

---

# Decoherence, control, and encoding of coupled solid-state quantum bits

Markus János Storcz

---



München 2005



---

# Decoherence, control, and encoding of coupled solid-state quantum bits

Markus János Storcz

---

Dissertation  
an der Fakultät für Physik  
der Ludwig-Maximilians-Universität  
München

vorgelegt von  
Markus János Storcz  
aus Köln

München, den 11. August 2005

Erstgutachter: PD Dr. Frank K. Wilhelm

Zweitgutachter: Prof. Dr. Erwin Frey

Tag der mündlichen Prüfung: 14. November 2005

*We must be physicists in order to be creative since so far codes of values and ideals have been constructed in ignorance of physics or even in contradiction to physics.*

Friedrich Nietzsche



# Contents

<b>Abstract</b>	<b>xv</b>
<b>Outline</b>	<b>xvii</b>
<b>I General Introduction</b>	<b>1</b>
<b>1 Introduction</b>	<b>3</b>
1.1 Quantum computation . . . . .	5
1.2 Hardware requirements . . . . .	5
1.3 Qubit realizations . . . . .	6
<b>2 Solid-state quantum computation</b>	<b>11</b>
2.1 Superconducting qubits . . . . .	12
2.1.1 Superconducting charge qubits . . . . .	14
2.1.2 Superconducting flux qubits . . . . .	16
2.2 Semiconductor qubits . . . . .	24
<b>3 Quantum gate operations and readout</b>	<b>29</b>
<b>4 Decoherence</b>	<b>33</b>
4.1 Linear response and the fluctuation dissipation theorem . . . . .	35
4.2 The Spin-Boson model . . . . .	36
4.3 Bloch-Redfield formalism . . . . .	38
<b>5 Quantum optics in the solid-state</b>	<b>43</b>
<b>II Decoherence, control, encoding, and circuit-QED of coupled solid-state qubits</b>	<b>49</b>
<b>6 Decoherence and gate performance of coupled solid-state qubits</b>	<b>51</b>
6.1 Introduction . . . . .	51
Paper 1 . . . . .	54
Paper 2 . . . . .	72
Paper 3 . . . . .	89

<b>7</b>	<b>Decoherence of two coupled QD charge qubits</b>	<b>99</b>
7.1	Introduction . . . . .	99
	Paper . . . . .	101
<b>8</b>	<b>Design of coupling elements for superconducting qubits</b>	<b>113</b>
8.1	Introduction . . . . .	113
	Paper . . . . .	119
<b>9</b>	<b>Decoherence Free Subspace (DFS) encoding</b>	<b>123</b>
9.1	Introduction . . . . .	123
	Paper . . . . .	128
<b>10</b>	<b>Optimum control of superconducting solid-state qubits</b>	<b>135</b>
10.1	Introduction . . . . .	135
10.2	Optimal control theory . . . . .	136
10.3	System Hamiltonian . . . . .	137
10.4	Generalization to the three qubit Hamiltonian . . . . .	139
10.5	Energy levels and leakage . . . . .	141
10.6	Generation of entanglement . . . . .	143
10.7	Time evolution of the optimized CNOT gate . . . . .	144
10.8	The single-qubit Hadamard gate . . . . .	146
	Paper . . . . .	147
<b>11</b>	<b>EPR pairs in superconducting charge qubits</b>	<b>159</b>
11.1	Introduction . . . . .	159
	Paper . . . . .	161
<b>12</b>	<b>Circuit-QED – quantum optics in the solid-state</b>	<b>171</b>
12.1	Introduction . . . . .	171
12.2	Deterministic single microwave photon generation and detection . . . . .	172
12.3	Flux qubit inside a cavity . . . . .	174
12.3.1	The dispersive readout . . . . .	177
	Paper . . . . .	178
	<b>Conclusions</b>	<b>183</b>
	<b>III Appendix</b>	<b>185</b>
<b>A</b>	<b>Useful relations</b>	<b>187</b>
A.1	Operator relations . . . . .	187
A.2	Qubit states on the Bloch sphere . . . . .	188
<b>B</b>	<b>The dissipative TSS – connection to the Kondo model and DMRG</b>	<b>189</b>



---

<b>C</b>	<b>Comparison of coupling schemes for flux qubits</b>	<b>193</b>
<b>D</b>	<b>Decoherence rates for pure Ising-type zz-coupling</b>	<b>197</b>
<b>E</b>	<b>The driven multi-qubit system</b>	<b>201</b>
E.1	Implementation of the program . . . . .	205
E.2	Examples for simulations . . . . .	208
<b>F</b>	<b>Flux qubit inside a cavity</b>	<b>211</b>
F.1	Quantization of a 1D transmission line . . . . .	211
F.2	The microstrip resonator . . . . .	213
F.3	Derivation of the Jaynes-Cummings Hamiltonian . . . . .	215
F.4	The dispersive read-out . . . . .	216
<b>G</b>	<b>Landau-Zener tunneling</b>	<b>219</b>
	<b>Bibliography</b>	<b>223</b>
	<b>List of Publications</b>	<b>247</b>
	<b>Acknowledgements</b>	<b>249</b>
	<b>Deutsche Zusammenfassung</b>	<b>253</b>
	<b>Curriculum vitae</b>	<b>255</b>



# List of Figures

1.1	Linear ion trap loaded with 3 ions. . . . .	7
1.2	Ion trap quantum computer. . . . .	7
1.3	Setup for an optical cavity QED experiment. . . . .	8
1.4	5 qubit NMR quantum computer. . . . .	8
2.1	Equivalent circuit of the RCSJ model. . . . .	13
2.2	Potential energy in the RCSJ model. . . . .	13
2.3	Schematic circuit diagram of the rf-SQUID. . . . .	14
2.4	Potential energy in the RCSJ model. . . . .	14
2.5	Schematic of a charge qubit. . . . .	15
2.6	Plot of the potential energy for the rf-SQUID. . . . .	18
2.7	Effective potential of the rf-SQUID qubit. . . . .	19
2.8	Eigenergies of the two-state system. . . . .	19
2.9	Simplest flux qubit design with three Josephson junctions. . . . .	20
2.10	Equivalent circuit of a flux qubit. . . . .	20
2.11	Plot of the potential landscape for the 3jj-qubit. . . . .	21
2.12	Plot of the potential landscape of the 3jj-qubit in the rotated $(\phi_m, \phi_p)$ coordinate system. . . . .	22
2.13	Wavefunctions for the 3jj-qubit. . . . .	23
2.14	SEM picture of a QD (charge) qubit. . . . .	25
2.15	SEM picture of a QD (spin) qubit structure. . . . .	25
2.16	Design sketch of an array of QD spin qubits. . . . .	26
2.17	Schematic of a single lateral QD. . . . .	27
2.18	Energy levels inside a single lateral QD. . . . .	27
2.19	Transport through a QD. . . . .	28
3.1	SEM image of a flux qubit with readout DC-SQUID. . . . .	30
3.2	SEM image of a flux qubit. . . . .	30
5.1	Energy level structure for the Jaynes-Cummings Hamiltonian. . . . .	45
5.2	Mean number of photons for the Jaynes-Cummings Hamiltonian. . . . .	45
5.3	Mean number of photons for the driven Jaynes-Cummings Hamiltonian. . . . .	46
5.4	Photon number distribution for the driven Jaynes-Cummings Hamiltonian. . . . .	46

6.1	Circuit diagram for the CNOT gate. . . . .	52
8.1	Inductively coupled flux qubits. . . . .	114
8.2	Schematic drawing of a JoFET. . . . .	115
8.3	Flux transformer. . . . .	116
9.1	Schematic picture explaining a DFS code. . . . .	124
9.2	Partition of all the gates in $SU(4)$ . . . . .	124
9.3	Weyl chamber trajectory for the CNOT operation with xy-interaction. . . . .	125
9.4	Quantum state tomography of a DFS encoded photon state. . . . .	126
10.1	Experimental two charge qubit setup of the NEC group. . . . .	135
10.2	Open chain three charge qubit setup. . . . .	140
10.3	Eigenenergies of a SCB with two leakage levels (broad). . . . .	141
10.4	Eigenenergies of a SCB with two leakage levels (narrow). . . . .	142
10.5	Plot of the eigenenergies of the qubit levels and the two additional leakage levels around degeneracy. . . . .	143
10.6	Matrix elements of the propagator for the CNOT operation. . . . .	144
10.7	Time optimal single-qubit Hadamard gate. . . . .	146
12.1	Artist view of microstrip resonator and flux qubit. . . . .	175
12.2	Circuit design of the microstrip resonator. . . . .	176
A.1	Bloch sphere representation of a qubit state. . . . .	188
B.1	Phase diagram for the dissipative TSS. . . . .	190
E.1	Simple driven time evolution a single qubit. . . . .	208
E.2	Time evolution of a single qubit for realistic driving. . . . .	209
F.1	Schematic drawing of a resonator in 1D. . . . .	214

# List of Tables

10.1 Comparison of the trace fidelity for different pulse shapes. . . . .	145
C.1 Different coupling schemes for sc flux qubits. . . . .	194
D.1 Non-vanishing tensor elements for pure zz-coupling. . . . .	198



# Abstract

In this thesis the decoherence properties, gate performance, control of solid-state quantum bits (qubits), and novel design proposals for solid-state qubits analogous to quantum optics are investigated. The qubits are realized as superconducting nanocircuits or quantum dot systems. The thesis elucidates both very appealing basic questions, like the generation and detection of deeply nonclassical states of the electromagnetic field, *i.e.*, single photon Fock states, in the solid-state, but also presents a broad range of different strategies to improve the scalability and decoherence properties of solid-state qubit setups.

Solid-state qubits are promising candidates for the realization of quantum computing. They are potentially scalable to a quantum processor, the building block of a quantum computer. However, decoherence due to the many degrees of freedom of a solid-state environment usually considerably impairs their behavior. Thus, in order to develop a working quantum computer it is of crucial importance to analyze the different decoherence sources that affect the qubit. Additionally, most solid-state qubits are pseudo-spin qubits, where the qubit levels are separated from the other energy levels in the much larger complete system Hilbert space by an energy gap. The population of these *leakage levels* of the system Hilbert space is particularly important for quantum computation.

We are specifically interested to identify the most important decoherence mechanisms in these solid-state qubit systems to then propose possible improvements in the design and operation of experimentally available devices, which are operated at low cryogenic temperatures  $T \approx 10$  mK smaller than the qubit energy scale, which is typically  $E_q/h \approx 10$  GHz, corresponding to  $T_q \approx 0.5$  K. Yet, temperature effects play an important role in the solid-state qubits.

The decoherence of a single qubit has already been intensely studied. In two coupled qubits, entanglement can be realized and a far more involved decoherence model appears. From the detailed analysis of multiple qubits, possible improvements in the design and operation of experimentally available devices are proposed. The decoherence of systems of coupled qubits is studied from the master equation that describes the time evolution of the qubit system including the effects of the coupling to the hostile environment. The symmetries of the qubit-environment coupling help to understand decoherence in these systems, and the admissible degree of symmetry breaking in experiments is determined.

Once the main decoherence sources and their effects are understood, it is important to develop strategies to minimize or even avoid the impact of decoherence. Here, a *Decoherence Free Subspace* (DFS) encoding for coupled superconducting qubits is presented

and its performance with respect to different error sources is evaluated. A DFS encoding for capacitively coupled flux qubits is given, which completely decouples the logical qubits from the noise originating in the coupling elements and collective flux noise. This is due to the encoding and a restricted phase space of the logical qubits. Optimum control theory is used as a tool to find pulse shapes that drastically reduce the overall time needed for a quantum gate operation and dramatically improve the performance of the quantum gate operation at given decoherence. Further on, no harmful leakage to other states of the pseudo-spin system is introduced.

Finally, quantum optics concepts will be applied to qubits in the solid-state domain. A scheme to generate and detect single microwave photons is presented. This analysis is complemented by the calculation of the properties of a flux qubit inside a single mode microstrip resonator, *i.e.* a cavity. This setup also effectively decouples the qubit from the most important environmental sources of relaxation. The readout of the flux qubit can be performed directly via a *quantum non-demolition* (QND) measurement of the cavity field.



# Outline

The content of this thesis is divided into three major parts. In the first part of the thesis, a basic general introduction to quantum computation, the different realizations of solid-state qubits, and the description of the electromagnetic field in quantum optics is given. The second, main part, of the thesis is divided into several studies,

- (i) Decoherence and gate performance of systems of multiple solid-state qubits,
- (ii) Design of coupling elements for superconducting flux qubits,
- (iii) DFS encoding of superconducting qubits,
- (iv) Optimum control of superconducting qubits,
- (v) Generation, decoherence and tomography of maximally entangled Einstein-Podolsky-Rosen pairs in superconducting charge qubits
- (v) Circuit-QED for superconducting qubits and the deterministic generation and detection of single microwave photons in superconducting solid-state circuits.

For each of these studies, an introduction is given and then the corresponding preprint or paper is attached at the end of the chapter. In the third part, the appendix, several calculations and technical details are summarized that have been of relevance to this thesis.



# Part I

## General Introduction



# Chapter 1

## Introduction

*Denn es ist ausgezeichnete Menschen unwürdig, gleich Sklaven Stunden zu verlieren mit Berechnungen.*<sup>1</sup>

Gottfried Wilhelm von Leibniz, 1865

Basic calculating machines for the processing of information have already been envisioned by Leonardo da Vinci. But the first sophisticated mechanical calculators were invented in the 17th century, the Pascaline by Blaise Pascal, and the Stepped Reckoner by Leibniz. These machines, as well as current computers, store classical information. The classical information is normally desired to be in exactly one out of two well defined states “off” and “on” or “0” and “1”. This classical information for example can be stored and processed by classical transistors, which are present in modern microprocessors.

The processing of the classical information itself is controlled by other information, which is named a program. For these computations, Turing provided the important basic model [1], which was motivated by results of Gödel [2]. The so-called *Turing machine*, which is a mathematical model for a computing machine, has been shown to be able to solve any mathematical problem that can be solved by a certain given algorithm. Later von Neumann and others [3, 4] developed the notion that the computer programs are also only data or information, and that they can be manipulated by machines under the control of other programs. The *quantum Turing machine* was first introduced by Benioff [5] and further developed by Deutsch [6] and Yao [7]. A modern definition with connection to algorithmic complexity is given in Ref. [8]. Also a quantum circuit model of computations was introduced [9] and it was shown [7] that the quantum circuit model of computation is equivalent to the quantum Turing machine model.

Underlining the close connection between computer science and physics, Feynman proposed [10] already in 1982 to use a computer that not only obeys the laws of quantum mechanics but also operates in a regime where quantum effects are relevant and most importantly, the information is fundamentally of quantum nature. His idea was to efficiently simulate the behaviour of quantum systems with the help of another quantum system, *i.e.*,

---

<sup>1</sup>“For it is unworthy of excellent men to lose hours like slaves in the labour of calculation [which would safely be relegated to anyone else if machines were used].”

a computer working in the quantum regime. However, quantum information processing has gained great interest only recently because of the promise of up to an exponential speedup for certain algorithmic problems, *e.g.*, the factorization of large numbers into primes [11], which is of central importance for secure communication. Moreover, several other quantum algorithms with moderate speedups were discovered [12, 13] and in recent years the completely new and interdisciplinary field of *quantum information processing* emerged.

In comparison to classical digital technology, quantum information is stored in arbitrary superpositions of quantum mechanical states described by a wavefunction  $|\psi\rangle = \alpha|0\rangle + \beta|1\rangle$  ( $|0\rangle$  and  $|1\rangle$  are orthonormal basis states of a Hilbert space on  $\mathbb{C}$ ), which roughly speaking resembles an analog instrument, in contrast to the classical digital information. It is this superposition of computational states that finally leads to an exponential speedup for certain algorithms on a quantum computer. The basic building blocks of a quantum computer are quantum bits, *i.e.*, (pseudo) spin-1/2 systems. However, also three level systems, the so-called qutrits [14], or  $d$ -dimensional bi-partite systems named qudits [14–17], or even continuous variable multi-level systems named qunats [18, 19] could be used for efficient quantum computation and quantum cryptography [20].

Operations on a quantum computer are described by unitary operations that can be defined via the time evolution of a Hamiltonian  $\hat{H}(t)$  describing the system evolution,  $\hat{U} = \hat{T}\exp(i\int_{t_0}^t \hat{H}(t') dt')$ , where  $\hat{T}$  is the time ordering operator<sup>2</sup>. Ideally, quantum computation is reversible because of the unitary time evolution and thus it is, just like ideal classical reversible computation, also non-dissipative. However, in reality the coherent unitary time evolution that is required for quantum information processing is always impeded by decoherence. (Also in the classical case of reversible computation dissipation can not be avoided because of Gödel friction.<sup>3</sup>) The decoherence, *i.e.* energy relaxation and dephasing, is due to the coupling of the quantum bit (qubit) to the surrounding environmental degrees of freedom.

Solid-state quantum computers, such as semiconductor quantum dot (QD) or superconducting systems are potentially scalable. However, especially the solid-state environment possesses many environmental degrees of freedom and usually solid-state systems suffer from strong decoherence. Decoherence can be caused by many different mechanisms depending on the material properties and the design of the experiment. It is one of the main goals of this work to analyze the decoherence properties of different solid-state qubit systems and develop design requirements which allow to reduce the amount of decoherence in these systems. This research is at the core of condensed matter physics and includes the detailed investigation of many body phenomena such as correlation effects, *e.g.*, in quantum dot qubit structures and superconducting qubits.

---

<sup>2</sup>The time ordering operator reorders the times of an arbitrary product of operators,  $\hat{T}(\hat{O}_n(t_n)\cdots\hat{O}_1(t_1)) = \hat{O}_{i_n}(t_{i_n})\cdots\hat{O}_{i_1}(t_{i_1})$ , where the causal order of the related times on the rhs is such that  $t_{i_n} > t_{i_{n-1}} > \cdots > t_{i_1}$  [21, 22].

<sup>3</sup>Gödel friction refers to the dissipation of energy due to the logical incompleteness of formal mathematical systems given by Gödel's incompleteness theorem, see Refs. [2, 23].

## 1.1 Quantum computation

Quantum bits (qubits) can be described by spin-1/2 systems, the state of a qubit is generally expressed as a linear combination, *i.e.*, a superposition of states

$$|\psi\rangle = \alpha |0\rangle + \beta |1\rangle, \quad |\alpha|^2 + |\beta|^2 = 1, \quad (1.1)$$

with  $\alpha, \beta \in \mathbb{C}$ . The states  $|0\rangle$  and  $|1\rangle$  are taken as eigenstates of, *e.g.*, the Pauli spin operator  $\hat{\sigma}_z$  and are called computational basis.

For a system of more than one qubit, another important ingredient of quantum computation emerges, entangled qubit states. Entangled states are states that are not separable into single qubit states  $|\psi_1\rangle, \dots, |\psi_N\rangle$ , such that  $|\psi\rangle = |\psi_1\rangle \otimes \dots \otimes |\psi_N\rangle$ . These two basic properties of quantum bits, to be able to perform computations on a superposition of states and the notion of entanglement<sup>4</sup> are the basic properties leading to the speed-up of quantum computers.

Quantum information science emerged after the discovery of algorithms that provide a substantial (up to exponential) speed-up in comparison with classical computers. The most important one (both regarding the funding perspectives and the speed-up that is gained) of these algorithms is certainly Peter Shor's factoring algorithm [11] based on the quantum Fourier transform. Other examples are Grover's database search algorithm [13], the Deutsch-Josza algorithm [12] or the quantum random walk algorithm [25–27], which has been shown to hit exponentially faster than the classical random walk. Another well established application is quantum cryptography [28–30].

## 1.2 Hardware requirements

Quantum algorithms can only be performed reliably on quantum hardware that provides a well defined and scalable Hilbert space with control over the system evolution in the Hilbert space, the ability to prepare a well defined initial state, a sufficiently low amount of decoherence, and state-specific quantum measurements [31, 32]. These requirements provide a good starting point for analyzing possible qubit candidates, however, these requirements are not very strict. For example, in nuclear magnetic resonance (NMR) the initialization of the nuclear spins in a well defined state is not possible. Moreover, there is no local experimental control or read-out available for individual spins. On the other hand, the NMR quantum computers show very long decoherence times and the ensemble of spins is easily manipulated. This illustrates that the very good decoherence properties of the NMR quantum computer make workarounds possible, *i.e.*, they can (roughly speaking) compensate for the lack of compliance with another criteria. This is reflected in the great experimental success of NMR quantum computation [33, 34], even performing advanced algorithms on a small number of qubits [35].

From the analysis of Quantum Error Correction Codes (QECCs) [36] a threshold for the fidelity, which is the deviation of the propagator of a physical system from the ideal unitary

<sup>4</sup>There are several different measures to characterize entanglement, an introduction is given in Ref. [24].

propagator  $\hat{U}$ , can be derived. Originally, it has been found that for quantum operations to be useful for quantum information processing, the fidelity has to meet the threshold criterion to be closer to unity than  $\mathcal{F} = 1 - 10^{-4}$  [37], which corresponds to approximately  $10^4$  operations within the decoherence time. More recent work for stabilizer codes [38] gives  $\mathcal{F} = 1 - 10^{-3}$  and when huge resource requirements are acceptable in the specific qubit setup, the criterion can be softened even more to up to approximately  $\mathcal{F} = 10^{-2}$  [39]. Also, fault tolerant quantum error correcting codes in non Markovian environments have been investigated lately [40, 41]. For an excellent summary and review of this topic see Ref. [42].

### 1.3 Qubit realizations

Currently, many efforts to realize quantum bits in different ways are pursued. Among the most important ones are optical photon quantum computers, optical cavity quantum electrodynamics (cQED), ion traps, nuclear magnetic resonance and solid-state implementations. These proposals for a quantum computer will be briefly reviewed here.

In an optical quantum computer, the qubits are defined by the photon being located in different modes of the light field or by the polarization of the photons. Beamsplitters and phase shifters give the arbitrary transforms and nonlinear media can be used for two-qubit operations. These two-qubit operations are also hard to realize. Initial preparation of single photon states is usually done by strongly attenuating a coherent light source. The noise properties of the photon quantum computer are good because the photons hardly interact. It is also possible to realize an optical photon quantum computer based only on linear optics and photodectors, however, this approach has the disadvantage that the quantum gates are postselected, which introduces significant computational overhead [43].

The optical cQED [44, 45] quantum computer is very closely related to the photon quantum computer. In typical cQED experiments, neutral atoms fall through the cavity and interact during a finite cavity transit time with the light field inside the cavity. An important difference to the photon quantum computer is that the two-qubit operations, *i.e.*, the interactions between the individual photons, are mediated by the atoms that are passing through an optical cavity. This way, the light field, *i.e.*, the photons, interact with the atom. The theme of cQED will be discussed again in chapter 5, where a basic introduction to quantum optics and *circuit*-QED (cQED in the solid-state domain) is given, and in chapter 12 for microwave photons travelling inside a superconducting cavity. Also optical photons have been used to demonstrate a decoherence free subspace (DFS) encoding experimentally. Specifically, two logical qubits that were encoded into four physical qubits (photons) have been encoded into a DFS immune to collective dephasing. Then, the photons were transmitted through a noisy (artificial noise) channel and the DFS encoding has been shown to work [46]. Decoherence free subspaces will be discussed in more detail in chapter 9 of this thesis.

From the point of view of scalability and stability, ion trap quantum computers are very promising. Because these two ingredients are at the heart of quantum computation the ion



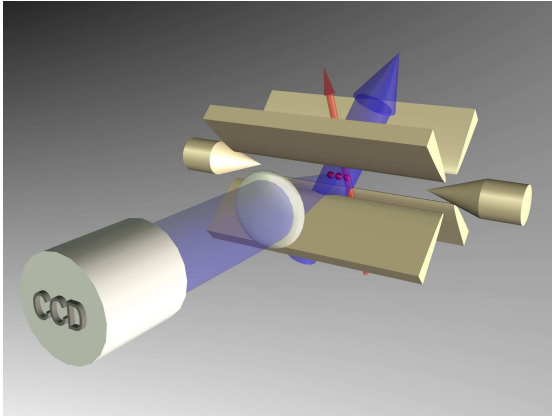


Figure 1.1: Schematic of a linear ion trap setup. The ion trap itself consists of elongated electrodes. The trap shown here is loaded with three ions which can be confined with electromagnetic fields to the center of the trap, aligned along the trap axis. Picture courtesy of the Blatt group, University of Innsbruck, Austria.

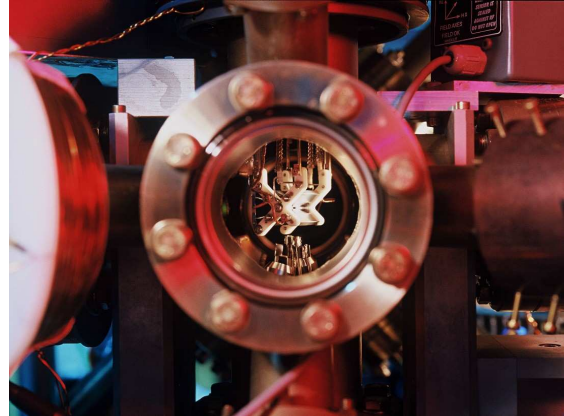


Figure 1.2: Picture of the ion trap that was used for the quantum teleportation experiment realized by the Blatt group [48]. Picture courtesy of the Blatt group, University of Innsbruck, Austria.

trap quantum computers are believed to be among the most promising qubit candidates [47]. A typical ion trap quantum computer consists of a linear Paul trap where a chain of several ions is trapped. The qubit itself is defined by the nuclear spin state or the phonon modes of an atom. By applying an oscillating electromagnetic field to two of the four electrodes of the trap, a confining potential for the atoms is generated, and laser cooling techniques prepare the atoms in their vibrational ground states. The individual atoms can then be manipulated by laser pulses and the measurement is performed by photodetectors, *i.e.*, by laser induced fluorescence techniques that provide a selective detection of the state of the ions with an readout efficiency close to unity. The interaction between different atoms is mediated by a common phonon mode. Quantum gate operations with a single ion [49] and also two-ion, and four-ion entangled states have been demonstrated [50, 51]. One problem of the ion trap quantum computer is that for strong ion-ion coupling the ions are spatially close, which makes it hard to address individual ions. However, this problem can be overcome by moving the atoms inside the trap [52] or by dark state schemes [48]. Especially scalable ion trap designs, the so-called *segmented multizone traps*, have been fabricated with multiple trapping regions where the ions are shuttled between the different parts of the trap [53, 54]. Recently, also ion trap devices on a chip have been developed [55]. Pictures 1.1 and 1.2 show a sketch of a typical ion trap setup for quantum computation and a picture of an experimental setup that was used to perform successful teleportation of the quantum state of an ion. A potential drawback of the ion trap quantum computer

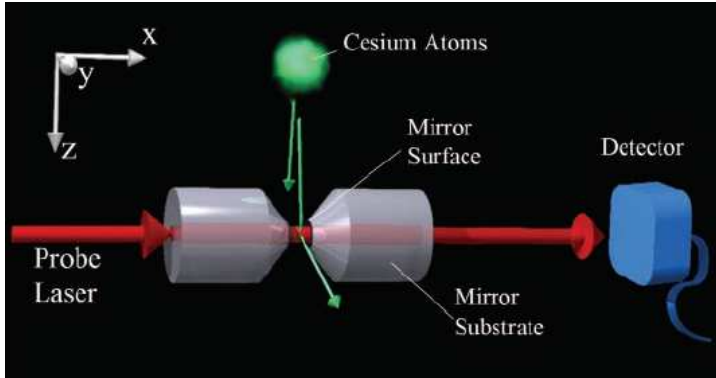


Figure 1.3: Sketch of a setup for an optical cavity QED experiment taken from the excellent review in Ref. [44]. In this experiment, the atoms are released from a magneto-optical trap and then fall into a Fabry-Perot type of cavity. Inside the cavity, the atom and the light field interact [45].

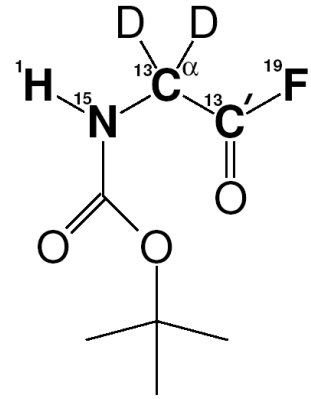


Figure 1.4: Molecule used for the implementation of the five qubit NMR quantum computer presented in Ref. [56].

is that the preparation of the ions in their motional ground states is hard to achieve [14]. The interaction of single atoms with a light field (or even single photons) inside a resonator is also the subject of the aforementioned cQED experiments [44, 45].

Although the experimental realizations of Nuclear Magnetic Resonance (NMR) quantum computers are the most advanced in terms of the manipulation and number of qubits, which can be manipulated nowadays, and also for the problem of state purification a promising solution has been found [57], the major problem of scalability remains. The evolution from the initial proposal [58] for an NMR quantum computer to the factorization of the number 15, see Ref. [35], was very fast, however, the major drawback is the scalability to many qubits which means that very complex molecules have to be synthesized [56]. One problem with the macroscopic samples for NMR quantum computation is that even when very large magnetic fields are applied, the net polarization of the spins in the sample is very small (around one part in a million) [59]. Thus, the initialization of the NMR qubits in a well defined state is impossible. But, it has been shown that it is not necessary to perform quantum computation with true pure states. Rather, a *pseudo-pure state* scheme has been first proposed in Ref. [57]. The idea of the pseudo-pure states is that quantum computation can be performed on a state described by the density matrix

$$\hat{\rho} = (1 - \epsilon)\hat{\mathbf{1}}/N + \epsilon|0\rangle\langle 0|, \quad (1.2)$$

which will evolve (if the quantum computer is otherwise error-free) to a state

$$\hat{\rho}' = (1 - \epsilon)\hat{\mathbf{1}}/N + \epsilon|\psi\rangle\langle\psi| \quad (1.3)$$

after the computation, where the initial state  $|0\rangle$  should, after an ideal quantum gate operation, end up in the desired state  $|\psi\rangle$ . For a regular quantum computer prepared in this mixed state, a random answer would be expected with probability  $1 - \epsilon$  and the correct answer would be expected to be returned with probability  $\epsilon$ . Now, it is important to note that it is possible to determine the desired answer by repeating the computation or to use an ensemble of qubits and take the ensemble averaged result. The ensemble averaged result is exactly what is used for NMR quantum computation [59]. After initial criticism on the pseudo-pure state method, the method has been clarified in Refs. [60, 61]. However, even the requirement to obtain pseudo-pure states for quantum computation is not strict for all algorithms, *e.g.*, it is not necessary for computing the Deutsch-Josza algorithm [62]. Moreover, NMR quantum computation on highly polarized spin states (not thermal states) is another possibility. In NMR quantum computation, the molecules are subjected to strong magnetic fields which are used to manipulate the state of the spins. These controls allow to steer the unitary evolution of the quantum system.

In the following chapters, this thesis will focus on solid-state implementations of quantum computers. These are especially scalable and relatively easily fabricated with present day technology. However, due to the requirement that thermal effects should be small in order to observe quantum behaviour, they need to be cooled down to cryogenic temperatures. The main challenge is to understand and describe decoherence in these qubit systems. The outline of the next chapters of this introduction is as follows.

First, in chapter 2, a detailed introduction to solid-state quantum computation, focused on superconducting and semiconductor qubits, will be given. Then the important decoherence mechanisms, *i.e.*, energy relaxation and dephasing, for QD and superconducting flux and charge qubits will be described and methods to analyze decoherence in solid-state qubits will be introduced. Namely, a general introduction to decoherence is given in chapter 4, including the treatment of decoherence and the derivation of a set of master equations in the so-called Bloch-Redfield formalism.



# Chapter 2

## Solid-state quantum computation

Already in the preceding chapter it could be recognized that there exists a rich diversity of different proposals for devices that could potentially be used as qubits, the basic building blocks of a much larger quantum computer. However, also in the solid-state domain qubits can be realized in many different ways. Lately, great progress has been made with qubits in superconducting structures. These are based on the charge degree of freedom or on the phase that is associated with the Cooper pair condensates in two pieces of superconductor separated by a Josephson junction. The Josephson tunnel junction is the main element of the superconducting qubits that are discussed in this thesis; it will be discussed in detail in the next section. The manipulation and readout of these superconducting qubits will be presented in more detail in the next chapter.

Among other promising realizations of solid-state qubits are semiconductor qubits, and especially Quantum Dot (QD) qubits. Quantum dots are devices in which a two-dimensional electron gas (2DEG), located around 100 nm below the surface, is confined via gate electrodes. Also for these devices, several different designs have been proposed, including using the spin of an electron [63, 64] and charge states in double quantum dots.

QDs are easily tunable via gate voltages, which can be applied to gate electrodes on top of the substrate. This tunability makes the QDs ideal devices for experimental studies. Because the QDs have small spatial dimensions, they exhibit a quantized level structure. A quantum dot is mainly characterized by its charging energy, which can be fabricated to be very large (up to  $1.5 \text{ meV} \simeq 15 \text{ K}$  as presented in Ref. [65]), therefore these charging effects are of relevance below temperatures  $T \sim 15 \text{ K}$ . QDs show charge quantization and (taking into account possible orbital excitations) energy quantization, and are thus also called *artificial atoms*.

Most generally, it is necessary in order to be able to observe quantum mechanical effects in small devices that the temperature scale is well below the typical energies of the two-state system. This holds for the solid-state devices investigated here. However, note that in these solid-state devices the overall energy scales (typically on the order of 10 GHz, which corresponds to  $T \approx 1/2 \text{ K}$ ) are much smaller compared to, *e.g.*, experiments in the optical domain.

## 2.1 Superconducting qubits

Superconducting qubits fulfill the basic criteria for quantum bits. They can in principle be scaled up to systems of many qubits, can be controlled by electromagnetic fields, can be read-out via standard detectors, *e.g.*, voltmeters and oscilloscopes, and due to the superconducting gap, quasiparticle excitations are suppressed. On the other hand, because of the many degrees of freedom in a solid-state system, decoherence remains a major issue and needs to be carefully investigated and avoided as much as possible. Here, we focus on qubits in superconducting structures that are based on the charge or phase (flux) degree of freedom associated with the Cooper pair condensate on a superconducting island or in a superconducting loop.

The Josephson junction is a tunnel barrier between two superconductors, *i.e.*, an insulating layer in between two superconductors. The basic schematic of a Josephson junction is depicted in Fig. 2.1. It shows two superconductors (electrodes) which are interrupted by a piece of insulating material, *e.g.*, an oxide barrier. The Josephson junction itself is usually labelled by a cross ( $\times$ ). B.D. Josephson derived [66, 67] that even if no voltage bias is applied, a finite supercurrent will flow between the two superconductors,

$$I_s = I_c \sin \Delta\phi, \quad (2.1)$$

where  $\Delta\phi$  is the phase difference between the Cooper-pair wavefunctions in the two superconducting electrodes. The critical current  $I_c$  is the maximum supercurrent that the junction can support; it also defines the so-called Josephson energy  $E_J = \hbar I_c / 2e$ . For a finite voltage bias of the junction, Josephson found that an alternating supercurrent of amplitude  $I_c$  and frequency  $\nu = 2eV/\hbar$  will develop according to

$$\frac{d(\Delta\phi)}{dt} = 2eV/\hbar. \quad (2.2)$$

In the presence of a gauge potential and in terms of the gauge invariant phase difference

$$\gamma = \Delta\phi - (2\pi/\Phi_0) \int \mathbf{A} \cdot d\mathbf{s}, \quad (2.3)$$

with the flux quantum  $\Phi_0 = h/2e$ . The free energy which is stored in the junction is [68]

$$F = \text{const.} - E_J \cos \gamma. \quad (2.4)$$

An easy description of the properties of the Josephson junction is given by the so-called resistively and capacitively shunted junction (RCSJ) model. In this model one takes into account the capacitance of the Josephson junction and a normal resistance of the junction, which is associated with the resistive dissipative quasiparticle channel. The capacitance depends quantitatively on the geometry of the Josephson tunnel junction between the two superconducting electrodes. Thus, a Josephson junction in principle behaves like a parallel circuit of the junction itself and a capacitance  $C$  and resistor  $R$ . The resistance  $R$  will be

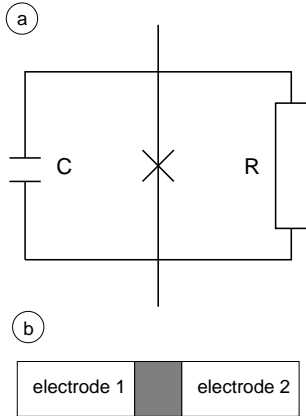


Figure 2.1: Part a) is the equivalent circuit of the resistively and capacitively shunted junction model. Part b) is a sketch of a basic Josephson junction.

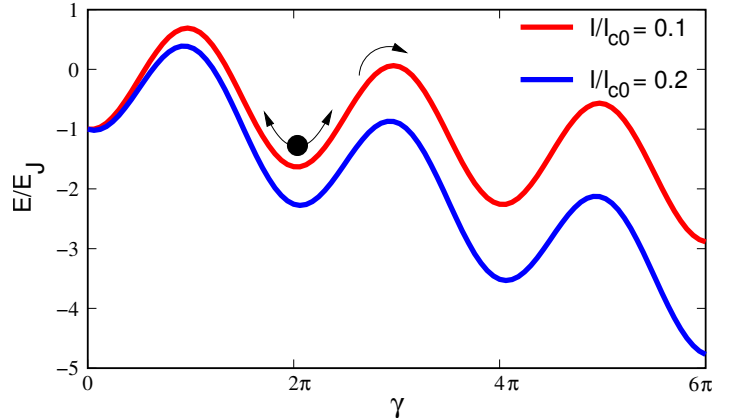


Figure 2.2: Potential energy (2.6) of a Josephson junction modeled via the RCSJ model for different magnitudes of the junction bias current  $I$ . This potential is the so-called *tilted-washboard* potential. The dynamics of the phase in the potential is indicated in the plot.

close to the normal state resistance  $R_n$  for superconductor-insulator-superconductor (S-I-S) junctions near  $T_c$ , whereas at lower temperatures it rises approximately as  $R_n \exp(\Delta/k_B T)$  for  $V < 2\Delta/e$ , where  $\Delta$  is the superconductor energy gap. For different kinds of junctions, like superconductor-normal conductor-superconductor (S-N-S) junctions the behaviour is generally different [68]. In the RCSJ model it is possible to derive a differential equation for the time dependence of the phase, namely

$$\frac{d^2\gamma}{d\tau^2} + \frac{1}{\omega_p RC} \frac{d\gamma}{d\tau} + \sin \gamma = \frac{I}{I_{c0}}, \quad (2.5)$$

where  $\omega_p = (2eI_{c0}/\hbar C)^{1/2}$  is the plasma frequency of the junction and the damping parameter  $\beta_c = (\omega_p RC)^2$  was first introduced by Stewart and McCumber [69, 70]. The differential equation (2.5) is written down in analogy to the equation of motion of a particle with mass  $(\hbar/2e)^2 C$  moving along the axis given by the gauge invariant phase difference  $\gamma$  in an effective potential given by

$$\frac{U(\gamma)}{E_J} = -\cos \gamma - \frac{I}{I_{c0}} \gamma, \quad (2.6)$$

which is shown in Fig. 2.2. Moreover, the particle is subjected to a drag force given by a term proportional to the effective velocity of the particle and the energy scale is given by  $E_J = (\hbar/2e)I_{c0}$  [68]. The Josephson tunnel junctions as described here, are used as basic building blocks of both superconducting charge and flux qubits.

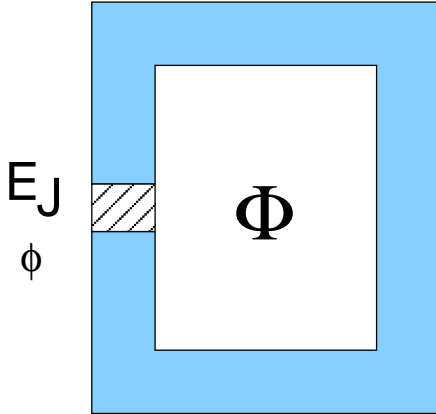


Figure 2.3: Schematic circuit diagram of the rf-SQUID. The rf-SQUID is formed by a superconducting loop that is interrupted by a single Josephson tunnel junction [72].

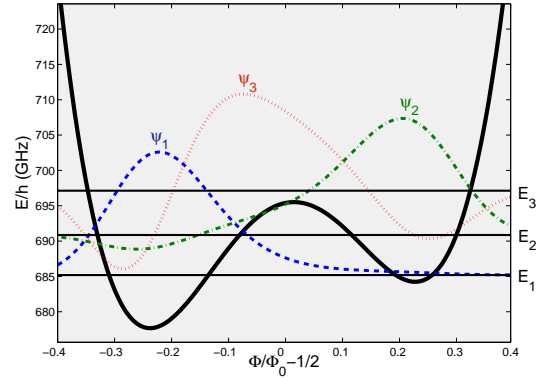


Figure 2.4: Plot of the wavefunctions and eigenenergies that correspond to the lowest three eigenstates of the rf SQUID Hamiltonian obtained from numerical simulations. The wavefunctions  $|\psi_1\rangle$  and  $|\psi_2\rangle$  are localized in one of the wells and the wavefunction associated with  $|\psi_3\rangle$  is delocalized over the double well. The parameters for the simulations are  $I_{c0} = 1.4 \mu\text{A}$ ,  $C_J = 0.13 \text{ pF}$ ,  $L = 270 \text{ pH}$ , and  $\Phi_x = 0.499\Phi_0$ , see also chapter 12.

One of the simplest qubit designs in these structures are single junction phase qubits (where the qubit degree of freedom is the superconducting phase across a Josephson tunnel junction [71]) and the so-called rf-SQUID, which we will investigate in more detail in section 2.1.2. The rf-SQUID is a superconducting ring that is interrupted by a single Josephson tunnel junction, see Fig. 2.3.

In the following section, these different types of superconducting qubits will be introduced.

### 2.1.1 Superconducting charge qubits

In Figure 2.5 a charge qubit circuit is schematically drawn in two different variations, where the setup presented in the right picture allows for the manipulation of the tunnel matrix element of the qubit via an external flux. In the superconducting charge qubit the qubit states  $|0\rangle$  and  $|1\rangle$  are defined as zero or one additional Cooper pair on a superconducting island. The superconducting island itself is connected via Josephson tunnel junctions to a superconducting reservoir, see the illustrations in Fig. 2.5. Compared to other types of Josephson junctions that have been investigated and used in practice [72, 73], the tunnel junction leads to a small damping term. The Hamiltonian of a superconducting charge qubit can be derived by writing down the total energy of the system, as the sum of the



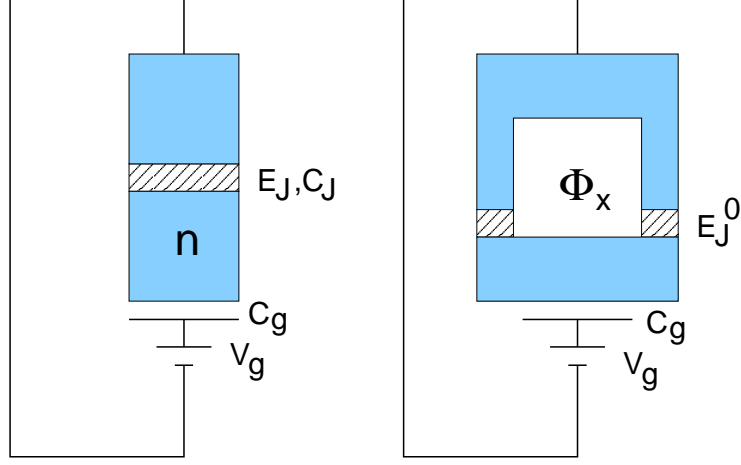


Figure 2.5: Schematic view of a charge qubit. The left circuit shows a superconducting island connected to a gate electrode via a capacitor  $C_g$  and a reservoir via a Josephson junction. The right circuit is a superconducting charge qubit in a superconducting quantum interference device (SQUID) geometry. Here, the single junction of the left circuit is split into two junctions. By applying an external flux through the SQUID loop, the tunnel matrix element of the qubit can be tuned [74].

free energy Eqn. (2.4), the work  $W$  done by the voltage source, which is connected to the charge qubit (see Fig. 2.5), and the electrostatic energy  $U$ ,

$$E = F + U - W = -E_J \cos \Delta\phi + \frac{(Q + C_g V_g)^2}{2(C_g + C_J)} + \frac{C_g V_g^2 (C_J - C_g)}{2(C_g + C_J)}. \quad (2.7)$$

In this system the two conjugate variables are the charge degree of freedom  $Q$  and the phase  $\Delta\phi$  across the Josephson junction. Here, the last term in Eqn. (2.7) just gives a constant energy offset (it is independent of  $Q$ ) and can be ignored when deriving the Hamiltonian of a single charge qubit. The charging energy of the Cooper pair box is defined as  $E_c = e^2/2(C_g + C_J)$ . For low temperatures such that  $k_B T < E_c < \Delta$ , where  $\Delta$  is the energy gap of the superconductor, the excess charge enters the island as Cooper pairs, *i.e.*,  $Q = 2ne$ . Therefore, the Hamiltonian can be expressed as

$$H = 4E_c(n - n_g)^2 - E_J \cos \gamma, \quad (2.8)$$

where  $n_g = -V_g C_g / 2e$  is the gate charge. This Hamiltonian can be described in either the charge basis or the phase basis; where the charge and phase are conjugate variables  $[n, \gamma] = i\hbar$ . If the charging energy  $E_c$  is larger than the Josephson energy  $E_J$ , the Hamiltonian (2.8) is conveniently expressed in the charge basis, where the charge states are characterized by the number of additional Cooper pairs on the superconducting island. By using the

relations for the displacement  $\exp(\pm i\gamma) |n\rangle = |n \pm 1\rangle$ , the Hamiltonian (2.8) reads

$$H = \sum_n \left( 4E_c(n - n_g)^2 |n\rangle \langle n| - \frac{E_J}{2} (|n\rangle \langle n+1| + |n+1\rangle \langle n|) \right). \quad (2.9)$$

When the gate voltage  $V_g$  is manipulated such that  $n_g \approx 1/2$  (note that the potential is periodic in the gate voltage) and at low temperatures the two states  $|0\rangle$  and  $|1\rangle$  corresponding to zero or one additional charge on the superconducting island are degenerate. Exactly at the degeneracy point there is an anticrossing of the eigenenergies of the qubit and the level splitting is given by the Josephson energy term in Eqn. (2.9). Near the degeneracy point, the Hamiltonian is truncated to two states

$$H \approx 4E_c(n_g^2 |0\rangle \langle 0| + (1 - n_g)^2 |1\rangle \langle 1|) - (1/2)(|0\rangle \langle 1| + |1\rangle \langle 0|). \quad (2.10)$$

Now, by introducing  $|1\rangle = (0, 1)^T$  and  $|0\rangle = (1, 0)^T$  as basis states and writing down the Hamiltonian in this basis one obtains

$$H = 2E_c(2n_g - 1)\hat{\sigma}_z + 2E_c(2n_g^2 - 2n_g + 1)\hat{\mathbf{1}} + \frac{E_J}{2}\hat{\sigma}_x, \quad (2.11)$$

where the Pauli spin matrices in standard representation have been used and  $\hat{\mathbf{1}}$  denotes the identity matrix. The second constant term just gives a global energy offset and can be neglected. In accordance with experiments with natural spin-1/2 systems, where electromagnetic fields are used to steer the dynamics of the spin, the parameters  $B_z = 4E_c(1 - 2n_g)$  and  $B_x = E_J$  are introduced. In the same way, arbitrary single-qubit operations can be performed on a superconducting charge qubit with manipulation of  $B_z$  and possibly  $B_x$  by an external gate voltage or (if the charge qubit is fabricated in SQUID geometry) by an external flux, respectively. When the charge qubit is fabricated in SQUID geometry, as shown in the right circuit of Fig. (2.5), the tunnel matrix element of the qubit can be tuned via the externally applied magnetic flux which is threading the SQUID loop. Then, effectively the parameter  $B_x$  is replaced by  $B_x(\Phi_x) = 2E_J \cos(\pi\Phi_x/\Phi_0)$ , where  $\Phi_x$  denotes the externally applied flux.

### 2.1.2 Superconducting flux qubits

The so-called superconducting flux qubits [74] are based either on rf-SQUID loops [75] (a superconducting loop interrupted by a single Josephson junction, cf. Fig. 2.3) or on SQUID loops with three Josephson junctions [76]. Here, the state of the qubit is defined by clockwise or counter-clockwise circulating currents in the SQUID loop. At degeneracy, the qubit state corresponds to an equal macroscopic superposition of clockwise and counter-clockwise circulating currents, cf. Fig. 2.8. In this picture, the energetically higher lying states correspond to circulating currents with much smaller current. The first implementation, an rf-SQUID, is a superconducting ring, which is interrupted by a single Josephson junction. It has been shown in experiment [75] that superpositions of truly macroscopic currents, *i.e.* currents that consist of  $\approx 10^{11}$  Cooper pairs, can be formed in the rf-SQUID devices.

The phase differences across the junctions in a SQUID device and the flux enclosed by the superconducting loop are related by the *fluxoid quantization* [77, 78]

$$\sum_i \gamma_i = 2\pi \frac{\Phi}{\Phi_0} + 2\pi n, \quad n \in \mathbf{N}. \quad (2.12)$$

For a rf-SQUID loop with only a single Josephson tunnel junction and thus only a single phase  $\gamma$ , the total flux through the loop and the phase can be used equivalently. The Hamiltonian that describes this system consists of parts describing the different circuit elements

- *The Josephson energy term*

The free energy of a Josephson junction is  $F = \text{const.} - E_J \cos \gamma$  in the presence of an electromagnetic gauge potential.

- *Self-inductance  $L$  of the loop*

There is also a term due to the self-inductance of the qubit loop, generated by the screening current in the superconductor. Namely, the total flux equals the sum of the screening flux and the externally applied flux,  $\Phi = \Phi_s + \Phi_x$ . Thus, the term in the Hamiltonian reads

$$\frac{LI_s^2}{2} = \frac{\Phi_s^2}{2L} = \frac{(\Phi - \Phi_x)^2}{2L}. \quad (2.13)$$

- *The charging energy*

The charging energy associated with the capacitance of the junction enters the Hamiltonian via  $Q^2/2C_J$ .

Therefore, the overall Hamiltonian can be expressed as

$$H = \frac{Q^2}{2C_J} - E_J \cos \left( 2\pi \frac{\Phi}{\Phi_0} \right) + \frac{(\Phi - \Phi_x)^2}{2L}, \quad (2.14)$$

where the last two terms determine the potential energy

$$U(\Phi) = U_0 \left[ \frac{1}{2} \left( \frac{2\pi(\Phi - \Phi_x)}{\Phi_0} \right)^2 - \beta_L \cos \left( 2\pi \frac{\Phi}{\Phi_0} \right) \right], \quad (2.15)$$

where  $U_0 = \Phi_0^2/(4\pi^2 L)$  and  $\beta_L = E_J/U_0$ . Here,  $Q = -i\hbar\partial/\partial\Phi \leftrightarrow \Phi$  are canonically conjugate variables  $[Q, \Phi] = i\hbar$ , just like coordinate  $X$  and momentum  $P$ . (Note that here the notation from Ref. [79] will be adopted mostly, *i.e.*,  $\hat{X} = \sqrt{m\omega/\hbar}X$ ,  $\hat{P} = 1/\sqrt{m\hbar\omega}P$  and correspondingly  $H = \hbar\omega\hat{H}$ .)

In Fig. 2.6. the plot of the potential close to  $\Phi_0/2$  for different  $\Phi_x$  and  $\beta_L$  is shown. It is found that for  $\beta_L > 1$  a double well structure develops close to a frustration of  $f = 1/2$

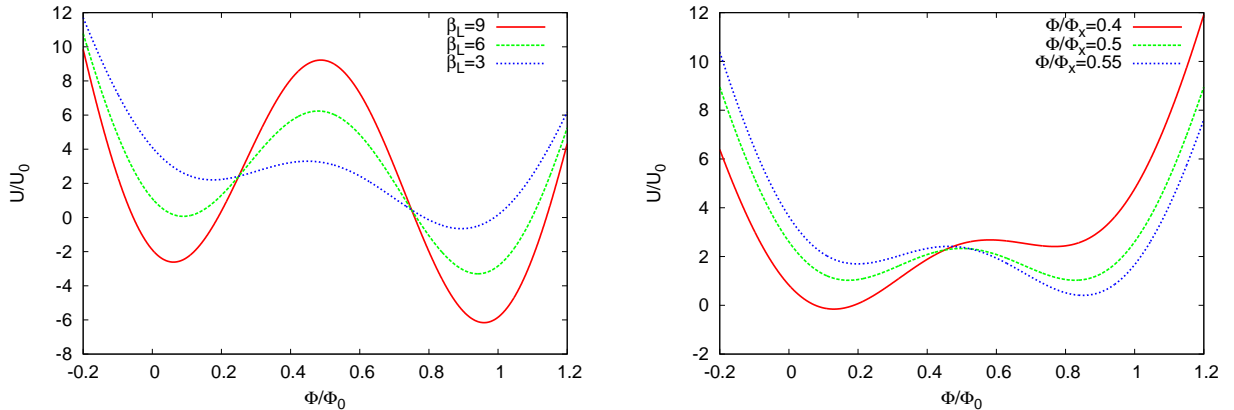


Figure 2.6: Plot of the potential energy Eqn. (2.15) of a rf-SQUID. The left plot depicts the potential for different values of  $\beta_L = E_J/U_0$ , *i.e.*, the increase of the barrier height with increasing Josephson energy  $E_J$  and the right plot shows the evolution of the asymmetry between the two wells due to a different external bias flux  $\Phi_x$ .

corresponding to  $\Phi = \Phi_0/2$ . This is because when  $E_J \gg E_C$  then the Josephson energy of the fully frustrated loop has two equivalent minima that correspond to states with currents circulating in opposite directions. The tunneling between these minima is given by a sum over all tunneling paths that connect both classical minima. The tunneling leads to a splitting  $\Delta$  between these two levels, which is given by the charges  $q_i$  (in units of  $2e$ ) that are induced on the islands [80]

$$\Delta = \Delta_0 |1 + e^{2\pi i q_1} + e^{2\pi i (q_1 + q_2)} + \dots + e^{2\pi i (q_1 + \dots + q_{N-1})}|. \quad (2.16)$$

The level splitting  $\Delta$  depends strongly on the interference pattern between these different tunneling paths. Note that when the flux through the loop is exactly half a flux quantum, the loop is invariant under flips that change the direction of the current [80]. In general, for the case when the Josephson energy is much larger than the charging energy, the only constraint on the potential is that the double degeneracy of the total Josephson energy as a function of the phases has to hold.

For low temperatures only the lowest state within each well is relevant. In this case two states  $|\psi_L\rangle$  and  $|\psi_R\rangle$  that are localized in the left and the right well are found. The Hamiltonian can then be truncated into the basis of the two states  $|\psi_L\rangle$  and  $|\psi_R\rangle$

$$H \approx \begin{pmatrix} \langle \psi_L | H | \psi_L \rangle & \langle \psi_L | H | \psi_R \rangle \\ \langle \psi_R | H | \psi_L \rangle & \langle \psi_R | H | \psi_R \rangle \end{pmatrix} = \begin{pmatrix} \varepsilon_L & \Delta \\ \Delta & \varepsilon_R \end{pmatrix} = \varepsilon \hat{\sigma}_z + \Delta \hat{\sigma}_x, \quad (2.17)$$

where  $\varepsilon = (\varepsilon_L - \varepsilon_R)/2$  and the constant offset  $(\varepsilon_L + \varepsilon_R)/2$  has been neglected.

Often, this Hamiltonian is conveniently parametrized by two perpendicular electromagnetic fields  $B_z(\Phi_x) = 4\pi\sqrt{6(\beta_L - 1)}E_J(\Phi_x/\Phi_0 - 1/2)$  and  $B_x$ , which depends on the barrier height and thus on the Josephson energy  $E_J$  [74]. The tunneling amplitude term  $B_x$  can

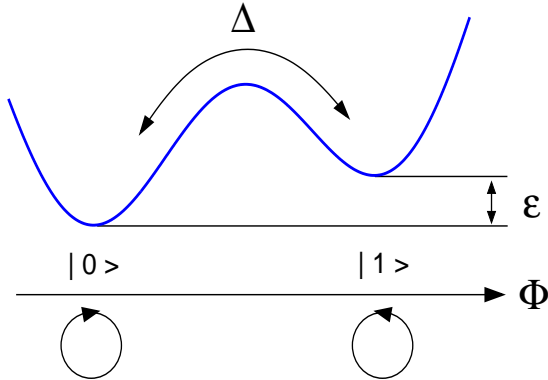


Figure 2.7: Effective potential of the rf-SQUID qubit as a two-state system. Here, the terms in the Hamiltonian Eqn. (2.18) are visualized;  $\Delta$  is the tunneling amplitude and  $\epsilon$  is the asymmetry, which can be tuned by the external flux  $\Phi_x$ , between the two wells.

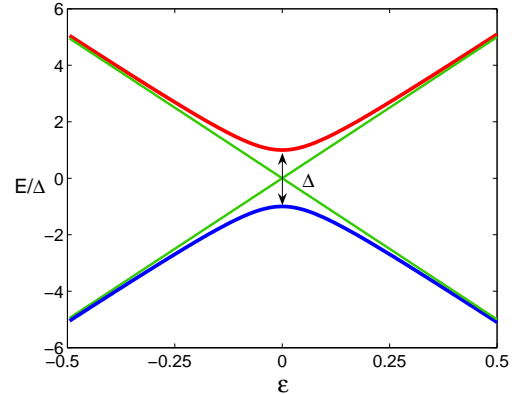


Figure 2.8: Plot of the eigenenergies of a two-state system. At the degeneracy point,  $\epsilon = 0$  the splitting between the energy levels is  $\Delta$  and the eigenstates are symmetric and antisymmetric superpositions of the basis states, *i.e.*, the clockwise/counter-clockwise rotating currents. Here, we set  $\Delta = 0.1$  and vary the energy bias  $\epsilon$ . This corresponds effectively to changing the magnetic flux through the SQUID loop of an rf-SQUID qubit or a flux qubit.

be calculated with the WKB method [76] or the aforementioned summation of different tunneling paths [80]. Thus, the effective two-state system is expressed in terms of the Pauli-matrices as

$$H = -\frac{1}{2}B_z\hat{\sigma}_z - \frac{1}{2}B_x\hat{\sigma}_x. \quad (2.18)$$

Although the system that is investigated here in general is a multi-level system, for an appropriate parameter regime a two-level system is obtained at low energies. It is separated by a significant gap from higher excitations. Thus, these kinds of qubits are called pseudo-spin systems because the system Hamiltonian can be expressed in the same form as “real” spin-1/2 systems [14].

In Fig. 2.7 the different terms in the two-state approximation of the rf-SQUID are depicted. The tunneling between the two-wells is determined by the tunneling amplitude  $\Delta$  and the energy bias between the wells is given by  $\epsilon$ . The energy bias can be tuned by varying the external flux through the qubit loop.

Although the aforementioned macroscopic superposition of currents has been shown in this type of rf-SQUID qubits [75], the drawback of qubits based on rf-SQUID devices is that  $\beta_L > 1$  implies that the product of the critical current of the Josephson junction and

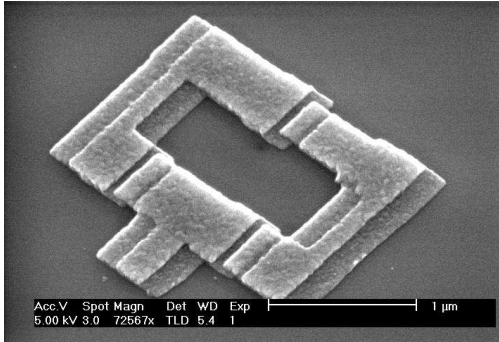


Figure 2.9: SEM picture of a small self-inductance three Josephson junction flux qubit [81]. The superconducting aluminium loop is interrupted by three Josephson junctions, with one of the junctions slightly smaller, cf. Fig. 2.10. The Josephson junctions are fabricated as thin insulating oxide layers in between the superconducting electrodes.

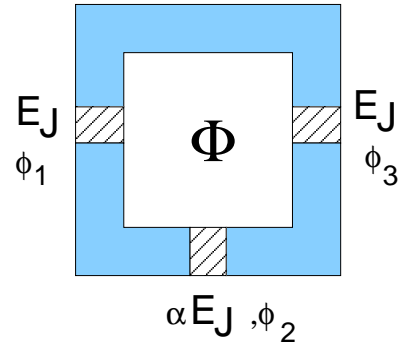


Figure 2.10: Schematic circuit diagram of a superconducting flux qubit. The superconducting islands are interrupted by three Josephson junctions, where one of the junctions is a factor  $\alpha$  smaller than the other junctions. In order to form an effective two-level potential for low temperatures,  $\alpha \approx 0.7 - 0.8$  [76]. The loop is threaded by the total flux  $\Phi$  and the qubit states are clockwise or counter-clockwise rotating currents, cf. Fig. 2.8.

its self-inductance is very large. This leads to two major drawbacks

1. Large critical currents require a large junction area; this leads to a large capacitance and due to the large capacitance quantum fluctuations of the phase and consequently tunneling between the lowest energy eigenstates, *i.e.*, the qubit states, is suppressed. Therefore in practice only a narrow parameter range is useful.
2. A large self-inductance of the rf-SQUID can only be achieved in large loops. Thus, because of the system dimensions the qubit is very susceptible to noise.

Due to these drawbacks that considerably hinder the development of qubits based on these SQUID devices, Mooij [82] and Feigel'man [83, 84] put forward a proposal to use a much smaller superconducting loop (smaller self-inductance) with more Josephson junctions embedded into the loop to still be able to design the double-well potential sufficiently. A picture of this so-called *flux qubit* design that is for example used at TU Delft [81, 85], MIT [86, 87], NTT [88] or IPHT Jena [89] is shown in Fig. 2.9 and an equivalent circuit is schematically drawn in Fig. 2.10. The flux qubit is a small superconducting SQUID loop made from aluminium or niobium interrupted by three Josephson tunnel junctions, which are thin isolating oxide layers in between the superconducting electrodes. The eigenstates of the qubit are again clockwise and counter-clockwise rotating *persistent currents*, the

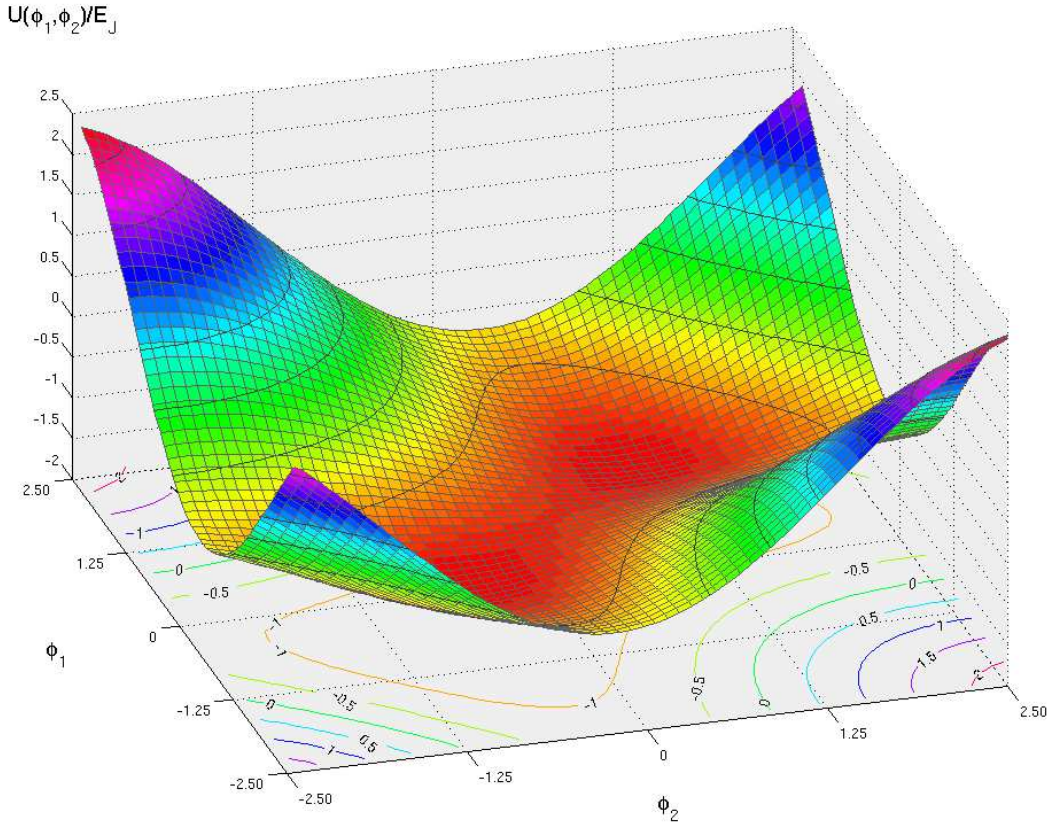


Figure 2.11: Plot of the potential energy  $U/E_J$ , Eqn. (2.20), for the 3 Josephson junction (3jj) qubit in a unit cell of the potential versus the phases. The isolines correspond to half-integer values of the potential energy (-1.0, 0, 0.5, 1.0, 1.5, 2.0), starting at -1.0 for the contour in the center of the plot.

difference in flux between these two states is  $2I_p L = 10^{-3}\Phi_0$  for typical qubit parameters  $I_p \approx 200$  nA and  $L \approx 5$  pH [90]. Thus, the two basis states are very close to each other and the coupling to external decoherence sources can be made small. However, this small difference between the two basis states translates into a truly *macroscopic* magnetic moment on the order of  $10^4 - 10^5 \mu_B$  [74], where  $\mu_B$  is the Bohr magneton.

Important characteristic features of a flux qubit are the small self-inductance of the superconducting SQUID loop and the fact that several Josephson junctions are used to form the potential landscape. However, the main ingredient for the appearance of a double well potential is again the frustration of the qubit loop. Because of the small self-inductance of the loop, the flux  $\Phi$  through the loop is close to the externally applied flux  $\Phi = \Phi_x + LI_s \approx \Phi_x$ , where  $L$  is the self-inductance of the qubit and  $I_s$  is the screening current, often also

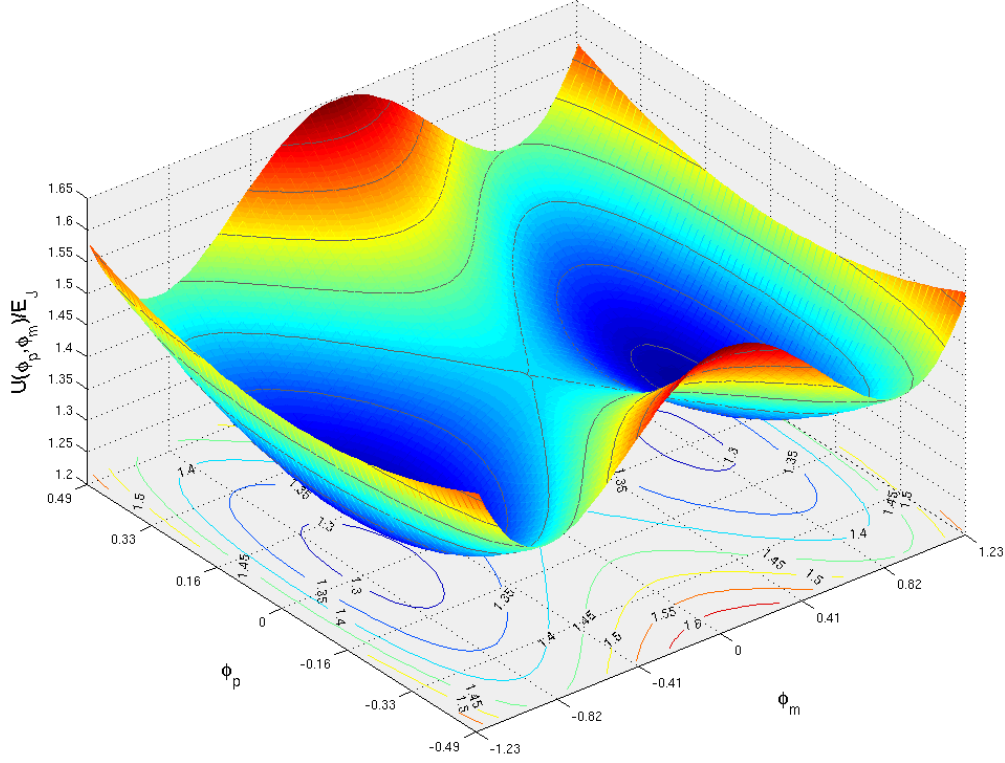


Figure 2.12: Plot of the potential energy term in Eqn. (2.21) for the 3 Josephson junction (3jj) qubit. The isolines correspond to the following values of the potential energy, starting from the bottom of the potential well (1.30, 1.35, 1.40, 1.45, 1.50, 1.55, 1.60). The double-well potential is chosen slightly asymmetric by setting  $f = 0.499$ .

called *circulating current*. Therefore fluxoid quantization Eqn. (2.12) leads to

$$\phi_1 + \phi_2 + \phi_3 = 2\pi \frac{\Phi_x}{\Phi_0} \quad (2.19)$$

where the  $\phi_i$ ,  $i = 1, \dots, 3$  are the gauge invariant phases for a three junction loop. Therefore, only  $\phi_1$  and  $\phi_2$  are the independent dynamical variables. For this three junction loop the potential energy is given by

$$U(\phi_1, \phi_2) = -E_J \cos \phi_1 - E_J \cos \phi_2 - \tilde{E}_J \cos(2\pi\Phi_x/\Phi_0 - \phi_1 - \phi_2), \quad (2.20)$$

where one of the Josephson junctions has been taken slightly smaller than the other two junctions, *i.e.*,  $\tilde{E}_J = \alpha E_J$  with  $\alpha = 0.7$  [76, 82]. Note that one of junctions is chosen



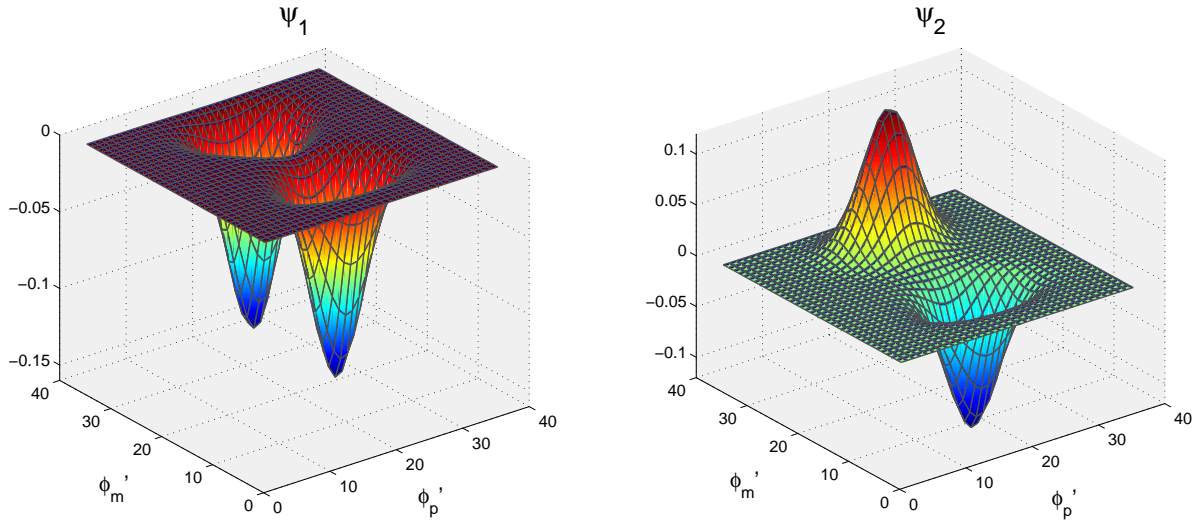


Figure 2.13: Plot of the wavefunctions of the 3jj flux qubit. The left plot depicts the eigen-wavefunction  $\psi_1$  of the lowest energy level and the right plot shows the eigen-wavefunction  $\psi_2$  associated with the second energy level in a unit cell. These wavefunctions are obtained from numerical determination of the eigenenergies and eigenstates of the Hamiltonian for the 3jj flux qubit, given in Eqn. (2.21). The wavefunctions are calculated for a typical set of parameters given in Ref. [76] and are seen to agree very well with the solutions from a tight-binding model presented in the aforementioned work. In more detail, the parameters used for the numerical calculations are  $\gamma = 0.02$ ,  $\alpha = 0.8$ ,  $E_J/E_C \approx 80$ ,  $L \approx 10$  pH, and  $I_0 \approx 400$  nA. Note that the values of the coordinates  $\phi'_p$  and  $\phi'_m$  are given in a unit cell, which is discretized on a 40x40 lattice, cf. Fig. 2.12.

slightly smaller in order to suppress interference from different tunneling paths in the potential [76, 80, 91].

For  $\tilde{E}_J/E_J > 0.5$  and a frustration close to half a flux quantum a double well potential is formed, see Fig. 2.11. Then, for low temperatures again only the two lowest states in each well contribute and the system effectively behaves as a two level system, see Eqn. (2.18). The full Hamiltonian can be expressed in terms of new coordinates  $\phi_p = (\phi_1 + \phi_2)/2$  and  $\phi_m = (\phi_1 - \phi_2)/2$ , and becomes [76]

$$\hat{H} = \frac{1}{2} \frac{P_p^2}{M_p} + \frac{1}{2} \frac{P_m^2}{M_m} + E_J(2 + \alpha - 2 \cos \phi_p \cos \phi_m - \alpha \cos(2\pi\Phi_x/\Phi_0 + 2\phi_m)), \quad (2.21)$$

where the conjugate momenta are defined via  $P_j = -i\hbar\partial/\partial\phi_j$ , the mass terms are  $M_p = (\Phi_0/2\pi)^2 2C(1 + \gamma)$  and  $M_m = (\Phi_0/2\pi)^2 2C(1 + 2\alpha + \gamma)$  and  $\gamma$  is defined via  $C_g = \gamma C$ . The potential is plotted in terms of these new coordinates in Fig. 2.12. In this rotated basis, the eigenenergies and wavefunctions for the Hamiltonian Eqn. (2.21) can be, *e.g.*, obtained numerically. Eigenenergies and wavefunctions that were obtained numerically from the

Hamiltonian are presented in Fig. 2.13.

Experiments with superconducting qubits have been very successful: macroscopic superpositions of states [81, 90] and macroscopic quantum coherence [85] have been demonstrated. Recently, also coupled qubits have been successfully realized [92]. The qubits were coupled via a direct inductive Ising-type coupling that can not be switched; the qubits were fabricated in a chain, which to first order leads to nearest neighbour interaction between the qubits. This type of flux (or current-current) coupling gives a  $\hat{\sigma}_z^{(i)} \otimes \hat{\sigma}_z^{(j)}$ -type of coupling in the Hamiltonian. However, flux qubit devices can for example also be coupled capacitively by connecting one of the superconducting islands of each qubit via a capacitor to each other, as will be discussed in chapter 9.

This introduction to superconducting qubits has so far only been focused on the most common charge and flux qubit designs, but of course there exist several other approaches. Namely, the Saclay group introduced an effective hybrid-design, where the qubit is based on a superconducting Cooper pair box and can be effectively decoupled from the measurement circuit during operation of the qubit. This is achieved by operating the qubit either in the charge or phase regime for manipulation and read-out [93]. In these experiments the qubit is operated at the “sweet spot” with respect to decoherence and therefore shows a large number of coherent Rabi oscillations within the decoherence time. Another elaborate read-out scheme for flux qubit devices has been realized by the Jena group [89]. It is based on coupling the flux qubit to a tank circuit, *i.e.*, a low frequency resonator. The read-out is then performed by monitoring the change in the properties of the resonator due to the qubit, *i.e.*, in the resonance frequency of the resonator and the amplitude of the response of the resonator to a high-frequency (HF) signal.

## 2.2 Semiconductor qubits

Currently, the most important semiconductor qubits are Quantum Dot (QD) or donor based qubits. The Quantum Dot (QD) qubits are mostly based on either self-assembled or lateral semiconductor heterostructures (typically GaAs/AlGaAs). The self-assembled QDs are grown epitaxially on lattice-mismatched crystalline materials. These are for example InAs or GaAs on Ge or Si, with a lattice mismatch between around 5-10% [96]. The self-assembled QDs form zero dimensional semiconductor nanostructures and their formation is steered by mechanical strain, or more generally by the growth conditions like the temperature and substrate properties. Typical sizes of these self-assembled QDs are around approximately 10 nm, thus the dots have a discrete level structure and electrons and holes are strongly confined in the QDs. Therefore, these systems can also be termed artificial atoms or even molecules [96–99]. The self-assembled QDs are manipulated with electromagnetic radiation in the optical domain and many studies regarding their properties and manipulation have been pursued [100–107]. Applications for the QDs are for example the realization of lasers or qubits. The qubits can be defined via charge or spin excitations in the QDs. From the quantum computation point of view, these devices possess long coherence times and are only weakly coupled to the environmental degrees of freedom.

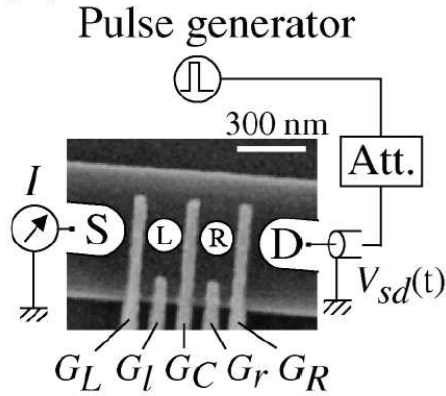


Figure 2.14: Lateral double quantum dot structure that was used for the realization of a charge qubit, the readout of the charge qubit is done by a bias voltage pulse, which transforms the system to a molecular state. Finally, a finite current depending on the state of the qubit is measured [94]. Note that the QD structures presented in Figs. 2.14 and 2.15 can in principle be used to realize both types of QD qubits.

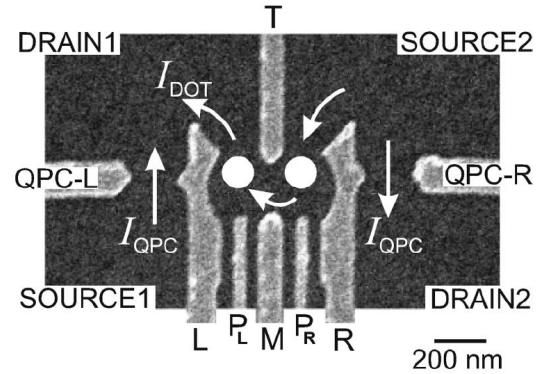


Figure 2.15: Lateral quantum dot structure used for the experimental realization of a QD spin qubit, the readout of the spin qubit is done via spin to charge conversion using the second dot of the double dot system. The spin state in the left dot (qubit spin) is transferred in a spin-dependent charge state in the right dot, which is then detected by the Quantum Point Contact (QPC) [95].

However, on the other hand, the fabrication of the QD structures is not yet fully deterministic and the coupling of several qubits is hard to control. Two qubits in self-assembled QDs can be coupled via their Coulomb (dipole-dipole) interaction or via a single mode of the electromagnetic field inside a cavity.

In contrast to self-assembled QDs, the system parameters of QDs formed in a two-dimensional electron gas (2DEG) in lateral semiconductor heterostructures are easily tunable. In these structures the 2DEG forms approximately a few hundred nanometers below the surface, near the interface of the two semiconducting materials. The 2DEG is confined by the gates on top of the substrate and the QD is defined. The gate voltages allow to precisely control the tunnel barriers between the QD and the reservoirs, *i.e.*, the source and drain leads, the coupling between the QDs in a double-dot system, and the shape of the QD (the electro-chemical potential inside the dot). For transport measurements with lateral QDs, a finite voltage is applied across the QD via leads connected to the quantum dot and thus a current is flowing through the QD.

In these QD structures, all electrons are bound and there is only a small number of additional free electrons (ranging from 0 to around 1000) [108]. Therefore, qubits based both on the charge degree of freedom [109–111] and the spin of individual electrons in a

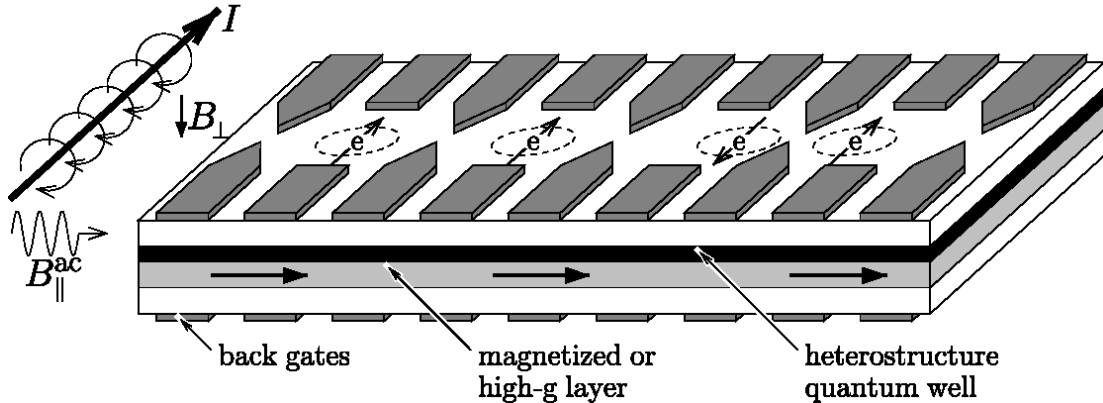


Figure 2.16: Sketch of an array of QD spin qubits, taken from Ref. [64]. The qubits are defined by the spin states of a single electron in a QD.

QD [64, 112] have been envisioned.

Up to now, in QD charge qubits, where the state of the qubit is defined by the position of an additional charge in a double-QD system, coherent oscillations have been demonstrated [94]. QD charge qubits are supposed to be hindered by strong decoherence due to phonons,  $1/f$ -noise due to background charges, electronic baths and co-tunneling, for a quantitative analysis see Ref. [113]. However, recently substantial experimental progress regarding the coherence times has been made [114].

In the QD spin qubit, the qubit is defined by the spin state of an electron in a single QD [112]. It is considered to be more stable with respect to decoherence due to the stability of the electron spin in the QD. On the other hand, the electron spin is also much harder to manipulate and to read out. The most important decoherence sources in QD spin qubits are expected to be hyperfine interactions between the electron spin and the nuclear spins in the bulk material [115] and spin-phonon or spin-orbit phonon coupling [116]. It has been shown that it is possible to fabricate QDs with just one electron in the dot [117] and also the readout of QD spin qubits has been demonstrated via spin-charge conversion and readout with a quantum point contact (QPC) [95]. In Fig. 2.16 an array of several coupled QD spin qubits for quantum computation is sketched.

A schematic view of a single lateral QD with several top gates for manipulation of the QD is shown in Fig. 2.17. The source-drain voltage corresponds to the difference in the electrochemical potentials  $\mu_S$  and  $\mu_D$ , cf. Fig. 2.18. In figure 2.18 a more detailed picture of the energy levels of a single lateral quantum dot is depicted. The chemical potentials of source and drain are denoted by  $\mu_S$  and  $\mu_D$ , respectively. The charge states inside the quantum dot are indicated by black lines, the grey line is an orbital excited state. The electrochemical potential of the quantum dot with  $N$  electrons is  $\mu(N)$ . It is defined as the energy that is required to add an electron to the dot. Without loss of generality, the local electron level (or electrochemical potential) is given for the difference between  $N - 1$

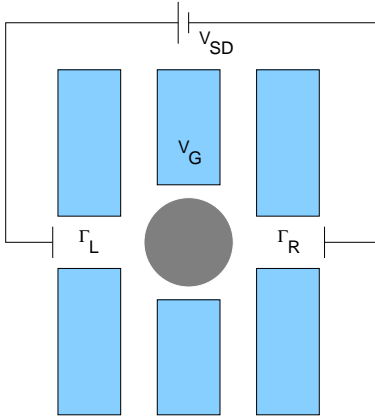


Figure 2.17: Schematic drawing of a single lateral quantum dot. The 2DEG that forms approximately 100 nm below the surface, constricted by the gate electrodes, is indicated by the grey circle. The gate voltage can be used to displace the charge levels inside the quantum dot, cf. Fig. 2.19. Moreover, it is also possible to manipulate the barrier heights  $\Gamma_L$  and  $\Gamma_R$  externally.

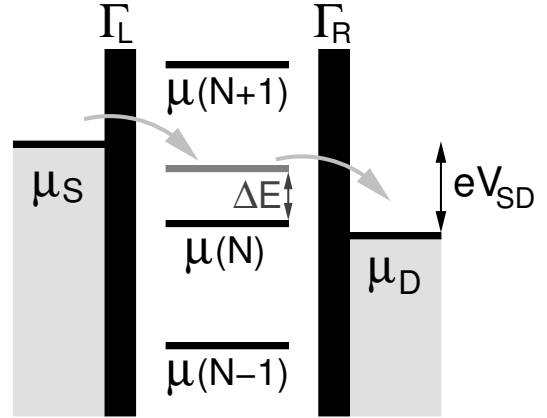


Figure 2.18: Energy levels inside a single lateral quantum dot. Depending on the source-drain voltage  $V_{SD}$ , transport through the quantum dot is possible. The charge levels are given by black lines and the orbital excited levels are drawn in grey. A gate voltage can be used to shift the energy levels upwards through the transport window given by  $V_{SD}$ . The Coulomb peaks in the transport current appear when the charge levels are inside the transport window, cf. Fig. 2.19. Picture taken from [113].

and  $N$  electrons [108, 118]

$$\begin{aligned} \mu(N) &\equiv U(N) - U(N-1) \\ &= \left(N - N_0 - \frac{1}{2}\right) E_C - \frac{E_C}{|e|} (C_S V_{SD} + C_g V_g) + E_N, \end{aligned} \quad (2.22)$$

where  $E_C = e^2/C$  is the charging energy of the dot and  $C$  is the capacitance given by the network of capacitances connected to the dot. The source-drain voltage  $V_{SD}$  and the gate voltage  $V_g$  are used to manipulate the local electron level according to Eqn. (2.22). Moreover,  $N_0$  is the number of electrons in the QD without applying a gate voltage and the  $C_i$  are the corresponding capacitances. The discrete levels in the QD are separated by the addition energy  $E_{\text{add}}(N)$ , which is given by [108, 118]

$$E_{\text{add}}(N) = \mu(N+1) - \mu(N) = E_C + \Delta E, \quad (2.23)$$

where  $\Delta E$  is the level spacing between two discrete quantum states, indicated in Fig. 2.18. Note that this energy  $\Delta E$  is zero when two electrons are added to the same spin-degenerate

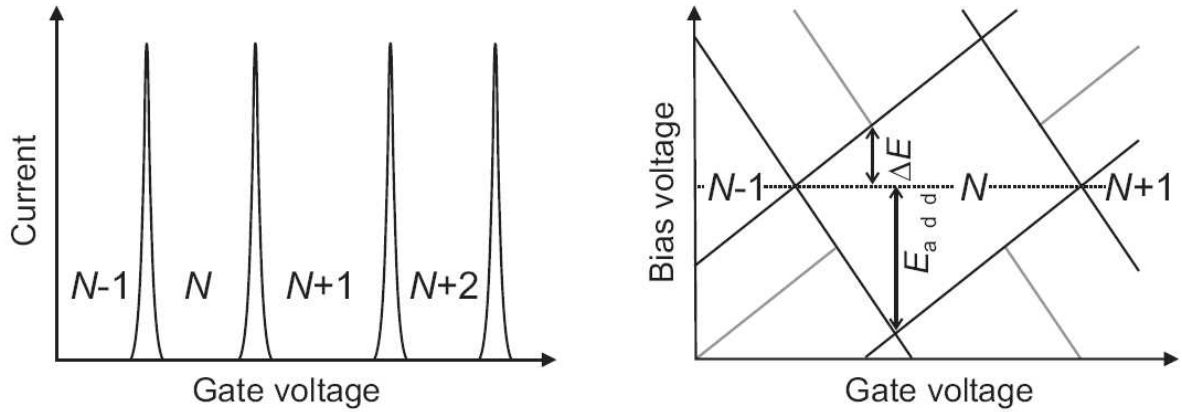


Figure 2.19: Transport through a QD. The left plot depicts the Coulomb peaks in the linear-response regime. The right plot shows the Coulomb diamonds in the differential conductance  $dI/dV_{SD}$ , where  $V_{SD}$  is the source-drain or bias voltage. The edges of the diamond-shaped regions (marked black) correspond to the onset of current. The grey lines indicate the onset of transport through excited states. Pictures are taken from Ref. [118].

level and the first term in the expressions for the addition energy, the charging energy  $E_C$ , is purely electrostatic.

In transport experiments with QDs, a finite source-drain voltage is applied across the quantum dot and when one of the charge levels is tuned by the gate voltage into the transport window, the so-called Coulomb peaks appear. Thus, in a single quantum dot there are charge ground states, however, there also exist elementary excitations just like in real atoms, which lead to orbital excited states.

There also exist other proposals for qubits in semiconductors. The most important ones are based on phosphorus donors in silicon. Again, a distinction between donor charge and spin qubits is made, the charge qubit states are given by lowest states of an electron which is localized in the potential generated by two  $P^+$  ions. The donor spin qubit is based on the nuclear spin of a positively charged donor in a semiconductor [119], the qubit can be manipulated by controlling the resonance frequency of the nuclear spins and the coupling between spins with external gates. Then ac electromagnetic fields are used at resonance to alter the state of the nuclear spin. The measurement of this type of qubit could be performed by spin-charge conversion [120, 121].

## Chapter 3

# Quantum gate operations and readout

A quantum gate operation in solid-state devices can be performed using electromagnetic fields, *i.e.*, by means of gate voltages and magnetic fields. The simplest experiment, yet the most important one to begin with, is to demonstrate coherent Rabi oscillations in a driven qubit circuit. These have been shown first in superconducting charge qubits [122] and later also for superconducting flux qubits [85].

Typically, in superconducting charge qubits quantum gate operations are performed via application of DC pulses, *i.e.*, short rectangular pulses. The individual pulses to complete a more complex quantum gate, for example a CNOT gate can be viewed as different single-qubit or two-qubit gates given by quantum mechanical propagators  $U = \exp(-i/\hbar)H\Delta t$ , where the length of the pulse is denoted by  $\Delta t$  and the time evolution is generated by a static Hamiltonian  $H$ . Recently, also manipulation schemes that are inspired by protocols from NMR quantum computation [123] have been presented [124]. In chapter 10, another method to manipulate superconducting charge qubits will be presented. There, a short pulse-trajectory of rather soft (small Fourier bandwidth compared to the time and frequency scale that is set by the pulse duration) pulses will be presented that drastically improves the gate performance of a charge qubit system and it is also feasible from the point of view of experiments. Superconducting flux qubits can also be manipulated with DC pulses. This is done by rapidly switching the two fields  $B_z$  and  $B_x$  that determine the energy bias and the tunnel matrix element of the qubit, respectively. Usually, the tunnel matrix element  $B_x$  is set fixed. However, it is possible to replace one of the junctions in a rf-SQUID or 3jj flux qubit by another SQUID loop with two Josephson junctions. Then, the tunnel matrix element  $B_x(\Phi_x)$  of the qubit can be tuned by adjusting the flux through the additional SQUID loop. Note that the requirement to steer two fluxes that act spatially very close is hard to achieve and flux crosstalk then will certainly degrade the performance of these types of qubits. Moreover, also an additional noise source is introduced to the system. With this control over  $B_x$  and  $B_z$  the elementary single-qubit gates could be performed.

However, flux qubits are most conveniently addressed by AC fields and resonant pulses. This is done in the following way. In these systems first a coherent flux driving of the type

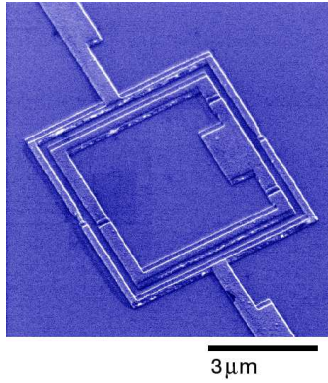


Figure 3.1: SEM image of a flux qubit with a readout DC-SQUID, which is surrounding the qubit loop. The qubit state can be measured using the current biased DC-SQUID, which will switch into the finite voltage state for different values of the bias current  $I_B$  depending on the state of the qubit. Image courtesy of TU Delft.

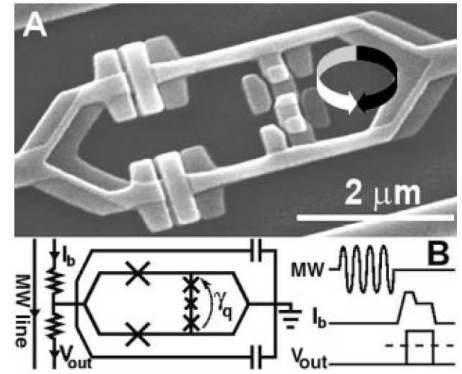


Figure 3.2: SEM image of a flux qubit and attached readout SQUID. In experiments performed with this kind of qubit coherent Rabi oscillations have been demonstrated. Below the image of the qubit circuit, an equivalent circuit diagram and the pulse sequence used for demonstration of Rabi oscillations are shown. Image courtesy of TU Delft.

$H_d = \delta\epsilon \cos(\omega t)$  is applied. The oscillatory driving field can be applied at the resonance frequency of the qubit like in NMR experiments [76]. Then the manipulation pulses are convoluted with the driving [125]. The effective manipulation of the qubit is then described best in the reference frame that rotates with the driving frequency. Two-qubit operations can be performed with the same technique, for example in a two-qubit system the level splitting of one qubit depends on the state of the other qubit. Therefore, the transition of the first qubit, will be conditionally shifted depending on the state of the first qubit, *e.g.*, when the second qubit is in the  $|1\rangle$  state. A pulse can only be resonant with the transition of the first qubit when the state of the second qubit (the control qubit) is correct. Obviously, the timescale of the irreducible two-qubit operations is determined by the coupling strength between the qubits.

Another possibility for qubit manipulation is the *adiabatic quantum computation* [126, 127]. This refers to a composite quantum system of qubits that is always kept in its ground state, where the Hamiltonian of the system is different for different quantum gates or algorithms and varied slowly. Here, it is important to note that the speed-up of the adiabatic quantum computer is due to an energy gap between ground state and excited states. Adiabatic quantum computation has been shown to be equivalent to standard quantum computation [128]. Qubit setups with flux qubits have been proposed for adiabatic quantum computation [129].



However, prior to the demonstration of single-qubit or two-qubit operations, the basic experiment is the aforementioned demonstration of coherent Rabi oscillations, where the frequency of the oscillations should vary linearly with the amplitude of the driving field, and Ramsey fringe experiments, where the coherent evolution in the  $\hat{\sigma}_x$ -component of the qubit is probed. The latter is done by two  $\pi/2$  pulses, before the coherent evolution and in the end to readout the pseudo-spin. Both of these experiments indicate whether the qubit system can really be manipulated quantum coherently. From these experiments the so-called *quality factor of quantum coherence*  $Q_\varphi = \pi\nu_q T_2$  [93] can be extracted, where  $\nu_q$  is the transition frequency of the qubit and  $T_2$  is the coherence time of a superposition of qubit states. It follows from the threshold theorem for QECCs, cf. section 1.2, that a  $Q_\varphi > 10^4 \nu_q t_{\text{op}}$  is required for quantum computation. Here,  $t_{\text{op}}$  is the duration of an elementary operation [130]. For superconducting phase qubits, the quality factor can be as large as  $Q_\varphi \approx 25000$ . For comparison, the QD qubits exhibit a much smaller quality factor, namely  $Q_\varphi \approx 7$  [94],  $Q_\varphi \approx 3$  [131], and  $Q_\varphi \approx 6$  [114], as summarized in [113]. However, not only the number of coherent oscillations within the decoherence time is an important benchmark for the qubit system but also the amplitude (“visibility”) of the coherent oscillations [132, 133]. Many experiments have observed [71, 93, 122, 134] and analyzed [135, 136] this loss of oscillation amplitude of the coherent oscillations. Thus, additionally to the exponential decay of the coherent oscillations due to decoherence the oscillations do *not* extrapolate back to the full expected amplitude at time  $t = 0$ , which is an indication for non-Markovian effects due to the environment [132, 137].

The readout of a flux qubit can be done by fabricating the flux qubit loop inside a DC-SQUID, which is then used for readout of the qubit state. For readout, the DC-SQUID is biased by a current  $I_B$ , which is increased until the DC-SQUID switches to the finite voltage state (where it also becomes dissipative, *i.e.*, it is not superconducting anymore). The point where the DC-SQUID switches to a finite voltage depends on the flux that is threading the DC-SQUID loop and therefore on the state of the qubit. Due to a signal-to-noise ratio (SNR) that is smaller than unity and the statistical nature of this measurement, a huge number of experiments have to be performed. However, there are many more readout schemes for flux qubits, which in the best cases even provide single-shot resolution, or are quantum-non-demolition (QND) measurements, as in the case of a flux qubit inside a cavity, which will be presented later.

In general, the ideal readout process should work as follows [138]. As long as the detector is switched off, the qubit should not experience any backaction from the detector, *i.e.*, dephasing and relaxation due to the detector circuit need to be avoided during the initialization and manipulation of the qubit. But when the detector is switched on to detect the state of the qubit, the qubit has to be dephased quickly by the detector in order to project the qubit state onto one of the basis states. Thus, for a fast measurement, the detector has to be coupled strongly to the qubit. During the readout process energy relaxation, which leads to mixing, should be suppressed, though. The relaxation of the qubit is also due to the coupling between the meter and the qubit, as long as the measurement is not a quantum non-demolition measurement (QND) for which the qubit and qubit-detector coupling terms in the Hamiltonian commute [138]. Note that the coupling strength of the

readout device, the meter, and the qubit during the measurement also determines the basis in which the qubit is read out. However, also measurements that do not lead to a complete collapse of the wavefunction can be performed repeatedly in order to obtain information about the system [139]. This is for example the case for the readout of superconducting flux qubits with a DC-SQUID [76, 81, 90].

In summary, the requirements that determine the quality of a readout switch are summarized as follows [140]

- The energy relaxation time of the qubit has to be sufficiently long when the detector is switched on.
- The dephasing time of the qubit has to be sufficiently long when the detector is turned off.
- The measurement time (the time taken by the measuring device to determine the state of the qubit with a signal-to-noise ratio (SNR) of 1), which describes the sensitivity of the switch, has to be sufficiently small.
- The dead time that is needed to reset the measuring device and the qubit after a measurement has to be sufficiently small. (These are determined by the energy expenditure associated with producing a signal strong enough for external detection.)

It is very hard to optimize all of these parameters at the same time [75, 87, 90, 141, 142]. However, it is of central importance to improve the readout fidelity and speed of the readout, and significant progress has been made with the dispersive readout of superconducting charge qubits inside a cavity, which is also a QND measurement [136]. In the aforementioned experiments, long coherence times of the superconducting charge qubit system on the order of  $\approx 500$  ns and a visibility close to unity have been demonstrated with the cavity readout scheme [136, 143].

# Chapter 4

## Decoherence

*Physicists learned to realize that whether they like a theory or they don't like a theory is not the essential question. Rather, it's whether or not the theory gives predictions that agree with experiment.*

Richard Feynman, 1985

*An expert is someone who knows some of the worst mistakes that can be made in his subject and who manages to avoid them.*

Werner Heisenberg, *Physics and beyond*, 1971

*A new scientific truth does not triumph by convincing its opponents and making them see the light, but rather because its opponents die, and a new generation grows up that is familiar with it.*

Max Planck, *Wissenschaftliche Selbstbiographie*, 1945

Decoherence denotes the influence of an environment, which can be a heat bath or reservoir, on a much smaller quantum system. However, in most cases one is not interested in the overall dynamics of the full system, including the reservoir and the quantum system (in the following called system, *e.g.*, a particle or an atom or qubit), but rather in the evolution of the smaller quantum system taking into account the influence of the reservoir due to their mutual coupling. Of course, also in classical physics examples exist, where one is concerned with the evolution of only a part of the system, *e.g.*, in *Brownian motion* processes. In these Brownian motion processes, particles exhibit a stochastic thermal movement, with collisions between the particles that broaden (and shift) the distribution function [144]. The Brownian motion of particles can be described by a *Langevin equation*, with friction forces that describe the effects of the collisions and damping, and a Langevin force that takes into account for fluctuations. A different tool is the *Fokker Planck equation* that can be used to describe the evolution of the statistical distribution function, *e.g.*, of the particles. In *Quantum Brownian motion* [145] stochastic relations for the quantum mechanical operators or states are utilized and an additional uncertainty due to quantum fluctuations even in the initial state completes the theory.

Returning to the description of the quantum system and the environment, the concept is that the particle (or quantum system) interacts with a very large reservoir with many degrees of freedom such that no macroscopic change of the reservoir is observed due to the coupling to the small system. In general, there are two relevant time scales, the time scale of fluctuations in the reservoir that perturbs the system, and a longer time scale that characterizes the dynamics of the system itself. This approach can also be adopted to the case when the system is an ensemble of particles, *e.g.*, an atom, a molecule, or (several) qubits, and the reservoir is a radiation field. In this particular case, the reservoir has an infinite number of degrees of freedom that correspond to an infinite number of modes of the electromagnetic field [146]. (The properties of a qubit (or atom) coupled to a single mode electromagnetic field are discussed in more detail in the chapters 5 and 12.) It is important to note that the correlation functions of the electromagnetic fields give the information about the dynamics of the fluctuations of the electromagnetic fields [146]. When the smaller system is just a single atom or qubit, then it is quite evident that the reservoir dynamics will only be affected very little by the atom-reservoir coupling. In many situations, the radiation field can be viewed as a perturbation, which changes fast on the atomic time scale. In summary, the effects of the system and reservoir dynamics can be interpreted as the system and reservoir fluctuating and polarizing each other. Returning to the notion of decoherence in the beginning of this section, in the case of a quantum system the aforementioned effects are called *decoherence*.

Decoherence includes both (energy) relaxation and dephasing. Dephasing leads to entropy production and the following long time behaviour [74] of the system density matrix

$$\langle \rho_{\pm}(t) \rangle = \langle \rho_{\pm}(0) \rangle e^{\mp iEt} e^{-t/\tau_{\varphi}}, \quad (4.1)$$

where the density matrix is written in the system eigenbasis,  $E$  is the level spacing of the qubit,  $\rho_{\pm} = (1/2)(\rho_x \pm i\rho_y)$ , and  $\tau_{\varphi}$  is the dephasing time. Additionally, the diagonal entries of the density matrix tend towards their thermal equilibrium values given by the Boltzmann factors due to relaxation with energy exchange, characterized by

$$\langle \rho_z(t) \rangle = \rho_z(\infty) + [\rho_z(0) - \rho_z(\infty)] e^{-t/\tau_R}, \quad (4.2)$$

where  $\rho_z(\infty)$  are the thermal equilibrium values and  $\tau_R$  is the relaxation time. In other words, the relaxation time is the timescale on which the diagonal elements of the reduced density matrix (in the preferred eigenbasis), *i.e.*, the density matrix of the system where the environmental degrees of freedom have been traced out, tend towards the Boltzmann factors. The dephasing time is the timescale on which the off-diagonal elements of the reduced density matrix, *i.e.*, the coherences, vanish. Thus, entropy production and energy exchange, which is irreversible, lead to dephasing and relaxation.

Decoherence can also be viewed as stemming from an asymmetry of dissipative systems under time-reversal. In other words as was already discussed before, the time-evolution of a dissipative system is *not* unitary.

When the coupling between the system and the reservoir has little effect during the correlation time of fluctuations of the reservoir, a master equation can be derived that

gives the coarse-grained rate of variation of the system density operator while treating the effects of the reservoir perturbatively [146–148]. The derivation of the master equation will be elucidated in section 4.3. This case is reminiscent of the weak-collision regime in Brownian motion. The condition that the coupling between reservoir and the system has a weak effect during the correlation time of the reservoir is known as the so-called *motional narrowing* condition. In more detail, let the dimensionless parameter  $\alpha$  describe the coupling strength between the system and the reservoir. This parameter characterizes also the dispersion of the values for the interaction  $\hat{H}_{\text{int}} = \sum_j \hat{S}_j \otimes \hat{B}_j$ , where the  $\hat{S}_j$  are system operators and the  $\hat{B}_j$  are bath operators. In other words, if the broadening of the spectral lines of the system produced by the coupling to the reservoir is not homogeneous, then the width of the spectral lines is large. However, because the interaction between the system and the bath fluctuates rapidly, the inhomogeneous width is reduced by a factor that is proportional to the correlation time of the reservoir, therefore the name motional narrowing evolved.

## 4.1 Linear response and the fluctuation dissipation theorem

For a macroscopic environment, the coupling of the quantum system to each distinct single mode of the reservoir can be considered very weak. Therefore one can assume that the system-reservoir coupling is *linear* in the bath coordinates for the large environment. Overall, the influence of the environment on the system can be large, though, because the influence of all the bath modes adds up and it is possible that there are many different modes in the environment [148]. The notion of this linear coordinate-coordinate coupling between the system and the reservoir coordinates is called *linear response theory*. The linear response theory clearly has the fluctuation-dissipation theorem at its heart [149], which says that the irreversible processes in weak non-equilibrium are necessarily related to thermal fluctuations in equilibrium. Namely, for an external perturbation coupling to a system quantity [150], *i.e.*,

$$\rho(t) \approx \rho(0) - \frac{i}{\hbar} \int_{t_0}^t dt' [V(t'), \rho(0)], \quad (4.3)$$

where  $V(t')$  denotes the coupling of the external perturbation to a physical quantity of the system. From this one can evaluate the expectation value of a physical observable  $O(\mathbf{r}, t)$  and the expectation value of the deviation  $\delta O(\mathbf{r}, t)$  from its unperturbed value. For  $t_0 \rightarrow -\infty$ , where  $Q_I$  is an observable in the interaction picture [150],

$$\langle \delta O(\mathbf{r}, t) \rangle = \frac{i}{\hbar} \int_{t_0 \rightarrow -\infty}^t dt' \int d\mathbf{r}' \text{tr} [\hat{\rho}_0 [O_I(\mathbf{r}, t), Q_I(\mathbf{r}', t')]] F(\mathbf{r}', t), \quad (4.4)$$

which defines the *generalized susceptibility* or *linear response function*

$$\langle \delta O(\mathbf{r}, t) \rangle = \int_{-\infty}^{\infty} dt' \int d\mathbf{r}' \chi(\mathbf{r}, t, \mathbf{r}', t') F(\mathbf{r}', t), \quad (4.5)$$

where from comparison of Eqns. (4.4) and (4.5) it is directly found that

$$\chi(\mathbf{r}, t, \mathbf{r}', t') = \frac{i}{\hbar} \text{tr} [\hat{\rho}_0 [O_I(\mathbf{r}, t), Q_I(\mathbf{r}', t')]] \theta(t - t'), \quad (4.6)$$

which is the so-called *Kubo formula*. In the case when the system is translation invariant, Fourier transformation gives  $\langle \delta O(\mathbf{k}, \omega) \rangle = \chi(\mathbf{k}, \omega) F(\mathbf{k}, \omega)$ . Next, we split up the generalized susceptibility into real and imaginary part  $\chi(\omega) = \chi'(\omega) + i\chi''(\omega)$ , where  $\chi'(\omega) = \chi(-\omega)$  and  $\chi''(\omega) = -\chi''(\omega)$ . In quantum mechanics the correlation function is defined via the symmetrized form

$$\langle \delta Q(t) \delta Q(t') + \delta Q(t') \delta Q(t) \rangle = \frac{1}{2} \text{tr} (\rho_0 [\delta Q(t) \delta Q(t') + \delta Q(t') \delta Q(t)]). \quad (4.7)$$

The calculation of the Fourier transform of this expression and comparison with the Fourier transformed Kubo formula gives the *fluctuation dissipation theorem* [151, 152]

$$\langle \delta Q \delta Q \rangle_{\omega} = \coth(\beta \hbar \omega / 2) \hbar \chi''(\omega). \quad (4.8)$$

Note that  $\chi''$  describes the change of energy and therefore the dissipation. The *Kramers-Kronig relations* are [150]

$$\text{Re} \chi(\omega) = \chi'(\omega) = \frac{1}{\pi} \mathcal{P} \int d\omega' \frac{\chi''(\omega')}{\omega' - \omega} \quad (4.9)$$

$$\text{Im} \chi(\omega) = \chi''(\omega) = -\frac{1}{\pi} \mathcal{P} \int d\omega' \frac{\chi'(\omega')}{\omega' - \omega}, \quad (4.10)$$

where  $\mathcal{P}$  denotes the principal value of the integral expression. With the Kramers-Kronig relations it is possible to calculate the imaginary part of the response function if the real part is known and vice versa. The real part  $\chi'$  of the generalized susceptibility  $\chi$  determines the classical dissipation and thus the relaxation time  $T_1$ , whereas the imaginary part  $\chi''$  gives the quantum fluctuations characterized by the dephasing time  $T_2$ . As was reasoned before, the linear response theory has a broad range of applicability and it shows that the oscillator-bath models, as presented in the next section, are universal within linear response.

## 4.2 The Spin-Boson model

Often, a physical system in contact with a dissipative environment can be described by a heat bath, which is sensitive to the position of the qubit or two-state system [153–155]. One

particular example is the following kind of interaction between the qubit and the collective bath mode as discussed in the last section

$$\hat{H}_I = \sum_j \hat{S}_j \otimes \hat{B}_j = \hat{\sigma}_z \otimes \hat{X}(t), \quad (4.11)$$

where  $S_j$  are system observables, the  $B_j$  are bath (reservoir) observables, as introduced in the last section. Here,  $\hat{X}(t)$  is a collective bath observable, which can be understood as the coordinate of the harmonic oscillator that is coupled to the system and jiggles the system. The collective bath mode can be expressed in terms of all modes  $x_i$  of the reservoir [148]

$$\hat{X}(t) = \frac{x_0}{2} \sum_{i=1}^N c_i x_i(t). \quad (4.12)$$

The heat bath acts like a fluctuating force on the system and causes decoherence in the system. In the case of Gaussian statistics, the heat bath can be modeled by a bath of harmonic oscillators, *i.e.*, bosons. This leads to the following ‘‘Spin-Boson’’ Hamiltonian in second quantization

$$H_{SB} = H_q - \frac{1}{2} \hat{\sigma}_z \sum_{i=1}^N \hbar \lambda_i (a_i + a_i^\dagger) + \sum_{i=1}^N \hbar \omega_i a_i^\dagger a_i, \quad (4.13)$$

where  $a^\dagger$  and  $a$  are the bosonic creation and annihilation operators,  $H_q$  is the Hamiltonian of the qubit. Next, the environmental effects can be cast into the spectral density, which characterizes the coupling and relates the  $c_i$  and  $\lambda_i$  [148],

$$J(\omega) = \sum_{i=1}^N \lambda_i^2 \delta(\omega - \omega_i) = \frac{\pi}{2} \sum_{i=1}^N \frac{c_i^2}{m_i \omega_i} \delta(\omega - \omega_i). \quad (4.14)$$

A realistic assumption, *e.g.*, for electromagnetic noise due to the wiring [81] are Ohmic spectral densities with a Drude-cutoff. This leads to integrals in the Bloch-Redfield rate expressions Eqn. (4.24) that are tractable by the residue theorem [156]. The cutoff frequency  $\omega_c$  for the spectral functions of the two qubits is then chosen to be the largest frequency in the problem. Namely,

$$J(\omega) = \frac{\alpha \hbar \omega}{1 + \frac{\omega^2}{\omega_c^2}}, \quad (4.15)$$

where the dimensionless parameter  $\alpha$  describes the strength of the dissipative effects that enter the Hamiltonian via the coupling to the environment. Note that in order for the Bloch-Redfield formalism, which is presented in section 4.3, to be valid, it is necessary to assume  $\alpha \ll 1$ . The reason for this restriction is that the Golden Rule rate expressions involve a Born approximation in the system-bath coupling. This corresponds to a description of the evolution of the system density matrix in the interaction picture in the linear response regime.

### 4.3 Bloch-Redfield formalism

In order to describe decoherence in the weak damping limit, the Bloch-Redfield-Formalism [147, 148, 157] can be used to derive a set of master equations for the system dynamics. Starting from the Liouville equation of motion for the density operator of the whole system

$$\frac{d}{dt}\hat{W}(t) = -\frac{i}{\hbar}[\hat{H}, \hat{W}(t)], \quad (4.16)$$

where the Hamiltonian  $\hat{H}$  and the corresponding Liouvillian  $\mathcal{L}$  can be decomposed in the form

$$\hat{H}(t) = \hat{H}_S(t) + \hat{H}_B + \hat{H}_I \text{ and } \mathcal{L} = \mathcal{L}_S + \mathcal{L}_B + \mathcal{L}_I. \quad (4.17)$$

Here,  $\hat{H}_S(t)$  is the system part of the Hamiltonian,  $\hat{H}_B$  describes the bath, and  $H_I$  is the system-bath interaction term. Next, one extracts the reduced system part of the whole system  $\hat{W}(t)$  describing the dynamics of the relevant macroscopic observables. This can be done by defining a projector  $\hat{P}$ , where  $\rho(t) = \text{tr}_B(\hat{W}(t))$  is the so-called *reduced density matrix* and  $\hat{P}^2 = \hat{P}$  holds such that the full density matrix can be split into two parts

$$\hat{W}(t) = \hat{P}\hat{W}(t) + (\hat{\mathbf{1}} - \hat{P})\hat{W}(t). \quad (4.18)$$

The second part of this expression describes the environmental degrees of freedom and correlations between system and environment. Note that the normalization  $\text{tr}_B\rho_\beta = 1$  has to be fulfilled [158]. Here, the action of the projector  $\hat{P}$  is to effectively trace out the environmental (bath) degrees of freedom, *i.e.*,  $\hat{P}\hat{W}(t) = \rho(t)$ . The thermal equilibrium density matrix is given by

$$\rho_\beta = \left[ \text{tr}_B \exp(-\hat{H}_B\beta(T)) \right]^{-1} \exp(-\hat{H}_B\beta(T)), \quad (4.19)$$

where  $\beta(T) = (k_B T)^{-1}$ ,  $T$  is the temperature and  $k_B$  is Boltzmann's constant. Next, the expression for  $\hat{W}(t)$  from Eqn. (4.18) is inserted into Eqn. (4.16) and two coupled equations for the relevant and irrelevant parts are found. Integration of the latter one and substitution of this result into the equation for the relevant part finally gives the exact generalized master equation for the reduced density matrix, the Nakajima-Zwanzig equation [159, 160]

$$\dot{\rho}(t) = \hat{P}\mathcal{L}\rho(t) + \int_0^t dt' \hat{P}\mathcal{L}\exp[(1 - \hat{P})\mathcal{L}t'](1 - \hat{P})\mathcal{L}\rho(t - t') + \hat{P}\mathcal{L}\exp[(1 - \hat{P})\mathcal{L}t](1 - \hat{P})\hat{W}(0), \quad (4.20)$$

where the system and bath density matrix were assumed to factorize at the initial time. Now, one uses a projection operator such that the irrelevant part  $(\hat{\mathbf{1}} - \hat{P})\hat{W}(0)$  can be disregarded, which puts the condition on the noise that it is not biased. Moreover, if  $\hat{P}$  commutes with  $\mathcal{L}_s$ , considering the kernel only in second order in  $\mathcal{L}_I$  and disregarding retardation effects, the master equation in Born approximation

$$\dot{\rho}(t) = \hat{P}(\mathcal{L}_s + \mathcal{L}_I)\rho(t) + \int_0^t dt' \hat{P}\mathcal{L}_I e^{(1 - \hat{P})(\mathcal{L}_s + \mathcal{L}_R)t'} (1 - \hat{P})\mathcal{L}_I\rho(t) \quad (4.21)$$



is obtained. Here, the Born approximation is made in the coupling strength to the environment. Here, also a Markov approximation can be made. It refers to the assumption of a memoryless reservoir [148]. In the master equation (4.21) a Markov assumption can be made by letting the integration bound  $t \rightarrow \infty$  in the integral term. The Born approximation is valid for weak coupling of the system to the environment, whereas the Markov assumption, which means that memory effects are negligible, can straightforwardly be lifted. This derivation of the master equation provides a systematic way of finding a set of coupled master equations, which describes the dynamics of the reduced (*i.e.* the reservoir coordinates are traced out) density matrix for a given system in contact with a dissipative environment. It has recently been shown to be numerically equivalent to a path-integral approach [158].

The Hamiltonian of our two qubit system in contact with a dissipative environment, Eqn. (4.17) is of the generic system-bath form. In the aforementioned Born approximation and when the system is only weakly coupled to the environment, Bloch-Redfield theory provides the following set of equations for the reduced density matrix  $\rho$  describing the dynamics of the system in the system eigenbasis [147, 148]

$$\dot{\rho}_{nm}(t) = -i\omega_{nm}\rho_{nm}(t) - \sum_{k\ell} R_{nmk\ell}\rho_{k\ell}(t), \quad (4.22)$$

where  $\omega_{nm} = (E_n - E_m)/\hbar$ . The Redfield relaxation tensor  $R_{nmk\ell}$  comprises the dissipative effects of the coupling of the system to the environment. The elements of the Redfield tensor are given by Golden Rule expressions [148]

$$R_{nmk\ell} = \delta_{\ell m} \sum_r \Gamma_{nrrk}^{(+)} + \delta_{nk} \sum_r \Gamma_{\ell rrm}^{(-)} - \Gamma_{\ell mnk}^{(+)} - \Gamma_{\ell mnk}^{(-)}, \quad (4.23)$$

and the Golden Rule rates are

$$\Gamma_{\ell mnk}^{(+)} = \hbar^{-2} \int_0^{\infty} dt e^{-i\omega_{nk}t} \langle \tilde{H}_{I,\ell m}(t) \tilde{H}_{I,nk}(0) \rangle_{\beta}, \quad (4.24)$$

$$\Gamma_{\ell mnk}^{(-)} = \hbar^{-2} \int_0^{\infty} dt e^{-i\omega_{\ell m}t} \langle \tilde{H}_{I,\ell m}(0) \tilde{H}_{I,nk}(t) \rangle_{\beta}. \quad (4.25)$$

Note, that  $\tilde{H}_I(t) = \exp(i\hat{H}_B t/\hbar) \hat{H}_I \exp(-i\hat{H}_B t/\hbar)$  is the interaction part of the Hamiltonian in the interaction picture with respect to the bath and  $\langle \cdot \rangle_{\beta}$  denotes thermal averaging over the bath degrees of freedom. These rate expressions can also be derived from lowest order diagrams in the Keldysh technique, see Ref. [74]. The two-time averages in the master equation are related to two categories of statistical functions, the symmetric correlation functions that describe the dynamics of the fluctuations of the observables of the system and the reservoir, and the linear susceptibilities that describe the linear response of each system to an external perturbation [146]. In more detail, the correlation functions that

enter the Redfield tensor elements describe the bath correlations. The general two-time correlation function for the bath observables

$$G(t', t'') = \text{tr}_B \left( \rho_\beta \hat{B}(t') \hat{B}(t'') \right) \quad (4.26)$$

can be split into real and imaginary parts. The real part of this function is the symmetric correlation function that describes the dynamics of the fluctuations of the bath observable  $\hat{X}(t)$  in the state  $\rho_\beta$ , whereas the imaginary part is related to a linear susceptibility [146]. In other words, the real part describes the classical fluctuations, whereas the imaginary part specifies the quantum part of the noise.

When the reservoir is in a stationary state and the interaction between the system and the bath is taken to be of bilinear form  $\hat{H}_I = \sum_i \hat{S}_i \otimes \hat{B}_i$  of the coupling between the system  $\hat{S}_i$  and bath operators  $\hat{B}_i$ , then  $G(t', t'')$  depends only on the time difference  $\tau = t' - t''$

$$G(\tau) = \text{tr}_B(\rho_B \hat{B}(\tau) \hat{B}(0)). \quad (4.27)$$

The symmetric correlation function and the linear susceptibility function can be used to characterize the effects of the bath (reservoir) on the system. In the most general situation both the small system and the reservoir fluctuate and can polarize each other. There exist both processes, where the system dynamics evolves unperturbed but affects (polarizes) the reservoir, which then also modifies the evolution of the system, and phenomena in which the fluctuations of the bath strongly influence the dynamics and properties of the system. Note also that the coarse-grained rate of variation of the system density operator in the Bloch-Redfield master equations corresponds to an intrinsic time averaging introduced in the Bloch-Redfield formalism over a timescale determined by the motional narrowing condition.

Using the secular approximation, it is possible to define decoherence rates, *i.e.*, dephasing and relaxation rates from the Redfield tensor Eqn. (4.23). The overall relaxation rate of a system of qubits is defined as the sum of the eigenvalues (or the trace) of the relaxation part of the Redfield tensor [161], *i.e.*, of the matrix  $\tilde{R}$  with matrix elements  $\tilde{R}_{nm} = R_{n,n,m,m}$ . Therefore, the relaxation and dephasing rates are defined as

$$\Gamma_R = \text{tr}(\tilde{R}), \text{ and } \Gamma_{\varphi_{nm}} = R_{n,m,n,m}. \quad (4.28)$$

Note that these rate expressions are derived in secular approximation (they are not obtained from the full Redfield tensor) for

- non-degenerate levels  $\max_{n,m,k,\ell} |\text{Re}(R_{nmkl})| < \min_{n \neq m} |\omega_{nm}|$  [161],
- and in the absence of Liouvillian degeneracy  $|\omega_{nm} - \omega_{k\ell}| > |R_{abcd}|$ , where  $a, b, c, d \in \{k, \ell, m, n\}$  [162].

The corresponding relaxation and dephasing times of a single qubit are given by  $T_1 = T_R = 1/\Gamma_R$  and  $T_2 = T_\varphi$ ; for a larger system, the dephasing times are defined via  $T_{\varphi_{ij}} = 1/\Gamma_{\varphi_{ij}}$ .

The system frequencies  $\omega_{nm}$  are renormalized by the imaginary part of the Redfield tensor [161] via  $\omega_{nm} \rightarrow \omega'_{nm} = \omega_{nm} - \text{Im } R_{n,m,n,m}$ . At small temperatures these renormalization effects do *not* depend on temperature. The renormalization effects diverge logarithmically with the cutoff frequency  $\omega_c$  [163].

It is interesting to note that the Lindblad operators [164] derived from the Bloch-Redfield formalism for the corresponding *Lindblad equation* preserve complete positivity only in the pure dephasing case [165], *i.e.*, when  $[\hat{H}_S, \hat{H}_I] = 0$  is fulfilled, or at high temperatures. Then the Markovian approximations are of Lindblad type and the nice mathematical form of the Lindblad equation is recovered [165].

For a numerical solution of the set of Redfield equations Eqn. (4.22), which are a set of coupled differential equations, it is convenient to collapse  $\rho$  into a vector. Then, in general the Redfield equations without driving, *i.e.*, without explicit time dependence in the Redfield tensor  $R_{nmkl}$  and for a static Hamiltonian, are solved by an ansatz of the type  $\rho(t) = B \exp(\tilde{R}') B^{-1} \rho(0)$ , where  $\tilde{R}'$  is a diagonal matrix. Possible computational drawbacks of this ansatz are discussed in Refs. [166, 167]. (See appendix E for numerical computations of a more general scenario including driven qubit dynamics.) The entries of this diagonal matrix are the eigenvalues of the Redfield tensor, written in matrix form, including the dominating coherent term  $i\omega_{nm}$ , cf. Eqn. (4.22). Here, the reduced density matrix  $\rho = (\rho_{11}, \dots, \rho_{44})^T$  is written in vector form and the matrix  $B$  describes the basis change to the eigenbasis of  $\tilde{R}$ , in which  $\tilde{R}'$  has diagonal form.

Note that for  $1/f$ -noise that is well approximated as Markovian and Gaussian, the effects of  $1/f$ -noise on the qubit system can be taken into account within the presented theory of a Spin-Boson model with the set of Bloch-Redfield master equations. This is done by setting the zero frequency component of the spectral function  $J_{1/f}(0)$  to an experimentally or theoretically determined value for the magnitude of the  $1/f$ -noise. However, in many cases the noise turns out to be non-Markovian and/or non-Gaussian, leading to non-exponential decay, which can neither be treated by Bloch-Redfield theory nor parameterized by a single rate. The  $1/f$ -noise due to hopping *background charges* or general *quantum bistable fluctuations* in superconducting qubits has been intensively studied [168–171]. Recently, there have been several investigations of  $1/f$ -noise caused by a single moving background charge [172] or several background charges [173] treated in an impurity model.



## Chapter 5

# Quantum optics in the solid-state

In this chapter a small overview of several ingredients from the field of quantum optics [174, 175], which will be required for describing circuit-Quantum Electrodynamics (cQED) [176] experiments in the solid-state, will be given. First, we start from the general Hamiltonian of the electromagnetic (photon) field [174]

$$\hat{H} = \frac{1}{2} \int (\varepsilon_0 \mathbf{E}^2 + \mu_0 \mathbf{H}^2) d\mathbf{r} = \sum_k \hbar \omega_k \left( a_k^\dagger a_k + \frac{1}{2} \right), \quad (5.1)$$

where the last equality holds in second quantization for mode functions that form a complete orthonormal set and satisfy the transversality condition [174] and  $a_k^\dagger$ ,  $a_k$  are the bosonic creation and annihilation operators. The bosonic operators obey the usual bosonic commutation relations  $[a_i, a_j] = [a_i^\dagger, a_j^\dagger] = 0$  and  $[a_i, a_j^\dagger] = \delta_{ij}$ . There are two different kinds of field states that will be most important for further considerations, the so-called Fock states or number states and the so-called coherent states. The Fock states are the eigenstates  $|n_k\rangle$  of the Hamiltonian Eqn. (5.1) with eigenvalues  $\hbar \omega_k (n_k + 1/2)$  ( $n_k = 0, 1, 2, \dots$ ), *i.e.*, they are eigenstates of the number operator  $\hat{n}_k = a_k^\dagger a_k$  with eigenvalue  $n_k$ . The following relations hold for the state of the field mode

$$a_k |0\rangle = 0, \quad \langle 0 | \hat{H} | 0 \rangle = \frac{1}{2} \sum_k \hbar \omega_k, \quad (5.2)$$

$$a_k |n_k\rangle = n_k^{1/2} |n_k - 1\rangle, \quad a_k^\dagger |n_k\rangle = (n_k + 1)^{1/2} |n_k + 1\rangle, \quad (5.3)$$

$$\langle n_k | m_k \rangle = \delta_{mn}, \quad \sum_{n_k=0}^{\infty} |n_k\rangle \langle n_k| = 1. \quad (5.4)$$

The state vector for higher lying excited states is obtained from the vacuum state  $|0\rangle$  by repeated application of the bosonic creation operators, Eqn. (5.3),

$$|n_k\rangle = \frac{(a_k^\dagger)^{n_k}}{\sqrt{n_k!}} |0\rangle, \quad n_k = 0, 1, 2, \dots \quad (5.5)$$

Thus, the Fock states have a well defined number of photons in each state, however, on the other hand the coherent states can have an indefinite number of photons in a state with a well defined phase. This is because the product of the uncertainty in amplitude and phase has to fulfill the Heisenberg uncertainty relation. In summary, the coherent states can be expressed in terms of the number states

$$|\alpha\rangle = e^{-|\alpha|^2/2} \sum_n \frac{\alpha^n}{\sqrt{n!}} |n\rangle. \quad (5.6)$$

The coherent states can be generated by application of the *displacement operator*

$$D(\alpha) = \exp(\alpha a^\dagger - \alpha^* a) = e^{-|\alpha|^2/2} e^{\alpha a^\dagger} e^{-\alpha^* a} \quad (5.7)$$

to the vacuum state  $|\alpha\rangle = D(\alpha)|0\rangle$ . The photons in a coherent state follow a Poissonian distribution

$$P(n) = |\langle n|\alpha\rangle|^2 = |\alpha|^{2n} e^{-|\alpha|^2} / n!. \quad (5.8)$$

One more class of states are the squeezed states, these have less noise in one quadrature than the coherent states, while the noise in the other quadrature is larger than in a coherent state due to the requirement that the state has to fulfill the Heisenberg uncertainty relation [174]. This leads to sub-Poissonian and super-Poissonian statistics in the two quadratures.

After introduction of these basic properties of the electromagnetic field, now the properties of the light field inside a cavity and the interaction of the light field with an (artificial) atom, *i.e.* a qubit, inside the cavity are discussed. The Hamiltonian of a qubit interacting with a single field mode inside the cavity is the so-called *Jaynes-Cummings Hamiltonian* [177] obtained in the electric dipole and rotating wave approximations

$$H = H_S + H_C + H_I = \hbar\omega\hat{\sigma}_z + \hbar\omega_r a^\dagger a + \hbar g(a\hat{\sigma}^+ + a^\dagger\hat{\sigma}^-), \quad (5.9)$$

where  $H_S$  is the Hamiltonian of the qubit,  $H_C$  is the free energy of the cavity field and  $H_I$  describes the interaction between the qubit and the cavity field. The rapidly oscillating terms in the qubit-cavity interaction Hamiltonian, which were neglected in the derivation, do not conserve energy and would correspond for example to the excitation of an atom together with the emission of a photon. The spin operators in the last term are defined as  $\hat{\sigma}^+ = (\hat{\sigma}_x + i\hat{\sigma}_y)/2$  and  $\hat{\sigma}^- = (\hat{\sigma}_x - i\hat{\sigma}_y)/2$ . Here, without loss of generality the qubit-field coupling strength  $g$  was taken to be a real number. See chapter 12 and appendix F for a derivation of the Jaynes-Cummings Hamiltonian for a flux qubit inside a cavity.

In Fig. 5.1 the level structure for the uncoupled ( $g = 0$ ) and coupled qubit-cavity system described by the Jaynes-Cummings Hamiltonian at resonance  $\omega = \omega_r$  is illustrated. Here, damping is neglected. In the case of a non-zero coupling strength  $g$ , the degeneracy of the qubit and resonator energy levels is lifted and the diagonalization of the Hamiltonian would yield the so-called *dressed states* [143, 174]. The mean number of photons inside the cavity at resonance and for the qubit initially prepared in the excited state, is depicted in Fig. 5.3. Nicely, the vacuum Rabi oscillations, *i.e.*, the periodic exchange of energy between the qubit and the cavity is observed.

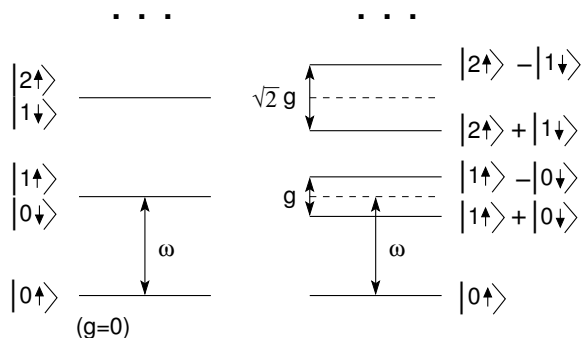


Figure 5.1: Energy level structure for the Jaynes-Cummings Hamiltonian. The left part depicts the degenerate energy levels for the uncoupled ( $g = 0$ ) qubit-cavity Hamiltonian. The right part shows the level structure for finite coupling between the qubit and the cavity. In this case, the degeneracy of the energy levels is lifted by the qubit-cavity coupling [162, 174].

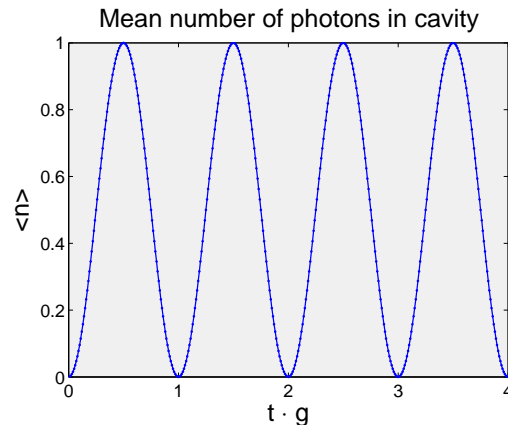


Figure 5.2: Mean number of photons for the resonant Jaynes-Cummings Hamiltonian without an external driving and without taking into account the qubit or cavity decay. Here, the qubit and the cavity are exactly on resonance and the qubit is initially prepared in the excited state. Clearly, coherent oscillations in the mean number of photons are observed due to the periodic energy exchange between qubit and cavity. Here,  $\omega = \omega_r = g$ , and  $\eta = 0$ .

In recent experiments with superconducting qubits inside a cavity [143, 178], the basic concepts of quantum optics have been demonstrated in the domain of microwave photon fields. The qubit (the artificial atom) is fabricated inside a coplanar resonator, which provides the cavity, whereas the coupling between the qubit and the cavity is due to a capacitive coupling of the single Cooper pair box or charge qubit to the electric field inside the resonator. For manipulation and readout of the qubit, an external coherent driving field is applied to the cavity either at a frequency given by the qubit splitting or at the cavity resonance frequency. This corresponds to a classical antenna driving the cavity mode and is known as the so-called *driven Jaynes-Cummings model* [179] described by the Hamiltonian

$$\hat{H} = \hbar\omega\hat{\sigma}_z + \hbar\omega_r a^\dagger a + \hbar g(a\hat{\sigma}^+ + a^\dagger\hat{\sigma}^-) + \hbar\eta(ae^{i\omega_{mw}t} + a^\dagger e^{-i\omega_{mw}t}), \quad (5.10)$$

where  $\eta$  is the amplitude of the driving field and  $\omega_{mw}$  is the frequency of the classical coherent microwave source. A classical field, which is not quantized, has no free energy Hamiltonian. It is given by inexhaustible external sources. Thus, the time-dependence stems only from the plane wave expressions. Note that the (phase) stability of a regular

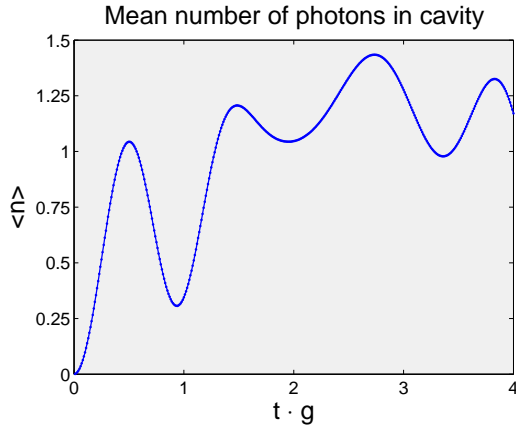


Figure 5.3: Mean number of photons for the resonantly driven Jaynes-Cummings Hamiltonian, but without taking into account the qubit or cavity decay (thus the mean number of photons steadily increases). Here, the qubit, cavity and the coherent driving are exactly on resonance and the qubit is initially prepared in the excited state. A steady increase of the photon number inside the cavity with additional coherent oscillations in the mean number of photons are observed. Here,  $\omega = \omega_r = g$ , and  $\eta = 0.15g$ .

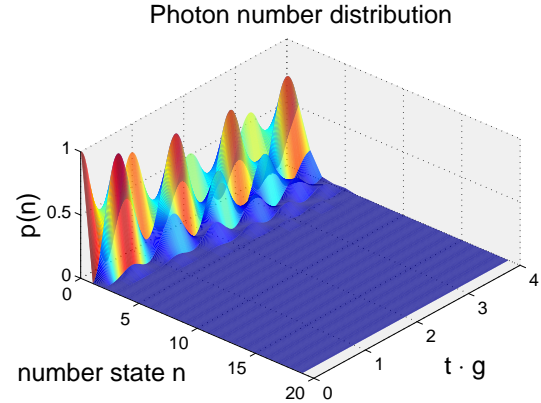


Figure 5.4: Photon number distribution for the driven Jaynes-Cummings Hamiltonian. The qubit is initially prepared in the excited state, and coherent oscillations are observed. With increasing time higher number states are populated. Here,  $N = 20$  number states were taken into account,  $\omega = \omega_r = g$ , and  $\eta = 0.15g$ .

continuous wave (cw) microwave source is better than the stability of a laser [180]. Figure 5.3 shows the mean number of photons inside the cavity for the driven Jaynes-Cummings Hamiltonian without damping, *i.e.*, the number of photons inside the cavity increases steadily. Compared to the case without driving, the coherent oscillations are still visible. In Fig. 5.4, the photon number distribution for the driven Jaynes-Cummings model, which was obtained from numerical simulations of the time evolution is shown. The simulations were obtained from a numerical simulation of the Hamiltonian evolution for consideration of 20 number states. In these simulations both the cavity and qubit decay were disregarded. Without the external classical driving, which corresponds to  $\eta = 0$  in the (classically) driven Jaynes-Cummings Hamiltonian Eqn. (5.10), and in the case where the qubit and the cavity are resonant, the system shows vacuum Rabi oscillations due to constantly exchanging energy between the oscillator (resonator) and the qubit, when the qubit is prepared in the excited state. For finite driving and in the case where the qubit, cavity and the classical driving are resonant, it is nicely observed that in the course of time the occupation of the number states varies and increases and is peaked at around 2 photons



---

for an appropriately chosen mild driving strength. As was mentioned before, neither qubit decay nor cavity leakage was taken into account here. Note that the cavity decay rate, *i.e.*, the cavity leakage rate needs to be of appreciable magnitude in order to be able to measure the photon field (and thus also infer the state of the qubit). Interestingly, the quality factor  $Q$  is very large in microwave cavities, thus the photon inside the cavity essentially never leaks, it rather leaks in transverse direction of the cavity mirrors. Thus it is impossible to measure the output field. However, in the scheme that will be presented in chapter 12, the quality factor of the cavity is chosen such that the cavity leakage rate is approximately  $\kappa \approx 1$  MHz, which leads to a sufficient signal strength such that the output field can be measured.

Now, the statistics of the light field inside the cavity will be investigated in more detail. For the pioneering experiments [178], the strength  $\eta$  of the classical driving is such that the average number of photons in the cavity is approximately one, *i.e.*, the cavity decay rate  $\kappa$  equals the magnitude of the photon flux into the cavity. At this point it is interesting to note the differences in the statistics of the photon distribution. Clearly, a classical antenna that is driving a quantized mode generates coherent states with Poissonian statistics. On the other hand, a pure Jaynes-Cummings Hamiltonian can generate Fock states [174] and has also been proposed to be used in charge qubit setups [181]. However, the classically driven Jaynes-Cummings Hamiltonian in the discussed experiments *can not* lead to a Fock state, even if the mean number of photons in the field is equal to one. Simulations show that a quasi-coherent state, *i.e.*, a mixture of many number states, develops inside the cavity.

In summary, in this section the basic properties of the electromagnetic field that interacts with a single atom or qubit inside a cavity, were introduced and applied to the particular case of a superconducting qubit inside a cavity, where the cavity is driven by a cw microwave source, which models current experiments [178].



## Part II

Decoherence, control, encoding,  
and circuit-QED of coupled  
solid-state qubits



# Chapter 6

## Decoherence and gate performance of coupled solid-state qubits

### 6.1 Introduction

For superconducting flux or charge qubits, one of the most important noise sources is noise from the electronics (Nyquist noise) in the flux or the gate voltages. This noise can be modeled by a linear coupling of the pseudo-spin system to the collective coordinate of a bath of harmonic oscillators determining the environmental influence on the qubit system, see section 4.2. This Spin-Boson model, which is characterized by its power spectrum, has been successfully applied [74, 161, 163].

In the following papers, the decoherence properties of a two-qubit system coupled via an Ising-type  $zz$ -interaction are evaluated. For a system of two qubits there are two general cases of different mutually uncorrelated bath couplings. Both qubits could be coupled to a single bosonic bath or each qubit to one of two different baths. From the evaluation of the dynamics of the reduced density matrix within the Bloch-Redfield formalism it is found that in general these two cases cause nearly identical decoherence properties. Here, the qualitative and quantitative behaviour of the dissipative dynamics is determined by the symmetry properties of the spin part of the interaction Hamiltonian and the system Hamiltonian. When the commutator  $[\hat{H}_I, \hat{H}_s] = 0$  vanishes, *i.e.*, in the case when the coupling to the bath and the qubit system Hamiltonian do commute (or in other words, the Hamiltonians are parallel), only *pure dephasing* processes contribute to the overall decoherence. It is worth noting that the pure dephasing rates will vanish in the case of an Ohmic spectrum for  $T \rightarrow 0$ . (Moreover, for a super-Ohmic spectral function the pure dephasing will always vanish, cf. chapter 9.) However, as soon as the coupling to the bath and the system Hamiltonian are not completely parallel anymore, there will be a significant noise level even for  $T \rightarrow 0$ , the noise saturates.

It is not only important to investigate the decoherence rates, but also the effects of decoherence on the ability of the system to perform quantum gate operations. Therefore, the so-called *gate quality factors* are investigated. These quantify how good the system

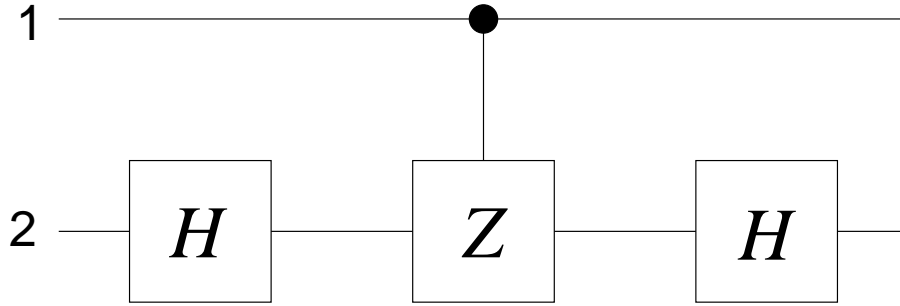


Figure 6.1: Circuit diagram for the CNOT gate, decomposed into the elementary Hadamard single qubit gate on the second qubit and a CONTROLLED-PHASE operation, cf. Refs. [14] and [163].

can perform a given quantum gate operation under the influence of the environment. The gate quality factors [182] are the purity  $\mathcal{P}$ , which is a measure for the decoherence effects, the fidelity  $\mathcal{F}$ , which is the overlap between the propagator for the ideal quantum gate operation and the gate operation with decoherence, and two measures for the non-local nature of the qubit states after performing the gate operation. The latter two are the quantum degree  $\mathcal{Q}$  and the entanglement capability  $\mathcal{C}$  [183]. The entanglement capability has been shown to be closely related to the negativity  $E_N$  of a state, which is a non-entropic entanglement monotone and corresponds to the well-known concurrence [24], cf. chapter 11.

The effect of the variation of the bath coupling operator can be investigated by allowing the spin operator that couples to the environment to lie arbitrarily in the x-z plane on the Bloch sphere. Then it is found that the best gate performance for a gate depends on whether the coupling to the bath mimics the composition of the system Hamiltonian during the gate sequence. For example, the CNOT operation in superconducting qubits (as given in Fig. 6.1), which are coupled via an Ising-type of zz-interaction, can be realized just by two Hadamard gates

$$U_H^{(2)} = \exp \left( i \frac{\pi}{2} \left( \frac{\hat{\mathbf{1}} \otimes \hat{\sigma}_z + \hat{\mathbf{1}} \otimes \hat{\sigma}_x}{\sqrt{2}} \right) \right), \quad (6.1)$$

the two-qubit coupling operation, and three additional z-type single qubit gates. Interestingly, when the coupling to the bath resembles this small admixture of  $\hat{\sigma}_x$ , the gate performance of the two-qubit system is best.

In experiment, a fabrication spread of qubit parameters can not be avoided. Thus, it is important to analyze the influence of asymmetric qubit parameters on the decoherence properties of the qubit system. Again, decoherence is very sensitive to the direction of the spin coupling to the bath. In the case of a perpendicular system Hamiltonian and bath coupling, the decoherence rates increase exponentially when increasing one of the qubit energies in the system, which corresponds to increasing the asymmetry between the qubits. In this case, the largest energy scale in the system naturally determines the

magnitude of the decoherence.

Recently, the finding that for low temperatures the relaxation of the qubit system, which is prepared in an excited state, into the ground state occurs via the population of intermediate states, has been verified by experiments [184]. In these experiments the cryogenic temperature is about  $T \approx 10$  mK. However, the microwave lines that are fed through the cryostat to the sample, which are needed for the qubit spectroscopy and manipulation of the qubits, are not as well thermally decoupled. Therefore, the microwave lines introduce a new higher effective (noise) temperature, which can leave the qubit system in an excited state. The noise from the flux and microwave lines has been associated in experiments with two environmental heat baths with different bath temperature that are coupled to both qubits in the same correlated manner. This scenario is closely connected to the situation that is analyzed in the papers in this chapter.

In another experiment proposed by Zorin [185, 186] for a charge-phase qubit with radio frequency readout, the coupling to the decoherence due to voltage fluctuations in the charge control line is exactly of the form  $\hat{H}_I = (\hat{\sigma}_x \sin \theta + \hat{\sigma}_z \cos \theta) \hat{X}$  as evaluated in the third paper in this chapter, see Ref. [187]. Especially the decoherence properties of quantum logic gates with coupled superconducting phase qubits [188] for which the aforementioned variable noise coupling is anticipated, are modeled in detail in the third paper in this chapter.

Thus, obviously several of the properties of the two-qubit systems that were predicted in the following papers have been verified by measurements [184]. The theoretical papers presented in this chapter model precisely the properties of experimental setups that are currently under investigation [186], albeit allowing for general statements about the influence of (dynamical) symmetries on the noise level of the qubit system.

Recently, other theoretical works on the dynamics of the dissipative two-qubit system [189, 190] verified the importance of symmetries in the coupling between the qubit and the bath and extended the analysis to non-Markovian environments, *i.e.* environments with a memory.

The aforementioned findings are derived and presented in great detail in the following papers.





PHYSICAL REVIEW A **67**, 042319 (2003)**Decoherence and gate performance of coupled solid-state qubits**

Markus J. Storcz\* and Frank K. Wilhelm

*Sektion Physik and CeNS, Ludwig-Maximilians-Universität, Theresienstrasse 37, 80333 München, Germany*

(Received 16 December 2002; published 23 April 2003; publisher error corrected 28 April 2003)

Solid-state quantum bits are promising candidates for the realization of a *scalable* quantum computer. However, they are usually strongly limited by decoherence due to the many extra degrees of freedom of a solid-state system. We investigate a system of two solid-state qubits that are coupled via  $\sigma_z^{(i)} \otimes \sigma_z^{(j)}$  type of coupling. This kind of setup is typical for *pseudospin* solid-state quantum bits such as charge or flux systems. We evaluate decoherence properties and gate quality factors in the presence of a common and two uncorrelated baths coupling to  $\sigma_z$ , respectively. We show that at low temperatures, uncorrelated baths do degrade the gate quality more severely. In particular, we show that in the case of a common bath, optimum gate performance of a controlled-PHASE gate can be reached at very low temperatures, because our type of coupling commutes with the coupling to the decoherence, which makes this type of coupling interesting as compared to previously studied proposals with  $\sigma_y^{(i)} \otimes \sigma_y^{(j)}$  coupling. Although less pronounced, this advantage also applies to the controlled-NOT gate.

DOI: 10.1103/PhysRevA.67.042319

PACS number(s): 03.67.Lx, 03.65.Yz, 05.40.-a, 85.25.-j

**I. INTRODUCTION**

Quantum computation has been shown to perform certain tasks much faster than classical computers [1–3]. Presently, very mature physical realizations of this idea originate in atomic physics, optics, and nuclear magnetic resonance. These systems are phase coherent in abundance, however, scaling up the existing few-qubit systems is not straightforward. Solid-state quantum computers have the potential advantage of being arbitrarily scalable to large systems of many qubits [4–6]. Their most important drawback is the coupling to the many degrees of freedom of a solid-state system. Even though recently, there has been fast progress in improving the decoherence properties of experimentally realized solid-state quantum bits [7–11], this remains a formidable task.

Quite a lot is known about decoherence properties of single solid-state qubits, see, e.g., Refs. [12–14], but much less is known about systems of two or more coupled qubits [15–17]. However, only for systems of at least two qubits, the central issue of entanglement can be studied. The physically available types of qubit coupling can be classified as Heisenberg-type exchange that is typical for real spin-1/2 systems, and Ising-type coupling, which is characteristic for *pseudospin* setups, where the computational degrees of freedom are not real spins. In the latter, the different spin components typically correspond to distinct variables, such as charge and flux [10,18] whose couplings can and have to be engineered on completely different footing. Previous work [16,17] presented the properties of a system of two coupled solid-state qubits that are coupled via  $\sigma_y^{(i)} \otimes \sigma_y^{(j)}$  type coupling as proposed in Ref. [14] as the current-current coupling of superconducting charge quantum bits.

On the other hand, many systems such as inductively coupled flux qubits [6], capacitively coupled charge qubits [7,8], and other pseudospin systems [19] are described by a

$\sigma_z^{(i)} \otimes \sigma_z^{(j)}$  Ising-type coupling. This indicates that the computational basis states are coupled, which, i.e., in the case of flux qubits are magnetic fluxes, whereas  $\sigma_{x/y}$  are electric charges. The  $\sigma_z$  observable is a natural way of coupling, because it is typically easy to couple to. We will study a two qubit-system coupled this way that is exposed to Gaussian noise coupling to  $\sigma_z$ , the “natural” observable. This example accounts for the crucial effect of electromagnetic noise in superconducting qubits. We will compare both the cases of noise that affects both qubits in a correlated way and the case of uncorrelated single-qubit errors. We determine the decoherence properties of the system by application of the well-known Bloch-Redfield formalism and determine quality factors of a controlled-NOT (CNOT) gate for both types of errors and feasible parameters of the system.

**II. MODEL HAMILTONIAN**

We model the Hamiltonian of a system of two qubits, coupled via Ising-type coupling. Each of the two qubits is a two-state system that is described in pseudospin notation by the single-qubit Hamiltonian [13]

$$\mathbf{H}_{sq} = -\frac{1}{2} \epsilon \hat{\sigma}_z - \frac{1}{2} \Delta \hat{\sigma}_x, \quad (1)$$

where  $\epsilon$  is the energy bias and  $\Delta$  the tunnel matrix element. The coupling between the qubits is determined by an extra term in the Hamiltonian  $\mathbf{H}_{qq} = -(K/2) \hat{\sigma}_z^{(1)} \otimes \hat{\sigma}_z^{(2)}$  that represents e.g., inductive interaction (directly or via flux transformer) in the case of flux qubits [6,20]. Thus, the complete two-qubit Hamiltonian in the absence of a dissipative environment reads

$$\mathbf{H}_{2qb} = \sum_{i=1,2} \left( -\frac{1}{2} \epsilon_i \hat{\sigma}_z^{(i)} - \frac{1}{2} \Delta_i \hat{\sigma}_x^{(i)} \right) - \frac{1}{2} K \hat{\sigma}_z^{(1)} \hat{\sigma}_z^{(2)}. \quad (2)$$

The dissipative (bosonic) environment is conveniently modeled as either a common bath or two distinct baths of har-

\*Electronic address: storcz@theorie.physik.uni-muenchen.de

M. J. STORCZ AND F. K. WILHELM

PHYSICAL REVIEW A 67, 042319 (2003)

monic oscillators, coupling to the  $\sigma_z$  components of the two qubits. This approach universally models baths which produce *Gaussian* fluctuations, such as the noise from linear electrical circuits. An example for a situation described by a common bath is long correlation length electromagnetic noise from the experimental environment or noise generated or picked up by coupling elements such as flux transformers [6]. Short correlation length radiation or local readout and control electronics coupling to individual qubits [13] might be described as coupling to two uncorrelated baths of harmonic oscillators.

One should note that if the number of qubits is increased to more than two, there might also occur dissipative effects that neither affect all qubits nor only a single qubit, but rather a cluster of qubits, thus, enhancing the complexity of our considerations [21].

In the case of two uncorrelated baths, the full Hamiltonian reads

$$\mathbf{H}_{2qb}^{2b} = \sum_{i=1,2} \left( -\frac{1}{2} \epsilon_i \hat{\sigma}_z^{(i)} - \frac{1}{2} \Delta_i \hat{\sigma}_x^{(i)} + \frac{1}{2} \hat{\sigma}_z^{(i)} \hat{X}^{(i)} \right) - \frac{1}{2} K \hat{\sigma}_z^{(1)} \hat{\sigma}_z^{(2)} + \mathbf{H}_{B_1} + \mathbf{H}_{B_2}, \quad (3)$$

where each qubit couples to its own, distinct harmonic oscillator bath  $\mathbf{H}_{B_i}$ ,  $i=1,2$ , via the coupling term  $\hat{\sigma}_z^{(i)} \hat{X}^{(i)}$ ,  $i=1,2$ , that bilinearly couples a qubit to the collective bath coordinate  $\hat{X}^{(i)} = \zeta \sum_\nu \lambda_\nu x_\nu$ . We again sum over the two qubits. In the case of two qubits coupled to one common bath, we model our two-qubit system with the Hamiltonian

$$\mathbf{H}_{2qb}^{1b} = -\frac{1}{2} \sum_{i=1,2} (\epsilon_i \hat{\sigma}_z^{(i)} + \Delta_i \hat{\sigma}_x^{(i)}) - \frac{1}{2} K \hat{\sigma}_z^{(1)} \hat{\sigma}_z^{(2)} + \frac{1}{2} (\hat{\sigma}_z^{(1)} + \hat{\sigma}_z^{(2)}) \hat{X} + \mathbf{H}_B, \quad (4)$$

where  $\mathbf{H}_B$  denotes one common bath of harmonic oscillators.

The appropriate starting point for our further analysis is the singlet/triplet basis, consisting of  $|\uparrow\uparrow\rangle := (1,0,0,0)^T$ ,  $(1/\sqrt{2})(|\uparrow\downarrow\rangle + |\downarrow\uparrow\rangle) := (0,1,0,0)^T$ ,  $|\downarrow\downarrow\rangle := (0,0,1,0)^T$ , and the singlet state  $(1/\sqrt{2})(|\uparrow\downarrow\rangle - |\downarrow\uparrow\rangle) := (0,0,0,1)^T$ . In the case of flux qubits, the  $\uparrow$  and  $\downarrow$  states correspond to clockwise and counterclockwise currents respectively.

In this basis, the undamped Hamiltonian  $\mathbf{H}_{2qb}$ , Eq. (2), of the two-qubit system assumes the matrix form

$$\mathbf{H}_{2qb} = -\frac{1}{2} \begin{pmatrix} \epsilon + K & \eta & 0 & -\Delta\eta \\ \eta & -K & \eta & \Delta\epsilon \\ 0 & \eta & K - \epsilon & \Delta\eta \\ -\Delta\eta & \Delta\epsilon & \Delta\eta & -K \end{pmatrix}, \quad (5)$$

with  $\epsilon = \epsilon_1 + \epsilon_2$ ,  $\eta = (\Delta_1 + \Delta_2)/\sqrt{2}$ ,  $\Delta\eta = (\Delta_1 - \Delta_2)/\sqrt{2}$ , and  $\Delta\epsilon = \epsilon_1 - \epsilon_2$ . From now on, for simplicity, we concentrate on the case of equal parameter settings,  $\Delta_1 = \Delta_2$  and  $\epsilon_1 = \epsilon_2$ .

If we now also express the coupling to the dissipative environment in this basis, we find in the case of coupling to two uncorrelated distinct baths that

$$\mathbf{H}_{2qb}^{2b} = -\frac{1}{2} \begin{pmatrix} \epsilon - s + K & \eta & 0 & 0 \\ \eta & -K & \eta & -\Delta s \\ 0 & \eta & K - \epsilon + s & 0 \\ 0 & -\Delta s & 0 & -K \end{pmatrix}, \quad (6)$$

with  $s = X_1 + X_2$  and  $\Delta s = X_1 - X_2$ . Here, the bath mediates transitions between the singlet and triplet states, the singlet is not a protected subspace.

In the case of two qubits with equal parameters that are coupled to one common bath, we obtain the matrix

$$\mathbf{H}_{2qb}^{1b} = -\frac{1}{2} \begin{pmatrix} \epsilon - s + K & \eta & 0 & 0 \\ \eta & -K & \eta & 0 \\ 0 & \eta & K - \epsilon + s & 0 \\ 0 & 0 & 0 & -K \end{pmatrix}, \quad (7)$$

where  $s = 2X$  and  $\Delta s = 0$ . One directly recognizes that compared to Eq. (6) in this case, thermalization to the singlet state is impeded, because Eq. (7) is block diagonal in the singlet and triplet subspaces. The singlet and triplet are completely decoupled from each other, and in the case of one common bath the singlet is also completely decoupled from the bath and thus, protected from dissipative effects. Therefore, a system in contact with one common bath that is prepared in the singlet state will never experience any decoherence effects. The singlet state is a decoherence free subspace (DFS) [22], although a trivial, one-dimensional one.

### III. EIGENERGIES AND EIGENSTATES OF THE TWO-QUBIT HAMILTONIAN

We calculate exact analytical eigenvalues and eigenvectors of the unperturbed two-qubit system Hamiltonian in the aforementioned symmetric case of Eq. (5), which reads

$$\mathbf{H}_{2qb} = -\frac{1}{2} \begin{pmatrix} \epsilon + K & \eta & 0 & 0 \\ \eta & -K & \eta & 0 \\ 0 & \eta & K - \epsilon & 0 \\ 0 & 0 & 0 & -K \end{pmatrix}. \quad (8)$$

This Hamiltonian is block diagonal and the largest block, the triplet, is three dimensional, i.e., it can be diagonalized using Cardano's formula. Details of that calculation are given in Ref. [23]. The case of nonidentical qubits is more easily handled numerically.

In the following,  $|E1\rangle$ ,  $|E2\rangle$ ,  $|E3\rangle$ , and  $|E4\rangle$  denote the eigenstates of the two-qubit system. The eigenenergies of the unperturbed Hamiltonian (8) depend on the three parameters  $K$ ,  $\epsilon$ , and  $\eta$ . Fig. 1 displays the eigenenergies in more detail for typical experimentally accessible values. The values that are chosen for the parameters  $\epsilon$ ,  $\eta$ , and  $K$  in Fig. 1 correspond to what can be reached in flux qubits. They typically assume values of a few GHz resembling the parameters

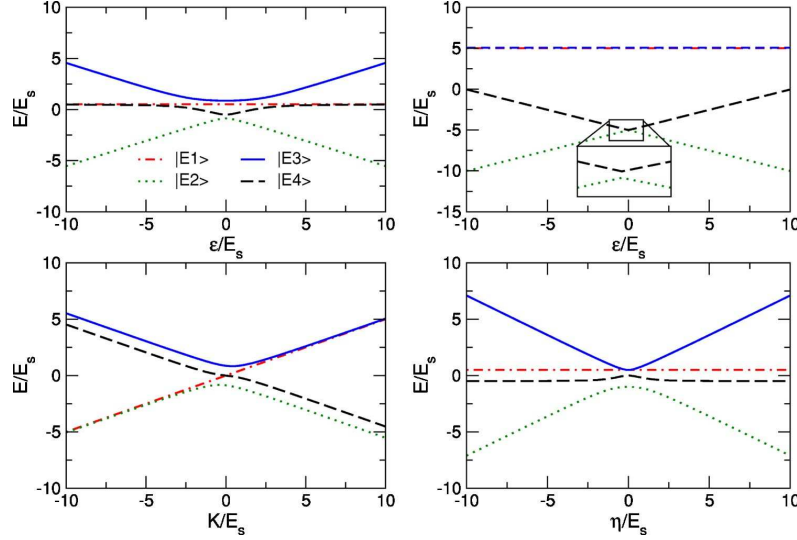


FIG. 1. Plot of the eigenenergies of the eigenstates  $|E1\rangle$ ,  $|E2\rangle$ ,  $|E3\rangle$ , and  $|E4\rangle$ . From upper left to lower right: (1)  $K = \eta = E_s$  and  $\epsilon$  is varied; (2)  $K = 10E_s$ ,  $\eta = E_s$ , and  $\epsilon$  is varied; the inset resolves the avoided level crossing due to the finite transmission amplitude  $\eta$ ; (3)  $\eta = \epsilon = E_s$  and  $K$  is varied; (4)  $K = \epsilon = E_s$  and  $\eta$  is varied.

of known single- and two-qubit experiments in Delft [13] and at MIT [24]. Therefore, we will use a characteristic energy scale  $E_s$ , which is typically  $E_s = 1$  GHz. The corresponding scales are  $t_s = 1$  ns,  $\omega_s = 2\pi \times 1$  GHz, and  $T_s = \nu_s(h/k_B) = 4.8 \times 10^{-2}$  K. Panel (1) shows that for large values of  $\epsilon$ , two of the eigenenergies are degenerate (namely, for  $\epsilon \gg \eta, K$  the states  $|E1\rangle$  and  $|E4\rangle$  equal the states  $(1/\sqrt{2})(|\uparrow\downarrow\rangle - |\downarrow\uparrow\rangle)$  and  $(1/\sqrt{2})(|\uparrow\downarrow\rangle + |\downarrow\uparrow\rangle)$ , hence the eigenenergies are degenerate) while near zero energy bias (magnetic frustration  $f = 1/2$ ) all four eigenenergies might be distinguished. Note also that, at zero energy bias, the transition frequency  $\omega_{14} = -\omega_{41}$  has a local *maximum*, which, as will be shown below, can only be accessed via nonsymmetric driving.

If  $K$  is set to a big positive value corresponding to large ferromagnetic coupling [Fig. 1, panel (2),  $K = 10E_s$ ], the Hamiltonian (8) is nearly diagonal and, hence, the eigenstates in good approximation are equal to the singlet/triplet basis states. In this case,  $|E3\rangle$  equals the triplet state  $(1/\sqrt{2})(|\uparrow\downarrow\rangle + |\downarrow\uparrow\rangle)$ ,  $|E2\rangle$  and  $|E4\rangle$  equal  $|\uparrow\uparrow\rangle$  and  $|\downarrow\downarrow\rangle$ , respectively, for positive values of  $\epsilon$ . For large negative values of  $\epsilon$ , the two states  $|E2\rangle$  and  $|E4\rangle$  become equal  $|\downarrow\downarrow\rangle$  and  $|\uparrow\uparrow\rangle$  with a pseudo-spin-flip between clockwise and counterclockwise rotating currents at  $\epsilon = 0$  when going from positive to negative  $\epsilon$ . In the case of large ferromagnetic coupling, the ground state tends towards the superposition  $(1/\sqrt{2})(|\uparrow\uparrow\rangle + |\downarrow\downarrow\rangle)$ . Panel (2) shows that only for  $\epsilon$  equal to zero, both  $|E2\rangle = |\uparrow\uparrow\rangle$  ( $|E2\rangle = |\downarrow\downarrow\rangle$ , for negative  $\epsilon$ ) and  $|E4\rangle = |\downarrow\downarrow\rangle$  ( $|E4\rangle = |\uparrow\uparrow\rangle$ , for negative  $\epsilon$ ) have the same energies (which one would expect if the  $-(1/2)K\sigma_z^{(1)}\sigma_z^{(2)}$  term in the Hamiltonian dominates), because if  $\epsilon$  is increased, the  $\epsilon_i\hat{\sigma}_z^{(i)}$  ( $i = 1, 2$ ) terms in the Hamiltonian change the energy.

For large antiferromagnetic coupling,  $|-K| \gg \epsilon, \Delta$  the states  $|\uparrow\downarrow\rangle$  and  $|\downarrow\uparrow\rangle$  are favorable. In this limit, the ground state tends towards  $(1/\sqrt{2})(|\uparrow\downarrow\rangle + |\downarrow\uparrow\rangle)$  and the energy splitting between  $(1/\sqrt{2})(|\uparrow\downarrow\rangle + |\downarrow\uparrow\rangle)$  and  $(1/\sqrt{2})(|\uparrow\uparrow\rangle - |\downarrow\downarrow\rangle)$  vanishes asymptotically, leaving the ground state nearly degenerate.

From Fig. 1, panel (3), one directly recognizes that the singlet eigenenergy crosses the triplet spectrum, which is a consequence of the fact that the singlet does not interact with any triplet states. At zero energy bias (magnetic frustration  $f = 1/2$ , for a flux qubit), none of the eigenstates equal one of the triplet basis states (e.g., as observed for a large energy bias  $\epsilon$ ), they are rather nontrivial superpositions. This is elucidated further in the following paragraph. The inset of panel (2) depicts the level anticrossing between the eigenenergies of the two states  $|E2\rangle$  and  $|E4\rangle$  due to quantum tunneling.

In general, the eigenstates are a superposition of singlet/triplet states. Figure 2 shows how singlet/triplet states combine into eigenstates for different qubit parameters. The first eigenstate  $|E1\rangle$  equals  $(1/\sqrt{2})(|\uparrow\downarrow\rangle - |\downarrow\uparrow\rangle)$  for all times while the other eigenstates  $|E2\rangle$ ,  $|E3\rangle$ , and  $|E4\rangle$  are in general superpositions of the singlet/triplet basis states. For large values of  $|\epsilon|$ , the eigenstates approach the singlet/triplet basis states. In particular, at typical working points, where  $\epsilon \approx 5\Delta$  [13], the eigenstates already nearly equal the singlet/triplet basis states. Hence, although the anticrossing described above corresponds to the anticrossing used in Refs. [9, 25] to demonstrate Schrödinger's cat states, *entanglement* is prevalent away from the degeneracy point. For an experimental proof, one still would have to show that one has successfully prepared coherent couplings by spectroscopically tracing the energy spectrum. Note that, for clarity, in

M. J. STORCZ AND F. K. WILHELM

PHYSICAL REVIEW A 67, 042319 (2003)

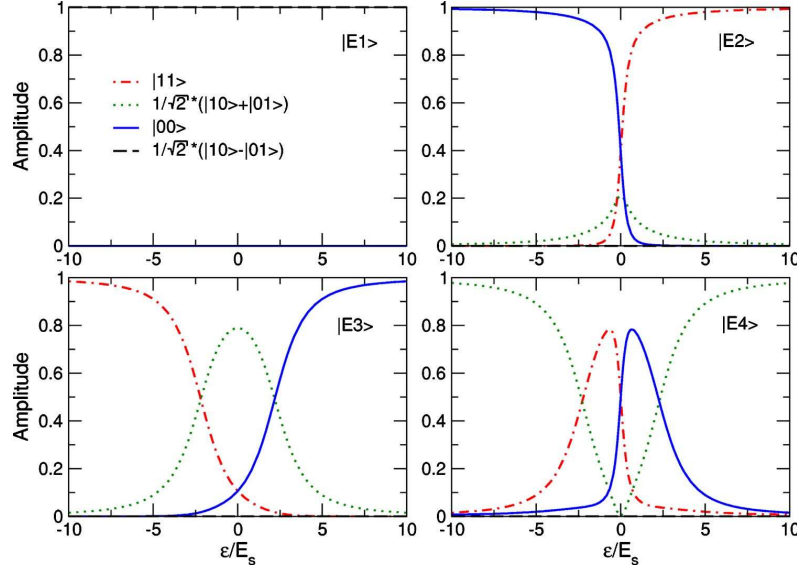


FIG. 2. Plot of the amplitude of the different singlet (triplet) states of which the eigenstates denoted by  $|E1\rangle$ ,  $|E2\rangle$ ,  $|E3\rangle$ , and  $|E4\rangle$  are composed for the four eigenstates. In all plots  $\epsilon$  is varied, and  $K$  and  $\eta$  are fixed to  $E_s$ .

Fig. 2, the interqubit coupling strength  $K$  is fixed to a rather large value of  $E_s$  that also sets the width of the anticrossing, which potentially can be very narrow.

### Spectroscopy

As a first technological step towards demonstrating coherent manipulation of qubits, usually the transition frequencies between certain energy levels are probed [9,25], i.e., the energy *differences* between the levels. Figures 3 and 4 depict the transition frequencies between the four eigenstates. The transition frequencies are defined as  $\omega_{nm} = (E_n - E_m)/\hbar$  and

$\omega_{nm} = -\omega_{mn}$ . The transitions between the singlet state  $|E1\rangle$  and the triplet states are forbidden in the case of one common bath, due to the special symmetries of the Hamiltonian (4), if the system is driven collectively through a time-dependent energy bias  $\epsilon_1(t) = \epsilon_2(t)$ . However, in the case of two distinct baths, the environment can mediate transitions between the singlet and the triplet states.

Not all transition frequencies have local minima at  $\epsilon = 0$ . The frequencies  $\omega_{41}$  and  $\omega_{34}$  have local maxima at zero energy bias  $\epsilon$ . This can already be inferred from Fig. 1, panel (1), the energy of the eigenstate  $|E4\rangle$  has a local minimum at  $\epsilon = 0$ . Similarly, the substructure of  $\omega_{34}$  can be understood from Fig. 1: the frequency  $\omega_{34}$  has a local maximum at  $\epsilon$

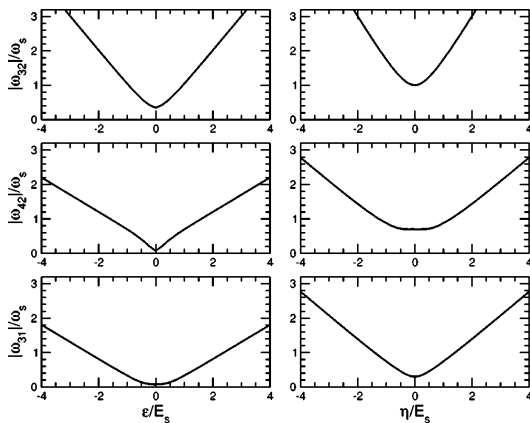


FIG. 3. Plot of the absolute value of the transition frequencies  $\omega_{32}$ ,  $\omega_{42}$ , and  $\omega_{31}$ . In the left column  $K = \eta = 0.2E_s$  and  $\epsilon$  is varied. In the right column,  $K = 0.2E_s$ ,  $\epsilon = E_s$ , and  $\eta$  is varied.

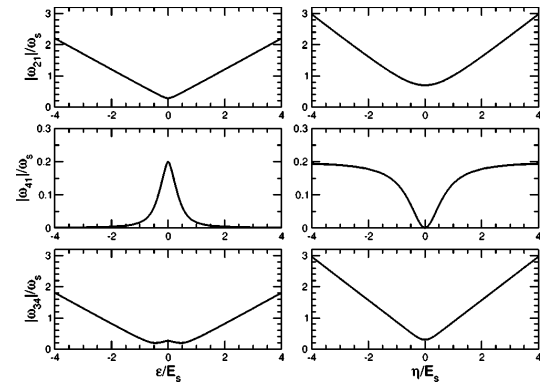


FIG. 4. Plot of the transition frequencies  $\omega_{21}$ ,  $\omega_{41}$ , and  $\omega_{34}$ . In the left column,  $K = \eta = 0.2E_s$  and  $\epsilon$  is varied. In the right column,  $K = 0.2E_s$ ,  $\epsilon = E_s$ , and  $\eta$  is varied.

=0, because of the local minimum of the eigenenergy of the state  $|E4\rangle$ . First, if  $\epsilon$  is increased, the level spacing of  $|E4\rangle$  and  $|E3\rangle$  decreases. Then, for larger values of  $\epsilon$ , the level spacing of  $|E4\rangle$  and  $|E3\rangle$  increases again. Thus, the structure observed for  $\omega_{34}$  around  $\epsilon=0$  emerges in Fig. 4.

#### IV. BLOCH-REDFIELD FORMALISM

In order to describe decoherence in the weak damping limit, we use the Bloch-Redfield Formalism [26]. It provides a systematic way of finding a set of coupled master equations which describes the dynamics of the reduced (i.e., the reservoir coordinates are traced out) density matrix for a given system in contact with a dissipative environment and has recently been shown to be numerically equivalent to the more elaborate path-integral scheme [27]. The Hamiltonian of our two-qubit system in contact with a dissipative environment, Eqs. (3) and (4), has the generic ‘‘system+bath’’ form

$$\mathbf{H}_{op}(t) = \mathbf{H}_{2qb} + \mathbf{H}_B + \mathbf{H}_{int}, \quad (9)$$

where  $\mathbf{H}_B$  is a bath of harmonic oscillators and  $\mathbf{H}_{int}$  inherits the coupling to a dissipative environment. In our case, the effects of driving are not investigated. In Born approximation and when the system is only weakly coupled to the environment, Bloch-Redfield theory provides the following set of equations for the reduced density matrix  $\rho$  describing the dynamics of the system [28,29]:

$$\dot{\rho}_{nm}(t) = -i\omega_{nm}\rho_{nm}(t) - \sum_{kl} R_{nmk\ell}\rho_{k\ell}(t), \quad (10)$$

where  $\omega_{nm} = (E_n - E_m)/\hbar$ , and  $\max_{n,m,k,\ell} |\text{Re}(R_{nmk\ell})| < \min_{n \neq m} |\omega_{nm}|$  must hold. The Redfield relaxation tensor  $R_{nmk\ell}$  comprises the dissipative effects of the coupling of the system to the environment. The elements of the Redfield relaxation tensor are given through golden rule rates [28]

$$R_{nmk\ell} = \delta_{\ell m} \sum_r \Gamma_{nrk}^{(+)} + \delta_{nk} \sum_r \Gamma_{\ell rm}^{(-)} - \Gamma_{\ell mnk}^{(+)} - \Gamma_{\ell mnk}^{(-)}. \quad (11)$$

##### A. Two qubits coupled to two distinct baths

We now evaluate the Golden rule expressions in Eq. (11) in the case of two qubits, each coupled to a distinct harmonic oscillator bath. Here,  $\tilde{H}_I(t) = \exp(iH_B t/\hbar) H_I \exp(-iH_B t/\hbar)$  denotes the coupling between system and bath in the interaction picture, and the bracket denotes thermal average of the bath degrees of freedom. Writing down all contributions gives

$$\begin{aligned} \Gamma_{\ell mnk}^{(+)} &= \hbar^{-2} \int_0^\infty dt e^{-i\omega_{nk}t} \langle e^{i(H_{B_1} + H_{B_2})t/\hbar} \\ &\times (\sigma_{z,\ell m}^{(1)} \otimes \hat{X}^{(1)} + \sigma_{z,\ell m}^{(2)} \otimes \hat{X}^{(2)}) e^{-i(H_{B_1} + H_{B_2})t/\hbar} \\ &\times (\sigma_{z,nk}^{(1)} \otimes \hat{X}^{(1)} + \sigma_{z,nk}^{(2)} \otimes \hat{X}^{(2)}) \rangle, \end{aligned} \quad (12)$$

where  $\sigma_{z,nm}^{(i)}$  ( $i=1,2$ ) are the matrix elements of  $\hat{\sigma}_z^{(i)}$  with respect to the eigenbasis of the unperturbed Hamiltonian (8) and likewise for  $\Gamma_{\ell mnk}^{(-)}$ .

We assume Ohmic spectral densities with a Drude cutoff. This is a realistic assumption, i.e., for electromagnetic noise [13] and leads to integrals in the rates which are tractable by the residue theorem. The cutoff frequency  $\omega_c$  for the spectral functions of the two qubits is typically assumed to be the largest frequency in the problem, this is discussed further in Sec. IV E,

$$J_1(\omega) = \frac{\alpha_1 \hbar \omega}{\omega^2 + \frac{\omega^2}{\omega_c^2}} \quad \text{and} \quad J_2(\omega) = \frac{\alpha_2 \hbar \omega}{\omega^2 + \frac{\omega^2}{\omega_c^2}}. \quad (13)$$

The dimensionless parameter  $\alpha$  describes the strength of the dissipative effects that enter the Hamiltonian via the coupling to the environment, described by  $s$  and  $\Delta s$ . In order for the Bloch-Redfield formalism, which involves a Born approximation in the system-bath coupling, to be valid, we have to assume  $\alpha_{1/2} \ll 1$ . After tracing out over the bath degrees of freedom, the rates read

$$\begin{aligned} \Gamma_{\ell mnk}^{(+)} &= \frac{1}{8\hbar} [\Lambda^1 J_1(\omega_{nk}) + \Lambda^2 J_2(\omega_{nk})] [\coth(\beta \hbar \omega_{nk}/2) - 1] \\ &+ \frac{i}{4\pi \hbar} [\Lambda^2 M^-(\omega_{nk}, 2) + \Lambda^1 M^-(\omega_{nk}, 1)] \end{aligned} \quad (14)$$

with  $\Lambda^1 = \Lambda_{\ell mnk}^1 = \sigma_{z,\ell m}^{(1)} \sigma_{z,nk}^{(1)}$ ,  $\Lambda^2 = \Lambda_{\ell mnk}^2 = \sigma_{z,\ell m}^{(2)} \sigma_{z,nk}^{(2)}$ , and

$$M^\pm(\Omega, i) = \mathcal{P} \int_0^\infty d\omega \frac{J_i(\omega)}{\omega^2 - \Omega^2} [\coth(\beta \hbar \omega/2) \Omega \pm \omega], \quad (15)$$

here  $\mathcal{P}$  denotes the principal value. Likewise,

$$\begin{aligned} \Gamma_{\ell mnk}^{(-)} &= \frac{1}{8\hbar} [\Lambda^1 J_1(\omega_{\ell m}) + \Lambda^2 J_2(\omega_{\ell m})] [\coth(\beta \hbar \omega_{\ell m}/2) + 1] \\ &+ \frac{i}{4\pi \hbar} [\Lambda^2 M^+(\omega_{\ell m}, 2) + \Lambda^1 M^+(\omega_{\ell m}, 1)]. \end{aligned} \quad (16)$$

The rates  $\Gamma_{\ell mnk}^{(+)}$  and  $\Gamma_{\ell mnk}^{(-)}$  might be inserted into Eq. (11) to build the Redfield tensor. Note, here, that for  $\omega_{nk} \rightarrow 0$ , and  $\omega_{\ell m} \rightarrow 0$  respectively, the real part of the rates (which is responsible for relaxation and dephasing) is of value  $\Gamma_{\ell mnk}^{(+)} = \Gamma_{\ell mnk}^{(-)} = (1/4\beta \hbar) [\sigma_{z,\ell m}^{(1)} \sigma_{z,nk}^{(1)} \alpha_1 + \sigma_{z,\ell m}^{(2)} \sigma_{z,nk}^{(2)} \alpha_2]$ .

To solve the set of differential equations (10), it is convenient to collapse  $\rho$  into a vector. In general, the Redfield equations (10) without driving are solved by an ansatz of the type  $\rho(t) = B \exp(\tilde{R}t) B^{-1} \rho(0)$ , where  $\tilde{R}$  is a diagonal matrix. The entries of this diagonal matrix are the eigenvalues of the Redfield tensor (11), written in matrix form, including the dominating term  $i\omega_{nm}$  [cf. Eq. (10)]. Here, the reduced density matrix  $\rho = (\rho_{11}, \dots, \rho_{44})^T$  is written as a vector. The

M. J. STORCZ AND F. K. WILHELM

PHYSICAL REVIEW A 67, 042319 (2003)

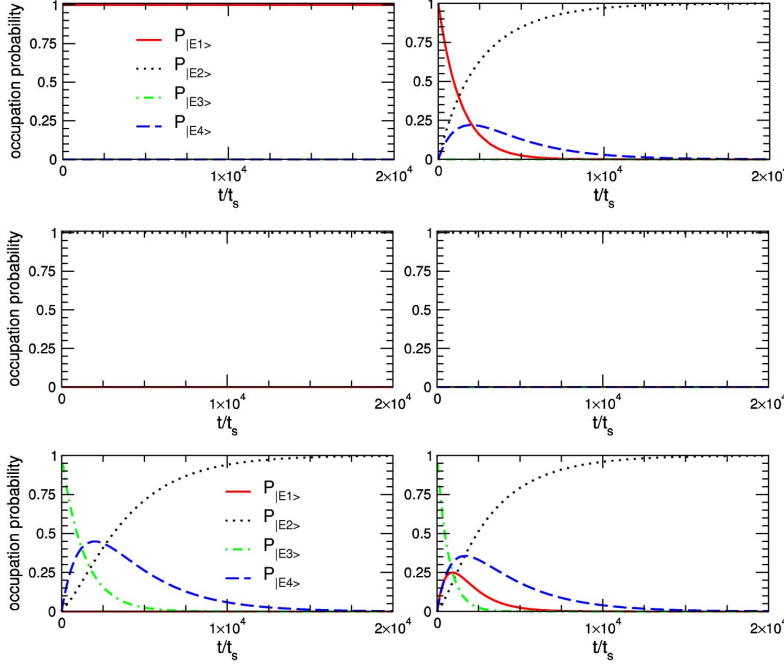


FIG. 5. Plot of the occupation probability of the four eigenstates  $|E1\rangle$ ,  $|E2\rangle$ ,  $|E3\rangle$ , and  $|E4\rangle$  for initially starting in one of the eigenstates  $|E1\rangle$  (first row),  $|E2\rangle$  (second row), or  $|E3\rangle$  (third row) at  $T=0$ . The left column illustrates the case of two qubits coupling to one common bath and the right column the case of two qubits coupling to two distinct baths. The energies  $K$ ,  $\epsilon$ , and  $\eta$  are all fixed to  $E_s$ . The characteristic time scale  $t_s$  is  $t_s = 1/\nu_s$ .

matrix  $B$  describes the basis change to the eigenbasis of  $\tilde{R}$ , in which  $\tilde{R}$  has diagonal form.

### B. Two qubits coupled to one common bath

For the case of two qubits coupled to one common bath, we perform the same calculation as in the preceding section, which leads to expressions for the rates analogous to Eqs. (16)

$$\Gamma_{\ell mnk}^{(+)} = \frac{1}{8\hbar} \Lambda J(\omega_{nk}) [\coth(\beta\hbar\omega_{nk}/2) - 1] + \frac{i\Lambda}{4\pi\hbar} \times \mathcal{P} \int_0^\infty d\omega \frac{J(\omega)}{\omega^2 - \omega_{nk}^2} [\coth(\beta\hbar\omega/2) \omega_{nk} - \omega], \quad (17)$$

with  $\Lambda = \Lambda_{\ell mnk} = \sigma_{z,\ell m}^{(1)} \sigma_{z,nk}^{(1)} + \sigma_{z,\ell m}^{(1)} \sigma_{z,nk}^{(2)} + \sigma_{z,\ell m}^{(2)} \sigma_{z,nk}^{(1)} + \sigma_{z,\ell m}^{(2)} \sigma_{z,nk}^{(2)}$  and

$$\Gamma_{\ell mnk}^{(-)} = \frac{1}{8\hbar} \Lambda J(\omega_{\ell m}) [\coth(\beta\hbar\omega_{\ell m}/2) + 1] + \frac{i\Lambda}{4\pi\hbar} \times \mathcal{P} \int_0^\infty d\omega \frac{J(\omega)}{\omega^2 - \omega_{\ell m}^2} [\coth(\beta\hbar\omega/2) \omega_{\ell m} + \omega]. \quad (18)$$

The difference between the rates for the case of two distinct baths (14) and (16) are the two extra terms  $\sigma_{z,\ell m}^{(1)} \sigma_{z,nk}^{(2)}$  and

$\sigma_{z,\ell m}^{(2)} \sigma_{z,nk}^{(1)}$ . They originate when tracing out the bath degrees of freedom. In the case of one common bath, there is only one spectral function, which we also assume to be Ohmic  $J(\omega) = (\alpha\hbar\omega)/(1 + \omega^2/\omega_c^2)$ . For  $\omega_{nk} \rightarrow 0$ , and  $\omega_{\ell m} \rightarrow 0$ , respectively, the real part of the rates is of the value  $\Gamma_{\ell mnk}^{(+)} = \Gamma_{\ell mnk}^{(-)} = (\alpha/4\beta\hbar)\Lambda$ , for  $\omega_{\ell m}, \omega_{nk} \rightarrow 0$ .

### C. Dynamics of coupled flux qubits with dissipation

The dissipative effects affecting the two-qubit system lead to decoherence, which manifests itself in two ways. The system experiences energy relaxation on a time scale  $\tau_R = \Gamma_R^{-1}$  ( $\Gamma_R$  is the sum of the relaxation rates of the four diagonal elements of the reduced density matrix;  $\Gamma_R = -\sum_n \Theta_n$  and  $\Theta_n$  are the eigenvalues of the matrix that consists of the tensor elements  $R_{n,m,n,m}$ ,  $n, m = 1, \dots, 4$ ), called relaxation time, into a thermal mixture of the system's energy eigenstates. Therefore, the diagonal elements of the reduced density matrix decay to the value given by the Boltzmann factors. The quantum coherent dynamics of the system are superimposed on the relaxation and decay on a usually shorter time scale  $\tau_{\varphi_{ij}} = \Gamma_{\varphi_{ij}}^{-1}$  ( $i, j = 1, \dots, 4; i \neq j$  and  $\Gamma_{\varphi_{nm}} = -\text{Re} R_{n,m,n,m}^{1b,2b}$ ) termed dephasing time. Thus, dephasing causes the off-diagonal terms (coherences) of the reduced density matrix to tend towards zero.

First, we investigate the incoherent relaxation of the two-qubit system out of an eigenstate. At long times, the system is expected to reach thermal equilibrium,  $\rho_{eq} = (1/Z)e^{-\beta H}$ . Special cases are  $T=0$ , where  $\rho_{eq}$  equals the projector on

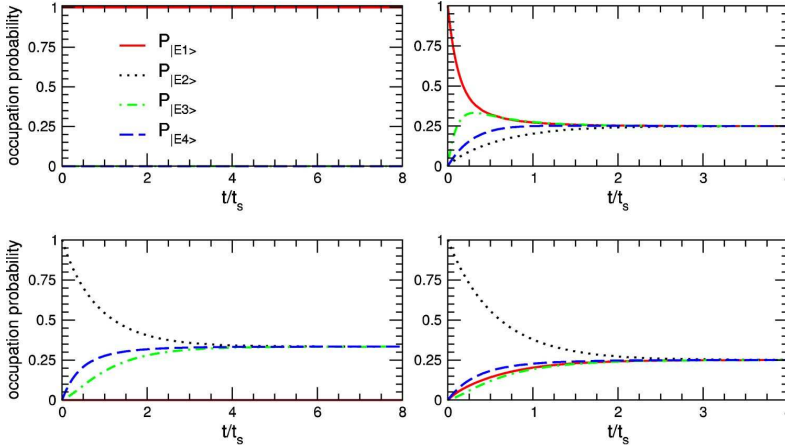


FIG. 6. Plot of the occupation probability of the four eigenstates  $|E1\rangle$ ,  $|E2\rangle$ ,  $|E3\rangle$ , and  $|E4\rangle$  for initially starting in one of the eigenstates  $|E1\rangle$  (upper row) or  $|E2\rangle$  (lower row) at  $T=2.1T_s$ . The left column illustrates the case of two qubits coupling to one common bath and the right column the case of two qubits coupling to two distinct baths. The energies  $K$ ,  $\epsilon$ , and  $\eta$  are all fixed to  $E_s$ . The characteristic time scale  $t_s$  is  $t_s=1/\nu_s$ .

the ground state and  $T \rightarrow \infty$ , where all eigenstates are occupied with the same probability, i.e.,  $\rho_{\text{eq}} = (1/4)\hat{I}$ . Figures 5 and 6 illustrate the relaxation of the system prepared in one of the four eigenstates for temperatures  $T=0$  and  $T=2.1T_s$  respectively. The qubit energies  $K$ ,  $\epsilon$ , and  $\eta$  are all set to  $E_s$  and  $\alpha$  is set to  $\alpha=10^{-3}$ . From Fig. 1, one recognizes relaxation into the eigenstate  $|E2\rangle$ , the ground state for this set of parameters.

At low temperatures ( $T=0$ ), we observe that for the case of two distinct uncorrelated baths, a system prepared in one of the four eigenstates always relaxes into the ground state. In the case of two qubits coupling to one common bath, this is not always the case, as can be seen in the upper left panels of Figs. 5 and 6. This can be explained through our previous observation, that the singlet is a protected subspace: Neither the free nor, unlike in the case of distinct baths, the bath-mediated dynamics couple the singlet to the triplet space. Moreover, we can observe that relaxation to the ground state happens by populating intermediate eigenstates with a lower energy than the initial state the system was prepared in at  $t=0$  (cf. Fig. 1).

For high temperatures ( $T \approx 2.1T_s$ ), the system thermalizes into thermal equilibrium, where all eigenstates have equal occupation probabilities. Again, in the case of one common bath, thermalization of the singlet state is impeded and the three eigenstates  $|E2\rangle$ ,  $|E3\rangle$  and  $|E4\rangle$  have equal occupation probabilities of  $1/3$  after the relaxation time.

If the system is prepared in a superposition of eigenstates, e.g.,  $|E3\rangle$  and  $|E4\rangle$  as in Fig. 7, which are not in a protected subspace, we observe coherent oscillations between the eigenstates that are damped due to dephasing and after the decoherence time, the occupation probability of the eigenstates is given by the Boltzmann factors. This behavior is depicted in Fig. 7. Here, for  $\alpha=10^{-3}$ , the cases of  $T=0$  and  $T=2.1T_s$  are compared. When the temperature is low enough, the system will relax into the ground state  $|E2\rangle$ , as illustrated by the right column of Fig. 7. Thus, the occupation probability of the state  $(1/\sqrt{2})(|E3\rangle+|E4\rangle)$  goes to zero. Here, in the case of zero temperature, the decoherence

times for the case of one common or two distinct baths are of the same order of magnitude. The left column illustrates the behavior when the temperature is increased. At  $T=2.1T_s$ , the system relaxes into an equally populated state on times much shorter than for  $T=0$ . For low temperatures, the characteristic time scale for dephasing and relaxation is somewhat shorter for the case of one common bath ( $\tau^{1b}/\tau^{2b} \approx 0.9$ , for  $\alpha=10^{-3}$ ). This can be explained by observing the temperature dependence of the rates shown in Fig. 8. Though for the case of one common bath, two of the dephasing rates are zero at  $T=0$ , the remaining rates are always slightly bigger for the case of one common bath compared to the case of two distinct baths. If the system is prepared in a general superposition, here  $|E3\rangle$  and  $|E4\rangle$ , nearly all rates become important thus compensating the effect of the two rates that are approximately zero at zero temperature and leading to faster decoherence.

If  $\alpha$  and, therefore, the strength of the dissipative effects is increased from  $\alpha=10^{-3}$  to  $\alpha=10^{-2}$ , the observed coherent motion is significantly damped. Variation of  $\alpha$  leads to a phase shift of the coherent oscillations, due to renormalization of the frequencies [16]. However, in our case, the effects of renormalization are very small, as discussed in Sec. IV E, and cannot be observed in our plots.

#### D. Temperature dependence of the rates

Figure 8 displays the dependence of typical dephasing rates and the relaxation rate  $\Gamma_R$  on temperature. These decoherence rates are the inverse decoherence times. The rates are of the same magnitude for the cases of one common bath and two distinct baths. As a notable exception, in the case of one common bath, the dephasing rates  $\Gamma_{\varphi_{21}} = \Gamma_{\varphi_{12}}$  go to zero when the temperature is decreased, while all other rates saturate for  $T \rightarrow 0$ . This phenomenon is explained later on. If the temperature is increased from  $T_s = (h/k_B)\nu_s = 4.8 \times 10^{-2}$  K, the increase of the dephasing and relaxation rates follows a power-law dependence. It is linear in temperature  $T$  with a slope given by the prefactors of the expression in the Red-

M. J. STORCZ AND F. K. WILHELM

PHYSICAL REVIEW A 67, 042319 (2003)

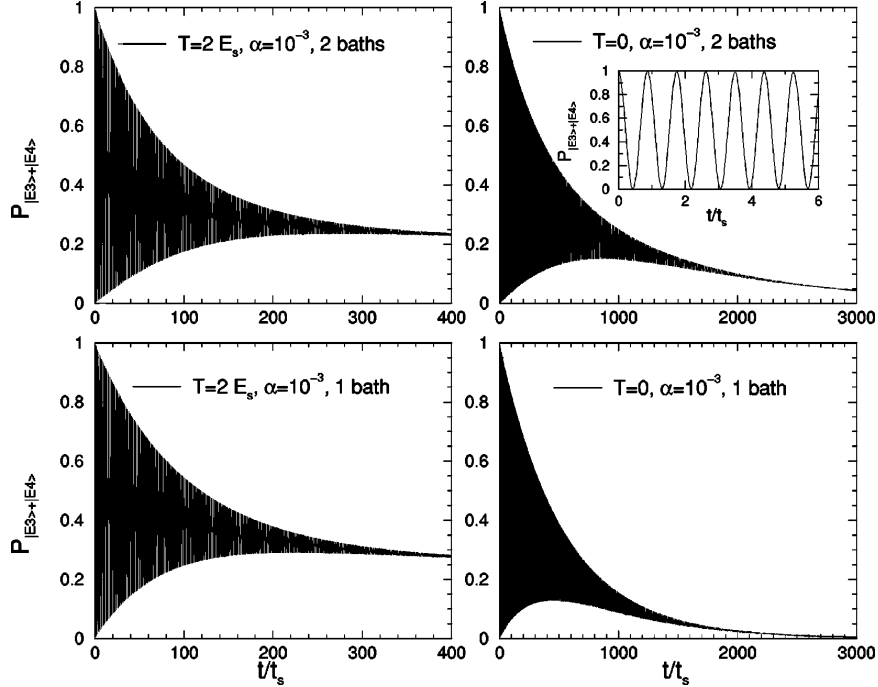


FIG. 7. Plot of the occupation probability  $P_{(1/\sqrt{2})(|E3\rangle+|E4\rangle)}(t)$  when starting in the initial state  $(1/\sqrt{2})(|E3\rangle+|E4\rangle)$ , which is a superposition of eigenstates  $|E3\rangle$  and  $|E4\rangle$ . The first row shows the behavior for two qubits coupling to two uncorrelated baths. The lower row shows the behavior for two qubits coupled to one common bath. The qubit parameters  $\epsilon$ ,  $\eta$ , and  $K$  are set to  $E_s$  and  $\alpha$  is set to  $\alpha = 10^{-3}$ . The inset resolves the time scale of the coherent oscillations.

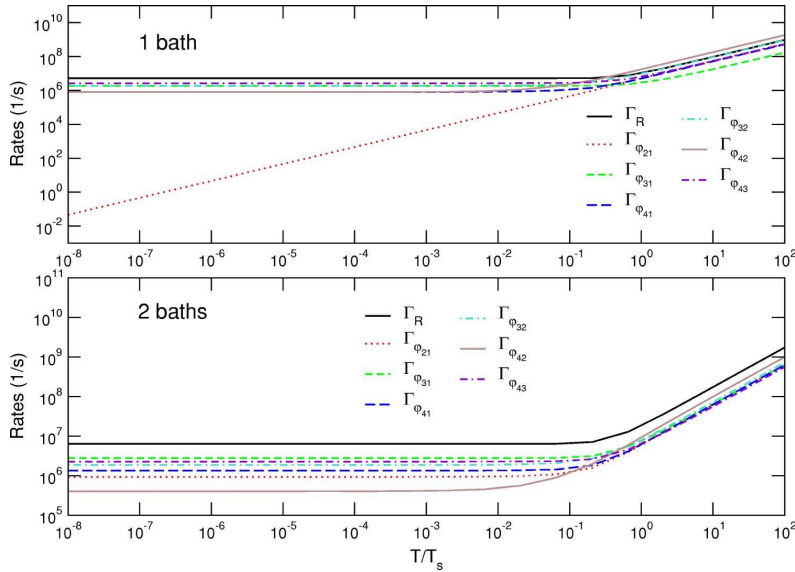


FIG. 8. Log-log plot of the temperature dependence of the sum of the four relaxation rates and selected dephasing rates. Qubit parameters  $K$ ,  $\epsilon$ , and  $\eta$  are all set to  $E_s$  and  $\alpha = 10^{-3}$ . The upper panel shows the case of one common bath and the lower panel the case of two distinct baths. At the characteristic temperature of approximately  $0.1T_s$ , the rates increase very steeply.



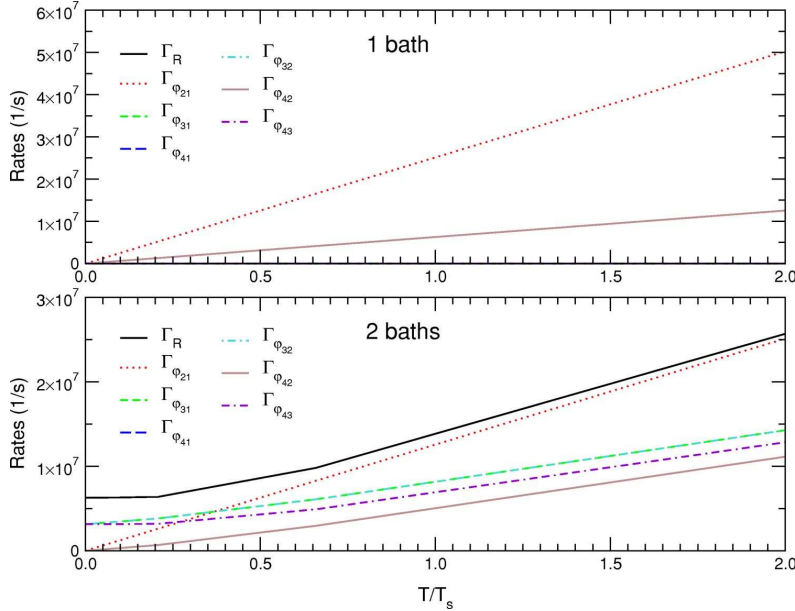


FIG. 9. Plot of the temperature dependence of the sum of the four relaxation rates and selected dephasing rates. Qubit parameters  $\epsilon$  and  $\eta$  are set to 0,  $K$  is set to  $E_s$ , and  $\alpha=10^{-3}$  corresponding to the choice of parameters used for the  $U_{\text{XOR}}$  operation. The upper panel shows the case of one common bath and the lower panel the case of two distinct baths. In the case of one common bath the system will experience no dissipative effects at  $T=0$ .

field rates that depends on temperature. At temperature  $T \approx 0.1T_s$ , the rates show a sharp increase for both cases. This roll-off point is set by the characteristic energy scale of the problem, which in turn is set by the energy bias  $\epsilon$ , the transmission matrix element  $\eta$ , and the coupling strength  $K$ . For the choice of parameters in Fig. 8, the characteristic energy scale expressed in temperature is  $T \approx 0.1T_s$ .

Note that there is also dephasing between the singlet and the triplet states. When the system is prepared (by application of a suitable interaction) in a coherent superposition of singlet and triplet states, the phase evolves coherently. Then two possible decoherence mechanisms can destroy phase coherence. First, “flipless” dephasing processes, where  $\langle E \rangle$  remains unchanged. These flipless dephasing processes are described by the terms for  $\omega_{\ell m}, \omega_{nk} \rightarrow 0$  in the rates, Eqs. (16) and (18). Obviously, these terms vanish for  $T \rightarrow 0$ , as the low-frequency component of Ohmic Gaussian noise is strictly thermal. Second, relaxation due to emission of a boson to the bath is also accompanied by a loss of phase coherence. This process in general has a *finite* rate at  $T=0$ . This explains the  $T$  dependence of the rates in the single-bath case:  $|E1\rangle$  alone is protected from the environment. As there are incoherent transitions between the triplet eigenstates even at  $T=0$ , the relative phase of a coherent oscillation between  $|E1\rangle$  and any of those is randomized, and the decoherence rates  $\Gamma_{\varphi_{3/4,1}}$  are finite even at  $T=0$ . As a notable exception,  $|E2\rangle$ , the lowest-energy state in the triplet subspace, can only be flipped through absorption of energy, which implies that the dephasing rate  $\Gamma_{\varphi_{21}}$  also vanishes at low temperature. The described behavior can be observed in Fig. 8.

If the parameters  $\epsilon$  and  $\eta$  are tuned to zero, thus  $K$  being the only nonvanishing parameter in the Hamiltonian, all dephasing and relaxation rates will vanish for  $T=0$  in the

case of one common bath. This behavior is depicted in Fig. 9. It originates from the special symmetries of the Hamiltonian in this case and the fact that for this particular two-qubit operation, the system Hamiltonian and the coupling to the bath are diagonal in the same basis. This special case is of crucial importance for the quantum gate operation as described in Sec. V and affects the gate quality factors.

### E. Renormalization effects

Next to causing decoherence, the interaction with the bath also renormalizes the qubit frequencies. This is mostly due to the fast bath modes, and can be understood analogous to the Franck-Condon effect, the Lamb shift, or the adiabatic renormalization [30]. Renormalization of the oscillation frequencies  $\omega_{nm}$  is controlled by the imaginary part of the Redfield tensor [16]

$$\omega_{nm} \rightarrow \tilde{\omega}_{nm} := \omega_{nm} - \text{Im}R_{nmnm}. \quad (19)$$

Note that  $\text{Im}R_{nmnm} = -\text{Im}R_{mnmn}$  due to the fact that the correlators in the Golden Rule expressions have the same parity. The imaginary part of the Redfield tensor is given by

$$\text{Im}\Gamma_{\ell mnk}^{(+)} = C_{\ell mnk}^{1b,2b} \frac{1}{\pi\hbar} \mathcal{P} \int_0^\infty d\omega J(\omega) \left( \frac{1}{\omega^2 - \omega_{nk}^2} \right) \times [\coth(\beta\hbar\omega/2)\omega_{nk} - \omega] \quad (20)$$

M. J. STORCZ AND F. K. WILHELM

PHYSICAL REVIEW A 67, 042319 (2003)

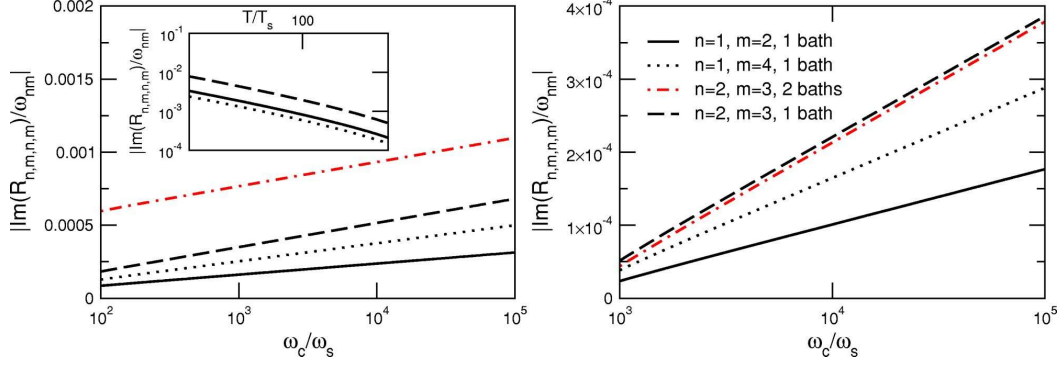


FIG. 10. The left plot depicts the ratio of the renormalization effects and the corresponding transition frequencies. Parameters:  $\alpha = 10^{-3}$ ,  $T=0$ , and  $\omega_c/\omega_s$  is varied between  $10^2$  and  $10^5$  for several frequencies ( $\omega_{12}$ ,  $\omega_{14}$ , and  $\omega_{23}$ ) for the case of two baths and in the case of  $\omega_{23}$  also for the case of one common bath. The parameters for the right plot are  $\alpha = 10^{-3}$ ,  $T = 2.1T_s$ , and  $\omega_c/\omega_s$  is varied between  $10^3$  and  $10^5$ . The inset of the left plot shows a log-log plot of the temperature dependence of the renormalization effects. Here  $\alpha = 10^{-3}$  and  $\omega_c = 10^{13}$ . Note that for small temperatures the renormalization effects do *not* depend on temperature. (This is elucidated further in Sec. IV E.) The plots are scaled logarithmically to emphasize the logarithmic divergence of the renormalization effects with  $\omega_c$ .

$$\text{Im}\Gamma_{\ell mnk}^{(-)} = C_{\ell mnk}^{1b,2b} \frac{1}{\pi\hbar} \mathcal{P} \int_0^\infty d\omega J(\omega) \left( \frac{1}{\omega^2 - \omega_{\ell m}^2} \right) \times [\coth(\beta\hbar\omega/2) \omega_{\ell m} + \omega], \quad (21)$$

where  $\mathcal{P}$  denotes the principal value, and  $C_{\ell mnk}^{1b,2b}$  are prefactors defined, in the case of two distinct baths, according to  $C_{\ell mnk}^{2b} = \frac{1}{4} [\sigma_{z,\ell m}^{(1)} \sigma_{z,nk}^{(1)} + \sigma_{z,\ell m}^{(2)} \sigma_{z,nk}^{(2)}]$  and in the case of one common bath  $C_{\ell mnk}^{1b} = \frac{1}{4} \Lambda$ . Here, for simplicity, we assumed  $\alpha_1 = \alpha_2 = \alpha$  and thus,  $J_1(\omega) = J_2(\omega) = J(\omega)$ . Evaluation of the integral leads to the following expression for  $\Gamma_{\ell mnk}^{(+)}$ :

$$\text{Im}\Gamma_{\ell mnk}^{(+)} = C_{\ell mnk}^{1b,2b} \frac{\alpha\omega_c^2\omega_{nk}}{2\pi(\omega_c^2 + \omega_{nk}^2)} \left[ \psi(1+c_2) + \psi(c_2) - 2\text{Re}[\psi(ic_1)] - \pi \frac{\omega_c}{\omega_{nk}} \right], \quad (22)$$

with  $c_1 := (\beta\hbar\omega_{nk})/(2\pi)$  and  $c_2 := (\beta\hbar\omega_c)/(2\pi)$ . In the case of  $\Gamma_{\ell mnk}^{(-)}$ , the expression is

$$\text{Im}\Gamma_{\ell mnk}^{(-)} = C_{\ell mnk}^{1b,2b} \frac{\alpha\omega_c^2\omega_{\ell m}}{2\pi(\omega_c^2 + \omega_{\ell m}^2)} \left[ \psi(1+c_2) + \psi(c_2) - 2\text{Re}[\psi(ic_1)] + \pi \frac{\omega_c}{\omega_{\ell m}} \right], \quad (23)$$

with  $c_1 := (\omega_{\ell m}\beta\hbar)/(2\pi)$ . The terms in Eqs. (22) and (23) which are linear in  $\omega_c$  give no net contribution to the imaginary part of the Redfield tensor [16]. To illustrate the size of the renormalization effects, the ratio of the renormalization effects to the frequencies which are renormalized is depicted in Fig. 10.

If  $c_1$  and  $c_2$  are large, and the digamma functions can be approximated by a logarithm, the resulting expression for the renormalization effects will be independent of temperature.

The temperature dependence of Eqs. (22) and (23) at higher temperatures, where  $c_1$  and  $c_2$  are small and the renormalization effects are very weak, is shown in Fig. 10. The rates (22) and (23) diverge logarithmically with  $\omega_c$  in analogy to the well-known ultraviolet-divergence of the spin boson model [30]. When comparing the left ( $T=0$ ) and right ( $T=2.1T_s$ ) panel, one recognizes that for the first case, one common bath gives somewhat smaller renormalization effects than two distinct baths, while in the second case for  $T=2.1T_s$ , the renormalization effects deviate only slightly (see the behavior for  $\omega_{23}$ ) and the renormalization effects are smaller for the case of two distinct baths. The effects of renormalization are always very small [ $|\text{Im}(R_{n,m,n,m})/\omega_{nm}|$  below 1% for our choice of parameters] and are therefore, neglected in our calculations. However, having calculated Eqs. (22) and (23), these are easily incorporated in our numerical calculations. The case of large renormalization effects is discussed in Ref. [31].

We only plotted the size of the renormalization effects for  $\omega_{12}$ ,  $\omega_{14}$ , and  $\omega_{34}$ , because in general, all values of  $\omega_{nk}$  are of the same magnitude and give similar plots. The size of the renormalization effects diverges linearly with  $\alpha$ , the dimensionless parameter that describes the strength of the dissipative effects.

For flux qubits, the cutoff frequency  $\omega_c$  is given by the circuit properties. For a typical first order low-pass LR filter [32] in a qubit circuit [13], one can insert  $R = 50 \Omega$  (typical impedance of coaxial cables) and  $L \approx 1$  nH (depends on the length of the circuit lines) into  $\omega_{LR} = R/L$ , and gets that  $\omega_{LR} \approx 5 \times 10^{10}$  Hz.  $\omega_{LR}$  is the largest frequency in the problem (see again Ref. [13], Chap. 4.5) and  $\omega_c \gg \omega_{LR}$  should hold. Then  $\omega_c \approx 10^{13}$  Hz ( $= 10^4 E_s$ ) as cutoff frequency is a reasonable assumption.

## V. GATE QUALITY FACTORS

In Sec. IV, we evaluated the dephasing and relaxation rates of the two-qubit system that is affected by a dissipative

environment. Furthermore, we visualized the dynamics of the two-qubit system. This does not yet allow a full assessment of the performance as a quantum logic element. These should perform unitary gate operations and based on the rates alone, one can not judge how well quantum gate operations might be performed with the two-qubit system. Therefore, to get a quantitative measure of how our setup behaves when performing a quantum logic gate operation, one can evaluate gate quality factors [33]. The performance of a two-qubit gate is characterized by four quantities: the fidelity, purity, quantum degree, and entanglement capability. The fidelity is defined as

$$\mathcal{F} = \frac{1}{16} \sum_{j=1}^{16} \langle \Psi_{in}^j | U_G^\dagger \rho_G^j U_G | \Psi_{in}^j \rangle, \quad (24)$$

where  $U_G$  is the unitary matrix describing the desired ideal gate and the density matrix obtained from attempting a quantum gate operation in a hostile environment is  $\rho_G^j = \rho(t_G)$ , which is evaluated for all initial conditions  $\rho(0) = |\Psi_{in}^j\rangle\langle\Psi_{in}^j|$ . The fidelity is a measure of how well a quantum logic operation was performed. Without dissipation, the reduced density matrix  $\rho_G^j$  after performing the quantum gate operation, applying  $U_G$  and the inverse  $U_G^\dagger$  would equal  $\rho(0)$ . Therefore, the fidelity for the ideal quantum gate operation should be 1.

The second quantifier is the purity

$$\mathcal{P} = \frac{1}{16} \sum_{j=1}^{16} \text{tr}((\rho_G^j)^2), \quad (25)$$

which should be 1 without dissipation and 1/4 in a fully mixed state. The purity characterizes the effects of decoherence.

The third quantifier, the quantum degree, is defined as the maximum overlap of the resulting density matrix after the quantum gate operation with the maximally entangled states, the Bell states

$$\mathcal{Q} = \max_{j,k} \langle \Psi_{me}^k | \rho_G^j | \Psi_{me}^k \rangle, \quad (26)$$

where the Bell states  $\Psi_{me}^k$  are defined according to

$$|\Psi_{me}^{00}\rangle = \frac{|\downarrow\downarrow\rangle + |\uparrow\uparrow\rangle}{\sqrt{2}}, \quad |\Psi_{me}^{01}\rangle = \frac{|\downarrow\uparrow\rangle + |\uparrow\downarrow\rangle}{\sqrt{2}}, \quad (27)$$

$$|\Psi_{me}^{10}\rangle = \frac{|\downarrow\downarrow\rangle - |\uparrow\uparrow\rangle}{\sqrt{2}}, \quad |\Psi_{me}^{11}\rangle = \frac{|\downarrow\uparrow\rangle - |\uparrow\downarrow\rangle}{\sqrt{2}}. \quad (28)$$

For an ideal entangling operation, e.g., the controlled-NOT gate, the quantum degree should be one. The quantum degree characterizes nonlocality. It has been shown [34] that all density operators that have an overlap with a maximally entangled state that is larger than the value 0.78 [17] violate the Clauser-Horne-Shimony-Holt inequality and are thus nonlocal.

The fourth quantifier, the entanglement capability  $\mathcal{C}$ , is the smallest eigenvalue of the partially transposed density matrix for all possible unentangled input states  $|\Psi_{in}^j\rangle$ . (see below). It has been shown [35] to be negative for an entangled state. This quantifier should be  $-0.5$ , e.g., for the ideal  $U_{\text{XOR}}$ , thus characterizing a maximally entangled final state. Two of the gate quality factors, namely, the fidelity and purity might also be calculated for single-qubit gates [12]. However, entanglement can only be observed in a system of at least two qubits. Therefore, the quantum degree and entanglement capability cannot be evaluated for single-qubit gates.

To form all possible initial density matrices, needed to calculate the gate quality factors, we use the 16 unentangled product states  $|\Psi_{in}^j\rangle$ ,  $j=1, \dots, 16$  defined [17] according to  $|\Psi_a\rangle_1 |\Psi_b\rangle_2$  ( $a, b=1, \dots, 4$ ), with  $|\Psi_1\rangle = |\downarrow\rangle$ ,  $|\Psi_2\rangle = |\uparrow\rangle$ ,  $|\Psi_3\rangle = (1/\sqrt{2})(|\downarrow\rangle + |\uparrow\rangle)$ , and  $|\Psi_4\rangle = (1/\sqrt{2})(|\downarrow\rangle + i|\uparrow\rangle)$ . They form one possible basis set for the superoperator  $\nu_G$  with  $\rho(t_G) = \nu_G \rho(0)$  [17,33]. The states are chosen to be unentangled for being compatible with the definition of  $\mathcal{C}$ .

## A. Implementation of two-qubit operations

### 1. Controlled phase-shift gate

To perform the controlled-NOT operation, it is necessary to be able to apply the controlled phase-shift operation together with arbitrary single-qubit gates. In the computational basis ( $|00\rangle, |01\rangle, |10\rangle, |11\rangle$ ), the controlled phase-shift operation is given by

$$U_{CZ}(\varphi) = \begin{pmatrix} 1 & 0 & 0 & 0 \\ 0 & 1 & 0 & 0 \\ 0 & 0 & 1 & 0 \\ 0 & 0 & 0 & e^{i\varphi} \end{pmatrix}, \quad (29)$$

and for  $\varphi = \pi$ , up to a global phase factor,

$$U_{CZ} = \exp\left(i\frac{\pi}{4}\sigma_z^{(1)}\right) \exp\left(i\frac{\pi}{4}\sigma_z^{(2)}\right) \exp\left(i\frac{\pi}{4}\sigma_z^{(1)}\sigma_z^{(2)}\right). \quad (30)$$

Note that in Eq. (30) only  $\sigma_z$  operations, which commute with the coupling to the bath, are needed. The controlled phase-shift operation together with two Hadamard gates and a single-qubit phase-shift operation then gives the controlled-NOT gate.

### 2. Controlled-NOT gate

Due to the fact that the set consisting of the  $U_{\text{XOR}}$  (or controlled-NOT) gate and the one-qubit rotations, is complete for quantum computation [36], the  $U_{\text{XOR}}$  gate is a highly important two-qubit gate operation. Therefore we further investigate the behavior of the four gate quality factors in this case. The  $U_{\text{XOR}}$  operation switches the second bit, depending on the value of the first bit of a two bit system. In the computational basis, this operation has the following matrix form:

M. J. STORCZ AND F. K. WILHELM

TABLE I. Parameters of the Hamiltonians which are needed to perform the  $U_{\text{XOR}}$  gate operation; only the nonzero parameters are listed:  $\xi = E_s$  in our case.

No.	Operation	Parameters ( $E_s$ )	Time (s)
1	$\exp\left[-i\frac{\pi}{2}\left(\frac{\sigma_x^2 + \sigma_z^2}{\sqrt{2}}\right)\right]$	$\epsilon_2 = -\xi, \Delta_2 = -\xi$	$\tau_1 = \frac{\sqrt{2}}{2\xi}$
2	$\exp\left(i\frac{\pi}{2}\sigma_z^1\right)$	$\epsilon_1 = \xi$	$\tau_2 = \frac{1}{2\xi}$
3	$\exp\left(i\frac{\pi}{4}\sigma_z^1\sigma_z^2\right)$	$K = \xi$	$\tau_3 = \frac{1}{4\xi}$
4	$\exp\left(i\frac{\pi}{4}\sigma_z^2\right)$	$\epsilon_2 = \xi$	$\tau_4 = \frac{1}{4\xi}$
5	$\exp\left(i\frac{\pi}{4}\sigma_z^1\right)$	$\epsilon_1 = \xi$	$\tau_5 = \frac{1}{4\xi}$
6	$\exp\left[-i\frac{\pi}{2}\left(\frac{\sigma_x^2 + \sigma_z^2}{\sqrt{2}}\right)\right]$	$\epsilon_2 = -\xi, \Delta_2 = -\xi$	$\tau_6 = \frac{\sqrt{2}}{2\xi}$

$$U_{\text{XOR}} = \begin{pmatrix} 1 & 0 & 0 & 0 \\ 0 & 1 & 0 & 0 \\ 0 & 0 & 0 & 1 \\ 0 & 0 & 1 & 0 \end{pmatrix}. \quad (31)$$

Up to a phase factor, the two-qubit  $U_{\text{XOR}}$  (or CNOT) operation can be realized by a sequence of five single-qubit and one two-qubit quantum logic operations. Each of these six operations corresponds to an appropriate Hamiltonian undergoing free unitary time evolution  $\exp[-(i/\hbar)\mathbf{H}_{op}t]$ . The single-qubit operations are handled with Bloch-Redfield formalism, like the two-qubit operations. We assume dc pulses (instantaneous on and off switching of the Hamiltonian with zero rise time of the signal) or rectangular pulses

$$U_{\text{XOR}} = \exp\left[-i\frac{\pi}{2}\left(\frac{\sigma_x^{(2)} + \sigma_z^{(2)}}{\sqrt{2}}\right)\right] U_{CZ}(\pi) \times \exp\left(i\frac{\pi}{2}\sigma_z^{(1)}\right) \exp\left[-i\frac{\pi}{2}\left(\frac{\sigma_x^{(2)} + \sigma_z^{(2)}}{\sqrt{2}}\right)\right], \quad (32)$$

where  $U_{CZ}(\pi)$  is given by Eq. (30). This generic implementation has been chosen in order to demonstrate the comparison to other coupling schemes [17] as well as for computational convenience, it is not necessarily the optimum scheme for application under cryogenic conditions, where slow rise-time ac pulses are preferred. Table I shows the parameters we inserted into the one- and two-qubit Hamiltonian to receive the  $U_{\text{XOR}}$  operation. In our case, we assumed  $\xi = E_s$ . However, there is no restriction in the use of other values for  $\xi$ . For a typical energy scale of 1 GHz, the resulting times from Table I are in the nanosecond range.

To better visualize the pulse sequence needed to perform the quantum  $U_{\text{XOR}}$  operation, which was already given in

PHYSICAL REVIEW A 67, 042319 (2003)

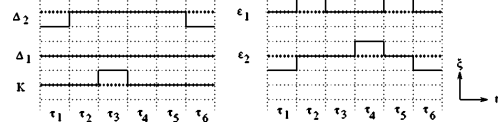


FIG. 11. Pulse sequence needed to perform the quantum  $U_{\text{XOR}}$  operation. Here, the elements of the unperturbed single- and two-qubit Hamiltonian needed to perform a certain operation undergoing free unitary time evolution are shown. The dotted horizontal lines denote  $\xi=0$ , and the horizontal lines are spaced by  $|\xi|=E_s$ . The durations of each pulse are not equal in general  $\tau_j \neq \tau_i, i, j = 1, \dots, 6$  (cf. Table I).

Table I, Fig. 11 depicts the values of the elements of the Hamiltonians. Interestingly enough, we find that for the only two-qubit operation included in the  $U_{\text{XOR}}$  operation,  $\epsilon$  and  $\eta$  are zero. Thus,  $K$  is the only nonzero parameter and  $\mathbf{H}_{2,qb}$  assumes diagonal form. For flux qubits, implementing the pulse sequence Fig. 11 involves negative and positive values tuning the magnetic frustration through the qubit loop below or above  $f=1/2$ . Note that, e.g., for realistic models of inductively coupled flux qubits, it is very difficult to turn on the interaction Hamiltonian between the two qubits without the individual  $\sigma_z$  terms in the Hamiltonian. However, for the pulse sequence given in Eq. (32), we might simply perform the third, fourth, and fifth operations of Eq. (32) at once using only the Hamiltonian with both the individual  $\sigma_z$  terms and the interqubit coupling.

To obtain the final reduced density matrix after performing the six unitary operations (32), we iteratively determine the density matrix after each operation with Bloch-Redfield theory and insert the attained resulting density matrix as initial density matrix into the next operation. This procedure is repeated for all possible unentangled initial states given in the preceding section. We inserted no additional time intervals between the operations. This is usually needed, if one applies Bloch-Redfield formalism, because it is known to violate complete positivity on short time scales. However, we circumvent this problem in our calculations by dropping the memory after each operation, when we iteratively calculate the reduced density matrix. This procedure may lead to small inaccuracies as compared to using QUAPPI [17], which, however, should not affect our main conclusions.

## B. Temperature dependence

### 1. Controlled phase-shift gate

We have analyzed the gate quality factors in the cases of a common and of two distinct baths, respectively. In Fig. 12, the temperature dependence of the deviations of the four gate quality factors from their ideal values are depicted as a log-log plot. At temperatures below  $T = 2.5 \times 10^{-2} \text{ K} \approx 0.5T_s$ , the purity and fidelity are clearly higher for the case of one common bath, but if temperature is increased above this characteristic threshold, fidelity and purity are slightly higher for the case of two baths.

In the case of one common bath the fidelity, purity, and entanglement capability are approaching their ideal value 1,

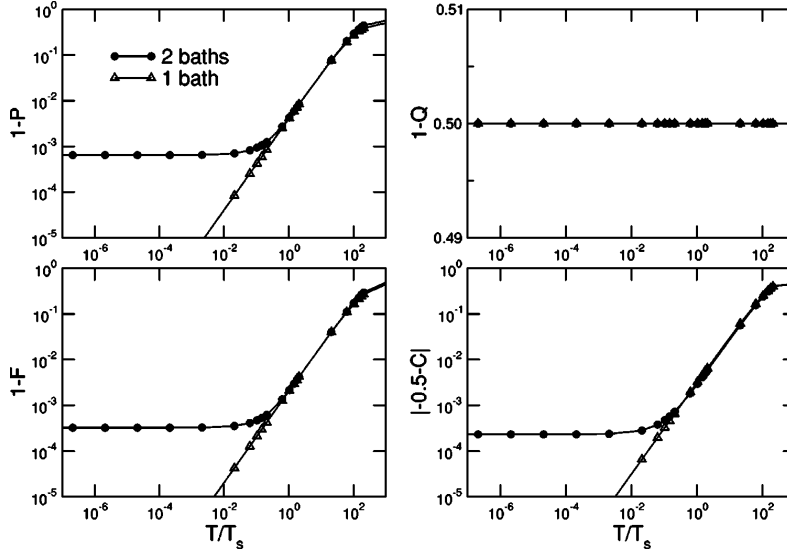


FIG. 12. Log-log plot of the temperature dependence of the deviations of the four gate quantifiers from their ideal values after performing the controlled phase-shift (CPHASE) gate operation. In all cases,  $\alpha = \alpha_1 = \alpha_2 = 10^{-3}$ . The full curves are provided as guides to the eye.

when temperature goes to zero. This is related to the fact that in the case of one common bath all relaxation and dephasing rates vanish during the two-qubit step of the controlled phase-shift gate due to the special symmetries of the Hamiltonian, when temperature goes to zero as depicted in Fig. 9.

The controlled phase-shift operation creates entanglement. The creation of entanglement is impeded by decoherence effects that vanish when temperature approaches zero. Therefore, the entanglement capability exhibits the same behavior as the fidelity and purity. For zero dissipation ( $\alpha = 0$ ), the quantum degree has the value 0.5 but the entanglement capability is  $-0.5$  thus, characterizing a maximum entangled state. The reason is that the Bell-states, which are generated by the controlled phase-shift gate from the input states, result in a basis that is different from the used basis, but can be transformed using only local transformations.

Furthermore, for finite dissipation, Fig. 9 shows that also for the case of two distinct baths, there are only three nonvanishing rates for  $T \rightarrow 0$ . The system, being prepared in one of the 16 initial states, might relax into one of the eigenstates that is an entangled state.

We observe the saturation of the deviation for the case of two baths and can directly recognize the effects of the symmetries of the controlled phase-shift operation. For given  $\alpha$ , the fidelity and purity cannot be increased anymore by lowering the temperature in the case of two distinct baths. Interestingly enough, we find that for two qubits coupling to one common bath, the situation is different for temperatures below  $0.5T_s$ . Above a temperature of  $T_s = 4.8 \times 10^{-2}$  K, the decrease of the gate quality factors shows a linear dependence on temperature for both cases of one common or two distinct heat baths before it again saturates at about  $10^2$  K  $\approx 2 \times 10^3 T_s$ . Finite decoherence effects in the fidelity, purity and entanglement capability at  $T=0$  for the case of two distinct baths are resulting from the coupling of the system to the environment of harmonic oscillators, which (at  $T=0$ ) are

all in their ground states and can be excited through spontaneous emission. But for the case of one common bath, the deviation from the ideal fidelity goes to zero, when temperature goes to zero. This is due to the special symmetries ( $K$  is the only *nonvanishing* parameter in the two-qubit operation) of the Hamiltonian, which rules out spontaneous emission. These symmetries are also reflected in the temperature dependence of the rates, Fig. 9. There, for one common bath, all rates vanish for  $T \rightarrow 0$ . Note that these rates only describe the two-qubit part of the operation. However, the single-qubit part behaves similarly, because the terms in the single-qubit Hamiltonian are also  $\propto \sigma_z$ .

## 2. Controlled-NOT gate

Different to the preceding section, we now add two single-qubit operations (Hadamard gates) to the controlled phase-shift operation that do *not* commute with the coupling to the bath. In Fig. 13, the deviations of the gate quality factors from their ideal values are depicted as a log-log plot. Again, at temperatures below  $T = 2.5 \times 10^{-2}$  K  $\approx 0.5T_s$ , the purity and fidelity are higher for the case of one common bath, but if temperature is increased above this characteristic threshold, fidelity and purity are higher for the case of two baths. Note that, we have chosen a rather large  $\alpha$ , this value can substantially be improved by means of engineering [13]. The fidelity and purity are clearly higher for the case of one common bath, when temperature is decreased below  $0.5T_s$ . This is related to the fact that in the case of one common bath, all relaxation and dephasing rates vanish during the two-qubit-step of the  $U_{\text{XOR}}$ , due to the special symmetries of the Hamiltonian, when temperature goes to zero as discussed in the preceding paragraph. However, the quantum degree and the entanglement capability tend towards the same value for both the case of one common and two distinct baths. This is due to the fact that both quantum degree and entanglement capability are, different than fidelity and purity, not defined

M. J. STORCZ AND F. K. WILHELM

PHYSICAL REVIEW A 67, 042319 (2003)

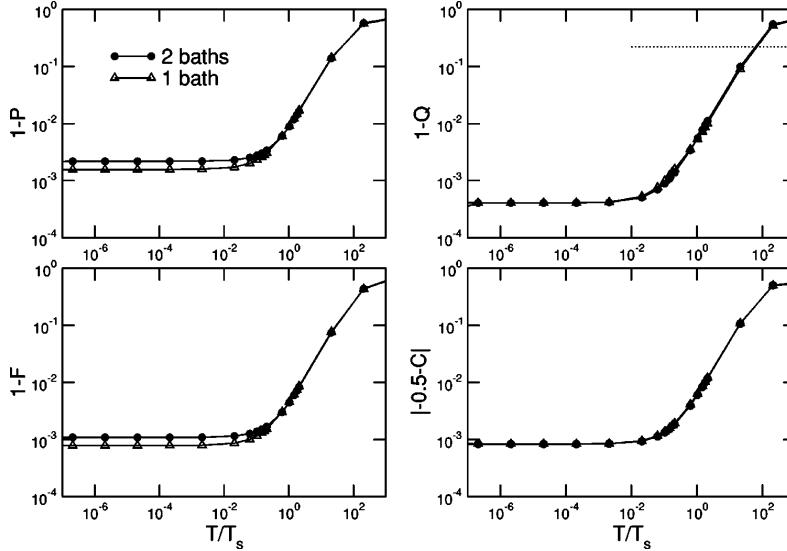


FIG. 13. Log-log plot of the temperature dependence of the deviations of the four gate quantifiers from their ideal values after performing the  $U_{\text{XOR}}$  gate operation. In all cases,  $\alpha = \alpha_1 = \alpha_2 = 10^{-3}$ . The dotted line indicates the upper bound set by the Clauser-Horne-Shimony-Holt inequality. The full curves are provided as guides to the eye.

as mean values but rather characterize the “best” possible case of all given input states. This results in the same value for both cases.

In the recent work by Thorwart and Hänggi [17], the  $U_{\text{XOR}}$  gate was investigated for a  $\sigma_y^{(i)} \otimes \sigma_y^{(j)}$  coupling scheme and one common bath. They find a pronounced degradation of the gate performance, in particular, the gate quality factors only weakly depend on temperature. They set the strength of the dissipative effects to  $\alpha = 10^{-4}$ . Their choice of parameters was  $\epsilon \approx 10E_s$ ,  $\Delta \approx 1E_s$ , and  $K \approx 0.5E_s$ , which is on the same order of magnitude as the values given in Table I. As can be seen in Fig. 13, we also observe only a weak decrease of the gate quality factors for both the cases of one common bath and two distinct baths in the same temperature range discussed by Thorwart and Hänggi, both for  $\alpha = 10^{-3}$  and  $\alpha = 10^{-4}$  and overall substantially better values. This is due to the fact that for  $\sigma_y^{(i)} \otimes \sigma_y^{(j)}$  coupling, the Hamiltonian does *not* commute with the coupling to the bath during the two-qubit steps of the  $U_{\text{XOR}}$  pulse sequence.

We observe the saturation of the deviation for both the cases of two baths and one common bath. For given  $\alpha$ , the fidelity and purity can not be increased anymore by lowering the temperature, different from the behavior for the controlled phase-shift gate that was discussed in the preceding section. This is due to the application of the Hadamard gate whose Hamiltonian does not commute with the coupling to the bath. Above a temperature of  $T_s$ , the decrease of the gate quality factors shows a linear dependence on temperature for both cases. Here, different from the controlled phase-shift gate, we observe finite decoherence effects in all four gate quantifiers also at  $T=0$ , both for the case of one common or two distinct heat baths. These decoherence effects are resulting from the coupling of the system to the environment of harmonic oscillators, which (at  $T=0$ ) are all in their ground states and can be excited through spontaneous emission as already described above.

The dotted line in Fig. 13 shows that the temperature has to be less than about  $T = 21T_s = 1$  K in order to obtain values of the quantum degree being larger than  $Q \approx 0.78$ . Only then, the Clauser-Horne-Shimony-Holt inequality is violated and nonlocal correlations between the qubits occur as described in Ref. [17].

### C. Dependence on the dissipation strength

The deviations from the ideal values of the gate quantifiers possess a linear dependence on  $\alpha$  as expected. Generally (if no special symmetries of the Hamiltonian are present), there are always finite decoherence effects also at  $T=0$ . Therefore, we can not improve the gate quality factors below a certain saturation value, when lowering the temperature [17], as was also discussed in the preceding section. By better isolating the system from the environment and by carefully engineering the environment [13], one can decrease the strength of the dissipative effects characterized by  $\alpha$ . In order to obtain the desired value of 0.99999 for  $\mathcal{F}$ ,  $\mathcal{P}$ , and  $\mathcal{Q}$  [17],  $\alpha$  needs to be below  $10^{-6}$  at  $T = 0.21T_s = 10$  mK.

### D. Time resolved controlled-NOT operation

To investigate the anatomy of the  $U_{\text{XOR}}$  quantum logic operation, we calculated the occupation probabilities of the singlet/triplet states after each of the six operations, of which the  $U_{\text{XOR}}$  consists. This time resolved picture of the dynamics of the two-qubit system, when performing a gate operation, gives insight into details of our implementation of the  $U_{\text{XOR}}$  operation and the dissipative effects that occur during the operation. Thus, we are able to characterize the physical process, which maps the input density matrix  $\rho_0$  to  $\rho_{out}$  in an open quantum system [33]. When the system is prepared in the state  $|\downarrow\downarrow\rangle = |00\rangle$ , the  $U_{\text{XOR}}$  operation (31) does not alter the initial state and after performing the  $U_{\text{XOR}}$  operation, the final state should equal the initial state  $|\downarrow\downarrow\rangle = |00\rangle$ . This can

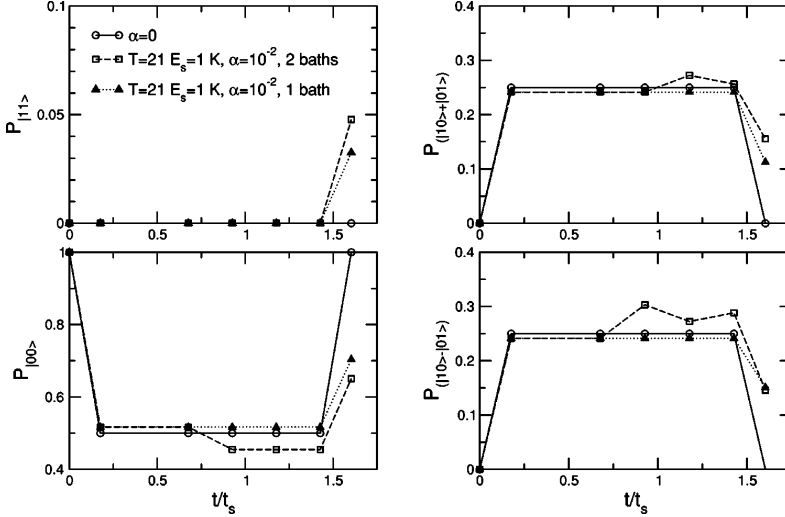


FIG. 14. Time resolved  $U_{XOR}$  operation. The system is initially prepared in the state  $|00\rangle$ . Occupation probabilities of the singlet/triplet states are shown after completion of a time step  $\tau_i$  ( $i = 1, \dots, 6$ ). For  $\alpha = \alpha_1 = \alpha_2 = 10^{-2}$  and  $T = 21T_s = 1$  K clear deviations from the ideal case can be observed. Qubit parameters are set according to Table I. The lines are provided as guides to the eye.

clearly be observed in Fig. 14. During the  $U_{XOR}$  operation, occupation probabilities of the four states change according to the individual operations given in Eq. (32). At  $T = 21T_s$ , the case of two baths differs significantly from the case of one common bath. After the third operation (the two-qubit operation; only there the distinction between one common or two distinct baths makes sense), occupation probabilities are different for both environments resulting in a less ideal result for the case of two baths.

In Fig. 14, the resulting state after performing the  $U_{XOR}$  operation always deviates more from the ideal value (for  $\alpha = 0$ , i.e., no dissipation) for the case of two distinct baths, if all other parameters are fixed and set to the same values for both cases. The state  $P_{|00\rangle}$  is less close to the ideal occupation probability one and the other singlet/triplet states are

also less close to their ideal value for the case of two distinct baths. The case of two distinct baths also shows bigger deviations from the ideal case ( $\alpha = 0$ ) during the  $U_{XOR}$  operation (see Fig. 14). But, if the system is initially prepared in the state  $|\uparrow\uparrow\rangle = |11\rangle$ , the case of two distinct baths shows bigger deviations from the ideal case during the  $U_{XOR}$  operation, while the resulting state is closer to the ideal case for two distinct baths compared to one common bath.

In Figs. 14 and 15, it looks like there would be no decoherence effects (or at least much weaker decoherence effects) after performing the (first two) single-qubit operations. However, not all input states are affected by the decoherence effects the same way. And when we regard all possible input states, there are finite decoherence effects. This can be explained with Fig. 16. Figure 16 depicts the time resolved

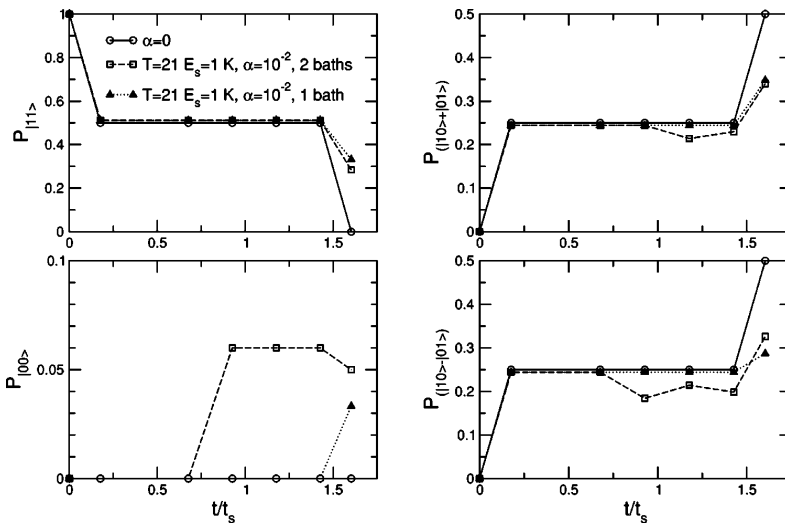


FIG. 15. Time resolved  $U_{XOR}$  operation. The system is initially prepared in the state  $|11\rangle$ . Occupation probabilities of the singlet/triplet states are shown after completion of a time step  $\tau_i$  ( $i = 1, \dots, 6$ ). For  $\alpha = \alpha_1 = \alpha_2 = 10^{-2}$  and  $T = 21T_s = 1$  K, deviations from the ideal case can be observed. Qubit parameters are set according to Table I. The lines are provided as guides to the eye.

M. J. STORCZ AND F. K. WILHELM

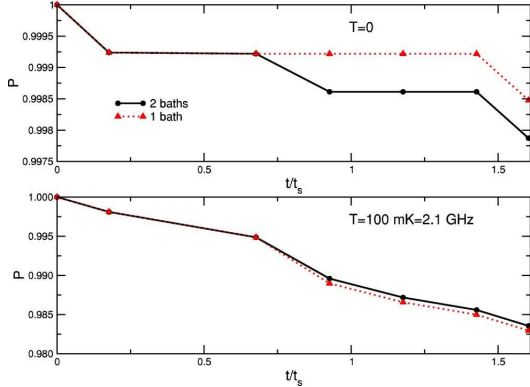
PHYSICAL REVIEW A **67**, 042319 (2003)

FIG. 16. Time resolved purity for the  $U_{\text{XOR}}$  operation. The value of the purity after each time step  $\tau_i$  ( $i=1, \dots, 6$ ) is shown. Here  $\alpha = \alpha_1 = \alpha_2 = 10^{-2}$ , and  $T = 2.1T_s = 100$  mK (lower panel) or  $T = 0$  (upper panel). Qubit parameters are set according to Table I. The lines are provided as guides to the eye.

purity when performing the  $U_{\text{XOR}}$  operation. We clearly observe that there are finite decoherence effects for the first single-qubit operations in Eq. (32) as well. The difference between the single-qubit and two-qubit operations is the steeper decrease of the purity due to stronger decoherence in the case of the two-qubit operation. The upper panel in Fig. 16 depicts the behavior of the purity for  $T \rightarrow 0$ . Decoherence due to the  $\sigma_z$  terms in the Hamiltonian will vanish for  $T \rightarrow 0$  in the case of one common bath.

## VI. CONCLUSION

We presented a full analysis of the dynamics and decoherence properties of two solid-state qubits coupled to each other via a generic type of Ising coupling and coupled, moreover, either to a common bath, or two independent baths.

We calculated the dynamics of the system and evaluated decoherence times. From the temperature dependence of the decoherence rates (Fig. 8), we conclude that both types of environments show a similar behavior; however, in the case of one common bath, two of the decoherence rates are zero, and the remaining ones are slightly larger than in the case of two distinct baths. This temperature dependence is also reflected in the characteristics of the gate quality factors from quantum information theory, which are introduced as robust

measures of the quality of a quantum logic operation. We illustrate that the gate quality factors depend linearly on  $\alpha$ , as expected. The time resolved  $U_{\text{XOR}}$  operation (Figs. 14 and 15) again illustrates the difference between one common and two distinct baths, and moreover, we observe that single-qubit decoherence effects  $\propto \sigma_z$  during the  $U_{\text{XOR}}$  operation are weak. The time scales of the dynamics of the coupled two qubit system are comparable to the time scales, which were already observed in experiments and discussed in the literature [13].

The question, whether one common bath or two distinct baths are less destructive regarding quantum coherence can not be clearly answered. For low enough temperatures, coupling to one common bath yields better results. However, when the temperature is increased, two distinct baths do better; in both temperature regimes, though, the gate quantifiers are only slightly different for both cases.

Compared to the work of Thorwart [17], the interaction part of our model Hamiltonian possesses symmetries (the Hamiltonian of the two-qubit operation and the errors commute) that lead to better gate quality factors. Furthermore, analysis of the symmetries and error sources of our model system can lead to improved coupling schemes for solid-state qubits. Milburn and co-workers on the other hand focused on comparison of classical and quantum mechanical dynamics [15] and estimated the decoherence properties of two coupled two-state systems.

Governale [16] determined the decoherence properties of two coupled charge qubits whose Hamiltonian differs from Eq. (2) by the type of interqubit coupling, namely,  $\sigma_y^{(1)} \otimes \sigma_y^{(2)}$  coupling. However, introducing the quality factors gives a measure to judge how certain qubit designs perform quantum gate operations.

As a next step, one should consider driving, to be able to observe and discuss Rabi oscillations in systems of two coupled qubits. It should be investigated, how the decoherence properties are modified, if one adds more qubits to the system.

## ACKNOWLEDGMENTS

We thank B. Singh, L. Tian, C. H. van der Wal, M. Governale, M. C. Goorden, A. C. J. ter Haar, H. Aschauer, R. Raussendorf, A. J. Leggett, P. Hänggi, C. J. P. M. Harmans, H. Gutmann, U. Hartmann and J. von Delft for fruitful discussions. We acknowledge financial support from ARO, under Contract No. P-43385-PH-QC, and from DAAD under Contract No. DAAD/NSF D/0104619.

- [1] P. Shor, in *Proceedings of 35th Annual Symposium on the Foundations of Computer Science*, edited by S. Goldwasser (IEEE Computer Society Press, Los Alamitos, 1994), pp. 124–134.  
 [2] L.K. Grover, *Phys. Rev. Lett.* **79**, 325 (1997).  
 [3] D. Deutsch, *Proc. R. Soc. London, Ser. A* **400**, 97 (1985).  
 [4] D.P. DiVincenzo, *Science* **269**, 225 (1995).  
 [5] B.E. Kane, *Nature (London)* **393**, 133 (1998).

- [6] T.P. Orlando *et al.*, *Phys. Rev. B* **60**, 15 398 (2000); J.E. Mooij *et al.*, *Science* **285**, 1036 (1999).  
 [7] Yu.A. Pashkin, T. Yamamoto, O. Astafiev, Y. Nakamura, D.V. Averin, and J.S. Tsai, *Nature (London)* **421**, 823 (2003).  
 [8] Y. Nakamura, Yu.A. Pashkin, and J.S. Tsai, *Nature (London)* **398**, 786 (2002).  
 [9] J.R. Friedman, V. Patel, W. Chen, S.K. Tolpygo, and J.E. Lukens, *Nature (London)* **406**, 43 (2000).



- DECOHERENCE AND GATE PERFORMANCE OF COUPLED . . . PHYSICAL REVIEW A **67**, 042319 (2003)
- [10] D. Vion, A. Aassime, A. Cottet, P. Joyez, H. Pothier, C. Urbina, D. Esteve, and M.H. Devoret, *Science* **296**, 886 (2002).
- [11] Y. Nakamura (private communication).
- [12] M.C. Goorden, Masters thesis, Delft University of Technology, 2002 (unpublished); M.C. Goorden and F.K. Wilhelm (unpublished).
- [13] C.H. van der Wal, *Quantum Superpositions of Persistent Josephson Currents* (Delft University Press, Delft, 2001); C.H. van der Wal, F.K. Wilhelm, C.J.P.M. Harmans, and J.E. Mooij, *Eur. Phys. J. B* **31**, 111 (2003).
- [14] Y. Makhlin, G. Schön, and A. Shnirman, *Rev. Mod. Phys.* **73**, 357 (2001).
- [15] G.J. Milburn, R. Laflamme, B.C. Sanders, and E. Knill, *Phys. Rev. A* **65**, 032316 (2002).
- [16] M. Governale, M. Grifoni, and G. Schön, *Chem. Phys.* **268**, 273 (2001).
- [17] M. Thorwart and P. Hänggi, *Phys. Rev. A* **65**, 012309 (2002).
- [18] F.K. Wilhelm and J.E. Mooij (unpublished).
- [19] R.H. Blick and H. Lorenz, in *ISCAS 2000 Proceedings* (unpublished), pp. II245-II248.
- [20] J.B. Majer (private communication).
- [21] D.A. Lidar, I.L. Chuang, and K.B. Whaley, *Phys. Rev. Lett.* **81**, 2594 (1998).
- [22] J. Kempe, D. Bacon, D.A. Lidar, and K.B. Whaley, *Phys. Rev. A* **63**, 042307 (2001).
- [23] M.J. Storz, Masters thesis, University of Bonn, 2002 (unpublished).
- [24] K. Segall *et al.*, *IEEE Trans. Appl. Supercond.* (to be published).
- [25] C.H. van der Wal *et al.*, *Science* **290**, 773 (2000).
- [26] P.N. Argyres and P.L. Kelley, *Phys. Rev.* **134**, A98 (1964).
- [27] L. Hartmann, I. Goychuk, M. Grifoni, and P. Hänggi, *Phys. Rev. E* **61**, R4687 (2000); L. Hartmann, *Driven Tunneling Dynamics of Dissipative Two-State Quantum Systems* (Shaker Verlag, Aachen, 2000).
- [28] U. Weiss, *Quantum Dissipative Systems*, 2nd ed. (World Scientific, Singapore, 1999).
- [29] K. Blum, *Density Matrix Theory and Applications*, 1st ed. (Plenum, New York, 1981).
- [30] A.J. Leggett *et al.*, *Rev. Mod. Phys.* **59**, 1 (1987).
- [31] S. Kehrein and M. Vojta, e-print cond-mat/0208390.
- [32] P. Horowitz and W. Hill, *The Art of Electronics*, 2nd ed. (Cambridge University Press, Cambridge, 1989).
- [33] J.F. Poyatos, J.I. Cirac, and P. Zoller, *Phys. Rev. Lett.* **78**, 390 (1997).
- [34] C.H. Bennett, G. Brassard, S. Popescu, B. Schumacher, J.A. Smolin, and W.K. Wootters, *Phys. Rev. Lett.* **76**, 722 (1996); J.F. Clauser, M.A. Horne, A. Shimony, and R.A. Holt, *ibid.* **23**, 880 (1969).
- [35] A. Peres, *Phys. Rev. Lett.* **77**, 1413 (1996).
- [36] A. Barenco, C.H. Bennett, R. Cleve, D.P. DiVincenzo, N. Margolus, P. Shor, T. Sleator, J.A. Smolin, and H. Weinfurter, *Phys. Rev. A* **52**, 3457 (1995).



## Decoherence of Flux Qubits Coupled to Electronic Circuits

F. K. Wilhelm<sup>1</sup>, M. J. Storcz<sup>1</sup>, C. H. van der Wal<sup>2</sup>,  
C. J. P. M. Harmans<sup>3</sup>, and J. E. Mooij<sup>3</sup>

<sup>1</sup> Sektion Physik and CeNS, Ludwig-Maximilians-Universität  
80333 München, Germany

<sup>2</sup> Dpt. of Physics, Harvard University  
Cambridge, MA 02138, USA

<sup>3</sup> Dpt. of Nanoscience, Delft University of Technology  
2600 GA Delft, Netherlands

**Abstract.** On the way to solid-state quantum computing, overcoming decoherence is the central issue. In this contribution, we discuss the modeling of decoherence of a superconducting flux qubit coupled to dissipative electronic circuitry. We discuss its impact on single qubit decoherence rates and on the performance of two-qubit gates. These results can be used for designing decoherence-optimal setups.

### 1 Introduction

Quantum computation is one of the central interdisciplinary research themes in present-day physics [1]. It promises a detailed understanding of the often counterintuitive predictions of basic quantum mechanics as well as a qualitative speedup of certain hard computational problems. A generic, although not necessarily exclusive, set of criteria for building quantum computers has been put forward by DiVincenzo [2]. The experimental realization of quantum bits has been pioneered in atomic physics, optics and NMR. There, the approach is taken to use microscopic degrees of freedom which are well isolated and can be kept quantum coherent over long times. Efficient controls are attached to these degrees of freedom. Even though these approaches are immensely successful demonstrating elementary operations, it is not evident how they can be scaled up to macroscopic computers.

Solid-state systems on the other hand have proven to be scalable in present-day classical computers. Several proposals for solid-state based *quantum* computers have been put forward, many of them in the context of superconductors [3]. As solid-state systems contain a macroscopic number of degrees of freedom, they are very sensitive to decoherence. Mastering and optimizing this decoherence is a formidable task and requires deep understanding of the physical system under investigation. Recent experimental success [4,5] suggests that this task can in principle be performed.

In this contribution, we are going to study decoherence of superconducting qubits coupled to an electromagnetic environment which produces Johnson-Nyquist noise. We show, how the decoherence properties can be engineered

764 F. K. Wilhelm et al.

by carefully designing the environmental impedance. We will discuss how the decoherence affects the performance of a CNOT operation.

## 2 Superconducting Flux Qubits

Superconducting qubits [3,4,5,6] are very well suited for the task of solid-state quantum computation, because two of the most obvious decoherence sources in solid-state systems are suppressed: Quasiparticle excitations experience an energy gap and phonons are frozen out at low temperatures [7]. The computational Hilbert space is engineered using Josephson tunnel junctions that are characterized by two competing energy scales: The Josephson coupling of a junction with critical current  $I_c$ ,  $E_J = I_c \Phi_0 / 2\pi$ , and the charging energy  $E_{ch} = 2e^2 / C_J$  of a single Cooper pair on the geometric capacitance  $C_J$  of the junction. Here  $\Phi_0 = h/2e$  is the superconducting flux quantum. There is a variety of qubit proposals classified by the ratio of these energies. Whereas another contribution in this volume [8] focuses on the case of charge qubits,  $E_{ch} > E_J$ , this contribution is motivated by flux qubit physics,  $E_J > E_{ch}$ . However, most of the discussion has its counterpart in other superconducting setups as well. Specifically, we discuss a three junction qubit [6,9], a micrometer-sized low-inductance superconducting loop containing three Josephson tunnel junctions (Fig. 1). By applying an external flux  $\Phi_q$  a persistent supercurrent can be induced in the loop. For values where  $\Phi_q$  is close to a half-integer number of flux quanta, two states with persistent currents of opposite sign are nearly degenerate but separated by an energy barrier. We will assume here that the system is operated near  $\Phi_q = \frac{1}{2}\Phi_0$ . The

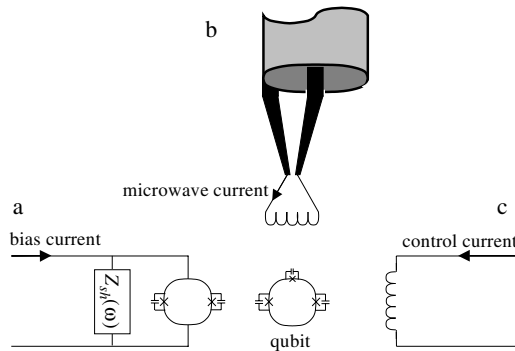


**Fig. 1.** Experimental setup for measurements on a flux qubit. The qubit (*center*) is a superconducting loop that contains three Josephson junctions. It is inductively coupled to a DC-SQUID (a), and superconducting control lines for applying magnetic fields at microwave frequencies (b) and static magnetic fields (c). The DC-SQUID is realized with an on-chip shunt circuit with impedance  $Z(\omega)$ . The circuits a)-c) are connected to filtering and electronics (not drawn)

persistent currents in the classically stable states have here a magnitude  $I_p$ . Tunneling through the barrier causes a coupling between the two states, and at low energies the loop can be described by a Hamiltonian of a two state system [6,9],

$$\hat{H}_q = \frac{\varepsilon}{2}\hat{\sigma}_z + \frac{\Delta}{2}\hat{\sigma}_x, \quad (1)$$

where  $\hat{\sigma}_z$  and  $\hat{\sigma}_x$  are Pauli matrices. The two eigenvectors of  $\hat{\sigma}_z$  correspond to states that have a left or a right circulating current and will be denoted as  $|L\rangle$  and  $|R\rangle$ . The energy bias  $\varepsilon = 2I_p(\Phi_q - \frac{1}{2}\Phi_0)$  is controlled by the externally applied field  $\Phi_q$ . We follow [10] and define  $\Delta$  as the tunnel splitting at  $\Phi_q = \frac{1}{2}\Phi_0$ , such that  $\Delta = 2W$  with  $W$  the tunnel coupling between the persistent-current states. This system has two energy eigen values  $\pm\frac{1}{2}\sqrt{\Delta^2 + \varepsilon^2}$ , such that the level separation  $\nu$  gives  $\nu = \sqrt{\Delta^2 + \varepsilon^2}$ . In general  $\Delta$  is a function of  $\varepsilon$ . However, it varies on the scale of the single junction plasma frequency, which is much above the typical energy range at which the qubit is operated, such that we can assume  $\Delta$  to be constant for the purpose of this paper.

In the experiments  $\Phi_q$  can be controlled by applying a magnetic field with a superconducting coil at a distance from the qubit and for local control one can apply currents to superconducting lines, fabricated on-chip in the vicinity of the qubit. The qubit's quantum dynamics will be controlled with resonant microwave pulses (i. e. by Rabi oscillations). In recent experiments the qubits were operated at  $\varepsilon \approx 5\Delta$  or  $\varepsilon \approx 0$  [4,9]. The numerical values given in this paper will concentrate on the former case. At this point, there is a good trade-off between a system with significant tunneling, and a system with  $\hat{\sigma}_z$ -like eigenstates that can be used for qubit-qubit couplings and measuring qubit states [6]. The qubit has a magnetic dipole moment as a result of the clockwise or counter-clockwise persistent current. The corresponding flux in the loop is much smaller than the applied flux  $\Phi_q$ , but large enough to be detected with a SQUID. This will be used for measuring the qubit states. For our two-level system Eq. (1), this means that both manipulation and readout couple to  $\hat{\sigma}_z$ . Consequently, the Nyquist noise produced by the necessary external circuitry will couple in as flux noise and hence couple to  $\hat{\sigma}_z$ , giving  $\varepsilon$  a small, stochastically time-dependent part  $\delta\varepsilon(t)$ .

Operation at  $\varepsilon \approx 0$  has the advantage that the flux noise leads to less variation of  $\nu$ . In the first experiments [4] this has turned out to be crucial for observing time-resolved quantum dynamics. Here, the qubit states can be measured by incorporating the qubit inside the DC-SQUID loop. While not working that out in detail, the methods that we present can also be applied for the analysis of this approach. This also applies to the analysis of the impact of electric dipole moments, represented by  $\hat{\sigma}_x$ . With  $E_{ch} \ll E_J$ , these couple much less to the circuitry and will hence not be discussed here.

As the internal baths are well suppressed, the coupling to the electromagnetic environment (circuitry, radiation noise) becomes a dominant source of decoherence. This is a subtle issue: It is not possible to couple the circuitry

766 F. K. Wilhelm et al.

arbitrarily weakly or seal the experimental setup, because it has to remain possible to control the system. One rather has to engineer the electromagnetic environment to combine good control with low unwanted back-action.

Any linear electromagnetic environment can be described by an effective impedance  $Z_{\text{eff}}$ . If the circuit contains Josephson junctions below their critical current, they can be included through their kinetic inductance  $L_{\text{kin}} = \Phi_0 / (2\pi I_c \cos \bar{\phi})$ , where  $\bar{\phi}$  is the average phase drop across the junction. The circuitry disturbs the qubit through its Johnson-Nyquist noise, which has Gaussian statistics and can thus be described by an effective Spin-Boson model [11]. In this model, the properties of the oscillator bath which forms the environment are characterized through a spectral function  $J(\omega)$ , which can be derived from the external impedance. Note, that other nonlinear elements such as tunnel junctions which can produce non-Gaussian shot noise are generically *not* covered by oscillator bath models.

As explained above, the flux noise from an external circuit leads to  $\epsilon = \epsilon_0 + \delta\epsilon(t)$  in Eq. (1). We parametrize the noise  $\delta\epsilon(t)$  by its power spectrum

$$\langle \{\delta\epsilon(t), \delta\epsilon(0)\} \rangle_\omega = \hbar^2 J(\omega) \coth(\hbar\omega/2k_B T). \quad (2)$$

Thus, from the noise properties calculated by other means one can find  $J(\omega)$  as was explained in Detail in [12]. In this contribution, we would like to outline an alternative approach pioneered by Leggett [13], where  $J(\omega)$  is derived from the classical friction induced by the environment. In reality, the combined system of SQUID and qubit will experience fluctuations arising from additional circuit elements at different temperatures, which can be treated in a rather straightforward manner.

### 3 Decoherence from the Electromagnetic Environment

#### 3.1 Characterizing the Environment from Classical Friction

We study a DC-SQUID in an electrical circuit as shown in Fig. 1. It contains two Josephson junctions with phase drops denoted by  $\gamma_{1/2}$ . We start by looking at the average phase  $\gamma_{\text{ex}} = (\gamma_1 + \gamma_2)/2$  across the read-out SQUID. Analyzing the circuit with Kirchhoff rules, we find the equation of motion

$$2C_J \frac{\Phi_0}{2\pi} \ddot{\gamma}_{\text{ex}} = -2I_{c,0} \cos(\gamma_i) \sin \gamma_{\text{ex}} + I_{\text{bias}} - \frac{\Phi_0}{2\pi} \int dt' \dot{\gamma}_{\text{ex}}(t') Y(t-t'). \quad (3)$$

Here,  $\gamma_{\text{in}} = (\gamma_1 - \gamma_2)/2$  is the dynamical variable describing the circulating current in the loop which is controlled by the flux,  $I_{\text{bias}}$  is the bias current imposed by the source,  $Y(\omega) = Z^{-1}(\omega)$  is the admittance in parallel to the whole SQUID and  $Y(\tau)$  its Fourier transform. The SQUID is described by the junction critical currents  $I_{c,0}$  which are assumed to be equal, and their capacitances  $C_J$ . We now proceed by finding a static solution which sets the operation point  $\gamma_{\text{in/ex},0}$  and small fluctuations around them,  $\delta\gamma_{\text{in/ex}}$ . The

static solution reads  $I_{\text{bias}} = I_{c,\text{eff}} \sin \gamma_{\text{ex},0}$  where  $I_{c,\text{eff}} = 2I_{c,0} \cos \gamma_{\text{in},0}$  is the effective critical current of the SQUID. Linearizing Eq. 3 around this solution and Fourier-transforming, we find that

$$\delta\gamma_{\text{ex}}(\omega) = \frac{2\pi I_b \tan \gamma_{\text{in},0} Z_{\text{eff}}(\omega)}{i\omega\Phi_0} \delta\gamma_i(\omega) \quad (4)$$

where  $Z_{\text{eff}}(\omega) = (Z(\omega)^{-1} + 2i\omega C_J + (i\omega L_{\text{kin}})^{-1})^{-1}$  is the effective impedance of the parallel circuit consisting of the  $Z(\omega)$ , the kinetic inductance of the SQUID and the capacitance of its junctions. Neglecting self-inductance of the SQUID and the (high-frequency) internal plasma mode, we can straightforwardly substitute  $\gamma_{\text{in}} = \pi\Phi/\Phi_0$  and split it into  $\gamma_{\text{in},0} = \pi\Phi_{x,S}/\Phi_0$  set by the externally applied flux  $\Phi_{x,S}$  through the SQUID loop and  $\delta\gamma_i = \pi M_{\text{SQ}} I_Q/\Phi_0$  where  $M_{\text{SQ}}$  is the mutual inductance between qubit and the SQUID and  $I_Q(\varphi)$  is the circulating current in the qubit as a function of the junction phases, which assumes values  $\pm I_p$  in the classically stable states.

In order to analyze the backaction of the SQUID onto the qubit in the two-state approximation, Eq. (1), we have to get back to its full, continuous description, starting from the classical dynamics. These are equivalent to a particle, whose coordinates are the two independent junction phases in the three-junction loop, in a two-dimensional potential

$$\mathbf{C}(\Phi_0/2\pi)^2 \ddot{\boldsymbol{\varphi}} = -\nabla U(\boldsymbol{\varphi}, \Phi_{x,q} + I_S M_{\text{SQ}}). \quad (5)$$

The details of this equation are explained in [6].  $\mathbf{C}$  is the capacitance matrix describing the charging of the Josephson junctions in the loop,  $U(\boldsymbol{\varphi})$  contains the Josephson energies of the junctions as a function of the junction phases and  $I_S$  is the circulating current in the SQUID loop. The applied flux through the qubit  $\Phi_q$  is split into the flux from the external coil  $\Phi_{x,q}$  and the contribution from the SQUID. Using the above relations we find

$$I_S M_{\text{SQ}} = \delta\Phi_{\text{cl}} - 2\pi^2 M_{\text{SQ}}^2 I_B^2 \tan^2 \gamma_{\text{in},0} \frac{Z_{\text{eff}}}{i\omega\Phi_0^2} I_Q \quad (6)$$

where  $\delta\Phi_{\text{cl}} \simeq M_{\text{SQ}} I_{c,0} \cos \gamma_{\text{ex},0} \sin \gamma_{\text{in},0}$  is the non-fluctuating back-action from the SQUID.

From the two-dimensional problem, we can now restrict ourselves to the one-dimensional subspace defined by the preferred tunneling direction [6], which is described by an effective phase  $\varphi$ . The potential restricted on this direction,  $U_{\text{1D}}(\varphi)$  has the form of a double well [11,14] with stable minima situated at  $\pm\varphi_0$ . In this way, we can expand  $U_{\text{1D}}(\varphi, \Phi_q) \simeq U(\varphi, \Phi_q, x) + I_Q(\varphi) I_Q M_{\text{SQ}}$ . Approximating the phase-dependence of the circulating current as  $I_Q(\varphi) \approx I_p \varphi/\varphi_0$  where  $I_p$  the circulating current in one of the stable minima of  $\varphi$ , we end up with the classical equation of motion of the qubit including the backaction and the friction induced from the SQUID

768 F. K. Wilhelm et al.

$$\begin{aligned} & \left[ -C_{\text{eff}} \left( \frac{\Phi_0}{2\pi} \right)^2 \omega^2 + 2\pi^2 M_{\text{SQ}}^2 I_{\text{bias}}^2 \tan^2 \gamma_{\text{in},0} \frac{Z_{\text{eff}} I_{\text{p}}^2}{i\varphi_0 \omega \Phi_0^2} \right] \varphi \\ & = -\partial_\varphi U_{\text{1D}}(\varphi, \Phi_{x,q} + \delta\Phi_{\text{cl}}). \end{aligned} \quad (7)$$

From this form, encoded as  $D(\omega)\varphi(\omega) = -\partial U/\partial\varphi$  we can use the prescription given in [13] and identify the spectral function for the continuous, classical model as  $J_{\text{cont}} = \text{Im}D(\omega)$ . From there, we can do the two-state approximation for the particle in a double well [14] and find  $J(\omega)$  in analogy to [12]

$$J(\omega) = \frac{(2\pi)^2}{\hbar\omega} \left( \frac{M_{\text{SQ}} I_{\text{p}}}{\Phi_0} \right)^2 I_{\text{bias}}^2 \tan^2 \left( \frac{\pi\Phi}{\Phi_0} \right) \text{Re}\{Z_{\text{eff}}(\omega)\}. \quad (8)$$

### 3.2 Qubit Dynamics under the Influence of Decoherence

From  $J(\omega)$ , we can analyze the dynamics of the system by studying the reduced density matrix, i.e. the density matrix of the full system where the details of the environment have been integrated out, by a number of different methods. The low damping limit,  $J(\omega)/\omega \ll 1$  for all frequencies, is most desirable for quantum computation. Thus, the energy-eigenstates of the qubit Hamiltonian, Eq. (1), are the appropriate starting point of our discussion. In this case, the relaxation rate  $\Gamma_r$  (and relaxation time  $\tau_r$ ) are determined by the environmental spectral function  $J(\omega)$  at the frequency of the level separation  $\nu$  of the qubit

$$\Gamma_r = \tau_r^{-1} = \frac{1}{2} \left( \frac{\Delta}{\nu} \right)^2 J \left( \frac{\nu}{\hbar} \right) \coth \left( \frac{\nu}{2k_B T} \right), \quad (9)$$

where  $T$  is the temperature of the bath. The dephasing rate  $\Gamma_\phi$  (and dephasing time  $\tau_\phi$ ) is

$$\Gamma_\phi = \tau_\phi^{-1} = \frac{\Gamma_r}{2} + 2\pi\alpha \left( \frac{\varepsilon}{\nu} \right)^2 \frac{k_B T}{\hbar} \quad (10)$$

with  $\alpha = \lim_{\omega \rightarrow 0} J(\omega)/(2\pi\omega)$ . These expressions have been derived in the context of NMR [15] and recently been confirmed by a full path-integral analysis [10]. In this paper, all rates are calculated for this regime.

For performing efficient measurement, one can afford to go to the strong damping regime. A well-known approach to this problem, the noninteracting blip approximation (NIBA) has been derived in [13]. This approximation gives good predictions at degeneracy,  $\epsilon = 0$ . At low  $|\epsilon| > 0$  it contains an artifact predicting incoherent dynamics even at weak damping. At high bias,  $\epsilon \gg \Delta$  and at strong damping, it becomes asymptotically correct again. We will not detail this approach here more, as it has been extensively covered in [11,14].



If  $J(\omega)$  is not smooth but contains strong peaks the situation becomes more involved: At some frequencies,  $J(\omega)$  may fall in the weak and at others in the strong damping limit. In some cases, when  $J(\omega) \ll \omega$  holds at least for  $\omega \leq \Omega$  with some  $\Omega \gg \nu/\hbar$ , this can be treated approximately: one can first renormalize  $\Delta_{\text{eff}}$  through the high-frequency contributions [11] and then perform a weak-damping approximation from the fixed-point Hamiltonian. This is detailed in [16]. In the general case, more involved methods such as flow equation renormalization [17] have to be used.

## 4 Engineering the Measurement Apparatus

From Eq. (8) we see that engineering the decoherence induced by the measurement apparatus essentially means engineering  $Z_{\text{eff}}$ . This includes also the contributions due to the measurement apparatus. In this section, we are going to outline and compare several options suggested in literature. We assume a perfect current source that ramps the bias current  $I_{\text{bias}}$  through the SQUID. The fact that the current source is non-ideal, and that the wiring to the SQUID chip has an impedance is all modeled by the impedance  $Z(\omega)$ . The wiring can be engineered such that for a very wide frequency range the impedance  $Z(\omega)$  is on the order of the vacuum impedance, and can be modeled by its real part  $R_l$ . It typically has a value of 100  $\Omega$ .

### 4.1 R-Shunt

It has been suggested [18] to overdamp the SQUID by making the shunt circuit a simple resistor  $Z(\omega) = R_S$  with  $R_S \ll \sqrt{L_{\text{kin}}/2C_J}$ . This is inspired by an analogous setup for charge qubits, [3]. Following the parameters given in [12], a SQUID with  $I_{c,0} = 200\text{nA}$  at  $\Phi/\Phi_0 \simeq 0.75$  biased at  $I_{\text{bias}} = 120\text{nA}$ , we find  $L_{\text{kin}} \simeq 2 \cdot 10^{-9}H$ . Together with  $C_J \simeq 1\text{fF}$ , this means that the SQUID is overdamped if  $R \ll R_{\text{max}} = 1.4\text{k}\Omega$ . Using Eq. 8, we find that this provides an Ohmic environment with Drude-cutoff,  $J(\omega) = \alpha\omega/(1 + \omega^2/\omega_{LR}^2)$  where  $\omega_{LR} = R/L_{\text{kin}}$  and  $\alpha = (2\pi)^2/\hbar (M_{SQ}I_q/\Phi_0)^2 I_{\text{bias}}^2 \tan^2(\pi\Phi/\Phi_0)L_{\text{kin}}^2/R_S$ . Using the parameters from [12],  $M_{SQ}I_q/\Phi_0 = 0.002$ , we find  $\alpha R = 0.08\Omega$  and  $\omega_{LR}/R = 8.3\text{GHz}/\Omega$ . Thus, for our range of parameters (which essentially correspond to weak coupling between SQUID and qubit), one still has *low* damping of the qubit from the (internally overdamped) environment at reasonable shunt resistances down to tens of Ohms. For such a setup, one can apply the continuous weak measurement theory as it is outlined e.g. in [18]. This way, one can readily describe the readout through measurement of  $Z_{\text{eff}}$  which leaves the system on the superconducting branch. If one desires to read out the state by monitoring the voltage at bias currents *above* the  $I_{c,\text{eff}}$ , our analysis only describes the pre-measurement phase and at least shows that the system is hardly disturbed when the current is ramped.

770 F. K. Wilhelm et al.

#### 4.2 Capacitive Shunt

Next, we consider a large superconducting capacitive shunt (Fig. 2a, as implemented in [4,9]). The  $C$  shunt only makes the effective mass of the SQUID's external phase  $\gamma_{\text{ex}}$  very heavy. The total impedance  $Z_{\text{eff}}(\omega)$  and  $J(\omega)$  are modeled as before, see Fig. 3. As limiting values, we find

$$\text{Re}\{Z_{\text{eff}}(\omega)\} \approx \begin{cases} \frac{\omega^2 L_J^2}{R_l}, & \text{for } \omega \ll \omega_{LC} \\ R_l, & \text{for } \omega = \omega_{LC} \\ \frac{1}{\omega^2 C_{sh}^2 R_l}, & \text{for } \omega \gg \omega_{LC} \end{cases} \quad (11)$$

We can observe that this circuit is a weakly damped  $LC$ -oscillator and it is clear from (9) and (8) that one should keep its resonance frequency  $\omega_{LC} = 1/\sqrt{L_J C_{sh}}$ , where  $\text{Re}\{Z_{\text{eff}}(\omega)\}$  has a maximum, away from the qubit's resonance  $\omega_{\text{res}} = \nu/\hbar$ . This is usually done by choosing  $\omega_{LC} \ll \omega_{\text{res}}$ . For a  $C$ -shunted circuit with  $\omega_{LC} \ll \omega_{\text{res}}$ , this yields for  $J(\omega \approx \omega_{LC})$

$$J(\omega) \approx \frac{(2\pi)^2}{\hbar\omega^3} \left(\frac{MI_P}{\Phi_0}\right)^2 I_{\text{bias}}^2 \tan^2\left(\frac{\pi\Phi}{\Phi_0}\right) \frac{1}{C_{sh}^2 R_l} \quad (12)$$

The factor  $1/\omega^3$  indicates a natural cut-off for  $J(\omega)$ , which prevents the ultraviolet divergence [11,10] and which in much of the theoretical literature is introduced by hand. Using Eq. (9), we can directly analyze mixing times  $\tau_r$  vs  $\omega_{\text{res}}$  for typical sample parameters (here calculated with the

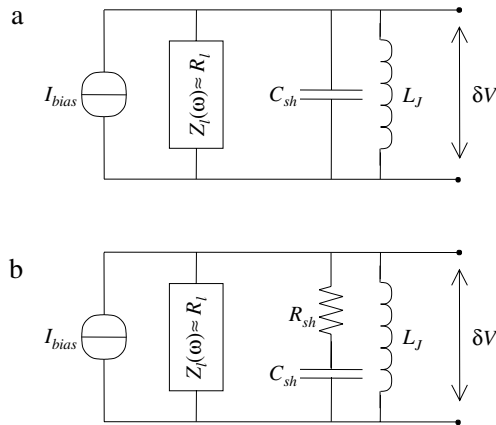


**Fig. 2.** Circuit models for the  $C$ -shunted DC-SQUID (a) and the  $RC$ -shunted DC-SQUID (b). The SQUID is modeled as an inductance  $L_J$ . A shunt circuit, the superconducting capacitor  $C_{sh}$  or the  $R_{sh}$ - $C_{sh}$  series, is fabricated on chip very close to the SQUID. The noise that couples to the qubit results from Johnson-Nyquist voltage noise  $\delta V$  from the circuit's total impedance  $Z_{\text{eff}}$ .  $Z_{\text{eff}}$  is formed by a parallel combination of the impedances of the leads  $Z_l$ , the shunt and the SQUID, such that  $Z_{\text{eff}}^{-1} = 1/Z_l + 1/(R_{sh} + 1/i\omega C_{sh}) + 1/i\omega L_J$ , with  $R_{sh} = 0$  for circuit (a)

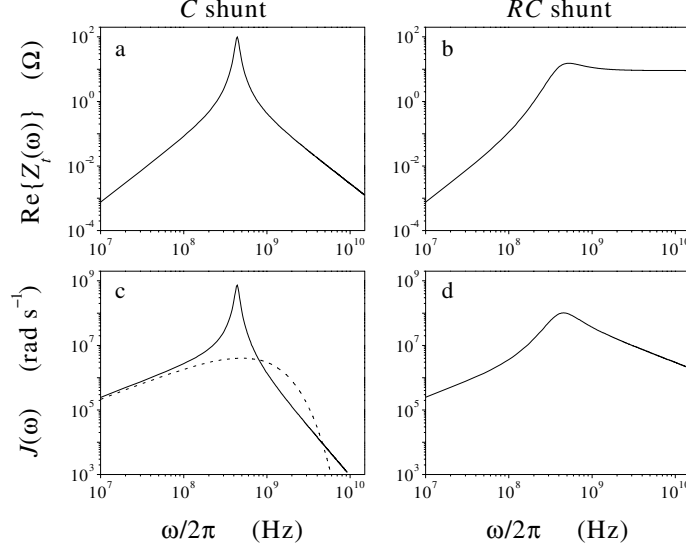


**Fig. 3.** A typical  $\text{Re}\{Z_t(\omega)\}$  for the  $C$ -shunted SQUID (a) and the  $RC$ -shunted SQUID (b), and corresponding  $J(\omega)$  in (c) and (d) respectively. For comparison, the dashed line in (c) shows a simple Ohmic spectrum,  $J(\omega) = \alpha\omega$  with exponential cut off  $\omega_c/2\pi = 0.5$  GHz and  $\alpha = 0.00062$ . The parameters used here are  $I_p = 500$  nA and  $T = 30$  mK. The SQUID with  $2I_{co} = 200$  nA is operated at  $f = 0.75\pi$  and current biased at 120 nA, a typical value for switching of the  $C$ -shunted circuit (the  $RC$ -shunted circuit switches at higher current values). The mutual inductance  $M = 8$  pH (i. e.  $MI_p/\Phi_0 = 0.002$ ). The shunt is  $C_{sh} = 30$  pF and for the  $RC$  shunt  $R_{sh} = 10$   $\Omega$ . The leads are modeled by  $R_l = 100$   $\Omega$

non-approximated version of  $\text{Re}\{Z_t(\omega)\}$ , see [12] for details. The mixing rate is then  $\Gamma_r \approx (2\pi\Delta/\hbar)^2 \omega_{\text{res}}^{-5} (MI_p/\Phi_0)^2 I_{\text{bias}}^2 \tan^2(\pi\Phi/\Phi_0) (2\hbar C_{sh}^2 R_l)^{-1} \coth(\hbar\omega_{\text{res}}/2k_B T)$ . With the  $C$ -shunted circuit it seems possible to get  $\tau_r$  values that are very long. They are compatible with the ramp times of the SQUID, but too slow for fast repetition rates. For the parameters used here they are in the range of 15  $\mu\text{s}$ . While this value is close to the desired order of magnitude, one has to be aware of the fact that at these high switching current values the linearization of the junction as a kinetic inductor may underestimate the actual noise. In that regime, phase diffusion between different minima of the washboard potential also becomes relevant and changes the noise properties [19,20].

### 4.3 RC-Shunt

As an alternative we will consider a shunt that is a series combination of a capacitor and a resistor (Fig. 2b) ( $RC$ -shunted SQUID). The  $RC$  shunt also adds damping at the plasma frequency of the SQUID, which is needed for

772 F. K. Wilhelm et al.

realizing a high resolution of the SQUID readout (i. e. for narrow switching-current histograms) [19]. The total impedance  $Z_t(\omega)$  of the two measurement circuits are modeled as in Fig. 2. For the circuit with the  $RC$  shunt

$$\operatorname{Re}\{Z_t(\omega)\} \approx \begin{cases} \frac{\omega^2 L_l^2}{R_l}, & \text{for } \omega \ll \omega_{LC} \\ \leq R_l, & \text{for } \omega = \omega_{LC} \ll \frac{1}{R_{sh} C_{sh}} \\ R_l // R_{sh}, & \text{for } \omega = \omega_{LC} \gg \frac{1}{R_{sh} C_{sh}} \\ R_l // R_{sh}, & \text{for } \omega \gg \omega_{LC} \end{cases}. \quad (13)$$

The difference mainly concerns frequencies  $\omega > \omega_{LC}$ , where the  $C$ -shunted circuit has a stronger cutoff in  $\operatorname{Re}\{Z_{\text{eff}}(\omega)\}$ , and thereby a relaxation rate, that is several orders lower than for the  $RC$ -shunted circuit. Given the values of  $J(\omega)$  from Fig. 3 one can directly see from the values of that an  $RC$ -shunted circuit with otherwise similar parameters yields at  $\omega_{res}/2\pi = 10$  GHz relaxation times that are about four orders of magnitude shorter.

## 5 Coupled Qubits

So far, we have applied our modeling only to single qubits. In order to study entanglement in a controlled way and to eventually perform quantum algorithms, this has to be extended to coupled qubits.

### 5.1 Hamiltonian

There is a number of ways how to couple two solid-state qubits in a way which permits universal quantum computation. If the qubit states are given through real spins, one typically obtains a Heisenberg-type exchange coupling. For other qubits, the three components of the pseudo-spin typically correspond to physically completely distinct variables. In our case,  $\hat{\sigma}_z$  corresponds to the flux through the loop whereas  $\hat{\sigma}_{x/y}$  are charges. Consequently, one usually finds Ising-type couplings. The case of  $\hat{\sigma}_y^{(1)} \otimes \hat{\sigma}_y^{(2)}$  coupling, i.e. coupling by a component which is orthogonal to all possible single-qubit Hamiltonians, has been extensively studied [21,22], because this type is straightforwardly realized as a *tunable* coupling of charge qubits [3]. We study the generic case of coupling the “natural” variables of the pseudospin to each other, which can be realized in flux qubits using a switchable superconducting transformer [6,23], but has also been experimentally utilized for coupling charge qubits by fixed capacitive interaction [24].

We model the Hamiltonian of a system of two qubits, coupled via Ising-type coupling. Each of the two qubits is described by the Hamiltonian Eq. (1). The coupling between the qubits is described by  $\hat{H}_{\text{qq}} = -(K/2)\hat{\sigma}_z^{(1)} \otimes \hat{\sigma}_z^{(2)}$  that represents e.g. inductive interaction. Thus, the complete two-qubit Hamiltonian in the absence of a dissipative environment reads

$$\hat{H}_{2qb} = -\frac{1}{2} \sum_{i=1,2} \left( \epsilon_i \hat{\sigma}_z^{(i)} + \Delta_i \hat{\sigma}_x^{(i)} \right) - \frac{1}{2} K \hat{\sigma}_z^{(1)} \hat{\sigma}_z^{(2)}. \quad (14)$$

For two qubits, there are several ways to couple to the environment: Both qubits may couple to a common bath such as picked up by coupling elements [6]. Local readout and control electronics coupling to individual qubits [6] can be described as coupling to two uncorrelated baths. In analogy to the procedure described above, one can determine the spectral functions of these baths by investigating the corresponding impedances.

In the case of two uncorrelated baths, the full Hamiltonian reads

$$\hat{H}_{2qb}^{2b} = \hat{H}_{2qb} + \sum_{i=1,2} \frac{1}{2} \hat{\sigma}_z^{(i)} \hat{X}^{(i)} + \hat{H}_{B_1} + \hat{H}_{B_2}, \quad (15)$$

$\hat{X}^{(i)} = \zeta \sum_{\nu} \lambda_{\nu} x_{\nu}$  are collective coordinates of the bath. In the case of two qubits coupling to one common bath we model our two qubit system in a similar way with the Hamiltonian

$$\hat{H}_{2qb}^{1b} = \hat{H}_{2qb} + \frac{1}{2} \left( \hat{\sigma}_z^{(1)} + \hat{\sigma}_z^{(2)} \right) \hat{X} + \hat{H}_B, \quad (16)$$

where  $\hat{X}$  is a collective bath coordinate similar to above.

## 5.2 Rates

We can derive formulae for relaxation and dephasing rates similar to Eqs. (9) and (10). Our Hilbert space is now four-dimensional. We label the eigenstates as  $|E1\rangle \dots |E4\rangle$ . We chose  $|E1\rangle$  to be the singlet state  $(|\uparrow\downarrow\rangle - |\downarrow\uparrow\rangle)/\sqrt{2}$ , which is always an eigenstate [25] whereas  $|E2\rangle \dots |E4\rangle$  are the energy eigenstates in the triplet subspace, which are typically *not* the eigenstates of  $\hat{\sigma}_z^{(1)} + \hat{\sigma}_z^{(2)}$ . As we have 4 levels, we have 6 independent possible quantum coherent oscillations, each of which has its own dephasing rate, as well as 4 relaxation channels, one of which has a vanishing rate indicating the existence of a stable thermal equilibrium point. The expressions for the rates, although of similar form as in Eqs. (9) and (10) are rather involved and are shown in [25]. Figure 4 displays the dependence of typical dephasing rates and the sum of all relaxation rates  $\Gamma_R$  on temperature for the case  $\Delta = \epsilon = K = h\nu_S$  with  $\nu_S = 1\text{GHz}$ . The rates are of the same magnitude for the case of one common bath and two distinct baths. If the temperature is increased above the roll off point set by the intrinsic energy scales,  $T_s = (h/k_B)\nu_s = 4.8 \cdot 10^{-2}\text{K}$ , where  $E_s = 1\text{GHz}$ , the increase of the dephasing and relaxation rates follows a linear dependence, indicating that the environmental fluctuations are predominantly thermal. As a notable exception, in the case of one common bath the dephasing rates  $\Gamma_{\varphi_{21}} = \Gamma_{\varphi_{12}}$  go to zero when the temperature is decreased while all other rates saturate for  $T \rightarrow 0$ . This can be understood as follows: the singlet state  $|E1\rangle$  is left invariant by the Hamiltonian of coupled qubits in a common bath, Eq. (16), i.e. it is an energy eigenstate left unaffected by the environment. Superpositions of the singlet with *another* eigenstate are usually still unstable, because the other eigenstate generally suffers from

774 F. K. Wilhelm et al.

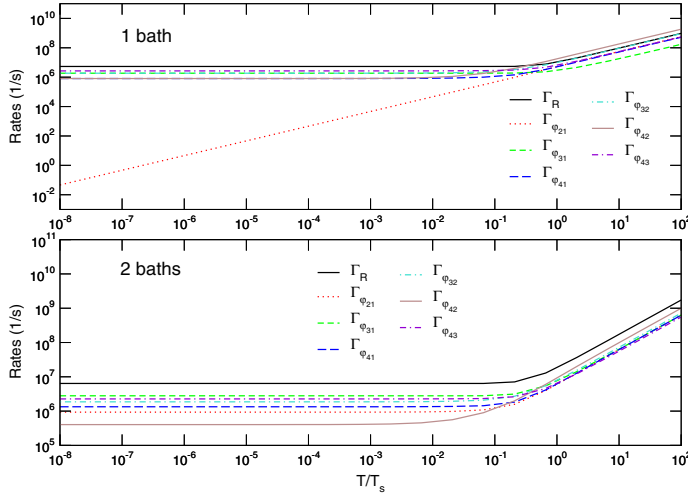


**Fig. 4.** Log-log plot of the temperature dependence of the sum of the four relaxation rates and selected dephasing rates. Qubit parameters  $K$ ,  $\epsilon$  and  $\eta$  are all set to  $E_s$  and the bath is assumed to be Ohmic  $\alpha = 10^{-3}$ . The *upper panel* shows the case of one common bath, the *lower panel* the case of two distinct baths. At the characteristic temperature of approximately  $0.1 \cdot T_s$  the rates increase very steeply

decoherence. However, the lowest-energy state of the triplet subspace  $|E2\rangle$  cannot decay by spontaneous emission and flip-less dephasing vanishes at  $T = 0$ , hence the dephasing rate between eigenstates  $|E1\rangle$  and  $|E2\rangle$  vanishes at low temperatures, see Fig. 4. As shown in [25], there can be more “protected” transitions of this kind if the qubit parameters are adjusted such that the symmetry between the unperturbed qubit and the coupling to the bath is even higher, e.g. at the working point for a CPHASE operation.

### 5.3 Gate Performance

The rates derived in the previous section are numerous and do strongly depend on the tunable parameters of the qubit. Thus, they do not yet allow a full assessment of the performance as a quantum logic element. A quantitative measure of how well a two-qubit setup performs a quantum logic gate operation are the gate quality factors introduced in [26]: the fidelity, purity, quantum degree and entanglement capability. These factors characterize the density matrices obtained after attempting to perform the gate operation in a hostile environment, starting from all possible initial conditions  $\rho(0) = |\Psi_{in}^j\rangle\langle\Psi_{in}^j|$ . To form all possible initial density matrices needed to calculate the gate quality factors, we use the 16 unentangled product states  $|\Psi_{in}^j\rangle$ ,  $j = 1, \dots, 16$  defined [22] according to  $|\Psi_a\rangle_1 |\Psi_b\rangle_2$ , ( $a, b = 1, \dots, 4$ ), with  $|\Psi_1\rangle = |0\rangle$ ,  $|\Psi_2\rangle = |1\rangle$ ,  $|\Psi_3\rangle = (1/\sqrt{2})(|0\rangle + |1\rangle)$ , and  $|\Psi_4\rangle = (1/\sqrt{2})(|0\rangle + i|1\rangle)$ .

They form one possible basis set for the superoperator  $\nu_G$  which describes the open system dynamics such that  $\rho(t_G) = \nu_G \rho(0)$  [22,26]. The CNOT gate is implemented using rectangular DC pulses and describing dissipation through the Bloch-Redfield equation as described in [3,25].

The fidelity is defined as  $F = (1/16) \sum_{j=1}^{16} \langle \Psi_{in}^j | U_G^\dagger \rho_G^j U_G | \Psi_{in}^j \rangle$ . The fidelity is a measure of how well a quantum logic operation was performed. Clearly, the fidelity for the ideal quantum gate operation is equal to 1. The second quantifier is the purity  $P = (1/16) \sum_{j=1}^{16} \text{tr} [(\rho_G^j)^2]$ , which should be 1 in a pure and 1/4 in a fully mixed state. The purity characterizes the effects of decoherence. The quantum degree measures nonlocality. It is defined as the maximum overlap of the resulting density matrix after the quantum gate operation with the maximally entangled Bell-states  $Q = \max_{j,k} \langle \Psi_{me}^k | \rho_G^j | \Psi_{me}^k \rangle$ . For an ideal entangling operation, e.g. the CNOT gate, the quantum degree should be 1. It has been shown [27] that all density operators that have an overlap with a maximally entangled state that is larger than the value 0.78 [22] violate the Clauser-Horne-Shimony-Holt (CHSH) inequality and are thus non-local. The entanglement capability  $\mathcal{C}$  is the smallest eigenvalue of the partially transposed density matrix for all possible unentangled input states  $|\Psi_{in}^j\rangle$ . (see below). It has been shown [28] to be negative for an entangled state. This quantifier should be -0.5, e.g. for the ideal CNOT, thus characterizing a maximally entangled final state.

In Fig. 5, the deviations due to decoherence of the gate quality factors from their ideal values are shown. Similar to most of the rates, all gate quality factors saturate at temperatures below a threshold set by the qubit energy scales. The deviations grow linearly at higher temperatures until they reach their theoretical maximum. Comparing the different coupling scenarios, we see that at low temperatures, the purity and fidelity are higher for the case of one common bath, but if temperature is increased above this threshold, fidelity and purity are approximately equal for both the case of one common and two distinct baths. This is related to the fact that in the case of one common bath all relaxation and dephasing rates vanish during the two-qubit-step of the CNOT (see [25] for details), due to the special symmetries of the Hamiltonian, when temperature goes to zero as discussed above. Still, the quantum degree and the entanglement capability tend towards the same value for both the case of one common and two distinct baths. This is due to the fact that both quantum degree and entanglement capability are, different than fidelity and purity, not defined as mean values but rather characterize the “best” possible case of all given input states.

In the recent work by Thorwart and Hänggi [22], the CNOT gate was investigated for a  $\hat{\sigma}_y^{(i)} \otimes \hat{\sigma}_y^{(j)}$  coupling scheme and one common bath. They find a pronounced degradation of the gate performance with gate quality factors only weakly depending on temperature. If we set the dissipation and the intrinsic energy scale to the same values as in their work, we also observe only a weak decrease of the gate quality factors for both the case of one com-

776 F. K. Wilhelm et al.

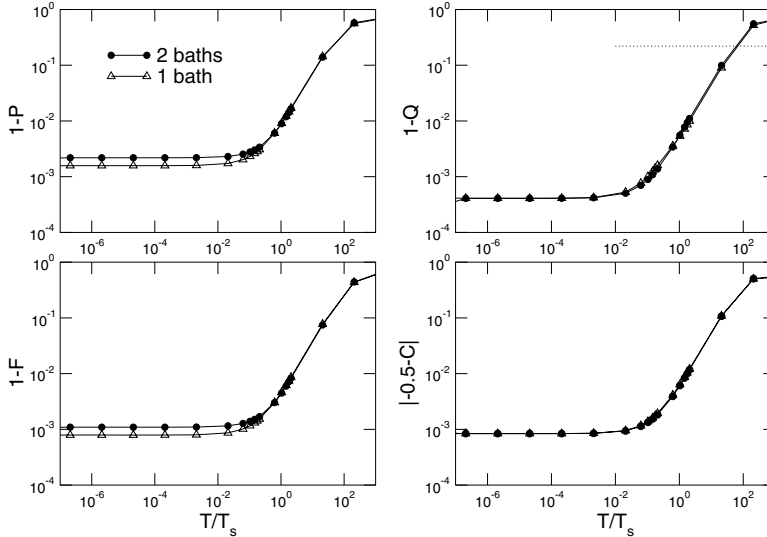


**Fig. 5.** Log-log plot of the temperature dependence of the deviations of the four gate quantifiers from their ideal values. Here the temperature is varied from  $\approx 0$  to  $2 \cdot E_s$ . In all cases  $\alpha = \alpha_1 = \alpha_2 = 10^{-3}$ . The dotted line indicates the upper bound set by the Clauser-Horne-Shimony-Holt inequality

mon bath and two distinct baths in the same temperature range discussed by Thorwart and Hänggi. However, see Fig. 5, overall we find substantially better values. This is due to the fact that for  $\hat{\sigma}_y \otimes \hat{\sigma}_y$  coupling, the Hamiltonian does *not* commute with the coupling to the bath during the two-qubit steps of the pulse sequence, i.e. the symmetries of the coupling to the bath and the inter-qubit coupling are not compatible. The dotted line in Fig. 5 shows that already at comparably high temperature, about 20 qubit energies, a quantum degree larger than  $\mathcal{Q} \approx 0.78$  can be achieved. Only then, the Clauser-Horne-Shimony-Holt inequality is violated and non-local correlations between the qubits occur as described in [22]. Thus, even under rather modest requirements on the experimental setup which seem to be feasible with present day technology, it appears to be possible to demonstrate nonlocality and entanglement between superconducting flux qubits.

## 6 Summary

It has been outlined, how one can model the decoherence of an electromagnetic environment inductively coupled to a superconducting flux qubit. We have exemplified a procedure based on analyzing the classical friction induced by the environment for the specific case of the read-out SQUID. It is shown that the SQUID can be effectively decoupled from the qubit if no bias cur-



rent is applied. The effect of the decoherence on relaxation and dephasing rates of single qubits has been discussed as well as the gate performance of coupled qubits. We have shown that by carefully engineering the impedance and the symmetry of the coupling, one can reach excellent gate quality which complies with the demands of quantum computation.

### Acknowledgements

We would like to thank M. Governale, T. Robinson, and M. Thorwart for discussions. FKW and MJS acknowledge support from ARO under contract-No. P-43385-PH-QC.

### References

1. see e.g. D. Bouwmeester, A.K. Ekert, and A. Zeilinger, *The Physics of Quantum Information* (Springer, Berlin, Heidelberg, 2000). 763
2. D. DiVincenzo, *Science* **270**, 255 (1995). 763
3. Yu. Makhlin, G. Schön, and A. Shnirman, *Rev. Mod. Phys.* **73**, 357 (2001). 763, 764, 769, 772, 775
4. I. Chiorescu, Y. Nakamura, C.J.P.M. Harmans, and J.E. Mooij, *Science* **299**, 1869 (2003). 763, 764, 765, 770
5. Yu.A. Pashkin, T. Yamamoto, O. Astafiev, Y. Nakamura, D.V. Averin, and J.S. Tsai, *Nature* **421**, 823 (2003). 763, 764
6. J.E. Mooij, T.P. Orlando, L. Levitov, L. Tian, C.H. van der Wal, and S. Lloyd, *Science* **285**, 1036 (1999); T.P. Orlando, J.E. Mooij, L. Tian, C.H. van der Wal, L.S. Levitov, S. Lloyd, and J.J. Mazo, *Phys. Rev. B* **60**, 15398 (1999). 764, 765, 767, 772, 773
7. L. Tian, L.S. Levitov, C.H. van der Wal, J.E. Mooij, T.P. Orlando, S. Lloyd, C.J.P.M. Harmans, and J.J. Mazo in I. Kulik and R. Ellitiogly, *Quantum Mesoscopic Phenomena and Mesoscopic Devices in Microelectronics* (Kluwer, Dordrecht, 2000), 429. 764
8. Yu. Makhlin *et al.*, this volume. 764
9. C.H. van der Wal, A.C.J. ter Haar, F.K. Wilhelm, R.N. Schouten, C.J.P.M. Harmans, T.P. Orlando, S. Lloyd, and J.E. Mooij, *Science* **290**, 773 (2000). 764, 765, 770
10. M. Grifoni, E. Paladino, U. Weiss, *Eur. Phys. J. B* **10**, 719 (1999). 765, 768, 770
11. A.J. Leggett, S. Chakravarty, A.T. Dorsey, M.P.A. Fisher, A. Garg, and W. Zwerger, *Rev. Mod. Phys.* **59**, 1 (1987). 766, 767, 768, 769, 770
12. C.H. van der Wal, F.K. Wilhelm, C.J.P.M. Harmans, and J.E. Mooij, *Eur. Phys. J. B* **31**, 111 (2003). 766, 768, 769, 771
13. A.J. Leggett, *Phys. Rev. B* **30**, 1208 (1984). 766, 768
14. U. Weiss, *Quantum Dissipative Systems*, (World Scientific, Singapore, ed. 2, 1999). 767, 768
15. A. Abragam, *Principles of Nuclear Magnetism* (Oxford University Press, Oxford, 1961). 768
16. F.K. Wilhelm, submitted to *Phys. Rev. B*. 769

778 F. K. Wilhelm et al.

17. S. Kleff, S. Kehrein, and J. von Delft, to appear in *Physica E*. 769
18. Yu. Makhlin, G. Schön, and A. Shnirman, *Physica C* **368**, 276 (2002). 769
19. P. Joyez, D. Vion, M. Götz, M.H. Devoret, D. Esteve, J. Supercond. **12**, 757 (1999). 771, 772
20. W.T. Coffey, Y.P. Kalmykov, J.T. Waldron, *The Langevin Equation; with Applications in Chemistry and Electrical Engineering*, (World Scientific, Singapore, 1996). 771
21. M. Governale, M. Grifoni, G. Schön, *Chem. Phys.* **268**, 273 (2001). 772
22. M. Thorwart, P. Hänggi, *Phys. Rev. A* **65**, 012309 (2002). 772, 774, 775, 776
23. J.B. Majer, priv. comm. (2002). 772
24. Yu.A. Pashkin, T. Yamamoto, O. Astafiev, Y. Nakamura, D.V. Averin, J.S. Tsai, *Nature* **421**, 823 (2003). 772
25. M.J. Storcz and F.K. Wilhelm, *Phys. Rev. A* **67**, 042319 (2003). 773, 774, 775
26. J.F. Poyatos, J.I. Cirac, P. Zoller, *Phys. Rev. Lett.* **78**, 390 (1997). 774, 775
27. C.H. Bennett, G. Brassard, S. Popescu, B. Schumacher, J.A. Smolin, and W.K. Wootters, *Phys. Rev. Lett.* **76**, 722 (1996). 775
28. A. Peres, *Phys. Rev. Lett.* **77**, 1413 (1996). 775



PHYSICAL REVIEW A **72**, 052314 (2005)**Decoherence of a two-qubit system away from perfect symmetry**

M. J. Storcz,\* F. Hellmann, C. Hrelescu, and F. K. Wilhelm

*Physics Department, Arnold Sommerfeld Center for Theoretical Physics, and Center for NanoScience, Ludwig-Maximilians-Universität München, Theresienstrasse 37, 80333 München, Germany*

(Received 13 June 2005; published 14 November 2005)

The decoherence of an asymmetric two-qubit system that is coupled via a variable interaction term to a common bath or two individual baths of harmonic oscillators is examined. The dissipative dynamics are evaluated using the Bloch-Redfield formalism. It is shown that the behavior of the decoherence effects is affected mostly by the symmetries between the qubit operator that is coupled to the environment and the temperature, whereas the differences between the two bath configurations are very small. Moreover, it is elaborated that small imperfections of the qubit parameters do not necessarily lead to a drastic enhancement of the decoherence rates.

DOI: [10.1103/PhysRevA.72.052314](https://doi.org/10.1103/PhysRevA.72.052314)

PACS number(s): 03.67.Lx, 03.65.Yz, 05.40.-a, 85.25.-j

**I. INTRODUCTION**

Quantum computation provides a substantial speedup for several important computational tasks [1–4]. A general quantum bit (qubit) consists of a two level quantum system with a controllable Hamiltonian of sufficient generality to implement a universal set of quantum logic gates [5]. From such a set, an arbitrary quantum algorithm can be implemented to any desired accuracy limited only by decoherence. A universal two qubit system requires just single-qubit rotations and one additional entangling two qubit gate. One important example for an entangling two qubit gate is the controlled-NOT (CNOT) gate that switches the state of the second qubit depending on the state of the first qubit.

Superconducting Josephson charge and persistent current (flux) qubits have been shown to possess the necessary properties [4] to act as quantum bits. They have been manipulated coherently and coherence times in the  $\mu s$  range have been demonstrated experimentally [6–12] with a corresponding quality factor of quantum coherence of up to  $Q_\varphi \approx 10^4$  [10]. In a two qubit system, where the coupling was achieved using a shared Josephson junction, coherent Rabi oscillations between states of a coupled qubit system were observed [13,14] and in a two charge qubit system a conditional gate operation was performed [12]. All of these experiments suffer from material imperfections which lead to nonideal time evolutions of the quantum states due to a parameter spread in the characteristic energies of the system Hamiltonian. Thus, it is of general importance to theoretically model these asymmetric qubit systems and their decoherence properties to optimize the decoherence in experimental setups. In this paper, the dependence of the decoherence rates and gate quality factors on the parameter spread of the qubits will be elaborated theoretically. In perspective, this is of crucial importance for connecting the experimental status and prospects to these central concepts in quantum information science: which degree of parameter uniformity do experiments have to achieve for symmetry-based protection schemes to

work—do these schemes have to be extended in order to accommodate experimental restrictions?

On the other hand, for high symmetry of the qubit parameters, the qubit coherence can be intrinsically strongly protected. This extends from the protection of the singlet in a symmetric qubit setup [15] to the general concept of decoherence-free subspaces (DFS's) [16,17]. General considerations on the stability of such DFS's can be found in Ref. [18]. In this paper the experimental conditions for these intrinsic protection mechanisms are investigated and direct conclusions for the decoherence of a two qubit system are given.

Also, variable bath couplings to the decohering environment have already been identified as a novel parameter for engineering decoherence, e.g., in Ref. [19]. It is exactly these decoherence properties of a qubit bath interaction operator that lies in the  $xz$  plane on the Bloch sphere that will be investigated in this work.

In Sec. II, we will introduce the global model of two qubits with a general bath coupling operator and how coherence can be protected by symmetry. In Sec. III, we specify how decoherence is parameterized and handled using the Bloch-Redfield approach, which helps to compute the gate quality factors introduced in Sec. IV. Results are summarized in the two subsequent sections: Section V shows how decoherence and gate quality depends on the coupling angle whereas Sec. VI discusses the experimentally important case of asymmetrically fabricated qubits.

**II. THE MODEL**

The Hamiltonian of a typical pseudo-spin system can be expressed in terms of the Pauli matrices as

$$\mathbf{H}_q = -\frac{1}{2}(\epsilon\hat{\sigma}_z + \Delta\hat{\sigma}_x), \quad (1)$$

where  $\epsilon$  is the energy bias and  $\Delta$  is the tunneling amplitude. In a two qubit system, an additional interaction term is required to implement the universal two qubit gate. In superconducting implementations [6,8–11,20,21] this coupling

\*Email address: storcz@theorie.physik.uni-muenchen.de

STORCZ *et al.*PHYSICAL REVIEW A **72**, 052314 (2005)

term is typically proportional to  $\hat{\sigma}_z^{(1)}\hat{\sigma}_z^{(2)}$ . Here, the superscripts are the qubit indices. In particular, inductively coupled flux qubits [15,22] and capacitively coupled charge qubits [23] are coupled this way. Thus, the two qubit Hamiltonian is

$$\mathbf{H}_{2q} = -\frac{1}{2} \sum_{i=1}^2 (\epsilon^{(i)} \hat{\sigma}_z^{(i)} + \Delta^{(i)} \hat{\sigma}_x^{(i)}) - \frac{\gamma}{2} \hat{\sigma}_z^{(1)} \hat{\sigma}_z^{(2)}. \quad (2)$$

In the singlet/triplet basis,  $(1,0,0,0)^T = |\uparrow\uparrow\rangle$ ,  $(0,1,0,0)^T = (|\uparrow\downarrow\rangle + |\downarrow\uparrow\rangle)/\sqrt{2}$ ,  $(0,0,1,0)^T = |\downarrow\downarrow\rangle$ ,  $(0,0,0,1)^T = (|\uparrow\downarrow\rangle - |\downarrow\uparrow\rangle)/\sqrt{2}$  that exhibits the symmetry properties of the coupling most clearly, this Hamiltonian takes the following explicit matrix form:

$$\mathbf{H}_{2q} = -\frac{1}{2} \begin{pmatrix} \epsilon & \eta & \gamma & -\Delta\eta \\ \eta & -\gamma & \eta & -\Delta\epsilon \\ \gamma & \eta & -\epsilon & \Delta\eta \\ -\Delta\eta & -\Delta\epsilon & \Delta\eta & \gamma \end{pmatrix}, \quad (3)$$

with  $\epsilon = \epsilon^{(1)} + \epsilon^{(2)}$ ,  $\Delta\epsilon = \epsilon^{(1)} - \epsilon^{(2)}$  and  $\eta = (\Delta^{(1)} + \Delta^{(2)})/\sqrt{2}$ ,  $\Delta\eta = (\Delta^{(1)} - \Delta^{(2)})/\sqrt{2}$ . Using this Hamiltonian the CNOT gate can be implemented through a sequence of elementary quantum gates [15,24]

$$U_{\text{CNOT}} = U_H^{(2)} \exp\left(-i\frac{\pi}{4} \hat{\sigma}_z^{(1)}\right) \exp\left(-i\frac{\pi}{4} \hat{\sigma}_z^{(2)}\right) \\ \times \exp\left(-i\frac{\pi}{4} \hat{\sigma}_z^{(1)} \hat{\sigma}_z^{(2)}\right) \exp\left(-i\frac{\pi}{4} \hat{\sigma}_z^{(1)}\right) U_H^{(2)}, \quad (4)$$

where  $U_H^{(2)}$  denotes the Hadamard gate operation performed on the second qubit. It involves one two-qubit operation at step three only. For our numerical calculations we applied the characteristic energies that were used in Ref. [15] as a viable example for superconducting solid-state flux or charge qubits. Following this approach also gate sequences optimized with respect to decoherence have been studied [25]. Disregarding the Hadamard gates, the gate operation Eq. (4) forms a controlled-phase (CPHASE) gate

$$U_{\text{CPHASE}} = \begin{pmatrix} 1 & 0 & 0 & 0 \\ 0 & 1 & 0 & 0 \\ 0 & 0 & 1 & 0 \\ 0 & 0 & 0 & e^{i\phi} \end{pmatrix}, \quad (5)$$

with  $\phi = \pi$ .

### III. DECOHERENCE

In experimental realizations of this model, additional effects always impair the capability of the system to operate as a qubit. In condensed matter implementations, the most pronounced is the coupling to environmental degrees of freedom. This leads to relaxation, i.e., classical thermalization of the states as well as, on a much shorter time scale, to dephasing. Decoherence causes the system to act similar to a classical ensemble eliminating all potential computational benefits of quantum algorithms. For a wide range (e.g., Refs.

[15,23,26]) of solid state implementations the dominant decoherence effects caused by coupling to linear environments such as electric circuits obey Gaussian statistics and can be effectively modeled with a bath of harmonic oscillators. It is assumed here that there is only one decoherence source in the dominating order of magnitude in the coupling parameter and possible weaker noise sources are ignored. To model this source each qubit is either coupled to an individual or to a common bath of harmonic oscillators. The system Hamiltonian then takes the form

$$\mathbf{H}_{2qB}^{\text{2B}} = \mathbf{H}_{2q} + \frac{1}{2} (\hat{\sigma}_s^{(1)} \hat{X}^{(1)} + \hat{\sigma}_s^{(2)} \hat{X}^{(2)}) + \mathbf{H}_B^{(1)} + \mathbf{H}_B^{(2)} \quad (6)$$

or

$$\mathbf{H}_{2qB}^{\text{1B}} = \mathbf{H}_{2q} + \frac{1}{2} (\hat{\sigma}_s^{(1)} + \hat{\sigma}_s^{(2)}) \hat{X} + \mathbf{H}_B, \quad (7)$$

where  $\hat{\sigma}_s$  is the spin representation of the qubit operator talking to the environment that depends on the specific implementation of the qubit. For the special case of superconducting flux qubits, which only experience flux noise, and superconducting charge qubits which are only subject to charge noise, this would correspond to  $\hat{\sigma}_s = \hat{\sigma}_z$ . Here,  $\hat{X}$  is the collective coordinate of the harmonic oscillator bath and the superscript distinguishes between the single bath and the two bath case. The general form is

$$\hat{\sigma}_s = (\vec{c} \cdot \vec{\sigma}) = \sqrt{2} (c_x \hat{\sigma}_x + c_y \hat{\sigma}_y) + c_z \hat{\sigma}_z, \quad (8)$$

where the factor  $\sqrt{2}$  in front of  $c_x$  and  $c_y$  was chosen for convenience in the singlet/triplet basis in which the qubit-bath interaction becomes

$$\mathbf{H}_{\text{int}} = \frac{1}{2} \begin{pmatrix} c_z \hat{X} & c_- \hat{X} & 0 & -c_- \Delta \hat{X} \\ c_+ \hat{X} & 0 & c_- \hat{X} & c_z \Delta \hat{X} \\ 0 & c_+ \hat{X} & -c_- \hat{X} & c_+ \Delta \hat{X} \\ -c_+ \Delta \hat{X} & c_z \Delta \hat{X} & c_- \Delta \hat{X} & 0 \end{pmatrix}, \quad (9)$$

with  $c_{\pm} = c_x \pm ic_y$ ,  $\hat{X} = \hat{X}^{(1)} + \hat{X}^{(2)}$ . Here,  $\Delta \hat{X} = \hat{X}^{(1)} - \hat{X}^{(2)}$  for the case of two baths and  $\Delta \hat{X} = 0$  for one common bath.

In the following we will, without loss of generality, characterize the results by the angle  $\theta$  between the  $\hat{\sigma}_x$  and  $\hat{\sigma}_z$  component of the coupling

$$\hat{\sigma}_s \hat{X} = (\hat{\sigma}_x \sin \theta + \hat{\sigma}_z \cos \theta) \hat{X}. \quad (10)$$

This is completely analogous to the bath coupling that is encountered in proposed experimental qubit realizations, e.g., for charge qubits [19]. The bath coupling angle  $\theta$  is defined for  $\theta \in [0, \pi/2]$ .

DECOHERENCE OF A TWO-QUBIT SYSTEM AWAY FROM...

PHYSICAL REVIEW A **72**, 052314 (2005)

Following the lines of Refs. [15,26], the Bloch-Redfield formalism is applied to calculate the effects of decoherence. The Bloch-Redfield equations and decoherence rates are given analytically. However, in comparison to a fully analytic evaluation of the dynamics of the two-qubit system [27], with this method the time evolution of the reduced density matrix can also be determined numerically for a wide range of system Hamiltonians.

The environment, i.e., the bath of harmonic oscillators, is characterized by its spectral density. The strength of the dissipative effects is given by the dimensionless parameter  $\alpha$ . The bath spectral function is assumed to be linear in frequency up to a cutoff frequency  $\omega_c$ . Thus,  $J(\omega) = \alpha\hbar\omega/[1 + (\omega/\omega_c)^2]$ , i.e., we employ an Ohmic spectrum with a Drude cutoff. The cutoff frequency is chosen two orders of magnitude above the largest frequency which is typical for a flux qubit system,  $\omega_c = 10^{13}$  Hz [7].

We choose a rather large coupling strength to the environment of  $\alpha = 10^{-3}$ , which is still in the weak coupling regime, to be able to observe pronounced decoherence effects. The Bloch-Redfield equations describe the evolution of the density matrix in the eigenbasis of the unperturbed Hamiltonian [28,29]

$$\dot{\rho}_{nm} = -i\omega_{nm}\rho_{nm} - \sum_{kl} R_{nmkl}\rho_{kl}, \quad (11)$$

where the Redfield tensor  $R_{nmkl}$  is given by

$$R_{nmkl} = \delta_{lm} \sum_r \Gamma_{nr rk}^{(+)} + \delta_{nk} \sum_r \Gamma_{lr rm}^{(-)} - \Gamma_{lmnk}^{(-)} - \Gamma_{lmnk}^{(+)}, \quad (12)$$

and the rates  $\Gamma$  are given by the Golden Rule expressions

$$\Gamma_{lmnk}^{(+)} = \hbar^{-2} \int_0^\infty dt e^{-i\omega_{nk}t} \langle \tilde{H}_{l,lm}(t) \tilde{H}_{l,nk}(0) \rangle_\beta, \quad (13)$$

$$\Gamma_{lmnk}^{(-)} = \hbar^{-2} \int_0^\infty dt e^{-i\omega_{ml}t} \langle \tilde{H}_{l,lm}(0) \tilde{H}_{l,nk}(t) \rangle_\beta, \quad (14)$$

where  $\tilde{H}_{l,ij}(t)$  is the matrix element of the bath/system coupling part of the Hamiltonian in the interaction picture. Here,  $\beta$  indicates averaging over the degrees of freedom of the thermal bath. In the following  $\beta = 1/k_B T$ , where  $T$  is the temperature of the bath. Evaluating this, we find according to Ref. [15] for one common bath the rates

$$\begin{aligned} \Gamma_{lmnk}^{(\pm)} &= \frac{1}{8\hbar} \Lambda J(\omega_{ab}) [\coth(\beta\hbar\omega_{ab}/2) \mp 1] + \frac{i\Lambda}{4\pi\hbar} \\ &\times \mathcal{P} \int_0^\infty d\omega \frac{J(\omega)}{\omega^2 - \omega_{ab}^2} [\coth(\beta\hbar\omega/2) \omega_{ab} \mp \omega], \end{aligned} \quad (15)$$

where  $ab = nk$  for the plus rate and  $ab = lm$  for the minus rate and  $\Lambda = \Lambda_{lmnk} = \hat{\sigma}_{s,lm}^{(1)} \hat{\sigma}_{s,nk}^{(1)} + \hat{\sigma}_{s,lm}^{(1)} \hat{\sigma}_{s,nk}^{(2)} + \hat{\sigma}_{s,lm}^{(2)} \hat{\sigma}_{s,nk}^{(1)} + \hat{\sigma}_{s,lm}^{(2)} \hat{\sigma}_{s,nk}^{(2)}$ . For two distinct baths one finds analogously

$$\begin{aligned} \Gamma_{lmnk}^{(\pm)} &= \frac{1}{8\hbar} [\Lambda^1 J_1(\omega_{ab}) + \Lambda^2 J_2(\omega_{ab})] [\coth(\beta\hbar\omega_{ab}/2) \mp 1] \\ &+ \frac{i}{4\pi\hbar} [\Lambda^2 M_2^\pm(\omega_{ab}) + \Lambda^1 M_1^\pm(\omega_{ab})], \end{aligned} \quad (16)$$

with  $\Lambda^1 = \Lambda_{lmnk}^1 = \hat{\sigma}_{s,lm}^{(1)} \hat{\sigma}_{s,nk}^{(1)}$ ,  $\Lambda^2 = \Lambda_{lmnk}^2 = \hat{\sigma}_{s,lm}^{(2)} \hat{\sigma}_{s,nk}^{(2)}$  and

$$M_i^\pm(\Omega) = \mathcal{P} \int_0^\infty d\omega \frac{J_i(\omega)}{\omega^2 - \Omega^2} [\coth(\beta\hbar\omega/2) \Omega \mp \omega], \quad (17)$$

where  $\mathcal{P}$  denotes the principal value. The limit of  $\omega_{ab}$  tending towards zero can be evaluated separately

$$\begin{aligned} \Gamma_{lmnk}^{(+)} = \Gamma_{lmnk}^{(-)} &= \frac{\alpha}{4\beta\hbar} (\hat{\sigma}_{s,lm}^{(1)} \hat{\sigma}_{s,nk}^{(1)} + \hat{\sigma}_{s,lm}^{(1)} \hat{\sigma}_{s,nk}^{(2)} + \hat{\sigma}_{s,lm}^{(2)} \hat{\sigma}_{s,nk}^{(1)} \\ &+ \hat{\sigma}_{s,lm}^{(2)} \hat{\sigma}_{s,nk}^{(2)}) \end{aligned} \quad (18)$$

for one bath, and

$$\Gamma_{lmnk}^{(+)} = \Gamma_{lmnk}^{(-)} = \frac{1}{4\beta\hbar} (\alpha_1 \hat{\sigma}_{s,lm}^{(1)} \hat{\sigma}_{s,nk}^{(1)} + \alpha_2 \hat{\sigma}_{s,lm}^{(2)} \hat{\sigma}_{s,nk}^{(2)}) \quad (19)$$

for two baths. All calculations were performed in the same parameter regime as in Ref. [15], thus renormalization effects of the frequencies are weak and will be neglected. This structure of the rates nicely shows the relation to symmetry and DFS: The matrix elements of the  $\hat{\sigma}_s$  in the eigenbasis determine the simultaneous symmetry properties of the qubit Hamiltonian and the system bath coupling. The energy splittings  $\omega_{ab}$  determine the relevant segment of environmental phase space and depend on symmetry much more weakly.

#### IV. GATE QUALITY FACTORS

The ability of a realistic device, or in our case a more realistic model of a device, to operate a quantum gate is characterized by the four gate quality factors introduced in Ref. [30]. Those are the fidelity  $\mathcal{F}$ , purity  $\mathcal{P}$ , quantum degree  $\mathcal{Q}$ , and entanglement capability  $\mathcal{C}$ . The quantum degree and entanglement capability characterize entangling operations. They are unique to multiqubit gates. We will collectively refer to these as nonlocal gate quality factors (GQFs) as opposed to fidelity and purity, which are both well defined for an arbitrary number of qubits, in particular also for a single qubit, and will be referred to as the local gate quality factors.

The fidelity can be evaluated, following Ref. [24], as follows:

$$\mathcal{F} = \overline{\langle \Psi_{\text{in}} | U^\dagger \hat{\rho}_{\text{out}} U | \Psi_{\text{in}} \rangle}. \quad (20)$$

The overline indicates the average over a discrete set of unentangled input states  $|\Psi_{\text{in}}\rangle$  that can serve as a basis for all possible input density matrices. The propagator  $U$  is the ideal unitary evolution of the desired gate, and  $\hat{\rho}_{\text{out}}$  is the density matrix after applying the realistic gate to  $|\Psi_{\text{in}}\rangle$ . Thus a perfect gate reaches a fidelity of unity and the deviation from unity characterizes the deviation from the ideal process. The purity  $\mathcal{P}$  is indicative of the decoherence effects

STORCZ *et al.*PHYSICAL REVIEW A **72**, 052314 (2005)

$$\mathcal{P} = \overline{\text{tr}(\hat{\rho}_{\text{out}}^2)}. \quad (21)$$

Again, the overbar indicates the input state average. A pure output state leads to  $\mathcal{P}=1$ , whereas as the state becomes increasingly mixed, the square of the weight of the contributions no longer sums up to unity and goes down to a minimum of one divided by the dimension of the Hilbert space of the system,  $1/4$  in our case.

Whereas the preceding two factors can be defined for any number of qubits, the following two are particular to the higher-dimensional case:

$$\mathcal{Q} = \max_{\rho_{\text{out}}|\Psi_{\text{me}}\rangle} \langle \Psi_{\text{me}} | \rho_{\text{out}} | \Psi_{\text{me}} \rangle. \quad (22)$$

Here, the  $\rho_{\text{out}}$  are the density operators after the gate operation relating to unentangled input states, whereas the  $|\Psi_{\text{me}}\rangle$  are the maximally entangled states, also known as Bell states. Therefore, this measures the ability of the gate to create quantum entanglement.

Finally, the entanglement capability  $\mathcal{C}$  is the smallest eigenvalue of the density matrix resulting from transposing the density matrix of one qubit. As shown in Ref. [31], the non-negativity of this smallest eigenvalue is a necessary condition for the separability of the density matrix into two unentangled systems. After separation, the partially transposed density matrix is a valid density matrix as well, with non-negative eigenvalues. The negativity of the smallest eigenvalue thus indicates that the states are not separable and therefore nonlocal. It approaches  $-0.5$  for the ideal CNOT gate. The dynamics of entanglement in a two-qubit system has been studied in Ref. [32]. The entanglement capability is closely related to the *negativity*  $E_N$  of a state [33], which is a nonentropic entanglement monotone [34].

### V. COMBINATION OF $\hat{\sigma}_x$ AND $\hat{\sigma}_z$ ERRORS

Now, the spin-boson model with a variable coupling operator to the harmonic oscillator baths, Eq. (10), is studied in more detail. We start with the CPHASE gate, which is entangling and forms the core part of the CNOT operation. The

TABLE I. Maxima of the gate quality factors for the CNOT and the CPHASE gate operation. Here  $T$  indicates the temperature and  $T_S = E_S/k_B$  is the characteristic temperature scale, which corresponds to the qubit energy scale during the gate operation. Both the preferred bath configuration and qubit operator coupling to the bath are given.

CNOT	local GQFs	nonlocal GQFs	preferred case
$T \ll T_S$	close to $\hat{\sigma}_z$	close to $\hat{\sigma}_z$	1 bath
$T \gg T_S$	close to $\hat{\sigma}_z$	at $\hat{\sigma}_x$	1 bath
CPHASE	local GQFs	nonlocal GQFs	preferred case
$T \ll T_S$	at $\hat{\sigma}_z$	at $\hat{\sigma}_z$	— <sup>a</sup>
$T \gg T_S$	at $\hat{\sigma}_z$	at $\hat{\sigma}_x$	2 baths

<sup>a</sup>There is no clear tendency observed in this case, see Fig. 1. Close to pure  $\hat{\sigma}_z$  coupling two baths are preferred, and close to  $\hat{\sigma}_x$  one bath.

quantum degree for the CPHASE gate is always smaller than the ideal value because the CPHASE gate cannot create entangled Bell states in this particular basis. Thus, we did not consider the quantum degree for the CPHASE gate. The different error coupling configurations achieve the best gate quality factors for different coupling operators to the environmental baths. The scenarios are summarized in Table I.

Two qualitatively different temperature regimes are found, separated by a smooth crossover. Temperatures are measured in units of  $T_S$ , where  $E_S/h = (k_B/h)T_S$  is the characteristic energy scale, which corresponds to the typical qubit energy scale during the quantum gate operation and is typically of the order of a few GHz. For low temperatures  $T \ll T_S$ , spontaneous emission processes dominate. When  $T_S$  is approached, thermal effects become important and for  $T \approx T_S$  temperature is the dominating energy scale as will be discussed in more detail below.

The CPHASE gate, for pure  $\hat{\sigma}_z$  coupling, is protected by symmetry because the gate operation and the coupling to the bath commute. As was shown previously, all disturbances vanish here in the limit of low temperatures. In this case,

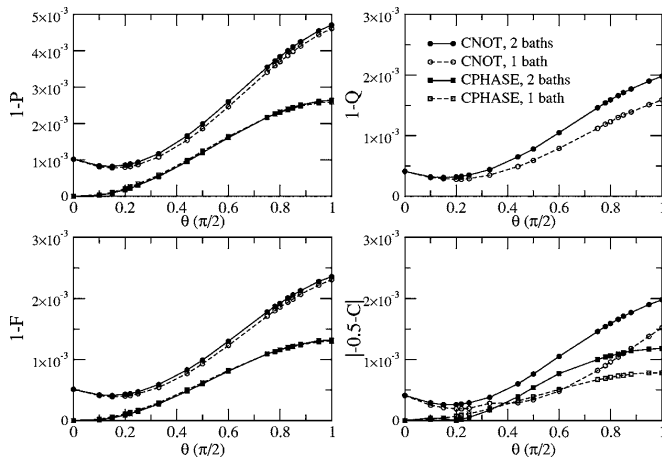


FIG. 1. Dependence of the gate quality factors on the bath coupling angle  $\theta$  defined in Eq. (10) for the CNOT and CPHASE operation at  $T \approx 0 \ll T_S$ . Here, the behavior of the gate quality factors for both the single bath and two bath case is shown. The characteristic energy scale for the gate operation is  $E_S/h = 1$  GHz [15]. The lines are provided as guides to the eye.

DECOHERENCE OF A TWO-QUBIT SYSTEM AWAY FROM...

PHYSICAL REVIEW A 72, 052314 (2005)

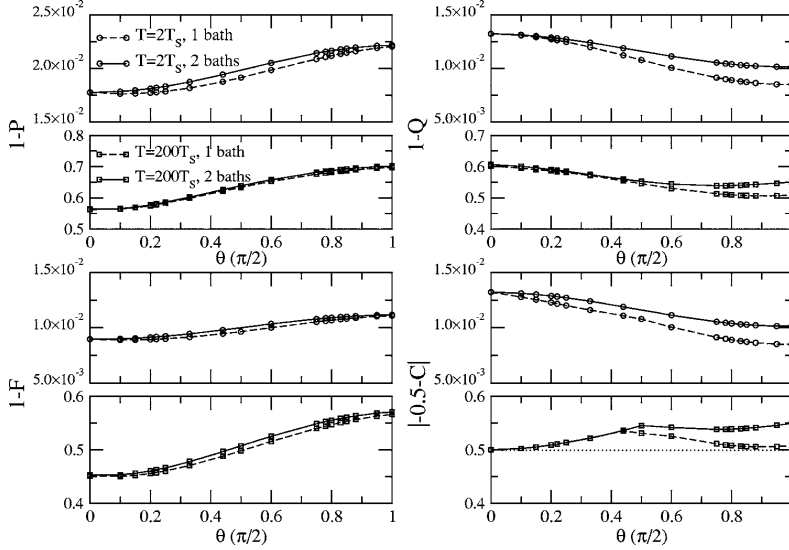


FIG. 2. Dependence of the gate quality factors on the bath coupling angle  $\theta$  defined in Eq. (10) for the CNOT operation at large temperatures  $T=2T_S$  and  $T=200T_S$ . The characteristic energy scale for the gate operation is  $E_S/\hbar=1$  GHz [15]. The lines are provided as guides to the eye.

spontaneous emission processes are the dominating decoherence mechanism because absorption and excitation processes are effectively suppressed due to the bath coupling (i.e., matrix elements for these processes are restricted due to symmetries of the bath coupling operators) and the temperature. In this case, the low-temperature regime can be referred to as the emission limited regime.

The additional  $\hat{\sigma}_x$  operation in the CNOT gate Eq. (4) during the single qubit Hadamard operations leads to nonvanishing decoherence rates even in the low-temperature limit. The reason is again the competition of pure dephasing with emission and absorption processes which show a different dependence on the coupling angle  $\theta$ .

However, the Hadamard part of the CNOT operation is short compared to the overall length of the gate operation (4). Thus, it is found that for low temperatures the best values for the GQFs are obtained very close to pure  $\hat{\sigma}_z$  coupling as depicted in Fig. 1. This implies that the overall decoherence effects are smallest if the bath coupling angle  $\theta$  throughout the gate is adjusted to the distribution of gate operations, which are characterized by different directions on the Bloch sphere.

For the CNOT gate better results are observed for the single bath case throughout the low-temperature regime, see Fig. 1. For the single bath configuration, close to pure  $\hat{\sigma}_x$  coupling to the bath, the difference becomes quite significant and for the nonlocal GQFs actually approaches a factor of 2, but reduces again as pure  $\hat{\sigma}_x$  coupling is reached. The CPHASE gate (see Fig. 1) prefers a two bath configuration unless the coupling is  $\hat{\sigma}_x$  dominated. Again, the nonlocal GQFs are affected most.

For the pure  $\hat{\sigma}_z$  case ( $\theta=0$  or correspondingly  $c_x=c_y=0$  and  $c_z=1$ ) little difference between the two bath and the single bath behavior is found in the CNOT case and none at all for the CPHASE. It is observed that the single bath configuration is certainly preferred as soon as there is a signifi-

cant  $\hat{\sigma}_x$  contribution in the gate operation. This means that the additional protection from the one-dimensional decoherence free subspace [15,16] involved is mainly beneficial if the commutator of the qubit operator, which couples to the bath and the qubit Hamiltonian (the Hamiltonian that is needed to perform the individual parts of the gate operation) has appropriate matrix elements, i.e., if there is a significant noncommuting part in the bath coupling and the gate operations. However, in a  $\hat{\sigma}_z$  dominated case the individual coupling is preferred as it does not induce any additional indirect couplings between the qubits. It is natural that the two qubit GQFs should notice this more strongly than the single qubit GQFs for which the differences never become more than about one fifth of the individual deviations.

For the high-temperature regime, drastically different behavior in the nonlocal GQFs is found, see Fig. 2. Both  $Q$  and  $C$  now achieve their best values at a pure  $\hat{\sigma}_x$  coupling for both gates, the local GQFs achieve their maximum at a pure  $\hat{\sigma}_z$  value. The protection that the CPHASE gate enjoyed in the low temperature regime breaks down here. The high-temperature case is essentially scale free, i.e., high temperatures symmetrize the system. In this case the system eigenbasis is given by the qubit operator which couples to the bath. This can be nicely shown when considering the single qubit dephasing rates within the spin-boson model [21]

$$\Gamma_\varphi = \frac{1}{T_2} = \frac{\epsilon^2}{2E^2} S(0) + \frac{\Delta^2}{2E^2} S(E), \quad (23)$$

where  $E$  is the single qubit energy splitting and  $S(E)$  denotes the power spectrum of the noise. The expression Eq. (23) becomes  $\Gamma_\varphi \approx 2\pi ak_B T/\hbar$  for  $T \gg E$  and does not depend on the ratio  $\Delta/\epsilon$ .

Thermalization is determined by the off-diagonal bath couplings in the basis of the corresponding system Hamiltonian which is required for a certain gate operation. It will



STORCZ *et al.*

PHYSICAL REVIEW A 72, 052314 (2005)

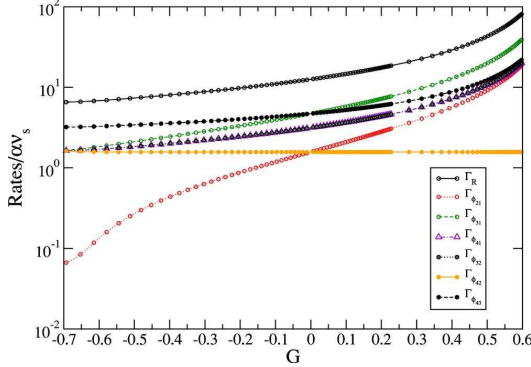


FIG. 3. (Color online) Dependence of the decoherence rates on the qubit asymmetry. Here, we set  $K=0$ ,  $\epsilon_i=0$ ,  $\Delta_2=E_S$ , and vary  $\Delta_1$ . The single and two bath cases behave identically, thus only the single bath case is shown. The strength of the decoherence effects is set to  $\alpha=10^{-3}$  and  $T \approx 0.5T_S$ . We set the bath coupling angles (24) to  $\theta_1=0$  and  $\theta_2=0$ , i.e., the bath coupling operator and the Hamiltonian are perpendicular. The decoherence rates are scaled by  $\alpha\nu_s$ , with  $\nu_s=E_S/h$ . The lines are provided as guides to the eye.

be strongly dominated by the noncommuting contributions, i.e., the  $\hat{\sigma}_x$  bath coupling for the CPHASE part of the CNOT gate. The single qubit Hadamard part of the CNOT gate will be additionally also affected by the  $\hat{\sigma}_z$  bath coupling. The two-qubit operation (CPHASE), or in other words the nonlocal part, of the CNOT gate is of the  $\hat{\sigma}_z^{(1)}\hat{\sigma}_z^{(2)}$  type and the single qubit Hadamard gates contain both  $\hat{\sigma}_x$  and  $\hat{\sigma}_z$  contributions. Thus, during the gate operation the thermalization is dominated strongly by the  $\hat{\sigma}_x$  part of the bath coupling for the nonlocal and by the  $\hat{\sigma}_z$  part for the local GQFs, implying that for thermal fluctuations the  $\hat{\sigma}_x$ -type couplings are more important in inducing interqubit transitions, while  $\hat{\sigma}_z$  primarily affects the single qubit gate quantifiers. What implementation to choose for a gate here, becomes a question of what gate quantifiers are desired to be optimized. The differences between the one bath and two bath scenario are now small.

For pure  $\hat{\sigma}_z$  coupling of the qubit to the bath, a peculiar effect is observed. In this case, the minimal eigenvalue of the partially transposed density matrix that is the entanglement capability remains negative even for  $T \gg T_S$  (Fig. 2). The negativity of the eigenvalue of the partially transposed density matrix is not just a necessary but also a sufficient criterion for the nonseparability of the system in our case [31]. Thus, no matter what the temperature or strength of the dissipative effects in our system during the CNOT gate operation, entanglement will never be eliminated completely. This can be explained by rapid thermalization into a protected entangled state. Furthermore, this effect carries over well into the regime where both  $\hat{\sigma}_x$  and  $\hat{\sigma}_z$  noise are present.

Overall, the temperature (and the coupling strength) has the largest influence on the GQFs. At  $T \ll T_S$  ( $T \approx 10^{-3}$  K), we observe deviations of the GQFs from the ideal value which are less than  $10^{-3}$ . At  $T \gg T_S$  ( $T \approx 1$  K) the deviations are  $10^{-1}$  and quickly increasing further at larger temperatures. The different coupling operators to the bath are the next strongest

effect. Rotating the coupling operator from  $\hat{\sigma}_z$  to  $\hat{\sigma}_x$  causes, in the worst cases, three to four times stronger deviations from the ideal value than the  $\hat{\sigma}_z$  noise. Finally, the change due to different types of bath couplings is generally small compared to the differences between  $\hat{\sigma}_x$  and  $\hat{\sigma}_z$  type coupling. This also suggests that we do not need to worry about noise sources with at least one order of magnitude weaker coupling strength, even if they couple through a less favorable coupling operator.

As an intermediate conclusion, it is found that for the decoherence dominated regime the CPHASE operation reached the optimum value of the GQFs for a pure  $\hat{\sigma}_z$  coupling to the bath. In the case of the CNOT operation, the minimum is located slightly shifted to the  $\hat{\sigma}_x$  component because of the mixture of  $\hat{\sigma}_x$  parts during the Hadamard operations, compare with Fig. 1. For the CNOT operation, the optimum values of the four gate quantifiers are encountered at different bath couplings, which are characterized by the mixing angle Eq. (10), especially for large temperatures.

Thus, the differences between the case of one common bath and two baths are much less important than the symmetries between the gate operation and the bath operators. In particular, the difference between the case of one or two baths disappears for pure  $\hat{\sigma}_z$  coupling to the bath. Here, decoherence due to flux noise or charge noise in coupled superconducting flux or charge qubits was explored. Decoherence due to  $1/f$  noise, caused by background charges or bistable fluctuators, was not treated. If still in the motional narrowing limit, it can be included in the Redfield equations by introducing a peak at zero frequency in the spectral function with a magnitude given by experiment [35]. More generally, microscopic calculations are needed [36].

## VI. NONIDENTICAL QUBITS

Now, we do not restrict the analysis to the case of a uniform error coupling Eq. (10) anymore. In general, both qubits can couple to the baths differently

$$\hat{\sigma}_s^{(i)} = \hat{\sigma}_x^{(i)} \sin \theta_i + \hat{\sigma}_z^{(i)} \cos \theta_i, \quad (24)$$

where  $i=1,2$  denotes one of the qubits. For the numerical calculations, the qubits are set to the degeneracy point  $K = \epsilon_i=0$  and  $\Delta_2$  is set to  $E_S$ , i.e., effectively this model describes a system of two uncoupled qubits. Here,  $\Delta_1$  and thus also the asymmetry  $G=(\Delta_1-\Delta_2)/(\Delta_1+\Delta_2)$  is varied.

Experimentally the spread of the qubit parameters due to fabrication imprecision is very important both because quantum algorithms (without further modification) require a certain level of precision and the decoherence effects in the system of qubits have to be sufficiently small [37].

Therefore, it is of central importance to investigate also the effects of the parameter spread in nonidentical qubits on the behavior of the decoherence rates. Superconducting qubits are preferably operated at the degeneracy point where decoherence effects are suppressed for superconducting charge and flux qubits. However, the tunnel matrix elements for superconducting qubits can differ significantly, on the order of several percent [12,14]. Thus, the dependence of the decoherence rates, i.e., dephasing rates and the relaxation

DECOHERENCE OF A TWO-QUBIT SYSTEM AWAY FROM...

PHYSICAL REVIEW A 72, 052314 (2005)

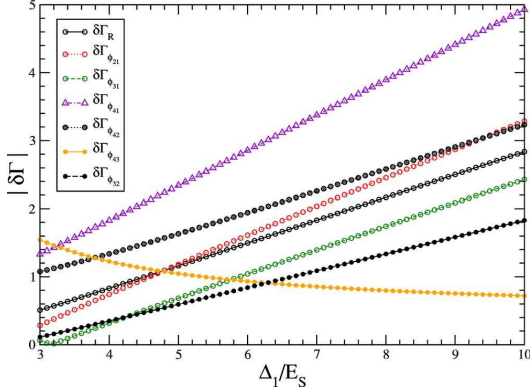


FIG. 4. (Color online) Dependence of the decoherence rates on the qubit asymmetry at  $T \approx 0.5T_S$ . Here, the case of one common bath is investigated. The tunnel matrix element of the second qubit and the interqubit coupling are set to  $\Delta_2 = K = E_S$  and  $\Delta_1$  is varied. For comparison with experiments, large asymmetry in the tunnel matrix elements of the individual qubits is investigated. The bath coupling angles are set to  $\theta_1 = 0$  and  $\theta_2 = 0$ . The strength of the dissipative effects is  $\alpha = 10^{-3}$ . The lines are provided as guides to the eye.

rate, close to the degeneracy point on the qubit asymmetry is an important property. The decoherence rates are defined according to Refs. [26,15]. Namely, the relaxation rate is  $\Gamma_R = -\sum_n \Lambda_n$ , where  $\Lambda_n$  are the eigenvalues of the matrix  $R_{n,n,m,m}$ ,  $n, m = 1, \dots, 4$ , and the dephasing rates are  $\Gamma_{\varphi_{nm}} = -\text{Re}R_{n,n,m,m}$ .

Figure 3 depicts the dependence of the decoherence rates on the qubit asymmetry  $G$  when the individual qubits are operated close to the degeneracy point. A Temperature  $T \approx 0.5T_S$ , which is typical for experimental situations, is chosen for this analysis.

We observe that for pure  $\hat{\sigma}_x$  coupling to the bath ( $\theta_1 = \pi/2$  and  $\theta_2 = \pi/2$ ), the asymmetry of the qubits is irrelevant because the coupling to the bath and the system Hamiltonian commute (the indices of qubit one and qubit two could be exchanged without changing the system). For mixed bath coupling of the  $\hat{\sigma}_x$  type for one qubit ( $\theta_1 = \pi/2$ ) and the  $\hat{\sigma}_z$  ( $\theta_2 = 0$ ) type for the other qubit, still the decoherence rates do not vary for different asymmetry. The reason for this behavior is that the  $\hat{\sigma}_x$  bath coupling of the first qubit *always* commutes with the qubit Hamiltonian, i.e., only flipless dephasing processes contribute to the decoherence rates of the first qubit. When we vary the asymmetry, essentially  $\Delta_1$  is varied ( $\Delta_2 = E_S$  is kept constant), which leads to a different contribution of the first qubit to the overall decoherence. However, these corrections are small compared to the full decoherence rates (i.e., not only flipless dephasing processes) that contribute in the case of qubit two where  $[H_{SB}, H_{sys}] \neq 0$  and  $\Delta_2$  stays constant.

Finally, Fig. 3 shows the case of exactly perpendicular system Hamiltonian and bath coupling. Here, the decoherence rates increase steeply for increasing asymmetry. Note here that due to the definition of  $G$  and  $\Delta_2$ , the two

cases  $G = -0.6 \rightarrow \Delta_1 = (1/4)E_S$  and  $G = 0.6 \rightarrow \Delta_1 = 4E_S$  are vastly different.

From the dependence of the decoherence rates on the asymmetry  $G$  of the two qubits at the degeneracy point, it is possible to estimate the maximum tolerable asymmetry for a given constraint on the deviation of the decoherence rates from their value for perfectly symmetric qubits. It is found that in order for the deviation of the relaxation rate from its value for perfectly symmetric qubits to stay below 1%, it is required that  $0.5\Delta_2 < \Delta_1 < 1.5\Delta_2$ ; i.e., the parameter spread of the two qubits could be remarkably large ( $\approx 50\%$ ) without considerably affecting the relaxation rates. However, detailed analysis shows that for the deviations of the dephasing rates, the increase happens much earlier. Moreover, there is a large spread among the dephasing rates, which are sensitive to the qubit asymmetries. Note that both the single bath and the two bath case behave identically for the relaxation rate. Differences between the two cases only occur for the dephasing rates. The angles of the bath coupling where the minimum dephasing rates are encountered are different for the different dephasing rates.

Typical experimental values for charge [12] and flux qubit [14] designs indicate that the parameter spread in the tunnel matrix amplitudes can be quite large, in the case of the charge qubit it is a factor of  $\Delta_2/\Delta_1 \approx 0.91$  and for the flux qubit  $\Delta_2/\Delta_1 \approx 4.22$ , which corresponds to deviations of approximately ten and up to several hundred percent, respectively. This difference of asymmetries is due to the fact, that fabrication parameters such as  $E_c$  and  $E_J$  enter the *exponent* of the tunnel splitting in the flux qubit case [6]. Thus, the parameter spread of the tunneling amplitudes for the flux qubit is larger and the decoherence rates will be considerably affected. These experimental values emphasize that it is important to study the evolution of the decoherence effects for nonidentical qubit parameters. Moreover, important information about the noise sources coupling to the qubit can be identified. From comparison of the decoherence rates for different qubit samples, which possess different asymmetries between the tunnel amplitudes, it is thus possible to identify the predominant bath coupling angle. In most qubit designs the bath coupling angle is then uniquely related to a certain noise source, e.g., flux noise in the case of flux qubits [38].

Figure 4 depicts the experimentally important [14] behavior of the decoherence rates when  $\Delta_2$  and  $K$  are fixed to  $E_S$  and  $\Delta_1 > \Delta_2$  is changed. We define the deviation of the decoherence, i.e., the relaxation or dephasing rates from their values at the degeneracy point as

$$\delta\Gamma_{R,\varphi_{ij}} = 1 - \frac{\Gamma_{R,\varphi_{ij}}(\Delta_1 \neq \Delta_2, K = E_S, \epsilon_i = 0)}{\Gamma_{R,\varphi_{ij}}(\Delta_1 = \Delta_2 = K = E_S, \epsilon_i = 0)}. \quad (25)$$

In this case the two qubits are permanently coupled, and embedded into one common environmental bath. The decoherence rates begin to increase linearly when  $\Delta_1$  is larger than  $\Delta_2$ .

Figure 5 illustrates the temperature dependence of the decoherence rates for the case of one common bath. The values of the decoherence rates for the two bath case differ insignificantly from the single bath case. We observe that the

STORCZ *et al.*

PHYSICAL REVIEW A 72, 052314 (2005)

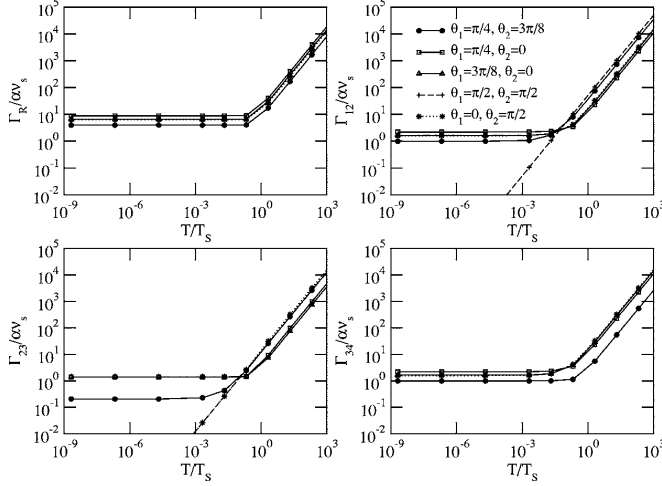


FIG. 5. Temperature dependence of selected decoherence rates for  $K=0$ ,  $\epsilon_i=0$ ,  $\Delta_1=E_S$ ,  $\Delta_2=0.9\Delta_1$ , for the single bath case. Here, temperature and the bath coupling angles are varied. The strength of the dissipative effects is set to  $\alpha=10^{-3}$ . The decoherence rates are scaled by  $\alpha\nu_S$ , where  $\nu_S=E_S/h$ . The lines are provided as guides to the eye.

spread of the magnitude of the different decoherence rates increases at intermediate mixing angles. As expected, the magnitude of the decoherence rates is maximum in the case where the system Hamiltonian and the coupling to the bath are perpendicular to each other. For the opposite case, where the system Hamiltonian and the coupling to the bath commute, the decoherence rates vanish for decreasing temperature, i.e., only flipless dephasing processes contribute to the overall decoherence. Note that in the case where the system Hamiltonian and the coupling to the bath commute ( $\theta_1=\pi/2$  and  $\theta_2=\pi/2$ ) the relaxation rate vanishes.

It is found that the dephasing rates depend strongly on the qubit asymmetry. Nevertheless the parameter spread of the qubit energies can be quite large (around 10%) without affecting the decoherence properties considerably for the case of a favorable bath coupling. However, for very large asymmetries and a bath coupling, which is perpendicular to the system Hamiltonian, the decoherence rates increase exponentially with asymmetry.

## VII. CONCLUSION

A system of two pseudospins coupled by an Ising-type  $\hat{\sigma}_z^{(1)}\hat{\sigma}_z^{(2)}$  interaction, which models e.g., superconducting charge or flux qubits, was investigated. It was shown that for the system of two pseudospins the optimum gate performance of different gate operations is closely related to their composition of elementary gates and the coupling to the bath. In more detail, the gate fidelity is enhanced when the coupling angle to the bath imitates the composition of the gate operation in terms of Hamiltonian parts pointing in different directions on the Bloch sphere. When considering the gate quality factors, the temperature and aforementioned special symmetries of the system-bath coupling have a large influence on the decoherence properties, whereas the differences for the single or two bath scenarios are minor. For the CPHASE operation at low temperatures, the optimum gate quality factors are at pure  $\hat{\sigma}_z$  system-bath coupling due to the fact that only in this case all individual Hamiltonians neces-

sary for performing the gate operations and the system bath coupling commute. Similarly, the CNOT gate operation approaches the best gate quality factors close to  $\hat{\sigma}_z$  system-bath coupling with a slight  $\hat{\sigma}_x$  admixture due to the Hadamard operations. These findings can be directly applied in systems where it is possible to engineer the decohering environment to a certain degree [39]. Moreover, special symmetries that are identified in experiments can also be used for the encoding of several physical qubits into logical qubits [16,17] to reduce the effects of the environmental bath.

For very large temperatures, the temperature effectively symmetrizes the system and thus entanglement is always preserved during a CNOT gate operation independently of the system-bath coupling. It is found that the parameter spread of the tunnel matrix elements of the qubits, when operated close to the degeneracy point can be quite large (approximately 10%) for a bath coupling which commutes with the system Hamiltonian without affecting the decoherence properties considerably; which again emphasizes the importance of using the symmetry properties of the system and bath to improve the decoherence of the qubit system. In the special case where the system Hamiltonian commutes with the system-bath coupling Hamiltonian, the differences in the decoherence rates stay below 1% for the aforementioned spread of the tunnel matrix elements. This special case can model the situation in superconducting flux qubits [13,14], where the dominating noise source is flux noise, quite well if the tunnel matrix elements of the individual qubits are small compared to the energy bias of the qubits and the interqubit coupling strength. However, in a more general setup with nonidentical qubits, the aforementioned symmetry properties are almost certainly not fulfilled and the performance of the qubits will be degraded quite significantly.

## VIII. OUTLOOK

Our results indicate, that in case of tunable bath coupling operators, decoherence may be further engineered. Moreover, they indicate that symmetry-induced coherence protec-

DECOHERENCE OF A TWO-QUBIT SYSTEM AWAY FROM...

PHYSICAL REVIEW A **72**, 052314 (2005)

tion is remarkably stable under realistic parameter spread. These results are expected to have significant impact on the analysis of the recent experiments [9,14,19]. Next to its practical importance, this emphasizes the role of the spatial correlations of the environmental noise that has been assumed here, but which needs to become an integral part of the experimental characterization of the environment.

## ACKNOWLEDGMENTS

This work was supported in part by DFG through SFB 631 and by NSA and ARDA under ARO Contract No. P-43385-PH-QC. We thank A.B. Zorin, W.D. Oliver, A. Marx, L.C.L. Hollenberg, S. Kohler, U. Hartmann, M. Mariani, and S. Ashhab for useful discussions.

- [1] P. Shor, in *Proceedings of the 35th Annual Symposium on the Foundations of Computer Science*, edited by S. Goldwasser (IEEE Computer Society Press, Los Alamitos, California, 1994), pp. 124–134.
- [2] L. K. Grover, *Phys. Rev. Lett.* **79**, 325 (1997).
- [3] D. Deutsch, *Proc. R. Soc. London, Ser. A* **400**, 97 (1985).
- [4] D. P. DiVincenzo, *Science* **269**, 225 (1995).
- [5] M. A. Nielsen and I. L. Chuang, *Quantum Computation and Quantum Information* (Cambridge University Press, Cambridge, 2000).
- [6] T. P. Orlando *et al.*, *Phys. Rev. B* **60**, 15398 (1999); J. E. Mooij *et al.*, *Science* **285**, 1036 (1999).
- [7] C. H. van der Wal, Ph.D. thesis, TU Delft, Delft, 2001.
- [8] Yu. A. Pashkin, T. Yamamoto, O. Astafiev, Y. Nakamura, D. V. Averin, and J. S. Tsai, *Nature (London)* **421**, 823 (2003).
- [9] Y. Nakamura, Yu. A. Pashkin, and J. S. Tsai, *Nature (London)* **398**, 786 (2002).
- [10] D. Vion, A. Aassime, A. Cottet, P. Joyez, H. Pothier, C. Urbina, D. Esteve, and M. H. Devoret, *Science* **296**, 886 (2002).
- [11] I. Chiorescu, Y. Nakamura, C. J. P. M. Harmans, and J. E. Mooij, *Science* **299**, 1869 (2003).
- [12] T. Yamamoto, Y. A. Pashkin, O. Astafiev, Y. Nakamura, and J. S. Tsai, *Nature (London)* **425**, 941 (2003).
- [13] A. C. J. ter Haar, Ph.D. thesis, TU Delft, Delft, 2005.
- [14] J. B. Majer, F. G. Paauw, A. C. J. ter Haar, C. J. P. M. Harmans, and J. E. Mooij, *Phys. Rev. Lett.* **94**, 090501 (2005).
- [15] M. J. Storcz and F. K. Wilhelm, *Phys. Rev. A* **67**, 042319 (2003).
- [16] J. Kempe, D. Bacon, D. A. Lidar, and K. B. Whaley, *Phys. Rev. A* **63**, 042307 (2001).
- [17] M. J. Storcz, J. Vala, K. R. Brown, J. Kempe, F. K. Wilhelm, and K. B. Whaley, *Phys. Rev. B* **72**, 064511 (2005).
- [18] D. Bacon, D. A. Lidar, and K. B. Whaley, *Phys. Rev. A* **60**, 1944 (1999).
- [19] A. B. Zorin, *JETP* **98**, 1250 (2004).
- [20] J. R. Friedman, V. Patel, W. Chen, S. K. Tolpygo, and J. E. Lukens, *Nature (London)* **406**, 43 (2000).
- [21] Y. Makhlin, G. Schön, and A. Shnirman, *Rev. Mod. Phys.* **73**, 357 (2001).
- [22] J. Q. You, Y. Nakamura, and F. Nori, *Phys. Rev. B* **71**, 024532 (2005).
- [23] Yu. A. Pashkin, T. Yamamoto, O. Astafiev, Y. Nakamura, D. V. Averin, and J. S. Tsai, *Nature (London)* **421**, 823 (2003).
- [24] M. Thorwart and P. Hänggi, *Phys. Rev. A* **65**, 012309 (2002).
- [25] I. A. Grigorenko and D. V. Khveshchenko, *Phys. Rev. Lett.* **94**, 040506 (2005).
- [26] M. Governale, M. Grifoni, and G. Schön, *Chem. Phys.* **268**, 273 (2001).
- [27] K. Rabenstein and D. V. Averin, *Turk. J. Phys.* **27**, 1 (2003).
- [28] U. Weiss, *Quantum Dissipative Systems*, 2nd ed. (World Scientific, Singapore, 1999).
- [29] K. Blum, *Density Matrix Theory and Applications*, 1st ed. (Plenum, New York, 1981).
- [30] J. F. Poyatos, J. I. Cirac, and P. Zoller, *Phys. Rev. Lett.* **78**, 390 (1997).
- [31] A. Peres, *Phys. Rev. Lett.* **77**, 1413 (1996).
- [32] V. M. Aji and J. E. Moore, cond-mat/0312145.
- [33] K. Zyczkowski, P. Horodecki, A. Sanpera, and M. Lewenstein, *Phys. Rev. A* **58**, 883 (1998).
- [34] J. Eisert, Ph.D. thesis, University of Potsdam, Potsdam, 2001.
- [35] O. Astafiev, Yu. A. Pashkin, Y. Nakamura, T. Yamamoto, and J. S. Tsai, *Phys. Rev. Lett.* **93**, 267007 (2004).
- [36] G. Falci, A. D'Arrigo, A. Mastellone, and E. Paladino, *Phys. Rev. Lett.* **94**, 167002 (2005).
- [37] D. Aharonov and M. Ben-Or, quant-ph/9906129.
- [38] C. H. van der Wal, F. K. Wilhelm, C. J. P. M. Harmans, and J. E. Mooij, *Eur. Phys. J. B* **31**, 111 (2003).
- [39] F. K. Wilhelm, M. J. Storcz, C. H. van der Wal, C. J. P. M. Harmans, and J. E. Mooij, *Adv. Solid State Phys.* **43**, 763 (2003).

# Chapter 7

## Decoherence of two coupled QD charge qubits

### 7.1 Introduction

Here, a system of two coupled quantum dot charge qubits is investigated. In these lateral quantum dot structures the qubit is defined by an additional charge in the left or right dot of a double quantum dot system. The tunnel coupling between the two dots, *i.e.*, the tunnel amplitude of the qubit can be tuned by an external gate voltage. In comparison to the superconducting qubits, this quantum dot system is not as well protected from excitations, it is coupled to several more degrees of freedom of the solid-state system. Namely, the most important decoherence sources for charge qubits in quantum dots have been identified as phonon decoherence,  $1/f$ -noise, electronics noise, and cotunneling, see Ref. [113]. Thus, a very important design issue for the quantum dot charge qubit system is how quantum dot charge qubits could be coupled and how the decoherence sources will act on such a setup.

In the following paper, the intrinsic decoherence due to the electron-phonon interactions is considered [191, 192] and the gate performance for a system of two coupled quantum dot charge qubits in a dissipative environment is evaluated. In this model for the electron-phonon decoherence, the assumption of Gaussian wavefunctions for each of the two dots is made, which corresponds to small tunnel couplings between the dots or large distances between the dot centers. The noise on the two qubits has both local and collective properties. It does neither fall completely in one of the standard classes of decoherence models for quantum registers, collective or local decoherence. From analyzing the decoherence properties of different classes of effective spectral functions, it is possible to propose a description of the noise in terms of multipole moments. The decoherence rates for the two-qubit setup can be made only slightly larger than the single qubit rates by adjusting the tunnel coupling between the dots to be small.

Because of the super-Ohmic spectrum of the phonons and the intrinsic type of bath coupling, which is diagonal in the eigenbasis of the system Hamiltonian, the gate quality of a CNOT gate operation is limited only by the single-qubit Hadamard gates. Thus, it is

possible by adjusting a weak tunnel coupling between the two dots that form one qubit, to significantly improve the gate performance despite a longer evolution time. Therefore, the overall gate performance is increased by slowing down the Hadamard operation and the threshold for quantum error correction, cf. section 1.2, can be met by the quantum dot charge qubit system.



## Intrinsic phonon decoherence and quantum gates in coupled lateral quantum dot charge qubits

Markus J. Storcz,<sup>1,\*</sup> Udo Hartmann,<sup>1,†</sup> Sigmund Kohler,<sup>2</sup> and Frank K. Wilhelm<sup>1</sup>

<sup>1</sup>*Physics Department, Arnold Sommerfeld Center for Theoretical Physics, and Center for NanoScience, Ludwig-Maximilians-Universität, Theresienstr. 37, D-80333 München, Germany*

<sup>2</sup>*Institut für Physik, Universität Augsburg, Universitätsstr. 1, D-86135 Augsburg, Germany*

Recent experiments by Hayashi *et al.* [Phys. Rev. Lett. **91**, 226804 (2003)] demonstrate coherent oscillations of a charge quantum bit (qubit) in laterally defined quantum dots. We study the intrinsic electron-phonon decoherence and gate performance for the next step: a system of two coupled charge qubits. The effective decoherence model contains properties of local as well as collective decoherence. Decoherence channels can be classified by their multipole moments, which leads to different low-energy spectra. It is shown that due to the super-Ohmic spectrum, the gate quality is limited by the single-qubit Hadamard gates. It can be significantly improved, by using double-dots with weak tunnel coupling.

PACS numbers: 03.67.Lx, 03.65.Yz, 73.21.La, 71.38.-k

### I. INTRODUCTION

In recent years, the experimental progress in analyzing transport properties in double quantum dots<sup>1</sup> has led to the fabrication of double dot structures with only one electron in the whole system<sup>2,3</sup>. This well-defined situation permits, although it is strictly speaking not necessary<sup>4</sup>, to use quantum dot systems as quantum bits (qubits). In order to define qubits in lateral quantum dot (QD) structures, the two degrees of freedom, spin and charge, are naturally used. For spin qubits<sup>5</sup>, the information is encoded in the spin of a single electron in one quantum dot, whereas for the charge qubit<sup>6,7,8</sup> the position of a single electron in a double dot system defines the logical states. Similar ideas can also be applied to charge states in Silicon donors<sup>9</sup>. Both realizations are interconnected: interaction and read-out<sup>2</sup> of spin qubits are envisioned<sup>5</sup> to be all-electrical and to make use of the charge degree of freedom.

Although the promises of spin coherence in theory<sup>10</sup> and in bulk measurements<sup>11</sup> are tremendous in the long run, it was the good accessibility of the *charge* degrees of freedom which lead to a recent break-through<sup>4</sup>, namely the demonstration of coherent oscillations in a quantum dot charge qubit. In this experiment, three relevant decoherence mechanisms for these charge qubits have been pointed out: a cotunneling contribution, the electron-phonon coupling, and  $1/f$ -noise or charge noise in the heterostructure defining the dots.

Recent theoretical results<sup>12</sup> predict that the cotunneling contribution can be very small, provided that the coupling between the dots and the connected leads is small. Thus, cotunneling is not a *fundamental* limitation. This, however, means that initialization and measurement protocols different from those of Ref. [4] are favorable<sup>2</sup>.

Other theoretical works<sup>13,14,15,16,17</sup> already describe the electron-phonon interaction for a single charge qubit in a GaAs/AlGaAs heterostructure. Moreover, also electronic Nyquist noise in the gate voltages affects the qubit

system<sup>18</sup>. Note that the physics of the electron-phonon coupling is different and less limiting in the unpolar material Si<sup>19</sup>, where the piezo-electric interaction is absent.

### II. MODEL

In this article, we analyze the decoherence due to the electron-phonon coupling in GaAs, which is generally assumed to be the dominant decoherence mechanism in a coupled quantum-dot setting. The recent experimental analysis shows that the temperature dependence of the dephasing rate in the experiment<sup>4</sup> can be modeled with the Spin-Boson model and hence is compatible with this assumption<sup>20</sup>. We develop a model along the lines of Brandes *et al.*<sup>21,22</sup> to describe the piezo-electric interaction between electrons and phonons in lateral quantum dots. Thereby, we assume the distance between the two dots to be sufficiently large and the tunnel coupling  $\Delta$  to be relatively small, which is a prerequisite for the validity of the model. The Hamiltonian for a system of two double dots with a tunnel-coupling within the double dots and electrostatic coupling between them, see Fig. 1, can be expressed as<sup>22</sup>

$$\hat{H}_{\text{total}} = \hat{H}_{\text{sys}} + \hat{H}_{\text{bath}} + \hat{H}_{\text{int}}, \quad (1)$$

where

$$\hat{H}_{\text{sys}} = - \sum_{i=1,2} \frac{1}{2} (\varepsilon_i \hat{\sigma}_{z,i} + \Delta_i \hat{\sigma}_{x,i}) - k \hat{\sigma}_{z,1} \otimes \hat{\sigma}_{z,2} \quad (2)$$

$$\hat{H}_{\text{bath}} = \sum_q \hbar \omega_q c_q^\dagger c_q \quad (3)$$

refer to the qubits and the heat bath, respectively.  $q$  is the phonon wave number. The system-bath interaction Hamiltonian  $\hat{H}_{\text{int}}$  depends on details of the setup such as the crystalline structure of the host semiconductor and the dot wave functions. We will distinguish between the



two extreme cases of long correlation length phonons resulting in coupling of both qubits to a single phonon bath, or two distinct phonon baths for short phonon correlation length. The former case is more likely<sup>23</sup> and applies to crystals which can be regarded as perfect and linear over the size of the sample, whereas the latter case describes systems that are strained or disordered and double quantum dots in large geometrical separation. The correlation length has to be distinguished from the wave length: The former indicates, over which distances the phase of the phonon wave is maintained, *i.e.*, over which distance the description as a genuine standing wave applies at all, whereas the latter indicates the internal length scale of the wave.

### A. One common phonon bath

In the case of a single phononic bath with a very long correlation length coupling to both charge qubits,  $\hat{H}_{\text{int}}$  can be written as

$$\begin{aligned} \hat{H}_{\text{int}} = & \sum_q \frac{1}{2} \left[ (\alpha_{q,1} + \beta_{q,1} + \alpha_{q,2} + \beta_{q,2}) \hat{\mathbf{1}}_1 \otimes \hat{\mathbf{1}}_2 + \right. \\ & + (\alpha_{q,1} - \beta_{q,1}) \hat{\sigma}_{z,1} \otimes \hat{\mathbf{1}}_2 + \\ & \left. + (\alpha_{q,2} - \beta_{q,2}) \hat{\mathbf{1}}_1 \otimes \hat{\sigma}_{z,2} \right] (c_q^\dagger + c_{-q}). \end{aligned} \quad (4)$$

The coefficients  $\alpha_{q,i}$  and  $\beta_{q,i}$  describe the coupling of a localized electron (one in each of the two double dot systems) to the phonon modes. They are given by

$$\alpha_{q,i} = \lambda_q \langle l, i | e^{i\vec{q}\vec{x}} | l, i \rangle, \quad (5)$$

$$\beta_{q,i} = \lambda_q \langle r, i | e^{i\vec{q}\vec{x}} | r, i \rangle, \quad (6)$$

where the  $|l, i\rangle$  and  $|r, i\rangle$  denote the wavefunctions of the electrons in the left or right dot of qubit  $i$ . We assume these wavefunctions to be two-dimensional Gaussians centered at the center of the dot, as sketched in Figure 1. These states approximate the ground state in the case of a parabolic potential and small overlap between the wavefunctions in adjacent dots. The coefficient  $\lambda_q$  is derived from the crystal properties<sup>22</sup>.

Henceforth, we investigate the case of two identical qubits. Due to the fact that the relevant distances are arranged along the  $x$ -direction, we obtain the coupling coefficients

$$\alpha_{q,1} = \lambda_q e^{iq(-l/2-d)} e^{-q^2\sigma^2/4}, \quad (7)$$

$$\beta_{q,1} = \lambda_q e^{-iq l/2} e^{-q^2\sigma^2/4}, \quad (8)$$

$$\alpha_{q,2} = \lambda_q e^{iq l/2} e^{-q^2\sigma^2/4}, \quad (9)$$

$$\beta_{q,2} = \lambda_q e^{iq(l/2+d)} e^{-q^2\sigma^2/4}. \quad (10)$$

Here,  $q$  is the absolute value of the wavevector  $\vec{q}$ . The second exponential function in each line is the overlap between the two Gaussian wavefunctions.

This two-qubit bath coupling Hamiltonian is quite remarkable, as it does not fall into the two standard

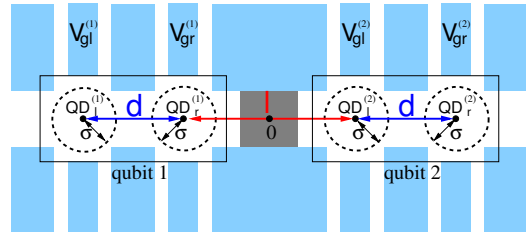


FIG. 1: (Colour online) Sketch of the two coupled identical charge qubits realized in a lateral quantum dot structure.  $d = 100$  nm is the distance of the dot centers in one qubit,  $l = 200$  nm is the distance between the right dot center of qubit 1 and the left dot center of qubit 2. The width of the Gaussian wavefunction of an electron in each dot is  $\sigma = 5$  nm. The values chosen for the distances  $d$  and  $l$  are slightly smaller than in experimental realizations<sup>2,4</sup> in order to provide a lower bound for the decoherence times. In principle, there could be tunneling processes between both qubits, *i.e.*, the QDs two and three in the chain, but we assume that the coupling is pinched off by applying appropriate gate voltages. The gray box between the qubits indicates that there is no tunneling between the qubits.

categories usually treated in literature (see, *e.g.*, Refs. [24,25,26] and references therein): On the one hand, there is clearly only one bath and each qubit couples to the bath modes with matrix elements of the same modulus, so the noise between the qubits is fully correlated. On the other hand, the Hamiltonian does *not* obey the familiar factorizing collective noise form  $\hat{H}_{\text{SB, coll}} = \hat{X}_{\text{system}} \otimes \hat{X}_{\text{bath}}$ . Such a form would lead to a high degree of symmetry and thus protection from the noise coupling<sup>24,25</sup>, however, the Hamiltonian  $\hat{H}_{\text{int}}$ , eq. 4, cannot be factorized in such a bilinear form. It is hence intriguing to explore where in between these cases the physics ends up to be. This is in particular important for finally finding strategies to protect the qubits against decoherence, and for estimating the scaling of decoherence in macroscopic quantum computers.

In order to obtain the dynamics of the reduced density matrix  $\rho$  for the coupled qubits, *i.e.*, for the degrees of freedom that remain after the environment is traced out, we apply Bloch-Redfield theory<sup>27,28,29</sup>. It starts out from the Liouville-von Neumann equation  $i\hbar\dot{\rho} = [\hat{H}, \rho_{\text{tot}}]$  for the total density operator. A perturbational treatment of the system-bath coupling Hamiltonian  $\hat{H}_{\text{int}}$  results in the master equation

$$\dot{\rho} = -\frac{i}{\hbar} [\hat{H}_{\text{sys}}, \rho] - \frac{1}{\hbar^2} \int_0^\infty d\tau \text{tr}_B [\hat{H}_{\text{int}}, [\hat{H}_{\text{int}}(-\tau), \rho \otimes \rho_B]], \quad (11)$$

where  $\rho_B = \exp(-\beta\hat{H}_B)/Z$  denotes the equilibrium density matrix of the bath. Evaluating the trace over all bath variables,  $\text{tr}_B$ , and decomposing the reduced density operator into the eigenbasis of the unperturbed system

Hamiltonian, we obtain<sup>28,30</sup>

$$\dot{\rho}_{nm} = -i\omega_{nm}\rho_{nm} - \sum_{k,\ell} R_{nmk\ell}\rho_{k\ell}, \quad (12)$$

where  $\omega_{nm} = E_n - E_m$ . The first term on the right hand side describes the unitary evolution and the Redfield relaxation tensor  $R_{nmk\ell}$  incorporates the decoherence effects. It is given by

$$R_{nmk\ell} = \delta_{\ell m} \sum_r \Gamma_{nrrk}^{(+)} + \delta_{nk} \sum_r \Gamma_{\ell rrm}^{(-)} - \Gamma_{\ell mnk}^{(-)} - \Gamma_{\ell mnk}^{(+)}, \quad (13)$$

where the rates  $\Gamma^{(\pm)}$  are determined by Golden Rule expressions<sup>28,30</sup>, see Eqs. (20) and (21), below. The Redfield tensor and the time evolution of the reduced density matrix are evaluated numerically to determine the decoherence properties of the system due to a weak electron-phonon coupling. Note that in addition, Ohmic electronic noise can be taken into account by employing the spectral function<sup>31</sup>  $J_{\Sigma}(\omega) = J_{\text{Ohmic}}(\omega) + J(\omega)$ , where  $J(\omega)$  contains only the phonon contribution. It is also possible to take  $1/f$ -noise in the quantum dot system into account in the same way. The  $1/f$ -noise essentially determines the magnitude of the dephasing part of the decoherence. Thus, it is in turn possible to impose for the zero frequency component  $J(0)$  the experimental value of the dephasing rates or a value from a microscopic model<sup>32</sup>. However, in many cases it turns out to be non-Markovian and/or non-Gaussian, leading to non-exponential decay, which can neither be described by Bloch-Redfield theory nor parameterized by a single rate.

In order to compute the rates, the electron-phonon interaction Hamiltonian has first to be taken from the localized representation to the computational basis, which is straightforward. To compute Bloch-Redfield rates, it is necessary to rotate into the eigenbasis of the system. After this basis change, the spectral densities  $J_{\ell mnk}(\omega)$  are calculated along the lines of Ref. [22] as

$$J_{\ell mnk}(\omega) = \langle (B^{-1}CB)_{\ell m} (B^{-1}CB)_{nk} \rangle_q, \quad (14)$$

where  $B$  is the matrix for the basis transformation from the computational basis  $\{|00\rangle, |01\rangle, |10\rangle, |11\rangle\}$  to the eigenbasis of the system and  $\langle \cdot \rangle_q$  denotes an averaging over all phonon modes  $q$  with frequency  $\omega$ . The matrix  $C$  is diagonal in the computational basis,  $C = \text{diag}(\alpha_{q,1} - \beta_{q,1} + \alpha_{q,2} - \beta_{q,2}, \alpha_{q,1} - \beta_{q,1} + \alpha_{q,2} - \beta_{q,2}, \alpha_{q,1} - \beta_{q,1} + \alpha_{q,2} - \beta_{q,2}, \alpha_{q,1} - \beta_{q,1} + \alpha_{q,2} - \beta_{q,2})$ .

The explicit derivation shows that it is most convenient to split the total spectral function  $J_{\ell mnk}(\omega)$  [see Eq. (14)] into odd and even components

$$J_{\ell mnk}(\omega) = e_{\ell mnk} J_e(\omega) + o_{\ell mnk} J_o(\omega), \quad (15)$$

where the prefactors  $e_{\ell mnk}$  and  $o_{\ell mnk}$  of the even/odd part of the spectral function are matrix elements coming from the basis change from the computational basis to the eigenbasis of the system and

$$J_{e/o}(\omega) = \frac{\pi}{4} \sum_q |\alpha_{q,1} - \beta_{q,1} \pm \alpha_{q,2} \mp \beta_{q,2}|^2 \delta(\omega - \omega_q). \quad (16)$$

They evaluate to

$$J_{e,o}(\omega) = \frac{\pi \hbar \omega g}{4} \left[ 2 - 2 \frac{\omega_d}{\omega} \sin\left(\frac{\omega}{\omega_d}\right) \mp \frac{\omega_l}{\omega} \sin\left(\frac{\omega}{\omega_l}\right) \pm 2 \frac{\omega_{l+d}}{\omega} \sin\left(\frac{\omega}{\omega_{l+d}}\right) \mp \frac{\omega_{l+2d}}{\omega} \sin\left(\frac{\omega}{\omega_{l+2d}}\right) \right] e^{-\omega^2/2\omega_c^2}, \quad (17)$$

where  $g = 0.05$  is the dimensionless electron-phonon coupling strength for the commonly used material GaAs<sup>21,22</sup> and  $c_S$  the speed of sound. The different frequencies represent the distances in the system:  $\omega_d = c_s/d$ ,  $\omega_l = c_s/l$ ,  $\omega_{d+l} = c_s/(d+l)$  and  $\omega_{2d+l} = c_s/(2d+l)$ , and  $\omega_c = c_s/\sigma$ . This structure can be understood as follows: The electron-phonon interaction averages out if the phonons are rapidly oscillating within a dot, *i.e.* if the wavelength is much shorter than the dot size — this provides the high-frequency cutoff at  $\omega_c$ . On the other hand, long-wavelength phonons do not contribute to decoherence between dots  $i$  and  $j$ , if the wavelength is much longer than their separation because then, the energy shift induced by the phonon displacement will only lead to a global phase. Furthermore, we can approximate the

leading order at low frequencies as

$$J_e(\omega) = \frac{2\pi \hbar g d^2}{3c_s^2} \omega^3 + \mathcal{O}(\omega^5), \quad (18)$$

$$J_o(\omega) = \frac{\pi \hbar g (l^2 d^2 + 2ld^3 + d^4)}{10c_s^4} \omega^5 + \mathcal{O}(\omega^7). \quad (19)$$

This different power-laws  $\omega^3$  to  $\omega^5$  can be understood physically as illustrated in Figure 2. “Even” terms are the natural extension of the one-qubit electron-phonon coupling, adding up coherently between the two dots. In the “odd” channel, the energy offset induced in one qubit is, for long wavelengths, cancelled by the offset induced in the other qubit. Thus, shorter wavelengths are required for finding a remaining net effect. An alternative point of view is the following: The distribution of

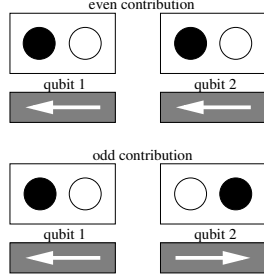


FIG. 2: Illustration of the even (top) and odd (bottom) contributions to the total rates. Filled circles indicate occupied dots. For long-wavelength modes, the energy shifts induced by underlying phonons in the two dots add up coherently in the even case but cancel in the odd case. Note, that moving charges from the black to the white dots changes the dipole moment in the even but not in the odd case.

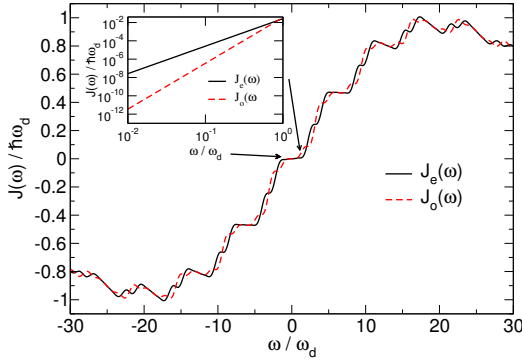


FIG. 3: (Colour online) Spectral functions  $J_{e,o}(\omega)$  in the case of one common phonon bath for the fixed parameters  $c_s = 5000$  m/s,  $g = 0.05$ ,  $d = 100$  nm,  $l = 200$  nm and  $\sigma = 5$  nm. Inset: zoom for small frequencies.

the two charges can be parameterized by a dipole and a quadrupole moment. The “even” channel couples to the dipole moment of the charge configuration similar to the one-qubit case. The “odd” channel couples to the quadrupole moment alone (see Figure 2). Thus, it requires shorter wavelengths and consequently is strongly suppressed at low frequencies. This explains the different low-frequency behavior illustrated for realistic parameters in Figure 3. Thus, we can conclude that for small frequencies the odd processes are suppressed by symmetry — even beyond the single-dot suppression and the suppression of asymmetric processes.

With these expressions for the spectral densities, one can proceed as in Ref. [26] and determine the rates that constitute the Redfield tensor to read

$$\Gamma_{\ell mnk}^{(+)} = \frac{J_{\ell mnk}(\omega_{nk})}{2\hbar} \left[ \coth\left(\frac{\hbar\omega_{nk}}{2k_B T}\right) - 1 \right], \quad (20)$$

$$\Gamma_{\ell mnk}^{(-)} = \frac{J_{\ell mnk}(\omega_{\ell m})}{2\hbar} \left[ \coth\left(\frac{\hbar\omega_{\ell m}}{2k_B T}\right) + 1 \right]. \quad (21)$$

For  $\omega_{ij} \rightarrow 0$ , these rates vanish due to the super-Ohmic form of the bath spectral function. From this, we find the time evolution of the coupled qubit system and finally also the gate quality factors.

## B. Two distinct phonon baths

When each qubit is coupled to its own phononic bath, the part of the Hamiltonian that describes the interaction with the environment  $H_{\text{int}}$  is given by

$$\begin{aligned} \hat{H}_{\text{int}} = & \sum_{q_1} \frac{1}{2} \left[ (\alpha_{q_1} + \beta_{q_1}) \hat{\mathbf{1}}_1 + (\alpha_{q_1} - \beta_{q_1}) \hat{\sigma}_{z,1} \right] \\ & \times (c_{q_1}^\dagger + c_{-q_1}) \otimes \hat{\mathbf{1}}_2 + \\ & + \sum_{q_2} \frac{1}{2} \left[ (\alpha_{q_2} + \beta_{q_2}) \hat{\mathbf{1}}_2 + (\alpha_{q_2} - \beta_{q_2}) \hat{\sigma}_{z,2} \right] \\ & \times (c_{q_2}^\dagger + c_{-q_2}) \otimes \hat{\mathbf{1}}_1. \end{aligned} \quad (22)$$

This scenario can be realized in different ways: One can split the crystal into two pieces by an etched trench. Alternatively, if there is lattice disorder and/or strong non-linear effects, the phonons between the dots may become uncorrelated.

The calculation of the coupling coefficients works in a similar way, but there are two different indices  $q_1$  and  $q_2$  to represent the phononic baths of each qubit

$$\alpha_{q_1} = \lambda_{q_1} e^{iq_1(-l/2-d)} e^{-q_1^2 \sigma^2/4}, \quad (23)$$

$$\beta_{q_1} = \lambda_{q_1} e^{-iq_1 l/2} e^{-q_1^2 \sigma^2/4}, \quad (24)$$

$$\alpha_{q_2} = \lambda_{q_2} e^{iq_2 l/2} e^{-q_2^2 \sigma^2/4}, \quad (25)$$

$$\beta_{q_2} = \lambda_{q_2} e^{iq_2(l/2+d)} e^{-q_2^2 \sigma^2/4}. \quad (26)$$

The expression for the spectral functions  $J_{\ell mnk}(\omega)$  turns out to be exactly the same as the one in the last section with the only difference that instead of  $\alpha_{q,i}$ , the coupling between electrons and phonons is now expressed as  $\alpha_{q_i}$  (with  $i = 1, 2$  for both qubits). Therefore, in order to obtain the spectral density  $J_{\ell mnk}(\omega)$ , one has to average over two distinct baths, *i.e.*

$$J_{\ell mnk}(\omega) = \langle (B^{-1}CB)_{\ell m} (B^{-1}CB)_{nk} \rangle_{q_1, q_2}. \quad (27)$$

Again, we find two different functions that we name in the same way as in the previous section,  $J_e(\omega)$  and  $J_o(\omega)$ , which are given by

$$J_{e,o}(\omega) = \frac{\pi \hbar \omega g}{4} \left[ 2 - 2 \frac{\omega_d}{\omega} \sin\left(\frac{\omega}{\omega_d}\right) \mp 2 \left( \frac{\omega_{\frac{l}{2}}}{\omega} \sin\left(\frac{\omega}{\omega_{\frac{l}{2}}}\right) - \frac{\omega_{d+\frac{l}{2}}}{\omega} \sin\left(\frac{\omega}{\omega_{d+\frac{l}{2}}}\right) \right)^2 \right] e^{-\omega^2/2\omega_c^2}. \quad (28)$$

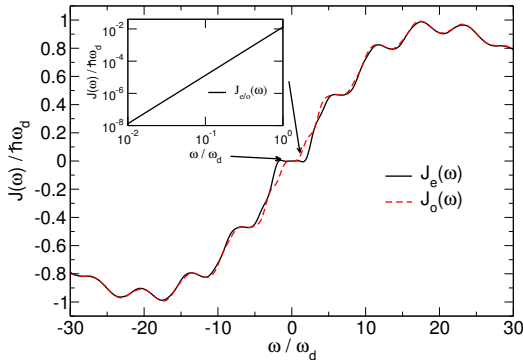


FIG. 4: (Colour online) Spectral functions  $J_{e,o}(\omega)$  in the case of two distinct phonon baths for the fixed parameters  $c_s = 5000$  m/s,  $g = 0.05$ ,  $d = 100$  nm,  $l = 200$  nm and  $\sigma = 5$  nm. Inset: magnification for small frequencies.

The prefactors from the basis change also enter the expressions for the rates in the same way as in the last section. The spectral functions  $J_{e,o}(\omega)$  are plotted in Figure 4; the inset depicts the proportionality to  $\omega^3$  for small frequencies.

### III. GOLDEN RULE RATES

We proceed as in Ref. [26] and determine the Golden rule rates that govern the Redfield tensor. Thereby, we find both the time evolution of the coupled system and the gate quality factors.

Let us first discuss the impact of this particular bath coupling on the dephasing and relaxation rates. The decoherence rates, *i.e.*, the relaxation and dephasing rates, are defined according to  $\Gamma_R = -\sum_n \Lambda_n$ , where  $\Lambda_n$  are the eigenvalues of the matrix composed of the elements  $R_{n,n,m,m}$ ,  $n, m = 1, \dots, 4$ , and  $\Gamma_{\varphi_{nm}} = -\text{Re}R_{n,m,n,m}$  for non-degenerate levels  $|\omega_{nm}| > |R_{n,m,n,m}|$  and in the absence of Liouvillian degeneracy,  $|\omega_{nm} - \omega_{kl}| > |R_{a,b,c,d}|$   $a, b, c, d, \in \{k, l, m, n\}$ , respectively<sup>31</sup>.

As a reference point, we study the rates in the uncoupled case. In this case, and in the absence of degeneracies between the qubits, there is a clear selection rule that the environment only leads to single-qubit processes, *i.e.*, decoherence can be treated at completely separate footing. As a result, all rates are identical between the qubits. To make this obvious, we rewrite the original Hamiltonian in

the one-bath case, combining Eq. (4) with eqs. (7)–(10) as

$$\hat{H}_{\text{int}} = \sum_q \left[ -2ie^{-q^2\sigma^2/4} \sin\left(\frac{qd}{2}\right) \left( e^{-iq(l+d)/2} \hat{\sigma}_{z,1} + e^{iq(l+d)/2} \hat{\sigma}_{z,2} \right) + E_0 \hat{\mathbf{1}} \right] (c_q^\dagger + c_{-q}) \quad (29)$$

which — besides a phase factor which is meaningless for single-qubit transitions — is identical to the standard electron-phonon Hamiltonian for double dots<sup>22</sup>.

Figure 5 shows the temperature dependence of the energy relaxation rate  $\Gamma_R$  and the two dephasing rates  $\Gamma_{\phi_{13}}$  and  $\Gamma_{\phi_{24}}$  compared to the single qubit relaxation and dephasing rates. In this notation,  $\Gamma_{\phi_{ij}}$  is the rate at which a superposition of energy eigenstates  $i$  and  $j$  is decays into a classical mixture. We considered the following three cases, characterized by values on the matrix element relative to a characteristic system energy scale  $E_s$ : (a) large difference of the  $\varepsilon_i$  and  $\Delta_i$  ( $i = 1, 2$ ) between both qubits and no coupling between the qubits ( $\varepsilon_1 = \Delta_1 = (1/40)E_s$ ,  $\varepsilon_2 = \Delta_2 = -(21/40)E_s$  and coupling energy  $K = 0$ ), (b) small asymmetry between the parameters for both qubits and no coupling ( $\varepsilon_1 = \Delta_1 = -(1/2)E_s$ ,  $\varepsilon_2 = \Delta_2 = -(21/40)E_s$  and  $K = 0$ ), and (c) without asymmetry between the qubits and a rather strong coupling between the qubits ( $\varepsilon_1 = \Delta_1 = -(1/2)E_s$ ,  $\varepsilon_2 = \Delta_2 = -(1/2)E_s$  and  $K = 10E_s$ ). One generally would expect a different value of the distance between the dot centers in the qubits  $d$ , when the tunneling coupling is varied. However, in our case of the dot wavefunctions which overlap only in their Gaussian tails, this effect is very small (below 1 nm for a change in the tunneling amplitude  $\Delta$  of approximately  $\sim (1/2)E_s$ ) for the lengthscales that we are considering. Note, that in Ref. 3 a substantial change of  $\Delta$  over more than an order of magnitude was obtained experimentally by a rather mild adjustment of the gate voltage, so it is consistent that a small change of  $\Delta$  can be achieved by a tiny adjustment. Therefore the value  $d = 100$  nm is used for the electron-phonon coupling encoded in  $J_e$  and  $J_o$  in all cases.

For case (a), we find that all rates are for all temperatures larger than the single qubit rates, as one would expect<sup>33</sup>. In more detail, for the single bath case, the ratio of the relaxation rates is approximately 1.9, the ratio of the single-qubit dephasing rate and the two-qubit dephasing rate  $\Gamma_{\phi_{24}}$  is around 0.9 and for the dephasing rate  $\Gamma_{\phi_{13}}$ , the ratio is 1.0. The behaviour of the even and odd parts of the spectral function in the single bath case can be explained from the spectral function Fig. 3,

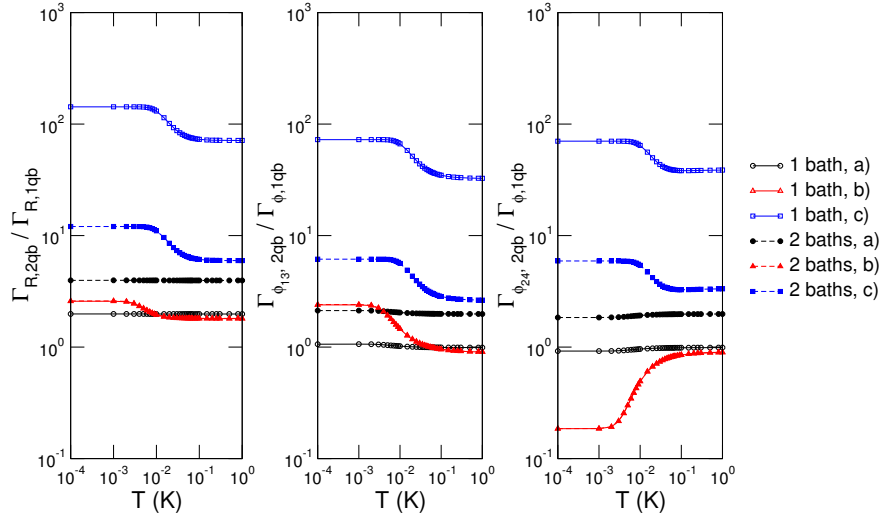


FIG. 5: (Colour online) Temperature dependence of the relaxation and dephasing rates normalized by the single-qubit relaxation and dephasing rates. The two-qubit relaxation rate is given by the trace of the relaxation part of the Redfield tensor in secular approximation. The energy scales for the two-qubit transitions  $1 \leftrightarrow 3$  and  $2 \leftrightarrow 4$  are comparable to the single qubit energy scale, the characteristic qubit energies are  $E_s = (1/8)$  GHz. The different cases are (a)  $\varepsilon_1 = \Delta_1 = (1/40)E_s$ ,  $\varepsilon_2 = \Delta_2 = -(21/40)E_s$ , and coupling energy  $K = 0$ , (b)  $\varepsilon_1 = \Delta_1 = -(1/2)E_s$ ,  $\varepsilon_2 = \Delta_2 = -(21/40)E_s$ , and  $K = 0$ , and (c)  $\varepsilon_1 = \Delta_1 = -(1/2)E_s$ ,  $\varepsilon_2 = \Delta_2 = -(1/2)E_s$  and  $K = 10E_s$ . Note that cases (a) and (b) model uncoupled qubits, especially for case (a) the overall relaxation rate for the two-qubit system is approximately twice the single-qubit relaxation rate when calculated for the dominating larger energy scale of the two-qubit system ( $\varepsilon_2 = \Delta_2 = -(21/40)E_s$ ).

for small  $\omega$  one finds that  $J_o < J_e$ . For the case of large frequencies, however, the even part of the spectral function increases and even dominates beyond the threshold  $\omega \gtrsim \omega_d$ . Overall, it is found that in the case of a single-bath the decoherence effects are significantly suppressed compared to the two-bath scenario. For the two-bath case, the ratios are for the relaxation rates approximately 3.9, for the dephasing rate  $\Gamma_{\phi_{24}}$  around 1.9 and for the dephasing rate  $\Gamma_{\phi_{13}}$  it is 2.0. Note that for the two-bath case  $J_e < J_o$  always and for the case where both tunnel matrix elements in the Hamiltonian vanish, the rate vanishes, too.

After decreasing the asymmetry between the two qubits as in case (b), the rates decreased but are still comparable with the single qubit rates, besides the last dephasing rate  $\Gamma_{\phi_{24}}$ . This can be understood, if one considers the energy spectrum of the eigenvalues of the system Hamiltonian. In cases (a) and (b) there is significant difference between the qubits, so it is straightforward to map the two-qubit rates onto the corresponding single qubit rates and they are largely determined by single-qubit physics. In case (c), we consider a fully symmetric case in the qubit parameters, but with a finite and large coupling between the qubits. This coupling lifts the degeneracy but makes the rate a generic two-qubit rate which belongs to a relatively robust transition with small transition matrix elements for the single bath

case. At high temperatures, these symmetry-related effects wash out as discussed in Ref. [34]. However, the high-temperature rates do *not* coincide with the single-qubit rates, as the underlying energy scales are still different and in generally larger for the two-qubit situation.

Overall, the ratio of the two-qubit and single-qubit relaxation rates decreases for increasing temperature due to the reduction of correlation effects in the double dot system, besides case c), where a symmetry based on the underlying Hamiltonian becomes important.

#### IV. QUANTUM GATE PERFORMANCE

For the characterization of the quantum gate performance of this two-qubit system, it is necessary to introduce suitable quantifiers. Commonly, one employs the four gate quality factors introduced in Ref. [35]; fidelity  $\mathcal{F}$ , purity  $\mathcal{P}$ , quantum degree  $\mathcal{Q}$ , and entanglement capability  $\mathcal{C}$  to characterize a gate operation within a hostile environment.

The fidelity, *i.e.*, the overlap between the ideal propagator and the simulated time evolution including the decoherence effects, is defined as

$$\mathcal{F} = \overline{\langle \Psi_{\text{in}} | \hat{U}^\dagger \rho_{\text{out}} \hat{U} | \Psi_{\text{in}} \rangle}, \quad (30)$$

where the bar indicates an average over a set of 36 unentangled input states  $|\Psi_{\text{in}}\rangle = |\psi_i\rangle|\psi_j\rangle$ , with  $i, j = 1, \dots, 6$ . The 6 single-qubit states  $|\psi_i\rangle$  are chosen such that they are symmetrically distributed over the Bloch sphere,

$$|\psi_1\rangle = |0\rangle, \quad |\psi_2\rangle = |1\rangle, \quad |\psi_{3,\dots,6}\rangle = \frac{|0\rangle + e^{i\phi}|1\rangle}{\sqrt{2}} \quad (31)$$

where  $\phi = 0, \pi/2, \pi, 3\pi/2$ . Here,  $\hat{U}$  is the ideal unitary time evolution for the given gate, and  $\hat{\rho}_{\text{out}}$  is the reduced density matrix resulting from the simulated time evolution. A perfect gate reaches a fidelity of unity. The purity  $\mathcal{P}$  measures the strength of the decoherence effects,

$$\mathcal{P} = \overline{\text{tr}(\rho_{\text{out}}^2)}. \quad (32)$$

Again, the bar indicates the ensemble average. A pure state returns unity and for a mixed state the purity can drop to a minimum given by the inverse of the dimension of the system Hilbert space, *i.e.* 1/4 in our case.

If the density operator  $\rho$  describes an almost pure state, *i.e.*, if the purity is always close to the ideal value 1, it is possible to estimate the purity loss during the gate operation from its decay rate along the lines of Ref. [36]. Thereby, one first evaluates the decay of  $(d/dt)\text{tr}\rho^2$  for an arbitrary pure qubit state  $\rho = |\psi\rangle\langle\psi|$ . From the basis-free version of the master equation (11), follows straightforwardly

$$\frac{d}{dt}\text{tr}\rho^2 = -\frac{2}{\hbar^2} \int_0^\infty d\tau \text{tr}_{S+B}[\hat{H}_{\text{int}}, [\hat{H}_{\text{int}}(-\tau), \rho \otimes \rho_B]]\rho. \quad (33)$$

By tracing out the bath variables, we obtain an expression that contains only qubit operators and bath correlation functions. This depends on the state  $|\psi\rangle$  via the density operator. Performing the ensemble average over all pure states as described in the Appendix A, we obtain

$$\dot{\mathcal{P}} = \frac{2}{\hbar^2(N+1)} \int_0^\infty d\tau \text{tr}([\hat{H}_{\text{int}}, \tilde{H}_{\text{int}}(-\tau)]_+)_B, \text{eq.} \quad (34)$$

where  $N = 4$  denotes the dimension of the system Hilbert space of the two qubits. We have used the fact that  $\text{tr}\hat{H}_{\text{int}} = 0$ . Although the discrete set of states employed in the numerical computation is obviously different from the set of all pure states, we find that both ensembles provide essentially the same results for the purity.

If the bath couples to a good quantum number, *i.e.*, for  $[\hat{H}_{\text{sys}}, \hat{H}_{\text{int}}] = 0$ , the system operator contained in the interaction picture operator  $\tilde{H}_{\text{int}}(-\tau)$  remains time-independent. Then, the  $\tau$ -integration in (34) is effectively the Fourier transformation of the symmetrically ordered bath correlation function in the limit of zero frequency. Thus, we obtain

$$\dot{\mathcal{P}} = -\frac{2}{N+1} \lim_{\omega \rightarrow 0} \sum_i J_i(\omega) \coth \frac{\hbar\omega}{2kT}, \quad (35)$$

where

$$J_i(\omega) = \frac{\pi}{4} \sum_q |\alpha_{q,i} - \beta_{q,i}|^2 \delta(\omega - \omega_q) \quad (36)$$

denotes the spectral density of the coupling between qubit  $i$  and the heat bath(s).

In the present case of a super-Ohmic bath, the limit  $\omega \rightarrow 0$  results for the coupling to a good quantum number in  $\mathcal{P} = 0$ . This means that whenever the tunnel coupling in the Hamiltonian (2) is switched off, *i.e.* for  $\Delta_1 = \Delta_2 = 0$ , the purity decay rate vanishes. Thus, we can conclude that the significant purity loss for the CNOT operation studied below [cf. Eq. (41)], stems from the Hadamard operation. This is remarkably different from cases with other bath spectra: For an ohmic bath, for which  $J_i(\omega) \propto \omega$ , expression (35) converges in the limit  $\omega \rightarrow 0$  to a finite value. By contrast, for a sub-ohmic bath, this limit does not exist and, consequently, the purity decay cannot be estimated by its decay rate. During the stage of the Hadamard operation,  $\Delta_2 = \Delta$  while  $\Delta_1 = 0$ . Then, the interaction picture versions of the qubit-bath coupling operators read

$$\tilde{\sigma}_{z,1}(-\tau) = \hat{\sigma}_{z,1}, \quad (37)$$

$$\tilde{\sigma}_{z,2}(-\tau) = \hat{\sigma}_{z,2} \cos(\Delta\tau/\hbar) - \hat{\sigma}_{y,2} \sin(\Delta\tau/\hbar). \quad (38)$$

In the case where both qubits couple to individual environments, the expression for the change of the purity can be evaluated for each qubit separately. For qubit 2, we still have a coupling to a good quantum number, while for qubit 1, the appearance of  $\cos(\Delta\tau/\hbar)$  results in a Fourier integral evaluated at the frequency  $\Delta/\hbar$ . Thus, we finally obtain

$$\dot{\mathcal{P}} = -\frac{4kT}{5} \lim_{\omega \rightarrow 0} \frac{J_1(\omega)}{\hbar\omega} - \frac{1}{5} J_2(\Delta/\hbar) \coth \frac{\Delta}{2kT}. \quad (39)$$

For the super-Ohmic bath under consideration [see eqs. (18) and (19)], the first term in Eqn. (39) vanishes.

In the case of one common heat bath, the estimate of the purity decay is calculated in the same way. The only difference is that we have to consider, in addition, cross terms of the type  $\hat{\sigma}_{1,z} \otimes \hat{\sigma}_{2,z}$ , *i.e.* terms that contain operators of different qubits. The contribution of these terms, however, vanishes when performing the trace over the bath variables in Eq. (34). Thus, we can conclude that within this analytical estimate, the purity decay rate is identical for both the individual bath model and the common bath model.

The so-called quantum degree

$$\mathcal{Q} = \max_{\rho_{\text{out}}, |\Psi_{\text{me}}\rangle} \langle \Psi_{\text{me}} | \rho_{\text{out}} | \Psi_{\text{me}} \rangle \quad (40)$$

is the overlap of the state obtained after the simulated gate operation and the maximally entangled Bell states. Finally the entanglement capability  $\mathcal{C}$  is defined as the smallest eigenvalue of the density matrix resulting from transposing the partial density matrix of one qubit. As

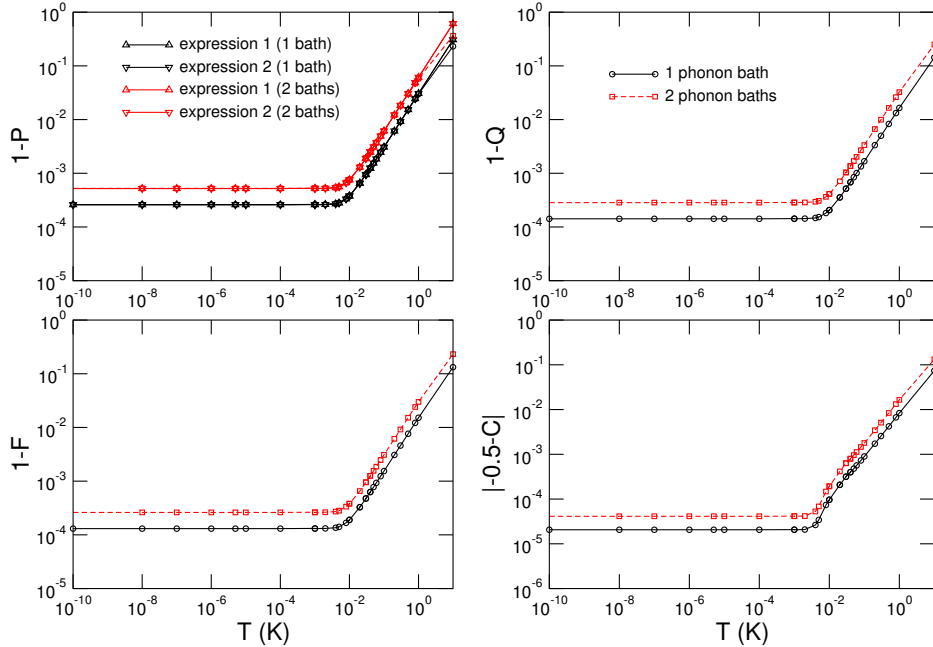


FIG. 6: (Colour online) Temperature dependence of the deviation of the four gate quality factors from their ideal values for the CNOT gate. The decoherence due to phonons is taken into account. The black line shows the results for a single phonon bath and the red line is for two phononic baths. The characteristic qubit energies are  $E_s = 1/4$  GHz and the tunnel amplitudes are  $\Delta_i = E_s$  ( $i = 1, 2$ ) due to the spacing of the double dots. In the curves for the deviation of the purity, we included lines for the analytical expressions 1 from Eq. (34) and 2 from Eq. (39).

shown in Ref. [37], the non-negativity of this smallest eigenvalue is a necessary condition for the separability of the density matrix into two unentangled systems. The entanglement capability approaches  $-0.5$  for the ideal CNOT gate.

It has been shown that the controlled-NOT (CNOT) gate together with single-qubit operations is sufficient for universal quantum computation. Here, we investigate the decoherence during a CNOT gate which generates maximally entangled Bell states from unentangled input states. In Figures 6 and 7 the simulated gate evolution in the presence of phonon baths is shown. Using the system Hamiltonian, the CNOT gate can be implemented through the following sequence of elementary quantum gates<sup>26,38</sup>

$$\begin{aligned}
 U_{\text{CNOT}} = & U_{\text{H}}^{(2)} \exp\left(-i\frac{\pi}{4}\hat{\sigma}_{z,1}\right) \exp\left(-i\frac{\pi}{4}\hat{\sigma}_{z,2}\right) \times \\
 & \times \exp\left(-i\frac{\pi}{4}\hat{\sigma}_{z,1}\hat{\sigma}_{z,2}\right) \exp\left(-i\frac{\pi}{2}\hat{\sigma}_{z,1}\right) U_{\text{H}}^{(2)},
 \end{aligned}
 \tag{41}$$

where  $U_{\text{H}}^{(2)}$  denotes the Hadamard gate operation performed on the second qubit. This gate sequence just involves one two-qubit operation at step three. The parameters for the numerical calculations are given below

Figs. 6 and 7.

In Fig. 6, the gate quality factors for the case of a single or two distinct phononic baths are shown. It is observed that for the case of a single phonon bath they achieve better values. This offset is due to the larger number of non-vanishing matrix elements in the coupling of the noise to the spin components for the two bath case. Here, due to several non-commuting terms in the coupling to the bath and the different Hamiltonians needed to perform the individual steps of the quantum gate, the gate quality factors saturate when the temperature  $T$  is decreased. This happens at around  $T = T_s = 12$  mK corresponding to  $E_s = 1/4$  GHz as the characteristic energy scale.

Figure 7, depicts the same behaviour of the gate quality factors as in Figure 6 with the only difference that the tunnel coupling  $\Delta_2$  is smaller by a factor of 4 during the Hadamard operation. The qualitative behavior is very similar to that in Figure 6, but the deviation from the ideal values for the gate quality factors is much smaller and already fulfills the criterion of an allowed deviation of  $10^{-4}$ . The reduction of the tunnel amplitudes by a factor 4 corresponds to a very small change of the distance  $d$  in the two qubits (namely, from 100.0 nm to 100.3 nm) ow-

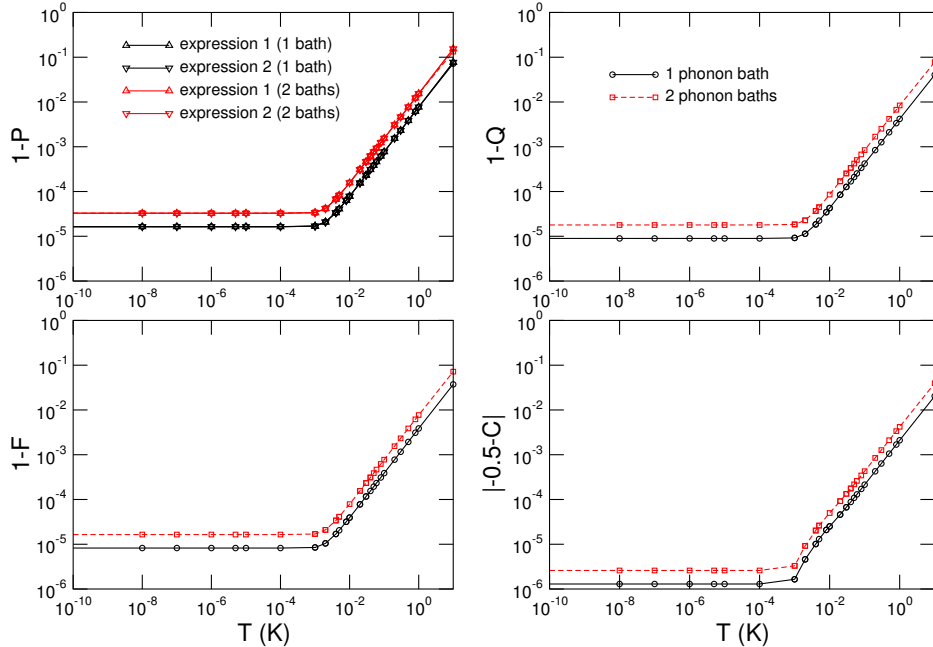


FIG. 7: (Colour online) Temperature dependence of the deviation of the four gate quality factors from their ideal values for the CNOT gate. The decoherence due to phonons is taken into account. The black line shows the results for a single phonon bath and the red line is for two phonon baths. The characteristic qubit energies are  $E_s = 1/4$  GHz and the tunnel amplitude during the Hadamard operation on the second qubit is  $\Delta_2 = 1/4E_s$ , *i.e.*, a factor 4 smaller than in Figure 6. In the curves for the deviation of the purity, we included lines for the analytical expressions 1 from Eq. (34) and 2 from Eq. (39).

ing to the Gaussian shape of the electron wavefunctions, provided their distance is sufficiently large<sup>22</sup>.

We have already mentioned that the phonon contribution to decoherence still allows for the fidelity values below the threshold  $1 - F < 10^{-4}$  from Ref. [39]. For a reliable quantum computer, however, such intrinsic decoherence mechanisms should beat the threshold at least by an order of magnitude. This can be achieved as follows: As we have seen, the Hadamard gate is the step limiting the performance as during the Hadamard the system is vulnerable against spontaneous emission at a rate  $\gamma \propto E^3$ , where  $E$  is the typical energy splitting of the single qubit. The duration of the Hadamard, on the other hand, scales as  $\tau \propto 1/E$ . Thus, the error probability and the purity decay reduces to  $1 - e^{-\gamma\tau} \simeq \gamma\tau \propto E^2$ . Thus, by making the Hadamard *slower*, *i.e.*, by working with small tunnel couplings between the dots, the gate performance can be increased. This works until Ohmic noise sources, electromagnetic noise on the gates and controls, takes over. This is demonstrated nicely in Fig. 7, where the CNOT gate for a modified Hadamard operation (on the second qubit) with  $\Delta_2 = \varepsilon_2 = (1/4)E_s$  is depicted. It is clearly observed that by decreasing the tunnel matrix element and by increasing the evolution time the deco-

herence is reduced and the threshold for the gate quality factors to allow universal quantum computation<sup>40</sup> can be achieved.

The gate quality of a CNOT under decoherence has been studied in Refs. [26,38] for standard collective and/or single-qubit noise in Ohmic environments. The single-qubit case for charge qubits in GaAs has been studied in Ref. [17] with emphasis on non-Markovian effects. Even in view of this, and in view of the emphasis of the strong tunneling regime, that work arrives at the related conclusion that intrinsic phonon decoherence in this system can be limited. Please note, that the approximations in the microscopic model give an upper bound of validity for the validity of effective Hamiltonians as studied in Ref. [17] as described in Refs. [7,15,21,22]. The work presented here is not affected by this restriction due to the emphasis of the case of small tunnel coupling.

## V. CONCLUSIONS

We have analyzed the influence of a phononic environment on four coupled quantum dots which represent two charge qubits. The effective error model resulting from



the microscopic Hamiltonian does not belong to the familiar classes of local or collective decoherence. It contains a dipolar and quadrupolar contribution with super-ohmic spectra at low frequencies,  $\omega^3$  and  $\omega^5$  respectively. The resulting decoherence is an intrinsic limitation of any gate performance. In particular, we have investigated within a Bloch-Redfield theory the relevant rates and the quality of a CNOT gate operation. The two employed models of coupling the qubits to individual heat baths versus a common heat bath, respectively, yield quantitative differences for the gate qualifiers. Still the qualitative behavior is the same for both cases.

Within an analytical estimate for the purity loss, we have found that the decoherence plays its role mainly during the stage of the Hadamard operation. The physics behind this is that during all the other stages, the bath couples to the qubits via a good quantum number. Consequently, during these stages, the decoherence rates are dominated by the spectral density of the bath in the limit of zero frequency which for the present case of a super-ohmic bath vanishes. The results of our analytical estimate compare favorably with the results from a numerical propagation.

The fact that on the one hand, the bath spectrum is super-ohmic, while on the other hand, the Hadamard operation is the part that is most sensitive to decoherence, suggests to slow down the Hadamard operation by using a rather small tunnel coupling. Then, decoherence is reduced by a factor that is larger than the extension of the operation time. This finally results for the complete gate operation in a reduced coherence loss. Thus, the gate quality is significantly improved for dots with weak tunnel coupling and can intrinsically meet the threshold for quantum error correction.

## VI. ACKNOWLEDGEMENTS

Our work was supported by DFG through SFB 631. We thank Stefan Ludwig for hinting on the idea of working with small tunneling and Peter Hänggi for interesting discussions.

### APPENDIX A: AVERAGE OVER ALL PURE STATES

In this appendix, we derive formulas for the evaluation of expressions of the type  $\text{tr}(\rho A)$  and  $\text{tr}(\rho A \rho B)$  in an ensemble average over all pure states  $\rho = |\psi\rangle\langle\psi|$ . The state  $|\psi\rangle$  is an element of an  $N$ -dimensional Hilbert space. Decomposed into an arbitrary orthonormal basis set  $\{|n\rangle\}_{n=1\dots N}$ , it reads

$$|\psi\rangle = \sum_n c_n |n\rangle, \quad (\text{A1})$$

where the only restriction imposed on the coefficients  $c_n$  is the normalization  $\langle\psi|\psi\rangle = \sum_n |c_n|^2 = 1$ . Hence the ensemble of pure states is fully described by the distribution

bution

$$P(c_1, \dots, c_N) = \gamma_N \delta(1 - \sum_n |c_n|^2). \quad (\text{A2})$$

We emphasize that  $P(c_1, \dots, c_N)$  is invariant under unitary transformations of the state  $|\psi\rangle$ . The prefactor  $\gamma_N$  is determined by the normalization

$$\int d^2 c_1 \dots d^2 c_N P(c_1, \dots, c_N) = 1 \quad (\text{A3})$$

of the distribution, where  $\int d^2 c$  denotes integration over the real and the imaginary part of  $c$ .

The computation of the ensemble averages of the coefficients with the distribution (A2) is straightforward and yields

$$\begin{aligned} \overline{c_m c_n^*} &= \frac{1}{N} \delta_{mn} \\ \overline{c_m c_n^* c_{m'} c_{n'}^*} &= \frac{1}{N(N+1)} (\delta_{mn} \delta_{m'n'} + \delta_{mn'} \delta_{nm'}). \end{aligned} \quad (\text{A4})$$

Using these expressions, we consequently find for the ensemble averages of the expressions  $\text{tr}(\rho A)$  and  $\text{tr}(\rho A \rho B)$  the results

$$\begin{aligned} \overline{\text{tr}(\rho A)} &= \overline{\langle\psi|A|\psi\rangle} = \frac{\text{tr} A}{N}, \\ \overline{\text{tr}(\rho A \rho B)} &= \overline{\langle\psi|A|\psi\rangle\langle\psi|B|\psi\rangle} = \frac{\text{tr}(A)\text{tr}(B) + \text{tr}(AB)}{N(N+1)} \end{aligned} \quad (\text{A5})$$

which have been used for deriving the purity decay (33) from Eq. (34).

While this averaging procedure is very convenient for analytical calculations, the numerical propagation can be performed with only a finite set of initial states. In the present case, the averages are computed with the set of 36 states given after Eq. (30). In the present case, we have justified numerically that both averaging procedures yield the same results. Thus, it is interesting whether this correspondence is exact.

For the case of one qubit,  $N = 2$ , the discrete set of states is given by the states  $|\psi\rangle = c_1|1\rangle + c_2|2\rangle$  where  $(c_1, c_2)$  is chosen from the set of 6 vectors

$$\begin{pmatrix} 1 \\ 0 \end{pmatrix}, \begin{pmatrix} 0 \\ 1 \end{pmatrix}, \frac{1}{\sqrt{2}} \begin{pmatrix} 1 \\ e^{i\phi} \end{pmatrix}, \quad (\text{A8})$$

where  $\phi = 0, \pi/2, \pi, 3\pi/2$ . Computing the averages for the states (A8) is now straightforward and shows that this discrete sample also fulfills the relations (A4) and (A5). Thus, we can conclude that for the computation of averages, both the discrete and the continuous sample.

For more than one qubit, however, arises a difference: While the sample of all pure states also contains entangled states, these are by construction excluded from set of direct products of the 6 one-qubit states (A8). Still our numerical results indicate that the different samples practically result in the same averages.

- \* markus.storcz@physik.lmu.de  
† udo.hartmann@physik.lmu.de
- <sup>1</sup> W.G. van der Wiel, S. De Franceschi, J.M. Elzerman, T. Fujisawa, S. Tarucha, and L.P. Kouwenhoven, *Rev. Mod. Phys.* **75**, 1 (2003).
  - <sup>2</sup> J.M. Elzerman, R. Hanson, J.S. Greidanus, L.H. Willems van Beveren, S. De Franceschi, L.M.K. Vandersypen, S. Tarucha, and L.P. Kouwenhoven, *Phys. Rev. B* **67**, 161308(R) (2003).
  - <sup>3</sup> A.K. Hüttel, S. Ludwig, K. Eberl, and J.P. Kotthaus, arXiv:cond-mat/0501012 (2005).
  - <sup>4</sup> T. Hayashi, T. Fujisawa, H.D. Cheong, Y.H. Jeong, and Y. Hirayama, *Phys. Rev. Lett.* **91**, 226804 (2003).
  - <sup>5</sup> D. Loss and D.P. DiVincenzo, *Phys. Rev. A* **57**, 120 (1998).
  - <sup>6</sup> R.H. Blick and H. Lorenz, *Proceedings of the IEEE International Symposium on Circuits and Systems*, II245 (2000).
  - <sup>7</sup> L. Fedichkin, M. Yanchenko and K.A. Valiev, *Nanotechnology* **11**, 387-391 (2000).
  - <sup>8</sup> W.G. van der Wiel, T. Fujisawa, S. Tarucha, and L.P. Kouwenhoven, *Jpn. J. Appl. Phys.* **40**, 2100 (2001).
  - <sup>9</sup> L.C.L. Hollenberg, A.S. Dzurak, C. Wellard, A.R. Hamilton, D.J. Reilly, G.J. Milburn, and R.G. Clark, *Phys. Rev. B* **69**, 113301 (2004).
  - <sup>10</sup> see e.g. V. Cerletti, W.A. Coish, O. Gywat, and D. Loss, *Nanotechnology* **16**, R27 (2005).
  - <sup>11</sup> J.M. Kikkawa, I.P. Smorchkova, N. Samarth, and D.D. Awschalom, *Science* **277** 1284 (1997).
  - <sup>12</sup> U. Hartmann and F.K. Wilhelm, *Phys. Rev. B* **69**, 161309(R)(2004).
  - <sup>13</sup> L. Fedichkin and A. Fedorov, *Phys. Rev. A* **69**, 032311 (2004).
  - <sup>14</sup> Z.-J. Wu, K.-D. Zhu, X.-Z. Yuan, Y.-W. Jiang, and H. Zheng, *Phys. Rev. B* **71**, 205323 (2005).
  - <sup>15</sup> S. Vorojtsov, E.R. Mucciolo, and H.U. Baranger, *Phys. Rev. B* **71**, 205322 (2005).
  - <sup>16</sup> V.N. Stavrou and X. Hu, arXiv:cond-mat/0503481 (2005).
  - <sup>17</sup> M. Thorwart, J. Eckel, E.R. Mucciolo, arXiv:cond-mat/0505621 (2005).
  - <sup>18</sup> F. Marquardt and V.A. Abalmassov, *Phys. Rev. B* **71**, 165325 (2005).
  - <sup>19</sup> J. Gorman, D.G. Hasko, and D.A. Williams, arXiv:cond-mat/0504451 (2005).
  - <sup>20</sup> A.J. Leggett et al., *Rev. Mod. Phys.* **59**, 1 (1987).
  - <sup>21</sup> T. Brandes and B. Kramer, *Phys. Rev. Lett.* **83**, 3021 (1999).
  - <sup>22</sup> T. Brandes, Habilitationsschrift, University of Hamburg (2000); *Phys. Rep.* **408**, 315 (2005).
  - <sup>23</sup> R.G. Ulbrich, V. Narayanamurti, and M.A. Chin, *Phys. Rev. Lett.* **45**, 1432 (1980).
  - <sup>24</sup> J. Kempe, D. Bacon, D. Lidar, K.B. Whaley, *Phys. Rev. A* **63**, 042307 (2001).
  - <sup>25</sup> P. Zanardi and M. Rasetti, *Phys. Rev. Lett.* **79**, 3306 (1997).
  - <sup>26</sup> M.J. Storcz and F.K. Wilhelm, *Phys. Rev. A* **67**, 042319 (2003).
  - <sup>27</sup> P.N. Agyres and P.L. Kelley, *Phys. Rev.* **134**, A98 (1964).
  - <sup>28</sup> U. Weiss, *Quantum dissipative systems, 2nd ed.*, (World Scientific, Singapore, 1999).
  - <sup>29</sup> L. Hartmann, I. Goychuk, M. Grifoni and P. Hänggi, *Phys. Rev. E* **61**, R4687 (2000).
  - <sup>30</sup> K. Blum, *Density Matrix Theory and Applications, 2nd ed.*, (Plenum Press, New York, 1996).
  - <sup>31</sup> M. Governale, M. Grifoni, and G. Schön, *Chem. Phys.* **268**, 273 (2001).
  - <sup>32</sup> G. Falci, A. D'Arrigo, A. Mastellone, and E. Paladino, *Phys. Rev. Lett.* **95**, 167002 (2005).
  - <sup>33</sup> W. Dür, C. Simon, and J.I. Cirac, *Phys. Rev. Lett.* **89**, 210402 (2002).
  - <sup>34</sup> M.J. Storcz, F. Hellmann, C. Hrlescu, and F.K. Wilhelm, arXiv:cond-mat/0504787 (2005).
  - <sup>35</sup> J.F. Poyatos, J.I. Cirac, P. Zoller, *Phys. Rev. Lett.* **78**, 390 (1997).
  - <sup>36</sup> K.M. Fonseca Romero, S. Kohler, and P. Hänggi, arXiv:cond-mat/0409774 (2004).
  - <sup>37</sup> A. Peres, *Phys. Rev. Lett.* **77**, 1413 (1996).
  - <sup>38</sup> M. Thorwart, P. Hänggi, *Phys. Rev. A* **65**, 012309 (2002).
  - <sup>39</sup> D. DiVincenzo, *Science* **270**, 255 (1995).
  - <sup>40</sup> D. Aharonov and M. Ben-Or, arXiv:quant-ph/9906129 (1999).

# Chapter 8

## Design of coupling elements for superconducting qubits

### 8.1 Introduction

A major milestone on the road to quantum computation is the development of systems of many coupled qubits while maintaining sufficient control over these qubits [14, 193]. For superconducting flux and charge qubits there exist several different proposals to couple individual qubits [74], *e.g.*, via a capacitor [194, 195], direct inductive coupling [92, 196], an LC-oscillator chain [197], or a flux transformer [81, 82]. A typical experimental setup for two flux qubits that share a common line and are coupled inductively (note that the kinetic inductance is increased greatly when the neighbouring qubits share a line) is shown in Fig. 8.1. In this design, each two flux qubits share a common line of superconductor and the circulating (screening) currents in each loop induce a flux through the neighbouring qubit loops, which will lead to  $\hat{\sigma}_z^{(i)} \otimes \hat{\sigma}_z^{(i+1)}$ -type coupling terms in the Hamiltonian. A drawback of this direct inductive coupling scheme is that the coupling can not be switched on and off, which would be very desirable in order to realize precise quantum gate operations. Another setup for a *tunable* coupling of flux qubits is the flux transformer, which is sketched in Fig. 8.3; a superconducting loop is fabricated on top of the two qubits separated by an insulating layer in-between. In the off-state, the transformer loop contains an integer number of flux quanta supplied by an external field. In this state the response of a current to a change in flux is small, however, when the the critical current of the device is increased a circulating current in the transformer loop builds up, which mediates the coupling. Alternatively, it is possible to replace the single Josephson junction that interrupts the coupling loop by a SQUID loop, which can be switched by the external flux that pierces this additional loop [82]. However, then the severe problem of flux cross-talk between the loops is introduced. Recently, also another scheme for a tunable coupling via a flux transformer has been proposed, see Ref. [199]. One possibility to simplify the original design of the flux transformer, is to replace the regular Josephson junction in the transformer circuit by junctions with an intrinsic  $\pi$ -shift [200–203] or based on trapped fluxoids

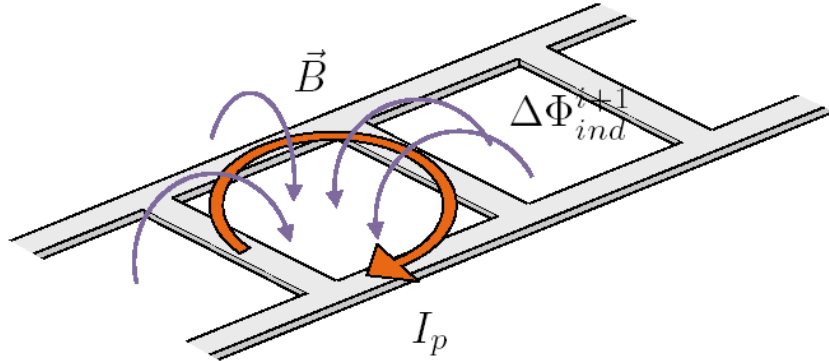


Figure 8.1: Sketch of an Ising chain of inductively coupled flux qubits, picture from [196].

in a regular superconducting ring [204]. This leads to a well-defined off-state of the flux transformer for zero flux bias, whereas for the original design the additional SQUID loop that replaces the Josephson junction of the flux transformer has to be biased by exactly half a flux quantum in the off-state, which is inconvenient and causes flux noise on the qubits even in the off-state of the coupler.

Here, the coupling via a flux transformer that will lead to an Ising type of  $zz$ -coupling will be investigated for flux qubits. In order to overcome the problems of inserting another SQUID loop to tune the interaction mediated by the flux transformer, it is proposed to use a so-called Josephson-Field-Effect-Transistor (JoFET). The JoFET [198, 205–209] can be viewed as a tunable Josephson junction. It resembles a regular metal-oxide-semiconductor field-effect transistor (MOSFET). In-between the source and drain contacts, a InGaAs/InAs layer is fabricated as depicted in figure 8.2 and under the channel defined by the  $\text{SiO}_2$  between the Nb contacts a two-dimensional electron gas (2DEG) is formed. The electron density of the 2DEG, which acts as a weak link between the two superconductors, can be tuned by an external gate voltage. Thus, it is possible to tune the critical current of the junction with an external gate voltage. This is very favorable compared to the direct inductive coupling, because the on/off state of the transformer is well defined and the problem of flux cross-talk can be avoided. For applications of the flux transformer, it is important to investigate the noise properties of switches for the transformer loop. The qubit should rest in a low noise environment and decoherence due to the coupling circuit should be suppressed. In the following paper, the decoherence properties of different switches for the flux transformer are investigated. It is found that the JoFET introduces no fundamental restrictions in terms of additional noise acting on the qubit.

First, the working principle of the flux transformer will be explained in more detail. The flux transformer consists of a SQUID loop around the two qubits with a Josephson junction as an on/off switch (cf. Fig. 8.3). In practice, the transformer loop is fabricated on top of the flux qubits with an insulating layer in between. Referring to this picture, the following equations for the flux through qubits one and two, generated by currents in the

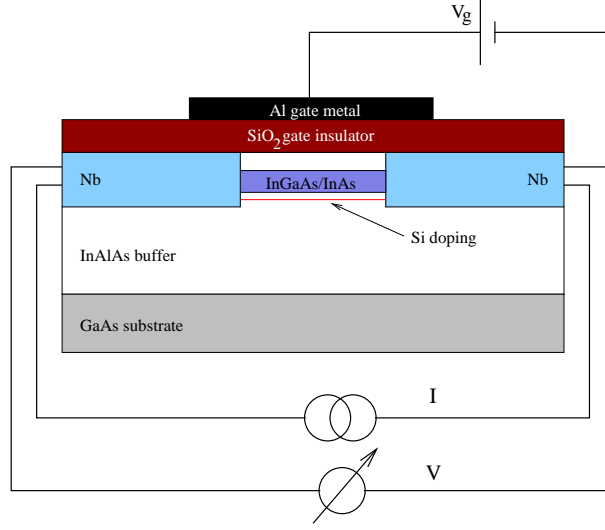


Figure 8.2: Schematic drawing of a JoFET, cf. [156]. The superconducting source and drain contacts are made from niobium. Under the channel defined by the  $\text{SiO}_2$  in between the contacts, the inversion layer constitutes a quasi two-dimensional electron gas (2DEG), which can be considered as a weak link between the superconducting electrodes. The electron density of the 2DEG can be manipulated with an external gate voltage. The critical current of such devices can be tuned by the applied gate voltage up to approximately  $50 \mu\text{A}$  at  $V_g = 20 \text{ V}$ , see Ref. [198].

qubits and the flux transformer, can be read off [72, 210]

$$\Delta\Phi_1 = L_1 I_{\text{circ}}^1 + M_{1,T} I_{\text{circ}}^T + M_{1,2} I_{\text{circ}}^2 \quad (8.1)$$

$$\Delta\Phi_2 = L_2 I_{\text{circ}}^2 + M_{2,T} I_{\text{circ}}^T + M_{2,1} I_{\text{circ}}^1, \quad (8.2)$$

where  $L = L_1 = L_2$  are the self-inductances of the qubits,  $M_{1,T} = M_{2,T} = M_T$  are the mutual inductances between the transformer and the qubit, and  $M_{1,2} \approx 0$  is the direct mutual inductance between qubits one and two. The so-called circulating currents  $I_{\text{circ}}$  are the screening currents in each of the qubit loops. In order to avoid confusion with the screening current in the transformer loop, these screening currents of the qubit loops will be referred to as *circulating currents* in accordance with literature [76, 81, 82]. Moreover, it is convenient to introduce the following notation,  $M_{TT}$  is the self-inductance of the transformer loop,  $M_{TQ} = M_{QT} = M_{i,T}$ ,  $i = 1, 2$  is the mutual inductance between the qubit and the transformer loop and  $M_{QQ} = L_i$ ,  $i = 1, 2$  is the self-inductance of the qubit.

The direct inductive mutual coupling between the two qubits is assumed to be small, *i.e.*, the qubits are fabricated in a substantial distance from each other. The extra flux  $\Delta\Phi_1$  and  $\Delta\Phi_2$  shifts the energy levels of the two qubits by an amount

$$\Delta\epsilon_{1,2} = \Delta\Phi_{1,2} \frac{\partial \epsilon_{1,2}}{\partial \Phi_{1,2}}. \quad (8.3)$$

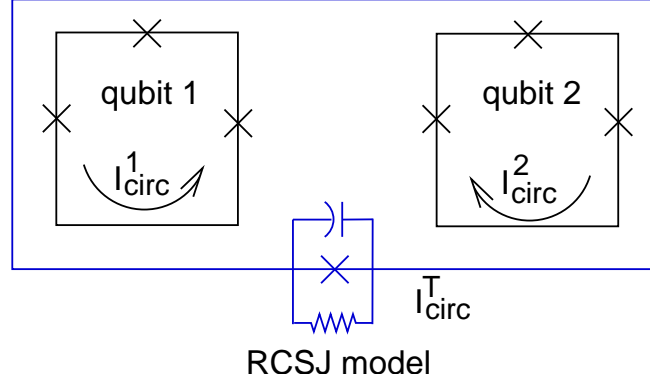


Figure 8.3: Sketch of a flux transformer that couples two superconducting flux qubit loops taken from [211].

From the Hamiltonian of the two-qubit system

$$H = \sum_{i=1}^2 \varepsilon_i \hat{\sigma}_z^{(i)} + \Delta_i \hat{\sigma}_x^{(i)} + K \hat{\sigma}_z^{(1)} \hat{\sigma}_z^{(2)}, \quad (8.4)$$

it is immediately immanent that in the case of two qubits with identical parameters, the energy shift  $\Delta\epsilon_{1,2}$  of both qubits by  $K = \Delta\epsilon_{1,2}$  can be denoted by

$$\begin{aligned} K &= \Delta\Phi_{1,2} \frac{\partial \varepsilon_{1,2}}{\partial \Phi_{1,2}} = \Delta\Phi_{1,2} \frac{\partial}{\partial \Phi_{1,2}} I_{\text{circ}}^{1,2} \left( \Phi_{1,2} - \frac{1}{2} \Phi_0 \right) \\ &= \Delta\Phi_{1,2} I_{\text{circ}}^{1,2} = \Delta\Phi_{1,2} I_C^{1,2} \sin(\gamma^{1,2}) \end{aligned} \quad (8.5)$$

where  $\gamma^{(1),(2)}$  denotes the gauge invariant phase difference resulting from the three Josephson junctions in each superconducting qubit loop.

Introducing the screening flux, which corresponds to the circulating current of the transformer loop,  $\Phi_S = \Delta\Phi_T$  and writing it in a similar form as equations (8.1) and (8.2) yields together with the equations for  $\Delta\Phi_1 = \Phi_1$  and  $\Delta\Phi_2 = \Phi_2$  (we introduced the abbreviations just for the sake of simplicity) in matrix form the system of equations

$$\begin{pmatrix} \vec{\Phi} \\ \Phi_S \end{pmatrix} = \mathbf{M} \vec{I} \quad \begin{pmatrix} \Phi_1 \\ \Phi_2 \end{pmatrix} = \begin{pmatrix} M_{TT} & M_{TQ} & M_{TQ} \\ M_{TQ} & M_{QQ} & 0 \\ M_{TQ} & 0 & M_{QQ} \end{pmatrix} \begin{pmatrix} I_S \\ I_1 \\ I_2 \end{pmatrix}, \quad (8.6)$$

where the direct mutual inductance between the qubits was assumed to be very small. By defining  $1/D := (M_{QQ}M_{TT} - 2M_{TQ}^2)$  we can conveniently write the matrix inverse  $\mathbf{M}^{-1}$ :

$$\mathbf{M}^{-1} = D \begin{pmatrix} M_{QQ} & -M_{TQ} & -M_{TQ} \\ -M_{TQ} & (M_{TT} - (M_{TQ}^2/M_{QQ})) & M_{TQ}^2/M_{QQ} \\ M_{TQ} & M_{TQ}^2/M_{QQ} & (M_{TT} - (M_{TQ}^2/M_{QQ})) \end{pmatrix} \quad (8.7)$$

And the screening current  $I_S$  can be conveniently expressed as

$$I_S = D(M_{QQ}\Phi_S - M_{TQ}\Phi_1 - M_{TQ}\Phi_2). \quad (8.8)$$

It is useful to insert experimental values in order to estimate the value of the average screening current in the transformer loop, *e.g.*, when the qubit system is in the state  $|\uparrow\uparrow\rangle$ . The following experimental values can be gathered,  $M_{QQ} \approx 13$  pH,  $M_{TT} \approx 30$  pH,  $M_{TQ} \approx 15$  pH,  $I_{\text{circ}}^{1,2} \approx 10^{-6}$  A,  $\gamma \approx 10^{-1}$  (strong coupling) and assumed two qubits with identical parameters (fluxoid quantization  $\Phi_S = \Phi_0 - \gamma/2\pi$  holds)

$$I_S = D(M_{QQ}\Phi_S - 2M_{TQ}(I_{\text{circ}}^{1,2}M_{QQ} + I_{\text{circ}}^T M_{QT})) \approx -4.4 \cdot 10^{-7} \text{ A} + 3.3 \cdot 10^{-3} I_C^T. \quad (8.9)$$

For the JoFET, a typical value of  $I_C^T \approx 25 \cdot 10^{-6}$  A and the screening current becomes  $|I_S| \approx |-4.4 \cdot 10^{-7} + 8.3 \cdot 10^{-8}| \text{ A} = 3.57 \cdot 10^{-7} \text{ A}$ . Thus, it is found that the coupling of the qubits to the transformer loop can be made reasonably large and a considerable screening current develops in the transformer loop. However, the transformer circuit will also introduce noise for the qubits. Thus, the noise properties of the transformer circuit have to be investigated in detail because even a very good coupler in terms of coupling strength and tunability is unemployable if it introduces strong noise for the qubits. For modeling the intrinsic noise of the JoFET (or Josephson junction) in the transformer loop, the resistively and capacitively shunted junction (RCSJ) model is employed [68]. In the RCSJ-model the dynamics of the gauge invariant phase are given by the differential equation

$$\frac{\hbar C}{2e} \ddot{\gamma} + \frac{\hbar}{2eR} \dot{\gamma} + I_C^T \sin(\gamma) + \delta I(t) = I_S. \quad (8.10)$$

The correlation of the current noise is given by the fluctuation-dissipation theorem

$$\langle \delta I \delta I \rangle_\omega = \coth(\beta \hbar \omega / 2) \hbar \chi''(\omega), \quad (8.11)$$

where  $\chi''(\omega)$  is the imaginary part of the generalized susceptibility. This equation can be rewritten in terms of the circuits admittance  $Y(\omega)$

$$\langle \delta I \delta I \rangle_\omega = \coth(\beta \hbar \omega / 2) \hbar \omega \text{Re} Y(\omega). \quad (8.12)$$

From Fig. 8.3 the real part of the admittance for the RCSJ model in the transformer loop can be calculated

$$\chi''(\omega) = \text{Re} \left( \frac{1}{i\omega C} + R^{-1} \right) = \frac{1}{R}, \quad (8.13)$$

which is thus found to lead to an Ohmic spectral function. From the effective circuit an intrinsic Drude-type of cutoff with  $\omega_c = R(M_{TT} + L_J)/M_{TT}L_J$  is found, where  $L_J$  is the Josephson inductance of the junction in the transformer loop. From Eqn. (8.11) one can then calculate the fluctuations in the energy bias using the relation  $\delta \varepsilon = 2I_{\text{circ}} \delta \Phi$ , see Ref. [211],

$$\langle \delta \varepsilon(t) \delta \varepsilon(0) \rangle_\omega = J(\omega) \coth(\beta \hbar \omega / 2). \quad (8.14)$$

In the following paper, the properties of different switches for the superconducting flux transformer are investigated. It is found that most noise from the coupler is imposed on the qubits during the switching of the transformer. Moreover, the JoFET as well as high- $T_c$  materials (note that the noise of the high- $T_c$  materials itself can be very challenging [212–214]) with an intrinsic  $\pi$ -shift are suitable as switches for the transformer loop, because they cause only little dissipation.





## Design of realistic switches for coupling superconducting solid-state qubits

Markus J. Storz<sup>a)</sup> and Frank K. Wilhelm

*Sektion Physik and CeNS, Ludwig-Maximilians-Universität, Theresienstr. 37, 80333 München, Germany*

(Received 16 June 2003; accepted 31 July 2003)

Superconducting flux qubits are a promising candidate for solid-state quantum computation. One of the reasons is that implementing a controlled coupling between the qubits appears to be relatively easy, if one uses tunable Josephson junctions. We evaluate possible coupling strengths and show how much extra decoherence is induced by the subgap conductance of a tunable junction. In light of these results, we evaluate several options of using intrinsically shunted junctions and show that based on available technology, Josephson field effect transistors and high- $T_c$  junctions used as  $\pi$  shifters would be a good option, whereas the use of magnetic junctions as  $\pi$  shifters severely limits quantum coherence. © 2003 American Institute of Physics. [DOI: 10.1063/1.1612901]

Quantum computation promises qualitative improvement of computational power as compared to today's classical computers. An important candidate for the implementation of a scalable quantum computer are superconducting qubits.<sup>1,2</sup> After experimental demonstration of basic features, e.g., in flux qubits,<sup>3,4</sup> the improvement of the properties of such setups involves engineering of couplings and decoherence, see, e.g., Ref. 5.

To perform universal quantum computation with a system of coupled qubits it is very desirable to be able to switch the couplings (although there are in principle workarounds).<sup>6</sup> It has already been described that for flux qubits, this can be achieved by using a superconducting flux transformer interrupted by a tunable Josephson junction,<sup>2</sup> i.e., a superconducting switch, as shown in Fig. 1. The primary and most straightforward proposal for the implementation of this switch is to use an unshunted dc-superconducting quantum interference device (SQUID) based on tunnel junctions utilizing the same technology as for the qubit junctions. Although this holds the promise of inducing very little extra decoherence, it suffers from two practical restrictions: (i) the SQUID loop has to be biased by exactly half a flux quantum in the off state and (ii) the external control parameter is a magnetic flux, which introduces the possibility of flux crosstalk between the qubits and the switch. The combination of (i) and (ii) implies that even small flux crosstalk will severely perturb the off state of the switch.

This can be avoided by using different switches: A voltage-controlled device such as a Josephson field effect transistor (JoFET)<sup>7</sup> or a super-normal-metal-conductor (SNS)-transistor completely avoids the cross-talk problem. As an intermediate step,<sup>8</sup> one can improve the SQUID by using a large  $\pi$  junction, in order to fix the off-state at zero field. Such  $\pi$  junctions can be found in high- $T_c$  systems<sup>9</sup> or in systems with a magnetic barrier.<sup>10</sup> All these junctions are damped by a large subgap conductance because they contain a large number of low-energy quasiparticles.

In this letter, we quantitatively evaluate the coupling

strength between two qubits coupled by a switchable flux transformer. We evaluate the strength of the decoherence induced by the subgap current modeled in terms of the resistively shunted junction (RSJ) model. Based on this result, we assess available technologies for the implementation of the switch.

We start by calculating the strength  $K$  of the coupling between the two qubits without a switch and then show how it is modified by the presence of the switch. From Fig. 1 and the law of magnetic induction we find the following equations for the flux through qubit 1 and 2 induced by currents in the qubits and the flux transformer

$$\delta \begin{pmatrix} \Phi_s \\ \Phi_1 \\ \Phi_2 \end{pmatrix} = \begin{pmatrix} M_{TT} & M_{TQ} & M_{TQ} \\ M_{TQ} & M_{QQ} & 0 \\ M_{TQ} & 0 & M_{QQ} \end{pmatrix} \begin{pmatrix} I_s \\ I_1 \\ I_2 \end{pmatrix}, \quad (1)$$

where  $M_{QQ}$  is the self-inductance of the qubits (assumed to be identical),  $M_{TQ}$  is the mutual inductance between the transformer and the qubits and the mutual inductance between the qubits is assumed to be negligible. The fluxes  $\delta\Phi$  in Eq. (1) are the screening fluxes in the transformer and the two qubits, i.e., the deviations from the externally applied values. Henceforth, we abbreviate Eq. (1) as  $\delta\Phi = \mathbf{M}I$ . These formulas are general and can be applied for any flux through

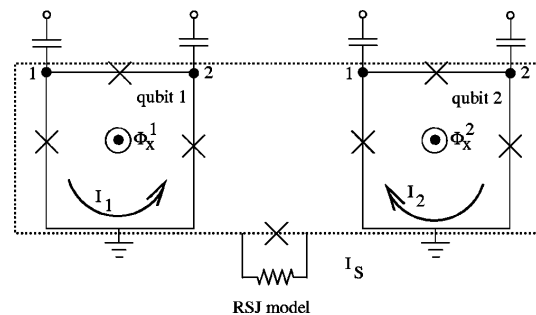


FIG. 1. The flux transformer inductively couples two flux qubits (see Ref. 2). It can be switched, e.g., by a dc-SQUID or by a tunable shunted Josephson junction.

<sup>a)</sup>Electronic mail: storcz@theorie.physik.uni-muenchen.de

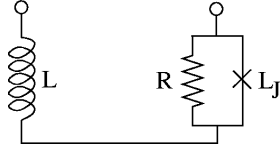


FIG. 2. Equivalent circuit diagram of the flux transformer circuit. The JoFET is modeled by a resistively shunted Josephson junction.

the transformer loop. It is most desirable to couple zero net flux through the device, which can be achieved by using a gradiometer configuration.<sup>11</sup> For this gradiometer case, we get  $I_S = -(M_{TQ}/M_{TT})(I_1 + I_2)$ , which we might insert into Eq. (1) and find for the inductive energy

$$E_{\text{ind}} = \left( M_{QQ} - \frac{M_{TQ}^2}{M_{TT}} \right) (I_1^2 + I_2^2) - 2 \frac{M_{TQ}^2}{M_{TT}} I_1 I_2. \quad (2)$$

The terms resulting from the off-diagonal elements of Eq. (1) can directly be identified as the interqubit coupling strength  $K = -2(M_{TQ}^2/M_{TT})I_1 I_2$  which enters the  $\hat{\sigma}_z \otimes \hat{\sigma}_z$  Ising-coupling described in Refs. 2 and 12. Note, that the dynamics of the qubit flux is dominated by the Josephson energies,<sup>2</sup> to which the diagonal term is only a minor correction.

We now introduce the tunable Josephson junction into the loop. Using fluxoid quantization, we rewrite the Josephson relation<sup>11</sup>  $I_S = I_c \sin[-2\pi(\Phi_S/\Phi_0)]$  and insert it into Eq. (1). The resulting nonlinear equation can be solved in the following cases: (i) If  $|I_S/I_c| \ll 1$  (“on” state of the switch) we find  $K = -2(M_{TQ}^2/M_{TT}^*)I_1 I_2$  with  $M_{TT}^* = M_{TT} + (\Phi_0/2\pi I_c) = M_{TT} + L_{\text{kin}}(0)$ . This can be understood as an effective increase of the self-inductance of the loop by the kinetic inductance of the Josephson junction at zero bias. (ii) In the case  $|I_S/I_c| \approx 1$ , “off” state, the circulating current is close to the critical current of the switch, hence the phase drop is  $\pm\pi/2$  and we find an analogous form  $K = -2(M_{TQ}^2/M_{TT}')I_1 I_2$  with  $M_{TT}' = M_{TT} + (\Phi_0/4|I_c|)$ , i.e., at low  $I_c$  the coupling can be arbitrarily weak due to the enormous kinetic inductance of the junction close to the critical current.

We now turn to the discussion of the decoherence induced by the subgap conductance of the tunable junction. The decoherence occurs due to the flux noise generated through the current noise from the quasiparticle shunt. Hence, both qubits experience the same level of noise. The decoherence of such a setup has been extensively studied in Ref. 12 as a function of the environment parameters. In this letter, we evaluate these environment parameters for our specific setup.

We model the junction by the RSJ-model for a sound quantitative estimate of the time scales even though the physics of the subgap conductance is usually by far more subtle than that. We evaluate the fluctuations of the current between two points of the flux transformer loop sketched in Fig. 1.  $L$  is the geometric inductance of the loop,  $L_J$  is the Josephson inductance characterizing the Josephson contact and  $R$  is the shunt resistance. The correlation is given by the fluctuation-dissipation theorem  $\langle \delta I \delta I \rangle_\omega = \coth(\beta \hbar \omega / 2) \hbar \omega \text{Re } Y(\omega)$ , where  $Y(\omega)$  is the admittance of the effective circuit depicted in Fig. 2. Following the lines of Ref. 5, this translates into a spectral function of the energy

fluctuations of the qubit of the shape  $\langle \delta \epsilon(t) \delta \epsilon(0) \rangle_\omega = J(\omega) \coth(\hbar \omega / 2k_B T)$  with  $J(\omega) = \alpha \omega^2 / (\omega^2 + \omega_c^2)$  with the important result that the dimensionless dissipation parameter here reads

$$\alpha = \frac{4I_{\text{circ}}^2 M_{TQ}^2 L_J^2}{\hbar R (L + L_J)^2} \quad (3)$$

and an intrinsic cutoff  $\omega_c = R(L + L_J) / LL_J$ . Here,  $L_J = \Phi_0 / 2\pi I_c$  is the kinetic inductance of the junction. From Eq. (3) we receive in the limit  $L \gg L_J$  the expression  $\alpha \propto 1/R I_c^2$  and for  $L \approx L_J$ ,  $L \ll L_J$  it follows that  $\alpha \propto 1/R$ . From the results of Ref. 12, we can conclude that  $\alpha \approx 10^{-6}$  poses an upper bound for gate operations to be compatible with quantum error correction. In the following sections we will evaluate  $\alpha$  for different types of junctions in the switch, a JoFET, a superconductor-ferromagnet-superconductor (SFS) junction and a high- $T_c$  junction by inserting typical parameters. We use the normal resistance  $R_N$  to estimate the shunt resistance in the RSJ model. Here, it is important to note that the parameters  $I_c$  and  $R_N$  of the junction determine the suitability of the device as a (low-noise) switch, which are given by a combination of material and geometry properties. In the following we exemplify the calculation of the dissipative effects with several experimental parameter sets.

For present day qubit technology<sup>13</sup> we can assume  $L \approx 1$  nH,  $I_{\text{circ}} \approx 100$  nA,  $M_{TQ} \approx 100$  pH. In the following, we estimate  $\alpha$  for a number of junction realizations, adjusting the junction area for sufficient critical current.

A JoFET can be understood as a SNS junction where the role of the normal metal is played by a doped semiconductor. By applying a gate voltage, it is possible to tune the electron density of the semiconductor.

The critical current of such a junction containing  $N_{\text{ch}}$  channels can be found using the formula of Kulik and Omel'yanchuk  $I_c = (\pi \Delta) / (R_N e)$ .<sup>11,14</sup>  $R_N = h / (2e^2 N_{\text{ch}})$  is the point-contact resistance. In a JoFET, the back gate essentially controls  $N_{\text{ch}}$ . The typical normal resistance is around  $R_N \approx 10 \Omega$ . For a JoFET the critical current of the Josephson junction is  $I_c \approx 30 \mu\text{A}$  and the Josephson inductance is  $L_J \approx 11$  pH.<sup>7</sup>

Inserting the earlier estimates we get  $\alpha \approx 7 \times 10^{-6}$ . This means that the dissipative effects are weak and a JoFET should be a reasonable switch that poses no new constraints. Besides the obvious technological challenge,<sup>7</sup> one drawback of JoFETs is that due to wide junctions with dimensions of around  $w = 500$  nm they are likely to trap vortices, which can cause  $1/f$  noise by hopping between different pinning sites. However, this can be reduced by pinning, e.g., by perforating the junction.

If we go away from the on state with the JoFET, we reduce both  $I_c$  and  $G_N$  linearly by depleting the density of states. Figure 3 shows that we find that the dissipative effects are strongest during the switching process when  $L_J(\rho_e / \rho_e^{\text{on}}) \approx L$ , and *not* in the on state of the switch. In the off state of the switch (for  $\rho_e(0) \rightarrow 0$ ) also  $\alpha$  goes to zero. If the switch is tuned from the off state to the on state,  $\alpha$  reaches a local maximum and then decreases again. This makes the JoFET a very attractive switch: It induces an acceptably low level decoherence in the on state and can be made completely silent in the off state.

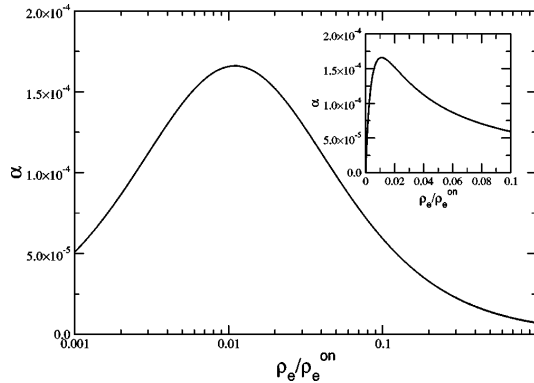


FIG. 3. The dimensionless dissipation parameter  $\alpha$  as a function of the electron density in the two-dimensional electron gas for a JoFET. The inset shows a linear plot of the region with the largest  $\alpha$ .

A SFS junction in the  $\pi$  state is based on a metallic material, thus the estimate of the shunt resistance in the RSJ model yields a much smaller result than in the case of the JoFET,  $R \approx 10^{-5} \Omega$ .<sup>10</sup> The critical current of the SFS junction is  $I_c \approx 0.2$  mA. Thus, leaving the transformer properties unchanged, we find  $L_J \approx 1.7$  pH. Using these estimates the strength of the dissipative effects is of the order of  $\alpha \approx 0.16$ . This makes such a device unsuitable at the present level of technology, however, it appears that superconductor-insulator-ferromagnet superconductor (SIFS) junctions<sup>15</sup> are

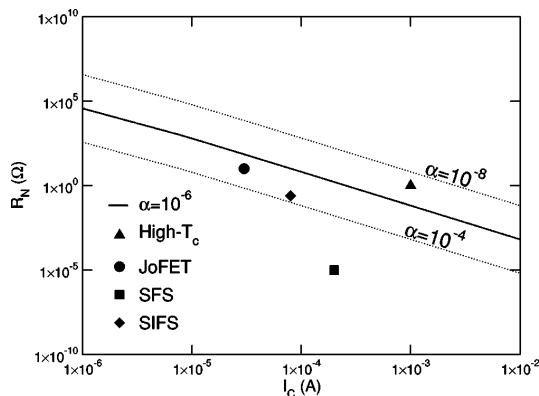


FIG. 4. Log-log plot of the normal state resistance vs the critical current of the junction. Here  $R_N$  is taken as an estimate for the shunt resistance of the junction. The solid line denotes  $\alpha = 10^{-6}$  and the two dotted lines are for  $\alpha = 10^{-4}$  (lower line) and  $\alpha = 10^{-8}$  (upper line). Parameters for the SIFS junction are  $I_c \approx 8.5 \times 10^{-5}$  A and  $R_N \approx 250$  m $\Omega$  (see Ref. 15).

by far closer to the desired values, see Fig. 4.

High- $T_c$  junctions can be realized in different ways. Here, we take from Ref. 9 parameters for a typical noble metal (Au)-bridge junction with a film thickness of about  $w \approx 100$  nm. The product  $I_c R_N \approx 1$  mV and  $\rho_N = 8.3 \Omega$  nm. We assume that in principle  $I_c$  for the  $\pi$  state and the 0 state are the same. For a contact area of around  $900 \text{ nm}^2$ ,  $I_c \approx 1$  mA and  $R_N \approx 1 \Omega$ . Now the strength of the dissipative effects is easily evaluated to be  $\alpha \approx 6.5 \times 10^{-8}$ , which is much better than SFS  $\pi$  junctions and even better than the JoFET.

We estimated the strength of the dissipative effects that will occur due to the switch for several possible switches. These results are summarized in Fig. 4 for typical parameters of the analyzed systems. We find that the noise properties of a JoFET and  $\pi$  shifters based on high- $T_c$  materials introduce no important noise source. On the other hand, the parameters found from  $\pi$  shifters based on magnetic materials are much less encouraging.

The authors would like to thank T. P. Orlando, P. Baars, and A. Marx for useful discussions. This work was supported in part by the National Security Agency (NSA) and Advanced Research and Development Activity (ARDA) under Army Research Office (ARO) contract No. P-43385-PH-QC.

<sup>1</sup> Yu. Makhlin, G. Schön, and A. Shnirman, Rev. Mod. Phys. **73**, 357 (2001).

<sup>2</sup> T. P. Orlando, J. E. Mooij, C. H. van der Wal, L. Levitov, S. Lloyd, and J. J. Mazo, Phys. Rev. B **60**, 15398 (1999); J. E. Mooij, T. P. Orlando, L. Levitov, L. Tian, C. H. van der Wal, and S. Lloyd, Science (Washington, DC, U.S.) **285**, 1036 (1999).

<sup>3</sup> C. H. van der Wal, A. C. J. ter Haar, F. K. Wilhelm, R. N. Schouten, C. J. P. M. Harmans, T. P. Orlando, S. Lloyd, and J. E. Mooij, Science (Washington, DC, U.S.) **290**, 773 (2000).

<sup>4</sup> I. Chiorescu, Y. Nakamura, C. J. P. M. Harmans, and J. E. Mooij, Science (Washington, DC, U.S.) **299**, 1869 (2003).

<sup>5</sup> C. H. van der Wal, F. K. Wilhelm, C. J. P. M. Harmans, and J. E. Mooij, Eur. Phys. J. B **31**, 111 (2003).

<sup>6</sup> X. Zhou, Z.-W. Zhou, G.-C. Guo, and M. J. Feldman, Phys. Rev. Lett. **89**, 197903 (2002).

<sup>7</sup> A. Richter, Adv. Solid State Phys. **40**, 321 (2000).

<sup>8</sup> G. Blatter, V. B. Geshkenbein, and L. B. Ioffe, Phys. Rev. B **63**, 174511 (2001).

<sup>9</sup> K. A. Delin and A. W. Kleinsasser, Supercond. Sci. Technol. **9**, 227 (1996).

<sup>10</sup> V. V. Ryazanov, V. A. Oboznov, A. Yu. Rusanov, A. V. Veretennikov, A. A. Golubov, and J. Aarts, Phys. Rev. Lett. **86**, 2427 (2001).

<sup>11</sup> M. Tinkham, *Introduction to Superconductivity*, 2nd ed. (McGraw-Hill, New York, 1996).

<sup>12</sup> M. J. Storcz and F. K. Wilhelm, Phys. Rev. A **67**, 042319 (2003).

<sup>13</sup> B. Singh and T. P. Orlando (private communication).

<sup>14</sup> I. O. Kulik and A. N. Omelyanchuk, Sov. J. Low Temp. Phys. **3**, 459 (1977).

<sup>15</sup> T. Kontos, M. Aprili, J. Lesueur, F. Genêt, B. Stephanidis, and R. Boursier, Phys. Rev. Lett. **89**, 137007 (2002).

# Chapter 9

## Decoherence Free Subspace (DFS) encoding

### 9.1 Introduction

Decoherence Free Subspaces (DFS) are generally considered as one possible tool to reduce or, in very special cases, even completely prevent environmental action on the qubit system, which results in decoherence. Historically, first the *conditions* for DFSs have been pointed out [215–218] and then investigations of the robustness of the decoherence free states [219] to perturbations which break the symmetry have been made.

Consider a general Hamiltonian

$$\hat{H} = \hat{H}_S + \hat{H}_{SB} + \hat{H}_B, \quad (9.1)$$

where the different parts of the Hamiltonian describe the system, the system-bath interaction, and the bath. Here, the system-bath interaction is taken bilinear in the system (spin) and bath operators,  $\hat{H}_I = \sum_{\alpha} \hat{S}_{\alpha} \otimes \hat{B}_{\alpha}$ . Obviously, for  $\hat{H}_{SB} = 0$ , system and bath are decoupled and evolve independently of each other, *i.e.*, the evolution of the system is *decoherence free* (DF). However, for non-vanishing system-bath interaction, one looks for subspaces of the full Hilbert space that fulfill the condition of DF dynamics.

The conditions for a DFS are [220],

1. There exists a set  $\{ |\tilde{k}\rangle \}$  of eigenvectors of the spin operators  $\hat{S}_{\alpha}$  with  $\hat{S}_{\alpha} |\tilde{k}\rangle = c_{\alpha} |\tilde{k}\rangle$  for all  $\alpha, |\tilde{k}\rangle$ . Here, the eigenvectors are degenerate, *i.e.*, the eigenvalue  $c_{\alpha}$  depends only on  $\alpha$  and not on  $k$ .
2. The system Hamiltonian  $\hat{H}_S$  leaves the subspace invariant and the evolution starts within this subspace.

As long as these requirements are met, the dynamics will be DF.

It has been shown that universal quantum computation can be performed within the encoded subspace for a single exchange Hamiltonian [221]. And the duality between quantum error correcting codes (QECCs) [36] and DFSs has also been pointed out, *e.g.*, in

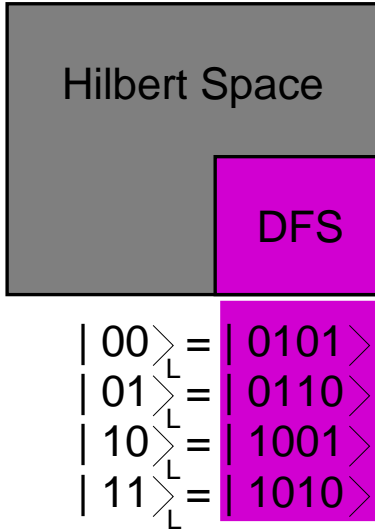


Figure 9.1: Schematic picture of a DFS encoding to protect from collective dephasing. The DFS is a subspace of the whole Hilbert space. The logical (encoded) states are denoted by the subscript “ $L$ ”.

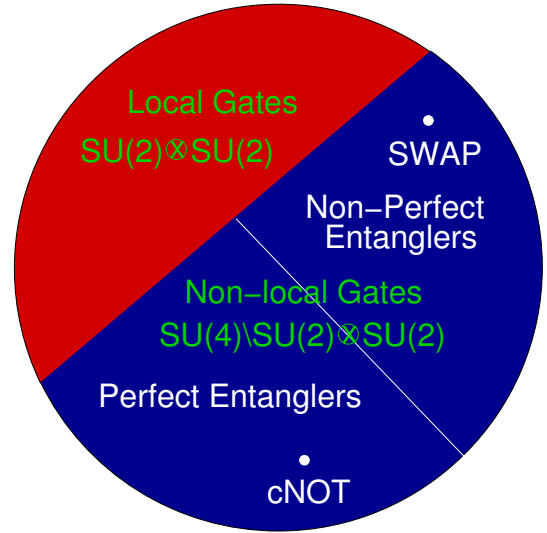


Figure 9.2: Cartoon of the partition of all the gates in  $SU(4)$  into local single-qubit gates and non-local two-qubit gates, taken from Ref. [222].

Refs. [220, 221]. Let us now exemplify one special case of collective dephasing for a system Hamiltonian that commutes with  $\hat{\sigma}_z^{(i)}$ . In this case the system-bath interaction is  $\hat{H}_{SB} = \left(\sum_i \hat{\sigma}_z^{(i)}\right) \otimes \hat{B}$ . Figure 9.1 depicts a DFS encoding for this example, here a system of four physical qubits is encoded into two logical qubits, denoted by the subscript “ $L$ ”.

When the collective spin operator  $\hat{S}$  in this example acts on the four states depicted in Fig. 9.1, all states lead to the same eigenvalue. Of course, one has to work out in detail that all conditions for a DFS are fulfilled, but this example nicely explains the advantages and design of DFSs. Investigations on the DFS encoding have been carried out for some physical realizations of qubits, in Ref. [223] DFSs have been introduced in the context of collective amplitude damping. Scalable schemes, *e.g.*, for ion trap quantum computation in decoherence-free subspaces [224] have been proposed and for NMR quantum computers the properties of a DFS have been intensively studied [225, 226].

Yet, the application of the DFS encoding to real solid-state physical systems is profound because of the many different decoherence sources and the fact that little is known about the correlations of the noise. Thus, despite the beautiful theoretical idea of DFSs, it is very hard in practice to identify systems that can take full advantage of the DFS encoding.

To exploit the full advantage of DFSs, it is necessary to identify systems that are subject to collective noise. Thus, it is important to identify the degree of correlation of the noise

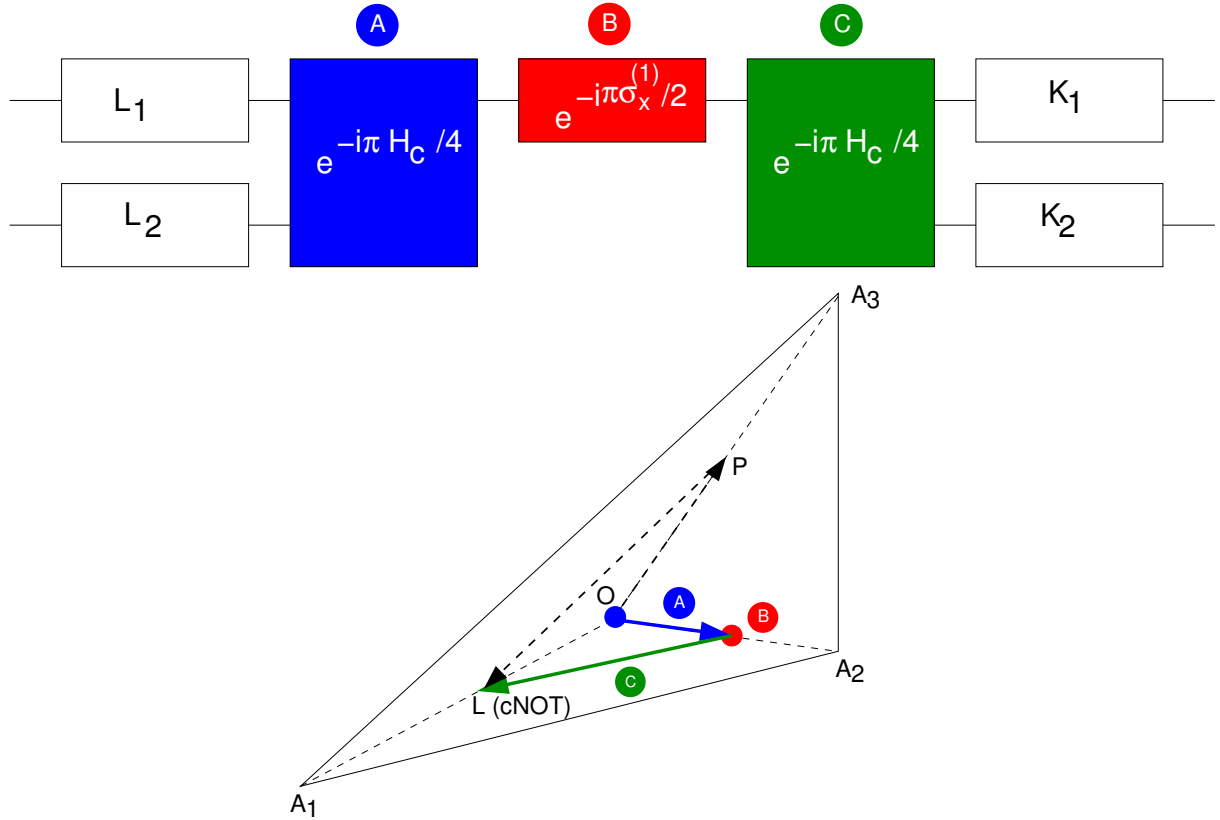


Figure 9.3: Weyl chamber trajectory illustrating the CNOT operation for the anisotropic exchange interaction, *i.e.*, for an inter-qubit coupling Hamiltonian  $H_c = \hat{\sigma}_x^{(1)}\hat{\sigma}_x^{(2)} + \hat{\sigma}_y^{(1)}\hat{\sigma}_y^{(2)}$ , obtained from the representation in the geometric theory presented in Ref. [222];  $L_{1,2}$  and  $K_{1,2}$  are local single-qubit gates.

in qubit systems to develop strategies to fight decoherence. The noise correlations are characterized by the correlation length scale.

Two-qubit gates can be represented geometrically in the Weyl chamber, which provides a projection of  $SU(4)$  into  $\mathbb{R}^3$  [227]. Namely, every unitary operation  $U \in SU(4)$  can be decomposed in [222]

$$U = k_1 \exp \left[ -i(c_1 \hat{\sigma}_x^{(1)} \hat{\sigma}_x^{(2)} + c_2 \hat{\sigma}_y^{(1)} \hat{\sigma}_y^{(2)} + c_3 \hat{\sigma}_z^{(1)} \hat{\sigma}_z^{(2)}) \right] k_2, \quad (9.2)$$

with  $k_1, k_2 \in SU(2) \otimes SU(2)$  and  $c_1, c_2, c_3 \in \mathbb{R}$ . In the Weyl chamber, all non-local operations can then be expressed in terms of the three parameters  $c_1, c_2$ , and  $c_3$ . These parameters are the three-dimensional coordinates in the Weyl chamber. By detailed analysis [222], it is found that the representation of non-local two-qubit operations is a tetrahedron in  $\mathbb{R}^3$ . Figure 9.3 exemplifies the trajectory for a CNOT gate with two coupled qubits as described in the paper in the following section. Note also that it was shown in [222] that any quantum gate can be implemented by three interactions and eight single-qubit

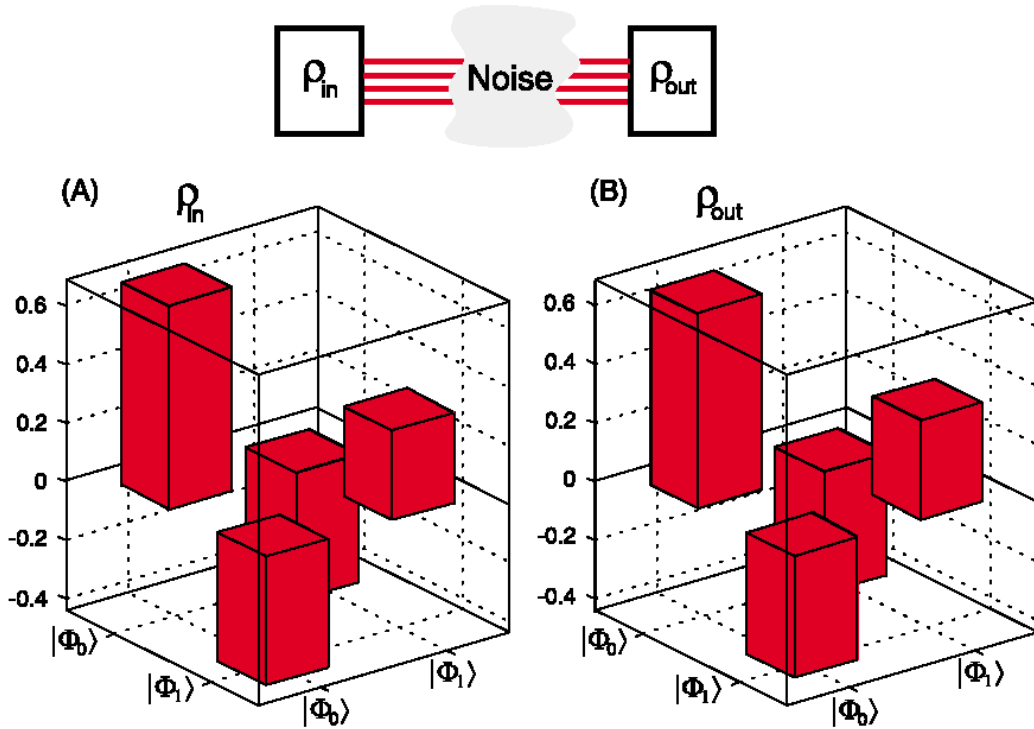


Figure 9.4: Experimental demonstration of quantum state tomography for a DFS encoded four-photon qubit state from [46]. The entries of the density matrix of the qubit before and after transmission through a noisy transmission channel are depicted. The DFS encoding protects the quantum state. The trace-fidelity of the transfer is  $F_{\rho_{\text{in}},\rho_{\text{out}}} = \text{tr} \left[ \left( \sqrt{\rho_{\text{out}}}\rho_{\text{in}}\sqrt{\rho_{\text{out}}} \right)^{1/2} \right] = 0.9958 \pm 0.0759$ .

gates. However, in a latter work [228] the authors discovered the quantum gate  $B$  that can implement any arbitrary two-qubit quantum operation with a minimal number of both two- and single-qubit gates, *i.e.*, any non-local two-qubit operation can be obtained from only two applications of the  $B$  gate, which is useful for physical systems where the  $B$  gate is easily implemented.

The general feasibility of DFS encoding has been demonstrated with photon states [46]. In this experiment, four-photon states have been generated by parametric down conversion and used to encode one qubit inside a DFS. Then these photons were transmitted via a noisy transmission channel, where the noise is simulated by transmission of the photons through quarter- and half-wave plates. Finally, quantum state tomography of the qubit states showed the immunity against the noise. These results are depicted in Fig. 9.4.

In the following paper [229], the DFS encoding for a realistic model of superconducting solid-state qubits is investigated. These qubits are coupled via the aforementioned anisotropic exchange interaction [195]. It turns out that the noise stemming from the coupling elements, which is assumed to be correlated between neighbouring qubits, can be



completely suppressed by encoding into a DFS. However, next to the DFS encoding also the special form of the bath spectral function needs to be exploited in order to provide perfect protection.

In more detail, the  $1/f$ -noise from the coupling elements that couples to a single qubit (here, for the sake of simplicity and without loss of generality only a single-qubit will be considered) can be described by the Hamiltonian

$$H_\phi = \frac{1}{2} \begin{pmatrix} \epsilon & \Delta e^{i\delta\phi} \\ \Delta e^{-i\delta\phi} & -\epsilon \end{pmatrix} + H_B = \frac{1}{2} e^{i\hat{\sigma}_z \delta\phi/2} \begin{pmatrix} \epsilon & \Delta \\ \Delta & -\epsilon \end{pmatrix} e^{-i\hat{\sigma}_z \delta\phi/2} + H_B \quad (9.3)$$

where  $H_B$  is the Hamiltonian that describes the environmental bath of harmonic oscillators with coordinates  $\hat{X}_i$  interacting with the qubit via the term  $\delta\phi = \sum_i c_i \hat{X}_i$ . This kind of Hamiltonian describes the effect of background charges on a flux qubit, which act via the Aharonov-Casher effect [230, 231]. It is well known that these background charges typically produce  $1/f$ -noise that can be described by a general semiclassical noise-correlation function in the frequency domain,

$$\frac{1}{2} \langle \delta\phi(t) \delta\phi(0) + \delta\phi(0) \delta\phi(t) \rangle_\omega = S_\phi(\omega) = \alpha_s \omega^s \omega_c^{1-s} e^{-\omega/\omega_c} \coth(\hbar\beta\omega/2), \quad (9.4)$$

in the limit when  $s \rightarrow 0$  and  $\omega \ll T$ , where  $S_\phi = (2T\alpha_s/\omega_c)1/\omega$ . Although the magnitude of the  $1/f$ -noise is usually small, the reason why  $1/f$ -noise is still noxious is that there is a large spectral weight at low frequencies.

The effect of the charge noise can be viewed as an effective unitary transformation which can be properly undone by an appropriate inverse transformation. Namely, the Hamiltonian Eqn. (9.4) can be mapped by using the unitary matrix  $U(t) = e^{-i\hat{\sigma}_z \delta\phi/2}$ . Here,  $\delta\phi(t)$  is an operator (or, in the Schrödinger picture, a time-dependent variable), thus the transformation of the wave function  $|\psi'\rangle = U|\psi\rangle$  corresponds to the transformation of the Hamiltonian  $H_\epsilon = UH_\phi U^\dagger + (i(d/dt)U)U^\dagger$ . Physically, this corresponds to going to the frame which is co-rotating with the noise and the extra term can be viewed as an inertial force. Thus, one can write

$$H_\epsilon = \begin{pmatrix} \epsilon & \Delta \\ \Delta & -\epsilon \end{pmatrix} + i\frac{1}{2} \delta\epsilon \hat{\sigma}_z + H_B,$$

where  $\delta\epsilon = \dot{\delta\phi}$  is the time-derivative of the phase. This corresponds to a spin-boson model, where the fluctuating force is the time-derivative of the phase. Note that the time-derivation corresponds to a factor  $i\omega$  in frequency space. Therefore, one can identify the spectral density of the corresponding spin-boson model

$$\frac{1}{2} \langle \delta\epsilon(t) \delta\epsilon(0) + \delta\epsilon(0) \delta\epsilon(t) \rangle_\omega = S_\epsilon(\omega) = \alpha_s \omega^{s+2} \omega_c^{1-s} e^{-\omega/\omega_c} \coth(\hbar\beta\omega/2), \quad (9.5)$$

which reduces to a super-Ohmic power spectrum  $S_\epsilon(\omega) = \alpha_0 \omega^2 / \omega_c$ . Thus, the transformation presented here effectively transforms  $1/f$ -noise to regular flux-noise with a super-Ohmic spectrum.



PHYSICAL REVIEW B 72, 064511 (2005)

**Full protection of superconducting qubit systems from coupling errors**M. J. Storz,<sup>1,\*</sup> J. Vala,<sup>2</sup> K. R. Brown,<sup>2</sup> J. Kempe,<sup>2,†</sup> F. K. Wilhelm,<sup>1</sup> and K. B. Whaley<sup>2</sup><sup>1</sup>*Physics Department, ASC, and CeNS, Ludwig-Maximilians-Universität, Theresienstr. 37, 80333 München, Germany*<sup>2</sup>*Department of Chemistry and Pitzer Center for Theoretical Chemistry, University of California, Berkeley, California 94720, USA*

(Received 18 April 2005; published 12 August 2005)

Solid state qubits realized in superconducting circuits are potentially scalable. However, strong decoherence may be transferred to the qubits by various elements of the circuits that couple individual qubits, particularly when coupling is implemented over long distances. We propose here an encoding that provides full protection against errors originating from these coupling elements, for a chain of superconducting qubits with a nearest neighbor anisotropic  $XY$ -interaction. The encoding is also seen to provide partial protection against errors deriving from general electronic noise.

DOI: 10.1103/PhysRevB.72.064511

PACS number(s): 03.67.Pp, 03.65.Yz, 03.67.Lx, 85.25.-j

Superconducting flux qubits have been shown to possess many of the necessary features of a quantum bit (qubit), including the ability to prepare superpositions of quantum states<sup>1,2</sup> and manipulate them coherently.<sup>3</sup> In these systems, the dominating error source appears to be decoherence due to flux noise.<sup>4</sup> Present designs for arrays of *multiple* flux qubits that are coupled through their flux degree of freedom are easily implemented from an experimental point of view.<sup>5</sup> However, when scaling up to large numbers of qubits, they suffer from technical restrictions such as possible flux crosstalk and a need for physically large coupling elements, which are expected to act as severe antennas for decoherence. The possibility of avoiding errors by prior encoding into decoherence free subspaces (DFS) that are defined by the physical symmetries of the qubit interaction with the environment is consequently very attractive. Such encoding is also attractive for superconducting charge qubits,<sup>6,7</sup> which are subject to similar decoherence sources.<sup>8</sup>

In this work, we show how to develop such protection for qubits coupled by the nearest neighbor  $XY$ -interaction that is encountered in both flux and charge qubit designs.<sup>9,10</sup> We demonstrate that for this coupling, a two-qubit encoding into a DFS provides full protection against noise from the coupling elements. Moreover, all encoded single-qubit operations are also protected from collective decoherence deriving from the electromagnetic environment. The protection is seen to result from a combination of symmetry in the coupling element and a restricted environmental phase space of the multi-qubit system—the DFS *alone* would not be sufficient. The analysis makes use of an exact unitary transformation of  $1/f$  phase noise in the coupling element (hence with a sub-Ohmic power spectrum) into regular nearest-neighbor correlated flux noise on the qubits that is characterized by a super-Ohmic power spectrum. To assess the performance of the encoding we add to this coupling-derived noise a single-qubit Ohmic noise source that represents the generic uncorrelated environmental factors and analyze the fidelity of encoded quantum gate operations.

The Hamiltonian of a linear chain of  $XY$  coupled qubits reads

$$\begin{aligned} \mathbf{H}_q &= \mathbf{H}_0 + \mathbf{H}_{\text{int}} \\ &= \sum_i \left[ \epsilon_i \hat{\sigma}_z^{(i)} + \Delta_i \hat{\sigma}_x^{(i)} + K_{i,i+1} (\hat{\sigma}_x^{(i)} \hat{\sigma}_x^{(i+1)} + \hat{\sigma}_y^{(i)} \hat{\sigma}_y^{(i+1)}) \right], \end{aligned} \quad (1)$$

where  $\mathbf{H}_0 = \sum_i [\epsilon_i \hat{\sigma}_z^{(i)} + \Delta_i \hat{\sigma}_x^{(i)}]$  is the uncoupled qubit Hamiltonian, and  $K_{i,i+1}$  is the strength of the inter-qubit coupling,  $\mathbf{H}_{\text{int}}$ . We assume that it is possible to switch the coupling  $K_{i,i+1}$  and the flux bias  $\epsilon_i(\Phi_{x,i})$  of each qubit separately. Such a Hamiltonian can be realized using flux qubits with capacitive coupling.<sup>10</sup> The switch for this interaction can in principle be implemented using PIN varactor diodes, micromechanical devices, or small Josephson junctions.<sup>11</sup> Switching on the coupling suppresses the tunnel amplitudes<sup>10</sup>  $\Delta_i$ . The Hamiltonian of Eq. (1) can also be readily implemented in charge qubits, i.e., Cooper pair boxes coupled by Josephson junctions,<sup>9</sup> whose coupling strength can be tuned through an external magnetic field. In both cases, the couplers are large objects and hence act as efficient antennas for charge and/or flux noise when the coupling is on. When the coupling is switched off, this noise is confined within the coupler and does not affect the qubits.

The decoherence sources relevant to Eq. (1) are background charges. This can be represented as  $1/f$  noise in the coupler as we explain below. In addition general electromagnetic (e.m.) noise, both local flux or electronics noise, couples to single qubits and, for long wavelength, also to multiple qubits. The e.m. noise is represented as usual by Ohmic noise which has both uncorrelated and collective components. The effect of these environmental decoherence sources on Eq. (1) is represented by the usual (linear) coupling to a bath of oscillators  $\mathbf{H}_b = \sum_i (a_i^\dagger a_i + \frac{1}{2})$ , characterized by a spectral density  $J(\omega) = \sum_i |\lambda_i|^2 \delta(\omega - \omega_i)$ , with the coupling strength characterized by a dimensionless parameter<sup>12</sup>  $\alpha$ .

We first show how the coupling and local noise are described in this framework. Background charge fluctuations  $\delta q(t)$  arising in the capacitive coupling elements between qubits  $i$  and  $i+1$ , induce geometric Aharonov-Casher<sup>13</sup> phases  $\delta\phi(t) \propto \delta q(t)$  when the qubit flux states tunnel between eigenstates of  $\hat{\sigma}_z$ . This results in a correlated two-qubit

STORCZ *et al.*PHYSICAL REVIEW B **72**, 064511 (2005)

error operator  $\exp[i\delta\phi(\hat{\sigma}_z^{(i)} + \hat{\sigma}_z^{(i+1)})]$  acting on  $\mathbf{H}_q$ . The low-frequency limit of this phase noise in the coupling elements can be approximated as a Gaussian  $1/f$  noise process deriving from coupling to a sub-Ohmic oscillator bath with associated spectral density<sup>12,13</sup>  $J_\phi^{2qb}(\omega) = (\alpha_0/\epsilon_0)\text{sign}(\omega)e^{-\omega/\omega_c}$ . Here and henceforth we set  $\hbar, k_B = 1$ . This leads to a classical power spectrum in the frequency domain

$$\begin{aligned} S_\phi(\omega) &= \frac{1}{2} \langle \delta\phi(t)\delta\phi(0) + \delta\phi(0)\delta\phi(t) \rangle_\omega \\ &= J_\phi^{2qb}(\omega) \coth(\omega/2T) \\ &\simeq (2T\alpha_0/\omega_c\omega) \end{aligned} \quad (2)$$

for  $\omega \ll T$ , which characterizes the environmental phase space of the correlated two-qubit errors due to capacitive coupling. Uncorrelated single qubit errors deriving from local electronic elements are represented here by bath coupling to the flux states, i.e.,  $\hat{\sigma}_z$  errors. This is typically represented by a bath having an Ohmic spectral density,<sup>14</sup>  $J_{\epsilon,\Omega}^{1qb} = \alpha_\Omega \omega \omega_c^2 / (\omega_c^2 + \omega^2)$ , which thus characterizes the environmental phase space of the uncorrelated single-qubit errors. We note that very recently,  $\hat{\sigma}_x$  single-qubit errors (i.e., bit flip errors) have also been identified.<sup>15</sup> The third source of errors, correlated errors deriving from long wavelength electromagnetic radiation, can be removed by encoding into a DFS as we show below, independent of the form of the spectral density associated with the source of such collective decoherence.

We can formally introduce the noise due to background charges into the total Hamiltonian  $\mathbf{H}_q + \mathbf{H}_b$  by transforming the total Hamiltonian with a unitary operator  $U_{qb} = \exp[i\delta\phi(\hat{\sigma}_z^{(i)} + \hat{\sigma}_z^{(i+1)})]$ , resulting in

$$\mathbf{H} = \mathbf{H}' + \mathbf{H}_b = U_{qb} \mathbf{H}_q U_{qb}^\dagger + \mathbf{H}_b, \quad (3)$$

with associated spectral density  $J_\phi^{2qb}(\omega)$ . Thus, the error acts in the interaction picture as a time-dependent unitary transformation and it can be eliminated by undoing the transformation. In NMR (nuclear magnetic resonance) language, this is a transformation to the ‘‘co-fluctuating’’ frame. The unitary transformation is properly undone by a time-dependent unitary transformation in the interaction picture, which transforms the states as  $|\psi'\rangle = U_{qb}^\dagger |\psi\rangle$  and the coupled Hamiltonian as

$$\mathbf{H}_{\text{eff}} = U_{qb}^\dagger \mathbf{H} U_{qb} - i U_{qb}^\dagger \frac{d}{dt} U_{qb}, \quad (4)$$

$$-i U_{qb}^\dagger \frac{d}{dt} U_{qb} = \frac{1}{2} [\hat{\sigma}_z^{(i)} + \hat{\sigma}_z^{(i+1)}] \delta\phi. \quad (5)$$

The last term is understood as an effective system-bath interaction, written more explicitly

$$\mathbf{H}_{\text{SB}} = -i U_{qb}^\dagger \frac{d}{dt} U_{qb} = \frac{1}{2} [\hat{\sigma}_z^{(i)} + \hat{\sigma}_z^{(i+1)}] \otimes \sum_n i \omega_n \lambda_n (a_n - a_n^\dagger). \quad (6)$$

Note that  $\mathbf{H}_q = U_{qb}^\dagger \mathbf{H}' U_{qb}$ . Physically, this arises from the transformation into the noninertial co-fluctuating frame as an inertial force. It is recognized that (6) is the regular spin

boson coupling  $\mathbf{H}_{\text{SB,eff}} = \sum_i (\lambda_i' a_i + \lambda_i'^* a_i^\dagger)$  with  $\lambda_i' = i\omega\lambda_i$ . In this transformed representation we now have correlated flux errors, i.e., pairwise coupling of the qubit  $\hat{\sigma}_z$  operators to energy fluctuations given by the time-derivative of the fluctuating correlated coupler phase,  $\delta\phi$ . Most importantly, the associated spectral density of the oscillator bath is also transformed, becoming  $J_\epsilon^{2qb}(\omega) = \omega^2 J_\phi^{2qb}(\omega) = \alpha_0 \omega^2 \text{sign}(\omega) / \epsilon_0$ , which is now super-Ohmic. Similar arguments can be applied to the flux noise arising when two charge qubits are coupled by a SQUID, except that here the coupling (flux) noise is usually Ohmic rather than sub-Ohmic, so that the transformed spectral density is proportional to  $\omega^3$  rather than to  $\omega^2$ . Note, that the flux states only get transformed by phase factors, hence computation and measurement carried out in this basis are unaffected by this transformation.

To protect against these correlated errors we employ a two-qubit encoding  $|0\rangle_L = |01\rangle$ ,  $|1\rangle_L = |10\rangle$  which is recognizable as the smallest DFS encoding that can protect against collective dephasing.<sup>16</sup> It, therefore, automatically protects against any correlated phase errors, including our third source of error deriving from long wavelength e.m. noise.

We will show that as a result of the symmetry in the bath, in particular, because of the form of its spectral density, this encoding also provides complete protection against the noise arising during capacitive coupling. This results in perfect performance of both encoded single qubit and two qubit operations when correlated errors during two-qubit operations are the only source of decoherence. Uncorrelated single qubit errors are then the only remaining mechanism leading to a reduced fidelity of quantum gates. We find below that for single qubit errors of less than or equal strength to two qubit errors, the DFS encoding still provides a significant, although now incomplete, protection.

The two logical qubits are encoded into four physical qubits using the encoding scheme  $|00\rangle_L = |0101\rangle_P$ ,  $|01\rangle_L = |0110\rangle_P$ ,  $|10\rangle_L = |1001\rangle_P$ ,  $|11\rangle_L = |1010\rangle_P$ , where  $L$  and  $P$  denote logical and physical states, respectively. We assume that the four physical qubits constitute a linear array (this need not be contiguous) which we label 1,2,3,4. This four-dimensional subspace is left invariant by collective errors involving qubits 1 and 2,  $U_{qb}$  with  $i=1$ , as well as by errors involving qubits 3 and 4,  $U_{qb}$  with  $i=3$ , but not by collective errors involving qubits 2 and 3, i.e.,  $U_{qb}$  with  $i=2$ , see Ref. 16. A simple counting argument shows that a DFS that protects against all two-qubit errors including those between the two encoded qubits does not exist.

The latter errors arise when switching on the coupling between qubits 2 and 3 with  $\mathbf{H}_{\text{int}}$  as described above, in order to perform logical two-qubit operations. Thus, in a Hamiltonian formulation within the basis spanned by the encoded subspace vectors, the coupling error  $\hat{\sigma}_z^{(2)} + \hat{\sigma}_z^{(3)}$  between qubits 2 and 3 does not have identical degenerate eigenvalues as would be required for a DFS.<sup>17</sup> Moreover, the physical single qubit errors also do not fulfill this requirement of degenerate eigenvalues. In the language of quantum error correcting codes (QECC)<sup>18</sup> where a DFS is a particular example of a degenerate QECC<sup>16</sup> we, therefore, conclude that our encoding is not fully degenerate under the action of both the correlated two-qubit and single qubit errors and does not

constitute a true DFS for both classes of errors. A true DFS would be completely degenerate, giving identical syndromes of unity for all of these errors. As a result of this lack of degeneracy, additional operations are in principle needed for correction of the uncorrelated noise, i.e., of the physical single-qubit errors, as well as for correction of the coupling error  $U_{qb}$ ,  $i=2$ . Nevertheless, we will see below that the latter coupling errors resulting from the background charge fluctuations are actually suppressed by the bath properties and its symmetry after application of the transformation  $U_{qb}$ , so that only the single qubit errors need to be actively corrected.

The encoded single-qubit operations, given here without loss of generality for the first encoded logical qubit only, can be shown to be

$$e^{-i\hat{\sigma}_z^{(1)}\tau} = e^{-i\hat{\sigma}_z^{(2)}\tau} \quad (7)$$

$$e^{-i\hat{\sigma}_x^{(1)}\tau} = e^{-i\tilde{\mathbf{H}}_{\text{int}}^{12}\tau} \quad (8)$$

$$e^{-i\hat{\sigma}_y^{(1)}\tau} = e^{i\hat{\sigma}_z^{(1)}\frac{\pi}{4}} e^{i\hat{\sigma}_x^{(1)}\tau} e^{-i\hat{\sigma}_z^{(1)}\frac{\pi}{4}}, \quad (9)$$

where  $\tilde{\mathbf{H}}_{\text{int}} = (\mathbf{H}_{\text{int}}/\epsilon_0)$  and  $\tau = t\epsilon_0$ . The first operation is straightforwardly achieved by tuning the flux bias. To implement the second operation,  $\hat{\sigma}_x^{(1)}$ , we need to cancel the effect of  $\mathbf{H}_0$ . This is also straightforward, if  $\epsilon_i$  and  $\Delta_i$  can be tuned to zero. If  $\Delta$  cannot be tuned to zero, it is nevertheless still possible to act with  $\mathbf{H}_{\text{int}}$  alone, by combining a short time Trotter expansion with operator conjugation as follows. First, we recognize that conjugation of  $\mathbf{H}_q$  with  $\hat{\sigma}_z$  can invert the sign of  $\Delta_i$

$$e^{-i\mathbf{H}_q(-\Delta_1, -\Delta_2)t} = e^{-i(\hat{\sigma}_z^{(1)} + \hat{\sigma}_z^{(2)})\pi/2} e^{-i\mathbf{H}_q(\Delta_1, \Delta_2)t} e^{i(\hat{\sigma}_z^{(1)} + \hat{\sigma}_z^{(2)})\pi/2}. \quad (10)$$

The alternation of  $\mathbf{H}_q(\Delta_1, \Delta_2, K_{12})$  with  $\mathbf{H}_q(-\Delta_1, -\Delta_2, K_{12})$  results in the desired action of  $\mathbf{H}_{\text{int}}$ , up to commutator errors between  $\mathbf{H}_{\text{int}}$  and  $\Delta\hat{\sigma}_x^{(i,j)}$  which can be suppressed by making a Trotter expansion:

$$\lim_{n \rightarrow \infty} (e^{-i\mathbf{H}_q(\Delta_1, \Delta_2, K_{12})t/2n} e^{-i\mathbf{H}_q(-\Delta_1, -\Delta_2, K_{12})t/2n})^n = e^{-i\tilde{\mathbf{H}}_{\text{int}}^{12}\tau}. \quad (11)$$

This scheme requires only relatively small values of  $n$  to be effective. Direct simulation shows that for  $n \sim 10$ , the relative deviation of individual matrix elements  $U_{nm}$  from  $U_{nm}^{\text{ideal}}$  is smaller than 1%. During all these encoded single qubit operations the encoded qubit remains in the DFS encoded subspace and so is fully protected against correlated two-qubit errors deriving from both the capacitive coupling and from any other electromagnetic correlated noise.

Encoded two-qubit operations require pairwise coupling of physical qubits from the two encoded qubits  $|0\rangle_L$  and  $|1\rangle_L$ , e.g., qubits 2 and 3 as mentioned above. The encoded  $\bar{U}_{zz}(t)$  two-qubit controlled-phase operation is

$$\bar{U}_{zz}(t) = e^{-i\hat{\sigma}_z^{(1)}\hat{\sigma}_z^{(2)}\tau} = e^{iS_x\frac{\pi}{4}} e^{i\tilde{\mathbf{H}}_{\text{int}}^{23}\pi/2} e^{-i\hat{\sigma}_x^{(2)}\frac{\pi}{2}} e^{i\tilde{\mathbf{H}}_{\text{int}}^{23}\pi/2} e^{iS_x'\frac{\pi}{4}}, \quad (12)$$

where  $S_x' = \hat{\sigma}_x^{(2)} - \hat{\sigma}_x^{(3)}$  and  $S_x = \hat{\sigma}_x^{(2)} + \hat{\sigma}_x^{(3)}$ . This can be combined with an encoded single qubit Hadamard gate to produce the controlled NOT (CNOT) gate.<sup>14</sup> Now the first element of  $\bar{U}_{zz}(t)$ ,  $e^{iS_x\pi/4}$ , takes the DFS states outside the subspace to form superpositions of DFS and non-DFS states and populate the non-DFS states  $|011\rangle$ ,  $|0100\rangle$ ,  $|1011\rangle$  and  $|1000\rangle$ . Detailed analysis reveals that the two-qubit operation Eq. (12) will always take the encoded qubits out of the DFS encoded subspace. However, during these excursions out of the DFS, when only coupling errors are present, only pure dephasing processes which do not flip eigenstates can contribute to decoherence,<sup>14</sup> since the coupling to the bath commutes with the interqubit coupling. The rates of these dephasing processes are proportional to  $S(0) = \lim_{\omega \rightarrow 0} \int_0^{2q_b} J_\epsilon^2(\omega) \coth(\omega/2T)$ , which vanishes as a result of the super-Ohmic shape of  $J_\epsilon^{2q_b}$  derived from the tunneling-flux transformation introduced above. Consequently these processes ‘‘lack phase space’’ in the environmental degrees of freedom and hence are fully suppressed. This excursion out of the DFS encoded subspace into a larger region of the full Hilbert space in which only pure dephasing processes contribute to the decoherence can alternatively be viewed as an excursion into a larger subspace that is characterized by suppression of relaxation processes.

We demonstrate the benefits of the DFS encoding by numerical studies of the CNOT gate, calculated from the simulated evolution of the reduced density matrix for the coupled flux qubits using the Bloch-Redfield description of the spin-boson model of the qubit and its bath coupling characterized by<sup>14</sup>  $J(\omega)$ . This approach is valid for  $\alpha_0, \alpha_\Omega \ll 1$ . To quantify the gate performance we evaluate the fidelity<sup>19</sup>  $\mathcal{F}$  of the encoded quantum gate operation, defined by  $\mathcal{F} = \frac{1}{16} \sum_{j=1}^{16} \langle \Psi_{in}^j | U_G^\dagger \rho_G^j U_G | \Psi_{in}^j \rangle$ . Here  $U_G$  is the unitary matrix describing the desired ideal gate, and  $\rho_G^j = \rho(t_G)$  is the density matrix obtained from attempting a quantum gate operation in a hostile environment, i.e., with errors, evaluated for all initially unentangled product states<sup>19</sup> from the encoded logical basis,  $\rho(0) = |\Psi_{in}^j\rangle\langle\Psi_{in}^j|$ . The states  $|\Psi_{in}^j\rangle$  are defined in Ref. 20.

Figure 1 shows the calculated gate fidelity for an encoded CNOT operation  $\bar{U}_{\text{CNOT}}$ , obtained from  $\bar{U}_{zz}$  together with the relevant encoded single qubit gates. We see that, as predicted by the above analysis, when only two-qubit errors are active ( $\alpha^{1\text{qb}}=0$ ) the gate performance is perfect. When additional uncorrelated single-qubit errors during single qubit operations occur ( $\alpha^{1\text{qb}}$ ), the gate fidelity is seen to decrease as the strength of these errors increases. The DFS encoding is thus seen to give 100% protection against the primary coupling errors in addition to correlated background errors. It does not protect against uncorrelated single qubit errors, in fact, due to the larger overhead, DFS encoding alone is sensitive against these (compare sets I and II). However, the uncorrelated single qubit errors can be well treated by active quantum error correction, particularly if the error rates for single

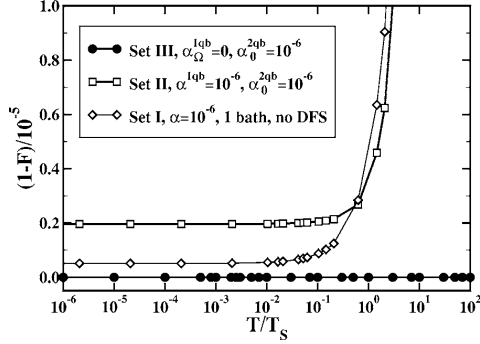
STORCZ *et al.*PHYSICAL REVIEW B **72**, 064511 (2005)

FIG. 1. Fidelity deviation  $1-\mathcal{F}$  vs temperature for the encoded CNOT operation, shown for two different combinations of super-Ohmic two-qubit noise (strength  $\alpha^{2qb}=\alpha_0$ ) and Ohmic single-qubit noise (strength  $\alpha^{1qb}=\alpha_\Omega$ ) acting on the physical qubits. The characteristic temperature scale is  $T_s=\epsilon_0(\hbar/k_B)$ , yielding  $T_s=48$  mK for qubits with energies  $\epsilon_i=\epsilon_0\equiv 1$  GHz,  $i=1, 2$ . Here,  $\epsilon_0$  is used as an energy unit for the correlation function. Solid lines are provided as guides to the eye. Ideal gate performance is achieved when  $\alpha^{1qb}=0$ . Detailed analysis shows that the fidelity depends linearly on  $\alpha^{1qb}$ . For comparison, set I shows the corresponding performance of the unencoded CNOT operation taken from Ref. 14.

qubit and correlated errors are comparable. It is also possible to combine this encoding scheme with a QECC in order to achieve fault-tolerance. Using the scheme proposed in Ref. 21, the leakage problem of standard QECC methods can be overcome.

Saturation of the gate quality at low temperatures occurs because all decohering processes (except spontaneous emission) are frozen out. This occurs when  $k_B T \approx E_{\min}$ , where  $E_{\min}$  is the lowest energy splitting in the system. Here,  $E_{\min}=\epsilon_0$ . Even during the excursion out of the DFS, transitions between the eigenstates of the Hamiltonian involving spontaneous emission are forbidden by symmetry. Thus, at low temperatures, only energy-conserving “pure dephasing” processes influence the gate. These are proportional to the noise power  $S(\omega \rightarrow 0)$ . For an Ohmic environment, this noise is purely thermal,<sup>14</sup>  $S(0) \propto T$ , so that the gate performance is still limited at any finite temperature. For the super-Ohmic case,  $S(0)=0$  at any  $T$  (Fig. 1). When  $\alpha_\Omega$  is small, the fidelity can be considerably increased because the errors from the coupling elements introduce no new constraints; i.e., if, for

equal coupling strength to the electromagnetic environment, the appropriate relative weight of two qubit errors is larger than that of one qubit errors, it is evident that the DFS encoding provides considerable protection. Thus, for optimizing two-qubit gates it is of crucial importance to identify, whether or not the noise is correlated between qubits. This is a critical challenge for experiment. An experimental signature of correlated noise is, e.g., the superior coherence of the states used as logical qubits in this work.

In conclusion, we have shown that using a DFS encoding of superconducting flux or charge qubits can significantly enhance their gate performance for the entangling two-qubit operations that are required to implement quantum computation. The DFS-encoding proposed here ensures that all *encoded* single-qubit operations are protected against  $1/f$  noise in the capacitive coupling elements, as well as from correlated electromagnetic noise. The latter are the errors originating from the coupling of the qubits to a common electromagnetic environment. When only the capacitive coupling errors arising during two-qubit operations are present, even though these are not automatically protected by this DFS encoding, we find that perfect fidelity can still be achieved. We have shown that this is a consequence of two symmetries of the bath. First, commutation of the system-bath coupling with the interqubit coupling results in elimination of spontaneous emission between qubit eigenstates. Second, a vanishing bath spectral density for dephasing processes results from the exact correspondence of the  $1/f$  sub-Ohmic charge noise in the coupler to super-Ohmic flux noise on the qubits.

The phase space restriction found here derives from the choice of the  $XY$ -interaction between the qubits: coupler noise from other interactions would explore the full phase space during the two-qubit operation. Thus the  $XY$ -coupling is a very attractive coupling scheme whenever decoherence is a major concern. From the results presented here, we expect that this DFS-inspired encoding, which is also very efficient, requiring only two physical qubits per logical qubit, will therefore be useful for reducing the noise in quantum circuits based on superconducting qubits.

#### ACKNOWLEDGMENTS

We thank T.L. Robertson for useful discussions. This work was supported in part by the NSA and ARDA under ARO contract number P-43385-PH-QC, in part by the National Science Foundation under the ITR program, Grant No. EIA-0205641, and by DFG through SFB 631.

\*Electronic address: storcz@theorie.physik.uni-muenchen.de

†Also affiliated with CNRS-LRI, UMR 8623, Université de Paris-Sud, 91405 Orsay, France.

<sup>1</sup>C. H. van der Wal, A. C. J. ter Haar, F. K. Wilhelm, R. N. Schouten, C. J. P. M. Harmans, T. P. Orlando, S. Lloyd, and J. E. Mooij, *Science* **290**, 773 (2000).

<sup>2</sup>J. R. Friedman, V. Patel, W. Chen, S. K. Tolpygo, and J. E. Lukens, *Nature (London)* **406**, 43 (2000).

<sup>3</sup>I. Chiorescu, Y. Nakamura, C. J. P. M. Harmans, and J. E. Mooij, *Science* **299**, 1869 (2003).

<sup>4</sup>F. K. Wilhelm, M. J. Storcz, C. H. van der Wal, C. J. P. M. Harmans, and J. E. Mooij, *Adv. Solid State Phys.* **43**, 763 (2003).

<sup>5</sup>J. B. Majer, F. G. Paauw, A. C. J. ter Haar, C. J. P. M. Harmans, J. E. Mooij, *Phys. Rev. Lett.* **94**, 090501 (2005).

<sup>6</sup>Y. A. Pashkin, T. Yamamoto, O. Astafiev, Y. Nakamura, D. V.

FULL PROTECTION OF SUPERCONDUCTING QUBIT...

PHYSICAL REVIEW B **72**, 064511 (2005)

- Averin, and J. S. Tsai, *Nature (London)* **421**, 823 (2003).
- <sup>7</sup>T. Yamamoto, Yu. A. Pashkin, O. Astafiev, Y. Nakamura, and J. S. Tsai, *Nature (London)* **425**, 941 (2003).
- <sup>8</sup>X. Zhou, M. Wulf, Z. Zhou, G. Guo, and M. J. Feldman, *Phys. Rev. A* **69**, 030301(R) (2004); J. Q. You, X. Hu, and F. Nori, preprint arXiv: cond-mat/0407423 (2004).
- <sup>9</sup>J. Siewert, R. Fazio, G. M. Palma, and E. Sciacca, *J. Low Temp. Phys.* **118**, 795 (2000).
- <sup>10</sup>L. S. Levitov, T. P. Orlando, J. B. Majer, and J. E. Mooij, preprint arXiv: cond-mat/0108266 (2001).
- <sup>11</sup>D. V. Averin and C. Bruder, *Phys. Rev. Lett.* **91**, 057003 (2003).
- <sup>12</sup>A. Shnirman, Yu. Makhlin, and G. Schön, *Phys. Scr., T* **102**, 147 (2002).
- <sup>13</sup>F. K. Wilhelm and J. E. Mooij, unpublished.
- <sup>14</sup>M. J. Storcz and F. K. Wilhelm, *Phys. Rev. A* **67**, 042319 (2003).
- <sup>15</sup>D. J. Van Harlingen, T. L. Robertson, B. L. T. Plourde, P. A. Reichardt, T. A. Crane, and J. Clarke, *Phys. Rev. B* **70**, 064517 (2004).
- <sup>16</sup>J. Kempe, D. Bacon, D. A. Lidar, and K. B. Whaley, *Phys. Rev. A* **63**, 042307 (2001).
- <sup>17</sup>D. A. Lidar and K. B. Whaley, in *Irreversible Quantum Dynamics*, edited by F. Benatti and R. Floreanini (Springer Lecture Notes in Physics, Berlin, 2003), Vol; 622, p.83.
- <sup>18</sup>A. M. Steane, in *Introduction to Quantum Computation and Information*, edited by H. K. Lo, S. Popescu, and T. P. Spiller (World Scientific, Singapore, 1999), p.184.
- <sup>19</sup>J. F. Poyatos, J. I. Cirac, and P. Zoller, *Phys. Rev. Lett.* **78**, 390 (1997).
- <sup>20</sup>M. Thorwart, P. Hänggi, *Phys. Rev. A* **65**, 012309 (2002).
- <sup>21</sup>M. Mohseni, D. A. Lidar, *Phys. Rev. Lett.* **94**, 040507 (2005).





# Chapter 10

## Optimum control of superconducting solid-state qubits

### 10.1 Introduction

Here, a system of two capacitively coupled Josephson charge qubits [194, 232] with full control only over the gate voltages of the two Cooper pair boxes (the superconducting islands) is investigated. The experimental setup is depicted in Fig. 10.1. In a recent experiment the CNOT gate (a conditional gate operation) has been demonstrated with this setup [232],

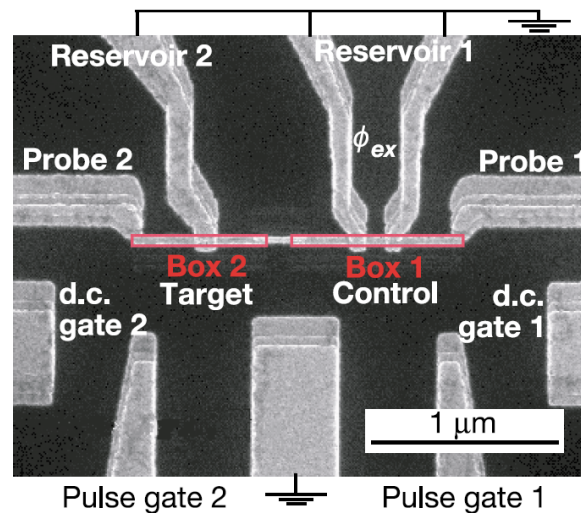


Figure 10.1: Picture of the experimental two charge qubit setup of the NEC group which was used for the demonstration of a conditional gate operation. The charge qubits are manipulated by dc pulses on the voltage gates. The first qubit is fabricated in SQUID geometry, *i.e.*, the tunnel amplitude can be changed on a timescale much longer than the experimentally realized gate operation. Picture taken from Ref. [232].

however, the fidelity of the gate operation, *i.e.*, the overlap of the experimental propagator and the ideal unitary propagator, was found to be below 50% [232]. The charge qubits in this experiment were manipulated by fast DC-pulses (rectangular pulses) of total durations 80 – 260 ps with rise-times of about 40 ps. In general, the approach of decomposing quantum gates into elementary operations is, for small system size, greatly outperformed by custom-built pulse sequences obtained from optimum control theory. However, clearly for larger systems the optimization problem can not be solved easily anymore. Thus, it would be still desirable to find small time or decoherence-optimal building blocks for extensive quantum gate operations on a larger quantum computer with many qubits. Clearly, not only in the context of a small system, pulse shaping techniques are an important tool for the manipulation of quantum systems and appropriate control might increase the gate fidelity drastically, as will be shown in the paper associated with this section.

## 10.2 Optimal control theory

In order to find a time-optimal pulse sequence for the manipulation of the qubit system, which leads to a time evolution of the system that is close to the desired ideal propagator, the time evolution is split in  $n$  small time steps

$$U = \exp(-it_n \hat{H}_{(n)}) \times \cdots \times \exp(-it_k \hat{H}_{(k)}) \times \cdots \times \exp(-it_1 \hat{H}_{(1)}). \quad (10.1)$$

Where the overall sequence should be time-optimal, *i.e.*,  $t = \sum_k t_k$  should be minimal and the Hamiltonians  $\hat{H}_{(k)}$  are piecewise constant [233]. It is most convenient to split the total Hamiltonian that is associated with the timestep  $t_k$  into a drift term (free evolution) and a control term (which can be manipulated, *e.g.*, by gate voltages)

$$\hat{H}_{(k)} = \hat{H}_d + \hat{H}_c = \hat{H}_d + \sum_j u_{(k)}^{(j)} \hat{H}_{(k)}^{(j)}, \quad (10.2)$$

where  $u_{(k)}^{(j)}$  is the value of the control, *e.g.*, the gate voltage, for the  $j$ -th qubit and the  $k$ -th timestep. When the gate fidelity is unity, *i.e.*, the obtained propagator equals the ideal desired propagator, it is found that

$$\|U - U_{\text{ideal}}\|_2 = \|U\|_2^2 + \|U_{\text{ideal}}\|_2^2 - 2\text{Re tr} \left( U_{\text{ideal}}^\dagger U \right) = 0, \quad (10.3)$$

and  $\text{Re tr} \left( U_{\text{ideal}}^\dagger U \right)$  has to be maximized for a fixed overall time  $t$ . This is done via optimal control theory, using the scalar-valued Hamiltonian function

$$h(U(t_k)) = \text{Re tr} \left( \lambda^\dagger(t_k) (-i(\hat{H}_d + \sum_j u_{(k)}^{(j)} \hat{H}_{(k)}^{(j)}) U(t_k)) \right), \quad (10.4)$$

derived from the equation of motion  $\dot{U}(t) = -i\hat{H}U(t)$  with the initial condition  $U(0) = \hat{1}$  with the Lagrange multiplier  $\lambda(t)$ , which satisfies  $\dot{\lambda}(t) = -i\hat{H}\lambda(t)$ . Then Pontryagin's

maximum principle [234] requires

$$\frac{\partial h(U(t_k))}{\partial u^{(j)}} = -\text{Im tr} \left( \lambda^\dagger(t_k) \hat{H}^{(k)} U(t_k) \right) = 0. \quad (10.5)$$

Then a gradient-flow based recursion method is employed [235, 236] to determine the amplitude of the  $j$ -th control for the  $k$ -th time-interval. Thus, it is found for the  $j$ -th control and the iteration step  $r + 1$

$$u_{r+1}^{(j)}(t_k) = u_r^{(j)}(t_k) + \epsilon \frac{\partial h(U(t_k))}{\partial u^{(j)}}, \quad (10.6)$$

with an appropriately chosen discretization stepsize  $\epsilon$ . Note that this procedure has to be repeated for a set of final times  $t_k$  that decrease to the minimal time  $t'$ , as long as the fidelity for the obtained propagator is large enough, *i.e.*, above a threshold that was set beforehand.

### 10.3 System Hamiltonian

First, the Hamiltonian of the two-qubit system in terms of Pauli spin-matrices will be derived. Starting from Eqn. (1) in [232] in the charge basis

$$\begin{aligned} \hat{H} = & \sum_{n_1, n_2=0,1} E_{n_1 n_2} |n_1, n_2\rangle \langle n_1, n_2| - \frac{E_{J1}}{2} \sum_{n_2=0,1} (|0\rangle \langle 1| + |1\rangle \langle 0|) \otimes |n_2\rangle \langle n_2| \\ & - \frac{E_{J2}}{2} \sum_{n_1=0,1} |n_1\rangle \langle n_1| \otimes (|0\rangle \langle 1| + |1\rangle \langle 0|), \end{aligned} \quad (10.7)$$

it is found that after expanding all terms of this expression gives

$$\begin{aligned} \hat{H} = & E_{00} |00\rangle \langle 00| + E_{01} |01\rangle \langle 01| + E_{10} |10\rangle \langle 10| + E_{11} |11\rangle \langle 11| \\ & - \frac{E_{J1}}{2} ((|0\rangle \langle 1| + |1\rangle \langle 0|) \otimes |0\rangle \langle 0| - \frac{E_{J1}}{2} ((|0\rangle \langle 1| + |1\rangle \langle 0|) \otimes |1\rangle \langle 1| \\ & - \frac{E_{J2}}{2} |0\rangle \langle 0| \otimes (|0\rangle \langle 1| + |1\rangle \langle 0|) - \frac{E_{J2}}{2} |1\rangle \langle 1| \otimes (|0\rangle \langle 1| + |1\rangle \langle 0|), \end{aligned} \quad (10.8)$$

where

$$E_{00} = E_{c1}(n_{g1} - 0)^2 + E_{c2}(n_{g2} - 0)^2 + E_m n_{g1} n_{g2}, \quad (10.9)$$

$$E_{01} = E_{c1}(n_{g1} - 0)^2 + E_{c2}(n_{g2} - 1)^2 + E_m n_{g1}(n_{g2} - 1), \quad (10.10)$$

$$E_{10} = E_{c1}(n_{g1} - 1)^2 + E_{c2}(n_{g2} - 0)^2 + E_m (n_{g1} - 1)n_{g2}, \quad (10.11)$$

$$E_{11} = E_{c1}(n_{g1} - 1)^2 + E_{c2}(n_{g2} - 1)^2 + E_m (n_{g1} - 1)(n_{g2} - 1). \quad (10.12)$$

Now a set of Pauli matrices in the computational basis  $|00\rangle, |01\rangle, |10\rangle, |11\rangle$  is introduced

$$\hat{\sigma}_z^{(1)} = \begin{pmatrix} -1 & 0 & 0 & 0 \\ 0 & -1 & 0 & 0 \\ 0 & 0 & 1 & 0 \\ 0 & 0 & 0 & 1 \end{pmatrix}, \quad \hat{\sigma}_z^{(2)} = \begin{pmatrix} -1 & 0 & 0 & 0 \\ 0 & 1 & 0 & 0 \\ 0 & 0 & -1 & 0 \\ 0 & 0 & 0 & 1 \end{pmatrix}, \quad \hat{\sigma}_z^{(1)} \hat{\sigma}_z^{(2)} = \begin{pmatrix} 1 & 0 & 0 & 0 \\ 0 & -1 & 0 & 0 \\ 0 & 0 & -1 & 0 \\ 0 & 0 & 0 & 1 \end{pmatrix}, \quad (10.13)$$

which are all diagonal in the computational basis. To rewrite the Hamiltonian (10.8) in terms of the Pauli-matrices we first treat the diagonal part of the Hamiltonian. It is useful to note that it is very simple to split up the diagonal part

$$\hat{H} = \begin{pmatrix} a & 0 & 0 & 0 \\ 0 & b & 0 & 0 \\ 0 & 0 & c & 0 \\ 0 & 0 & 0 & d \end{pmatrix} \quad (10.14)$$

into parts that are proportional to the Pauli matrices, because this space is spanned by  $\hat{\sigma}_z^{(1)}$ ,  $\hat{\sigma}_z^{(2)}$ ,  $\hat{\sigma}_z^{(1)} \otimes \hat{\sigma}_z^{(2)}$  and  $\hat{\mathbf{1}}$ . Therefore, the diagonal matrix Eqn. (10.14) can be split into

$$\hat{A}_1 = \hat{H} - \frac{1}{4}(a + b + c + d)\hat{\mathbf{1}} \quad (10.15)$$

$$\hat{A}_2 = \hat{A}_1 - \frac{1}{2}((A_1)_{11} + (A_1)_{22})\hat{\sigma}_z^{(1)} \quad (10.16)$$

$$\hat{A}_3 = \hat{A}_2 - \frac{1}{2}((A_2)_{22} + (A_1)_{44})\hat{\sigma}_z^{(2)} \quad (10.17)$$

$$\hat{A}_4 = \hat{A}_3 - \frac{1}{2}((A_3)_{22} + (A_3)_{33})\hat{\sigma}_z^{(1)}\hat{\sigma}_z^{(2)} = 0. \quad (10.18)$$

Thus, the diagonal part of the Hamiltonian reads

$$\begin{aligned} \hat{H}_{\text{diag}} &= - \left( \frac{1}{4}E_m(n_{g1} + 2n_{g2} - 1 - n_{g1}n_{g2} + n_{g1}(n_{g2} - 1)) + \frac{1}{2}E_{c1}(2n_{g1} - 1) \right) \hat{\sigma}_z^{(1)} \\ &+ \left( \frac{1}{4}E_m(n_{g1}(n_{g2} - 1) - n_{g1}n_{g2} - n_{g1} + 1) + \frac{1}{2}E_{c2}(1 - 2n_{g2}) \right) \hat{\sigma}_z^{(2)} \\ &- \left( \frac{1}{4}E_m(n_{g1}(n_{g2} - 1) - n_{g1}n_{g2} + n_{g1} - 1) \right) \hat{\sigma}_z^{(1)}\hat{\sigma}_z^{(2)}. \end{aligned} \quad (10.19)$$

This can be further simplified to become

$$\begin{aligned} \hat{H}_{\text{diag}} &= \frac{1}{4} \left( (E_m(1 - 2n_{g2}) + 2E_{c1}(1 - 2n_{g1}))\hat{\sigma}_z^{(1)} \right. \\ &\left. + (E_m(1 - 2n_{g1}) + 2E_{c2}(1 - 2n_{g2}))\hat{\sigma}_z^{(2)} + E_m\hat{\sigma}_z^{(1)}\hat{\sigma}_z^{(2)} \right). \end{aligned} \quad (10.20)$$

The off-diagonal part of the Hamiltonian is composed of the single-qubit spin-flip terms

$$\hat{H}_{\text{off}} = -\frac{E_{J1}}{2}\hat{\sigma}_x^{(1)} - \frac{E_{J2}}{2}\hat{\sigma}_x^{(2)}. \quad (10.21)$$

Therefore, the whole Hamiltonian expressed in terms of Pauli matrices is

$$\begin{aligned} \hat{H} &= \frac{1}{4}(E_m(1 - 2n_{g2}) + 2E_{c1}(1 - 2n_{g1}))\hat{\sigma}_z^{(1)} - \frac{E_{J1}}{2}\hat{\sigma}_x^{(1)} \\ &+ \frac{1}{4}(E_m(1 - 2n_{g1}) + 2E_{c2}(1 - 2n_{g2}))\hat{\sigma}_z^{(2)} - \frac{E_{J1}}{2}\hat{\sigma}_x^{(2)} + \frac{1}{4}E_m\hat{\sigma}_z^{(1)}\hat{\sigma}_z^{(2)}. \end{aligned} \quad (10.22)$$

From this expression it is clearly seen that due to the permanent coupling of the qubits, the controls  $n_{g,i}$  (the gate voltages  $V_{g,i}$ ) are mutually coupled. Next, after having derived the Hamiltonian of the two-qubit system, it is important to investigate the timescales and energy scales, which will determine the dynamics of the qubit evolution. From Ref. [232] the energies

$$\begin{aligned}
E_{c1} &= 580\mu\text{eV} = 140\text{GHz}, \\
E_{c2} &= 671\mu\text{eV} = 162\text{GHz}, \\
E_m &= 95\mu\text{eV} = 23\text{GHz}, \\
E_{J1} &= 45\mu\text{eV} = 11\text{GHz}, \\
E_{J2} &= 41\mu\text{eV} = 10\text{GHz},
\end{aligned} \tag{10.23}$$

are extracted. In Ref. [232], the controlled-NOT pulse takes 255 ps or 264 ps (depending on the input state – therefore, the CNOT operation is of course not unitary anymore) with a fall and rise-time of the pulses of about 40 ps.

## 10.4 Generalization to the three qubit Hamiltonian

Compared to the two charge qubit setup, the three charge qubit setup in an open chain geometry, *i.e.*, without connecting the third qubit to the first qubit (which would lead to a term proportional to  $\hat{\sigma}_z^{(1)} \otimes \hat{\sigma}_z^{(3)}$  in the three charge qubit Hamiltonian), the role of the middle qubit is special. This can be clearly observed in the Hamiltonian which shall be derived below. A typical three charge qubit setup is depicted in Fig. 10.4. There is a second important change on top of the different shape of the Hamiltonian. The charging energy of the second qubit will be significantly decreased due to the increase of the overall capacitance seen by the second qubit. This occurs *only* for the second (or middle) qubit due to the additional coupling capacitance seen by this qubit. In the case of a closed chain geometry this decrease of  $E_c$  would of course occur for all qubits.

The general expression (10.22) can easily be generalized for an open chain of N qubits and leads to nearest neighbour qubit-qubit interaction. The overall Hamiltonian is

$$\hat{H} = \sum_{i=1}^N B_i(t) \hat{\sigma}_z^{(i)} - \frac{E_{J_i}}{2} \hat{\sigma}_x^{(i)} + \sum_{i=1}^{N-1} J_{i,i+1} \hat{\sigma}_z^{(i)} \hat{\sigma}_z^{(i+1)}. \tag{10.24}$$

To derive the *pseudo* magnetic field strengths  $B_i$  (or in other words the qubit bias) and the qubit-qubit coupling strength  $J_{i,i+1}$  explicitly, we shall use the method from the last section and obtain for the diagonal elements of the Hamiltonian

$$\begin{aligned}
\hat{H}_{\text{diag}} &= -\frac{1}{4}(2E_{c1}(1 - 2n_{g1}) + E_{m1}(1 - 2n_{g2}))\hat{\sigma}_z^{(1)} \\
&\quad - \frac{1}{4}(2E_{c2}(1 - 2n_{g2}) + E_{m1}(1 - 2n_{g1}) + E_{m2}(1 - 2n_{g3}))\hat{\sigma}_z^{(2)}
\end{aligned}$$

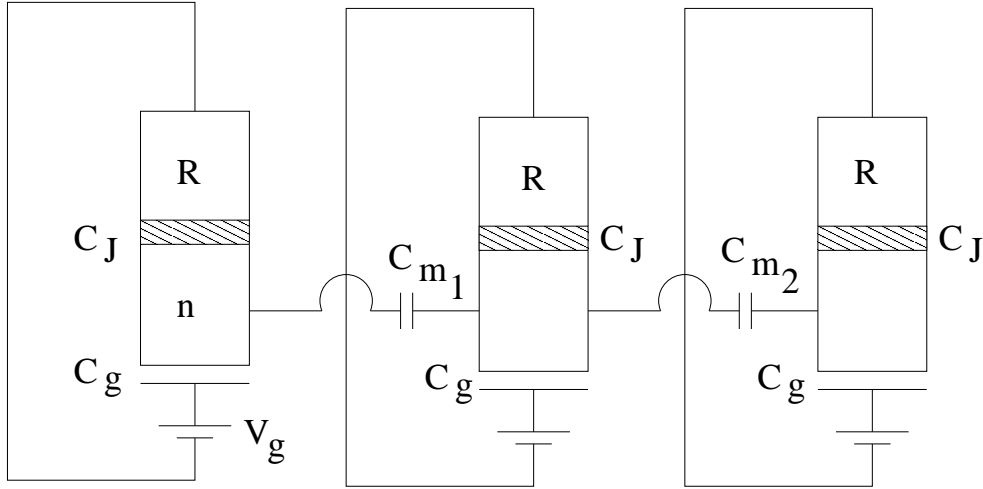


Figure 10.2: The three charge qubit setup in an open chain geometry. Each of the superconducting Cooper pair boxes is capacitively coupled to the neighbouring boxes. However, the last qubit in the chain is not connected to the first qubit in the chain. Due to this asymmetry, the charging energy of the middle qubit is decreased.

$$\begin{aligned}
& -\frac{1}{4}(2E_{c3}(1 - 2n_{g3}) + E_{m2}(1 - 2n_{g2}))\hat{\sigma}_z^{(3)} \\
& + \frac{1}{4}E_{m1}\hat{\sigma}_z^{(1)} \otimes \hat{\sigma}_z^{(2)} + \frac{1}{4}E_{m2}\hat{\sigma}_z^{(2)} \otimes \hat{\sigma}_z^{(3)}
\end{aligned} \tag{10.25}$$

From comparison of Eqns. (10.24) and (10.25) the elements  $B_i$  and  $J_{i,i+1}$  of the Hamiltonian are easily identified. Please note that the tunneling terms in the Hamiltonian remain unchanged. Thus, it was again sufficient to calculate only the diagonal elements because the qubit coupling is diagonal in the computational basis and thus only the well known single qubit tunneling terms survive as off-diagonal elements. Moreover, it is important to note that (due to the given geometry) additionally only the diagonal terms proportional to  $\hat{\sigma}_z^{(1)}$ ,  $\hat{\sigma}_z^{(2)}$ ,  $\hat{\sigma}_z^{(3)}$ ,  $\hat{\sigma}_z^{(1)} \otimes \hat{\sigma}_z^{(2)}$ , and  $\hat{\sigma}_z^{(2)} \otimes \hat{\sigma}_z^{(3)}$  can occur in the Hamiltonian.

Note again that one could probably also find a closed chain geometry for a three charge qubit design that would not only lead to the nearest neighbour interaction terms given above, *i.e.*, for the closed chain setup all coupling terms  $\hat{\sigma}_z^{(1)} \otimes \hat{\sigma}_z^{(2)}$ ,  $\hat{\sigma}_z^{(2)} \otimes \hat{\sigma}_z^{(3)}$ , and  $\hat{\sigma}_z^{(1)} \otimes \hat{\sigma}_z^{(3)}$  would appear in the Hamiltonian and the decrease of the qubit charging energies would occur isotropic. The coupling topology also predetermines the overall time needed to perform quantum gate operations [233]. In particular, the information flow in a system of qubits where each qubit is coupled to every other qubit is optimal in terms of the execution time of any quantum algorithm.

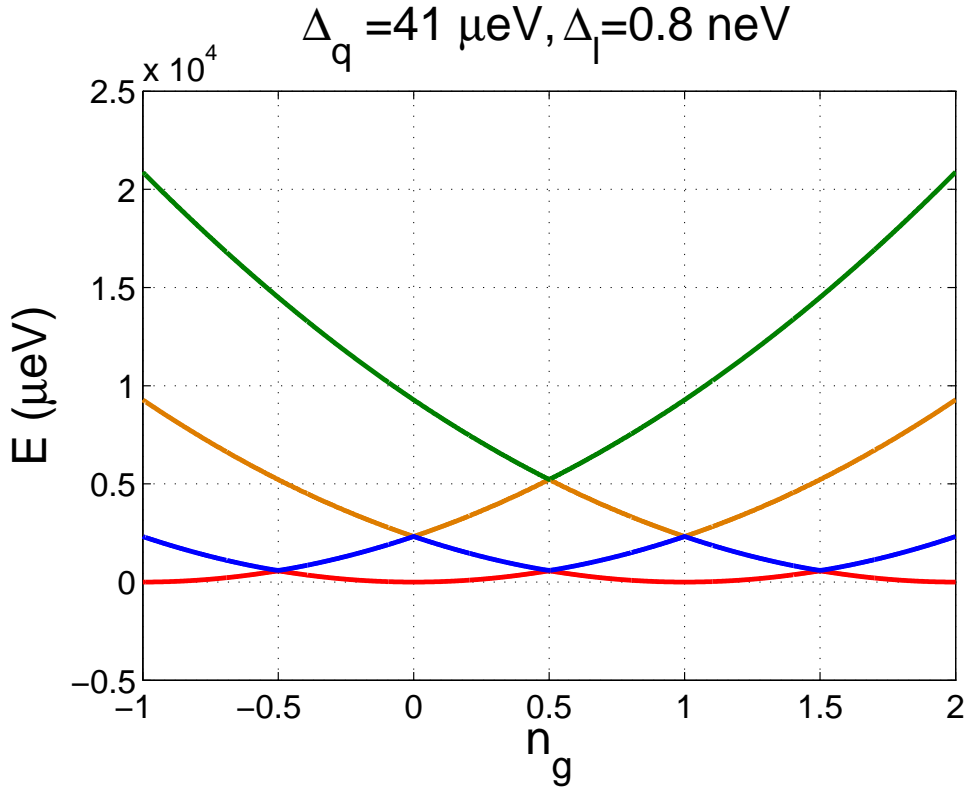


Figure 10.3: Plot of the eigenenergies of the single charge qubit Hamiltonian including two leakage levels for a gate charge  $n_g \in [-1, 2]$ . Here,  $\Delta_q$  denotes the qubit energy splitting at degeneracy,  $\Delta_l$  is the splitting of the leakage levels at the qubit degeneracy.

## 10.5 Energy levels and leakage

Fig. 10.3 depicts the energy levels over a broad range of gate voltages  $V_g = 2en_g/C_g$ . From Figs. 10.3 and 10.4 it is found that anticrossings between one of the leakage levels and one of the qubit levels are present at  $n_g = 0$  and  $n_g = 1.5$ ; close to the qubit degeneracy point, the splitting between the qubit levels and the leakage levels is more than  $10^3 \mu\text{eV}$ . Thus, simple spectroscopic arguments indicate that the leakage levels are only of minor significance during the manipulation of the two-qubit system with pulsed controls because the magnitude of the gate voltages is such that  $n_g$  is varied between approximately  $n_g = 0$  and  $n_g = 0.6$ .

In this section, leakage into higher charge states is considered, for a detailed description of the leakage problem for superconducting charge qubits see also Refs. [237–239]. For each qubit the basis states expressed in terms of the number of Cooper pairs on the island are  $|n\rangle = |-1\rangle, |0\rangle, |1\rangle, |2\rangle$ . In the first instance and for the sake of simplicity only a single charge qubit is considered. However, all simulations of the time-evolution

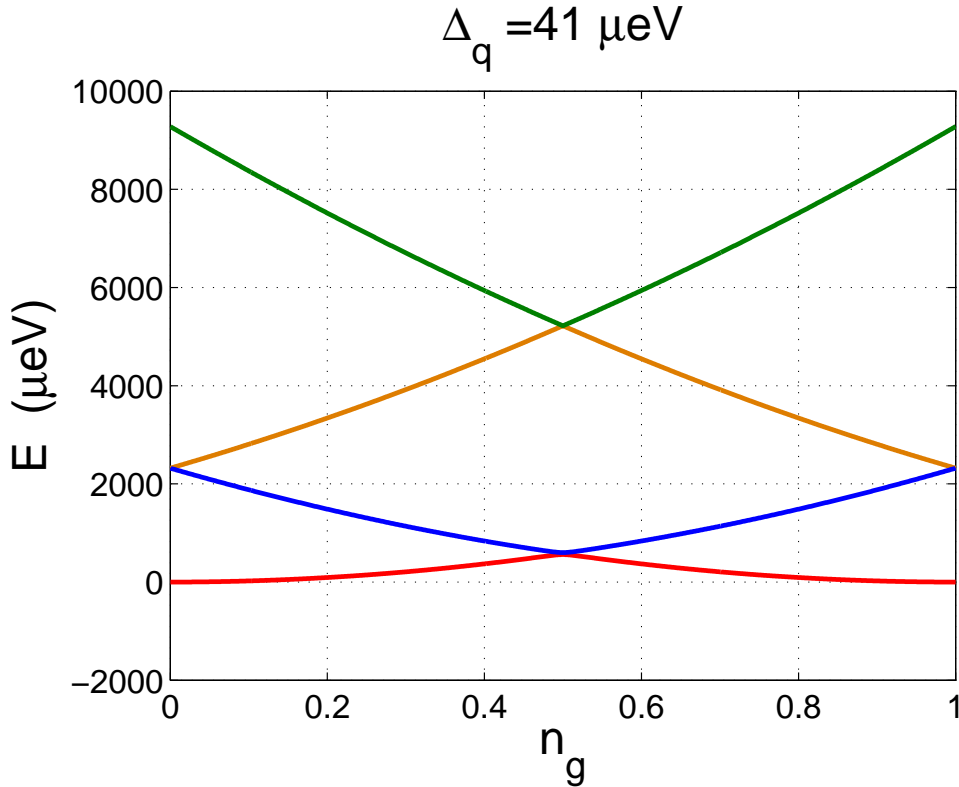


Figure 10.4: Plot of the eigenenergies of the single charge qubit Hamiltonian including the leakage levels. Here,  $\Delta_q$  denotes the qubit splitting at degeneracy. Clearly, the leakage levels are separated from the qubit levels by a large energy gap around  $n_g = 0.25 \sim 0.5$ .

of the qubits under the optimized controls that are presented in the following sections are calculated using the full Hamiltonian of two superconducting charge qubits with two additional leakage levels each.

From the diagonalization of the full leakage Hamiltonian for a single qubit the corresponding energy levels are found. These are shown in Figs. 10.3 and 10.4, whereas Fig. 10.5 depicts the anticrossing of the qubit levels (the working transition) and the anticrossing of the leakage levels at the degeneracy point, where the gate charge is  $n_g = 1/2$ . Here, the characteristic parameters of the single qubit are taken from the experiments [232],  $E_c = 580 \mu\text{eV}$  and  $E_J = 41 \mu\text{eV}$ . Note that  $E_J$  directly determines the energy splitting of the qubit at the degeneracy point.



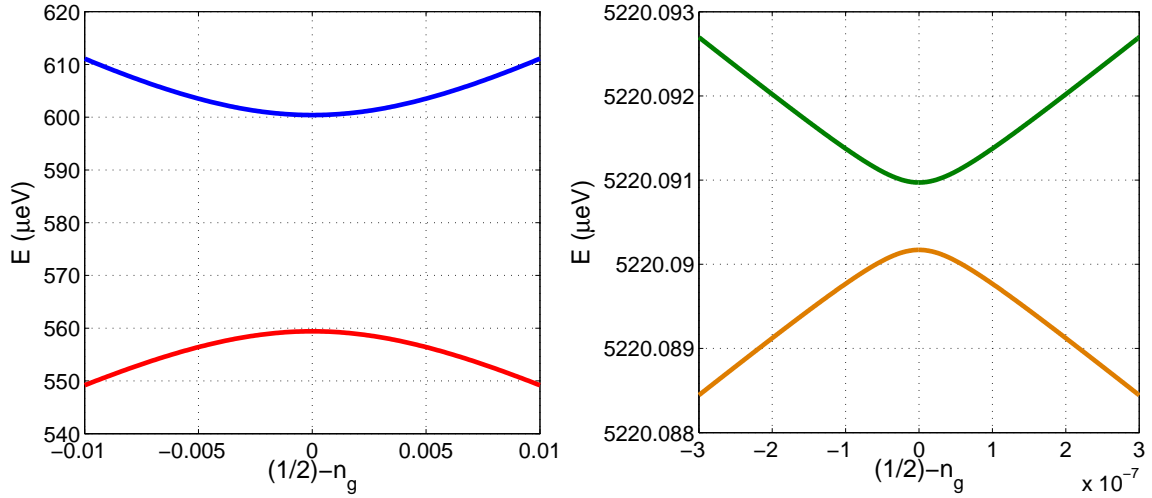


Figure 10.5: Plot of the eigenenergies of the qubit Hamiltonian around degeneracy. Both plots resolve the anticrossings of the qubit levels and the leakage levels at the degeneracy point. The left plot shows the qubit splitting, the right plot shows the splitting of the next anticrossing (leakage levels) at degeneracy.

## 10.6 Generation of entanglement

The concurrence of a bipartite quantum state is defined as  $C = \langle \psi^* | \hat{\sigma}_y^{(1)} \otimes \hat{\sigma}_y^{(2)} | \psi \rangle$ , where the concurrence  $C \in [0, 1]$ . Here,  $C = 1$  characterizes a non-separable entangled state and  $C = 0$  is a separable state that can be written as a product state. Interestingly, the concurrence for the input state  $|\psi_i\rangle = \frac{1}{\sqrt{2}}(|0\rangle + |1\rangle) \otimes |1\rangle$  is  $C_{\text{NEC}} = 0.688$  in the case of the pioneering experiments performed at NEC [232] and for the optimized pulse sequence it is found that  $C_{\text{optimized}} = 0.998$ . Thus, a huge increase in the value of the concurrence is readily observed for the optimized pulse sequence. From this one would be tempted to conclude that the degree of entanglement that is generated by the CNOT gate in the pioneering experiments is quite small. However, this is not true. The so-called Horodecki criterion  $M(\rho) > 1$ , where  $M$  measures the non-locality of a state encoded in its density matrix  $\rho$  [240], is fulfilled for both realizations. Thus, also for the imperfect and not pulse optimized experimental realization of the CNOT gate, the CNOT gate clearly generates entanglement and the outcome for several examples of factorized input states (see below) violates at least one of Bell's inequalities. When the stability of the entanglement creation characterized by the averaged concurrence is concerned, though, it becomes clear that the optimized pulse sequence is uniformly stable. Namely, the average concurrence for input states that lead to completely entangled states when the CNOT gate is performed, for example when averaged over the states  $\frac{1}{\sqrt{2}}(|0\rangle + |1\rangle) \otimes |0\rangle$  and  $\frac{1}{\sqrt{2}}(|0\rangle + |1\rangle) \otimes |1\rangle$ , gives  $C_{\text{NEC}} = 0.794$  and still  $C_{\text{optimized}} = 0.998$ . In summary, non separable entangled states are

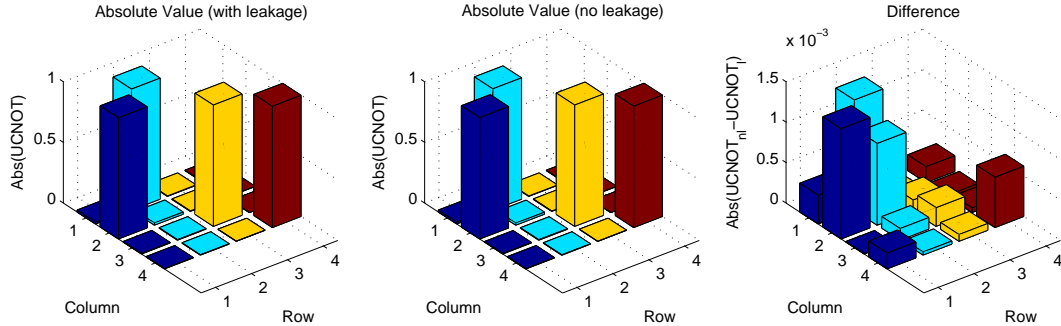


Figure 10.6: Weighted (with the phase angle) absolute values of the propagator matrix elements for the simulated CNOT operation performed with Gaussian pulses. The trajectory of the Gaussian pulses was fitted to the pulse sequence obtained from optimal control theory. The right plot depicts the difference between the operations with and without taking leakage into account. The excellent fidelity is clearly visible.

created even for the CNOT gate performed by the NEC group. Weyl chamber trajectories (see chapter 9 for an introduction to the Cartan decomposition and the Weyl chamber) for the pioneering CNOT gate that was performed by the group at NEC [232] and the optimized CNOT gate are both presented in the supplementary material given with the following paper.

## 10.7 Time evolution of the optimized CNOT gate

For the experimental implementation of the optimized pulse sequence it is useful to fit the theoretically determined trajectory for the gate voltage controls on the two qubits, *e.g.*, with superpositions of several experimentally realizable Gaussian or harmonic pulses. The fitted pulse sequence of harmonic pulses is discussed in detail in the following paper, however, the results for decomposition of the overall pulse sequence into Gaussian pulses will be discussed here.

First, the fidelity of the optimized pulses is evaluated. The trace fidelity is defined as

$$F = \frac{1}{N} |\text{tr}(U_{\text{cnot}}^\dagger U)|, \quad (10.26)$$

where  $U_{\text{cnot}}$  is the propagator of the ideal CNOT gate and  $U$  is the propagator for the simulated CNOT gate including the leakage levels.

The numerical calculation of the time propagation gives the results presented in table 10.1 for a set of Gaussian or harmonic pulses that were fitted to the optimized trajectory for the qubit controls; this trajectory was evaluated via optimal control theory. The results were obtained for a simulation with a pulse duration of  $t = 55$  ps and 250 or 50 discretization steps (Gaussian pulses or harmonic pulses). For the CNOT gate realized with Gaussian

Pulse	F (no leakage)	F (leakage)
Gaussian	0.999834	0.997976
Harmonic	0.989471	0.984742

Table 10.1: Comparison of the trace fidelity for different shapes of the control pulses that are applied to the two superconducting charge qubits.

pulses the resulting propagator with and without leakage and the difference between the two cases in terms of the matrix elements of the propagator is shown in Fig. 10.6. Again, for all simulations the characteristic parameters of the Hamiltonian are taken from the pioneering paper by the NEC group, see Ref. [232]; namely,  $E_{c1} = 580\mu\text{eV}$ ,  $E_{c2} = 671\mu\text{eV}$ ,  $E_m = 95\mu\text{eV}$ ,  $E_{J1} = 45\mu\text{eV}$  and  $E_{J2} = 41\mu\text{eV}$ .

## 10.8 The single-qubit Hadamard gate

The optimized pulses obtained from optimal control theory provide a possibility of effectively manipulating only a single qubit in a two-qubit system while leaving the other qubit unaffected. This is demonstrated here with the example of a Hadamard gate that is performed on one of the permanently coupled qubits only. The ideal propagator for this gate reads  $U = \hat{H}^{(1)} \otimes \hat{1}^{(2)}$ .

It is found that both qubits need to be manipulated (pulsed) in order to achieve an effective idle operation on one of the qubits and the Hadamard operation on the other qubit. The time-optimal trajectories for the manipulation pulses are illustrated in Fig. 10.7. Here,

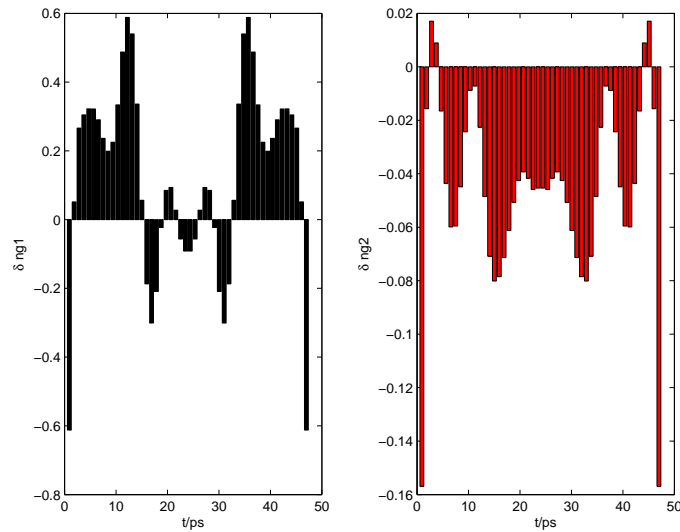


Figure 10.7: Time optimal single-qubit Hadamard gate for a system of two constantly coupled Josephson charge qubits. The qubit parameters for the simulations are those of Ref. [232]. Plot courtesy of A. Spörl, TU München.

the Hamiltonian again is splitted into a drift and control part  $H = H_d + H_c$  and the qubit energies are taken from the experimental work presented in Ref. [232], namely  $E_{J_1} = 41\mu$  eV,  $E_{J_2} = 45\mu$  eV, and  $E_{12} = 95\mu$ eV. From the figure, it is recognized that the pulse amplitudes can become relatively large ( $\delta n_{g1} \approx -0.6 \dots 0.6$ ) for the qubit on which the Hadamard gate is performed, however, this pulse sequence is not yet optimized for small amplitudes in the same way it was done for the CNOT gate. The trace fidelity Eqn. (10.26) is  $F = 0.9999678$  for this pulse sequence and it is again remarkably good. However, note that here no leakage to other than the qubit levels was taken into account in the simulations. The duration of the pulses is  $t_{\text{Hadamard}} = 47$  ps. Thus, the optimized pulses can also help to effectively decouple a perpetually coupled system of two (or more) qubits.

In the following paper the optimization of the control of superconducting charge qubits for a two-qubit CNOT and three-qubit TOFFOLI gate will be discussed.



## Optimal Control of Coupled Josephson Qubits

A. Spörl,<sup>1</sup> T. Schulte-Herbrüggen,<sup>1,\*</sup> S.J. Glaser,<sup>1</sup> V. Bergholm,<sup>2</sup> M.J. Storz,<sup>3</sup> J. Ferber,<sup>3</sup> and F.K. Wilhelm<sup>3,†</sup><sup>1</sup>Department of Chemistry, Technische Universität München, Lichtenbergstrasse 4, 85747 Garching, Germany.<sup>2</sup>Materials Physics Laboratory, POB 2200 (Technical Physics) FIN-02015 HUT, Helsinki University of Technology, Finland.<sup>3</sup>Physics Department, ASC, and CeNS, Ludwig-Maximilians-Universität, Theresienstr. 37, 80333 Munich, Germany.

(Dated: September 26, 2005)

*This paper is dedicated to the memory of Martti Salomaa.*

In two and three coupled Josephson charge qubits we exemplify how to take pulse controls for realising quantum gates from fidelity-limited pioneering stages to the decoherence limit of near timeoptimal high-fidelity controls. Thus a CNOT gate can be obtained with a trace fidelity  $> 1 - 10^{-9}$  for the two qubits. Even when including higher charge states, the leakage is below 1%, although the pulses are non adiabatic. The controls are five times faster than the pioneering experiment (*Nature* **425**, 941 (2003)) for otherwise identical parameters—*i.e.* a progress towards the error-correction threshold by a factor of 100. We outline schemes to generate these shaped pulses by few LCR-circuits. The approach generalises to larger systems, as shown by realising a TOFFOLI gate in three linearly coupled charge qubits 13 times faster than a circuit of nine CNOTs of above experimental work. In view of the next generation of fast pulse-shape generators, the combination of methods is designed to find wide application in quantum control of pseudospin and macroscopic quantum systems such as charges in super- and semiconductors, excitons, and Bose-Einstein condensates.

PACS numbers: 85.25.Cp, 85.35.Gv, 82.56.Jn, 03.67.Lx

Regarding Hamiltonian simulation and quantum computation recent years have seen an increasing array of quantum systems that can be coherently controlled. Next to natural microscopic quantum systems, a particular attractive candidate for *scalable* setups are superconducting devices based on Josephson junctions [1–3]. Due to the ubiquitous bath degrees of freedom in the solid-state environment, the quantum coherence time remains limited, even in light of recent progress [4, 5] approaching theoretical bounds. Thus it is a challenge to generate the gates fast and accurately enough to meet the error correction threshold. This poses fundamental questions, such as (i) to which extent are gate accuracies and speeds limited by the presence of nearby higher levels? (ii) does a constant and relatively strong interaction promote or hinder the gate performance and which parameter is limiting the gate time? and (iii) given the challenge in building control electronics: which properties do pulses for quantum gates in these pseudospin systems have to have?

Recently, progress has been made in applying optimal control techniques to steer quantum systems [6] in a robust, relaxation-minimising [7] or timeoptimal way [8, 9]. Spin systems are a particularly powerful paradigm of quantum systems [10]:  $N$  spins- $\frac{1}{2}$  are fully controllable, if (i) all spins can be addressed selectively by *rf*-pulses and (ii) if the spins form an arbitrary connected graph of weak (Ising-type) coupling interactions. The optimal control techniques of spin systems can be extended to pseudospin systems, such as charge or flux states in superconducting setups, provided their Hamiltonian dynamics can be expressed to sufficient accuracy within a closed Lie algebra, *e.g.*,  $\mathfrak{su}(2^N)$  in a system of  $N$  qubits.

As a practically relevant and illustrative example, we

consider two capacitively coupled charge qubits controlled by DC pulses as in Ref. [1]. The infinite-dimensional Hilbert space of charge states in the device can be mapped to its low-energy part defined by zero or one excess charge on the respective islands [2]. Identifying these charges as pseudospins, the Hamiltonian can be written as  $H_{\text{tot}} = H_{\text{drift}} + H_{\text{control}}$ , where the drift or static part reads (for constants see caption to Fig. 1)

$$H_{\text{drift}} = - \left( \frac{E_m}{4} + \frac{E_{c1}}{2} \right) (\sigma_z^{(1)} \otimes \mathbf{1}) - \frac{E_{J1}}{2} (\sigma_x^{(1)} \otimes \mathbf{1}) \\ - \left( \frac{E_m}{4} + \frac{E_{c2}}{2} \right) (\mathbf{1} \otimes \sigma_z^{(2)}) - \frac{E_{J2}}{2} (\mathbf{1} \otimes \sigma_x^{(2)}) \\ + \frac{E_m}{4} (\sigma_z^{(1)} \otimes \sigma_z^{(2)}) \quad , \quad (1)$$

while the controls can be cast into

$$H_{\text{control}} = \left( \frac{E_m}{2} n_{g2} + E_{c1} n_{g1} \right) (\sigma_z^{(1)} \otimes \mathbf{1}) \\ + \left( \frac{E_m}{2} n_{g1} + E_{c2} n_{g2} \right) (\mathbf{1} \otimes \sigma_z^{(2)}) \quad . \quad (2)$$

Note that the Pauli matrices involved constitute a minimal generating set of the Lie algebra  $\mathfrak{su}(4)$ ; hence the system is fully controllable. The control amplitudes  $n_{g\nu}$ ,  $\nu = 1, 2$  are gate charges controlled by external voltages via  $n_{g\nu} = V_{g\nu} C_{g\nu} / 2e$ . They are taken to be piecewise constant in each time interval  $t_k$ . This pseudospin Hamiltonian motivated by Ref. [1] also applies to other systems such as double quantum dots [11] and Josephson flux qubits [12], although in the latter case the controls are typically *rf*-pulses.

In a time interval  $t_k$  the system thus evolves under  $H_{\text{tot}}^{(k)} = H_{\text{drift}} + H_{\text{control}}^{(k)}$ . The task is to find a sequence of

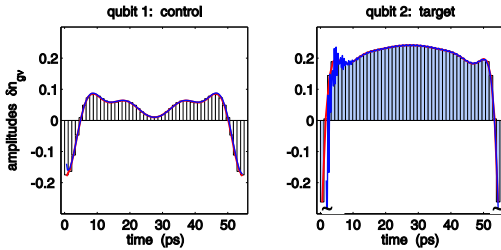


FIG. 1: (Colour online) Fastest gate charge controls obtained for realising a CNOT-gate on two coupled charge qubits (left part: control qubit, right part: working qubit). The total gate charges for the qubits are  $n_{g\nu} = n_{g\nu}^0 + \delta n_{g\nu}$  with  $\nu = 1, 2$ . Here,  $n_{g1}^0 = 0.24$ ,  $n_{g2}^0 = 0.26$  and the qubit energies  $E_{c1}/h = 140.2$  GHz,  $E_{c2}/h = 162.2$  GHz,  $E_{J1}/h = 10.9$  GHz,  $E_{J2}/h = 9.9$  GHz, and  $E_m/h = 23.0$  GHz were taken from the experimental values in [1]. The 50 piecewise constant controls are shown as bars (uniform width  $\Delta = t_k = 1.1$  ps); the trace fidelity is  $\frac{1}{2^N} |\text{tr}\{U_{\text{target}}^\dagger U_T\}| > 1 - 10^{-9}$ . Red lines give the analytic curves in Eqn. 3; the blue ones superimposed show a pulse synthesised by an LCR-filter (see below and Fig. 3).

control amplitudes for the intervals  $t_1, t_2, \dots, t_k, \dots, t_M$  such as to maximise a quality function, here the overlap with the desired quantum gate or element of an algorithm  $U_{\text{target}}$ . Moreover, for the decomposition of  $U_T = e^{-it_M H^M} e^{-it_{M-1} H^{M-1}} \dots e^{-it_k H^k} \dots e^{-it_1 H^1}$  into available controls  $\{H_\nu^{(k)}\}$  to be timeoptimal,  $T := \sum_{k=1}^M t_k$  has to be minimal. The gate fidelity is unity, if  $\|U_T - U_{\text{target}}\|_2^2 = 0 = \|U_T\|_2^2 + \|U_{\text{target}}\|_2^2 - 2\text{Re tr}\{U_{\text{target}}^\dagger U_T\}$ . Maximising  $\text{Re tr}\{U_{\text{target}}^\dagger U_T\}$  can be solved by optimal control: set  $h(U(t_k)) := \text{Re tr}\{\lambda^\dagger(t_k)(-i(H_d + \sum u_\nu H_\nu))U(t_k)\}$  with the Lagrange-type adjoint system  $\lambda(t)$  following the equation of motion  $\dot{\lambda}(t) = -i(H_d + \sum u_\nu H_\nu)\lambda(t)$ . Pontryagin's maximum principle requires  $\partial h/\partial u_\nu \equiv \text{Re tr}\{\lambda^\dagger(-iH_\nu)U\} = 0$  thus allowing to implement a gradient-flow based recursion. For the amplitude of the  $\nu^{\text{th}}$  control in iteration  $r+1$  at time interval  $t_k$  one finds with  $\varepsilon$  as a suitably chosen step size  $n_{g\nu}^{(r+1)}(t_k) = n_{g\nu}^{(r)}(t_k) + \varepsilon \frac{\partial h^{(r)}(t_k)}{\partial n_{g\nu}^{(r)}(t_k)}$  as explained in more detail in Refs. [13, 14].  $T$  is the shortest fixed final time allowing for a given fidelity to be obtained numerically.

Throughout the work, we take the parameters from the experiment [1]. Fig. 1 shows the fastest decompositions obtained by numerical optimal control for the CNOT gate into evolutions under available controls (Eqns. 1 and 2). In contrast to the 255 ps in Ref. [1],  $T = 55$  ps suffice to get  $\|U_T - U_{\text{target}}\|_2 = 5.3464 \times 10^{-5}$  corresponding to a trace fidelity of  $\frac{1}{2^N} |\text{tr}\{U_{\text{target}}^\dagger U_T\}| > 1 - 10^{-9}$ .

The supplementary material illustrates how the sequence of controls (Fig. 1) acts on specific input states by representing the quantum evolution on local Bloch

spheres complemented by showing the coupling evolution in the Weyl chamber. These pictures trigger physical insight: for a CNOT, the duration  $T = 55$  ps has to accommodate at least a  $\frac{\pi}{2}$  rotation under the coupling Hamiltonian ( $\frac{1}{2}\sigma_z \otimes \sigma_z$ ) lasting 21.7 ps concomitant to two  $\frac{\pi}{2}$   $x$ -rotations under the drift component ( $\frac{1}{2}\sigma_x^{(2)}$ ) each requiring 25.3 ps. This is in contrast to NMR, where the coupling interactions are some 100 times slower than the local ones, so timeoptimal controls can be envisaged as Riemannian geodesics in the symmetric space  $G/K = SU(4)/SU(2)^{\otimes 2}$  [8]. However, in our charge qubit system, the time scales of local and non-local interactions are comparable, and the local drifts in  $K$  generated by  $\sigma_x$  are even time-limiting, while phase shifts generated by  $\sigma_z$  via the gate charge are fast (*cf.* Eqns. 1-2). Assuming in a limiting simplification that *two*  $\frac{\pi}{2}$   $x$ -pulses are required, the total length cannot be shorter than 50.6 ps. A sigmoidal phase distortion from a geodesic state inversion is cheap timewise. While the duration of  $T = 55$  ps of our controls is close to the simplifying infimum of 50.6 ps, the controls in Ref. [1] last 255 ps; they entail several closed great circles on the Bloch sphere and are far from geodesic (details in the supplement).

Note that the time course of controls in charge qubits turns out palindromic (Fig. 1). Self-inverse gates ( $U_{\text{gate}}^2 = \mathbf{1}$ ) relate to the more general time-and-phase-reversal symmetry (TPR) observed in the control of spin systems [15]: for example, any sequence  $e^{-it_x \sigma_x} e^{-it_y \sigma_y} e^{-it_z \sigma_z}$  is inverted by transposition concomitant to time reversal  $t_\nu \mapsto -t_\nu$  and  $\sigma_y \mapsto -\sigma_y$ . Since the Hamiltonians in Eqns. 1-2 are real and symmetric, they will give the same propagator, no matter whether read forward or backward.

The pulses are not very complicated, as the time course of the controls on either qubit ( $\nu = 1, 2$ ) can be written with high accuracy as a sum of 6(7) harmonic functions (coefficients in Tab. 1 of the supplement)

$$n_{g\nu}(t) = \sum_{j=0}^{5(6)} a_\nu(j) \cos\left(2\pi\omega_\nu(j)\frac{t}{T} + \phi_\nu(j)\right). \quad (3)$$

The limited bandwidth allows to maintain high fidelity even if leakage levels formed from higher charge states of the qubit system are taken into account: we now explicitly apply the pulses to the extended system obtained by mapping the full Hamiltonian [1] to the subspaces of  $-1, \dots, 2$  extra charges per island. The two-qubit CNOT gate is thus embedded into the group  $SU(16)$ , still the full propagator generated by the above controls projects onto the CNOT gate giving a trace fidelity  $> 0.99$ . Even the time courses starting with any of the four canonical two-qubit basis vectors hardly ever leave the state space of the working qubits: at no time do the projections onto the leakage space exceed 0.6%. Clearly, optimisation including explicit leakage levels could improve the quality even further in systems where necessary [16].

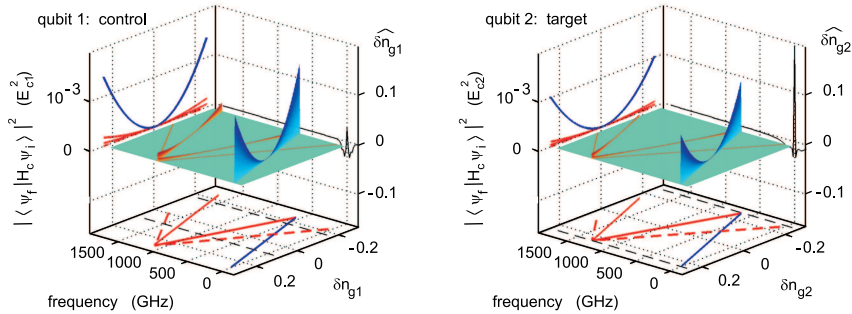


FIG. 2: (Colour online) Spectroscopic explanation of the high quality of the control sequences of Fig. 1: the spectral overlap of the Fourier-transforms (right walls) of the controls of Fig. 1 with the energy differences corresponding to the one-charge transitions into leakage levels (solid lines on the surface) is small at gate charges in the working range (within black dashed lines). In the 3D representation, intensities at allowed (solid lines) *vs* forbidden transitions (broken lines) into leakage levels are given in terms of transition-matrix elements (normalised by charging energies  $E_{c1}^2$ ,  $E_{c2}^2$ ) with an extended control Hamiltonian as in Eqn. 2 expressed by  $H_c(\delta n_{g\nu})$  in  $|\langle \Psi_f | H_c | \Psi_i \rangle|^2$ : the working transitions (blue) are far more probable than the allowed ones into leakage levels (red) that have no overlap with the excitation bandwidth of the pulses; forbidden ones are very weak.

In simplified terms, the high quality can be understood by relating the limited bandwidth to the transitions between the eigenstates of the local parts of  $H_{\text{drift}}$  in Eqn. 1: while *one-charge* transitions to leakage levels like  $|-1\rangle \leftrightarrow |0\rangle$  and  $|2\rangle \leftrightarrow |1\rangle$  are allowed, *two-charge* transitions like  $|-1\rangle \leftrightarrow |1\rangle$  and  $|2\rangle \leftrightarrow |0\rangle$  are forbidden in terms of the transition-matrix elements  $|\langle \Psi_{\text{final}} | H_{\text{control}} | \Psi_{\text{initial}} \rangle|^2$  as can be seen in Fig. 2. Note the charge control on gate 2 in Fig. 1 is around  $\delta n_{g2} = 0.2$  thus driving the working transition  $|0\rangle \leftrightarrow |1\rangle$ , while the ‘spectral overlap’ of the Fourier-transform of the time course in both controls with energy differences corresponding to one-charge leakage transitions in Fig. 2 is small. Hence simple spectroscopic arguments underpin the high fidelity.

The actual pulse shape generation is a challenging but possible task. Note that the minimal length of the pulse is given by the coupling strength. In the pertinent time scale, however, there are no commercially available devices for generating arbitrary wave forms. Yet, high-end pulse generators [17, 18] or ultrafast classical Josephson electronics [19] are close to the necessary specifications.

As a proof of principle, it is important to note how to generate these pulses experimentally, which can readily be exemplified using the well-established technique of shaping in Laplace space: we start with an input current pulse  $I_{\text{in}}(t)$  *shorter* than the desired one of a shape which is arbitrary as long as it contains enough spectral weight at the harmonics necessary for the desired pulse. Such pulses are easily generated optically or electrically [18]. This pulse is sent through an appropriately designed discrete electrical four-pole with transfer function  $Z_{12}$ . We have carried out this idea for a rectangular pulse of length  $\tau_r = 1.1\text{ps}$  as an input and our two gate pulses as outputs. We have developed a transfer function in Laplace

space  $Z_{12}(s)$  by fitting  $V_g(s) = Z_{12}(s)I_{\text{in}}(s)$ , see Fig. 3. Owing to causality, the poles of  $Z_{12}$  are either on the negative real axis or in conjugate pairs of poles on the left half plane. Each conjugate pair corresponds to an LCR-filter stage, whereas each real pole corresponds to an RC lowpass-filter [20]. With 8 LCR filters and two low-pass filters the pulses are very close to the desired ones, see Fig. 1, and a trace fidelity of 94 % can be achieved for the entire CNOT. Clearly, the quality could be further improved with more refined technology. This approach can also accommodate the generally frequency-dependent transfer function from the generator to the sample as shown in the Supplementary Material.

Note that our controls are fairly robust with regard to  $\pm 5\%$  variation of the tunneling frequencies  $E_{J_{1,2}}$  and the coupling term  $E_m$  as well as to Gaussian noise on the

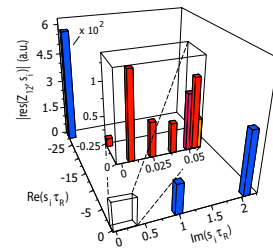


FIG. 3: (Colour online) Filter characteristic for shaping the pulse on the working gate. The bars show the poles  $s_i$  of the transfer function in the Laplace plane. Poles outside the negative imaginary axis also lead to the complex conjugate pole and can be implemented by an LCR-Filter. The height of the bar gives the modulus of the residue in this pole.



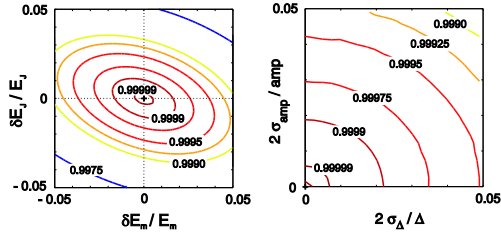


FIG. 4: (Colour online) Left: Trace fidelities resulting from the controls of Fig. 1 when the parameters  $E_m$  and  $E_J$  in Eqns. 1-2 vary by  $\pm 5\%$ . In this range, the quality profile can be fitted by a tilted 2D Gaussian (parameters in Supplement). Right: Fidelities under Gaussian noise on control amplitudes and time intervals parameterised by the standard deviations  $2\sigma_\Delta/\Delta$  and  $2\sigma_{\text{amp}}/\text{amp}$  ranging from 0 to 5%. (As in Fig. 1,  $\Delta := t_k$ ;  $\text{amp} := \delta n_{q\nu}$  with  $\nu = 1, 2$ .) Each data point is an average of 25'000 Monte-Carlo simulations.

control amplitudes and time-intervals as shown in Fig. 4.

Likewise, in a system of three linearly coupled charge qubits, we realised the TOFFOLI gate by experimentally available controls (Fig. 5), where the speed-up against a circuit of 9 CNOTs is by a factor of 2.8 with our CNOTs and by 13 with the CNOTs of Ref. [1]. Due to the comparatively strong qubit-qubit interactions in multiqubit setups, a direct generation of three-qubit gates is much faster than its composition by elementary universal gates. This also holds when developing simple algorithms [21] on superconducting qubit setups: a minimisation algorithm for searching control amplitudes in coupled Cooper pair boxes was applied in [22], where the optimisation was restricted to only very few values. In Ref. [23], an  $rf$ -pulse sequence for a CNOT with fixed couplings was introduced, which, however, is much longer and uses more of the available decoherence time.

In conclusion, we have shown how to take pulse controls for realising quantum gates in pseudospin systems from fidelity-limited pioneering stages to the decoherence limit of near timeoptimal high-fidelity controls. In superconducting charge qubits, the progress towards the error-correction threshold is by a factor of 100 (details in the Supplement). Limiting the optimal-control based shapes to low bandwidth allows for non-adiabatic pulses with remarkably low leakage to higher states thus justifying the pseudospin- $\frac{1}{2}$  truncation to the low-energy part of the spectrum. Moreover, shapes could be kept simple enough to be realised by few LCR-circuits, so the approach will find wide application, in particular for the next generation of fast pulse-shaping devices.

We expect the decoherence time scales dominated by  $1/f$  contributions to  $T_2$  will not change largely under the pulses, so time optimal controls provide a significant step towards the accuracy threshold for quantum computing, even if the optimisation of decoherence times reaches its

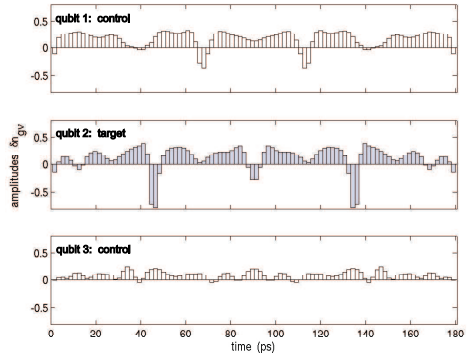


FIG. 5: Fastest gate charge controls obtained for realising a TOFFOLI gate on a linear chain of charge qubits coupled by nearest-neighbour interactions with a trace fidelity of  $\frac{1}{2N} |\text{tr}\{U_{\text{target}}^\dagger U_T\}| > 1 - 10^{-5}$ . Parameters:  $E_{c1}/h = 140.2$  GHz,  $E_{c2}/h = 120.9$  GHz,  $E_{c3}/h = 184.3$  GHz,  $E_{J1}/h = 10.9$  GHz,  $E_{J2}/h = 9.9$  GHz,  $E_{J3}/h = 9.4$  GHz,  $E_{m1,m2}/h = 23$  GHz,  $n_{g1}^0 = 0.24$ ,  $n_{g2}^0 = 0.26$ ,  $n_{g3}^0 = 0.28$ .

intrinsic limits.

We are indebted to N. Khaneja for continuous stimulating scientific exchange. We thank M. Marantoni for discussing experimental issues, as well as Y. Nakamura and the NEC group, J.M. Martinis, A. Ustinov, L.C.L. Hollenberg, T. Cubitt, and D. van der Weide. This work was supported by DFG in SPP 1078 (Gl 203/4-2) and SFB 631, by the Finnish Cultural Foundation, by ARDA and by NSA (ARO contract P-43385-PH-QC).

\* Electronic address: tosh@ch.tum.de

† Electronic address: frank.wilhelm@physik.lmu.de

- [1] T. Yamamoto, Y. A. Pashkin, O. Astafiev, Y. Nakamura, and J. S. Tsai, *Nature (London)* **425**, 941 (2003).
- [2] Y. Makhlin, G. Schön, and A. Shnirman, *Rev. Mod. Phys.* **73**, 357 (2001).
- [3] R. McDermott, R. W. Simmonds, M. Steffen, K. B. Cooper, K. Cicak, K. D. Osborn, S. Oh, D. P. Pappas, and J. M. Martinis, *Science* **307**, 1299 (2005).
- [4] P. Bertet, I. Chiorescu, G. Burkard, K. Semba, C. Harman, D. DiVincenzo, and J. Mooij, *cond-mat/0412485*.
- [5] O. Astafiev, Y. A. Pashkin, Y. Nakamura, T. Yamamoto, and J. S. Tsai, *Phys. Rev. Lett.* **93**, 267007 (2004).
- [6] A. G. Butkovskiy and Y. I. Samoilenko, *Control of Quantum-Mechanical Processes and Systems* (Kluwer, Dordrecht, 1990).
- [7] N. Khaneja, B. Luy, and S. J. Glaser, *Proc. Natl. Acad. Sci. USA* **100**, 13162 (2003).
- [8] N. Khaneja, R. W. Brockett, and S. J. Glaser, *Phys. Rev. A* **63**, 032308 (2001).
- [9] N. Khaneja, S. J. Glaser, and R. W. Brockett, *Phys. Rev. A* **65**, 032301 (2001).

- [10] S. J. Glaser, T. Schulte-Herbrüggen, M. Sieveking, O. Schedletsky, N. C. Nielsen, O. W. Sørensen, and C. Griesinger, *Science* **280**, 421 (1998).
- [11] T. Hayashi, T. Fujisawa, H. Cheong, Y. Yeong, and Y. Hirayama, *Phys. Rev. Lett.* **91**, 226804 (2003).
- [12] J. Majer, F. Paauw, A. ter Haar, C. Harmans, and J. Mooij, *Phys. Rev. Lett.* **94**, 090501 (2005).
- [13] N. Khaneja, T. Reiss, C. Kehlet, T. Schulte-Herbrüggen, and S. J. Glaser, *J. Magn. Reson.* **172**, 296 (2005).
- [14] T. Schulte-Herbrüggen, A. Spörl, N. Khaneja, and S. J. Glaser, *quant-ph/0502104*, *Phys. Rev. A.* (2005) in press.
- [15] C. Griesinger, C. Gemperle, O. W. Sørensen, and R. R. Ernst, *Molec. Phys.* **62**, 295 (1987).
- [16] S. Sklarz and D. Tannor, *quant-ph/0404081*.
- [17] H. Kim, A. Kozrev, S. Ho, and D. van der Weide, *proc. IEEE Microwave Symp.* 2005, in press.
- [18] H. Qin, R. Blick, D. van der Weide, and K. Eberl, *Physica E* **13**, 109 (2002).
- [19] D. Brock, *Int. J. High Sp. El. Sys.* **11**, 307 (2001).
- [20] W. Rupprecht, *Netzwerksynthese* (Springer, Berlin, 1972).
- [21] J. Vartiainen, A. Niskanen, M. Nakahara, and M. Salomaa, *Int. J. Quant. Inf.* **2**, 1 (2004).
- [22] A. Niskanen, J. Vartiainen, and M. Salomaa, *Phys. Rev. Lett.* **90**, 197901 (2003).
- [23] C. Rigetti, A. Blais, and M. Devoret, *Phys. Rev. Lett.* **94**, 240502 (2005).

## Supplementary Material: Optimal Control of Coupled Josephson Qubits

A. Spörl, T. Schulte-Herbrüggen, S.J. Glaser, V. Bergholm, M. Storz, J. Ferber, and F.K. Wilhelm  
(Dated: September 26, 2005)

### OVERVIEW

In the first place, it is the purpose of this supplement to illustrate the quality of the qubit dynamics under the pulse controls obtained numerically in order to provide more insight. Given these numerical controls, the second paragraph demonstrates how easily the pulse shapes can actually be generated by classical network synthesis. Moreover, we wish to emphasize that the controls obtained are fairly robust to  $\pm 5\%$  variation of the tunneling frequencies  $E_J$  as well as the coupling strength  $E_m$  thus embracing typical errors of spectroscopic parameter determination. Finally, we show that the current work gained two orders of magnitude towards approaching the error-correction threshold of  $\simeq 10^{-4}$ .

### QUALITY OF THE QUBIT DYNAMICS UNDER THE OPTIMISED CONTROLS

Figure 1 shows the qubit dynamics of the reduced system given by local Bloch-spheres. The left one belonging to qubit  $A$  (control), shows the projections  $\rho_A = \text{Tr}_B \rho$  and vice versa for the right one. The sigmoidal distortion of the inversion discussed in the main text is time-wise cheap due to fast local controls along  $\sigma_z$ . Bloch vectors inside the spheres indicate entanglement between the qubits as in Fig. 2. The experimental pulses used in Ref. [1] entail much longer trajectories with loops and several nearly closed great cycles (see Figs. 3-4); they are far from geodesic.

The Weyl chamber of Fig. 5 provides a visualisation complementary to the local Bloch spheres: under the controls of Fig. 1 (main text) it picks out the coupling evolution in  $G/K = SU(4)/SU(2)^{\otimes 2}$ . In NMR time scales, this is time-limiting, hence there time optima are geodesic [2], whereas here in the charge qubits, local and non-local evolutions take similar times thus giving a mildly recurrent curve.

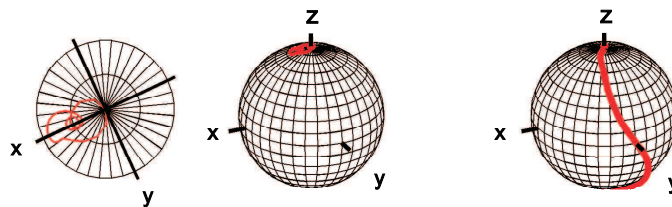


FIG. 1: Evolution of the product state  $|\Theta(0)\rangle = |0\rangle|0\rangle$  under the optimised controls resulting in  $|\Theta(T)\rangle = |0\rangle|1\rangle$ . The evolution  $0 \leq t \leq T$  with  $T = 55$  ps is represented by the reduced states  $\text{tr}_B |\Theta(t)\rangle\langle\Theta(t)|$  (left sphere) and  $\text{tr}_A |\Theta(t)\rangle\langle\Theta(t)|$  (right sphere) on the respective local Bloch spheres with the grid lines spaced by  $10^\circ$ . The blow-up shows the top of the left Bloch sphere.

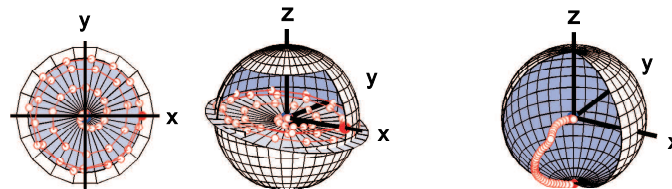


FIG. 2: Evolution of the Bell state  $|\Phi_+\rangle = \frac{1}{\sqrt{2}}(|00\rangle + |11\rangle)$  into the final state  $\frac{1}{\sqrt{2}}(|01\rangle + |11\rangle)$  (filled red dots). The Bell state is maximally entangled and hence has local representations in the centre of the respective Bloch spheres, while the final state is a product state represented by points (filled red dots) on their surfaces. The projection on the left is a view from the top onto the plane inserted into the left Bloch sphere.

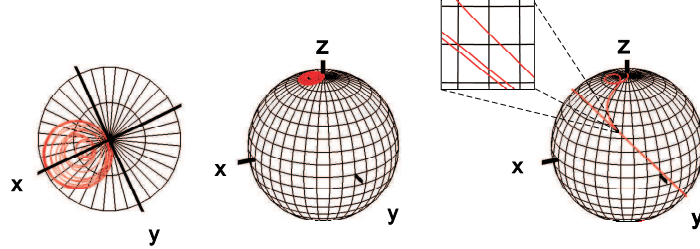


FIG. 3: For comparison: same evolution of the product state  $|\Theta(0)\rangle = |0\rangle|0\rangle$  as in Fig. 1, but using the pulse of the experiment in the NEC group [1]. The evolution  $0 \leq t \leq T$  with  $T = 255$  ps is represented by the reduced states  $tr_B|\Theta(t)\rangle\langle\Theta(t)|$  (left) and  $tr_A|\Theta(t)\rangle\langle\Theta(t)|$  (right) on the respective local Bloch spheres. The trajectory completes two full circles (see inset) before reaching its final state near the south pole. Grid lines are spaced by  $10^\circ$  on the Bloch spheres, and by  $1^\circ$  in the inset.

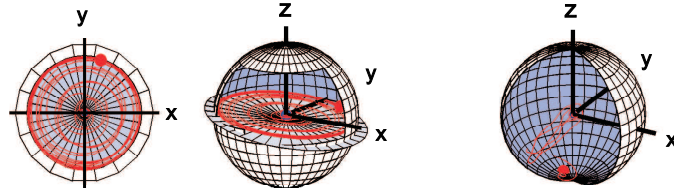


FIG. 4: Evolution of the Bell state  $|\Phi_+\rangle = \frac{1}{\sqrt{2}}(|00\rangle + |11\rangle)$  as Fig. 2, but using the control of the experiment [1]. Parameters of that pulse on the second qubit are:  $\delta n_{g2} = 0.25$ , total length 255 ps with 40 ps rise time and 40 ps fall time, digitisation: 1000 points. Note the different final states as compared to Figs. 1 and 2 indicative of a resulting gate whose matrix elements coincide with the proper CNOT in absolute value, but not in phase. (Actually, the phase deviations are not uniform throughout the elements).

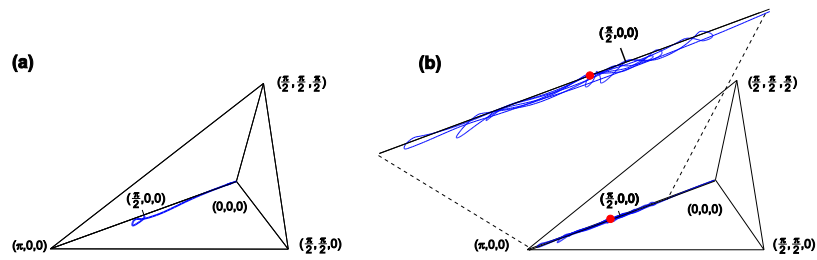


FIG. 5: Coupling evolution under the controls of Fig. 1 (main text) represented in the Weyl chamber. With local and non local controls being of comparable time scale, where the time for a *local*  $\pi$ -pulse is actually time-limiting, the time-optimised controls (a) give a mildly recurrent smooth curve which ends at the point  $(\frac{\pi}{2}, 0, 0)$  as expected for a CNOT requiring a  $\frac{\pi}{2}$  evolution under the coupling term  $\frac{1}{2}\sigma_z \otimes \sigma_z$ . In contrast, the coupling evolution under the controls of Ref. [1] is meandering back and forth (b) and terminates (red dot) without reaching  $\frac{\pi}{2}$  exactly.

TABLE I: Parameters giving the envelope to the control amplitudes  $n_{g\nu}(t)$  for the two qubits  $\nu = 1, 2$  as in Eqn. 3 in the main text.  $T = 55$  ps. The fits give  $\chi^2 = 0.008231$  for qubit 1 and  $\chi^2 = 0.003668$  for qubit 2.

$j$	$a_1(j)$	$\omega_1(j)$	$\phi_1(j)$	$a_2(j)$	$\omega_2(j)$	$\phi_2(j)$
0	- 4.4647	0	0	-17.4138	0	0
1	- 4.5071	0.0130	9.3846	-23.7277	0.4400	1.7869
2	6.5080	3.2896	- 0.7031	-10.0067	1.2108	2.5555
3	14.5596	3.3968	2.1083	- 8.5767	1.9801	3.3284
4	-14.2523	3.5523	1.6296	-15.5114	2.5745	4.6400
5	- 6.1681	3.6477	4.4777	-19.2964	2.8057	7.0698
6	-	-	-	- 8.4275	2.9355	9.8117

### PULSE SHAPING HARDWARE

This section details the pulse shaping scheme outlined in the main text. For the pulses of Fig. 1 of the paper, Table I gives the Fourier-type decompositions according to Eqn. 3 (main text).

The data in Fig. 3 of the paper and in Fig. 6 of this supplement have been obtained as follows: we have fitted a rational function  $Z_{12}(s)$  in Laplace space, such that  $V_{\text{out}}(s) = Z_{12}(s)I_{\text{in}}(s)$  where  $I_{\text{in}}$  is a 1 ps current pulse and  $n_{g,i} = C_{G,i}V_{\text{out},i}/2e$  for the two qubits,  $i = 1, 2$ . This function is represented best by its residue decomposition  $Z_{12} = \sum_i \frac{r_i}{s-s_i}$ . With this decomposition, there are a number of approaches to design a lumped circuit with this transfer function, such as the method of Gewertz [3] that systematically eliminates poles and introduces loops in the electrical circuit: one LCR-loop for each pair of complex conjugate poles, and one RC-filter for each pole on the real axis. Thus, the degree of the polynomial in the denominator gives a clear view on the size of the necessary circuit.

In reality, the transfer function from the pulse shaping circuit (which at room temperature can conveniently be placed to the sample) is not constant. Most reliably, it can be measured *e.g.* by using a capacitor simulating the qubit. In the linear case, it can be expressed as another four-pole impedance matrix  $Z_{\text{sample}}$ . The total transfer function of the series configuration of those four-poles will then be  $Z_{12} = Z_{12,\text{sample}}Z_{12,\text{filter}}/(Z_{22,\text{filter}} + Z_{11,\text{sample}})$ . This outlines, that unless the transfer function to the sample is not filtering out the relevant frequencies (i.e. becomes small for values of  $s$  important to  $V_{\text{out}}$ ), it will be possible to design an appropriate filter taking into account the properties of the experimental setup. With this approach, the *full* transfer function  $Z_{12}$  shapes the pulse.

When designing the filter as well as the pulse one can readily accommodate the experimental necessities. Due to unavoidable fabrication uncertainties, the optimum pulse will be slightly different for each individual pair of qubits. Thus the parameters for the Hamiltonians in Eqs. 1-2 of the main paper have to be determined spectroscopically before re-running our algorithm to adapt the optimal pulse shapes, which can easily be done on a regular PC.

Pulses can also be formed by other means, such as superimposing short pulses of shapes easy to generate with different heights, widths, and delays. The two main candidates for this approach are (i) Gaussian pulses [4], which can be generated at room temperature and pass the necessary cryogenic filtering nearly undistorted and (ii) SFQ pulses, which can be generated on chip (hence avoiding the filters) using ultrafast classical Josephson electronics [5].

Note, that our optimization method also applies to control by microwave Rabi-type pulses [6], where pulse shaping appears to be easier as time scales are usually longer.

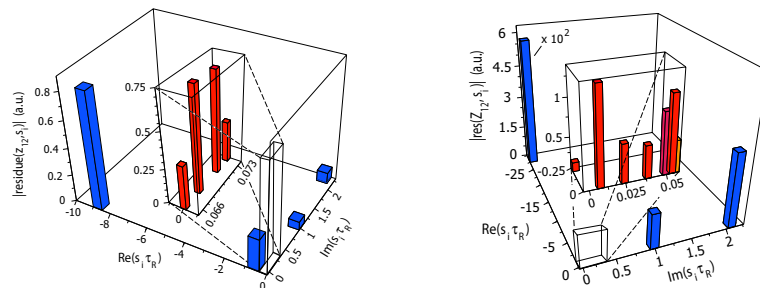


FIG. 6: Pole structure of the transfer functions necessary for shaping the pulses on both the control (left) and target (right) qubit. Parameters correspond to Fig. 3 of the main paper.

## ROBUSTNESS OF THE OPTIMISED CONTROLS

Interestingly, the controls of Fig. 1 (main text) are already remarkably robust with respect to joint variations of the tunneling energies  $E_{J\nu}$  ( $\nu = 1, 2$ ) as they may result from homogeneously differing oxygen content in the alloy of the junction material as well as deviating coupling strength  $E_m$ . These parameters have to be determined spectroscopically, where the relative error normally does not exceed 5%. Fig. 7a shows that even the time-optimised controls as short as  $T = 55$  ps cope with such variations. Significant improvement of the broad-band behaviour, however, could not be obtained by pulse sequences up to a total duration of  $T = 75$  ps thus suggesting that broad-band CNOT controls tailored for the special (and rare) instances with ill-defined experimental parameters will require considerably longer pulse schemes. A similar robustness is observed in Monte-Carlo simulations of Gaussian noise on the control amplitudes or time units as seen in Fig. 7b.

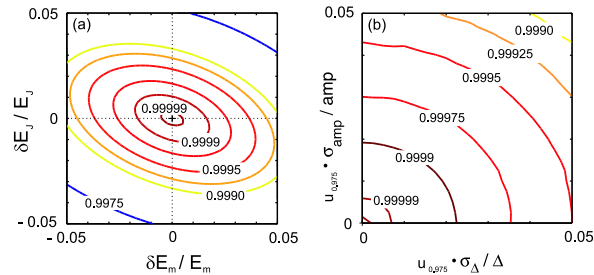


FIG. 7: (a) Trace fidelities resulting from the controls of Fig. 1 in the main text when the parameters  $E_m$  and  $E_J$  in Eqns. 1-2 vary by  $\pm 5\%$ . In this range, the quality profile can be fitted ( $\chi^2 = 3.84 \times 10^{-8}$ ) by a tilted 2D Gaussian distribution with standard deviations of 0.80 for  $\delta E_m/E_m$  and 1.27 for  $\delta E_J/E_J$ . The correlation coefficient is  $-0.38$  corresponding to a tilt angle of  $-30^\circ$  between the  $x$ -axis and the major principal axis of the ellipse. (b) Fidelities under Gaussian noise on control amplitudes and time intervals ranging from 0 to 5%. Scaling the standard deviations by  $1.96 \sigma_\Delta/\Delta$  and  $1.96 \sigma_{\text{amp}}/\text{amp}$  means 95% of the simulated noise values lie in the intervals  $0 \pm 1.96 \sigma$ . (As in Fig. 1,  $\Delta := t_k$ ;  $\text{amp} := \delta n_{q\nu}$  with  $\nu = 1, 2$ .) Each data point is an average of 25'000 Monte-Carlo simulations. At the origins (+) of (a) and (b), the trace fidelities are  $1 - 10^{-9}$ .

## TOWARDS THE ERROR-CORRECTION THRESHOLD: GUIDELINES AND FRONTIERS AHEAD

Apart from illustrating the results in the main text, it is the purpose of this Supplement to make a strong case for the next generation of fast pulse shapers. Actually we regard them as paramount for reaching the goal of scalable quantum computation with superconducting Josephson elements. Let  $F$  denote the fidelity of a gate of duration  $T$ , and let  $T_2$  be the pertinent overall decay time. Assuming independent errors, the quality of a gate is roughly determined by  $q \simeq F e^{-T/T_2} \simeq F(1 - \frac{T}{T_2})$ , where the error rate  $1 - q \simeq 10^{-4}$  is an estimate for the error-correction threshold (see e.g. [7]). This goal can be met by improvements on three frontiers:

1. fighting decoherence by making  $T_2$  longer,
2. cutting gate times by making  $T$  shorter,
3. improving fidelity by making  $F$  larger,

where this work shows how to cope with the latter two by means of optimal control.

(1) In fact the Josephson devices known today [1, 6, 8] have already undergone a great deal of hardware optimisation bringing decoherence down close to its theoretical limits. The observed decoherence times in charge qubits are on the scale of  $T_2 \simeq 0.5$  to 2.5 ns for two-qubit dynamics [9], and 10 ns for single qubits [10]. Both can be improved by using echo techniques [11], which hints at  $1/f$  noise as the limiting factor. Other improvements of  $T_2$  rely on operating with microwave pulses [6, 12] at an optimum bias point on the expense of much slower pulses limited by the Rabi frequency. Although our technique may incorporate both strategies, echo and microwave pulses, we base our technological estimate in the next section on an optimistic  $T_2$  of 10 ns, which appears to be accessible in a charge qubit setup as in [1].

(2) The pulse controls *currently available* are too slow to fully exploit the power of the experimental setting: within a decay time of 10 ns, just 40 CNOTs of the current duration of 250 ps can be performed (with the rise times in the order of 35 ps). On the other hand, the capacitively coupled Josephson hardware elements themselves have large intrinsic frequency scales allowing for fast operation and may well reach the decoherence-limited threshold—provided gates could be executed some 10 times faster than in the current experimental setting, where we have shown that within 10 ns, approx. 200 time-optimised high-fidelity CNOTs can be run.

(3) For obtaining sufficiently high fidelities experimentally, an important part of the future challenge will boil down to the accurate determination of the experimental system response: once this can be done, a non-ideal system response can easily be incorporated into our algorithms thus allowing for getting fidelities that are essentially limited by the robustness of the experimental setting (*cf.* Fig. 7). With fidelities of  $F$  up to  $1 - 10^{-9}$  being ideally accessible by our pulses, the total error rate is then entirely limited by decoherence ( $\frac{T}{T_2}$ ).

*Summary of the CNOT gate.* With the pulses presented here, the total error rate  $1 - q$  is limited by decoherence ( $\frac{T}{T_2}$ ) and amounts to  $1 - q = 0.0055$ , which does not reach the error correction threshold of  $1 - q \simeq 10^{-4}$  yet. However, it compares favorably to the one in the pioneering setting [1], where a fidelity of  $F \simeq 0.4188$  was obtained (largely limited by the phase twists) for a pulse of duration  $T = 250$  ps thus leading to a value of  $q = 0.4083$ . So our results present an improvement of two orders of magnitude in the error rates ( $1 - q = 0.0055$  instead of  $1 - q = 0.5917$ ).

*Summary for the TOFFOLI gate.* The effects are nearly as dramatic: in a linear chain of three qubits coupled by nearest-neighbour interactions, a TOFFOLI gate needs nine CNOTs, which gives an error rate of  $1 - q_{\text{pioneer}} = 1 - 0.4083^9 = 0.9997$  using the CNOTs of Ref. [1], an error rate of  $1 - q_{\text{network}} = 1 - 0.9945^9 = 0.0483$  with nine of our CNOTs, while the error rate of the TOFFOLI gate shown in Fig. 5 of the main text is  $1 - q_{\text{direct}} = 1 - 0.99999 e^{-180\text{ps}/10\text{ns}} = 0.0178$ , assuming for the moment that the  $T_2$  in a coupled three-qubit Josephson system would also be in the order of 10 ns. Clearly, the latter error rate is again entirely decoherence-limited and thus strongly suggests to generate quantum modules directly and in a time optimal way from the experimentally available controls rather than decomposing them into elementary universal quantum gates first.

### Concluding Guidelines

Our results make a strong case for faster pulse generation, both shorter in total length and with the possibility of shaping the external structure. This is a corner stone for future progress. In contrast, even though the current experimental controls could further be optimised fidelity-wise, a simple calculation already shows that this will not suffice for significant improvements given the time scales of current pulse shaping technology: in the case of a CNOT, the quality would always be limited by  $e^{-T/T_2} = 0.975$  even at fidelities of  $F = 1$ . On the same footing, if higher fidelity is achieved by additional compensation pulses, the total sequence becomes longer and the quality again deteriorates. Rather, one should strive for making the Josephson hardware system even faster without introducing higher  $T_2$  decay rates. Since with reasonable fidelities the limitation is entirely on decoherence, above all, the ultra-fast pulse-shaping devices being developed right now will enable significant progress. Clearly, this technological frontier has not been really explored so far, yet the timescales needed are not excessively short compared to what has been realized with electro-optical methods involving pulsed lasers and switches [13]. For getting sufficiently high fidelities experimentally, another frontier will rely on accurately determining the experimental system response, which should then be included into the numerical algorithms.

The combination of optimal control and network synthesis methods presented here thus gives a proof of principle by way of example, and the broadly applicable techniques will lead to similar improvements in further solid-state qubit setups, *e.g.*, semiconductor quantum dots. Other experimental settings, such as microwave pulses at optimum points, where both decoherence and control are slower will profit likewise. The tools of optimal quantum control are thus shown to be both very powerful and general and hence await broad application in spin and pseudospin systems.

- 
- [1] T. Yamamoto, Y. A. Pashkin, O. Astafiev, Y. Nakamura, and J. S. Tsai, *Nature (London)* **425**, 941 (2003).
  - [2] N. Khaneja, R. W. Brockett, and S. J. Glaser, *Phys. Rev. A* **63**, 032308 (2001).
  - [3] C. Gewertz, *J. Math. Phys.* **12**, 1 (1932).
  - [4] T. Hayashi, T. Fujisawa, H. Cheong, Y. Yeong, and Y. Hirayama, *Phys. Rev. Lett.* **91**, 226804 (2003).
  - [5] D. Brock, *Int. J. High Sp. El. Sys.* **11**, 307 (2001).
  - [6] R. McDermott, R. W. Simmonds, M. Steffen, K. B. Cooper, K. Cicak, K. D. Osborn, S. Oh, D. P. Pappas, and J. M. Martinis, *Science* **307**, 1299 (2005).
  - [7] M. Nielsen and I. Chuang, *Quantum Computation and Quantum Information* (Cambridge University Press, 2000).
  - [8] P. Bertet, I. Chiorescu, G. Burkard, K. Semba, C. Harmans, D. DiVincenzo, and J. Mooij, *cond-mat/0412485*.

- [9] Y. A. Pashkin, T. Yamamoto, O. Astafiev, Y. Nakamura, D. V. Averin, and J. S. Tsai, *Nature (London)* **421**, 823 (2003).
- [10] O. Astafiev, Y. A. Pashkin, Y. Nakamura, T. Yamamoto, and J. S. Tsai, *Phys. Rev. Lett.* **93**, 267007 (2004).
- [11] Y. Nakamura, Y. A. Pashkin, T. Yamamoto, and J. S. Tsai, *Phys. Rev. Lett.* **88**, 047901 (2002).
- [12] D. Vion, A. Aassime, A. Cottet, P. Joyez, H. Pothier, C. Urbina, D. Esteve, and M. H. Devoret, *Science* **296**, 286 (2002).
- [13] C.-C. Wang, M. Currie, R. Sobolewski, and T. Y. Hsiang, *Appl. Phys. Lett.* **67**, 79 (1995).



# Chapter 11

## EPR pairs in superconducting charge qubits

### 11.1 Introduction

In 1935, Einstein, Podolsky, and Rosen (EPR) in their famous work [241] raised the question whether quantum mechanics is *incomplete* through discussion of the correlations between two particles. Bohr in his comment to this work [242] showed that quantum theory is consistent, though, he did *not* argue whether quantum mechanics is complete or incomplete [231]. The claim by EPR implies an inequality that is not satisfied by some of the quantum correlations; namely Bell's inequalities are violated [243]. These have been generalized by Clauser, Horne, Shimony, and Holt (CHSH) [244] in order to allow to test the EPR correlations.

Here, the generation and quantum state tomography of EPR pairs, in superconducting charge qubits and the decoherence of the generated EPR states will be discussed. Therefore, the maximally entangled Bell states

$$|\psi_{\pm}\rangle = \frac{1}{\sqrt{2}}(|00\rangle \pm |11\rangle), \quad |\phi_{\pm}\rangle = \frac{1}{\sqrt{2}}(|01\rangle \pm |10\rangle). \quad (11.1)$$

are used to test the quantum mechanical correlations, *i.e.*, the entanglement.

The entanglement can be quantified by an entanglement measure [240], *e.g.*, the linearized entropy [24], entanglement capability [183], or concurrence [245]. In the following paper, the quantum mechanical correlations in the two charge qubit system will be metered by the concurrence as defined in Refs. [245, 246]. In more detail, the concurrence [245] of a state  $|\psi\rangle$  with a density matrix  $\rho = |\psi\rangle\langle\psi|$ , is given by  $C(\rho) = \max\{0, \sqrt{\lambda_1} - \sqrt{\lambda_2} - \sqrt{\lambda_3} - \sqrt{\lambda_4}\}$ , where the  $\lambda_i$  are the eigenvalues of  $\rho\tilde{\rho}$  in decreasing order of magnitude and

$$\tilde{\rho} = (\sigma_y^1 \otimes \sigma_y^2)\rho^*(\sigma_y^1 \otimes \sigma_y^2). \quad (11.2)$$

As an entanglement measure, the concurrence indicates non-locality. For maximally entangled states, *e.g.*, the Bell states which are the ideal EPR correlations, the concurrence is unity, whereas fully separable states yield zero as the value of the concurrence.

In the charge qubit system that is considered here, two important drawbacks restrict the performance of the quantum gate operations on the two charge qubit system, which are needed in order to generate and measure the EPR pairs. First, there is no full control over all terms in the Hamiltonian, *i.e.*, the coupling between the two qubits is fixed and set by a coupling capacitance. Here, we assume that one can tune the Josephson energy via an externally applied flux through the SQUID loop of the charge qubit (that is fabricated in SQUID geometry) and the gate charges, *i.e.*, the charge energies or bias of the qubit. Still, the coupling term between the qubits is not tunable and set constant. Thus, a scheme for manipulation of the qubits and quantum state tomography has to be developed that takes these special properties into account. Second, decoherence due to fluctuations of the control voltages and a smaller amount of  $1/f$ -noise (due to hopping background charges), which can be effectively modeled by Gaussian noise, affects the qubit (states) and can severely limit the decoherence times of the qubit system. Therefore, numerical simulations of the time evolution of the prepared EPR pairs that take decoherence into account were performed within the Bloch-Redfield formalism that is presented in chapter 4.3 of this thesis.

It will be shown how conditional gate operations on any qubit can be realized, also with the constant coupling term between the qubits. Starting from the natural ground state of the circuit, any EPR pair can be generated by a set of basic quantum gate operations. Moreover, the correlations can be verified by a test of Bell's inequality with the generated EPR pairs, which is described in detail. This test can be performed by obtaining the correlation function from repeated measurements of the qubit states.



## Macroscopic Einstein-Podolsky-Rosen pairs in superconducting circuits

L.F. Wei,<sup>1,2</sup> Yu-xi Liu,<sup>1</sup> Markus J. Storcz,<sup>1,3</sup> and Franco Nori<sup>1,4</sup>

<sup>1</sup>Frontier Research System, The Institute of Physical and Chemical Research (RIKEN), Wako-shi, Saitama, 351-0198, Japan

<sup>2</sup>Institute of Quantum Optics and Quantum Information, Department of Physics,  
Shanghai Jiaotong University, Shanghai 200030, P.R. China

<sup>3</sup>Physics Department, ASC, and CeNS, Ludwig-Maximilians-Universität, Theresienstrasse 37, 80333 München, Germany

<sup>4</sup>Center for Theoretical Physics, Physics Department, CSCS,  
The University of Michigan, Ann Arbor, Michigan 48109-1040, USA

(Dated: October 6, 2005)

We propose an efficient approach to prepare Einstein-Podolsky-Rosen (EPR) pairs in currently-existing Josephson nanocircuits with capacitive-couplings. In these fixed-coupling circuits, two-qubit logic gates could be easily implemented while, strictly speaking, single-qubit gates cannot be easily realized. For a known two-qubit state, conditional single-qubit operations could still be designed to evolve only the selected qubit and keep the other qubit unchanged; the rotations of the selected qubit depends on the state of the left one. These conditional single-qubit operations allow to deterministically generate the well-known Einstein-Podolsky-Rosen pairs, represented by EPR-Bell (or Bell) states, at a macroscopic level. Quantum-state tomography is further proposed to experimentally confirm the generation of these states. The decay of the prepared EPR pairs is analyzed using numerical simulations of the system dynamics. Possible applications of the generated macroscopic EPR pairs to test Bell's Inequality (BI) are also discussed.

PACS number(s): 03.67.Mn, 03.65.Wj, 85.25.Dq.

### I. INTRODUCTION

Quantum mechanics (QM) is a very successful theory. It has solved many physical mysteries in both macroscopic superconductivity and microscopic elemental-particle systems. Still, laboratory studies of its conceptual foundations and interpretation continue to attract much attention. One of the most important examples is the well-known Einstein-Podolsky-Rosen (EPR) "paradox", concerning the completeness of QM. Based on a *gedanken* experiment, Einstein, Podolsky and Rosen (EPR) claimed [1] that QM is incomplete and that so-called "hidden variables" should exist. This is because a two-particle quantum system might be prepared in a correlated state such that a measurement performed on one of the particles immediately changes the state (and thus the possible physical outcome) of the second particle, even though the two particles could be separated by large distances, without direct communication between them. This "paradox" lead to much subsequent, and still on-going, research. Bell proposed [2] an experimentally testable inequality to examine the existence of the hidden variables: if this inequality is ever *not* satisfied, then there are no so-called local "hidden variables" and thus there are quantum non-local correlations. Bell's Inequality (BI) has served as one of the most important witnesses of entanglement, which is a correlated feature of composite quantum systems and takes an important role in future quantum information processing.

During the past decade, a number of interesting experiments [3] using entangled photon pairs have been proposed and carried out to investigate the quantum nature of two-particle entangled states. These experiments showed that BI could be strongly violated, and thus agreed with quantum mechanical predictions. Yet, two essential loopholes have not been strictly closed in these experiments. First, the required EPR pairs were generated in a small subset of all pairs created

in certain spontaneous processes, and thus were not deterministically prepared. Second, besides the problem of detector efficiency, the expected locality could not be strictly satisfied as the individual experimental measurements of two particles were not realistically spacelike separated. Therefore, it is necessary to study two-particle entanglement in different, e.g., massive or macroscopic systems, instead of fast-escaping photons. Theoretical proposals include those with e.g., neutral Kaons [4], Rydberg atoms [5], ballistic electrons in semiconductors [6], and trapped ions [7]. Experimentally, in 1997 two Rydberg atoms had been first entangled to form EPR pairs in a high  $Q$  cavity by the exchange of a single photon [8]. Later, by exchanging the quanta of the common vibrational mode, EPR correlations of ultralong lifetime had been generated between a pair of trapped cold ions separated a few micrometers apart [9]. Consequently, experimental violations of BI have been verified with the EPR correlations between the two ions [10] and between an atom and a photon [11].

Recent developments of quantum manipulation in coupled Josephson systems [12, 13] allow to experimentally investigate the quantum correlations between two macroscopic degrees of freedom in a superconducting nano-electronic device [14]. Proposals have been made for producing quantum entanglement between two superconducting qubits, e.g., indirectly coupled by sequentially interacting with a current-biased information bus [15, 16], coupled inductively [17, 18], and coupled via a cavity mode [19]. It has also shown [20] that microwave pulses applied to the gate-voltages can entangle two charge-qubit coupled by a large Josephson junction. By introducing effective single-qubit operations, we have shown [21] that the BI could also be tested even in capacitively-coupled Cooper-pair boxes. The robustness of the scheme proposed there [21] is better suited for weak interbit couplings, e.g., when the ratio of the interbit-coupling energy  $E_m$  and the Josephson energy  $E_J$  of the qubit is small. Here, for an *arbi-*

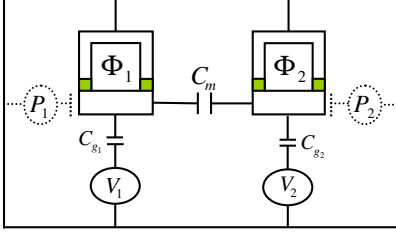


FIG. 1: Two capacitively-coupled SQUID-based charge qubits. The quantum states of two Cooper-pair boxes (i.e., qubits) are manipulated by controlling the applied gate voltages  $V_1, V_2$  and external magnetic fluxes  $\Phi_1, \Phi_2$  (penetrating the SQUID loops).  $P_1$  and  $P_2$  (dashed line parts) read out the final qubit states.

rary interbit coupling, we propose an approach for producing EPR correlations by manipulating the well-known EPR-Bell (or Bell) states

$$|\psi_{\pm}\rangle = \frac{1}{\sqrt{2}}(|00\rangle \pm |11\rangle), \quad (1)$$

and

$$|\phi_{\pm}\rangle = \frac{1}{\sqrt{2}}(|01\rangle \pm |10\rangle). \quad (2)$$

The outline of the paper is as follows. In Sec. II, we propose a few elementary quantum operations to deterministically manipulate two superconducting-quantum-interference-device (SQUID)-based Josephson charge qubits coupled capacitively. We show that conditional operations on any selected qubit, keeping the state of the other qubit unchanged, are still possible in the present constant-coupling circuit. By making use of these operations, in Sec. III, we propose a two-step approach to deterministically generate any EPR pairs from the circuit's ground state  $|\psi(0)\rangle = |00\rangle$ . Further, we discuss how to experimentally confirm the generation of EPR pairs by using a tomographic technique via various experimentally realizable projected measurements. In Sec. IV, considering the existence of typical voltage-noises and  $1/f$ -noise, we numerically analyze the decays of the prepared EPR correlations within the Bloch-Redfield formalism [22]. In Sec. V, we discuss the possibility of testing BI with the generated EPR pairs. Conclusions and discussions are given in Sec. VI.

## II. MANIPULATIONS OF TWO CAPACITIVELY-COUPLED JOSEPHSON CHARGE QUBITS

We consider the two-qubit nano-circuit sketched in Fig. 1, which was used in recent experiments [12, 23]. Two superconducting-quantum-interference-device (SQUID) loops with controllable Josephson energies produce two

Josephson qubits, fabricated separately (e.g., up to a few micrometers [12, 23]) and coupled via the capacitance  $C_m$ . The qubits work in the charge regime with  $k_B T \ll E_J^{(j)} \ll E_C^{(j)} \ll \Delta$  (with  $j = 1, 2$ ), wherein both quasi-particle tunnelling and excitations are effectively suppressed and the number  $n_j$  (with  $n_j = 0, 1, 2, \dots$ ) of Cooper-pairs in the boxes is a good quantum number. Here,  $k_B, T, \Delta, E_C^{(j)}$ , and  $E_J^{(j)}$  are the Boltzmann constant, temperature, superconducting gap, the charging and Josephson energies of the  $j$ th qubit, respectively.

Following Refs. [12, 23], the dynamics of the system can be effectively restricted to the subspace spanned by only the four lowest charge states:  $|00\rangle, |10\rangle, |01\rangle$  and  $|11\rangle$ , and is thus described by the following simplified Hamiltonian

$$\hat{H} = \sum_{j=1,2} \frac{1}{2} \left[ E_C^{(j)} \sigma_z^{(j)} - E_J^{(j)} \sigma_x^{(j)} \right] + E_{12} \sigma_z^{(1)} \sigma_z^{(2)}, \quad (3)$$

with  $E_{12} = E_m/4, E_m = 4e^2 C_m / C_{\Sigma}$ ,  $E_J^{(j)} = 2\varepsilon_J^{(j)} \cos(\pi\Phi_j/\Phi_0)$ , and  $E_C^{(j)} = E_{C_j}(n_{g_j} - 1/2) + E_m(n_{g_k}/2 - 1/4)$ ,  $j \neq k = 1, 2$  being the coupling-, Josephson- and charge energies, respectively. Here,  $n_{g_j} = C_{g_j} V_j / (2e)$ ,  $E_{C_j} = 4e^2 C_{\Sigma_k} / C_{\Sigma}$ , and  $C_{\Sigma} = C_{\Sigma_1} C_{\Sigma_2} - C_m^2$ . Above,  $e$  is the electron charge and  $\Phi_0$  the flux quantum.  $\varepsilon_J^{(j)}$  and  $C_{\Sigma_j}$  are the Josephson energy of the single-junction and the sum of all capacitances connected to the  $j$ th box, respectively. The pseudospin operators are defined as  $\sigma_z = |0\rangle\langle 0| - |1\rangle\langle 1|$  and  $\sigma_x = |0\rangle\langle 1| + |1\rangle\langle 0|$ .

Obviously, the interbit-coupling energy  $E_{12} = E_m/4$  is determined by the coupling capacitance  $C_m$  and therefore given by fabrication and fixed, i.e., not controllable. However, the charge- and Josephson energies of the qubits,  $E_C^{(j)}$  and  $E_J^{(j)}$ , can be controlled by adjusting the applied gate-voltages  $V_j$  and fluxes  $\Phi_j$ . Although any evolution of this two-qubit system is solvable, we prefer certain relatively simple quantum operations for conveniently engineering arbitrary quantum states. These operations can be achieved by properly setting the above controllable parameters.

First, one can switch off all the charge- and Josephson energies and let the circuit evolve under the Hamiltonian  $\hat{H}_{\text{int}} = E_{12} \sigma_z^{(1)} \sigma_z^{(2)}$ , i.e., undergo a free time-evolution

$$\hat{U}_0(\tau) = \exp \left[ -i \frac{E_{12} \tau}{\hbar} \sigma_z^{(1)} \sigma_z^{(2)} \right], \quad (4)$$

in the operational delay  $\tau$ . We assume the circuit stays in this parameter setting, until any operation is applied to it. In this case, the Bell states Eqs. (1) and (2) will not evolve, once they have been generated.

Second, if  $n_{g_1} = n_{g_2} = 1/2$  (co-resonance point) and  $E_J^{(1)} = E_J^{(2)} = E_J$ , then the circuit has the Hamiltonian  $\hat{H}_{\text{co}} = -E_J(\sigma_x^{(1)} + \sigma_x^{(2)})/2 + E_{12} \sigma_z^{(1)} \sigma_z^{(2)}$ , which corresponds to the following compact time-evolution operator

$$\bar{U}_{\text{co}} = \frac{1}{2} \begin{pmatrix} a & b & b & c \\ b & a^* & c^* & b \\ b & c^* & a^* & b \\ c & b & b & a \end{pmatrix},$$

with  $a = \cos(t\Omega/\hbar) - iE_{12} \sin(t\Omega/\hbar)/\Omega + \exp(-itE_{12}/\hbar)$ ,  $b = iE_J \sin(t\Omega/\hbar)/\Omega$ ,  $c = \cos(t\Omega/\hbar) - iE_{12} \sin(t\Omega/\hbar)/\Omega - \exp(-itE_{12}/\hbar)$ , and  $\Omega = \sqrt{E_J^2 + E_{12}^2}$ . The sub-index ‘‘co’’ refers to ‘‘co-resonance’’. Thus, we can simultaneously flip the two qubits, i.e.,  $|00\rangle \rightleftharpoons |11\rangle$ , and  $|01\rangle \rightleftharpoons |10\rangle$ , by setting the duration as  $\cos(t\Omega/\hbar) = -\cos(tE_{12}/\hbar) = 1$ . Another specific two-qubit quantum operation

$$\hat{U}_{\text{co}} = \frac{1}{2} \begin{pmatrix} 1-i & 0 & 0 & 1+i \\ 0 & 1+i & 1-i & 0 \\ 0 & 1-i & 1+i & 0 \\ 1+i & 0 & 0 & 1-i \end{pmatrix} \quad (5)$$

can also be implemented, if the duration is set as  $\cos(t\Omega/\hbar) = \sin(tE_{12}/\hbar) = 1$ .

Note that a single-qubit logic gate cannot be strictly achieved in the system with strong constant interbit-coupling. Considering the correction of the constant-coupling, we have proposed an effective approach to approximately implement expected single-qubit logic operations [21]. Below, we want to manipulate only one qubit and leave the other one unaffected. Various conditional single-qubit quantum operations (thus, no strict single-qubit quantum logic gates) will be designed to evolve one selected qubit, depending on the state of the other one.

If we switch off all charge energies and one of the Josephson energies, e.g.,  $E_J^{(2)} = 0$ , this will typically yield a Hamiltonian  $\hat{H}_J^{(1)} = -E_J^{(1)}\sigma_x^{(1)}/2 + E_{12}\sigma_z^{(1)}\sigma_z^{(2)}$ . In this case the circuit undergoes the time evolution

$$\bar{U}_J^{(1)} = \begin{pmatrix} \zeta_1 & \xi_1 & 0 & 0 \\ \xi_1 & \zeta_1^* & 0 & 0 \\ 0 & 0 & \zeta_1^* & \xi_1 \\ 0 & 0 & \xi_1 & \zeta_1 \end{pmatrix},$$

with

$$\begin{aligned} \xi_1 &= i \sin \alpha_1 \sin \left( \frac{t\gamma_1}{\hbar} \right), \quad \cos \alpha_1 = \frac{E_{12}}{\gamma_1}, \\ \zeta_1 &= \cos \left( \frac{t\gamma_1}{\hbar} \right) - i \cos \alpha_1 \sin \left( \frac{t\gamma_1}{\hbar} \right), \\ \gamma_1 &= \frac{1}{2} \sqrt{(2E_{12})^2 + (E_J^{(1)})^2}. \end{aligned}$$

This implies that there are two invariant subspaces  $\{|00\rangle, |10\rangle\}$  and  $\{|01\rangle, |11\rangle\}$  for this conditional dynamics; the evolution of the first qubit depends on the state of the second qubit, although the later one is unchanged during the dynamics. This operation reduces to

$$\hat{U}_J^{(1)} = \frac{i}{\sqrt{2}} \begin{pmatrix} -1 & 1 & 0 & 0 \\ 1 & 1 & 0 & 0 \\ 0 & 0 & 1 & 1 \\ 0 & 0 & 1 & -1 \end{pmatrix}, \quad (6)$$

if the Josephson energy is set beforehand to  $E_J^{(1)} = 2E_{12}$  and the duration is set to satisfy the condition  $\sin(\gamma_1 t/\hbar) = 1$ .

Similarly, the conditional quantum evolution of the second qubit, keeping the first qubit unchanged, can be implemented

by only switching on the Josephson energy of the second qubit. For example, if  $E_J^{(2)} = 2E_{12}$  is set beforehand and the duration satisfies the condition  $\sin(\gamma_2 t/\hbar) = 1$ ,  $\gamma_2 = E_{12}\sqrt{2}$ , then

$$\hat{U}_J^{(2)} = \frac{i}{\sqrt{2}} \begin{pmatrix} -1 & 0 & 1 & 0 \\ 0 & 1 & 0 & 1 \\ 1 & 0 & 1 & 0 \\ 0 & 1 & 0 & -1 \end{pmatrix}, \quad (7)$$

can be obtained.

The above conditional manipulations on a selected qubit can be further engineered by introducing other controllable parameters, e.g., switching on the charging energies of qubits. In fact, under the Hamiltonian  $\hat{H}_{\text{CJ}}^{(1)} = E_C^{(1)}\sigma_z^{(1)}/2 - E_J^{(1)}\sigma_x^{(1)}/2 + E_{12}\sigma_z^{(1)}\sigma_z^{(2)}$ , the circuit undergoes a time-evolution

$$\bar{U}_{\text{CJ}}^{(1)} = \begin{pmatrix} \mu_+ & \nu_+ & 0 & 0 \\ \nu_+ & \mu_+^* & 0 & 0 \\ 0 & 0 & \mu_- & \nu_- \\ 0 & 0 & \nu_- & \mu_-^* \end{pmatrix},$$

with

$$\begin{aligned} \mu_{\pm} &= \cos \left( \frac{t\gamma_{\pm}}{\hbar} \right) - i \cos \alpha_{\pm} \sin \left( \frac{t\gamma_{\pm}}{\hbar} \right), \\ \nu_{\pm} &= i \sin \alpha_{\pm} \sin \left( \frac{t\gamma_{\pm}}{\hbar} \right), \quad \sin \alpha_{\pm} = \frac{E_J^{(1)}}{2\gamma_{\pm}}, \\ \gamma_{\pm} &= \frac{1}{2} \sqrt{[E_C^{(1)}/2 \pm 2E_{12}]^2 + [E_J^{(1)}]^2}. \end{aligned}$$

If the charge energy of the first qubit is beforehand set as  $E_C^{(1)} = 2E_{12}$  (thus  $\cos \alpha_- = 0$ ), and the duration is set as  $\cos(t\gamma_+/ \hbar) = 1$ , then the following two-qubit Deutsch gate [24]

$$\hat{U}_+^{(1)}(\theta_1) = \begin{pmatrix} 1 & 0 & 0 & 0 \\ 0 & 1 & 0 & 0 \\ 0 & 0 & \cos \theta_1 & i \sin \theta_1 \\ 0 & 0 & i \sin \theta_1 & \cos \theta_1 \end{pmatrix}, \quad \theta_1 = \frac{tE_J^{(1)}}{2\hbar}, \quad (8)$$

is obtained. This gate implies that the target qubit (here it is the second one) undergoes a quantum evolution only if the control qubit (here, the first qubit) is in the logical state ‘‘1’’. If the duration is set to simultaneously satisfy the two conditions:  $\sin \theta_1 = 1$  and  $\cos(t\gamma_+/ \hbar) = 1$ , then the above two-qubit operation is equivalent to the well-known controlled-NOT (CNOT) gate, apart from a phase factor. Obviously, if the charge energy of the first qubit is set beforehand as  $E_C^{(1)} = -2E_{12}$ , then the target qubit undergoes the same evolution only if the control qubit is in the logic state ‘‘0’’, i.e.,

$$\hat{U}_-^{(1)}(\theta_1) = \begin{pmatrix} \cos \theta_1 & i \sin \theta_1 & 0 & 0 \\ i \sin \theta_1 & \cos \theta_1 & 0 & 0 \\ 0 & 0 & 1 & 0 \\ 0 & 0 & 0 & 1 \end{pmatrix}. \quad (9)$$

Note that, due to the presence of the constant interbit-coupling  $E_{12}$ , the charge energy  $E_C^{(1)}$  depends on both gate-voltages applied to the two Cooper-pair boxes. Switching

off the charge energy  $E_C^{(2)} = 0$  requires that the two gate-voltages should be set to satisfy  $(n_{g_2} - 1/2)/(n_{g_1} - 1/2) = -2E_{12}/E_{C_2}$ . Under this condition the charge energy  $E_C^{(1)}$  could still be controlled by adjusting either  $V_1$  or  $V_2$ .

### III. MACROSCOPIC EPR-CORRELATIONS: DETERMINISTIC GENERATIONS AND TOMOGRAPHIC CONFIRMATIONS

Now, it will be shown how to deterministically generate EPR correlations between the above two capacitively-coupled Josephson qubits. Then, we propose an effective approach, which is experimentally feasible, to confirm the generation of the EPR states by using tomographic techniques in the present fixed-coupling system. Naturally, we begin with the ground state of the circuit  $|\psi(0)\rangle = |00\rangle$ , which can be easily initialized by letting the circuit work far from the co-resonance point via a large voltage bias.

First, we superpose two logical states of a selected qubit, e.g., the first one. This can be achieved by simply using a pulse of duration  $t_1$  to implement the above quantum operation (9), i.e.,

$$|\psi_0\rangle \xrightarrow{\hat{U}_+^{(1)}(\theta_1)} |\psi_1\rangle = \frac{1}{\sqrt{2}}(|00\rangle \pm i|10\rangle). \quad (10)$$

Here, the plus sign corresponds to the time durations for  $\theta_1 = E_J^{(1)}t_1/(2\hbar) = \pi/4$ , and  $5\pi/4$ . The minus sign corresponds to  $\theta_1 = E_J^{(1)}t_1/(2\hbar) = -\pi/4$ , and  $7\pi/4$ .

We next conditionally flip the second qubit, keeping the first one unchanged. The expected operations can be simply expressed as either  $|00\rangle \rightarrow |01\rangle$ , keeping  $|10\rangle$  unchanged, or  $|10\rangle \rightarrow |11\rangle$ , keeping  $|00\rangle$  unchanged. The former (latter) operation requires to flip the second qubit if and only if the first qubit is in logic state “0” (“1”). These manipulations can be achieved by evolving the circuit under the Hamiltonian  $\hat{H}_{CJ}^{(2)} = E_C^{(2)}\sigma_z^{(2)}/2 - E_J^{(2)}\sigma_x^{(2)}/2 + E_{12}\sigma_z^{(1)}\sigma_z^{(2)}$ . When the charging energy  $E_C^{(2)}$  is set beforehand to  $E_C^{(2)} = -2E_{12}$ , two of the Bell states can be deterministically created as follows

$$|\psi_1\rangle \xrightarrow{\hat{U}_-^{(2)}(\theta_2)} |\phi_{\pm}\rangle = \frac{1}{\sqrt{2}}(|01\rangle \pm |10\rangle), \quad (11)$$

by accurately setting the duration  $t_2$  of the manipulation

$$\hat{U}_-^{(2)}(\theta_2) = \begin{pmatrix} \cos\theta_2 & 0 & i\sin\theta_2 & 0 \\ 0 & 1 & 0 & 0 \\ i\sin\theta_2 & 0 & \cos\theta_2 & 0 \\ 0 & 0 & 0 & 1 \end{pmatrix} \quad (12)$$

to simultaneously satisfy the conditions  $\sin\theta_2 = 1$  and  $\cos(\gamma't_2/\hbar) = 1$ . Here,  $\theta_2 = E_J^{(2)}t_2/(2\hbar)$ , and  $\gamma' = \sqrt{(E_C^{(2)})^2 + (E_J^{(2)}/2)^2}$ . Inversely, by setting  $E_C^{(2)} = 2E_{12}$  beforehand, the other two Bell states can be produced as

$$|\psi_1\rangle \xrightarrow{\hat{U}_+^{(2)}(\theta_2)} |\psi_{\pm}\rangle = \frac{1}{\sqrt{2}}(|00\rangle \pm |11\rangle), \quad (13)$$

by using the single-step operation

$$\hat{U}_+^{(2)}(\theta_2) = \begin{pmatrix} 1 & 0 & 0 & 0 \\ 0 & \cos\theta_2 & 0 & i\sin\theta_2 \\ 0 & 0 & 1 & 0 \\ 0 & i\sin\theta_2 & 0 & \cos\theta_2 \end{pmatrix} \quad (14)$$

of the duration satisfying the conditions  $\sin\theta_2 = -1$  and  $\cos(\gamma't_2/\hbar) = 1$ .

The fidelity of these EPR correlations can be experimentally measured by quantum-state tomography, i.e., reconstructing the density matrix of the prepared quantum state. From this reconstructed density matrix, relevant quantum information quantities, such as the degree of entanglement and entropy, can be calculated. For the complete characterization of an unknown two-qubit state with a  $4 \times 4$  density matrix  $\rho = (\rho_{ij,kl})$  (with  $i, j, k, l = 0, 1$ ), we need to determine 15 independent real parameters, due to  $\text{tr}\rho = \sum_{i,j=0,1} \rho_{ij,ij} = 1$ , and  $\rho_{ij,kl} = \rho_{kl,ij}^*$ . This can be achieved by a series of measurements on a sufficient number of identically prepared copies of the measured quantum state. The operations presented above for the generation of EPR pairs could provide enough copies of any expected EPR pairs to be reconstructed. Experimentally, Bell states of pseudo-spins (e.g., in nuclear magnetic resonance systems [25], two-level trapped cold ions [9], and the photon pairs [26]) have been tomographically reconstructed by only using a series of single-qubit manipulations. Recently, we have proposed a generic approach to tomographically measure solid-state qubits with switchable interactions [27]. Due to the relatively strong interbit-coupling, which is always on in the circuits considered here, specific operations are required to realize the tomographic reconstruction of the EPR pairs generated.

The state of a charge qubit is often read out by capacitively coupling a single-electron transistor (SET) to the measured qubit [28]. The dissipative current  $I_c^{(j)}$  flowing through the  $j$ th SET, coupled to the  $j$ th qubit, is proportional to the probability of a projective-operator measurement  $\hat{P}_j = |1_j\rangle\langle 1_j|$  on the state of density matrix  $\rho$ , i.e.,  $I_c^{(j)} = \text{tr}(\rho\hat{P}_j)$ . Such a projective measurement is equivalent to the measurement of  $\sigma_z^{(j)}$ , as  $\sigma_z^{(j)} = (\hat{I}_j - \hat{P}_j)/2$  with  $\hat{I}_j$  being the unit operator. For the present system one may perform three kinds of projective measurements: i) the  $P_1$ -measurement (with projected operator  $\hat{P}_1 \otimes \hat{I}_2$ ) acting only on the first qubit (independent of the state of the second qubit); ii) the  $P_2$ -measurement (with projected operator  $\hat{I}_1 \otimes \hat{P}_2$ ) operating only on the second qubit (independent of the state of the first qubit); and iii) the  $P_{12}$ -measurement (with projected operator  $\hat{P}_1 \otimes \hat{P}_2$ ) simultaneously acting on both Cooper-pair boxes.

All diagonal elements of the density matrix  $\rho$  can be directly determined by performing these three kinds of projective measurements on the system. In fact,  $\rho_{11,11}$  can be determined by the  $P_{12}$ -measurement as

$$\rho_{11,11} \propto I_c^{(12)} = \text{tr}(\rho\hat{P}_1 \otimes \hat{P}_2). \quad (15)$$

Next,  $\rho_{10,10}$  could be determined by  $P_1$ -measurement as

$$\rho_{10,10} + \rho_{11,11} \propto I_c^{(1)} = \text{tr}(\rho\hat{P}_1 \otimes \hat{I}_2). \quad (16)$$

Also, we can determine  $\rho_{01,01}$  by the  $P_2$ -measurement as

$$\rho_{01,01} + \rho_{11,11} \propto I_c^{(2)} = \text{tr}(\rho \hat{I}_1 \otimes \hat{P}_2). \quad (17)$$

The remaining element  $\rho_{00,00}$  could be determined by the normalization condition  $\text{tr} \rho = 1$ .

The 12 non-diagonal elements which are left, should be transformed to the diagonal positions of new density matrix  $\rho' = \hat{W} \rho \hat{W}^\dagger$ , by performing a proper quantum operation  $\hat{W}$  on the original density matrix  $\rho$ . For example, after a quantum manipulation  $\hat{U}_j^{(1)}$ , evolving the system to  $\bar{\rho} = \hat{U}_j^{(1)} \rho \hat{U}_j^{(1)\dagger}$ , we can perform the  $P_{12}$ -measurement to obtain

$$\begin{aligned} \bar{I}_c^{(12)} &\propto \text{tr}[\bar{\rho} \hat{P}_1 \otimes \hat{P}_2] \\ &= \frac{1}{2}[\rho_{01,01} + \rho_{11,11} - 2 \text{Re}(\rho_{01,11})], \end{aligned} \quad (18)$$

for determining  $\text{Re}(\rho_{01,11})$ ; and perform the  $P_1$ -measurement to obtain

$$\bar{I}_c^{(2)} \propto \text{tr}[\bar{\rho} \hat{P}_1 \otimes \hat{I}_2] = \frac{1}{2}[1 + 2 \text{Re}(\rho_{00,10} - \rho_{01,11})], \quad (19)$$

for determining  $\text{Re}(\rho_{00,10})$ . All the remaining 10 off-diagonal elements of  $\rho$  can be similarly determined.

Table I summarizes such a procedure for tomographic characterization of an unknown two-qubit state in this fixed-coupling two-qubit system. We need to first apply to  $\rho$  the quantum operations listed in the first column of Table I. Afterwards, the projected measurements listed in the second column of Table I must be made. In this way, all the matrix elements of  $\rho$  can be determined. Of course, this is not a unique approach for determining all fifteen independent elements of the density matrix. In fact, the expected tomographic reconstruction could also be achieved by only using the  $\hat{P}_1$ - and  $\hat{P}_2$ -measurements, and making the  $\hat{P}_{12}$ -measurement unnecessary.

With the density matrix  $\rho$  obtained by the above tomographic measurements and comparing to the density matrix of ideal Bell states, e.g.,

$$\rho_{|\psi_{\pm}\rangle} = \begin{pmatrix} 1 & 0 & 0 & \pm 1 \\ 0 & 0 & 0 & 0 \\ 0 & 0 & 0 & 0 \\ \pm 1 & 0 & 0 & 1 \end{pmatrix}, \quad \rho_{|\phi_{\pm}\rangle} = \begin{pmatrix} 0 & 0 & 0 & 0 \\ 0 & 1 & \pm 1 & 0 \\ 0 & \pm 1 & 1 & 0 \\ 0 & 0 & 0 & 0 \end{pmatrix},$$

the fidelity of the EPR pairs generated above can be defined as  $F_{|\psi_{\pm}\rangle} = \text{tr}(\rho \rho_{|\psi_{\pm}\rangle})$  and  $F_{|\phi_{\pm}\rangle} = \text{tr}(\rho \rho_{|\phi_{\pm}\rangle})$ , respectively.

So far, we have shown that macroscopic EPR correlations could be produced between two capacitively-coupled Cooper-pair boxes. Further, these macroscopic entangled states can be characterized by using tomographic techniques via a series of projective measurements. Below, we will numerically estimate the lifetimes of these macroscopic quantum entangled states and discuss their possible application to test Bell's inequality.

TABLE I: Tomographic characterization of an unknown two-qubit state  $\rho = (\rho_{ij,kl})$  with  $i, j, k, l = 0, 1$  in capacitively-coupled Josephson circuits. Each row of this table requires operating on an identically prepared initial state  $\rho$ .

Operations	Measurement	Determining
No	$\hat{P}_1 \otimes \hat{P}_2$	$\rho_{11,11}$
No	$\hat{P}_1 \otimes \hat{I}_2$	$\rho_{10,10}$
No	$\hat{I}_1 \otimes \hat{P}_2$	$\rho_{01,01}$
$\hat{U}_j^{(1)}$	$\hat{P}_1 \otimes \hat{P}_2$	$\text{Re}(\rho_{01,11})$
$\hat{U}_j^{(1)}$	$\hat{P}_1 \otimes \hat{I}_2$	$\text{Re}(\rho_{00,10})$
$\hat{U}_j^{(2)}$	$\hat{P}_1 \otimes \hat{P}_2$	$\text{Re}(\rho_{10,11})$
$\hat{U}_j^{(2)}$	$\hat{I}_1 \otimes \hat{P}_2$	$\text{Re}(\rho_{00,01})$
$\hat{U}_-^{(1)}(\frac{\pi}{4}) \hat{U}_+^{(2)}(\frac{\pi}{4})$	$\hat{P}_1 \otimes \hat{I}_2$	$\text{Re}(\rho_{00,11})$
$\hat{U}_+^{(1)}(\frac{\pi}{4}) \hat{U}_+^{(2)}(\frac{\pi}{4})$	$\hat{P}_1 \otimes \hat{P}_2$	$\text{Re}(\rho_{01,10})$
$\hat{U}_-^{(1)}(\frac{\pi}{4})$	$\hat{I}_1 \otimes \hat{P}_2$	$\text{Im}(\rho_{00,10})$
$\hat{U}_+^{(1)}(\frac{\pi}{4})$	$\hat{I}_1 \otimes \hat{P}_2$	$\text{Im}(\rho_{01,11})$
$\hat{U}_-^{(2)}(\frac{\pi}{4})$	$\hat{I}_1 \otimes \hat{P}_2$	$\text{Im}(\rho_{00,01})$
$\hat{U}_+^{(2)}(\frac{\pi}{4})$	$\hat{I}_1 \otimes \hat{P}_2$	$\text{Im}(\rho_{10,11})$
$\hat{U}_{co}$	$\hat{P}_1 \otimes \hat{P}_2$	$\text{Im}(\rho_{00,11})$
$\hat{U}_{co}$	$\hat{I}_1 \otimes \hat{P}_2$	$\text{Im}(\rho_{01,10})$

#### IV. DECAY OF MACROSCOPIC EPR PAIRS DUE TO GATE-VOLTAGE NOISE

The EPR pairs generated above are the eigenstates of the idle (i.e., no operations on it) circuit without any charge- and Josephson energies, and thus are long-lived, at least theoretically. Considering the influence of various disturbing perturbations, these pure quantum states will finally decay to the corresponding mixed states. In fact, experimental solid-state circuits are very sensitive to decoherence because of the coupling to the many degrees of freedom of the solid-state environment. However, coherent quantum manipulations on the generated EPR pairs are still possible if their decay times are not too short.

The typical noise sources in Josephson circuits consist of linear fluctuations of the electromagnetic environment (e.g., circuitry and radiation noises) and the low-frequency noise due to fluctuations in various charge/current channels (e.g., the background charge and critical current fluctuations). Usually, the former one behaves as Ohmic dissipation [29] and the latter one produces a  $1/f$  spectrum [30], which is still not fully understood in solid-state circuits (see, e.g., [31]). Here, we assume that the decay of the EPR pairs arises from linear environmental noises, i.e., we investigate the fluctuations of the gate voltages applied to the qubits. Moreover, the effect of background charges that cause dephasing are modeled by setting the zero-frequency part of the bath spectral function to a value given by the experimentally obtained [32] dephasing rates for the charge qubit system. The effect of gate-voltage noise on a single charge qubit has been discussed in [29]. We now study two such noises in a capacitively-coupled circuit. Each electromagnetic environment is treated as a quantum



system with many degrees of freedom and modeled by a bath of harmonic oscillators. Furthermore, each of these oscillators is assumed to be weakly coupled to the Cooper-pair boxes.

The Hamiltonian containing the fluctuations of the applied gate voltages can be generally written as

$$\tilde{H} = \hat{H} + \hat{H}_B + \hat{V},$$

with

$$\hat{H}_B = \sum_{j=1,2} \sum_{\omega_j} \left( \hat{a}_{\omega_j}^\dagger \hat{a}_{\omega_j} + \frac{1}{2} \right) \hbar \omega_j, \quad (20)$$

and

$$\hat{V} = \sigma_z^{(1)}(X_1 + \beta X_2) + \sigma_z^{(2)}(X_2 + \gamma X_1), \quad (21)$$

being the Hamiltonians of the two baths and their interactions with the two boxes. Here,

$$X_j = \frac{E_{C_j} C_{g_j}}{4e} \sum_{\omega_j} (g_{\omega_j}^* \hat{a}_{\omega_j}^\dagger + g_{\omega_j} \hat{a}_{\omega_j})$$

with  $\hat{a}_{\omega_j}, \hat{a}_{\omega_j}^\dagger$  being the Boson operators of the  $j$ th bath, and  $g_{\omega_j}$  the coupling strength between the oscillator of frequency  $\omega_j$  and the non-dissipative system. Due to the mutual coupling of the two Cooper pair boxes, there will be crosstalk of the noise affecting each qubit. This is modelled in the spin-boson model with two bosonic baths presented above by the terms with the additional factors  $\beta$  and  $\gamma$ . The amount of this crosstalk is given by the network of capacitances or the corresponding energies only; namely,  $\beta = E_m/2E_{C_2}$  and  $\gamma = E_m/2E_{C_1}$ , and by inserting experimental values one finds that  $\beta \approx \gamma \approx 1/10$ .

The effects of these noises can be characterized by their power spectra. The spectral density of the voltage noise for Ohmic dissipation can be expressed as

$$J(\omega) = \pi \sum_{\omega_j} |g_{\omega_j}|^2 \delta(\omega - \omega_j) \sim \pi \alpha \hbar \omega. \quad (22)$$

Here, a Drude cutoff with cutoff frequency  $\omega_c = 10^4$  GHz, which is well above all relevant frequency scales of the system, is introduced via  $J(\omega) = \alpha \hbar \omega \omega_c^2 / (\omega_c^2 + \omega^2)$ . Here,  $\alpha$  is a dimensionless constant characterizing the strength of the environmental effects. Introducing the impedance,  $Z_t(\omega) = 1/[i\omega C_t + Z^{-1}(\omega)]$ , the spectral function for these fluctuations could be expressed as  $J(\omega) = \omega \text{Re}(Z_t(\omega))$ . Here,  $Z(\omega) \sim R_V$  is the Ohmic resistor and  $C_t$  is the total capacitance connected to the Cooper-pair box.

The well-established Bloch-Redfield formalism [22, 33] provides a systematic way to obtain a generalized master equation for the reduced density matrix of the system, weakly influenced by dissipative environments. A subtle Markov approximation is also made in this theory such that the resulting master equation is local in time. In the regime of weak coupling to the bath and low temperatures, this theory is numerically equivalent to a full non-Markovian path-integral approach [34]. For the present case, a set of master equations

are obtained in the eigenbasis of the unperturbed Hamiltonian [29]

$$\dot{\rho}_{nm} = -i\omega_{nm} \rho_{nm} - \sum_{kl} R_{nmkl} \rho_{kl}, \quad (23)$$

with the Redfield tensor elements  $R_{nmkl}$  given by

$$R_{nmkl} = \delta_{\ell m} \sum_r \Gamma_{nrrk}^{(+)} + \delta_{nk} \sum_r \Gamma_{\ell rrm}^{(-)} - \Gamma_{\ell mnk}^{(-)} - \Gamma_{\ell mnk}^{(+)}, \quad (24)$$

and the rates  $\Gamma^{(\pm)}$  are given by the Golden Rule expressions

$$\Gamma_{\ell mnk}^{(+)} = \hbar^{-2} \int_0^\infty dt e^{-i\omega_{nk}t} \langle H_{I,\ell m}(t) H_{I,nk}(0) \rangle,$$

$$\Gamma_{\ell mnk}^{(-)} = \hbar^{-2} \int_0^\infty dt e^{-i\omega_{nk}t} \langle H_{I,\ell m}(0) H_{I,nk}(t) \rangle.$$

Here,  $H_{I,\ell m}(t)$  is the matrix element of the bath/system coupling term of the Hamiltonian in the interaction picture, and the brackets denote thermal average.

The strength of the dissipative effects is characterized by the dimensionless parameter  $\alpha$ . From experimental measurements of the noise properties of the charge qubit system [35], it is found that the strength of the Ohmic noise is given by

$$\alpha = \frac{4e^2 R}{\hbar \pi} \approx 1.8 \cdot 10^{-3}, \quad (25)$$

where  $R \approx 6 \Omega$ . Thus, current technology gives a noise floor of approximately  $\alpha \sim 10^{-3}$ , which will be used for the numerical simulations. For visualization of the decay of the Bell states, we compute the concurrence [36], given by

$$C = \max\{0, \sqrt{\lambda_1} - \sqrt{\lambda_2} - \sqrt{\lambda_3} - \sqrt{\lambda_4}\}. \quad (26)$$

Here, the  $\lambda_i$  are the eigenvalues of  $\rho \tilde{\rho}$  and  $\tilde{\rho} = (\sigma_y^1 \otimes \sigma_y^2) \rho^* (\sigma_y^1 \otimes \sigma_y^2)$ . The concurrence is a measure for entanglement and indicates non-locality. The maximally entangled Bell states (i.e., the ideal EPR correlations) yield a value of 1 whereas a fully separable state gives 0. The results of the simulations are shown in Fig. 2, where the time evolution of the concurrence  $C$  shows the decays of all Bell states, for temperature set to an experimentally feasible value of 10 mK. Compared to the durations of quantum manipulations ( $\sim 100$  ps), the lifetimes of the operationally idle EPR pairs are sufficiently long.

For the case where only the coupling term between the qubits is present and all single-qubit terms in the Hamiltonian are suppressed, Fig. 2(a) shows that the Bell states exponentially decay. In this case, only pure dephasing, i.e., the zero frequency value  $J(\omega = 0)$ , contributes to overall decoherence rates, as  $\hat{H} = \hat{H}_{\text{int}} = E_{12} \sigma_z^{(1)} \sigma_z^{(2)}$  and  $[\hat{H}, \hat{V}] = 0$ , see Ref. [37]. The results from microscopic calculations of the magnitude of  $1/f$ -noise in these structures are incorporated by introducing a peak in the spectral function at zero frequency. The magnitude of this peak is then determined

by the microscopic derivations of the strength of the  $1/f$ -noise in the superconducting charge qubits. Namely, here we set the zero frequency contribution, i.e., the dephasing due to the  $1/f$ -noise to an experimentally reported value of  $\Gamma_\varphi \approx 10^7$  Hz [32]. Note that the individual contributions from different noise sources sum up in the spectral function  $J(\omega) = J_f(\omega) + J_{1/f}(\omega)$ , which also holds at  $\omega = 0$ . It is interesting to note that the decay time is independent of the inter-qubit coupling strength  $E_{12}$ . In more detail, when the coupling energy  $E_{12}$  in the Hamiltonian is increased the decay does not change. The reason for this behavior is that the pure dephasing is only affected by the zero frequency part of the spectrum, which is obviously independent of the individual frequency splittings, i.e., the characteristic energy scale of the Hamiltonian. Also, one of the most important results from our numerical results (i.e., *the decay time of  $|\phi_\pm\rangle$  is longer than that of  $|\psi_\pm\rangle$* ) is consistent with the analog experimental one in ion traps [9]. This is because  $|\phi_\pm\rangle$  is superposed by two states with the same energy, while  $|\psi_\pm\rangle$  corresponds to higher energy and is more sensitive to such perturbations.

When the Josephson-tunneling terms exist, e.g.,  $E_J^{(1)} = E_J^{(2)} = E_J$ , we see from Fig. 2(b) that the decays of the generated EPR pairs are significantly faster than in the former case without any tunneling. This is because the additional Josephson tunneling provides additional decoherence channels since the Hamiltonian of the circuit now does not commute with the couplings to the baths. Moreover, also the overall energy scale in the Hamiltonian increases. In this case, the weaker interbit-coupling corresponds to the slower decay of the EPR pairs.

## V. TESTING BELL'S INEQUALITY

A possible application of the deterministically generated EPR pairs is to test BI at the macroscopic level. Due to the existence of interbit constant-coupling, the required local operations of encoding classical information  $\{\theta_j\}$  into the EPR pairs cannot be strictly implemented. In Ref. [21] we proposed an approach to overcome this difficulty by introducing the effective single-qubit operations including corrections due to the constant-coupling. Instead, here we approximately perform the encoded procedure by sequentially using the conditional single-qubit operations

$$\hat{U}_J^{(1)} = \begin{pmatrix} \vartheta_1 & \chi_1 & 0 & 0 \\ \chi_1 & \vartheta_1^* & 0 & 0 \\ 0 & 0 & \vartheta_1^* & \chi_1 \\ 0 & 0 & \chi_1 & \vartheta_1 \end{pmatrix},$$

and

$$\hat{U}_J^{(2)} = \begin{pmatrix} \vartheta_2 & 0 & \chi_2 & 0 \\ 0 & \vartheta_2^* & 0 & \chi_2 \\ \chi_2 & 0 & \vartheta_2^* & 0 \\ 0 & \chi_2 & 0 & \vartheta_2 \end{pmatrix},$$

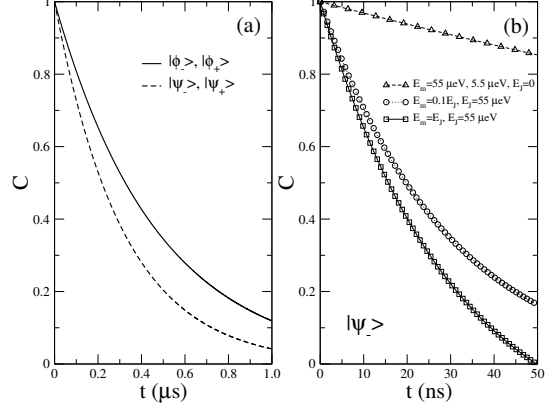


FIG. 2: Simulated time evolution of the concurrence  $C$  for a two-qubit system coupled to a noisy environment and initially prepared in the Bell states. Here, the temperature is set to  $T = 10$  mK and the strength of the dissipative effects for the two baths is  $\alpha^1 = \alpha^2 = 10^{-3}$ . (a) captures the long-time decay of the concurrence for different entangled input states in the case of vanishing single-qubit terms, i.e., when only the inter-qubit coupling terms are present. (b) compares the decays of  $|\psi_-\rangle$  for different interbit-couplings ( $E_m = E_J$ , and  $0.1E_J$ ) without ( $E_J^{(1)} = E_J^{(2)} = 0$ ), and with Josephson tunneling ( $E_J^{(1)} = E_J^{(2)} = E_J = 55 \mu\text{eV}$ ).

individually on the two qubits. The operation  $\hat{U}_J^{(j)}$  is not a strict single-qubit operation (although it only evolves the  $j$ th qubit), as it depends on the state of the  $k$ th qubit  $j \neq k = 1, 2$ . Above,  $\chi_j = i \sin \alpha_j \sin \beta_j$ ,  $\vartheta_j = \cos \beta_j - i \cos \alpha_j \sin \beta_j$ ,  $\cos \alpha_j = E_{12}/\gamma_j$ , and  $\gamma_j = \sqrt{E_{12}^2 + (E_J^{(j)}/2)^2}$ ,  $\beta_j = t\gamma_j/\hbar$ . For the case of  $\alpha_1 = \alpha_2 = \alpha$ , the validity of the above quasi-local encodings could be described by the variation of the degree of entanglement (i.e., *concurrence*) of the EPR pairs

$$\Delta C = 1 - \sqrt{1 - [\sin(2\alpha)(1 - \cos(2\varphi_1 + 2\varphi_2))]^2} \quad (27)$$

with  $\varphi_j = 2\beta_j$ . Obviously,  $\Delta C = 0$  corresponds to the ideal locality or maximal locality. After the encoding, we simultaneously detect [13] the populations of qubits and check if they are in the same logic states: the excited one  $|1\rangle$  or the ground state  $|0\rangle$ .

Theoretically, the correlation of two local variables,  $\varphi_1$  and  $\varphi_2$ , can be defined as the expectation value of the operator  $\hat{P}_T = |11\rangle\langle 11| + |00\rangle\langle 00| - |10\rangle\langle 10| - |01\rangle\langle 01| = \hat{\sigma}_z^{(1)} \otimes \hat{\sigma}_z^{(2)}$  and reads

$$E(\varphi_1, \varphi_2) = \cos^2 \alpha + \sin^2 \alpha \cos(\varphi_1 + \varphi_2). \quad (28)$$

Experimentally, all the above operational steps can be repeated many times in a controllable way for various parameter sets. As a consequence, the correlation function  $E$  can be measured by

$$E(\varphi_1, \varphi_2) = \frac{N_{\text{same}}(\varphi_1, \varphi_2) - N_{\text{diff}}(\varphi_1, \varphi_2)}{N_{\text{same}}(\varphi_1, \varphi_2) + N_{\text{diff}}(\varphi_1, \varphi_2)}, \quad (29)$$

TABLE II: Variations of the concurrence,  $\Delta C$ , correlations  $E$ , and CHSH-functions  $f$ , for certain typical parameters of the interbit coupling  $E_m$  and the controllable classical variables  $\varphi_1$  and  $\varphi_2$ .

$E_m$	$(\varphi_1, \varphi_2)$	$\Delta C$	$E(\varphi_1, \varphi_2)$	$f$
$E_J$	$(-\pi/8, -\pi/8)$	0.00699	0.76569	2.6627
	$(-\pi/8, 3\pi/8)$	0.00699	0.76569	
	$(3\pi/8, -\pi/8)$	0.00699	0.76569	
	$(3\pi/8, 3\pi/8)$	0.26943	-0.36569	
$E_J/10$	$(-\pi/8, -\pi/8)$	0.00238	0.72434	2.8264
	$(-\pi/8, 3\pi/8)$	0.00011	0.70784	
	$(3\pi/8, -\pi/8)$	0.00011	0.70784	
	$(3\pi/8, 3\pi/8)$	0.00363	-0.70285	
$E_J/100$	$(-\pi/8, -\pi/8)$	0.00001	0.70711	2.8284
	$(-\pi/8, 3\pi/8)$	0.00001	0.70711	
	$(3\pi/8, -\pi/8)$	0.00001	0.70711	
	$(3\pi/8, 3\pi/8)$	0.00004	-0.70706	

for any pair of chosen classical variables  $\varphi_1$  and  $\varphi_2$ . Here,  $N_{\text{same}}(\varphi_1, \varphi_2)$  ( $N_{\text{diff}}(\varphi_1, \varphi_2)$ ) are the number of events with two qubits found in the same (different) logic states. With these measured correlation functions, one can experimentally test the BI in macroscopic systems.

We consider the following typical set of angles:  $\{\varphi_j, \varphi'_j\} = \{-\pi/8, 3\pi/8\}$  and the interbit couplings  $E_m = 4E_{12} = E_J, E_J/10, E_J/100$ , respectively. The corresponding variations  $\Delta C$  of the concurrence and the correlation  $E(\varphi_1, \varphi_2)$ , which yields the Clauser, Horne, Shimony and Holt (CHSH) [3] function  $f = |E(\varphi_1, \varphi_2) + E(\varphi'_1, \varphi_2) + E(\varphi_1, \varphi'_2) - E(\varphi'_1, \varphi'_2)|$ , are given in Table II. It is seen that the variations  $\Delta C$  of the concurrence after the quasi-local operations  $\hat{U}_j^{(j)}$ ,  $j = 1, 2$  decrease with decreasing interbit coupling. For very weak coupling, e.g.,  $E_m/E_J = 0.1$  (or 0.01), the applied conditional single-qubit operations can be regarded as local, away from 0.4%, (or 0.004%). Besides these tiny loopholes of locality, Table II shows that the CHSH-type Bell's inequality [3]

$$f(|\psi'_+\rangle) < 2 \quad (30)$$

is obviously violated.

## VI. DISCUSSION AND CONCLUSION

Similar to other theoretical schemes (see, e.g., Ref. [18]) the realizability of the present proposal also faces certain technological challenges, such as the rapid switching of the charge-

and Josephson energies of the SQUID-based qubits and decoherence due to the various environmental noises. Our numerical results, considering various typical fluctuations, showed that the lifetime of the generated EPR pairs adequately allows to perform the required operations for experimentally testing Bell's inequality. Indeed, for current experiments [12], the decay time of a *two*-qubit excited state is as long as  $\sim 0.6$  ns, even for the very strong interbit coupling, e.g.,  $E_m \simeq E_J$ . Longer decoherence times are possible for weaker interbit couplings. In addition, for testing this, the influence of the environmental noises and operational imperfections is not fatal, as the nonlocal correlation  $E(\varphi_i, \varphi_j)$  in Bell's inequality is statistical — its fluctuation could be effectively suppressed by the averages of many repeatable experiments.

In summary, for the experimentally demonstrated capacitively-coupled Josephson nanocircuits, we found that several typical two-qubit quantum operations (including simultaneously flipping the two qubits and only evolving a selected qubit in the case of leaving the other one unchanged) could be easily implemented by properly setting the controllable parameters of circuits, e.g., the applied gate voltages and external fluxes. As a consequence of this, macroscopic EPR correlated pairs could be deterministically generated from the ground state  $|00\rangle$  by two conditional single-qubit operations; only superposing two logic states of the selected qubit and then only flipping one of the two qubits. During these operations, the left qubit does not evolve. To experimentally confirm the proposed generation schemes, we also propose an effective tomographic technique for determining all density matrix elements of the prepared states by a series of quantum projective measurements. The deterministically generated EPR pairs provide an effective platform to test, at the macroscopic level, certain fundamental principles, e.g., the non-locality of quantum entanglement via violating the Bell's inequality.

The approach proposed here can be easily modified to engineer quantum entanglement in other “fixed-interaction” solid-state systems, e.g., capacitively (inductively) coupled Josephson phase (flux) system and Ising (Heisenberg)-spin chains.

## Acknowledgments

We acknowledge useful discussions with Drs. J.Q. You, J.S. Tsai, O. Astafiev, S. Ashhab and F.K. Wilhelm. MJS gratefully acknowledges financial support of RIKEN and the DFG through SFB 631. This work was supported in part by the National Security Agency (NSA) and Advanced Research and Development Activity (ARDA) under Air Force Office of Research (AFOSR) contract number F49620-02-1-0334, and by the National Science Foundation grant No. EIA-0130383.

[1] A. Einstein, B. Podolsky, N. Rosen, Phys. Rev. **41**, 777 (1935).

[2] J. Bell, Phys. **1**, 195 (1964).

[3] See, e.g., G. Weihs, T. Jennewein, C. Simon, H. Weinfurter,

and A. Zeilinger, Phys. Rev. Lett. **81**, 5039 (1998); A. Aspect, J. Dalibard, and G. Roger, *ibid.* **49**, 1804 (1982); W. Tittel, J. Brendel, H. Zbinden, and N. Gisin, *ibid.* **81**, 3563 (1998).

- [4] A. Barmon, *Phys. Rev. Lett.*, **83**, 1 (1999).
- [5] B.J. Oliver and C.R. Stroud, Jr., *J. Opt. Soc. Am. B*, **4**, 1426 (1987); J.I. Cirac and P. Zoller, *Phys. Rev. A* **50**, R2799 (1994).
- [6] R. Ionicioiu, P. Zanardi, and F. Rossi, *Phys. Rev. A* **63**, 050101(R) (2001).
- [7] L.F. Wei and F. Nori, *Europhys. Lett.* **65**, 1 (2004); L.F. Wei, Yu-xi Liu, and F. Nori, *Phys. Rev. A* **70**, 063801 (2004); E. Solano, R.L. de Matos Filho, and Z. Zagury, *Phys. Rev. A* **59**, R2539 (1999).
- [8] E. Hagley, X. Maitre, G. Nogues, C. Wunderlich, M. Brune, J.M. Raimond, and S. Haroche, *Phys. Rev. Lett.* **79**, 1 (1997).
- [9] C. F. Roos, G. P. T. Lancaster, M. Riebe, H. Häffner, W. Hänsel, S. Gulde, C. Becher, J. Eschner, F. Schmidt-Kaler, and R. Blatt, *Phys. Rev. Lett.* **92**, 220402 (2004).
- [10] M.A. Rowe, D. Kiepiniski, V. Meyer, C.A. Sackett, W.M. Itano, C. Monroe, and D.J. Wineland, *Nature* **409**, 791 (2001).
- [11] D. L. Moehring, M. J. Madsen, B. B. Blinov, and C. Monroe, *Phys. Rev. Lett.* **93**, 090410 (2004).
- [12] Yu. P. Pashkin, T. Yamamoto, O. Astafiev, Y. Nakamura, D.V. Averin, and J.S. Tsai, *Nature*, **421**, 823 (2003).
- [13] R. McDermott, R.W. Simmonds, M. Steffen, K.B. Cooper, K. Cicak, K.D. Osborn, S. Oh, D.P. Pappas, and J.M. Martinis, *Science*, **307**, 1299 (2005).
- [14] G. P. Berman, A. R. Bishop, D. I. Kamenev, and A. Trombettoni, *Phys. Rev. B* **71**, 014523 (2005).
- [15] A. Blais, A. M. van den Brink, and A. M. Zagoskin, *Phys. Rev. Lett.* **90**, 127901 (2003).
- [16] L. F. Wei, Yu-xi Liu, and F. Nori, *Europhys. Lett.* **67**, 1004 (2004); *Phys. Rev. B* **71**, 134506 (2005).
- [17] H. Tanaka, Y. Sekine, S. Saito, and H. Takayanagi, *Super. Sci. Tech.* **14**, 1161 (2001).
- [18] Y. Makhlin, G. Schön, A. Shnirman, *Nature* **398**, 305 (1999); J.Q. You, S.J. Tsai, and F. Nori, *Phys. Rev. Lett.* **89**, 197902 (2002).
- [19] J. Q. You and F. Nori *Phys. Rev. B* **68**, 064509 (2003); G.P. He, S.L. Zhu, Z.D. Wang, and H.Z. Li, *Phys. Rev. A* **68**, 012315 (2003).
- [20] J. Q. You, J. S. Tsai, and F. Nori, *Phys. Rev. B* **68**, 024510 (2003).
- [21] L.F. Wei, Yu-xi Liu, and F. Nori, arXiv: quant-ph/0408089; *Phys. Rev. B* (in press).
- [22] P.N. Argyres and P.L. Kelley, *Phys. Rev.* **134**, A98 (1964).
- [23] T. Yamamoto, Yu. P. Pashkin, O. Astafiev, Y. Nakamura, and J.S. Tsai, *Nature*, **425**, 941 (2003).
- [24] A. Barenco, C.H. Bennett, R. Cleve, D.P. DiVincenzo, N. Margolus, P. Shor, T. Sleator, J.A. Smolin, and H. Weinfurter, *Phys. Rev. A* **52**, 3457 (1995).
- [25] I. L. Chuang, N. Gershenfeld, M. G. Kubinec, and D. Leung, *Proc. R. Soc. London, Ser. A* **454**, 447 (1998).
- [26] A. G. White, D. F. V. James, W. J. Munro, and P. G. Kwiat, *Phys. Rev. A* **65**, 012301 (2001); A. G. White, D. F. V. James, P. H. Eberhard, and P. G. Kwiat, *Phys. Rev. Lett.* **83**, 3103 (1999).
- [27] Yu-xi Liu, L.F. Wei, and F. Nori, *Europhys. Lett.* **67**, 874 (2004); *Phys. Rev. B* **72**, 014547 (2005).
- [28] Y. Nakamura, Yu. A. Pashkin and J.S. Tsai, *Nature*, **398**, 786 (1999).
- [29] U. Weiss, *Quantum Dissipative systems*, 2nd ed., World Scientific, Singapore, 1999; Y. Makhlin, G. Schön, and A. Shnirman, *Rev. Mod. Phys.* **73**, 357 (2001).
- [30] A. Shnirman, G. Schön, I. Martin, and Y. Makhlin, *Phys. Rev. Lett.* **94**, 127002 (2005); E. Paladino, L. Faoro, G. Falci, and R. Fazio, *Phys. Rev. Lett.* **88**, 228304 (2002).
- [31] H. Gutmann, F.K. Wilhelm, W.M. Kaminsky, S. Lloyd, cond-mat/0308107; G. Falci, A. D'Arrigo, A. Mastellone, E. Paladino, cond-mat/0312442.
- [32] O. Astafiev, private communication (2005).
- [33] M.C. Goorden and F.K. Wilhelm, *Phys. Rev. B* **68**, 012508 (2003).
- [34] L. Hartmann, I. Goychuk, M. Grifoni, and P. Hänggi, *Phys. Rev. E* **61**, R4687 (2000).
- [35] O. Astafiev, Yu. A. Pashkin, Y. Nakamura, T. Yamamoto, and J. S. Tsai *Phys. Rev. Lett.* **93**, 267007 (2004).
- [36] W.K. Wootters, *Phys. Rev. Lett.* **80**, 2245 (1997).
- [37] M. J. Storcz and F. K. Wilhelm, *Phys. Rev. A* **67**, 042319 (2003).

# Chapter 12

## Circuit-QED – quantum optics in the solid-state

### 12.1 Introduction

Quantum optics and cavity quantum electrodynamics (cQED), as already introduced in chapter 5, have been very successful in the exploration of fundamental physics of quantum systems (including the measurement process and decoherence) and quantum computation [44, 45, 174, 176]. In quantum optics, the generation of photons in entangled states can be achieved by using the atomic cascades or parametric down-conversion [176], which converts a photon into two entangled photons of smaller energy. Moreover, in quantum optics, the polarization of photon states can be manipulated and the photons can be detected with a high detector efficiency [174, 176]. The generation of non-classical states of light [247], the teleportation of quantum states [248–250], and quantum cryptography with correlated photons [251, 252] are just a few examples of important successful experiments that were performed in quantum optics. Yet, a drawback of the quantum optics setups for quantum computation is that there is no efficient coupling between photons.

In cavity quantum electrodynamics (cQED) mixed atom and photon systems that can interact inside a resonator are considered [176]. In cQED experiments, a neutral atom falls through high finesse cavities, *i.e.*, resonators with a large quality factor, and strong coupling between the atom and the photon (field) is achieved [253]. The cQED setup has been used to investigate quantum effects in great detail [254, 255], however, the fast time evolution in optical systems hindered the direct study of entanglement in these systems. Photon states with a fixed number of photons have been generated on demand in cQED [256] and even the measurement of the Wigner functions of an optical single-photon Fock state with quantum state tomography has been performed [257]. Microwave cQED [258] experiments show little relaxation and the atom and cavity are easily prepared in pure states, moreover, as was already mentioned before, the setups are operated in the strong coupling regime.

The strong coupling regime refers to the regime where the coupling between the atom

and the photon field inside the cavity is strong compared to the cavity loss rate  $\kappa$  and the atom decay rate  $\gamma$ . For 3D microwave cavities, the vacuum Rabi frequency that characterizes the coupling strength between the atom and the cavity is typically on the order of  $g/\pi \approx 50$  kHz, the cavity decay rate is  $\kappa \approx 1$  kHz, and the atom decay rate is  $\gamma \approx 30$  kHz [176].

The idea of operating a superconducting solid-state qubit inside a cavity has been introduced already some time ago for both charge qubit [259] and flux qubit (rf-SQUID) setups [260, 261]. Also the preparation of macroscopic superpositions of cavity field states for this type of cavity-qubit setup [262] and the generation of nonclassical photon states [263] has been proposed. The successful experiments performed with a superconducting charge qubit inside a cavity (a coplanar resonator) [178] showed a very impressive agreement with the theoretical predictions both for the dynamics and decoherence of the cavity-qubit system [143]. However, the generation of true quantum entanglement with artificial atoms and photons inside a cavity [176] has not been demonstrated yet for a solid-state qubit setup. Still, many of the concepts from quantum optics, such as for example electromagnetically induced transparency that can be exploited to generate macroscopic quantum coherence in superconducting qubits [264], are successfully applied to artificial atoms in solid-state systems.

In summary, the important advantages of the solid-state setup compared to quantum optics setups are that the coupling strength between the qubit and the cavity can be made very large and that the qubit is fixed inside the cavity, *i.e.*, the interaction time between the qubit and the cavity field is very large. Differently from quantum optics, in the solid-state setup the cavity field is measured and not the atom. The state of the qubit can be inferred by measuring the output field of the cavity. Thus, in order to achieve an appreciable signal strength for the measurement, it is necessary that the quality factor  $Q$  of the resonator is not too large (or in other words the cavity decay rate has to be sufficiently large).

## 12.2 Deterministic single microwave photon generation and detection

A single microwave photon that is created by a certain transition in one qubit carries information about the state of the qubit and can be used as an information bus, *e.g.*, to mediate entanglement between qubits. Also, these single photons could be used for quantum cryptography applications in solid-state devices and are eventually just the starting point for interfacing the solid-state and the quantum optics domain.

The special setting of a superconducting resonator as a cavity that is operated with photons in the microwave domain is quite different from the setups in quantum optics experiments. First experiments with microwave photons travelling in conductors used *Hanbury Brown and Twiss* (HBT) correlations [265–267] to measure the super-Poissonian and Poissonian photon statistics of a thermal and a coherent photon source [180].

Now, important differences and properties of the solid-state setup compared to quantum

optics experiments will be discussed. First, note that the normal conducting part of the setup, *e.g.*, the microwave generators at room temperature, has *no* shot noise but Johnson-Nyquist noise, whereas the superconducting part has no intrinsic electronic shot noise but photon shot noise. A single microwave photon that is generated from a transition in a rf-SQUID or 3jj flux qubit and travels through the superconducting resonator can be viewed as a plane wave inside the waveguide. There are several possible loss mechanisms for this electromagnetic wavepacket, namely

- Static or dynamic charge disorder,
- Magnetic impurities in the superconductor,
- Dispersion of the electromagnetic wavepacket.

For the superconducting waveguide, the fabrication in niobium (Nb) technology will be considered in most detail. Static or dynamic charge disorder have been shown to be negligible, see Ref. [268], which follows from the large quality factor  $Q$  for the resonances that are associated with the Mooij-Schön modes [268] because the photon itself can also be viewed as a quantum of the Mooij-Schön mode [268, 269]. Magnetic impurities in the Nb can be analyzed via data for the density of states in the gap or subgap tunnel conductance. The data presented in Ref. [270] suggests that the effect of magnetic impurities is also negligible. Thus, it can be shown from an effective circuit model of the superconducting waveguide or transmission line that the dispersion relation for the photon wavepacket is linear. Therefore, the wavepacket will be destroyed only after a significant distance that is estimated to be about one kilometer in the superconductor.

The microwave photon inside the cavity can be generated by an appropriate transition of a rf-SQUID or a 3jj flux qubit, cf. chapter 2.1.2. Here, it is favorable to make use of the rf-SQUID or 3jj flux qubit as a multi-level system. This is due to the fact that if a driving that is resonant with the qubit is applied in order to populate the excited qubit level for the generation of photons, the cavity will also be driven. This happens because the cavity has to be on resonance with the transition that will generate the photon. Thus, a more elaborate scheme is required for the single photon generation. It can be realized, *e.g.*, via stimulated Raman adiabatic passage [271] or a Raman pulse.

For the general rf-SQUID  $N$ -level system, the interaction Hamiltonian that describes the coupling between the system and the cavity [260, 272, 273] is given by

$$H_I = -\frac{1}{L}(\hat{\Phi} - \Phi_x)\hat{\Phi}_c \quad (12.1)$$

$$= (a + a^\dagger)\left(\sum_i g_{ii} |i\rangle \langle i| + g_{01}a |0\rangle \langle 1| + g_{01}a^\dagger |0\rangle \langle 1| + g_{12}a |1\rangle \langle 2| + \dots\right), \quad (12.2)$$

where the coupling constants are defined as

$$g_{ij} = -\frac{1}{L}\sqrt{\hbar\omega_c}2\mu_0(\langle i|\hat{\Phi}|j\rangle - \delta_{ij}\Phi_x)\Phi'_c, \quad (12.3)$$

where  $\Phi'_c = \int_S \mathbf{B}(\mathbf{r}) \cdot d\mathbf{S}$  is the time independent part of the flux generated by the resonator field, which is threading the qubit loop. The complete expression for the cavity flux, cf. also appendix F, is

$$\Phi_c = \int_S \mathbf{B}(\mathbf{r}, t) \cdot d\mathbf{S}, \text{ with } \mathbf{B}(\mathbf{r}, t) = \sqrt{\frac{\hbar\omega_c}{2\mu_0}} (a(t) + a^\dagger(t)) \mathbf{B}(\mathbf{r}, t). \quad (12.4)$$

For calculation of the coupling strength between the cavity and the qubit, which is determined by the  $g_{ij}$ , it is necessary to compute the eigenstates  $|i\rangle$  of the system Hamiltonian. This can be easily done numerically either in the charge or phase basis. The total flux in the qubit loop is the sum of the externally applied flux and the so-called screening flux, which appears because of the finite self inductance of the qubit loop

$$\Phi = \Phi_x + \Phi_s. \quad (12.5)$$

For a 3jj flux qubit with a negligible self-inductance, the so-called *screening current* is usually disregarded. In this case the expectation value of the total flux  $\langle i|\Phi|j\rangle$  will vanish at the degeneracy point of the qubit, where the state of the qubit is in an equal superposition state of clockwise and counter-clockwise rotating currents. Due to the small but finite self-inductance of the real qubit, it is most convenient to view the screening current as a perturbation

$$\Phi_s = LI_s = LI_c \sin(\phi_1) = LI_c \sin(\phi_2), \quad (12.6)$$

which is induced in the qubit loop. The screening current essential gives the coupling between the cavity and the qubit. In the qubit eigenbasis it can be viewed as completely off-diagonal, mediating the coupling strengths  $g_{ij}$  with  $i \neq j$ . The coupling strengths that are presented in the paper of this chapter were calculated from numerical simulations of the cavity-qubit Hamiltonian and the mutual inductive coupling.

Next, a detection scheme for the detection of photons with different frequencies is required. This can be realized, *e.g.*, by a (non-)linear mixing with another radiation at a certain reference frequency. The basic interferometric setup is the same both for a homodyne and a heterodyne readout scheme. In a homodyne scheme, the reference radiation, *i.e.*, the local oscillator, stems from the same source as the photon, or more generally, the signal that is to be measured. For heterodyne detection the difference is that the reference radiation comes from a different source. For example in a laser scattering experiment with homodyne detection, the laser light is separated into two beams. Then one of the beams is used to perform an experiment and the scattered photons should be read out after the experiment. This radiation is mixed with the other laser beam that acts as a local oscillator. Then the resulting measurement can be made insensitive to fluctuations of the laser frequency.

### 12.3 Flux qubit inside a cavity

A flux qubit could be coupled either to the e.m. field inside a coplanar waveguide or to the field inside a microstrip resonator. The microstrip resonator, which is essentially a coil



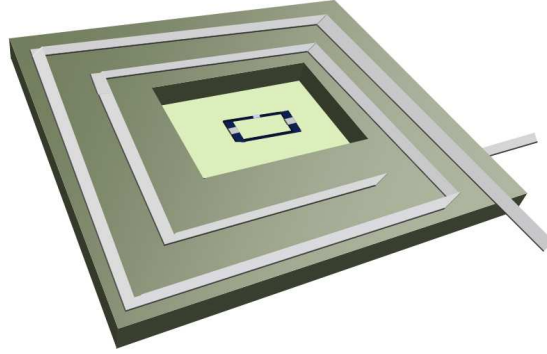


Figure 12.1: Artist view of the microstrip resonator (coil shape) with a flux qubit fabricated inside. The capacitors at the input and output ports of the microstrip coil set the boundary conditions for the electromagnetic waves inside the resonator. The qubit is to be fabricated in Al technology and the resonator in Nb technology, parameters are given in the text.

with a ground plane that is at both ends interrupted by capacitors, has the advantage of very strong inductive coupling to the qubit, see appendix F.

The resonance frequency of the microstrip resonator is carefully designed to be approximately 10 GHz, *i.e.*, it is in the microwave domain. Microstrip resonators have already been fabricated and operated with resonance frequencies ranging from several hundred MHz [275] up to several GHz [276].

The qubit is then fabricated in the middle of the resonator loop. It is directly inductively coupled to the resonator, which is wrapped up as a coil around the qubit loop in order to maximize the mutual coupling. This mutual inductive coupling via a current-current coupling of the type  $H_I = M_{qc} \hat{I}_q \hat{I}_c$ , leads to a coupling of the qubit  $\hat{\sigma}_z$ -coordinate to the cavity field. The Hamiltonian of the joint qubit-resonator system is [260, 261, 272, 277]

$$H = -\frac{1}{2}\epsilon\hat{\sigma}_z - \frac{1}{2}\Delta\hat{\sigma}_x - \hbar g(a^\dagger + a)\hat{\sigma}_z + \hbar\omega_r \left( a^\dagger a + \frac{1}{2} \right). \quad (12.7)$$

The coupling strength  $g$  between the qubit and the cavity mode is analytically estimated in appendix F. Numerical simulations of the cavity-qubit Hamiltonian and the mutual inductive coupling between the qubit and the microstrip resonator loop agree well with these calculations. For typical qubit parameters [90] and assuming that the microstrip resonator is fabricated as a Nb coil, a coupling strength of  $g/\pi \approx 100 - 200$  MHz is found<sup>1</sup>

In the eigenbasis of the system part of the Hamiltonian, the full Hamiltonian becomes

$$H = -\frac{1}{2}E\rho_z + \hbar g(a^\dagger + a)(\sin(\theta)\rho_x + \cos(\theta)\rho_z) + H_c, \quad (12.8)$$

<sup>1</sup>The calculations of the mutual inductive coupling were performed with the software FastHenry (developed at the Research Laboratory of Electronics, MIT Cambridge, MA USA).

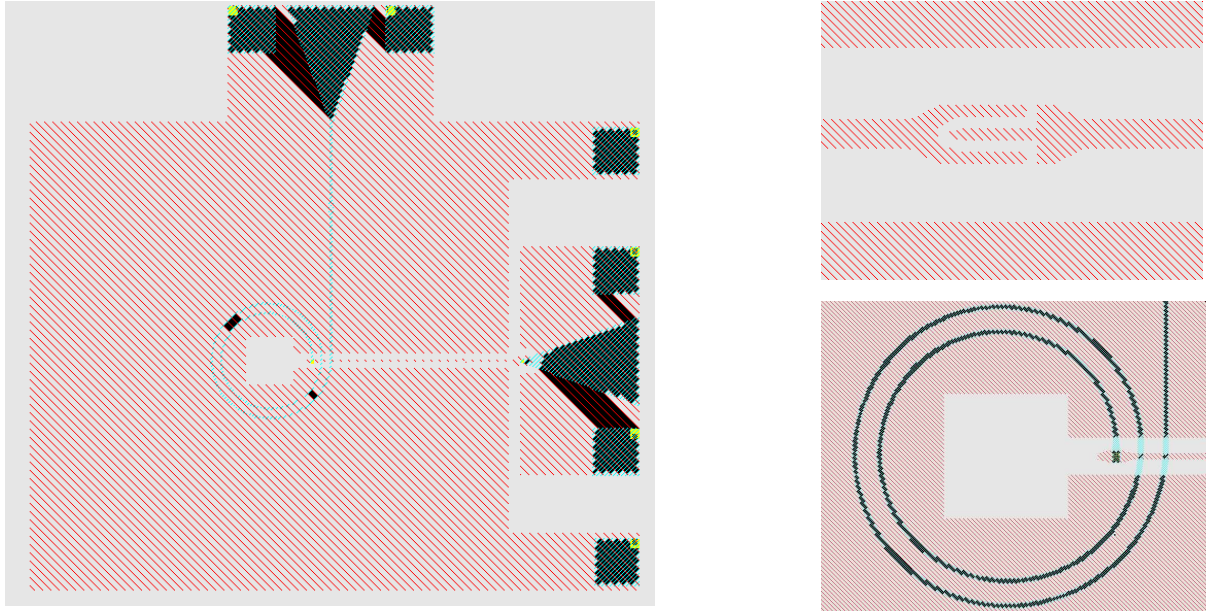


Figure 12.2: Circuit design of the microstrip resonator. The left panel shows the whole circuit board, whereas the upper right panel depicts one of the capacitances that define the boundary conditions. The lower right panel is a close up of the microstrip coil. The qubit will be fabricated inside the coil, cf. Fig. 12.1. The pictures are from the actual sample design that was developed at the Walther-Meissner-Institute in Garching [274].

where  $E = \sqrt{\epsilon^2 + \Delta^2}$ ,  $\theta = \arctan(\Delta/\epsilon)$  is the so-called *mixing angle* [74], and  $H_c$  is the free energy of the cavity mode. At the qubit degeneracy point  $\theta = \pi/2$  and thus

$$H = -\frac{1}{2}\Delta\rho_z + \hbar g(a^\dagger\rho^- + a\rho^+) + H_c + H_\kappa + H_\gamma, \quad (12.9)$$

where a rotating wave approximation that neglects the rapidly rotating terms was made in the qubit-cavity coupling and the two extra terms  $H_\kappa$  and  $H_\gamma$  describe the cavity and qubit decay, respectively. The cavity decay rate  $\kappa = \omega_c/Q$  can, depending on the quality factor of the cavity, be fabricated to be approximately 1 MHz. Here, the tradeoff is between having a sufficiently strong signal for the readout and a sufficiently small decay rate in order to be still in the strong coupling regime  $g/\pi \gg \gamma, \kappa$  of cQED. The qubit decay rates are typically on the order of a MHz, corresponding to coherence times of approximately 1  $\mu s$  [85, 93].

Due to the effective impedance transformation of the cavity, the qubit can be very well decoupled from electronics noise. However, it is of course not possible to decouple from noise that is intrinsic to the qubit, *e.g.*, fluctuators in the Josephson tunnel junctions.

It is also interesting to note that it is possible to generate squeezed vacuum states with the non-linearities inherently present in SQUID devices [278].

### 12.3.1 The dispersive readout

The Hamiltonian of the cavity-qubit system at the qubit degeneracy point, and with neither taking into account the qubit nor the cavity decay, is given in the interaction picture with regard to the oscillator mode as

$$H = -\frac{1}{2}\Delta\rho_z + \hbar g(a^\dagger e^{i\Omega t}\rho^- + ae^{-i\Omega t}\rho^+), \quad (12.10)$$

where  $\Omega = \omega_{\text{mw}} - \omega_c$  is given by the frequency of the external driving and the cavity resonance frequency. The transformation of this Hamiltonian into the interaction picture with respect to the qubit system leads to

$$H_I''(t) = \hbar g(|e\rangle\langle g| ae^{-i\Omega t}e^{i\Delta/\hbar t} + |g\rangle\langle e| a^\dagger e^{i\Omega t}e^{i\Delta/\hbar t}), \quad (12.11)$$

where  $|g\rangle$  and  $|e\rangle$  denote the ground and excited states in the qubit eigenbasis. When the frequency difference between the qubit system and the resonator  $\delta = \Omega - \Delta/\hbar$  is introduced the Hamiltonian can be simplified further

$$H_I''(t) = \hbar g(|e\rangle\langle g| ae^{-i\delta t} + |g\rangle\langle e| a^\dagger e^{i\delta t}). \quad (12.12)$$

Thus, in this interaction picture the time-dependent Hamiltonian can be written in the form [279]

$$H_I(t) = \hbar \sum_j \left[ A_j^\dagger e^{-i\delta_j t} + A_j e^{i\delta_j t} \right], \quad (12.13)$$

where  $A_j^\dagger$  is composed of time-independent system operators, and obtained from comparison of Eqns. (12.12) and (12.13). It has been shown [279, 280] that for  $|\delta_j| \gg g_j, \forall j$ , and  $|\delta_j + \delta_k| \gg g_k, \forall j \neq k$ , the Dyson series for the propagator associated with the Hamiltonian Eqn. (12.13) can be written as  $U = \exp(-iH_{\text{eff}}t/\hbar)$  with

$$H_{\text{eff}} = \hbar \sum_j \frac{[A_j^\dagger, A_j]}{\delta_j}. \quad (12.14)$$

This method can be applied to the Hamiltonian Eqn. (12.12) and yields the effective Hamiltonian

$$H_{\text{eff}} = \hbar \frac{g^2}{\delta} (|e\rangle\langle e| (a^\dagger a + 1) - |g\rangle\langle g| a^\dagger a), \quad (12.15)$$

which clearly shows the AC-Stark shift in the dispersive regime  $|\delta| \gg g$ , *i.e.*, the cavity frequency is shifted depending on the state of the qubit. Note that this readout scheme is a QND measurement, because clearly  $[H_S, \hat{\sigma}_z] = 0$ .



## Generation of Microwave Single Photons and Homodyne Tomography on a Chip

M. Mariani<sup>1,\*</sup>, M.J. Storz<sup>2</sup>, F.K. Wilhelm<sup>2</sup>, W.D. Oliver<sup>3</sup>,  
A. Emmert<sup>1</sup>, A. Marx<sup>1</sup>, R. Gross<sup>1</sup>, H. Christ<sup>4</sup>, and E. Solano<sup>4,5</sup>

<sup>1</sup>Walther-Meissner-Institut, Bayerische Akademie der Wissenschaften,  
Walther-Meissner-Strasse 8, D-85748 Garching, Germany

<sup>2</sup>Department Physik, CeNS and ASC, LMU, Theresienstrasse 37, D-80333 München, Germany

<sup>3</sup>MIT Lincoln Laboratory, 244 Wood Street, Lexington, Massachusetts 02420, USA

<sup>4</sup>Max-Planck Institute for Quantum Optics, Hans-Kopfermann-Strasse 1, D-85748 Garching, Germany

<sup>5</sup>Sección Física, Departamento de Ciencias, Pontificia Universidad Católica del Perú, Apartado 1761, Lima, Peru

We show that flux-based qubits can be coupled to superconductive resonators by means of a quantum-optical Raman excitation scheme and utilized for the deterministic generation of propagating microwave single photons. We introduce also a microwave quantum homodyning technique that enables the detection of single photons and other weak signals, and full state reconstruction via quantum tomography, realizing linear optics on a chip. These generation and detection protocols are building blocks for the advent of quantum information processing in the field of circuit QED.

PACS numbers: 85.25.-j, 42.50.Pq, 42.50.Dv, 03.65.Wj

arXiv:cond-mat/0509737 v1 28 Sep 2005

A two-level atom coupled to a single mode of a quantized electromagnetic field is arguably the most fundamental system exhibiting matter-radiation interplay. Their interaction, described by the Jaynes-Cummings (JC) model, arises naturally in the realm of cavity quantum electrodynamics (CQED) in the microwave [1] and optical domains [2]. There, a variety of nonclassical states (e.g., squeezed, Schrödinger cat, and Fock states [3]), among other remarkable phenomena and applications (e.g., entanglement and elements of quantum logic [4]), have been proposed and realized. Other physical systems, like trapped ions [5], can reproduce the JC dynamics and, consequently, exploit this analogy for similar purposes. The intracavity field in CQED and the motional field in trapped ions are typically detected through a suitable transfer of information to measurable atomic degrees of freedom [1, 5]. In the case of propagating photonic fields [6], homodyne detection leads to full state reconstruction by means of quantum tomography [7]. Given its relevance for quantum communication, single-photon sources have been pursued in the optical domain [8, 9]. Recently, several CQED-related experiments have been performed in tunable, solid-state systems. Quantum dots in photonic band-gap structures have been used as single photon sources [10] and superconducting charge qubits [11] have been coupled to on-chip cavities [12]. In addition, microwave squeezing with Josephson parametric amplifiers [13] and aspects of the quantum-statistical nature of GHz photons in mesoscopic conductors have been demonstrated [14].

In this Letter, we show how to implement a deterministic source of microwave single photons at the output of a superconducting resonator containing a flux qubit. A Raman-like scheme [15] determines the coupling between the cavity and the qubit, consisting of the two ground states of a three-level system in a  $\Lambda$ -type configuration [16, 17]. Furthermore, we show that these sin-

gle photons can be measured by means of a microwave quantum homodyne detection (MQHD) scheme, based on a superconducting hybrid ring [18] acting as an on-chip microwave beam splitter (MBS). In this way, full state reconstruction of an arbitrary traveling field can be realized via microwave quantum homodyne tomography (MQHT), a natural application of homodyning techniques [7]. The generation of propagating microwave single photons in a controlled way and an appropriate measurement apparatus represent building blocks to establish on-chip quantum information transfer between qubits.

A prototypical example of a flux-based quantum circuit is the radio-frequency (RF) superconducting quantum-interference device (SQUID) [19], a superconducting loop interrupted by a single Josephson tunnel junction. The RF SQUID Hamiltonian is

$$\hat{H}_S = \frac{\hat{Q}^2}{2C_j} + \frac{(\hat{\Phi} - \Phi_x)^2}{2L_s} - E_J \cos\left(2\pi \frac{\hat{\Phi}}{\Phi_0}\right), \quad (1)$$

where  $\hat{Q}$  is the charge stored on the junction capacitor  $C_j$ ,  $\hat{\Phi}$  is the total flux threading the loop (with  $[\hat{\Phi}, \hat{Q}] = i\hbar$ ),  $\Phi_x$  is an externally applied quasi-static flux bias,  $L_s$  is the self-inductance of the loop,  $E_J \equiv I_{c0}\Phi_0/2\pi$  is the Josephson coupling energy,  $I_{c0}$  is the junction critical current, and  $\Phi_0 = h/2e$  is the flux quantum. For appropriate design parameters, and close to half-integer values of  $\Phi_x/\Phi_0$ , the RF SQUID potential profile becomes a relatively shallow double well whose asymmetry can be tuned by setting  $\Phi_x$  (see Fig. 1). In this case, the two lowest eigenstates  $|g\rangle$  and  $|e\rangle$  are localized in the left and right wells, respectively, whereas the second excited state  $|h\rangle$  is delocalized with energy above the barrier. As will be shown later, these levels are suitable for implementing a Raman excitation scheme. The energy levels can be tuned by statically biasing  $\Phi_x$  during the experiment, and transitions between states are driven by pulsed ac excitations. Other flux-based devices can also be used

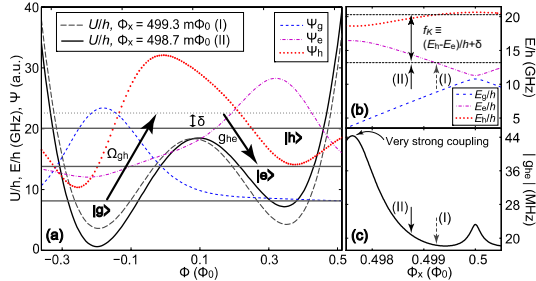


FIG. 1: (a) (Color online) Potential profile of the RF SQUID for two distinct values of  $\Phi_x$  (I) and (II) and wave functions for the first three lowest energy levels ( $|g\rangle$ ,  $|e\rangle$ , and  $|h\rangle$ ). Parameters are given in Table I. The Raman scheme is indicated with arrows. (b) RF SQUID energy-band diagram near  $\Phi_0/2$  plotted vs.  $\Phi_x$ . Zero detuning case, point (I), and large detuning case, point (II). (c) Absolute value of the vacuum Rabi frequency  $g_{he}$  as a function of  $\Phi_x$ . The coupling reaches 40 MHz at the anticrossing between levels  $|e\rangle$  and  $|h\rangle$ .

for the purposes of this work, for instance, persistent-current (PC) qubits [20], which have been demonstrated to possess relatively large excited-state lifetimes [21].

The segment of superconducting coplanar waveguide (CWG) shown in Figs. 2 (a), (b), and (d) is one realization of a monolithic resonator. Such a resonator is characterized by eigenenergies with transition angular frequencies  $\omega_k$  that are much larger than the thermal energy at cryogenic temperatures. Its Hamiltonian is  $\hat{H}_C = \sum_k \hbar\omega_k (\hat{a}_k^\dagger \hat{a}_k + 1/2)$ , where  $\hat{a}_k^\dagger$  and  $\hat{a}_k$  are the bosonic creation and annihilation operators for mode  $k$ . Voltage and current, corresponding to electric and magnetic fields, respectively, are conjugate operators associated with the quantized resonator,  $\hat{I}_C(z, t) = (\partial/\partial t) \hat{v}(z, t)$ , where  $z$  is the spatial coordinate for the superconducting inner strip and  $\hat{v}(z, t)$  is the normal mode expansion of the cavity field. The vacuum rms current of a single mode  $k = K$  of the cavity is  $I_{c,K}^0(z) = \sqrt{\hbar\omega_K/2(Dl)} |\sin(2\pi z/D - K\pi/2)|$ . Here,  $D$  is the length of the resonator and  $l$  is its total series inductance per unit length. The cavity is chosen to be a  $\lambda/2$  open-circuited resonator operated at the second mode,  $K = 2$ , and coupled capacitively to a CWG transmission line, as in Figs. 2 (a), (b), and (d). Such a cavity can reach external quality factors  $Q_x = 10^4$  at  $f_K = \omega_K/2\pi \approx 10$  GHz [12], corresponding to a cavity decay rate  $\kappa_c/2\pi \approx 1$  MHz. Hence, at a base temperature  $T_b \approx 50$  mK, the mean number of thermal photons is  $\langle n_{th} \rangle = [\exp(\hbar\omega_K/k_B T_b) - 1]^{-1} \approx 10^{-4}$  and the cavity mode can be considered to be in the vacuum state  $|0\rangle$ .

Embedding the RF SQUID in the CWG resonator [see Figs. 2 (a), (b) and (c)] allows a strong, inductive coupling between any two levels of the RF SQUID and the

single cavity mode  $K$ . The resulting interaction Hamiltonian is  $\hat{H}_I = -M_{cs} \hat{I}_{c,K} \hat{I}_s$ , where  $\hat{I}_{c,K}$  and  $\hat{I}_s$  are resonator and RF SQUID current operators, respectively, and  $M_{cs}$  is their mutual inductance. Explicitly, we find

$$\hat{H}_I = - (M_{cs}/L_s) I_{c,K}^0(z) (\hat{\Phi} - \Phi_x) i [\hat{a}_K^\dagger(t) - \hat{a}_K(t)]. \quad (2)$$

The RF SQUID can be positioned near one of the antinodes of the vacuum current [Fig. 2 (a)] and can be biased to yield maximum coupling for any two of its eigenstates  $|i\rangle$  and  $|j\rangle$ . The interaction matrix element between these levels represents their coupling strength with mode  $K$  and it is used to define the vacuum Rabi frequency  $g_{ij} = - (M_{cs}/L_s) I_{c,K}^0(z) \langle i | \hat{\Phi} | j \rangle / \hbar$ . Moreover, when operating the cavity mode largely detuned from any two levels of the RF SQUID, the corresponding lifetimes become strongly enhanced and an effective decay rate  $\gamma_{ij}^{\text{eff}} \leq \kappa_c f_K^2 g_{ij}^2 / (\delta_{tr}^4)$  can be assumed, where  $\delta_{tr} \gg (\kappa_c/2\pi)$  is the detuning between mode  $K$  and the transition under consideration. The coupling  $g_{he}$ , the effective decay rate  $\gamma_{he}^{\text{eff}}/2\pi$ , and other relevant quantities have been calculated for both RF SQUIDs and PC qubits and the results are reported in Table I.

A main application of the system illustrated above is the generation of single photons at frequency  $f_K$  in a manner similar to a quantum-optical Raman scheme [9, 15]. After preparing the RF SQUID in level  $|g\rangle$ , the transition  $|g\rangle \leftrightarrow |h\rangle$  is driven by a classical excitation with Rabi frequency  $\Omega_{gh}$  and detuned by the amount  $\delta$ . The same transition is detuned from the resonator mode  $K$  by an amount  $\Delta \gg \delta$ , resulting in a comparatively negligible coupling. On the other hand, the  $|h\rangle \leftrightarrow |e\rangle$  transition is the only one coupled to mode  $K$ , and it is also detuned by  $\delta$  [see Figs. 1 (a) and (b)]. Choosing  $\delta \gg \max[\Omega_{gh}, g_{he}]$ , level  $|h\rangle$  can be adiabatically eliminated [9, 15], thus leading to the effective second-order Hamiltonian

$$\hat{H}_{\text{eff}} = \hbar \frac{\Omega_{gh}^2}{\delta} |g\rangle \langle g| + \hbar \frac{g_{he}^2}{\delta} |e\rangle \langle e| \hat{a}_K^\dagger \hat{a}_K + \hbar g_{\text{eff}} (|g\rangle \langle e| \hat{a}_K + |e\rangle \langle g| \hat{a}_K^\dagger), \quad (3)$$

where  $g_{\text{eff}} = (\Omega_{gh}/\delta) g_{he}$  is the effective Raman coupling. The first two terms at the r.h.s. of Eq. (3) are ac Zeeman shifts, while the last term describes an effective anti-JC dynamics, inducing transitions within the  $\{|g\rangle|n\rangle, |e\rangle|n+1\rangle\}$  subspaces. The ac Zeeman shifts associated with the transition of interest,  $\{|g\rangle|0\rangle, |e\rangle|1\rangle\}$ , can be compensated by retuning the classical driving frequency. When the strong-coupling regime is reached,  $g_{\text{eff}} \gtrsim \max[\kappa_c/2\pi, \gamma_{he}^{\text{eff}}/2\pi]$ , an effective  $\pi$ -pulse realizes a complete transfer of population from state  $|g\rangle|0\rangle$  to state  $|e\rangle|1\rangle$ . This process leads to the creation of a microwave Fock state  $|1\rangle$  inside the resonator that will leak out in a time  $\sim 2\pi/\kappa_c$ . Alternatively, in the case of weak-coupling, the photon leaks to the outer world as soon as it is generated inside the cavity, thereby realizing

a deterministic single-photon source. Tailoring the photon pulse shape would require a time-dependent classical driving  $\Omega_{\text{gh}}(t)$  [9].

The proposed Raman scheme solves a technical problem of on-chip microwave single-photon generators: the difficulty to initialize superconducting qubits in the excited state  $|e\rangle$  without inevitably populating the cavity (recall that the state  $|g\rangle|0\rangle$  is a dark state of the JC dynamics) [12]. Raman pulses profit from the well defined RF SQUID-resonator coupling [9], while adiabatic-passage techniques are recommended for loosely trapped qubits [8, 16]. The so-generated single photons can then be guided through superconducting CWGs and transferred as propagating electromagnetic modes over appreciable distances, typically beyond the few centimeters required for on-chip quantum communication.

Detection schemes based on classical homodyning [12, 18] are insufficient to resolve nonclassical states of the electromagnetic radiation. On the other hand, microwave single-photon detectors in mesoscopic systems do not exist to our knowledge. Here, we introduce an on-chip MQHD technique as a means to detect weak quantum signals, even at the level of single photons. It can be implemented in three main steps. First, a signal (S) and a local oscillator (LO), characterized by the same angular frequency  $\omega_S = \omega_{\text{LO}}$ , are coherently superposed at a suitably designed MBS [Fig. 2 (a)]. This unitary manipulation of the input fields, the quantum part of the measurement process, is performed at cryogenic temperatures. Second, the microwave fields at the MBS output ports are amplified at low temperatures and then downconverted to dc signals via classical homodyning, which is carried out with image-rejection mixers (IRMs) at room temperature [18]. Finally, the dc signals are detected as rms voltages  $V_d$  with an oscilloscope and then processed to calculate the corresponding powers  $P_d = V_d^2/Z_c$ , where  $Z_c$  is the characteristic network impedance.

The MBS is realized using a superconducting four-port device: the hybrid ring, depicted in Fig. 2 (a). The advantageous coplanar design proposed here can be easily scaled and integrated with resonators in monolithic circuits that can be fabricated with Nb technology [see Fig. 2 (b)]. We now extend the classical theory of hybrid rings in Ref. [18] to the quantum regime by analogy with an optical beam splitter. With only the vacuum incident

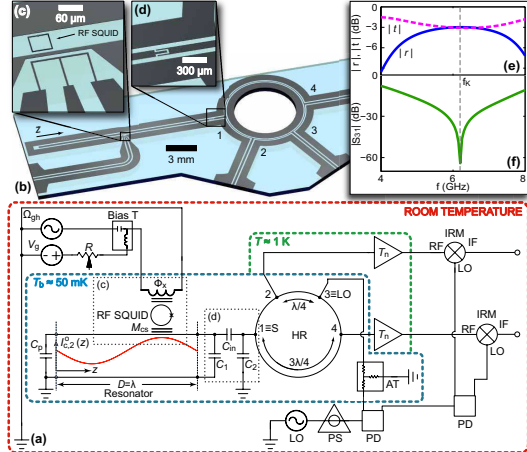


FIG. 2: (a) (Color online) Sketch of the entire generation and detection network ( $C_{\text{in}}$ ,  $C_1$ , and  $C_2$ : capacitive  $\Pi$  network representing the resonator input port;  $C_p$ : parasitic capacitor at the cavity open-circuit ending; HR: hybrid ring; PS: phase shifter; PD: power divider; AT: attenuator). (b) Asymmetric CWG resonator with integrated HR. (c) On-chip antenna providing the classical driving  $\Omega_{\text{gh}}$ . (d) Resonator-CWG coupling region. (e) The waves traveling around the HR interfere in the plotted reflection and transmission amplitude patterns. (f) Isolation between ports three and one of the HR.

at ports two and four, and up to a global phase common to both input beams, the reduced quantum input-output relations of a (superconducting) lossless MBS are

$$\begin{bmatrix} \hat{a}_2 \\ \hat{a}_4 \end{bmatrix} = \begin{bmatrix} r & t \\ -t^* & r^* \end{bmatrix} \begin{bmatrix} \hat{a}_S \\ \hat{a}_{\text{LO}} \end{bmatrix}, \quad (4)$$

where  $r$  and  $t$  are the complex, frequency-dependent reflection and transmission coefficients,  $\hat{a}_S$  and  $\hat{a}_{\text{LO}}$  are the signal and LO port operators, respectively. The latter is chosen to be a classical coherent field which is characterized by its complex amplitude  $\alpha_{\text{LO}} = |\alpha_{\text{LO}}| \exp(i\theta_r)$  [3], where  $|\alpha_{\text{LO}}|$  is the real part of this field and  $\theta_r$  is its relative phase with respect to S. The numerical simulations plotted in Fig. 2 (e) show that the MBS can be *balanced* over a broad bandwidth around the desired operation frequency  $f_K$ , i.e.,  $r = t = 1/\sqrt{2}$  (−3 dB).

A balanced MQHD is implemented subtracting the powers associated to the measured voltages at ports two and four of the IRMs,

$$P_{d,2} - P_{d,4} \propto N_2 - N_4 = 2 |\alpha_{\text{LO}}| X_{\theta_r}, \quad (5)$$

where the quantity  $(N_2 - N_4)$  represents different realizations of the measured observable  $(\hat{n}_2 - \hat{n}_4)$ , with  $\hat{n}_2 = \hat{a}_2^\dagger \hat{a}_2$ ,  $\hat{n}_4 = \hat{a}_4^\dagger \hat{a}_4$ , and  $\hat{a}_2 = (\hat{a}_S + \hat{a}_{\text{LO}})/\sqrt{2}$ ,  $\hat{a}_4 = (-\hat{a}_S + \hat{a}_{\text{LO}})/\sqrt{2}$ . Furthermore,  $X_{\theta_r}$  represents different realizations of the measured quadratures  $\hat{X}_{\theta_r} \equiv$

TABLE I: Typical parameters and calculated relevant quantities for the RF SQUID and the PC qubit [22], coupled to a 50  $\Omega$  resonator with dimensions given in Ref. [23].

	$I_{c0}$	$C_j$	$L_s$	$M_{cs}$	$\frac{\Delta E_{\text{ah}}}{h}$	$I_{c,2}^0$	$ g_{\text{he}} $	$\frac{\gamma_{\text{he}}^{\text{eff}}}{2\pi}$
	( $\mu\text{A}$ )	(fF)	(pH)	(pH)	(GHz)	(nA)	(MHz)	(kHz)
RF SQUID	1.4	100	266	22	6.2	16.1	20	9.5
PC qubit	0.6	7	10	1	6	16.2	5.7	106.4

$(\hat{a}_S^\dagger e^{i\theta_r} + \hat{a}_S e^{-i\theta_r})/2$ , where the LO operators were replaced by their complex amplitudes. Equation (5) contains the essence of the balanced MQHD technique and reveals that the quadrature of the *weak* signal S is *amplified* by a factor  $2|\alpha_{\text{LO}}|$ , and thus, for large LO voltages, can overcome the detector (a cold amplifier) noise floor. MQHD can be used for measuring any quadrature moment  $\langle \hat{X}_{\theta_r}^p \rangle$  of signal S. It also allows one to reconstruct the quadrature probability histogram  $\text{pr}(X_{\theta_r})$  by repeating the measurements of  $\hat{X}_{\theta_r}$  for  $0 \leq \theta_r < 2\pi$  [see PS in Fig. 2 (a)], a crucial step for the realization of MQHT. The function  $\text{pr}(X_{\theta_r})$  is then related to the Wigner function of S, a phase-space representation of its corresponding density operator, through an inverse Radon transform [7]. MQHD and MQHT are powerful techniques, allowing not only for the detection of single photons, but also for full state reconstruction of any weak signal S.

The rms voltages  $V_d$  are the measured quantities from which computing the powers  $P_d$  in Eq. (5). At the output port of one of the IRMs we find

$$V_d = G_{\text{eff}} |\delta_m| \sqrt{\frac{N \hbar \omega_K Z_c}{\tau_m}}, \quad (6)$$

where  $G_{\text{eff}}$  is the effective gain of the network,  $\delta_m$  is the downconversion coefficient of the IRM,  $N$  is any of  $N_2, N_4$ ,  $\tau_m$  is the measurement time [e.g., in the case of strong coupling,  $\tau_m = 4\pi/(\kappa_c + \gamma_{\text{he}}^{\text{eff}})$ ], and  $Z_c = 50 \Omega$ . The quantum efficiency of the MQHD can be shown to be almost unity. The two output ports of the hybrid ring are connected to two cryogenic amplifiers [see Fig. 2 (a)]. The noise floor of each amplifier, as expressed through its noise temperature  $T_n$ , leads to a mean photon number  $\langle \bar{n}_{\text{amp}} \rangle = k_B T_n / \hbar \omega_K$ . This quantity must be exceeded by the mean number of signal photons at the amplifier input, which is  $\propto |\alpha_{\text{LO}}|$ , in order to realize a signal-to-noise-ratio  $\text{SNR} > 1$ . The LO power  $P_{\text{LO}}$  required to reach this condition is then  $(|\alpha_{\text{LO}}|^2 \hbar \omega_{\text{LO}}) / \tau_m = V_{\text{LO}}^2 / (2Z_c) \geq (\hbar \omega_K \langle \bar{n}_{\text{amp}} \rangle) / \tau_m$ , where  $V_{\text{LO}}$  is the (real) LO voltage amplitude. Assuming  $T_n \approx 10 \text{ K}$  (corresponding to  $\sim 21$  photons at  $\omega_K = 2\pi \times 10^{10} \text{ rad/s}$ ) and  $\tau_m \approx 1 \mu\text{s}$ , a lower bound for  $P_{\text{LO}}$  is approximately  $-130 \text{ dBm}$ . Increasing the LO power would in principle further enhance the weak quantum signal. However, the trade off to large LO powers is the leakage to the resonator resulting from the finite isolation of the hybrid ring given by the scattering-matrix parameter between LO and cavity ports,  $S_{31}$ . Assuming  $|S_{31}| \approx -40 \text{ dB}$  [see Fig. 2 (f)], a power of  $-130 \text{ dBm}$  at the LO port would be attenuated to  $-170 \text{ dBm}$  at the cavity port. This power would populate the cavity with  $\langle n_{\text{LO}}^{\text{eff}} \rangle \approx 2 \times 10^{-3}$  photons. Thus, an increase of the LO power up to  $-110 \text{ dBm}$  is admissible and single photons, or other weak quantum signals, can be measured.

In conclusion, we presented a new scheme for the deterministic generation of microwave single photons based on a Raman pulse. Also, we showed how to realize MQHD

for measuring quadrature moments and MQHT for realizing full state reconstruction of quantum weak signals. These proposals are essential tools for the implementation of quantum-optical CQED (e.g., Raman schemes, selective interactions, quantum computing) and linear optics (e.g., heterodyne detection, Mach-Zehnder interferometry, and entangled-photon chains) in the microwave domain on a chip. Moreover, they represent an important step for the advent of quantum information processing in the field of circuit QED [24], e.g., quantum logic and on-chip quantum communication with internal flying qubits.

The authors would like to acknowledge K. R. Brown and D. E. Oates for fruitful discussions. MM and WDO thank T. P. Orlando and M. Gouker for their support during the early stages of this work. This work has been partially supported by the DFG through SFB 631. ES acknowledges EU support through RESQ project.

\* Electronic address: Matteo.Mariantoni@wmi.badw.de

- [1] J.M. Raimond, M. Brune, and S. Haroche, *Rev. Mod. Phys.* **73**, 565 (2001).
- [2] H. Mabuchi and A.C. Doherty, *Science* **298**, 1372 (2002).
- [3] *Theory of Nonclassical States of Light*, edited by V.V. Dodonov and V.I. Man'ko (Taylor & Francis, London, 2003).
- [4] M.A. Nielsen and I.L. Chuang, *Quantum Computation and Quantum Information*, (Cambridge University Press, Cambridge, 2000).
- [5] D. Leibfried, R. Blatt, C. Monroe, and D. Wineland, *Rev. Mod. Phys.* **75**, 281 (2003).
- [6] A.I. Lvovsky *et al.*, *Phys. Rev. Lett.* **87**, 050402 (2001).
- [7] U. Leonhardt, *Measuring the Quantum State of Light* (Cambridge University Press, Cambridge, 1997).
- [8] A. Kuhn, M. Hennrich, and G. Rempe, *Phys. Rev. Lett.* **89**, 067901 (2002).
- [9] M. Keller *et al.*, *Nature* **431**, 1075 (2004).
- [10] A. Badolato *et al.*, *Science* **308**, 1158 (2005).
- [11] Y. Makhlin, G. Schön, and A. Shnirman, *Rev. Mod. Phys.* **73**, 357 (2001).
- [12] A. Wallraff *et al.*, *Nature* **431**, 162 (2004).
- [13] R. Movshovich *et al.*, *Phys. Rev. Lett.* **65**, 1419 (1990).
- [14] J. Gabelli *et al.*, *Phys. Rev. Lett.* **93**, 056801 (2004).
- [15] M. França Santos, E. Solano, and R.L. de Matos Filho, *Phys. Rev. Lett.* **87**, 093601 (2001).
- [16] C.-P. Yang, S.-I. Chu, and S. Han, *Phys. Rev. Lett.* **92**, 117902 (2004).
- [17] J. Siewert, T. Brandes, and G. Falci (submitted).
- [18] R.E. Collin, *Foundations for Microwave Engineering*, 2nd ed. (Wiley-IEEE Press, New Jersey, 2000).
- [19] J.R. Friedman *et al.*, *Nature* **406**, 43 (2000).
- [20] C.H. van der Wal *et al.*, *Science* **290**, 773 (2000).
- [21] Y. Yu *et al.*, *Phys. Rev. Lett.* **92**, 117904 (2004).
- [22] The flux  $\Phi_x$  was set to  $0.499 \Phi_0$  and  $0.480 \Phi_0$  for the two qubits, respectively. For the PC qubit  $\alpha = 0.8$  [20].
- [23] E.g., conductor width  $W = 118 \mu\text{m}$ , slot  $S = 80 \mu\text{m}$ , capacitance and inductance per unit length  $c \approx 0.17 \text{ nFm}^{-1}$  and  $l \approx 435 \text{ nHm}^{-1}$ , resp., and length  $D \approx 18.4 \text{ mm}$ .
- [24] J.Q. You and F. Nori, *Phys. Rev. B* **68**, 064509 (2003).



# Conclusions

In this thesis macroscopic solid-state circuits envisaged as quantum bits were investigated. These solid-state qubits fulfill the basic criteria for quantum bits [32]. Here, the decoherence of these qubits was analyzed and different strategies to improve the gate performance of these qubits were presented. Moreover, a scheme for the deterministic generation of single microwave photons as well as their detection was given.

In **chapter 6**, the decoherence and gate performance of a two-qubit system in a setup typical for solid-state qubits (such as superconducting charge or flux qubits) was analyzed. It was found that the gate performance crucially depends on the symmetries of the qubit-bath coupling, which suggests to try to engineer the qubit-bath coupling for optimized decoherence of the qubit system. Recent experiments [92, 184] verify these findings and engineer the electromagnetic environment in order to decrease the level of imperfections.

**Chapter 7** deals with the decoherence of two QD charge qubits, namely a double double-QD system. In this system, the most important intrinsic decoherence source is decoherence due to the electron-phonon coupling and decoherence in this system is carefully analyzed. It is found that due to the qubit-coupling to the noise, which is diagonal in the preferred qubit eigenbasis, the decoherence can be significantly reduced, by reducing the tunnel matrix elements in a single qubit (double dot).

The coupling of two flux qubits with a flux transformer is investigated in **chapter 8**. It is proposed to use a JoFET, which is essentially a Josephson tunnel junction with a tunable critical current, as a switch for the transformer loop. The JoFET as well as non-switchable junctions that provide an intrinsic  $\pi$ -shift, are analyzed with regard to the decoherence that they impose on the qubits. It is found that the noise due to the coupling elements introduces only a small additional noise source with correlated noise between the qubits. Moreover, it is verified that the switching process itself should be performed rather fast because most decoherence occurs during the switching of the switch that steers the coupling between the qubits.

In **chapter 9**, a Decoherence Free Subspace encoding is given for a specific design of superconducting charge or flux qubits. For the case of flux qubits it is shown that the most important decoherence source, namely  $1/f$ -noise that affects the coupling elements, can be fully eliminated by the encoding together with a restricted phase space of the logical qubits. Both of these properties alone would be insufficient for a complete protection from the noise. Moreover, the encoding also fully protects from collective dephasing on the qubits.

At present, carefully optimized pulse sequences are not yet commonly used for the manipulation of superconducting solid-state qubits. In **Chapter 10** *optimal control theory* is introduced to the domain of superconducting charge qubits. In this system, only the single-qubit bias terms can be individually controlled, but even these are mutually coupled. Optimized pulse sequences found by this technique for a setup of two permanently coupled superconducting charge qubits are presented. Astonishingly, the pulse sequence found with optimal control theory, leads to a simulated fidelity, *e.g.*, of the CNOT gate of  $F > 99\%$ , even taking into account leakage to higher levels of the pseudo-spin system embedded into an infinite Hilbert space. Thus, it is impressively shown that in these experiments the pulse sequence and pulse shapes, and *not* decoherence is the limiting factor. Especially the optimization of the former that leads to a major improvement in the gate performance makes the potential of the charge qubit devices obvious.

Non-locality of entangled quantum states is a fascinating property of quantum mechanics. The generation, decoherence and tomography of maximally entangled Einstein-Podolsky-Rosen (EPR) pairs is presented in **chapter 11**. Measurements on these states are proposed that can verify the completeness of quantum mechanics in the sense of the original work by EPR [241] for macroscopic states, non-local correlations between the states can clearly be identified.

In **chapter 12**, circuit-QED, *i.e.*, the realization of ideas from quantum optics and cavity QED in the solid-state, is introduced and a scheme for the deterministic generation and detection of single microwave photons is proposed. Here, an rf-SQUID or a strongly biased flux qubit inside a resonator is used to generate single microwave photons that can be detected by the circuit analog of a beamsplitter/interferometer setup in quantum optics. This detection scheme provides intrinsic amplification of the signal associated with the single microwave photon. Thus, even though the noise floor on the amplifiers that will be used for the final measurements is on the order of at least 20 photons, the signal from the single photon, which was in such a way pre-amplified can easily be detected. Moreover, it is proposed to embed a superconducting flux qubit inside a microstrip resonator that acts as the cavity. Here, compared to quantum optics setups, the atom (or qubit) is fixed inside the cavity and the field inside the cavity can be measured to infer the state of the atom. Also, the cavity effectively filters the external decoherence from the electromagnetic environment due to the narrow bandwidth of the cavity resonances. These devices that realize linear quantum optics on a chip could be used for on-chip quantum communication and to mediate long-range interactions between qubits.

# Part III

## Appendix



# Appendix A

## Useful relations

### A.1 Operator relations

The following exact relations for the matrix exponential of an operator [281], its time derivative [281], and commutation relations [281–283] are useful, *e.g.*, for the computation of exponentials of time-dependent operators in a Polaron transformation [284].

$$\frac{d}{dt}(e^{\hat{A}t}) = \hat{A} \cdot e^{\hat{A}t} = e^{\hat{A}t} \cdot \hat{A}, \quad (\text{A.1})$$

$$\frac{d}{dt}e^{\hat{A}(t)} = \int_0^1 ds \cdot e^{s\hat{A}} \cdot \frac{d\hat{A}}{dt} \cdot e^{(1-s)\hat{A}} = \int_0^1 ds \cdot e^{(1-s)\hat{A}} \cdot \frac{d\hat{A}}{dt} \cdot e^{s\hat{A}}, \quad (\text{A.2})$$

$$(e^{\hat{A}})' = \hat{A}' + \frac{1}{2!}(\hat{A}\hat{A}' + \hat{A}'\hat{A}) + \frac{1}{3!}(\hat{A}\hat{A}\hat{A}' + \hat{A}\hat{A}'\hat{A} + \hat{A}'\hat{A}\hat{A}) + \dots, \quad (\text{A.3})$$

$$[\hat{A}, e^{\hat{B}t}] = \int_0^t ds \cdot e^{(t-s)\hat{B}}[\hat{A}, \hat{B}]e^{s\hat{B}} = \int_0^t ds \cdot e^{s\hat{B}}[\hat{A}, \hat{B}]e^{(t-s)\hat{B}}, \quad (\text{A.4})$$

$$[e^{\lambda\hat{A}}, e^{\mu\hat{B}}] = \int_0^\lambda dt \int_0^\mu ds \cdot e^{(s-t)\hat{A}} e^{(\mu-s)\hat{B}}[\hat{A}, \hat{B}]e^{s\hat{B}} e^{t\hat{A}}. \quad (\text{A.5})$$

## A.2 Qubit states on the Bloch sphere

The state of a qubit can be represented geometrically on the Bloch sphere as depicted in Fig. A.1. The qubit state is decomposed as

$$|\psi\rangle = \cos(\theta/2) |0\rangle + e^{i\varphi} \sin(\theta/2) |1\rangle, \quad (\text{A.6})$$

where  $\varphi$  and  $\theta$  are the angles on the Bloch sphere that describe the position of the spin vector. The poles of the sphere are the  $\hat{\sigma}_z$  eigenstates.

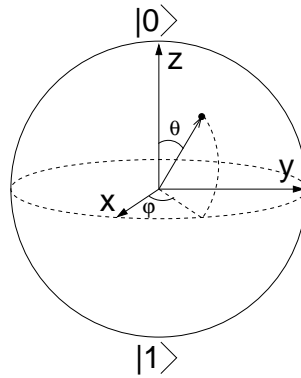


Figure A.1: Bloch sphere representation of a qubit state. The poles of the sphere are the eigenstates  $|0\rangle$  and  $|1\rangle$  of  $\hat{\sigma}_z$ . The angles  $\varphi$  and  $\theta$  are defined in Eqn. (A.6).

Each single qubit gate can be expressed in terms of a rotation of the state vector on the Bloch sphere around a normalized axis  $\vec{n}$  as [14, 285].

$$R_{\vec{n}}(\theta) = \exp(-i(\theta/2)\vec{n}\vec{\sigma}) = \cos(\theta/2)\hat{\mathbf{1}} - i\sin(\theta/2)(\vec{n}\vec{\sigma}), \quad (\text{A.7})$$

especially for  $\hat{A}^2 = 1$ , which is the case for the Pauli matrices, it holds that

$$\exp(\pm i\hat{A}\theta) = \cos(\theta)\hat{\mathbf{1}} \pm i\sin(\theta)\hat{A}. \quad (\text{A.8})$$

When the spin is subjected to a static magnetic field  $\mathbf{B}_z$  in z-direction, the state vector evolves according to

$$|\psi\rangle = \cos(\theta/2)e^{-i\omega_0 t/2} |0\rangle + e^{i\varphi} \sin(\theta/2)e^{i\omega_0 t/2} |1\rangle, \quad (\text{A.9})$$

*i.e.*, the spin precesses with the *Larmor frequency*  $\omega_0 \propto |B_z|$  around the z-axis.

# Appendix B

## The dissipative TSS – connection to the Kondo model and DMRG

The dissipative two-state system (TSS) (the qubit) has been analyzed in detail in chapters 4 and 6 for a small coupling strength  $\alpha$  between the qubit and the environment. In this chapter different approaches that extend the description of this system to large  $\alpha$  (*i.e.* a strong coupling to the environment) are presented. First, for simplicity a single qubit that is coupled to an environmental bath of harmonic oscillators is considered

$$H = H_q + H_I + H_B = -\frac{\Delta}{2}\hat{\sigma}_x + \hat{\sigma}_z\hat{X} + \hat{H}_B, \quad (\text{B.1})$$

where  $\hat{H}_B = \sum_i^N \omega_i a_i^\dagger a_i$  is the Hamiltonian that describes the bath. The system-bath coupling term can be rewritten as

$$\hat{H}_I = \hat{\sigma}_z \otimes \hat{X} = \hat{\sigma}_z \frac{1}{2} \sum_{i=1}^N f_i (a_i^\dagger + a_i), \quad (\text{B.2})$$

with coupling strengths  $f_i$  for the individual modes. The spectral function that characterizes the bosonic bath is taken as [286]

$$J(\omega) = \pi \sum_{i=1}^N f_i^2 \delta(\omega - \omega_i) = \begin{cases} 2\pi\alpha\omega, & \text{for } \omega \ll \omega_c, \\ 0, & \text{for } \omega \gg \omega_c, \end{cases} \quad (\text{B.3})$$

where in the last step the spectral function was taken Ohmic with a high frequency cutoff. This is the special case of an Ohmic spectral function and in general  $J(\omega) \propto \omega^k$ , where the spectral function is called sub-Ohmic for  $k < 1$ , Ohmic for  $k = 1$ , and super-Ohmic for  $k > 1$ . For the Ohmic spectral function, the model presented in Eqn. (B.1) is equivalent to the anisotropic Kondo model [287]. Here, the dimensionless parameter  $\alpha$  parametrizes the coupling strength to the environmental bath. The different phases of the dissipative TSS are depicted in Fig. B.1. The figure summarizes the different phases as a function of  $\alpha$ , the dimensionless parameter that parametrizes the coupling to the environment. It turns

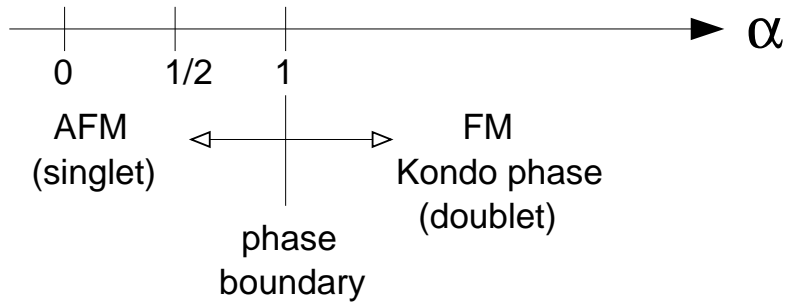


Figure B.1: Phases of the dissipative two-state system in terms of the coupling strength  $\alpha$  [287]. The phase transition from the anti-ferromagnetic (AFM) phase to the ferromagnetic (FM) phase is at  $\alpha = 1$ . At the Toulouse point  $\alpha = 1/2$ , the anisotropic Kondo model can be solved exactly [288].

out based on NRG and Bethe ansatz calculations that depending on  $\alpha$  the system has different ground states, *i.e.*, a variation of  $\alpha$  can drastically change the properties of the system resulting in a phase transition. The phase boundary between the antiferromagnetic (singlet) phase and the ferromagnetic phase is at a value of the coupling strength  $\alpha = 1$ . The properties of the dissipative TSS have been evaluated in detail. It was found that generally three regimes are important, damped coherent oscillations ( $0 < \alpha < 1/2$ ), exponential decay ( $1/2 < \alpha < 1$ ), and localization of the (pseudo-)spin ( $\alpha > 1$ ) [148, 155, 289–291]. Moreover, it is found that the tunnel splitting of the TSS is renormalized, *i.e.*, it diverges for  $\alpha \rightarrow 1$ , when  $\Delta > \omega_c$ , and the effective tunnel splitting is given by

$$\Delta_{\text{eff}} = \Delta \left( \frac{\Delta}{\omega_c} \right)^{\frac{\alpha}{1-\alpha}}. \quad (\text{B.4})$$

The resonance around  $\Delta_{\text{eff}}$  corresponds to coherent oscillations with a width that is given by the decoherence rate of the dissipative TSS.

The Kondo problem deals with a single magnetic impurity and associated spin-1/2. It interacts via an exchange scattering potential with a band of conduction electrons. In the Kondo model, there is a constant density of electron-hole excitations close to the Fermi surface, which also gives rise to Anderson’s orthogonality catastrophe, see Ref. [292], and to logarithmic infrared divergences in, *e.g.*, the static magnetic susceptibility [148]. Kondo himself referred to these effects as the Fermi surface effects [293]. The connection between the Spin-Boson and the Kondo model is due to the fact that the low-energy electron-hole excitations have bosonic character and can be viewed in terms of density fluctuations [294]. In 1D there exists an exact mapping between fermions and bosons [295, 296], which is useful for the treatment of strongly correlated electron systems in one dimension.

The original Kondo problem deals with a single localized impurity of spin-1/2. The localized spin interacts strongly below the so-called Kondo temperature  $T_K$  with its surrounding conduction electrons in the host materials. In the anisotropic Kondo model only



s-wave scattering occurs, which allows to reduce the anisotropic Kondo model essentially to 1D. In the anisotropic Kondo model only a narrow band, which is chosen to be symmetric around the Fermi energy  $E_F$ , interacts with the impurity. Following Ref. [148], after linearization of the dispersion relation  $E(k) - E_F \equiv \hbar\epsilon_k = \hbar v_F k$ , the Kondo Hamiltonian is given by

$$H_K = \hbar v_F \sum_{k,\sigma} k c_{k,\sigma}^\dagger c_{k,\sigma} + \frac{\hbar J'}{4} \tau_z \sum_{\sigma} \sigma c_{\sigma}^\dagger c_{\sigma} + \frac{\hbar J''}{2} \left( \tau_+ c_{\downarrow}^\dagger c_{\uparrow} + \tau_- c_{\uparrow}^\dagger c_{\downarrow} \right), \quad (\text{B.5})$$

where  $J'$  and  $J''$  describe impurity scattering for conserved spin polarization and spin-flip scattering, respectively. Here,  $\tau_{\pm} = (\tau_x \pm i\tau_y)/2$ . Note that  $J'$  and  $J''$  are related to the coupling strength  $\alpha$ . It has been shown by Yuval and Anderson [297] that this Hamiltonian is equivalent to the Spin-Boson model introduced in chapter 4. The numerical renormalization group technique (NRG) formulated by Wilson [298–303] has proven to be extremely powerful in the context of Kondo physics. This numerical technique is working only for a fermionic conduction band. As can be readily seen, this is not the case for the Hamiltonian Eqn. (B.1). Current developments are extending the NRG to treat bosonic bands [304].

An alternative approach to solving the dissipative TSS is White's *density matrix renormalization group* (DMRG) approach [305, 306]. Coming back to the model of the dissipative TSS, it is possible to apply DMRG techniques to reduce the many degrees of freedom of the bosonic Hilbert space of the environmental bath. Note that due to the absence of the Pauli principle, already a single boson (oscillator) spans an infinite-dimensional Hilbert space. The truncation of the Hilbert space can be performed in several different ways [148]. One possibility is to represent the bosonic states in terms of the occupation number and disregard states that exceed a certain occupation number. The numerical renormalization technique proposed by White et al. [305, 306] reduces the dimensionality of each oscillator to only a few states [306]. For an excellent overview of the DMRG method see the review Ref. [307]. The DMRG method is especially efficient when the oscillator equilibrium position is shifted by an external force via coordinate-coordinate coupling, which is for example the case for the well-known Spin-Boson model.

Now, an outline of the analysis of the dissipative tunneling is given, following the approach presented in Ref. [287]. First, the important quantities for the analysis of the dissipative TSS are given and then the calculation of these quantities with DMRG codes is sketched. The dynamical correlation function

$$C(t) = \frac{1}{2i} \langle [\hat{\sigma}_z(t), \hat{\sigma}_z(0)] \rangle \quad (\text{B.6})$$

is calculated because it contains information about *non-equilibrium* processes [155], like relaxation, which is known from linear response theory [149]. Equivalently, one can calculate the Fourier transform of the dynamical correlation function, the response function

$$\chi''(\omega) = \frac{1}{2} \int_{-\infty}^{\infty} dt e^{i\omega t} \langle [\hat{\sigma}_z(t), \hat{\sigma}_z(0)] \rangle \quad (\text{B.7})$$

$$= \text{Im} \left( \langle \hat{\sigma}_z \frac{1}{\omega + E_g - H + i\eta} \hat{\sigma}_z \rangle - \langle \hat{\sigma}_z \frac{1}{\omega - E_g + H - i\eta} \hat{\sigma}_z \rangle \right) \quad (\text{B.8})$$

$$= \text{Im} G(\omega), \quad (\text{B.9})$$

where  $G(\omega)$  is the Fourier transform of the imaginary-time Green function [21]. Note that the inverse matrix of the total Hamiltonian can *not* be computed, however, the expectation value needed for the evaluation of Eqn. (B.8) can be computed using the Lanczos method [287], which involves the continued fraction formula

$$\langle f_0 | \frac{1}{Z - H} | f_0 \rangle = \frac{\langle f_0 | f_0 \rangle}{z - \alpha_0 - \frac{\beta_1^2}{z - \alpha_1 - \dots}}, \quad (\text{B.10})$$

where the coefficients  $|f_{i+1}\rangle$ ,  $\alpha_i$ , and  $\beta_i^2$  are given by the Lanczos tridiagonal elements. For the frequency range of interest  $\approx \Delta_{\text{eff}}$  it is usually possible to truncate the iteration scheme at approximately 100th order [287]. After calculation of the response function, the power spectrum of the environmental noise is extracted straightforwardly as  $S(\omega) = \chi''(\omega)/\omega$ .

The dynamics of entanglement of a single spin system (*e.g.*, a qubit) and a bosonic environment have also been evaluated using the *numerical renormalization group* (NRG) method [298–303]. The NRG model has been shown to give very confident results for the anisotropic Kondo model or other quantum impurity models [291]. Note that, however, for lattice models like the Heisenberg spin chain, the DMRG method gives very reliable results, whereas the NRG method does not [291, 305]. The breakdown of the NRG method has been identified as being due to not properly taking into account the effect of boundary conditions during iterations [305]. Thus, from a quantum computation point of view the NRG method does not take into account the contribution that entanglement gives to the correlations in the ground state. Therefore, the failure of the NRG method for lattice models has been attributed to the fact that DMRG manifestly takes into account the entanglement, whereas the NRG method does not [308].

Interestingly, apart from the DMRG and NRG studies, exact results that avoid the boundary terms (by taking an odd number of lattice sites) have been obtained [309]. These study the dynamics of entanglement in a spin-1/2 chain with an XY exchange coupling in a transverse electromagnetic field. The entanglement and the scaling of entanglement close to the quantum phase transition in this system is classified in the framework of scaling theory. A major difference between the classical correlations and the entanglement is that the entanglement in general remains short ranged while the classical correlation length diverges close to the phase transition. Note that due to the universality principle, the critical behaviour depends only on the dimension of the system and the symmetry of the order parameter [309], which underlines the significance of these results.

# Appendix C

## Comparison of coupling schemes for flux qubits

In order to perform quantum computation it is necessary to be able to scale the solid-state qubit setups up to systems of many qubits. Naturally, superconducting charge or flux qubits are coupled via the charge or flux degrees of freedom. Thus, in table C.1 some of these basic coupling schemes for superconducting flux qubits are shown. The schemes No. 1,3 and 4 refer to an inductive coupling between one of the SQUID loops of each flux qubit [76]. In scheme No. 2, the qubits are mutually coupled via a LC-oscillator [74]. Finally, in scheme No. 5, the flux qubits are coupled capacitively to each other. Namely, one of the superconducting islands of a flux qubit is coupled to one of the superconducting islands of the neighbouring qubit [195]. Note that this qubit setup has to be designed very carefully in order to allow for a mutual capacitance between two neighbouring superconducting islands whilst suppressing most of the mutual flux crosstalk between the flux qubits. Also, the flux qubits can be coupled via interaction with photons inside a cavity, cf. chapter 12. Note that for the superconducting charge qubit, a variable electrostatic transformer for the realization of a controllable capacitive coupling between qubits has been proposed [310], which could potentially also be useful for qubit setups with superconducting flux qubits. Moreover, it is not always strictly necessary to be able to tune the coupling, see chapters 9 and 11, and the schemes for universal computations with untunable couplings in Ref. [311].

Here, the parameters for the basic coupling schemes for superconducting flux qubits (which are presented in table C.1) corresponding to classical short range nearest neighbour interaction are summarized. Note that this short range interaction leads to a substantial swapping overhead when performing quantum gate operations [14] as compared to an ideally desirable “quantum” coupling between any pair of qubits. Together with the corresponding energy scales for the Hamiltonian elements, also the anticipated qubit operators that are coupled to the environmental noise are given. The energy scales are  $\epsilon$  (single-qubit bias),  $\Delta$  (single-qubit tunneling amplitude), and  $K$  (coupling strength between neighbouring qubits). The tunneling amplitude  $\Delta$  is fabricated to be approximately between 1 – 10 GHz.

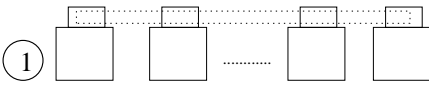
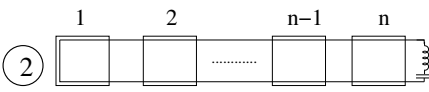
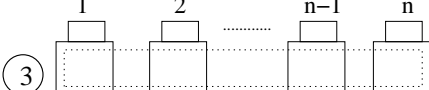
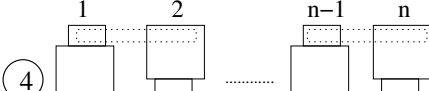
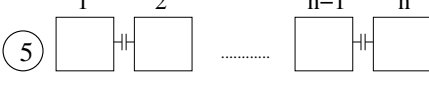
Type of coupling	Hamiltonian
	$\sum_i (\epsilon_i \sigma_z^{(i)} + \Delta_i \sigma_x^{(i)}) + K_i \sigma_x^{(1)} \otimes \dots \otimes \sigma_x^{(n)}$ or $\dots + \sum_{i,j} K_{ij} \sigma_x^{(i)} \otimes \sigma_x^{(j)}$ (nearest neighbor interaction easier)
	$\sum_i (\epsilon_i \sigma_z^{(i)} + \Delta_i \sigma_x^{(i)}) + K_i \sigma_y^{(1)} \otimes \dots \otimes \sigma_y^{(n)}$ or $\dots + \sum_{i,j} K_{ij} \sigma_y^{(i)} \otimes \sigma_y^{(j)}$
	$\sum_i (\epsilon_i \sigma_z^{(i)} + \Delta_i \sigma_x^{(i)}) + K_i \sigma_z^{(1)} \otimes \dots \otimes \sigma_z^{(n)}$ or $\dots + \sum_{i,j} K_{ij} \sigma_z^{(i)} \otimes \sigma_z^{(j)}$ (nearest neighbor interaction easier)
	$\sum_i (\epsilon_i \sigma_z^{(i)} + \Delta_i \sigma_x^{(i)}) + \sum_{i,j} K_{ij} \sigma_x^{(i)} \otimes \sigma_z^{(j)}$
	$\sum_i (\epsilon_i \sigma_z^{(i)} + \Delta_i \sigma_x^{(i)})$ $+ \sum_i K_{i,i+1} (\sigma_x^{(i)} \otimes \sigma_x^{(i+1)} + \sigma_y^{(i)} \otimes \sigma_y^{(i+1)})$

Table C.1: Simple schemes for coupling of superconducting flux qubits via the flux or charge degree of freedom. In the lower part of the table the energy scales in the Hamiltonian and potential noise sources are listed.

1. **xx-type of coupling**, the energy scales in the Hamiltonian are  $\epsilon \approx 5\Delta$ ,  $K \approx 0.1\Delta$ ; important noise sources are flux noise from the transformer loop  $\propto \sigma_x^i$ , which is correlated and regular flux noise  $\propto \sigma_z^i$ ; here,  $\Delta$  and  $\epsilon$  are tunable, whereas the coupling strength  $K$  is fixed but can be switched (on/off).
2. **yy-type of coupling**, the energy scales in the Hamiltonian are  $\epsilon \approx 5\Delta$ ,  $K \approx 1 \dots 0.01\Delta$ ; important noise sources are  $1/f$ -noise due to hopping background charges, which is uncorrelated and regular flux noise  $\propto \sigma_z^i$ ; here,  $\Delta$  and  $\epsilon$  are tunable, whereas the coupling strength  $K$  is fixed but possibly switchable.
3. **zz-type of coupling**, the energy scales in the Hamiltonian are  $\epsilon \approx 5\Delta$ ,  $K \approx \Delta$ ; important noise sources are correlated flux noise from the transformer loop  $\propto \sigma_z^i$ ; here,  $\epsilon$  is tunable, the coupling  $K$  is possibly switchable, and the  $\Delta$  are fixed.
4. **xz-type of coupling**, the energy scales in the Hamiltonian are  $\epsilon \approx 5\Delta$ ,  $K \approx 0.1\Delta$ ; important noise sources are correlated flux noise due to transformer loop  $\propto \sigma_x^i$  and

regular flux noise  $\propto \sigma_z^i$ ; here,  $\Delta$  and  $\epsilon$  are tunable, while the coupling  $K$  is fixed but is possibly switchable.

5. **xy-type of coupling**, the energy scales in the Hamiltonian are  $\epsilon \approx 5\Delta$ ,  $K \approx 0.1 \dots 0.01\Delta$ ; important noise sources are  $1/f$ -noise and regular flux noise  $\propto \sigma_z^i$ ; here  $\epsilon$  is tunable,  $K$  and  $\Delta$  are fixed.

The inductive coupling schemes are easiest to fabricate from an experimental point of view. However, one of the most promising coupling schemes is to couple the qubits via a photon field inside a superconducting cavity, see chapters 5, 12, F, which can also reduce the external electronics noise on the qubits drastically.



# Appendix D

## Decoherence rates for pure Ising-type zz-coupling

Here, the Bloch-Redfield rate expressions for pure Ising-type  $zz$ -coupling will be derived. In the case where the Hamiltonian of the coupled two-qubit system in the singlet-triplet basis is simply given by

$$\hat{H}_S = -\frac{1}{2}K\hat{\sigma}_z^{(1)} \otimes \hat{\sigma}_z^{(2)} = -\frac{1}{2} \text{diag}(K, -K, K, -K). \quad (\text{D.1})$$

Obviously, the eigenbasis of this system Hamiltonian is the singlet-triplet basis and the eigenenergies can directly be written down,  $\lambda_{1,3} = -(1/2)K$  and  $\lambda_{2,4} = (1/2)K$ . In the same spirit, the transition frequencies  $\omega_{ij} = (\lambda_i - \lambda_j)/h$  are extracted as

$$\begin{aligned} \omega_{12} &= \omega_{14} = \omega_{32} = \omega_{34} = -K/h, \\ \omega_{21} &= \omega_{23} = \omega_{41} = \omega_{43} = K/h, \\ \omega_{13} &= \omega_{24} = \omega_{31} = \omega_{42} = 0, \end{aligned} \quad (\text{D.2})$$

and for  $i = j$  trivially  $\omega_{ii} = 0$ . Therefore, the Golden-Rule expressions are of the following form for the two bath case

$$\Gamma_{\ell mnk}^+ = \frac{1}{8\hbar} \left[ \sigma_{z,\ell m}^{(1)} \sigma_{z,nk}^{(1)} J_1(\omega_{nk}) + \sigma_{z,\ell m}^{(2)} \sigma_{z,nk}^{(2)} J_2(\omega_{nk}) \right] (\coth(\beta\hbar\omega_{nk}/2) - 1), \quad (\text{D.3})$$

$$\Gamma_{\ell mnk}^- = \frac{1}{8\hbar} \left[ \sigma_{z,\ell m}^{(1)} \sigma_{z,nk}^{(1)} J_1(\omega_{\ell m}) + \sigma_{z,\ell m}^{(2)} \sigma_{z,nk}^{(2)} J_2(\omega_{\ell m}) \right] (\coth(\beta\hbar\omega_{\ell m}/2) + 1), \quad (\text{D.4})$$

and correspondingly for the single bath case, where the only difference are the additional cross-terms of the form  $\sigma_{z,ab}^{(i)} \sigma_{z,cd}^{(j)}$  with  $i \neq j$ . In more detail, for a single bath it is found that

$$\begin{aligned} \Gamma_{\ell mnk}^+ &= \frac{1}{8\hbar} \left[ \sigma_{z,\ell m}^{(1)} \sigma_{z,nk}^{(1)} + \sigma_{z,\ell m}^{(1)} \sigma_{z,nk}^{(2)} + \sigma_{z,\ell m}^{(2)} \sigma_{z,nk}^{(1)} + \sigma_{z,\ell m}^{(2)} \sigma_{z,nk}^{(2)} \right] \times \\ &\quad \times J(\omega_{nk}) (\coth(\beta\hbar\omega_{nk}/2) - 1), \end{aligned} \quad (\text{D.5})$$

$$\begin{aligned} \Gamma_{\ell mnk}^- &= \frac{1}{8\hbar} \left[ \sigma_{z,\ell m}^{(1)} \sigma_{z,nk}^{(1)} + \sigma_{z,\ell m}^{(1)} \sigma_{z,nk}^{(2)} + \sigma_{z,\ell m}^{(2)} \sigma_{z,nk}^{(1)} + \sigma_{z,\ell m}^{(2)} \sigma_{z,nk}^{(2)} \right] \times \\ &\quad \times J(\omega_{\ell m}) (\coth(\beta\hbar\omega_{\ell m}/2) + 1). \end{aligned} \quad (\text{D.6})$$

Tensor element (two baths)	Tensor element (single bath)
11 11	11 11
11 33	11 33
24 24	–
24 42	–
33 11	33 11
33 33	33 33
42 24	–
42 42	–

Table D.1: Non-vanishing Redfield tensor elements for pure Ising-type zz-coupling between the qubits and  $\sigma_z$ -coupling to the bath. The labelling is according to the basis states in the Hamiltonian given in the singlet-triplet basis.

For vanishing frequency  $\omega_{nk} \rightarrow 0$ ,  $\omega_{\ell m} \rightarrow 0$ , and for Ohmic spectral functions  $J(\omega) = \alpha\omega$ , these rate expressions become

$$\Gamma_{\ell mnk}^{(\pm)} = \frac{1}{4\beta\hbar} \left[ \sigma_{z,\ell m}^{(1)} \sigma_{z,nk}^{(1)} \alpha_1 + \sigma_{z,\ell m}^{(2)} \sigma_{z,nk}^{(2)} \alpha_2 \right], \quad (\text{D.7})$$

where the  $\alpha_i$  are dimensionless parameters that characterize the strength of the dissipative effects for the corresponding baths. Again, the rate expressions are very similar for the single-bath case with the aforementioned differences. For simplicity, we now assume  $\alpha = \alpha_1 = \alpha_2$  and therefore also  $J(\omega) = J_1(\omega) = J_2(\omega) = \alpha\omega\hbar/(1 + \omega^2/\omega_c^2)$ , where in the last equation a Drude cutoff was introduced into the Ohmic spectral function.

Now, we would like to find the non-zero rates that constitute the Redfield tensor  $R_{nmkl}$ . Therefore, it is most useful to first investigate the symmetry properties of the spin coupling to the bath. Obviously  $[\hat{H}_S, \hat{H}_I] = 0$ , where  $\hat{H}_I$  is the coupling Hamiltonian between the system and the bath, holds. In more detail, the spin part of the bath coupling Hamiltonian is given in the singlet-triplet basis by

$$\hat{\sigma}_z^{(1)} = \begin{pmatrix} 1 & 0 & 0 & 0 \\ 0 & 0 & 0 & 1 \\ 0 & 0 & -1 & 0 \\ 0 & 1 & 0 & 0 \end{pmatrix} \quad \text{and} \quad \hat{\sigma}_z^{(2)} = \begin{pmatrix} 1 & 0 & 0 & 0 \\ 0 & 0 & 0 & -1 \\ 0 & 0 & -1 & 0 \\ 0 & -1 & 0 & 0 \end{pmatrix}. \quad (\text{D.8})$$

Both spin matrices have the same matrix entries non-zero. Thus, one can conclude that  $\sigma_{z,ab}^{(i)} \neq 0$  is the case for  $ab \in \{11, 24, 33, 42\} = \kappa$ , *i.e.*, possible indices for non-zero rate expressions are all possible combinations of elements of the set  $\kappa$ . Here, the labelling is according to the basis states for the Hamiltonian in matrix form in singlet-triplet basis. Additionally, from consideration of the parity of the different products of  $\hat{\sigma}_z$  matrix elements, it follows that only the Redfield tensor elements given in table D.1 do *not* vanish. The reason why in the single bath case the rates belonging to the transitions  $2 \leftrightarrow 4$  vanish,



is that the bath can only induce these transitions in the two bath case, which is observed when considering the full Hamiltonian

$$\hat{H} = \hat{H}_S + \hat{H}_I + \hat{H}_B = -\frac{1}{2} \begin{pmatrix} K - S & 0 & 0 & 0 \\ 0 & -K & 0 & -\Delta S \\ 0 & 0 & K + S & 0 \\ 0 & -\Delta S & 0 & -K \end{pmatrix} + \hat{H}_B, \quad (\text{D.9})$$

where  $S = \hat{X}_1 + \hat{X}_2$  and  $\Delta S = \hat{X}_1 - \hat{X}_2$  are the sum and difference of the bath (oscillator) coordinates. Clearly, for a single bath  $\hat{X} = \hat{X}_1 = \hat{X}_2$  and  $\Delta S = 0$  – thus, the bath can induce the aforementioned transitions only in the single bath case. Note also that in the single bath case the bath coordinates are only coupled to the first and third diagonal element reflecting the remaining Redfield tensor elements for the single bath case given in table D.1.



# Appendix E

## The driven multi-qubit system

Here, a general recipe for the simulation of driven dissipative multi-qubit systems for weak coupling to the environment will be given. Note that no Markov approximation will be made, so that this approach can be compared to exact semi-analytical calculations within lowest-order Born approximation, cf. Ref. [312]. Similar to the approach presented in Ref. [158], first the projectors  $\hat{\gamma}_{nm} \equiv |n\rangle\langle m|$  are introduced, where  $n, m$  denote the possible basis states of the multi-qubit system. The matrix elements of the stochastic force operator are given by  $\hat{\zeta}_{nm}$ . Thus it is possible to rewrite the system Hamiltonian and the system-bath interaction

$$\begin{aligned}\hat{H}_S &= \sum_i -\frac{1}{2}\Delta_i \hat{\sigma}_x^{(i)} - \frac{1}{2}\epsilon_i(t) \hat{\sigma}_z^{(i)} - \frac{K}{2} \hat{\sigma}_z^{(i)} \hat{\sigma}_z^{(i+1)} \\ &= \sum_i -\frac{1}{2}\Delta_1 (|00\rangle\langle 01| + |01\rangle\langle 00|) + \dots \\ &= \sum_{n,m} H_{nm}(t) \hat{\gamma}_{nm},\end{aligned}\tag{E.1}$$

$$\begin{aligned}\hat{H}_{SB} &= -\frac{1}{2} (|00\rangle\langle 00| - |01\rangle\langle 01|) \sum_i c_i x_i - \frac{1}{2} (|10\rangle\langle 10| - |11\rangle\langle 11|) \sum_j c_j x_j \\ &= \sum_{n,m} \hat{\gamma}_{nm} \hat{\zeta}_{nm}.\end{aligned}\tag{E.2}$$

Then the matrix elements  $\rho_{nm} = \langle n|\rho|m\rangle$  of the reduced density matrix in Born approximation read [158]

$$\dot{\rho}_{nm}(t) = -i \sum_{n',m'} L_{nmn'm'}(t) \rho_{n'm'}(t) - \int_0^t dt' \sum_{n'm'} \Gamma_{nmn'm'}(t, t') \rho_{n'm'}(t'),\tag{E.3}$$

where both the Liouville superoperator that describes the coherent part of the system evolution

$$L_{nmn'm'}(t) = \langle n|\mathcal{L}_S \hat{\gamma}_{n'm'}|m\rangle = H_{nn'} \delta_{mm'} - H_{mm'} \delta_{nn'}\tag{E.4}$$

and the Redfield relaxation tensor [313]

$$\begin{aligned}\Gamma_{nmm'm'}(t, t') &= \langle n | \langle \mathcal{L}_{\text{SB}}(t) \mathcal{S}_0(t, t') \mathcal{L}_{\text{SB}}(t') \rangle_{\beta} \hat{\gamma}_{n'm'} | m \rangle \\ &= \sum_{kk', rr'} \left( K_{rr'kk'}(t - t') \langle n | [\hat{\gamma}_{rr'}, \mathcal{S}_{\text{S}}(t, t') \hat{\gamma}_{kk'} \hat{\gamma}_{n'm'}] | m \rangle - \right. \\ &\quad \left. - K_{kk'rr'}(t' - t) \langle n | [\hat{\gamma}_{rr'}, \mathcal{S}_{\text{S}}(t, t') \hat{\gamma}_{n'm'} \hat{\gamma}_{kk'}] | m \rangle \right)\end{aligned}\quad (\text{E.5})$$

were introduced. Here, the bath correlation function is defined as

$$K_{kk'rr'}(\tau) = \langle \exp(i\hat{H}_{\text{B}}\tau) \hat{\zeta}_{kk'} \exp(-i\hat{H}_{\text{B}}\tau) \hat{\zeta}_{rr'} \rangle_{\beta}, \quad (\text{E.6})$$

where  $\tau = t - t'$ , and the evolution superoperators act according to

$$\mathcal{S}_0(t, 0) = \exp(-i\mathcal{L}_{\text{B}}t) \hat{T} \exp\left(-i \int_0^t dt' \mathcal{L}_{\text{S}}(t')\right) =: \mathcal{S}_{\text{B}}(t) \mathcal{S}_{\text{S}}(t, 0) \quad (\text{E.7})$$

and

$$\exp(i\mathcal{L}_{\text{B}}t) \hat{O} = \exp(i\hat{H}_{\text{B}}t/\hbar) \hat{O} \exp(-i\hat{H}_{\text{B}}t/\hbar). \quad (\text{E.8})$$

For our purpose

$$\mathcal{S}_{\text{S}}(t, t') = \hat{T} \exp\left(-i \int_{t'}^t d\tau \mathcal{L}_{\text{S}}(\tau)\right). \quad (\text{E.9})$$

From quantum mechanics it is well known (e.g. see page 290/291 of [22]) that the time-evolution operator can be rewritten in terms of a product of infinitesimal time-evolution operators

$$\begin{aligned}\hat{U}(t, t') &= \hat{T} \exp\left(-\frac{i}{\hbar} \int_{t'}^t d\tau H(\tau)\right) \\ &= \exp\left(-\frac{i}{\hbar} H(t' + \Delta t(n-1)) \Delta t\right) \times \cdots \times \exp\left(-\frac{i}{\hbar} H(t') \Delta t\right),\end{aligned}\quad (\text{E.10})$$

with  $\Delta t = (t - t')/n$  and  $n \rightarrow \infty$ . For solving the Bloch-Redfield equations numerically on a computer, we now discretize the right hand side of (E.10) by taking  $n$  large, but finite. To gain more insight into the structure of the elements of the Redfield relaxation tensor, we explicitly write down equation (E.5)

$$\begin{aligned}\Gamma_{nmm'm'}(t, t') &= \sum_{kk', rr'} \left( K_{rr'kk'}(t - t') \langle n | [\hat{\gamma}_{rr'}, \mathcal{S}_{\text{S}}(t, t') \hat{\gamma}_{kk'} \hat{\gamma}_{n'm'}] | m \rangle - \right. \\ &\quad \left. - K_{kk'rr'}(t' - t) \langle n | [\hat{\gamma}_{rr'}, \mathcal{S}_{\text{S}}(t, t') \hat{\gamma}_{n'm'} \hat{\gamma}_{kk'}] | m \rangle \right) \\ &= \sum_{kk', rr'} \left( K_{rr'kk'}(t - t') [\langle n | r \rangle \langle r' | \mathcal{S}_{\text{S}}(t, t') | k \rangle \langle k' | n' \rangle \langle m' | m \rangle - \right. \\ &\quad \left. - \langle n | \mathcal{S}_{\text{S}}(t, t') | k \rangle \langle k' | n' \rangle \langle m' | r \rangle \langle r' | m \rangle] - \right.\end{aligned}\quad (\text{E.11})$$

$$\begin{aligned}
& - K_{kk'rr'}(t' - t)[\langle n|r\rangle \langle r'| \mathcal{S}_S(t, t')|n'\rangle \langle m'|k\rangle \langle k'|m\rangle - \\
& - \langle n|\mathcal{S}_S(t, t')|n'\rangle \langle m'|k\rangle \langle k'|r\rangle \langle r'|m\rangle] \\
= & \sum_{k,r} K_{nrkn'}(t - t')S_{rmkm'}(t, t') + K_{mrkm'}(t - t')S_{nrn'k}(t, t') - \\
& - K_{rnkm'}(t - t')S_{rmn'k}(t, t') - K_{rmkn'}(t - t')S_{nrkm'}(t, t'). \quad (\text{E.12})
\end{aligned}$$

Where we simplified the expression by defining the matrix elements of the system evolution superoperator

$$S_{nmn'm'}(t, t') = \langle n|\mathcal{S}_S(t, t')\hat{\gamma}_{n'm'}|m\rangle = \langle n|\hat{U}_S(t, t')\hat{\gamma}_{n'm'}\hat{U}_S^\dagger(t, t')|m\rangle = U_{nn'}(t, t')U_{mm'}^*(t, t'), \quad (\text{E.13})$$

where  $\hat{U}_S(t, t')$  is the time evolution operator of the unperturbed driven system. The  $U_{ij}(t, t')$  are the corresponding matrix elements. The  $K_{nmkl}$  are the bath correlation functions that are defined via

$$K_{nmkl}(\tau) = \langle \exp(i\hat{H}_B\tau)\hat{\zeta}_{nm} \exp(-i\hat{H}_B\tau)\hat{\zeta}_{kl} \rangle_\beta. \quad (\text{E.14})$$

After these basic considerations, one can proceed to calculate the system dynamics by solving the master equation for the system. For the weak coupling regime the Bloch-Redfield equations (E.5) can be solved. The master equation itself needs to be discretized in order to be solved numerically on a (classical) computer. Here, the master equation will be given for a discretized stepwise propagation, *i.e.*, the evolution is propagated forward only a single small step  $\Delta t$  and then the time evolution operator  $\hat{U}(t_0 + \Delta t, t_0) = \exp(-i/\hbar H(t_0)\Delta t)$  is calculated. Therefore, also the matrix elements of the system evolution superoperator (E.13) are determined. When an infinitesimal time step  $\Delta t$  is considered, the right part of the differential equation (E.3) can be written as

$$\begin{aligned}
\dot{\rho}_{nm}(t + \Delta t) & = -i \sum_{n',m'} L_{nmn'm'}(t + \Delta t)\rho_{n'm'}(t + \Delta t) - \\
& - \sum_{n',m'} \int_{t_0}^{t+\Delta t} \Gamma_{nmn'm'}(t + \Delta t, t')\rho_{n'm'}(t') dt' \quad (\text{E.15})
\end{aligned}$$

$$\begin{aligned}
& = -i \sum_{n',m'} \left[ \left( L_{nmn'm'}(t_0) + \Delta t \dot{L}_{nmn'm'}(t_0) \right) (\rho_{n'm'}(t) + \dot{\rho}_{n'm'}(t)\Delta t) \right. \\
& - \Delta t \Gamma_{nmn'm'}(t_0, t_0)\rho_{n'm'}(t_0) - \int_0^t dt' \Gamma_{nmn'm'}(t, t')\rho_{n'm'}(t') \\
& \left. - \Delta t \int_0^{t_0} dt' \frac{\partial \Gamma_{nmn'm'}}{\partial t}(t, t')\rho(t') \right] \quad (\text{E.16})
\end{aligned}$$

$$\begin{aligned}
& = \dot{\rho}_{nm}(t) + \Delta t \sum_{n',m'} \left[ (-i \dot{L}_{nmn'm'}(t)\rho_{n'm'}(t) - i L_{nmn'm'}(t)\dot{\rho}_{n'm'}(t)) \right. \\
& \left. - \Gamma_{nmn'm'}(t_0, t_0)\rho_{n'm'}(t_0) - \int_0^{t_0} dt' \frac{\partial \Gamma_{nmn'm'}}{\partial t}(t, t')\rho_{n'm'}(t') \right]. \quad (\text{E.17})
\end{aligned}$$

For the Markov approximation the last two terms can be simplified to become

$$\begin{aligned} \dot{\rho}_{nm}(t_0 + \Delta t) &= \dot{\rho}_{nm}(t_0) + \Delta t \sum_{n',m'} \left[ (-i\dot{L}_{nmn'm'}(t_0)\rho_{n'm'}(t_0) - iL_{nmn'm'}(t_0)\dot{\rho}_{n'm'}(t_0)) \right. \\ &\quad - \frac{\Delta t}{2} \left[ 2\Gamma_{nmn'm'}(t + \Delta t, t)\rho_{n'm'}(t) \right. \\ &\quad \left. \left. + \Gamma_{nmn'm'}(t + \Delta t, t + \Delta t)(\rho_{n'm'}(t) + \Delta t\dot{\rho}_{n'm'}(t)) \right) \right], \end{aligned} \quad (\text{E.18})$$

where the integration step was performed via the trapezoid rule.

After all, this scheme works, for small enough step size and if their period is long enough, also for more sophisticated pulse shapes like a sine or cosine. In the program one may choose an arbitrary memory time of the environment, which has to fit into the memory of the computer, though. The memory will consist of a number of steps  $n_{\text{memory}}$ . All values of  $\rho_{nm}[n_t]$  and  $\dot{\rho}_{nm}[n_t]$  which are calculated prior to the current time step  $n'_t$  will be held in memory, to calculate the integral in Eqn. (E.17) that depends on the state of the system at earlier times.

The integration of the master equation could be done with the well-established Runge-Kutta integration method. Here, the basic working principle will be explained, however, for application of this method, a variable step size algorithm should be implemented additionally [314]. Of course, this method is also applicable to a system of coupled differential equations.

The following differential equation should be solved

$$\dot{\rho} = f(t, \rho), \text{ where } \rho(t_0) = \rho_0. \quad (\text{E.19})$$

In the following we will use equidistant sampling points with a given step size  $h$

$$t_i = t_0 + ih \text{ for } i = 0, 1, 2, \dots \quad (\text{E.20})$$

then the solution of (E.19) when going from  $t_0$  to  $t_1 = t_0 + h$  is given by the following scheme.

$t$	$\rho$	$k = hf(t, \rho)$
$t_0$	$\rho_0$	$k_1$
$t_0 + h/2$	$\rho_0 + k_1/2$	$k_2$
$t_0 + h/2$	$\rho_0 + k_2/2$	$k_3$
$t_0 + h$	$\rho_0 + k_3$	$k_4$
$t_1 = t_0 + h$	$\rho_1 = \rho_0 + \frac{1}{6}(k_1 + 2k_2 + 2k_3 + k_4)$	

For the next time steps, the scheme is simply iterated. From Ref. [315] it is known that the time steps  $h$  should be chosen rather small, *i.e.* time resolution should be rather fine grained.

## E.1 Implementation of the program

It is first necessary to define a Hamiltonian. For a flux qubit that is driven via a continuous wave microwave signal, the Hamiltonian is for example

$$H = \begin{pmatrix} \epsilon_0 + \delta \sin(\omega t) & \Delta \\ \Delta & -\epsilon_0 - \delta \sin(\omega t) \end{pmatrix}, \quad (\text{E.21})$$

with the matrix elements  $H_{nm}(t)$ . The time derivative of the Hamiltonian is

$$\dot{H} = \begin{pmatrix} \omega\delta \cos(\omega t) & 0 \\ 0 & -\omega\delta \cos(\omega t) \end{pmatrix}. \quad (\text{E.22})$$

In the following, the implementation of a code for numerical simulation of the dissipative dynamics of a (multi-)qubit system will be sketched. The individual parts will be described in an easy pseudo-code. For the calculation of the time-evolution operator we use the following procedure, which is derived from a series approximation of the time evolution operator for short time intervals  $\Delta t$

```

U(t, t') := function(t, t')
  U =  $\hat{\mathbf{1}}$ 
  told = 0
   $\Delta t = \frac{|t-t'|}{n}$ 
  for i = 1 → n
    tnew = told +  $\Delta t$ 
    U = [ $\hat{\mathbf{1}} - \frac{i}{\hbar} H(\epsilon, \omega, \delta, \Delta, (t' + \Delta t(i-1))\Delta t)$ ]U
    told = tnew
  end.

```

Note that the time evolution operator is stored in a matrix (or array), whose size is determined by the dimension of the Hilbert space for the corresponding Hamiltonian. The Matrix elements of the propagator, kernel and rates are then defined via

$$\dot{U}(t, t') = i\hbar H(\epsilon, \omega, \delta, \Delta, t)U$$

$$S_{nmkl}(t, t') = \text{first calculate } U(t, t') \text{ and } \dot{U}(t, t') \\ \text{return } (U_{\text{mat}})_{nk} (U_{\text{mat}}^\dagger)_{ml}$$

$$\dot{S}_{nmkl}(t, t') = \text{first calculate } U(t, t') \text{ and } \dot{U}(t, t') \\ \text{return } (\dot{U}_{nk} (\dot{U}^\dagger)_{ml} + (U_{nk} (\dot{U}_{ml}))$$

$$L_{nmkl}(t) = \frac{1}{\hbar} (H_{nk}(t)\delta_{ml} - H_{lm}(t)\delta_{nk})$$

$$\dot{L}_{nmkl}(t) = \frac{1}{\hbar} (\dot{H}_{nk}(t)\delta_{ml} - \dot{H}_{lm}(t)\delta_{nk})$$

$$K_{nmkl}(\tau) = \frac{2A_{nmkl}\alpha}{\hbar\beta(T)^2\pi} \left( \psi \left( 1, \frac{\omega_c\tau i+1}{\hbar\beta(T)\omega_c} \right) + \psi \left( 1, \frac{\hbar\beta(T)\omega_c - \omega_c\tau i+1}{\hbar\beta(T)\omega_c} \right) \right)$$

$$\begin{aligned} \dot{K}_{nmkl}(\tau) \\ \tau > 0 \\ &= -\alpha(8 * \text{Im}(\dots)) \\ \tau \leq 0 \\ &= \dots \end{aligned}$$

$$\Gamma_{nmkl}(t, t') = \sum_{i,j=1}^{N_{\text{dim}}} (K_{nikj}(t-t')S_{imjm}(t, t') + K_{mijl}(t-t')S_{nikj}(t, t') - K_{injl}(t-t')S_{imkj}(t, t') - K_{imjk}(t-t')S_{nijl}(t, t'))$$

$$\begin{aligned} \Gamma'_{nmkl}(t, t') &= \sum_{i,j=1}^{N_{\text{dim}}} (\dot{K}_{nikj}(t-t')S_{imjm}(t, t') + K_{nikj}(t-t')\dot{S}_{imjm}(t, t') \\ &+ \dot{K}_{mijl}(t-t')S_{nikj}(t, t') + K_{mijl}(t-t')\dot{S}_{nikj}(t, t') \\ &- \dot{K}_{injl}(t-t')S_{imkj}(t, t') - K_{injl}(t-t')\dot{S}_{imkj}(t, t') \\ &- \dot{K}_{imjk}(t-t')S_{nijl}(t, t') - K_{imjk}(t-t')\dot{S}_{nijl}(t, t')) \end{aligned}$$

where, *e.g.*,  $A_{nmkl} = \sigma_{z,nm}^{(1)}\sigma_{z,kl}^{(1)}$  in the particular basis. Here, the expressions for the kernel are taken for an Ohmic spectral function with an exponential cutoff at frequency  $\omega_c$ , *i.e.*,  $J(\omega) = \alpha\hbar\omega\exp(-\omega/\omega_c)$ , cf. Ref. [315]. For an Ohmic spectral function with a Drude cutoff  $J(\omega) = \alpha\hbar\omega/(1 + \omega^2/\omega_c^2)$ , the kernel has real and imaginary parts (different from the classical case), which can be evaluated [316] and is given here for a pure  $\hat{\sigma}_z$ -type of coupling to the bath

$$K_{nmkl}(\tau) = -\frac{1}{4}\delta_{nm}\delta_{kl}(-1)^{1-\delta_{n\ell}}\alpha \left( \frac{\pi}{\hbar\beta^2}\sinh^{-2}(\pi t/\hbar\beta) + i\frac{\hbar\omega_c}{2}\text{sign}(t)e^{-\omega_c|t|} \right). \quad (\text{E.23})$$

Note that also more sophisticated spectral functions can be used in the simulations, *e.g.*, peaked spectral functions [317, 318].

The main algorithm of the program treats the solution of the master equation by stepwise integration. First, an initial value for the reduced density matrix and its time derivative is defined

$$\rho(0) = \begin{pmatrix} 1 & 0 \\ 0 & 0 \end{pmatrix}, \quad \dot{\rho}(0) = \begin{pmatrix} 0 & \frac{i}{\hbar}\Delta \\ -\frac{i}{\hbar}\Delta & 0 \end{pmatrix}.$$

Then one can proceed to write down the main part of the program. Note that the time is discretized in steps of size  $\Delta t$ , *i.e.*, the matrix elements of the density matrix are characterized by the number of time steps  $n_t$  with  $t = n_t\Delta t$ . Now the main algorithm will be given in a simplified pseudo-code.



```

 $n_t = 1 \rightarrow N_{\text{steps}}$ 
 $t = (n_t - 1)\Delta t$ 
→ calculate the eigenbasis of the Hamiltonian at this time -
this is needed to calculate, e.g., the time evolution operator
 $p_1 = \dot{\rho}_{nm}[n_t - 1]$ 
 $p_2 = \Delta t(-i(\sum_{k,\ell} \dot{L}_{nmk\ell}(t)\rho_{k\ell}[n_t - 1] + L_{nmk\ell}(t)\dot{\rho}_{k\ell}[n_t - 1]))$ 
 $p_3 = -\Delta t \sum_{k,\ell} \Gamma_{nmk\ell}(t, t)\rho_{k\ell}[n_t - 1]$ 
 $t_0 = t - n_{\text{memory}}\Delta t$ 
 $t_0 < 0? \Rightarrow t_{\text{lowerlimit}} := 0$ 
 $p_4 = -\Delta t \int_{t_0}^t \sum_{k,\ell} \Gamma'_{nmk\ell}(t, t')\tilde{\rho}_{k\ell}(t') dt'$ 
(remark:  $\tilde{\rho}$  is continuous and it is interpolated
between two discrete neighbouring values of  $\rho$ 
that define the interval  $[n_{t1}\Delta t, n_{t2}\Delta t]$ .)
 $\dot{\rho}_{nm}[n_t] = \sum_{i=1}^4 p_i$ 
 $\rho_{nm}[n_t] = \rho_{nm}[n_t - 1] + \dot{\rho}_{nm}[n_t - 1]\Delta t$ 
end

```

Note that the integration step in the last equation can be improved by use of the trapezoid rule. Alternatively, the calculation of the term  $p_4$  can be done via

$$dt = \frac{|t_0 - t|}{N}$$

$$p_4 = -\Delta t \frac{dt}{2} \sum_{n=0}^N \sum_{k,\ell} \Gamma'_{nmk\ell}(t, t_0 + n \cdot dt) \tilde{\rho}_{k\ell}(t_0 + n \cdot dt)$$

## E.2 Examples for simulations

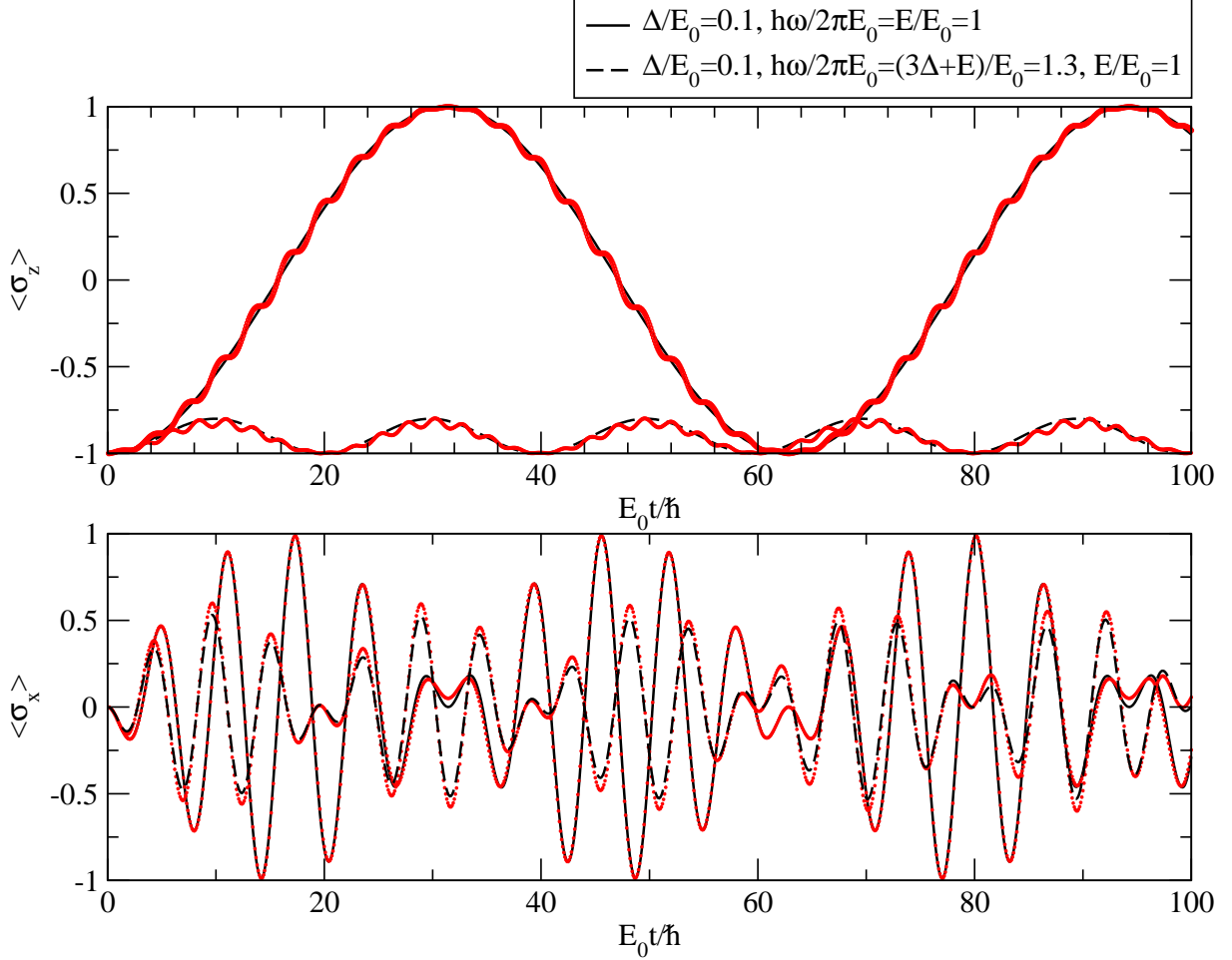


Figure E.1: Simulated time evolution of the expectation values  $\langle \hat{\sigma}_z \rangle$  and  $\langle \hat{\sigma}_x \rangle$  obtained from a numerical integration of the master equation. The black lines denote the case of a rotating wave driving, cf. Eqn. (E.24), and the red lines denote the case of a cos-driving that includes also counter-rotating terms. The cases of a resonant driving (solid lines) and a detuned driving (dashed lines) are shown.

Some simple examples for the simulated time evolution of the reduced density matrix without decoherence, *i.e.*, for  $\alpha = 0$ , are shown in Figs. E.1 and E.2. Figure E.1 depicts the time evolution both for the rotating wave Hamiltonian

$$H = \frac{1}{2} \begin{pmatrix} \epsilon_0 & \Delta e^{-i\omega t} \\ \Delta e^{i\omega t} & -\epsilon_0 \end{pmatrix}, \quad (\text{E.24})$$

and a cosine driving (the terms  $e^{\pm i\omega t}$  in Eqn. (E.24) are replaced by a cosine with otherwise the same parameters). Additionally the case of a fully resonant driving and a detuned

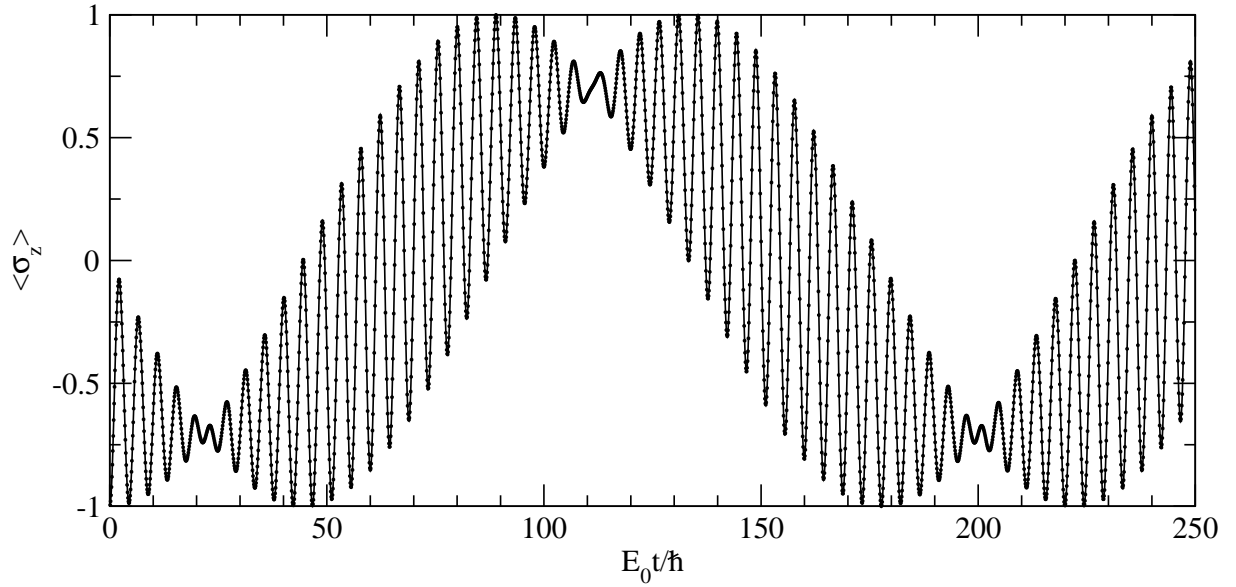


Figure E.2: Time evolution of the expectation value  $\langle \hat{\sigma}_z \rangle$  for the realistic driven flux qubit Hamiltonian Eqn. (E.21).

driving are shown. It is observed that in the case of the resonant driving, the expectation values of  $\hat{\sigma}_z$  and  $\hat{\sigma}_x$  oscillate between their maximal values, which is not the case for the off-resonant driving as expected. Additionally, the cosine-driving shows small oscillations (“wiggles”) on a shorter time scale, which are due to the counter-rotating terms in the expressions for the cosine (Bloch-Siegert shift). In Fig. E.2, the time evolution of the Hamiltonian for a realistic driving of flux qubits Eqn. (E.21) is shown. Here,  $\epsilon_0/E_0 = \Delta/E_0 = 1$ ,  $\delta/E_0 = 0.1$ , where the resonance condition [146] for  $\hbar\omega = \sqrt{\epsilon_0^2 + \Delta^2}$  is fulfilled. It is observed that with this realistic driving again coherent Rabi oscillations are observed with a beating due to the additional frequency scales.



# Appendix F

## Flux qubit inside a cavity

In this appendix, the cavity-qubit system will be investigated in more detail for the specific setup of a flux qubit inside a superconducting (microstrip) resonator, as presented in chapter 12.3. Here, a simplified analytical estimation of the coupling strength  $g$  between the qubit and the cavity is given. Therefore, the problem of the two-dimensional microstrip resonator will be mapped onto the problem of a one-dimensional transmission line. Then the field inside the resonator is quantized, the circuit Lagrangian will be derived, and the coupling strength of the qubit to the cavity field will be estimated. In the last section, the dispersive regime is analyzed.

The two-dimensional problem of the microstrip resonator can be reduced to a one-dimensional problem by assuming that the coil of the microstrip resonator has a circular shape with a mean radius that defines the length of the 1D transmission line via  $L = \lambda = 2\pi\langle R\rangle N$ , where  $N$  is the number of turns of the microstrip coil,  $\langle R\rangle$  is the mean radius of the microstrip coil, and  $L$  is the overall length of the 1D transmission line. This can be viewed as “unwrapping” the microstrip resonator onto a line, which is possible because of the symmetric shape of the microstrip resonator and the electromagnetic fields.

### F.1 Quantization of a 1D transmission line

First, the electromagnetic field of a general 1D transmission line will be quantized. Starting from the general Lagrange density [319]

$$\mathcal{L} = \int_{-L/2}^{L/2} dx \left( \frac{\ell}{2} \dot{j}^2 - \frac{1}{2c} q^2 \right), \quad (\text{F.1})$$

where  $\ell$  and  $c$  are the inductance and capacitance per unit length and  $q(x, t)$  is the charge density, the electromagnetic fields inside the cavity are calculated. Note here again that we consider not the Lagrange function but rather the Lagrange density, *i.e.*,

$$L = \sum_i L_i(q_i, \dot{q}_i) \rightarrow \int \mathcal{L}(\phi_k, \partial^\alpha \phi_k) d^3x \quad (\text{F.2})$$

$$\frac{d}{dt} \left( \frac{\partial L}{\partial \dot{q}_i} \right) = \frac{\partial L}{\partial q_i} \rightarrow \partial^\beta \frac{\partial \mathcal{L}}{\partial (\partial^\beta \phi_k)} = \frac{\partial \mathcal{L}}{\partial \phi_k} \quad (\text{F.3})$$

$$i \rightarrow x^\alpha, k \quad (\text{F.4})$$

$$q_i \rightarrow \phi_k(x) \quad (\text{F.5})$$

$$\dot{q}_i \rightarrow \partial^\alpha \phi_k. \quad (\text{F.6})$$

By introducing  $\Theta(x, t) \equiv \int_{-L/2}^x dx' q(x', t)$ , Eqn. (F.1) can be written as

$$\mathcal{L} = \int_{-L/2}^{L/2} \left( \frac{\ell}{2} \dot{\Theta}^2 - \frac{1}{2c} (\nabla \Theta)^2 \right). \quad (\text{F.7})$$

From this follows the Euler-Lagrange equation (in our case  $\Theta = \Theta(\varphi, t)$ )

$$\partial_\varphi \frac{\partial \mathcal{L}}{\partial (\partial_\varphi \Theta)} + \partial_t \frac{\partial \mathcal{L}}{\partial (\partial_t \Theta)} = \frac{\partial \mathcal{L}}{\partial \Theta} \quad (\text{F.8})$$

$$\partial_\varphi (c^{-1} \Theta') + \ell \ddot{\Theta} = 0. \quad (\text{F.9})$$

Note especially that in the 1D case  $\nabla \Theta = \partial_\varphi \Theta = \Theta'$ . Proceeding along the lines of [143], for the 1D case this can be written as

$$\frac{\partial^2 \Theta}{\partial x^2} = \frac{1}{v^2} \frac{\partial^2 \Theta}{\partial t^2}, \text{ with } v = \frac{1}{\sqrt{\ell c}}. \quad (\text{F.10})$$

This is the one-dimensional wave equation [320]. The boundary conditions are given by the specific cavities used for superconducting qubits, *i.e.*, for a

- superconducting **charge qubit** inside a linear cavity [143],  $\Theta(-L/2, t) = \Theta(L/2, t) = 0$ , and accordingly for a
- superconducting **flux qubit** embedded into a superconducting microstrip resonator (a curled stripline),  $\Theta(\varphi = -N\pi, t) = \Theta(\varphi = N\pi, t) = 0$ , where  $\varphi$  is the angle in the plane in polar coordinates and  $N$  is the number of turns of the resonator loop.

Furthermore, we need to define initial conditions

$$\Theta(x, 0) = f(x), \quad (\text{F.11})$$

$$\frac{\partial \Theta}{\partial t}(x, 0) = g(x). \quad (\text{F.12})$$

We can solve the one-dimensional wave equation by separation of variables [320]. (Or Fourier transform method or d'Alembert's solution.) Here, a factorization ansatz  $\Theta(\varphi, t) = \Phi(\varphi)T(t)$  will be used. This leads to

$$\frac{\Phi''(\varphi)}{\Phi(\varphi)} = \frac{T''(t)}{v^2 T(t)} = -\lambda^2, \quad (\text{F.13})$$

where the boundary conditions are  $\Phi(-N\pi) = \Phi(N\pi) = 0$ . This can be written as two separated problems

$$\Phi''(\varphi) + \lambda^2\Phi(\varphi) = 0, \quad -N\pi < \varphi < N\pi, \quad \Phi(-N\pi) = \Phi(N\pi) = 0 \quad (\text{F.14})$$

$$\text{and } T''(t) + v^2\lambda^2T(t) = 0, \quad t > 0. \quad (\text{F.15})$$

We find the solution ( $\lambda^2 = \lambda_n^2 = (n/2N)^2$ ,  $n = 1, 2, \dots$ ), where  $N$  was the number of turns of the resonator loop

$$\Phi_n(\varphi) = A_n \sin(n\varphi/2N) + B_n \cos(n\varphi/2N). \quad (\text{F.16})$$

Of course it is possible, using the same ansatz, to write down also a solution for  $T_n(t)$ . However, we do not need to write this down explicitly. Thus, the general solution reads

$$\Theta(\varphi, t) = \sum_{n=1}^{\infty} A_n \sin(n\varphi/2N)T_n(t) + B_n \cos(n\varphi/2N)T_n(t). \quad (\text{F.17})$$

The initial conditions require that for

- $n$  **odd**,  $\pm A_n = 0$  and
- $n$  **even**,  $B_n = 0$ .

In other words for  $n$  even, only terms  $A_n \sin(n\varphi/2N)$  (equals  $A_{2n} \sin(2n\varphi/2N)$ ) survive and for  $n$  odd, only terms  $B_n \cos(n\varphi/2N)$  (equals  $B_{2n-1} \cos((2n-1)\varphi/2N)$ ) survive. Now we can write down the whole solution again

$$\Theta(\varphi, t) = \sum_{n=1}^{\infty} A_{2n} \sin(n\varphi/2N)T_{2n}(t) + B_{2n-1} \cos((2n-1)\varphi/2N)T_{2n-1}(t). \quad (\text{F.18})$$

Moreover, we introduce  $\phi_{n_e}(t) = A_{2n}T_{2n}(t)$  and  $\phi_{n_o}(t) = B_{2n-1}T_{2n-1}(t)$  and recognize that the two terms in the sum characterize even and odd modes, respectively. Finally we arrive at

$$\Theta(\varphi, t) = \sum_{n_e=2}^{\infty} \phi_{n_e}(t) \sin(n_e\varphi/2N) + \sum_{n_o=1}^{\infty} \phi_{n_o}(t) \cos(n_o\varphi/2N), \quad (\text{F.19})$$

in analogy to the result obtained in Ref. [143], cf. Eqn. (A5). Please note again that it is easy to write down also the  $\phi_n(t)$  explicitly starting from a formal general solution for  $T_n(t)$  in the same way as  $\Phi_n(\varphi)$  was determined.

## F.2 The microstrip resonator

In this section, the coupling strength between the qubit and the photon field inside the cavity will be calculated. First, the problem of the microstrip resonator line is mapped onto a one dimensional problem, *i.e.*, we define an average radius  $\langle R \rangle$ , such that  $x = \langle R \rangle \varphi$ .

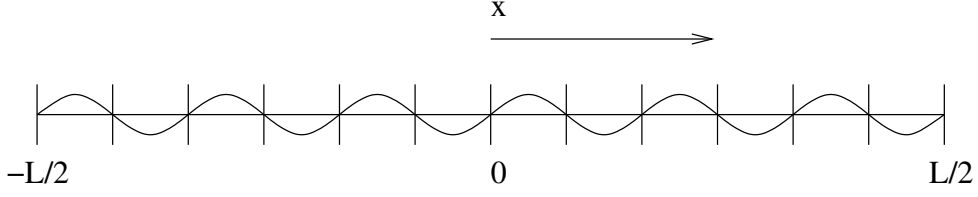


Figure F.1: Schematic drawing of the superconducting transmission line resonator unwrapped and mapped to the problem of a one dimensional transmission line.

The total length of the microstrip resonator in terms of this average radius is given by  $L = \lambda = 2\pi \langle R \rangle N$ . Starting from the solutions of the general Lagrangian that was derived in the first section

$$\mathcal{L} = \langle R \rangle \int_{-\pi N}^{+\pi N} d\varphi \left( \frac{1}{2} j^2 - \frac{1}{2c} q^2 \right), \quad (\text{F.20})$$

$$\Theta(\varphi, t) = \langle R \rangle \int_{-\pi N}^{\varphi} d\varphi' q(\varphi', t), \quad (\text{F.21})$$

with boundary conditions  $\Theta(-\pi N, t) = \Theta(\pi N, t) = 0$ , we find the solution

$$\Theta(\varphi, t) = \sqrt{\frac{2}{\lambda}} \left( \sum_{k_o=1}^{\infty} \phi_{k_o}(t) \cos\left(\frac{k_o \varphi}{2N}\right) + \sum_{k_e=2}^{\infty} \phi_{k_e}(t) \sin\left(\frac{k_e \varphi}{2N}\right) \right). \quad (\text{F.22})$$

Using second quantization we find for the variable  $\phi_k(t)$  and its conjugate momentum

$$\phi_k(t) = \sqrt{\frac{\hbar \omega_k c}{2}} \frac{\lambda}{k\pi} (a_k(t) + a_k^\dagger(t)), \quad (\text{F.23})$$

$$\pi_k(t) = -i \sqrt{\frac{\hbar \omega_k \ell}{2}} \frac{\lambda}{k\pi} (a_k(t) - a_k^\dagger(t)). \quad (\text{F.24})$$

The current is then given by the time derivative, i.e. the momentum, and reads

$$I(\varphi, t) = \sqrt{\frac{2}{\lambda}} \left( \sum_{k_o} \sqrt{\frac{\hbar \omega_{k_o}}{2\ell}} A_{k_o}(t) \cos\left(\frac{k_o \varphi}{2N}\right) + \sum_{k_e} \sqrt{\frac{\hbar \omega_{k_e}}{2\ell}} A_{k_e}(t) \sin\left(\frac{k_e \varphi}{2N}\right) \right). \quad (\text{F.25})$$

This can be inserted into the expression for the magnetic field. Here we neglect retardation effects, i.e., the dimensions of the qubit system are much larger than the wavelength of the incident electromagnetic field. Thus, we assume a uniform magnetic field such that it is sufficient to calculate the field in the center of the qubit loop which is a symmetry point where the vector potential  $\vec{A}$  vanishes

$$\vec{B}(\vec{r}) = \frac{\mu_0}{4\pi} \int_V dV \frac{j(\vec{r}') \times \vec{r}_{rr'}}{r_{rr'}^3}. \quad (\text{F.26})$$



The resulting expression can be inserted into the interaction part of the Hamiltonian that describes the qubit-cavity system when a flux qubit is placed in the center of the microstrip coil. to give the vacuum Rabi frequency which is approximately  $g/\pi \approx 160$  MHz for the first mode. Taking into account the effects of the ground plane, *i.e.*, the washer, the inductive coupling between the qubit and the cavity is increased [276, 321]. This is due to the cut in the ground plane. With a regular ground plane, the currents in the microstrip coil would induce currents in the ground plane that flow in the opposite direction and thus would decrease the coupling strength. However, taking the cut ground plane into account, the mutual coupling is *increased* [321]. Thus, the overall coupling strength between the qubit and the microstrip resonator increases to about  $g/\pi \approx 200$  MHz.

### F.3 Derivation of the Jaynes-Cummings Hamiltonian

For a flux qubit placed in the center of the microstrip resonator coil, the Hamiltonian of the qubit-cavity system is

$$H = H_c + H_S + H_I, \quad (\text{F.27})$$

where  $H_c$  is the cavity Hamiltonian,  $H_S$  is the qubit Hamiltonian and  $H_I$  is the interaction part of the Hamiltonian. The SQUID (or flux qubit) Hamiltonian reads [74]

$$\hat{H}_S = \frac{\hat{Q}^2}{2C} + \frac{(\hat{\Phi} - \Phi_x)^2}{2L} - E_J \cos\left(2\pi \frac{\hat{\Phi}}{\Phi_0}\right), \quad (\text{F.28})$$

see also section 2.1. The analysis is easily extended to a 3jj qubit inside the cavity, which does not change the shape of the cavity-qubit coupling as presented in the following. The cavity Hamiltonian describes a single-mode cavity  $H_c = \hbar\omega_r (a^\dagger a + \frac{1}{2})$  with resonant frequency  $\omega_r$ . Moreover, the coupling between the cavity and the qubit is a mutual inductive coupling,

$$H_I = -\frac{1}{L}(\hat{\Phi} - \Phi_x)\hat{\Phi}_c, \quad \Phi_c = \int_S \vec{B}(\vec{r}, t) \cdot d\vec{S}. \quad (\text{F.29})$$

If the self-inductance is large, the externally applied flux is close to  $\Phi_0/2$  and temperature is low, a double-well potential is formed where only the lowest states in the wells contribute. Therefore, the reduced Hamiltonian

$$\hat{H} = -\frac{1}{2}\epsilon\hat{\sigma}_z - \frac{1}{2}\Delta\hat{\sigma}_x \quad (\text{F.30})$$

is obtained. The bias, *i.e.*, the asymmetry of the double-well potential, reads [81]

$$\epsilon(\Phi_x) = 2I_p \left( \frac{\Phi}{\Phi_0} - \frac{1}{2} \right), \quad (\text{F.31})$$

where  $I_p$  denotes the magnitude of the persistent current in the loop. In the case of a flux qubit embedded into a microstrip resonator, the coupling (F.29) couples the magnetic field

mode of the cavity to the  $\hat{\sigma}_z$  component of the spin, due to the current-current coupling between the two loops [76]. The magnetic component  $\vec{B}(\vec{r}, t)$  of the cavity field has the form  $\vec{B}(\vec{r}, t) = \sqrt{\frac{\hbar\omega_r}{2\mu_0}}(a^\dagger + a)\vec{B}(\vec{r})$ . In spin-1/2 notation the Hamiltonian becomes

$$H_q = -\frac{1}{2}\epsilon\hat{\sigma}_z - \frac{1}{2}\Delta\hat{\sigma}_x - \sqrt{\frac{\hbar\omega_r}{2\mu_0}}(a^\dagger + a)\hat{\sigma}_z + \hbar\omega_r\left(a^\dagger a + \frac{1}{2}\right). \quad (\text{F.32})$$

Diagonalization of the Hamiltonian with respect to the unperturbed qubit terms

$$\hat{H}'_q = -\frac{\Omega}{2}\hat{\sigma}'_z - \sqrt{\frac{\hbar\omega_r}{2\mu_0}}(a^\dagger + a)(\cos(\theta)\hat{\sigma}'_z - \sin(\theta)\hat{\sigma}'_x) + \hbar\omega_r\left(a^\dagger a + \frac{1}{2}\right), \quad (\text{F.33})$$

with  $\Omega = \sqrt{\epsilon^2 + \Delta^2}$ . At the degeneracy point and in the eigenbasis, only the  $\hat{\sigma}'_x$ -component of the spin couples to the oscillator. By introducing the Pauli raising and lowering operators,

$$\hat{\sigma}'_\pm = \frac{\hat{\sigma}'_x \pm i\hat{\sigma}'_y}{2}, \quad (\text{F.34})$$

and defining  $g := \sqrt{\frac{\omega_r}{2\hbar\mu_0}}B_c$  we can re-express  $H_I$  as

$$H_I = \hbar g(\hat{\sigma}'_+ + \hat{\sigma}'_-)(a^\dagger + a). \quad (\text{F.35})$$

The terms that contain  $\hat{\sigma}'_+ a^\dagger$  and  $\hat{\sigma}'_- a$  oscillate in the interaction picture at twice the frequencies of interest  $\omega_r$  and  $\Omega$  and are therefore neglected. Thus, we finally arrive at the Jaynes-Cummings Hamiltonian

$$H_{\text{JC}} = -\frac{\Omega}{2}\sigma'_z + \hbar g(a^\dagger\sigma'_- + a\sigma'_+) + \hbar\omega_r\left(a^\dagger a + \frac{1}{2}\right), \quad (\text{F.36})$$

see also chapter 12.

## F.4 The dispersive read-out

To read-out the qubit one can employ a dispersive read-out scheme. It has been shown in chapter 12 that the ac-Stark shift will pull the resonance frequency of the cavity depending on the state of the qubit. The cavity resonance frequency in turn is easily probed by measuring the transmitted signal power when shining in microwave radiation on the cavity. If this microwave radiation is at one of the pulled frequencies of the cavity, the transmitted signal and the photon number in the cavity will be large in contrast to the case where both are detuned.

Without taking dissipative effects, e.g. cavity losses, in the cavity into account, the average photon number inside the cavity can be computed from the qubit-cavity Hamiltonian in the rotating frame

$$H' = UH U^\dagger \approx \hbar\left[\omega_r + \frac{g^2}{\Delta}\hat{\sigma}_z\right]a^\dagger a + \frac{\hbar}{2}\left[\Omega + \frac{g^2}{\Delta}\right]\hat{\sigma}_z \quad (\text{F.37})$$

and for the readout process an additional coherent driving term [143]

$$H_{\text{mw}} = \hbar\epsilon(t)(a^\dagger e^{-i\tilde{\omega}t} + a e^{i\tilde{\omega}t}) \quad (\text{F.38})$$

with time dependent amplitude  $\epsilon(t)$  is applied to the resonator circuit. From this one finds the equations of motion

$$\dot{\sigma}_z = 0 \quad (\text{F.39})$$

$$\begin{aligned} \dot{a} &= \frac{1}{i\hbar}[a, H' + H_{\text{mw}}] \\ &= -i \left( \omega_r a + \frac{g^2}{\Delta} a \sigma_z + \epsilon(t) e^{-i\tilde{\omega}t} \right) \end{aligned} \quad (\text{F.40})$$

$$\partial_t(a\sigma_z) = -i \left( \omega_r a \sigma_z + \frac{g^2}{\Delta} \mathbf{1} a + \epsilon(t) \sigma_z e^{-i\omega_{\text{mw}}t} \right). \quad (\text{F.41})$$

The time dependent solution for  $a(t)$  can be used to compute the average number of photons  $n = \langle a^\dagger a \rangle = \text{Tr}(\rho_\beta a^\dagger a)$  inside the cavity [174]. It can be obtained by Laplace transformation of the equation of motion for the intra-cavity field  $a(t)$  and taking into account that  $\sigma_z$  is a constant of motion. In the following  $\sigma_z$  denotes the expectation value  $\langle \hat{\sigma}_z \rangle$ . It is found

$$sa(s) - a(0) + i \left( \omega_r + \frac{g^2}{\Delta} \sigma_z \right) a(s) = -i \int_0^\infty \epsilon(t) e^{-i\omega_{\text{mw}}t} e^{-st} dt, \quad (\text{F.42})$$

*i.e.*, with  $\omega' = \omega_r + g^2/\Delta \langle \sigma_z \rangle$  one formally gets

$$a(s) = \frac{a(0)}{s + i\omega'} - \frac{i}{s + i\omega'} \int_0^\infty \epsilon(t) e^{-i\tilde{\omega}t} e^{-st} dt. \quad (\text{F.43})$$

Obviously the first term in Eqn. (F.43) will give an oscillating contribution in time and the second term in Eqn. (F.43) depends on the shape of the pulse which is given by the time-dependent amplitude  $\epsilon(t)$ .

The general solution for  $a(t)$  can also be obtained by a Green function solution [322]. Then, with the definition  $\omega_0 = \omega_r + g^2/\Delta \langle \hat{\sigma}_z \rangle$ , the general solution is

$$a(t) = e^{i\omega_0 t} \int_{-\infty}^t dt' \epsilon(t') e^{i\delta t'}, \quad (\text{F.44})$$

where  $\delta = \tilde{\omega} - \omega_0$  is the detuning. For an off-resonant driving and a finite pulselength the integral on the rhs has to be evaluated. In the case of a resonant driving, *only* the area under the pulse is important. In this case clearly the area theorem holds because the Jaynes-Cummings Hamiltonian includes a rotating wave approximation. Using the

presented approach, it is verified that for the driven Jaynes-Cummings Hamiltonian the limit of on average a single microwave photon in the cavity can be achieved. However, from this result a truly quantum mechanical behaviour, *i.e.*, generation of a Fock state in the cavity can not be deduced. Here, the pump rate of incoming photons and the loss rate are both on the order of  $10^6/s$ , *i.e.*, on average there is a single photon in the cavity. However, for a true (single photon) Fock state, also the deviation from the mean value has to be small.

Note that, by assuming a two-sided cavity with input and output fields at both ends [174] (accounting for cavity losses) the solution  $a(t)$  for the internal cavity field will be modified and the equation of motion for the internal field is given by (F.40) and

$$\dot{a}(t) = \dot{a}(t)_{\text{old}} - \frac{\gamma_1 + \gamma_2}{2}a(t) + \sqrt{\gamma_1}a_{\text{IN}}(t) + \sqrt{\gamma_2}b_{\text{IN}}(t), \quad (\text{F.45})$$

where the  $\gamma_i$  can be determined from the simulations of the cavity field configurations, and  $a_{\text{IN}}$ ,  $b_{\text{IN}}$  model the input fields at both ends of the cavity.

# Appendix G

## Landau-Zener tunneling

When a two-level system in its ground state is biased through an anticrossing, the Landau-Zener-Stückelberg (LZS) problem gives the probability for the system to make a transition to the excited state [323]. LZS transitions have been reported in recent experiments [324] with superconducting flux qubits, where a linear sweep of the bias flux was performed. Also indirect evidence for LZS transitions was found in other experiments with superconducting flux qubits [86, 87]. However, a detailed analytical description of the LZS problem for a finite sweep time and taking leakage to other states into account has not been developed yet.

Note that a system for which the sweep time through the anticrossing is infinitely long, undergoes a completely adiabatic evolution and would always stay in the ground state. Thus, for determining the probability for making a transition from the ground to the excited state, the interplay between the timescales set by the energy scale of the two-level system and the sweep time is important. This problem can be described with the following time-dependent Hamiltonian

$$H(t) = \frac{1}{2} \begin{pmatrix} vt & \Delta \\ \Delta & -vt \end{pmatrix}. \quad (\text{G.1})$$

The basis states of this Hamiltonian are the ground  $|g\rangle$  and excited state  $|e\rangle$ . In the original LZS problem the probability for finding the system, which is prepared in the state  $|g\rangle$  at time  $t_i = -\infty$ , at the final time  $t_f = \infty$  in the excited state  $|e\rangle$ , *i.e.*, for simplicity  $t_i = -t_f$ . Kayanuma [325] has presented an elegant solution to this problem. He calculates the probability for finding that the system remains in the initial state

$$P = |\langle g | \hat{T} \exp(-i \int_{t_f}^{t_f} H(t) dt) | g \rangle|^2 = |c|^2 \quad (\text{G.2})$$

by expanding the time-ordered exponential in powers of  $H$ , which leads to a sequence of coupled integrals, namely

$$c = \sum_n (-i\Delta/2)^{2n} \int_{-t_f}^{t_f} dt_{2n} \int_{-t_f}^{t_{2n}} dt_{2n-1} \cdots \int_{-t_f}^{t_2} dt_1 \exp\left(\frac{i\nu}{2} \sum_{j=1}^{2n} (-1)^j t_j^2\right). \quad (\text{G.3})$$

By introducing the following transformation

$$\begin{aligned} x_1 &= t_1 \\ x_k &= t_1 + \sum_{j=1}^{k-1} (t_{2j+1} - t_{2j}) \\ y_k &= t_{2k} - t_{2k-1}, \end{aligned} \quad (\text{G.4})$$

the integrations can be decoupled and finally the Landau-Zener probability

$$P_{\text{LZ}} = e^{-\frac{\Delta^2 \pi}{2v}} \quad (\text{G.5})$$

is obtained. Now, a more complicated scenario will be introduced in which the sweep time is finite and the upper level can decay with a rate  $\Gamma$  into a third state  $|h\rangle$ . Thus the effective two-level Hamiltonian reads

$$H'(t) = \frac{1}{2} \begin{pmatrix} vt & \Delta \\ \Delta & -vt - i\Gamma \end{pmatrix}. \quad (\text{G.6})$$

For the case where the sweep through the anticrossing happens in a finite time interval and taking the leakage out of the level  $|e\rangle$  into account, the following expression needs to be evaluated

$$\begin{aligned} c &= \sum_n \left( \frac{-i\Delta}{2} \right)^{2n} A_n \\ A_n &= \int_{-t_f}^{t_f} dx_1 \int_{-x_1}^{3t_f} dx_2 \cdots \int_{-x_{n-1}}^{(2n-1)t_f} dx_n \int_0^{2t_f} dy_1 \cdots \\ &\quad \cdots \int_0^{2t_f} dy_n \exp \left( iv \sum_{k=1}^n x_k y_k + \frac{iv}{2} \left( \sum_{k=1}^n y_k \right)^2 - \Gamma \sum_{k=1}^n y_k \right). \end{aligned} \quad (\text{G.7})$$

The problematic part of this integral is the first series of  $x_n$ -integrations, which are coupled and can not easily be decoupled. Thus, a short sketch of a derivation by complete induction is given. First, for  $n = 1$  the problematic  $x_k$ -integration simplifies and gives

$$A_1 = \int_0^{2t_f} dy_1 \frac{1}{ivy_1} e^{\frac{iv}{2} y_1^2 - \Gamma y_1} e^{ivy_1 t_f}. \quad (\text{G.8})$$

For the step  $n \rightarrow n + 1$ , the following expression is investigated

$$A_n = \int_{-t_f}^{t_f} dx_1 \int_{-x_1}^{3t_f} dx_2 \cdots \int_{-x_{n-1}}^{(2n-1)t_f} dx_n \int_0^{2t_f} dy_1 \cdots \int_0^{2t_f} dy_n \exp \left( iv \sum_{k=1}^n x_k y_k + c(y_p) \right) \quad (\text{G.9})$$

$$= \int_{-t_f}^{t_f} dx_1 \int_{-x_1}^{3t_f} dx_2 \cdots \int_{-x_{n-1}}^{(2n-1)t_f} dx_n \zeta(x_k, y_k), \quad (\text{G.10})$$

where  $c(y_p) = \frac{iv}{2} (\sum_{k=1}^n y_k)^2 - \Gamma \sum_{k=1}^n y_k$  includes all constant terms during the respective integration. The individual  $x_k$ -integrations yield factors of the form

$$\zeta = \frac{1}{(i)^n v y_n (y_{n-1} - y_n) \dots} \left( e^{iv y_n (2n-1)t_f} e^{iv y_{n-1} (2(n-1)-1)t_f} \dots - e^{iv y_n (2n-1)t_f} e^{-iv y_{n-1} x_{n-2}} \dots \right) e^c. \quad (\text{G.11})$$

Then the resulting  $y_k$ -integrations can be performed and  $A_n$  could be obtained in closed form. Note that for the leaky LZS problem perturbative solutions in lowest order of  $\Delta$  can be derived [326]. The resulting expression for finite leakage and a long sweep time is

$$A_1 = \frac{2}{v} \arctan \left( \frac{vt_f}{\Gamma} \right). \quad (\text{G.12})$$

In comparison to the case without damping ( $A_1 = \pi/v$ ), the leakage from one of the levels can enhance the survival probability because the arctangent always stays smaller than  $\pi/2$  for a positive argument. For  $t_f \rightarrow \infty$ , the result without leakage is recovered.





# Bibliography

- [1] A.M. Turing. *On Computable Numbers, with an Application to the Entscheidungsproblem*. Proc. London Math. Soc. **42**, 230–265 (1936).
- [2] K. Gödel. *Über formal unentscheidbare Sätze der Principia Mathematica und verwandter Systeme I*. Monat. Math. Phys. **38**, 173–198 (1931).
- [3] H. Klaeren. *Vom Problem zum Programm*. Teubner Verlag (Stuttgart, Germany) 1991.
- [4] N. Metropolis, J. Howlett and G. Rota. *A History of Computing in the Twentieth Century*. Academic Press (New York) 1980.
- [5] P. Benioff. *The computer as a physical system: A microscopic quantum mechanical Hamiltonian model of computers as represented by Turing machines*. J. Stat. Phys. **22**, 563–591 (1980).
- [6] D. Deutsch. *Quantum theory, the Church-Turing Principle and the universal quantum computer*. Proc. R. Soc. London A **400**, 97 (1985).
- [7] A.C. Yao. *Quantum circuit complexity*. Proc. of the 34th Ann. IEEE Symp. on Foundations of Computer Science pages 352–361 (1993).
- [8] E. Bernstein and U. Vazirani. *Quantum complexity theory*. SIAM J. Comput. **26**, 1411–1473 (1997).
- [9] D. Deutsch. *Quantum computational networks*. Proc. R. Soc. London A **425**, 73 (1989).
- [10] R.P. Feynman. *Simulating Physics with Computers*. Int. J. Theor. Phys. **V 21**, 467 (1982).
- [11] P. Shor. *Algorithms for quantum computation: Discrete logarithms and factoring*. in Proc. 35th Ann. Symp. on the Foundations of Computer Science (ed. S. Goldwasser), IEEE Computer Society Press, Los Alamitos, California **1**, 124–134 (1994).
- [12] D. Deutsch and R. Jozsa. *Rapid solution of problems by quantum computation*. Proc. Roy. Soc. London A **439**, 553–558 (1992).

- [13] L.K. Grover. *Quantum Mechanics Helps in Searching for a Needle in a Haystack*. Phys. Rev. Lett. **79**, 325 (1997).
- [14] M.A. Nielsen and I.L Chuang. *Quantum Computation and Quantum Information*. Cambridge University Press Cambridge, United Kingdom 2000.
- [15] G. Alber, A. Delgado, N. Gisin and I. Jex. *Efficient bipartite quantum state purification in arbitrary dimensional Hilbert spaces*. J. Phys. A **34**, 8821–8833 (2001).
- [16] P. Rungta, W.J. Munro, K. Nemoto, P. Deuar, G.J. Milburn and C.M. Caves. *Qudit Entanglement, p. 149-164 in Directions in Quantum Optics: A Collection of Papers Dedicated to the Memory of Dan Walls, edited by H. J. Carmichael, R. J. Glauber, and M. O. Scully*. Springer (Berlin, Germany) 1990.
- [17] R. Thew, K. Nemoto, A.G. White and W.J. Munro. *Qudit Quantum State Tomography*. Phys. Rev. A **66**, 012303 (2002).
- [18] D. Gottesman, A. Kitaev and J. Preskill. *Encoding a qubit in an oscillator*. Phys. Rev. A **64**, 012310 (2001).
- [19] F. Grosshans and P. Grangier. *Continuous variable quantum cryptography using coherent states*. Phys. Rev. Lett. **88**, 057902 (2002).
- [20] N.J. Cerf, M. Bourennane, A. Karlsson and N. Gisin. *Security of Quantum Key Distribution Using  $d$ -Level Systems*. Phys. Rev. Lett. **88**, 127902 (2002).
- [21] H. Kleinert. *Path Integrals in Quantum Mechanics, Statistics, Polymer Physics, and Financial Markets, 3rd ed.* World Scientific Singapore 2004.
- [22] F. Schwabl. *Quantenmechanik*. Springer Verlag (Berlin, Germany) 1998, 5th ed.
- [23] W.H. Zurek. *Algorithmic Randomness and Physical Entropy I*. Phys. Rev. A **40**, 4731–4751 (1989).
- [24] J. Eisert. *Entanglement in Quantum Information Theory*. PhD thesis University of Potsdam 2001.
- [25] N. Shenvi, J. Kempe and K.B. Whaley. *A Quantum Random Walk Search Algorithm*. Phys. Rev. A **67** (5), 052307 (2003). lanl-arXive quant-ph/0210064.
- [26] Julia Kempe. *Quantum random walks - an introductory overview*. Contemporary Physics **44** (4), 302–327 (2003). lanl-arXive quant-ph/0303081.
- [27] J. Kempe. *Discrete Quantum Walks Hit Exponentially Faster*. In *RANDOM-APPROX 2003 Lecture Notes in Computer Science* pages 354–369 Heidelberg 2003. Springer. lanl-arXiv quant-ph/0205083.

- [28] N. Gisin, G. Ribordy, W. Tittel and H. Zbinden. *Quantum cryptography*. Rev. Mod. Phys. **74**, 145–195 (2002).
- [29] Ch. Kurtsiefer, P. Zarda, Matthias Halder, H. Weinfurter, P.M. Gorman, P.R. Tapster and J.G. Rarity. *A step towards global key distribution*. Nature **419**, 450 (2002).
- [30] A. Beige, B.-G. Englert, Ch. Kurtsiefer and H. Weinfurter. *Secure communication with single-photon two-qubit states*. J. Phys. A **35**, L407–L413 (2002).
- [31] D.P. DiVincenzo. *Quantum Computation*. Science **270**, 255 (1995).
- [32] D.P. DiVincenzo and D. Loss. *Quantum information is physical*. Superlattices and Microstructures **23**, 419–432 (1998).
- [33] S. J. Glaser, T. Schulte-Herbrüggen, M. Sieveking, O. Schedletsky, N. C. Nielsen, O. W. Sørensen and C. Griesinger. *Unitary Control in Quantum Ensembles, Maximizing Signal Intensity in Coherent Spectroscopy*. Science **280**, 421–424 (1998).
- [34] S.J. Glaser. *NMR Quantum Computing*. Angew. Chem. Int. Ed. **40**, 147–149 (2001).
- [35] L.M.K. Vandersypen, M. Steffen, G. Breyta, C.S. Yannoni, M.H. Sherwood and I.L. Chuang. *Experimental realization of Shor’s quantum factoring algorithm using nuclear magnetic resonance*. Nature **414**, 883–887 (2001).
- [36] A.M. Steane. *Quantum Error Correction*. World Scientific, Singapore 1997.
- [37] D. Aharonov and M. Ben-Or. *Fault-Tolerant Quantum Computation With Constant Error Rate*. arXiv:quant-ph/9906129, submitted to SIAM J. Comp. 1999.
- [38] A.M. Steane. *Overhead and noise threshold of fault-tolerant quantum error correction*. Phys. Rev. A **68**, 042322 (2003).
- [39] E. Knill. *Quantum computing with realistically noisy devices*. Nature **434**, 39–44 (2005).
- [40] B.M. Terhal and G. Burkard. *Fault-Tolerant Quantum Computation For Local Non-Markovian Noise*. Phys. Rev. A **71**, 012336 (2005).
- [41] P. Aliferis, D. Gottesman and J. Preskill. *Quantum accuracy threshold for concatenated distance-3 codes*. arXiv:quant-ph/0504218 2005.
- [42] R. Alicki, D.A. Lidar and P. Zanardi. *Are the Assumptions of Fault-Tolerant Quantum Error Correction Internally Consistent?* arXiv:quant-ph/0506201 2005.
- [43] E. Knill. *Quantum gates using linear optics and postselection*. Phys. Rev. A **66**, 052306 (2002).

- [44] H. Mabuchi and A. C. Doherty. *Cavity quantum electrodynamics: coherence in context*. Science **298**, 1372–1377 (2002).
- [45] C.J. Hood, T.W. Lynn, A.C. Doherty, A.S. Parkins and H.J. Kimble. *The Atom-Cavity Microscope: Single Atoms Bound in Orbit by Single Photons*. Science **287**, 1447–1453 (2000).
- [46] M. Bourennane, M. Eibl, S. Gaertner, C. Kurtsiefer, A. Cabello and H. Weinfurter. *Decoherence-Free Quantum Information Processing with Four-Photon Entangled States*. Phys. Rev. Lett. **92**, 107901 (2004).
- [47] F. Schmidt-Kaler, H. Häffner, M. Riebe, S. Gulde, G.P.T. Lancaster, T. Deuschle, C. Becher, C.F. Roos, J. Eschner and R. Blatt. *Realization of the Cirac-Zoller controlled-NOT quantum gate*. Nature **422**, 408–411 (2003).
- [48] M. Riebe, H. Häffner, C.F. Roos, W. Hänsel, J. Benhelm, G.P.T. Lancaster, T.W. Körber, C. Becher, F. Schmidt-Kaler, D.F.V. James and R. Blatt. *Deterministic quantum teleportation with atoms*. Nature **429**, 734 (2004).
- [49] C. Monroe, D.M. Meekhof, B.E. King and D.J. Wineland. *A “Schrödinger Cat” Superposition State of an Atom*. Science **272**, 1131–1136 (1996).
- [50] Q.A. Turchette, C.S. Wood, B.E. King, C.J. Myatt, D. Leibfried, W.M. Itano, C. Monroe and D.J. Wineland. *Deterministic Entanglement of Two Trapped Ions*. Phys. Rev. Lett. **81**, 3631–3634 (1998).
- [51] C.A. Sackett, D. Kielpinski, B.E. King, C. Langer, V. Meyer, C.J. Myatt, M. Rowe, Q.A. Turchette, W.M. Itano, D.J. Wineland and C. Monroe. *Experimental entanglement of four particles*. Nature **404**, 256–259 (2000).
- [52] M.D. Barrett, J. Chiaverini, T. Schaetz, J. Britton, W.M. Itano, J.D. Jost, E. Knill, C. Langer, D. Leibfried, R. Ozeri and D.J. Wineland. *Deterministic quantum teleportation of atomic qubits*. Nature **429**, 737–739 (2004).
- [53] J. Chiaverini, J. Britton, D. Leibfried, E. Knill, M.D. Barrett, R.B. Blakestad, W.M. Itano, J.D. Jost, C. Langer, R. Ozeri, T. Schaetz and D.J. Wineland. *Implementation of the semiclassical quantum Fourier transform in a scalable system*. Science **308**, 997–1000 (2005).
- [54] T. Schaetz, D. Leibfried, J. Chiaverini, M.D. Barrett, J. Britton, B.L. DeMarco, W.M. Itano, J.D. Jost, C. Langer and D.J. Wineland. *Towards a scalable quantum computer/simulator based on trapped ions*. Appl. Phys. B **79**, 979–986 (2004).
- [55] J. Chiaverini, R.B. Blakestad, J. Britton, J.D. Jost, C. Langer, D. Leibfried, R. Ozeri and D.J. Wineland. *Surface-Electrode Architecture for Ion-Trap Quantum Information Processing*. arXiv:quant-ph/0501147, to appear in Quant. Inf. Comput., Vol. 5, No. 6 2005.

- [56] R. Marx, A.F. Fahmy, J.M. Myers, W. Bermel and S.J. Glaser. *Approaching Five-Bit NMR Quantum Computing*. Phys. Rev. A **62**, 012310–1–8 (2000).
- [57] D.G. Cory, A.F. Fahmy and T.F. Havel. *Nuclear magnetic resonance: an experimentally accessible paradigm for quantum computing*. In *Proc. of PhysComp '96* pages 87–91. (eds. M. Toffoli, M. Biafore, and J. Le ao) 1996.
- [58] D.P. DiVincenzo. *Two-bit gates are universal for quantum computation*. Phys. Rev. A **51**, 1015–1022 (1995).
- [59] J.A. Jones. *NMR Quantum Computation: A Critical Evaluation*. Fortschr. Phys. **48**, 909–924 (2000).
- [60] D.G. Cory, A.F. Fahmy and T.F. Havel. *Ensemble quantum computing by NMR spectroscopy*. Proc. Natl. Acad. Sci. USA **94**, 1634–1639 (1997).
- [61] D.G. Cory, M.D. Price and T.F. Havel. *Nuclear magnetic resonance spectroscopy: An experimentally accessible paradigm for quantum computing*. Physica D **120**, 82–101 (1998).
- [62] J.M. Myers, A.F. Fahmy, S.J. Glaser and R. Marx. *Rapid solution of problems by nuclear-magnetic-resonance quantum computation*. Phys. Rev. A **63**, 032302 (2001).
- [63] D. Loss and D.P. DiVincenzo. *Quantum computation with quantum dots*. Phys. Rev. A **57**, 120–126 (1998).
- [64] G. Burkard, H.-A. Engel and D. Loss. *Spintronics and Quantum Dots for Quantum Computing and Quantum Communication*. Fortschr. Phys. **48**, 965–986 (2000).
- [65] Y. Ji, M. Heiblum, D. Sprinzak, D. Mahalu and H. Shtrikman. *Phase Evolution in a Kondo-Correlated System*. Science **290**, 779–783 (2000).
- [66] B.D. Josephson. *Possible new effects in superconductive tunneling*. Phys. Lett. **1**, 251–253 (1962).
- [67] B.D. Josephson. *Supercurrents through Barriers*. Adv. Phys. **14**, 419 (1965).
- [68] M. Tinkham. *Introduction to Superconductivity*. Dover Publications, Inc. Mineola, New York 1996.
- [69] W.C. Stewart. *Current-Voltage Characteristics of Josephson Junctions*. Appl. Phys. Lett. **12**, 277–280 (1968).
- [70] D.E. McCumber. *Effect of ac Impedance on dc Voltage-Current Characteristics of Superconductor Weak-Link Junctions*. J. Appl. Phys. **39**, 3113–3118 (1968).
- [71] J.M. Martinis, S. Nam, J. Aumentado and C. Urbina. *Rabi Oscillations in a Large Josephson-Junction Qubit*. Phys. Rev. Lett. **89**, 117901 (2002).

- [72] J. Clarke and A.I. Braginski. *The SQUID Handbook*. Wiley-VCH Verlag (Weinheim) 2004.
- [73] K.K. Likharev. *Dynamics of Josephson Junctions and Circuits*. Gordon and Breach (New York) 1986.
- [74] Y. Makhlin, G. Schön and A. Shnirman. *Quantum-state engineering with Josephson-junction devices*. Rev. Mod. Phys. **73**, 357–400 (2001).
- [75] J.R. Friedman, V. Patel, W. Chen, S.K. Tolpygo and J.E. Lukens. *Quantum superposition of distinct macroscopic states*. Nature **406**, 43–46 (2000).
- [76] T.P. Orlando, J.E. Mooij, Lin Tian, Caspar H. van der Wal, L. Levitov, Seth Lloyd and J.J. Mazo. *A Superconducting Persistent Current Qubit*. Phys. Rev. B **60**, 15398 (1999).
- [77] B.S. Deaver and W.M. Fairbank. *Experimental Evidence for Quantized Flux in Superconducting Cylinders*. Phys. Rev. Lett. **7**, 43–46 (1961).
- [78] R. Doll and M. Näbauer. *Experimental Proof of Magnetic Flux Quantization in a Superconducting Ring*. Phys. Rev. Lett. **7**, 51–52 (1961).
- [79] C. Cohen-Tannoudji, B. Diu and F. Laloë. *Quantum Mechanics Vol. 1 & 2*. John Wiley & Sons, Inc. (New York, N.Y.) 1999.
- [80] D.A. Ivanov, L.B. Ioffe, V.B. Geshkenbein and G. Blatter. *Interference effects in isolated Josephson junction arrays with geometric symmetries*. Phys. Rev. B **65**, 024509 (2001).
- [81] C.H. van der Wal. *Quantum superpositions of persistent Josephson currents*. PhD thesis Technical University Delft 2001.
- [82] J.E. Mooij, T.P. Orlando, L. Levitov, Lin Tian, Caspar H. van der Wal and Seth Lloyd. *Josephson Persistent-Current Qubit*. Science **285**, 1036 (1999).
- [83] D.A. Ivanov and M.V. Feigel'man. *Coulomb effects in a ballistic one-channel S-S-S device*. JETP **87**, 349 (1998).
- [84] L.B. Ioffe, V.B. Geshkenbein, M.V. Feigel'man, A.L. Fauchere and G. Blatter. *Environmentally decoupled sds -wave Josephson junctions for quantum computing*. Nature **398**, 679–681 (1999).
- [85] I. Chiorescu, Y. Nakamura, C.J.P.M. Harmans and J.E. Mooij. *Coherent quantum dynamics of a superconducting flux-qubit*. Science **299**, 1869 (2003).
- [86] Y. Yu, D. Nakada, J.C. Lee, B. Singh, D.S. Crankshaw, T.P. Orlando, K.K. Berggren and W. D. Oliver. *Energy Relaxation Time between Macroscopic Quantum Levels in a Superconducting Persistent-Current Qubit*. Phys. Rev. Lett. **92**, 117904 (2004).

- [87] J.C. Lee, W.D. Oliver, T.P. Orlando and K.K. Berggren. *Resonant Readout of a Persistent Current Qubit*. IEEE Transactions on Applied Superconductivity **15**, 841–844 (2005).
- [88] S. Saito, M. Thorwart, H. Tanaka, M. Ueda, H. Nakano, K. Semba and H. Takayanagi. *Multiphoton Transitions in a Macroscopic Quantum Two-State System*. Phys. Rev. Lett. **93**, 037001 (2004).
- [89] E. Il'ichev, N. Oukhanski, A. Izmailkov, Th. Wagner, M. Grajcar, H.-G. Meyer, A.Yu. Smirnov, A. Maassen van den Brink, M.H.S. Amin and A.M. Zagoskin. *Continuous Monitoring of Rabi Oscillations in a Josephson Flux Qubit*. Phys. Rev. Lett. **91**, 097906 (2003).
- [90] C.H. van der Wal, A.C.J. ter Haar, F.K. Wilhelm, R.N. Schouten, C.J.P.M. Harmans, T.P. Orlando, S. Lloyd and J.E. Mooij. *Quantum superposition of macroscopic persistent-current states*. Science **290**, 773 (2000).
- [91] G. Blatter, V.B. Geshkenbein and L.B. Ioffe. *Design aspects of superconducting-phase quantum bits*. Phys. Rev. B **63**, 174511 (2001).
- [92] J.B. Majer, F.G. Paauw, A.C.J. ter Haar, C.J.P.M. Harmans and J.E. Mooij. *Spectroscopy on Two Coupled Superconducting Flux Qubits*. Phys. Rev. Lett. **94**, 090501 (2005).
- [93] D. Vion, A. Aassime, A. Cottet, P. Joyez, H. Pothier, C. Urbina, D. Esteve and M.H. Devoret. *Manipulating the quantum state of an electrical circuit*. Science **296**, 886–889 (2002).
- [94] T. Hayashi, T. Fujisawa, H.D. Cheong, Y.H. Jeong and Y. Hirayama. *Coherent Manipulation of Electronic States in a Double Quantum Dot*. Phys. Rev. Lett. **91**, 226804 (2003).
- [95] J.M. Elzerman, R. Hanson, L.H. Willems van Beveren, B. Witkamp, L.M.K. Vandersypen and L.P. Kouwenhoven. *Single-shot read-out of an individual electron spin in a quantum dot*. Nature **430**, 431–435 (2004).
- [96] W. Wegscheider, G. Schedelbeck, M. Bichler and G. Abstreiter. *Atomically precise quantum dots fabricated by twofold cleaved edge overgrowth: From artificial atoms to molecules*. Physica E **3**, 103–111 (1998).
- [97] P. Borri, W. Langbein, U. Woggon, M. Schwab, M. Bayer, S. Fafard, Z. Wasilewski and P. Hawrylak. *Exciton Dephasing in Quantum Dot Molecules*. Phys. Rev. Lett. **91**, 267401 (2003).
- [98] K. Karrai, R.J. Warburton, A. Högele, B. Urbaszek, C. Schulhauser, E.J. McGhee, A.O. Govorov, J.M. Garcia, B.D. Gerardot and P.M. Petroff. *Hybridisation of electronic states in quantum dots through photon emission*. Nature **427**, 135–138 (2004).

- [99] A. Högele, S. Seidl, M. Kroner, K. Karrai, R.J. Warburton, B.D. Gerardot and P.M. Petroff. *Voltage-controlled optics of a quantum dot*. Phys. Rev. Lett. **93**, 217401 (2004).
- [100] Y. Ducommun, M. Kroutvar, J.J. Finley, M. Bichler, A. Zrenner and G. Abstreiter. *Dynamics of optically stored charges in InGaAs quantum dots*. Physica E **21**, 886–891 (2004).
- [101] M. Kroutvar, Y. Ducommun, J.J. Finley, M. Bichler, G. Abstreiter and A. Zrenner. *Wavelength selective charge storage in self-assembled InGaAs/GaAs quantum dots*. Appl. Phys. Lett. **83**, 443–445 (2003).
- [102] R. Oulton, J.J. Finley, A.I. Tartakovskii, D.J. Mowbray, M.S. Skolnick, M. Hopkinson, A. Vasanelli, R. Ferreira and G. Bastard. *Continuum transitions and phonon coupling in single self-assembled Stranski-Krastanow quantum dots*. Phys. Rev. B **68**, 235301 (2003).
- [103] K. Brunner and G. Abstreiter. *Ordering and electronic properties of self-assembled Si/Ge quantum dots*. J. Appl. Phys. **40**, 1860–1865 (2001).
- [104] F. Findeis, M. Baier, E. Beham, A. Zrenner and G. Abstreiter. *Photocurrent and photoluminescence of a single self-assembled quantum dot in electric fields*. Appl. Phys. Lett. **78**, 2958–2960 (2001).
- [105] F. Findeis, M. Baier, A. Zrenner, M. Bichler and G. Abstreiter. *Optical excitations of a self-assembled artificial ion*. Phys. Rev. B **63**, 121309 (2001).
- [106] A. Zrenner, F. Findeis, E. Beham, M. Markmann, G. Böhm and G. Abstreiter. *Spectroscopy of single self-assembled quantum dots*. Journal of Luminescence **35**, 87–89 (2000).
- [107] J.J. Finley, M. Skalitz, M. Arzberger, A. Zrenner, G. Böhm and G. Abstreiter. *Electrical Detection of Optically-Induced Charge Storage in Self-Assembled InAs Quantum Dots*. Appl. Phys. Lett. **73**, 2618–2620 (1998).
- [108] W.G. van der Wiel, S. De Franceschi, J.M. Elzerman, T. Fujisawa, S. Tarucha and L.P. Kouwenhoven. *Electron transport through double quantum dots*. Rev. Mod. Phys. **75**, 1–22 (2003).
- [109] L. Fedichkin, M. Yanchenko and K.A. Valiev. *Coherent charge qubits based on GaAs quantum dots with a built-in barrier*. Nanotechnology **11**, 387–391 (2000).
- [110] R.H. Blick and H. Lorenz. *Possible Definition of Quantum Bits in Coupled Quantum Dots*. Proceedings of the IEEE International Symposium on Circuits and Systems pages II245–II248 (2000).



- [111] W.G. van der Wiel, T. Fujisawa, S. Tarucha and L.P. Kouwenhoven. *A Double Quantum Dot as an Artificial Two-level System*. Jpn. J. Appl. Phys. **40**, 2100 (2001).
- [112] D. Loss and D.P. DiVincenzo. *Quantum computation with quantum dots*. Phys. Rev. A **57**, 120–126 (1998).
- [113] U. Hartmann. *Decoherence and Measurement of Charge Qubits in Double Quantum Dots*. PhD thesis Ludwig-Maximilians-Universität München 2005.
- [114] J. Gorman, D.G. Hasko and D.A. Williams. *Charge-qubit operation of an isolated double quantum dot*. Phys. Rev. Lett. **95**, 090502 (2005).
- [115] A.C. Johnson, J.R. Petta, J.M. Taylor, A. Yacoby, M. D. Lukin, C.M. Marcus, M.P. Hanson and A.C. Gossard. *Triplet-singlet spin relaxation via nuclei in a double quantum dot*. Nature **435**, 925–928 (2005).
- [116] A.V. Khaetskii and Yu.V. Nazarov. *Spin-flip transitions between Zeeman sublevels in semiconductor quantum dots*. Phys. Rev. B **64**, 125316 (2001).
- [117] J.M. Elzerman, R. Hanson, J.S. Greidanus, L.H. Willems van Beveren, S. De Franceschi, L.M.K. Vandersypen, S. Tarucha and L.P. Kouwenhoven. *Few-Electron Quantum Dot Circuit with Integrated Charge Read-Out*. Phys. Rev. B **67**, 161308 (2003).
- [118] J. Elzerman. *Electron spin and charge in semiconductor quantum dots*. PhD thesis Technical University Delft 2004.
- [119] B.E. Kane. *A silicon-based nuclear spin quantum computer*. Nature **393**, 133–137 (1998).
- [120] L.C.L. Hollenberg, C.J. Wellard, C.I. Pakes and A.G. Fowler. *Single-spin readout for buried dopant semiconductor qubits*. Phys. Rev. B **69**, 233301 (2004).
- [121] A.D. Greentree, A.R. Hamilton, L.C.L. Hollenberg and R.G. Clark. *Electrical readout of a spin qubit without double occupancy*. Phys. Rev. B **71**, 113310 (2005).
- [122] Y. Nakamura, Yu.A. Pashkin and J.S. Tsai. *Coherent control of macroscopic quantum states in a single-Cooper-pair box*. Nature **398**, 786–788 (1999).
- [123] L.M.K. Vandersypen and I.L. Chuang. *NMR Techniques for Quantum Control and Computation*. Rev. Mod. Phys. **76**, 1037–1069 (2004).
- [124] C. Rigetti and M. Devoret. *Protocol for universal gates in optimally biased superconducting qubits*. arXiv:quant-ph/0412009 2004.
- [125] M.C. Goorden and F.K. Wilhelm. *Theoretical analysis of continuously driven dissipative solid-state qubits*. Phys. Rev. B **68**, 012508 (2003).

- [126] E. Farhi, J. Goldstone, S. Gutmann and M. Sipser. *Quantum Computation by Adiabatic Evolution*. arXiv:quant-ph/0001106 2000.
- [127] W.M. Kaminsky, S. Lloyd and T.P. Orlando. *Scalable Superconducting Architecture for Adiabatic Quantum Computation*. arXiv:quant-ph/0403090 2004.
- [128] D. Aharonov, W. van Dam, J. Kempe, Z. Landau, S. Lloyd and O. Regev. *Adiabatic Quantum Computation is Equivalent to Standard Quantum Computation*. In *Proc. 45th Annual IEEE Symp. on Foundations of Computer Science (FOCS)* pages 42–51. IEEE 2004.
- [129] M. Grajcar, A. Izmailkov and E. Il'ichev. *Possible implementation of adiabatic quantum algorithm with superconducting flux qubits*. Phys. Rev. B **71**, 144501 (2005).
- [130] J. Preskill. *Reliable quantum computers*. J. Proc. R. Soc. Lond. A **454**, 385–410 (1998).
- [131] J.R. Petta, A.C. Johnson, C.M. Marcus, M.P. Hanson and A.C. Gossard. *Manipulation of a Single Charge in a Double Quantum Dot*. Phys. Rev. Lett. **93**, 186802 (2004).
- [132] F.K. Wilhelm. *Reduced visibility of quantum oscillations in the spin-boson model*. arXiv:cond-mat/0507526 2005.
- [133] F. Meier and D. Loss. *Reduced visibility of Rabi oscillations in superconducting qubits*. Phys. Rev. B **71**, 094519 (2005).
- [134] I. Chiorescu, P. Bertet, K. Semba, Y. Nakamura, C.J.P.M. Harmans and J.E. Mooij. *Coherent dynamics of a flux-qubit coupled to a harmonic oscillator*. Nature **431**, 159 (2004).
- [135] R.W. Simmonds, K.M. Lang, D.A. Hite, S. Nam, D.P. Pappas and J.M. Martinis. *Decoherence in Josephson Phase Qubits from Junction Resonators*. Phys. Rev. Lett. **93**, 77003 (2004).
- [136] A. Wallraff, D.I. Schuster, A. Blais, L. Frunzio, J. Majer, S.M. Girvin and R.J. Schoelkopf. *Approaching Unit Visibility for Control of a Superconducting Qubit with Dispersive Readout*. Phys. Rev. Lett. **95**, 060501 (2005).
- [137] D.P. DiVincenzo and D. Loss. *Rigorous Born Approximation and beyond for the Spin-Boson Model*. Phys. Rev. B **71**, 035318 (2005).
- [138] V.B. Braginsky and F.Ya. Khalili. *Quantum measurement*. Cambridge University Press (Cambridge, UK) 1992.
- [139] F.K. Wilhelm. *An asymptotical von-Neumann measurement strategy for solid-state quantum bits*. Phys. Rev. B **68**, 060503(R) (2003).

- [140] M.H. Devoret, A. Wallraff and J.M. Martinis. *Superconducting Qubits: A Short Review*. arXiv:cond-mat/0411174 2004.
- [141] O. Astafiev, Yu.A. Pashkin, T. Yamamoto, Y. Nakamura and J.S. Tsai. *Single-shot measurement of the Josephson charge qubit*. Phys. Rev. B **69**, 180507 (2004).
- [142] O. Astafiev, Yu.A. Pashkin, Y. Nakamura, T. Yamamoto and J.S. Tsai. *Quantum Noise in the Josephson Charge Qubit*. Phys. Rev. Lett. **93**, 267007 (2004).
- [143] A. Blais, R.-S. Huang, A. Wallraff, S.M. Girvin and R. J. Schoelkopf. *Cavity quantum electrodynamics for superconducting electrical circuits: an architecture for quantum computation*. Phys. Rev. A **69**, 062320 (2004).
- [144] E. Frey and K. Kroy. *Brownian motion: a paradigm of soft matter and biological physics*. Ann. Phys. (Leipzig) **14**, 20–50 (2005).
- [145] P. Hänggi and G.-L. Ingold. *Fundamental Aspects of Quantum Brownian Motion*. Chaos **15**, 026105 (2005).
- [146] C. Cohen-Tannoudji, J. Dupont-Roc and G. Grynberg. *Atom-photon interactions: basic processes and applications*. John Wiley & Sons, Inc. (New York, N.Y.) 1992.
- [147] K. Blum. *Density Matrix Theory and Applications*. Plenum Press New York 1996, 2nd edition.
- [148] U. Weiss. *Quantum Dissipative Systems*. World Scientific Singapore 1999, 2nd edition.
- [149] R. Kubo. *Brownian Motion and Nonequilibrium Statistical Mechanics*. Science **233**, 330–334 (1986).
- [150] G. Schön. *Statistische Physik*. <http://www-tfp.physik.uni-karlsruhe.de/~schoen/findex.html>, University of Karlsruhe 1998.
- [151] H.B. Callen and T.A. Welton. *Irreversibility and Generalized Noise*. Phys. Rev. **83**, 34–40 (1951).
- [152] H.B. Callen and R.F. Greene. *On a Theorem of Irreversible Thermodynamics*. Phys. Rev. **86**, 702–710 (1952).
- [153] A.O. Caldeira and A.J. Leggett. *Influence of Dissipation on Quantum Tunneling in Macroscopic Systems*. Phys. Rev. Lett. **46**, 211–214 (1981).
- [154] A.O. Caldeira and A.J. Leggett. *Quantum tunnelling in a dissipative system*. Ann. Phys. (N.Y.) **149**, 374–456 (1984).
- [155] A.J. Leggett, S. Chakravarty, A.T. Dorsey, M.P.A. Fisher, A. Garg and W. Zwerger. *Dynamics of the dissipative two-state system*. Rev. Mod. Phys. **59**, 1–85 (1987).

- [156] M.J. Storcz. *Decoherence of coupled solid state qubits*. Master's thesis University of Bonn 2002.
- [157] P.N. Argyres and P.L. Kelley. *Theory of Spin Resonance and Relaxation*. Phys. Rev. **134**, A98 (1964).
- [158] L. Hartmann. *Driven Tunneling Dynamics of Dissipative Two-State Quantum System*. PhD thesis Universität Augsburg 2000.
- [159] S. Nakajima. *On Quantum Theory of Transport Phenomena - Steady Diffusion*. Prog. Theor. Phys. **20**, 948–959 (1958).
- [160] R. Zwanzig. *Ensemble method in the theory of irreversibility*. J. Chem. Phys. **33**, 1338–1341 (1960).
- [161] M. Governale, M. Grifoni and G. Schön. *Decoherence and dephasing in coupled Josephson qubits*. Chem. Phys. **268**, 273–283 (2001).
- [162] I. Rau, G. Johansson and A. Shnirman. *Cavity quantum electrodynamics in superconducting circuits: Susceptibility at elevated temperatures*. Phys. Rev. B **70**, 054521 (2004).
- [163] M.J. Storcz and F.K. Wilhelm. *Decoherence and gate performance of coupled solid state qubits*. Phys. Rev. A **67**, 042319 (2003).
- [164] G. Lindblad. *On the generators of completely positive semi-groups*. Commun. Math. Phys. **48**, 119 (1976).
- [165] H.P.G. Gutmann. *Description and control of decoherence in quantum bit systems*. PhD thesis Ludwig-Maximilians-Universität München 2005.
- [166] C. Moler and C. Van Loan. *Nineteen Dubious Ways to Compute the Exponential of a Matrix*. SIAM Review **4**, 801–836 (1978).
- [167] C. Moler and C. Van Loan. *Nineteen Dubious Ways to Compute the Exponential of a Matrix, Twenty-Five Years Later*. SIAM Review **45**, 3–49 (2003).
- [168] R. Bauernschmitt and Yu.V. Nazarov. *Detailed balance in single-charge traps*. Phys. Rev. B **47**, 9997–10000 (1993).
- [169] E. Paladino, M. Sassetti and G. Falci. *Modulation of dephasing due to a spin-boson environment*. Chem. Phys. **296**, 325–332 (2004).
- [170] G. Falci, A. D'Arrigo, A. Mastellone and E. Paladino. *Dynamical suppression of telegraph and  $1/f$  noise due to quantum bistable fluctuator*. Phys. Rev. A **70**, R40101 (2004).

- [171] E. Paladino, L. Faoro, G. Falci and R. Fazio. *Decoherence and  $1/f$  noise in Josephson qubits*. Phys. Rev. Lett. **88**, 228304 (2002).
- [172] E. Paladino, L. Faoro and G. Falci. *Decoherence due to discrete noise in Josephson qubits*. Adv. in Solid State Phys. **43**, 747–762 (2003).
- [173] G. Falci, A. D’Arrigo, A. Mastellone and E. Paladino. *Initial Decoherence in Solid State Qubits*. Phys. Rev. Lett. **94**, 167002 (2005).
- [174] D.F. Walls and G.J. Milburn. *Quantum Optics*. Springer-Verlag (Berlin, Germany) 1994.
- [175] M.O. Scully and M.S. Zubairy. *Quantum Optics*. Cambridge University Press (Cambridge, UK) 1997.
- [176] J.M. Raimond, M. Brune and S. Haroche. *Colloquium: Manipulating quantum entanglement with atoms and photons in a cavity*. Rev. Mod. Phys. **73**, 565–582 (2001).
- [177] B.W. Shore and P.L. Knight. *The Jaynes-Cummings model*. J. Mod. Opt. **40**, 1195–1238 (1993).
- [178] A. Wallraff, D.I. Schuster, A. Blais, L. Frunzio, R.-S. Huang, J. Majer, S. Kumar, S.M. Girvin and R.J. Schoelkopf. *Strong coupling of a single photon to a superconducting qubit using circuit quantum electrodynamics*. Nature **431**, 162–167 (2004).
- [179] P. Alsing, D.-S. Guo and H.J. Carmichael. *Dynamic Stark effect for the Jaynes-Cummings system*. Phys. Rev. A **45**, 5135–5143 (1992).
- [180] J. Gabelli, L.-H. Reydellet, G. Fève, J.-M. Berroir, B. Plaçais, P. Roche and D.C. Glattli. *Hanbury Brown-Twiss Correlations to Probe the Population Statistics of GHz Photons Emitted by Conductors*. Phys. Rev. Lett. **93**, 056801 (2004).
- [181] J.Q. You and F. Nori. *Quantum information processing with superconducting qubits in a microwave field*. Phys. Rev. B **68**, 064509 (2003).
- [182] J.F. Poyatos, J.I. Cirac and P. Zoller. *Complete Characterization of a Quantum Process: The Two-Bit Quantum Gate*. Phys. Rev. Lett. **78**, 390–393 (1997).
- [183] A. Peres. *Separability Criterion for Density Matrices*. Phys. Rev. Lett. **77**, 1413–1415 (1996).
- [184] A.C.J. ter Haar. *Single and coupled Josephson junction quantum bits*. PhD thesis Technical University Delft 2005.
- [185] A.B. Zorin. *Coupling and dephasing in Josephson charge-phase qubit with radio frequency readout*. arXiv:cond-mat/0407602 2004.

- [186] A.B. Zorin. *Josephson charge-phase qubit with radio frequency readout: coupling and decoherence*. Journal of Experimental and Theoretical Physics (JETP) **98**, 1250–1261 (2004).
- [187] M.J. Storcz, F. Hellmann, C. Hrlescu and F.K. Wilhelm. *Decoherence of a two-qubit system away from perfect symmetry*. Phys. Rev. A **72**, 052314 (2005).
- [188] F.W. Strauch, P.R. Johnson, A.J. Dragt, C.J. Lobb, J.R. Anderson and F.C. Wellstood. *Quantum Logic Gates for Coupled Superconducting Phase Qubits*. Phys. Rev. Lett. **91**, 167005 (2003).
- [189] A. Abliz, S.-S. Li, L.-L. Sun, S.-L. Feng and H.-Z. Zheng. *Decoherence of two Josephson charge qubits coupled via  $\sigma_x\sigma_x$ -type coupling and exposed to  $\sigma_x$ -noise*. Phys. Rev. A **69**, 052309 (2004).
- [190] S. Lutz. *Dekohärenz komplexer Quantengatter*. Master’s thesis University of Hamburg 2003.
- [191] T. Brandes and B. Kramer. *Spontaneous emission of phonons by coupled quantum dots*. Phys. Rev. Lett. **83**, 3021–3024 (1999).
- [192] T. Brandes. *The Dicke Effect in Electronic Systems*. Habilitation Thesis, University of Hamburg 2000.
- [193] A.J. Leggett. *Superconducting Qubits – a Major Roadblock Dissolved?* Science **296**, 861–862 (2002).
- [194] Yu.A. Pashkin, T. Yamamoto, O. Astafiev, Y. Nakamura, D.V. Averin and J.S. Tsai. *Quantum oscillations in two coupled charge qubits*. Nature **421**, 823–826 (2003).
- [195] L.S. Levitov, T.P. Orlando, J.B. Majer and J.E. Mooij. *Quantum spin chains and Majorana states in arrays of coupled qubits*. arXiv:cond-mat/0108266 2001.
- [196] J.R. Butcher. *Advances in persistent-current qubit research: Inductively coupled qubits and novel biasing methods*. Master’s thesis Delft University of Technology 2002.
- [197] Y. Makhlin, G. Schön and A. Shnirman. *Josephson-Junction Qubits with Controlled Couplings*. Nature **398**, 305–307 (1999).
- [198] P. Baars. *Transport and Microwave Properties of nanostructured InAs/Nb Hybrid Devices*. PhD thesis University of Hamburg 2004.
- [199] B.L.T. Plourde, J. Zhang, K.B. Whaley, F.K. Wilhelm, T.L. Robertson, T. Hime, S. Linzen, P.A. Reichardt, C.-E. Wu and J. Clarke. *Entangling flux qubits with a bipolar dynamic inductance*. Phys. Rev. B **70**, 140501(R) (2004).

- [200] K.A. Delin and A.W. Kleinsasser. *Stationary properties of high-critical-temperature proximity effect Josephson junctions*. Supercond. Sci. Technol. **9**, 227–269 (1996).
- [201] V.V. Ryazanov, V.A. Oboznov, A.Yu. Rusanov, A.V. Veretennikov, A.A. Golubov and J. Aarts. *Coupling of Two Superconductors through a Ferromagnet: Evidence for a  $\pi$  Junction*. Phys. Rev. Lett. **86**, 2427–2430 (2001).
- [202] T. Kontos, M. Aprili, J. Lesueur, F. Genêt, B. Stephanidis and R. Boursier. *Josephson Junction through a Thin Ferromagnetic Layer: Negative Coupling*. Phys. Rev. Lett. **89**, 137007 (2002).
- [203] A. Bauer, J. Bentner, M. Aprili, M.L. Della Rocca, M. Reinwald, W. Wegscheider and C. Strunk. *Spontaneous Supercurrent Induced by Ferromagnetic  $\pi$  Junctions*. Phys. Rev. Lett. **92**, 217001 (2004).
- [204] J.B. Majer, J.R. Butcher and J.E. Mooij. *Simple phase bias for superconducting circuits*. Phys. Rev. Lett. **80**, 3638–3640 (2002).
- [205] A. Richter, M. Koch, T. Matsuyama and U. Merkt. *Transport properties of Nb/InAs(2DEG)/Nb Josephson field-effect transistors*. Supercond. Sci. Technol. **12**, 874–876 (1999).
- [206] A. Richter. *Nb/InAs(2DEG)/Nb Hybrid Quantum Structures*. Adv. Solid State Phys. **40**, 321–332 (2000).
- [207] M. Ebel. *Current-Phase Relationship of Nb/InAs(2DES)/Nb Josephson Junctions*. PhD thesis University of Hamburg 2004.
- [208] M. Grajcar, M. Ebel, E. Il'ichev, R. Kürsten, T. Matsuyama and U. Merkt. *Supercurrent-phase relation of a Nb/InAs(2DEG)/Nb Josephson junction*. Physica C **372**, 27–30 (2002).
- [209] M. Grajcar, A. Izmalkov, E. Il'ichev, Th. Wagner, N. Oukhanski, U. Hübner, T. May, I. Zhilyaev, H.-E. Hoenig, Ya.S. Greenberg, V.I. Shnyrkov, D. Born, W. Krech, H.-G. Meyer, A. Maassen van den Brink and M.H.S. Amin. *Low-frequency measurement of the tunneling amplitude in a flux qubit*. Phys. Rev. B **69**, 060501 (2004).
- [210] T.P. Orlando and K.A. Delin. *Foundations of Applied Superconductivity*. Addison-Wesley Publishing Company (Reading, MA) 1990.
- [211] C.H. van der Wal. *Quantum superpositions of persistent Josephson currents*. Delft University Press (Delft, Netherlands) 2001.
- [212] F. Herbstritt, T. Kemen, A. Marx and R. Gross. *Transport and Noise Characteristics of Submicron High Temperature Superconductor Grain Boundary Junctions*. Appl. Phys. Lett. **78**, 955 (2001).

- [213] S. Keil, R. Straub, R. Gerber, R.P. Hübener, K. Barthel, D. Kölle and R. Gross. *Imaging of Vortices and  $1/f$  Noise Sources in YBCO dc SQUIDs Using Low Temperature Scanning Electron Microscopy*. IEEE Trans. Appl. Supercond. **9**, 2961 (1999).
- [214] A. Marx, Th. Kemen, L. Alff, D. Kölle and R. Gross. *Characterization of Individual Noise Sources in High Temperature Superconductor Josephson Junctions*. IEEE Trans. Appl. Supercond. **9**, 3982 (1999).
- [215] L.-M. Duan and G.-C. Guo. *Preserving Coherence in Quantum Computation by Pairing Quantum Bits*. Phys. Rev. Lett. **79**, 1953 (1997).
- [216] P. Zanardi and M. Rasetti. *Noiseless Quantum Codes*. Phys. Rev. Lett. **79**, 3306 (1997).
- [217] P. Zanardi and M. Rasetti. *Error Avoiding Quantum Codes*. Mod. Phys. Lett. B **11**, 1085 (1997).
- [218] L.-M. Duan and G.-C. Guo. *Reducing decoherence in quantum-computer memory with all quantum bits coupling to the same environment*. Phys. Rev. A **57**, 737 (1998).
- [219] D. Bacon, D.A. Lidar and K.B. Whaley. *Robustness of Decoherence-Free Subspaces for Quantum Computation*. Phys. Rev. A **60**, 1944 (1999).
- [220] D.A. Lidar and K.B. Whaley. *Decoherence-Free Subspaces and Subsystems* Band 622. Springer Lecture Notes in Physics, Berlin 2003.
- [221] J. Kempe, D. Bacon, D.A. Lidar and K.B. Whaley. *Theory of Decoherence-Free Fault-Tolerant Universal Quantum Computation*. Phys. Rev. A **63**, 042307 (2001).
- [222] J. Zhang, J. Vala, S. Sastry and K.B. Whaley. *Geometric theory of nonlocal two-qubit operations*. Phys. Rev. A **67**, 042313 (2003).
- [223] L.-M. Duan and G.-C. Guo. *Optimal quantum codes for preventing collective amplitude damping*. Phys. Rev. A **58**, 3491 (1998).
- [224] K.R. Brown, J. Vala and K.B. Whaley. *Scalable Ion Trap Quantum Computation with Pair-wise Interactions only*. Phys. Rev. A **67**, 012309 (2003).
- [225] L. Viola, E.M. Fortunato, M.A. Pravia, E. Knill, R. Laflamme and D.G. Cory. *Experimental Realization of Noiseless Subsystems for Quantum Information Processing*. Science **293**, 2059–2063 (2001).
- [226] E.M. Fortunato, L. Viola, M.A. Pravia, E. Knill, R. Laflamme, T.F. Havel and D.G. Cory. *Exploring noiseless subsystems via nuclear magnetic resonance*. Phys. Rev. A **67**, 062303 (2003).



- [227] W.Y. Hsiang. *Lectures on Lie Groups*. World Scientific Singapore 2000.
- [228] J. Zhang, J. Vala, S. Sastry and K.B. Whaley. *Minimum Construction of Two-Qubit Quantum Operations*. Phys. Rev. Lett. **93**, 020502 (2004).
- [229] M.J. Storz, J. Vala, K.R. Brown, J. Kempe, F.K. Wilhelm and K.B. Whaley. *Full protection of superconducting qubit systems from coupling errors*. Phys. Rev. B **72**, 064511 (2005).
- [230] Y. Aharonov and A. Casher. *Topological Quantum Effects for Neutral Particles*. Phys. Rev. Lett. **53**, 319–321 (1984).
- [231] Y. Aharonov and D. Rohrlich. *Quantum Paradoxes, Quantum Theory for the Perplexed*. Wiley-VCH (Weinheim) 2005.
- [232] T. Yamamoto, Yu.A. Pashkin, O. Astafiev, Y. Nakamura and J.S. Tsai. *Demonstration of conditional gate operation using superconducting charge qubits*. Nature **425**, 941–944 (2003).
- [233] T. Schulte-Herbrueggen, A.K. Spoerl, N. Khaneja and S.J. Glaser. *Optimal Control-Based Efficient Synthesis of Building Blocks of Quantum Algorithms Seen in Perspective from Network Complexity towards Time Complexity*. arXiv:quant-ph/0502104 2005.
- [234] L.S. Pontryagin, V.G. Bol'tanskii, R.S. Gamkrelidze and E.F. Mischenko. *The Mathematical Theory of Optimal Processes*. Pergamon Press (New York) 1964.
- [235] A.G. Butkovskiy and Y.I. Samoilenko. *Control of Quantum-Mechanical Processes and Systems*. Kluwer (Dordrecht, Netherlands) 1990.
- [236] N. Khaneja, T. Reiss, C. Kehlet, T. Schulte-Herbrüggen and S.J. Glaser. *Optimal control of coupled spin dynamics: design of NMR pulse sequences by gradient ascent algorithms*. J. Magn. Reson. **172**, 296–305 (2005).
- [237] R. Fazio, G.M. Palma and J. Siewert. *Fidelity and leakage of Josephson qubits*. Phys. Rev. Lett. **83**, 5385–5388 (1999).
- [238] R. Fazio, G.M. Palma, E. Sciacca and J. Siewert. *Leakage and fidelity of real qubits*. Physica B **284-288**, 1822–1823 (2000).
- [239] J. Siewert, R. Fazio, G.M. Palma and E. Sciacca. *Aspects of Qubit Dynamics in the Presence of Leakage*. J. Low Temp. Phys. **18**, 795–804 (2000).
- [240] R. Horodecki, P. Horodecki and M. Horodecki. *Violating Bell inequality by mixed spin- $\frac{1}{2}$  states: necessary and sufficient condition*. Phys. Lett. A **200**, 340–344 (1995).
- [241] A. Einstein, B. Podolsky and N. Rosen. *Can Quantum-Mechanical Description of Physical Reality Be Considered Complete?* Phys. Rev. **47**, 777–780 (1935).

- [242] N. Bohr. *Can Quantum-Mechanical Description of Physical Reality Be Considered Complete?* Phys. Rev. **48**, 696–702 (1935).
- [243] J.S. Bell. *On the Einstein Podolsky Rosen paradox.* Phys. Rev. **1**, 195–200 (1964).
- [244] J.F. Clauser, M.A. Horne, A. Shimony and R.A. Holt. *Proposed Experiment to Test Local Hidden-Variable Theories.* Phys. Rev. Lett. **23**, 880–884 (1969).
- [245] W.K. Wootters. *Entanglement of Formation of an Arbitrary State of Two Qubits.* Phys. Rev. Lett. **80**, 2245–2248 (1998).
- [246] N.A. Peters, T.-C. Wei and P.G. Kwiat. *Mixed-state sensitivity of several quantum-information benchmarks.* Phys. Rev. A **70**, 052309 (2004).
- [247] D.T. Smithey, M. Beck, M. Belsley and M.G. Raymer. *Sub-shot-noise correlation of total photon number using macroscopic twin pulses of light.* Phys. Rev. Lett. **69**, 2650–2653 (1992).
- [248] D. Bouwmeester, J.-W. Pan, K. Mattle, M. Eible, H. Weinfurter and A. Zeilinger. *Experimental quantum teleportation.* Nature **390**, 575–579 (1998).
- [249] D. Boschi, S. Branca, F. De Martini, L. Hardy and S. Popescu. *Experimental Realization of Teleporting an Unknown Pure Quantum State via Dual Classical and Einstein-Podolsky-Rosen Channels.* Phys. Rev. Lett. **80**, 1121–1125 (1998).
- [250] A. Furusawa, J.L. Sørensen, S.L. Braunstein, C.A. Fuchs, H.J. Kimble and E. S. Polzik. *Unconditional Quantum Teleportation.* Science **282**, 706–709 (1998).
- [251] J.G. Rarity, P.C.M. Owens and P.R. Tapster. *Quantum Random-number Generation and Key Sharing.* J. Mod. Opt. **41**, 2435–2444 (1994).
- [252] T. Jennewein, C. Simon, G. Weihs, H. Weinfurter and A. Zeilinger. *Quantum Cryptography with Entangled Photons.* Phys. Rev. Lett. **84**, 4729–4732 (2000).
- [253] R.J. Thompson, G. Rempe and H.J. Kimble. *Observation of normal-mode splitting for an atom in an optical cavity.* Phys. Rev. Lett. **68**, 1132–1135 (1992).
- [254] P. Münstermann, T. Fischer, P. Maunz, P.W.H. Pinkse and G. Rempe. *Dynamics of Single-Atom Motion Observed in a High-Finesse Cavity.* Phys. Rev. Lett. **82**, 3791–3794 (1999).
- [255] C.J. Hood, T.W. Lynn, A.C. Doherty, A.S. Parkins and H.J. Kimble. *The Atom-Cavity Microscope: Single Atoms Bound in Orbit by Single Photons.* Science **287**, 1447–1453 (2000).
- [256] S. Brattke, B.T.H. Varcoe and H. Walther. *Generation of Photon Number States on Demand via Cavity Quantum Electrodynamics.* Phys. Rev. Lett. **86**, 3534–3537 (2001).

- [257] G. Breitenbach, S. Schiller and J. Mlynek. *Measurement of the quantum states of squeezed light*. Nature **387**, 471–475 (1997).
- [258] S. Haroche. in *Fundamental Systems in Quantum Optics, les Houches summer school session LIII*, ed. J. Dalibart, J.M. Raimond, and J. Zinn-Justin. North-Holland (Amsterdam) 1992.
- [259] J.Q. You and F. Nori. *Quantum information processing with superconducting qubits in a microwave field*. Phys. Rev. B **68**, 064509 (2003).
- [260] C.-P. Yang, S.-I Chu and S. Han. *Possible realization of entanglement, logical gates, and quantum-information transfer with superconducting-quantum-interference-device qubits in cavity QED*. Phys. Rev. A **67**, 042311 (2003).
- [261] C.-P. Yang, S.-I Chu and S. Han. *Quantum Information Transfer and Entanglement with SQUID Qubits in Cavity QED: A Dark-State Scheme with Tolerance for Nonuniform Device Parameter*. Phys. Rev. Lett. **92**, 117902 (2004).
- [262] Y. x. Liu, L.F. Wei and F. Nori. *Preparation of macroscopic quantum superposition states of a cavity field via coupling to a superconducting charge qubit*. Phys. Rev. A **71**, 063820 (2005).
- [263] Y. x. Liu, L.F. Wei and F. Nori. *Generation of nonclassical photon states using a superconducting qubit in a microcavity*. Europhys. Lett. **67**, 941–947 (2004).
- [264] K.V.R.M. Murali, Z. Dutton, W.D. Oliver, D.S. Crankshaw and T.P. Orlando. *Probing Decoherence with Electromagnetically Induced Transparency in Superconductive Quantum Circuits*. Phys. Rev. Lett. **93**, 087003 (2004).
- [265] R. Hanbury Brown and R.Q. Twiss. *Correlation between photons in two coherent beams of light*. Nature **177**, 27–29 (1956).
- [266] R. Hanbury Brown and R.Q. Twiss. *The question of correlation between photons in coherent light rays*. Nature **178**, 1447–1448 (1956).
- [267] R. Hanbury Brown and R.Q. Twiss. *A test of a new type of stellar interferometer on Sirius*. Nature **178**, 1046–1048 (1956).
- [268] F. Parage, M.M. Doria and O. Buisson. *Plasma modes in periodic two-dimensional superconducting-wire networks*. Phys. Rev. B **58**, R8921–R8924 (1998).
- [269] J.E. Mooij and G. Schön. *Propagating Plasma Mode in Thin Superconducting Filaments*. Phys. Rev. Lett. **55**, 114–117 (1985).
- [270] A. Anthore, H. Pothier and D. Esteve. *Density of States in a Superconductor Carrying a Supercurrent*. Phys. Rev. Lett. **90**, 127001 (2003).

- [271] N.V. Vitanov and S. Stenholm. *Analytic properties and effective two-level problems in stimulated Raman adiabatic passage*. Phys. Rev. A **55**, 648–660 (1997).
- [272] R. Migliore and A. Messina. *Rabi Oscillations in the Dynamics of a Fully Quantized SQUID Ring-Electromagnetic Field System*. Optics and Spectroscopy **94**, 817–821 (2003).
- [273] R. Migliore and A. Messina. *Quantum superpositions of clockwise and counterclockwise supercurrent states in the dynamics of an rf-SQUID exposed to a quantized electromagnetic field*. Phys. Rev. B **67**, 134505 (2003).
- [274] T. Niemczyk and M. Mariantoni. *Sample design for the microstrip resonator*. private communication (2005).
- [275] M. Mariantoni. *Operation of a Microstrip SQUID Amplifier – and its Possible Applications*. Master’s thesis Chalmers University of Technology 2003.
- [276] M. Mück and J. Clarke. *The superconducting quantum interference device microstrip amplifier: Computer models*. J. Appl. Phys. **88**, 6910–6918 (2000).
- [277] R. Migliore and A. Messina. *Freezing the dynamics of a rf SQUID qubit via its strong coupling to a quantized microwave field*. J. Opt. B **6**, 136–141 (2004).
- [278] F.X. Kaertner and P. Russer. *Generation of squeezed microwave states by a dc-pumped degenerate parametric Josephson junction oscillator*. Phys. Rev. A **42**, 5601–5612 (1990).
- [279] E. Solano. *Effective Hamiltonians through Dyson series*. private communication (2005).
- [280] A.B. Klimov, L.L. Sanchez-Soto, A. Navarro and E.C. Yustas. *Effective Hamiltonians in quantum optics: a systematic approach*. J. Mod. Opt. **49**, 2211–2226 (2002).
- [281] A.M Dykhne and G.L. Yudin. *Sudden perturbations and quantum evolution (in Russian: Vnezapnye vozmuschenya and kvantovaya evolutsiya)*. Advances in Physics (Moscow) 1996.
- [282] I.S. Gradshteyn and I.M. Ryzhik. *Table of Integrals, Series, and Products*. Academic Press (San Diego) 2000.
- [283] M. Abramowitz and I.A. Stegun. *Handbook of mathematical functions*. Dover Publications (Mineola, N.Y.) 1970.
- [284] G. Schön. *Single-Electron Tunneling*. in *Quantum Transport and Dissipation*, ed. by T. Dittrich *et al.* pages 149–212 (1998).
- [285] T. Hecht. *Quantum Computation with Bose-Einstein Condensates*. Master’s thesis Technische Universität München 2004.

- [286] K. Völker. *Dynamical behavior of the dissipative two-state system*. Phys. Rev. B **58**, 1862–1871 (1998).
- [287] Y. Nishiyama. *Numerical analysis of the dissipative two-state system with the density-matrix Hilbert-space-reduction algorithm*. Eur. Phys. J. B **12**, 547–554 (1999).
- [288] A.M. Tsvelik and P.B. Wiegmann. *Exact results in the theory of Magnetic Alloys*. Adv. Phys. **32**, 453–713 (1983).
- [289] F. Lesage and H. Saleur. *Boundary Interaction Changing Operators and Dynamical Correlations in Quantum Impurity Problems*. Phys. Rev. Lett. **80**, 4370–4373 (1998).
- [290] T.A. Costi and G. Zarand. *Thermodynamics of the dissipative two-state system: A Bethe-ansatz study*. Phys. Rev. B **59**, 12398–12418 (1999).
- [291] T.A. Costi and R.H. McKenzie. *Entanglement between a qubit and the environment in the spin-boson model*. Phys. Rev. A **68**, 034301 (2003).
- [292] P.W. Anderson. *Infrared Catastrophe in Fermi Gases with Local Scattering Potentials*. Phys. Rev. Lett. **18**, 1049–1051 (1967).
- [293] J. Kondo. *in Fermi Surface Effects, Vol. 77 of Springer Series in Solid State Sciences, eds. J. Kondo and A. Yoshimori*. Springer Verlag (Berlin, Germany) 1988.
- [294] F. Guinea, V. Hakim and A. Muramatsu. *Bosonization of a two-level system with dissipation*. Phys. Rev. B **32**, 4410–4418 (1985).
- [295] F.D.M. Haldane. *Effective Harmonic-Fluid Approach to Low-Energy Properties of One-Dimensional Quantum Fluids*. Phys. Rev. Lett. **47**, 1840–1843 (1981).
- [296] J. von Delft and H. Schoeller. *Bosonization for Beginners - Refermionization for Experts*. Ann. Phys. (Leipzig) **7**, 225–306 (1998).
- [297] G. Yuval and P.W. Anderson. *Exact Results for the Kondo Problem: One-Body Theory and Extension to Finite Temperature*. Phys. Rev. B **1**, 1522–1528 (1970).
- [298] K. Wilson and J. Kogut. *The Renormalization Group and the  $\epsilon$  Expansion*. Phys. Rep. **12**, 75–200 (1974).
- [299] K.G. Wilson. *The renormalization group: Critical phenomena and the Kondo problem*. Rev. Mod. Phys. **47**, 773–840 (1975).
- [300] K.G. Wilson. *Renormalization Group Methods*. Advances in Mathematics **16**, 170–186 (1975).

- [301] H.R. Krishna-murthy, K.G. Wilson and J.W. Wilson. *Temperature-Dependent Susceptibility of the Symmetric Anderson Model: Connection to the Kondo Model*. Phys. Rev. Lett. **35**, 1101–1104 (1975).
- [302] H.R. Krishna-murthy, J.W. Wilkins and K.G. Wilson. *Renormalization-group approach to the Anderson model of dilute magnetic alloys. I. Static properties for the symmetric case*. Phys. Rev. B **21**, 1003–1043 (1980).
- [303] H.R. Krishna-murthy, J.W. Wilkins and K.G. Wilson. *Renormalization-group approach to the Anderson model of dilute magnetic alloys. II. Static properties for the asymmetric case*. Phys. Rev. B **21**, 1044–1083 (1980).
- [304] R. Bulla, H.-J. Lee, N.-H. Tong and M. Vojta. *Numerical Renormalization Group for Quantum Impurities in a Bosonic Bath*. Phys. Rev. B **71**, 045122 (2005).
- [305] S.R. White. *Density matrix formulation for quantum renormalization groups*. Phys. Rev. Lett. **69**, 2863–2866 (1992).
- [306] C. Zhang, E. Jeckelmann and S.R. White. *Density Matrix Approach to Local Hilbert Space Reduction*. Phys. Rev. Lett. **80**, 2661–2664 (1998).
- [307] U. Schollwöck. *The density-matrix renormalization group*. Rev. Mod. Phys. **77**, 259–315 (2005).
- [308] T.J. Osborne and M.A. Nielsen. *Entanglement, Quantum Phase Transitions, and Density Matrix Renormalization*. Quantum Information Processing **1**, 45–53 (2002).
- [309] A. Osterloh, L. Amico, G. Falci and R. Fazio. *Scaling of entanglement close to a quantum phase transition*. Nature **416**, 608–610 (2002).
- [310] D.V. Averin and C. Bruder. *Variable electrostatic transformer: controllable coupling of two charge qubits*. Phys. Rev. Lett. **91**, 057003 (2003).
- [311] X. Zhou, Z.-W. Zhou, G.-C. Guo and M.J. Feldman. *Quantum Computation with Untunable Couplings*. Phys. Rev. Lett. **89**, 197903 (2002).
- [312] D. Loss and D.P. DiVincenzo. *Exact Born Approximation for the Spin-Boson Model*. arXiv:cond-mat/0304118 2003.
- [313] I.A. Goychuk. *Kinetic equations for a dissipative quantum system driven by dichotomous noise: an exact result*. Phys. Rev. E **51**, 6267–6270 (1995).
- [314] I.N. Bronstein, K.A. Semendjajew, G. Musiol and H. Mühlig. *Taschenbuch der Mathematik*. Verlag Harri Deutsch Frankfurt am Main 1993.
- [315] M.C. Goorden. *Theory of Josephson persistent-current qubits with driving and dissipation*. Master’s thesis Delft University of Technology 2002.

- [316] G.-L. Ingold. *Path Integrals and Their Application to Dissipative Quantum Systems*. Lect. Notes Phys. **611**, 1–53 (2002).
- [317] S. Kleff, S. Kehrein and J. von Delft. *Flow equation renormalization of a spin-boson model with a structured bath*. Physica E (proc. of the 23rd International Conference on Low Temperature Physics, Hiroshima, Japan, 2002) **18**, 343–345 (2003).
- [318] F.K. Wilhelm, S. Kleff and J. von Delft. *The spin-boson model with a structured environment: A comparison of approaches*. Chem. Phys. **296**, 345–353 (2004).
- [319] J.D. Jackson. *Classical electrodynamics*. John Wiley & Sons, Inc. (New York, N.Y.) 1999, 3rd ed.
- [320] S.L. Sobolev. *Partial Differential Equations of Mathematical Physics*. Dover Publications, Inc. (Mineola, N.Y.) 1989.
- [321] M.B. Ketchen and J.M. Jaycox. *Ultra-low-noise tunnel junction dc SQUID with a tightly coupled planar input coil*. Appl. Phys. Lett. **40**, 736–738 (1982).
- [322] F.K. Wilhelm. *Two notes on open topics in circuit-QED*. private communication (2004).
- [323] M. Grifoni and P. Hänggi. *Driven Quantum Tunneling*. Phys. Rep. **304**, 229–354 (1998).
- [324] A. Izmalkov, M. Grajcar, E. Il'ichev, N. Oukhanski, Th. Wagner, H.-G. Meyer, W. Krech, M.H.S. Amin, A. Maassen van den Brink and A.M. Zagorskin. *Observation of macroscopic Landau-Zener transitions in a superconducting device*. Europhys. Lett. **65**, 844–849 (2004).
- [325] Y. Kayanuma. *Nonadiabatic Transitions in Level Crossing with Energy Fluctuation. I. Analytical Investigations*. J. Phys. Soc. Jpn. **53**, 108–117 (1984).
- [326] F.K. Wilhelm. *The leaky Landau-Zener-Stückelberg-Problem*. private communication (2004).





# List of Publications

The results presented in this thesis have been published in the following papers:

1. *Decoherence and gate performance of coupled solid state qubits*  
M.J. Storcz and F.K. Wilhelm  
Phys. Rev. A **67**, 042319 (2003)
2. *Decoherence of Flux Qubits Coupled to Electronic Circuits*  
F.K. Wilhelm, M.J. Storcz, C.H. van der Wal, C.J.P.M. Harmans, and J.E. Mooij  
Adv. Solid State Phys. **43**, 763 (2003)
3. *Design of realistic switches for coupling superconducting solid-state qubits*  
M.J. Storcz and F.K. Wilhelm  
Appl. Phys. Lett. **83**, 2389 (2003)
4. *Full protection of superconducting qubit systems from coupling errors*  
M.J. Storcz, J. Vala, K.R. Brown, J. Kempe, F.K. Wilhelm, and K.B. Whaley  
Phys. Rev. B **72**, 064511 (2005)
5. *Optimal Control of Coupled Josephson Qubits*  
A.K. Spörl, T. Schulte-Herbrüggen, S.J. Glaser, V. Bergholm, M.J. Storcz, J. Ferber,  
and F.K. Wilhelm  
submitted to Phys. Rev. Lett., arXiv:quant-ph/0504202
6. *Decoherence of a two-qubit system with a variable bath coupling operator*  
M.J. Storcz, F. Hellmann, C. Hrlescu, and F.K. Wilhelm  
Phys. Rev. A **72**, 052314 (2005)
7. *Intrinsic phonon decoherence and quantum gates in coupled lateral quantum dot charge qubits*  
M.J. Storcz, U. Hartmann, S. Kohler, and F.K. Wilhelm  
accepted for publication in Phys. Rev. B, arXiv:cond-mat/0507178
8. *Macroscopic Einstein-Podolsky-Rosen pairs in superconducting circuits*  
L.F. Wei, Y.-x. Liu, M.J. Storcz, and F. Nori  
submitted to Phys. Rev. A, arXiv:quant-ph/0508027

9. *Generation and Detection of Microwave Fock States: Linear Optics on a Chip*  
M. Mariani, M.J. Storcz, F.K. Wilhelm, W.D. Oliver, A. Emmert, A. Marx,  
R. Gross, H. Christ, and E. Solano  
submitted to Phys. Rev. Lett., arXiv:cond-mat/0509737
  
10. *Mesoscopic Superpositions, Nonclassical States, and their Measurement  
in Circuit QED*  
M.J. Storcz, M. Mariani, A. Emmert, R. Gross, F.K. Wilhelm,  
H. Christ, and E. Solano  
to be submitted

# Acknowledgements

I am indebted to Professor Dr. Jan von Delft and PD Dr. Frank K. Wilhelm for making it possible to join their research group in Munich and for the possibility of attending conferences and schools.

I am grateful to my advisor, Frank K. Wilhelm, for providing support for my research over the last three years. Discussions with him were crucial to gain a deeper understanding of the physics behind the different problems. Also, I am indebted to him for giving me the opportunity to collaborate with several experts in the field of quantum computing.

Moreover, I would like to thank Professor Dr. Erwin Frey for co-refereeing this thesis, Professor Dr. Rudolf Gross, Professor Dr. Harald Weinfurter, and Professor Dr. Axel Schenzle for being part of my Ph.D. examination committee.

My deep gratitude goes to my office-mate Udo Hartmann, for many useful discussions and friendship.

Most of the work presented in this thesis greatly benefited from the support, help and ideas of my excellent collaborators (and friends) during the last years. I would like to thank Professor Dr. Terry P. Orlando, Dr. William D. Oliver, Janice Lee, William Kaminisky, Professor Dr. K. Birgitta Whaley, Dr. Jiri Vala, Dr. Julia Kempe, Dr. Kenneth R. Brown, Dr. Simon Myrgren, Professor Dr. Franco Nori, Professor Dr. L.F. Wei, Dr. Yu-xi Liu, Dr. Sahel Ashhab, Robert Johansson, Dr. Sergey Savel'ev, and Dr. Slaver Mis'ko.

Especially, I would like to thank Professor Franco Nori, Sahel Ashhab, L.F. Wei, Yu-xi Liu and the whole group of the Digital Materials Laboratory at RIKEN for their hospitality and excellent collaboration during my stay at RIKEN, and Ai Sato and Sahel Ashhab for all their help with life in Japan. Also, I would like to thank the whole NEC group for many useful discussions.

Also, I am very grateful to all my excellent collaborators within the SFB 631 *quantum information processing*, Professor Dr. Peter Hänggi and PD Dr. Sigmund Kohler at the University of Augsburg, Professor Dr. Steffen Glaser, Dr. Thomas Schulte-Herbrüggen and A. Spörl at the Chemistry department of the TU Munich, Professor Dr. Rudolf Gross,

Dr. Achim Marx, Matteo Mariantoni, and Andreas Emmert at the Walther-Meissner Institute, Dr. Enrique Solano and Henning Christ at the Max Planck Institute for Quantum Optics, Francesco Nesi at the University of Regensburg, and Andreas K. Hüttel and Dr. Stefan Ludwig of the Nanophysics group.

Of course, I am very grateful to all the visitors that came to Munich and shared their thoughts and ideas with me, namely Marlies Goorden, Dr. Andreas Käck, Dr. Alexander Khaetskii, PD Dr. Mikhail Kiselev, Professor Dr. Lloyd C.L. Hollenberg, Dr. Ron Lifschitz, Jared Cole, and many more. Thanks also to the excellent students Frank Hellmann and Calin Hrlescu with whom I worked on several aspects of the decoherence of coupled qubits, I enjoyed very much discussing and working with you.

Moreover I would like to thank Lloyd Hollenberg, Florian Marquardt, Andreas K. Hüttel, Frank K. Wilhelm, Michael Sindel, Udo Hartmann, and Johannes Ferber for critical reading of this thesis, and Johannes Ferber also for many stimulating discussions.

I would like to thank all members of our group during the last years, Benjamin Abel, Dr. Robert Dahlke, Johannes Ferber, Andreas Friedrich, Dr. Dominique Gobert, Igor Gazuz, Henryk Gutmann, Theresa Hecht, Rolf Helmes, Konstanze Jähne, Dr. Alexander Khaetskii, PD Dr. Mikhail Kiselev, Dr. Silvia Kleff, Dr. Corinna Kollath, Dr. Rong Lü, Dr. Florian Marquardt, Michael Möckel, Professor Dr. Achim Rosch, Hamed Saberi, Ioana Serban, Professor Dr. Ulrich Schollwöck, Dr. Andreas Weichselbaum, and Professor Dr. Ulrich Zülicke with whom I enjoyed many stimulating discussions, a lot of insight into (solid-state) physics and for the nice working atmosphere at the chair for theoretical condensed matter physics. Stéphane Schoonover for her organizational help and Ralph Simmler for keeping the computers working.

Deep thanks to Dr. Michael Sindel and Dr. László Borda for the great time in Munich, which means many discussions about physics, life in general and much more.

Thanks go to the Center for Nanoscience (CeNS), especially Dr. Monika Kaempfe, Dr. Eva Natzer, Evelyn Morgenroth, and Barbara Pinto for their organizational help and support during the CeNS activities, the poster printing efforts, financial travel support, and scientific events organized by CeNS. And the Arnold Sommerfeld Center for Theoretical Physics (ASC) for providing a good working environment with excellent lecturers.

Financial support through the DFG Programm “Festkörperbasierte Quanteninformationsverarbeitung: Physikalische Konzepte und Materialaspekte” (SFB 631), from the National Security Agency and the Advanced Development Activity under Army Research Office contract no. P-43385-PH-QC, and DAAD is gratefully acknowledged.

My deepest gratitude goes to my parents for their encouraging and steady support during all the time and my girlfriend Silvia who kept supporting me.





# Deutsche Zusammenfassung

In dieser Arbeit werden verschiedene theoretische Studien zur Dekohärenz, Manipulierbarkeit und dem Auslesen von festkörperbasierten Quantenbits (Qubits) durchgeführt. Es werden grundlegende physikalische Konzepte, wie die Erzeugung und Detektion einzelner Photonen in einem Fock-Zustand, ausgearbeitet. Die Skalierbarkeit und Dekohärenz von Qubit-Systemen wird analysiert und verschiedene Vorschläge zur Verbesserung der Eigenschaften dieser Qubit-Systeme für die Quanteninformationsverarbeitung präsentiert.

Im ersten Teil der Arbeit wird zunächst eine Einführung in das physikalische System und die theoretischen Grundlagen zu seiner Beschreibung gegeben. Der zweite Teil der Arbeit, der Hauptteil, beschäftigt sich zuerst mit den Dekohärenzeigenschaften eines Systems zweier gekoppelter Qubits, wobei ein mögliches Qubit-System z.B. aus supraleitenden Josephson Qubits, oder auch Quantenpunkten in Halbleiterstrukturen, besteht. Hierbei werden speziell die Dekohärenzmechanismen für supraleitende Josephson Qubits und Ladungsqubits in Quantenpunkten im Detail untersucht. Es werden die sogenannten Gatterqualitätsfaktoren bestimmt, die ein Maß für die Exaktheit eines Quantengatters und die auftretende Dekohärenz sind. Hieraus folgt als wichtiges Ergebnis, daß die während der Gatteroperation auftretende Dekohärenz sehr stark von den Symmetrien im Qubitsystem bzw. der Qubit-Bad Kopplung abhängt; besonders in festkörperbasierten Systemen ist es möglich, die Qubit-Bad Kopplung teilweise gezielt zu konstruieren und dabei diese Erkenntnisse zu berücksichtigen.

Da die Kopplung zwischen den Quantenbits im idealen Fall schaltbar sein sollte, werden verschiedene Schalter für die Kopplung zwischen supraleitenden Josephson Fluss-Qubits, die mittels eines supraleitenden Fluß-Transformators gekoppelt sind, untersucht. Dabei stellt sich heraus, dass sich verschiedene Arten supraleitender Nanosysteme eignen würden. Außerdem sollte der Schaltvorgang, während dem die Kopplung zwischen den Qubits verstellt wird, möglichst schnell erfolgen, da der Rauscheinfluß auf das Qubit-System während des Schaltvorgangs am größten ist.

Nachdem der Einfluß der Dekohärenz untersucht wurde, wird die Kodierung mehrerer physikalischer Qubits in logische Qubits in sogenannten dekohärenzfreien Unterräumen (DFS) ausgearbeitet. Für kollektiv an alle Qubits koppelnde Rauschquellen ist es möglich, mit dieser Kodierung Rauscheinflüsse komplett auszuschließen. Es wird ebenfalls gezeigt, daß im speziellen Fall von zwei kapazitiv gekoppelten supraleitenden Fluß-Qubits diese Kodierung einen vollständigen Schutz vor dem  $1/f$ -Rauschen der Kopplungselemente bedingt.

Weiterhin wird die optimale Kontrolltheorie zur Verbesserung der zur Manipulation der Qubits notwendigen Pulssequenzen verwendet. Die optimierten Pulssequenzen sind deutlich kürzer und erreichen eine wesentlich größere Genauigkeit (Exaktheit) als bereits experimentell angewendete, aus elementaren nicht-optimierten Gattern aufgebaute, Gatteroperationen. Diese Ergebnisse verdeutlichen, daß für die untersuchten Systeme die Gatterqualität nicht durch Dekohärenz sondern die Pulssequenz beschränkt ist. Daher ist diese Methode sehr gut zur experimentellen Verbesserung der Genauigkeit realistischer Quantengatter geeignet.

Im letzten Teil der Arbeit werden verschiedene Konzepte aus der Quantenoptik auf Qubits in Festkörpersystemen angewendet. Hierbei wird insbesondere ein Schema zur Erzeugung und Detektion einzelner Photonen im Mikrowellenspektrum und die Realisierung eines Fluß-Qubits in einem Resonator, einer sogenannten Kavität, vorgeschlagen.





# Curriculum vitae

**Name:** Markus János Storcz

**Born:** October 25th, 1977 in Cologne

**School:** 1984 - 1988: Primary school in Cologne

1988 - 1996: Herder-Gymnasium, Buchheim, Cologne  
(grammar school)

06/1996: Abitur

**Studies:** 10/1997 - 09/1999: Studies of Physics and Computer Science  
at the University of Bonn

09/1999: *Vordiplom* in Physics (University of Bonn)

09/2002: *Diplom* in Physics (University of Bonn)

10/2001 - 09/2002: external master's thesis (*Diplomarbeit*)  
at the Ludwig-Maximilians-University Munich

10/2002 - 10/2005: Ph.D. studies in Theoretical Condensed Matter Physics,  
supervised by PD Frank K. Wilhelm  
and Prof. Dr. Jan von Delft,  
Physics Department, ASC, and CeNS,  
Ludwig-Maximilians-University Munich

**Thesis:** *Decoherence of coupled solid-state qubits*  
(*Diplomarbeit* 2002)

supervised by Prof. Dr. Jan von Delft

and Prof. Dr. Hartmut Monien,

(Physikalisches Institut, University of Bonn)